

JAN 21 1981

Item 830-H-14

NAS 1.26:3311

NASA Contractor Report 3311

ORIGINAL  
COMPLETED

Rotary Balance Data for a  
Single-Engine Agricultural  
Airplane Configuration for an  
Angle-of-Attack Range of  $8^\circ$  to  $90^\circ$

William Mulcay and Julio Chu

CONTRACT NAS1-14849  
DECEMBER 1980

**NASA**

NASA Contractor Report 3311

Rotary Balance Data for a  
Single-Engine Agricultural  
Airplane Configuration for an  
Angle-of-Attack Range of  $8^{\circ}$  to  $90^{\circ}$

William Mulcay and Julio Chu  
*Bibrle Applied Research, Inc.*  
*Jericho, New York*

Prepared for  
Langley Research Center  
under Contract NAS1-14849



National Aeronautics  
and Space Administration

Scientific and Technical  
Information Branch

1980



## SUMMARY

Aerodynamic characteristics obtained in a helical flow environment utilizing a rotary balance located in the Langley spin tunnel are presented in plotted form for a 1/10-scale, single-engine agricultural airplane model. The configurations tested include the basic airplane, various wing leading-edge and wing-tip devices, elevator, aileron and rudder control settings, and other modifications. Data are presented without analysis for an angle-of-attack range of  $8^{\circ}$  to  $90^{\circ}$ , and clockwise and counter-clockwise rotations covering an  $\frac{\Omega b}{2V}$  range from 0 to .9. This information is being obtained, along with that of other models, in order to establish a data base for analysis of the model and full-scale flight results, and to develop design charts for desirable stall/spin characteristics.

## INTRODUCTION

A wind-tunnel rotary balance measures forces and moments acting on an airplane model while subjecting it to steady, though not necessarily equilibrium, spin flow conditions. The need for these data was recognized early in aircraft development. For example, early researchers noted in 1928 that the use of "straight" force tests conduce to erroneous conclusions when applied to the spin. NACA investigators at that time developed a "spinning" balance installed in a 5-foot vertical tunnel; they reasoned that subjecting all portions of an aircraft model to a constant wind velocity vector during static force tests was an unsatisfactory simulation of flow conditions existing in a spin.

In recent years, NASA installed a rotary balance apparatus in the Langley full-scale tunnel and sponsored studies to determine the ability of current analytical techniques to compute the

flight motions of current fighter configurations. Again, these studies clearly demonstrated the need to model the effects of spin rotation rate on the aerodynamic characteristics in all phases of the spinning motion. This concern is certainly warranted in the case of the high  $\frac{\Omega b}{2V}$  (non-dimensionalized spin rate) values of today's general aviation airplane designs.

These values are high due to high rates of rotation and low rates of descent for low wing-loaded vehicles. Hence, a difference of up to  $90^\circ$  in angle of attack between wing tips and  $70^\circ$  in sideslip angle between nose and tail can be realized.

The NASA Langley Research Center has initiated a broad, general aviation stall/spin research program which includes spin tunnel and free-flight radio control model tests for a number of configurations typical of light, general aviation airplanes. To support these free-flight investigations, a rotary balance facility was developed in the Langley spin tunnel to rapidly identify an airplane's aerodynamic characteristics in a steady spin flow environment. The influence of spin radius, angle of attack, sideslip angle, rate of rotation and control settings on the aerodynamics can be measured, thereby permitting prediction of incipient and developed spin characteristics.

A 1/10-scale, single-engine agricultural airplane model was tested on the wind tunnel rotary balance in the NASA Langley 20-ft. spin tunnel. This report presents the data obtained for the basic configuration, various wing leading-edge and wing-tip devices, elevator, aileron and rudder control settings and other modifications.

Use of trade names or names of manufacturers in this report does not constitute an official endorsement of such products or manufacturers, either expressed or implied, by the National Aeronautics and Space Administration.

# SYMBOLS

The units for physical quantities used herein are presented in the International System of Units (SI) and U.S. Customary Units. The measurements were made in the U.S. Customary Units; equivalent dimensions were determined by using the conversion factors given in reference 1.

b	wing span, m (ft)
$\bar{c}$	mean aerodynamic chord, cm (in.)
$C_L$	lift-force coefficient, $\frac{\text{Lift force}}{qS}$
$C_N$	normal-force coefficient, $\frac{\text{Normal force}}{qS}$
$C_A$	axial-force coefficient, $\frac{\text{Axial force}}{qS}$
$C_Y$	side-force coefficient, $\frac{\text{Side force}}{qS}$
$C_l$	rolling moment coefficient, $\frac{\text{Rolling moment}}{qSb}$
$C_m$	pitching-moment coefficient, $\frac{\text{Pitching moment}}{qSc}$
$C_n$	yawing-moment coefficient, $\frac{\text{Yawing moment}}{qSb}$
q	free-stream dynamic pressure, N/m <sup>2</sup> (lb/ft <sup>2</sup> )
S	wing area, m <sup>2</sup> (ft <sup>2</sup> )
V	free-stream velocity, m/sec (ft/sec)
$\alpha$	angle of attack, deg
$\beta$	angle of sideslip, deg
$\Omega$	angular velocity about spin axis, rad/sec
$\frac{\Omega b}{2V}$	spin coefficient, positive for clockwise spin
$\delta_a$	aileron deflection, positive when right aileron is down ( $\delta_{a_{\text{right}}} - \delta_{a_{\text{left}}}$ )/2, deg
$\delta_e$	elevator deflection, positive when trailing edge is down, deg
$\delta_r$	rudder deflection, positive when trailing edge is to left, deg

Abbreviations:

cg     center of gravity  
LE     leading edge  
SR     spin radius

TEST EQUIPMENT

A photograph and sketch of the rotary balance apparatus installed in the Langley 20-Foot Spin Tunnel are shown in figures 1 and 2, respectively. The arm of the balance system rotates about a vertical axis and is mounted on the free end of a horizontal supporting boom, which is hinged at the wall. It is moved from the wall to the center of the tunnel by cables, secured, and then driven by a drive shaft through couplings and gears.

A test model is mounted on a strain gauge balance which is affixed to the bottom of the rotary balance apparatus. Controls located outside the tunnel are used to activate motors on the rig, which position the model to the desired attitude. The angle-of-attack range of the rig is 8 to 90 degrees, and the sideslip angle range is  $\pm 15$  degrees. The spin radius and lateral displacement motors allow the operator to position the moment center of the balance on the spin axis or at a specific distance from the spin axis. This is done for each combination of angle of attack and sideslip angle. The NASA six-component strain gauge balance mounted inside the model measures the normal, axial, and side forces, and the yawing, rolling, and pitching moments acting about the model body axis. Interactions among the six components are available from previous laboratory calibration tests and are used to correct the raw forces and moments output by the balance strain gauge transducers. For the data presented herein and the practice generally, the force and moment axes of the balance are mounted coincident with the body axes of the air-

plane, with the moment center at the cg location about which the aerodynamic moments are desired. Electrical current to and from the balance and to the positioning motors on the rig, and position-indicating potentiometer voltages are conducted through slip rings located at the rig head. Examples of how the rig is positioned for different angles of attack and side-slip angles are shown in figures 2a and 2b, respectively.

The model can be rotated up to 90 rpm in either direction. By using different rotational speeds and a specific airflow in the tunnel, the motions of an airplane in a steady spin can be simulated. The aerodynamic forces and moments can be measured at different values of  $\frac{\Omega b}{2V}$ , including the case of  $\frac{\Omega b}{2V} = 0$ , where static aerodynamic data are obtained.

Additional background for this apparatus is given in reference 2.

The data acquisition, reduction and presentation system for the rotary balance set-up includes an RPM indicator, a 12-channel scanner/voltmeter with a 14-bit variable gain analog to digital converter, and a mini-computer with graphics and a printer. With this equipment, immediate presentation of data in tabular and/or plotted form is possible.

#### TEST PROCEDURES

Rotary aerodynamic data are obtained in two steps. First, the inertial forces and moments (tares) acting on the model at different attitudes and rotational speeds are measured. To accomplish this, a covered bird cage like structure, which encloses the model without touching it, is mounted on the upper portion of the rig and rotates with the model. In this manner, the air immediately surrounding the model is trapped by the structure and constrained to rotate with it. As the rig is rotated at the desired attitude and rate, a pulse voltage from a magnetic

trigger device on the drive shaft begins the data sampling process. Eighty samples of the 6 balance output channels are taken over 10 revolutions, with the computer adjusting the timing, according to the RPM indicator, to sample at 8 fixed angular positions of the rotating rig. The inertial forces and moments thus measured are curve-fitted to a least-squares function of  $\frac{1}{100}$  and stored for later use on magnetic tape.

For the second step, the covered structure enclosing the model is removed and the total wind-on forces and moments are measured. The aerodynamic forces and moments are determined by subtracting the tare values from the total wind-on values at each tested RPM and angle of attack. The aerodynamic data are converted to coefficient form and stored on magnetic tape.

#### MODEL

A 1/10-scale fiberglass-epoxy, wood and aluminum model of a typical single-engine configuration used for agricultural purposes was tested in the present study. A three-view drawing of this model is shown in figure 3, dimensional characteristics of the model are presented in Table I, and a photograph of the model installed on the rotary balance located in the Langley 20-Foot Spin Tunnel is presented in figure 1.

The model was fabricated such that various modifications could be added. These consisted of a turbine nose, as shown in figure 4; canopy fairing and a wing-fuselage fillet, shown in figure 5; an outboard leading-edge wing droop, shown in figure 6; and a full span leading-edge wing slot, shown in figure 7. In addition, several wing-tip modifications designed to alter the characteristics of wing-tip vortex flow were tested. These consisted of winglets, wing-tip sails and Lockheed Vortex Diffuser Vanes, as shown in figures 8 and 9. The Lockheed Vortex Diffuser Vane is patented by the Lockheed-Georgia Aircraft Company.

The model control surfaces could be fixed at any position prior to the test. The maximum deflections for the control surfaces were:

Elevator, deg	27 up, 17 down
Rudder, deg	24 right, 24 left
Aileron, deg	21 up, 17 down

#### TEST CONDITIONS

The tests were conducted in the spin tunnel at a tunnel velocity of 7.62 m/sec (25ft/sec), which corresponds to a Reynolds number of approximately 120,000 based on the model mean aerodynamic chord. Unless otherwise noted in Table II, all the configurations were tested through an angle-of-attack range of 8 to 35°, with the spin axis in the plane of symmetry of the aircraft at a full-scale distance 152.4 cm (60 in.) forward of the cg location of .26c. In addition, for some configurations, data were obtained for angles of attack between 30 and 90°, with the spin axis through the cg location. Data were thus obtained at two spin radii for angles of attack of 30 and 35 degrees. At each spin attitude, measurements were obtained for nominal  $\frac{\Omega b}{2V}$  values of .1, .2, .3, .4, .5, .6, .7, .8, and .9, in both clockwise and counter-clockwise directions, as well as for  $\frac{\Omega b}{2V} = 0$  (static value).

#### DATA PRESENTATION

Table II identifies the configurations tested and the corresponding appendix figure numbers which present the aerodynamic data. The aerodynamic coefficients plotted vs.  $\frac{\Omega b}{2V}$  are presented for each configuration in six sequentially numbered figures in the following order:  $C_n$ ,  $C_l$ ,  $C_m$ ,  $C_N$ ,  $C_Y$ , and  $C_A$ . Each figure consists of two pages, which present the subject

aerodynamic coefficient plotted vs  $\frac{\Omega b}{2V}$  for the following angles of attack and spin radius:

a)  $\alpha = 8, 10, 12, 14, 16$  deg      SR = 152.4 cm (60 in.)

b)  $\alpha = 18, 20, 25, 30, 35$  deg      SR = 152.4 cm (60 in.)

and, in addition, for some configurations noted in Table II:

c)  $\alpha = 30, 35, 40, 45, 50$  deg      SR = 0

d)  $\alpha = 55, 60, 70, 80, 90$  deg      SR = 0

All the moment data are presented for a cg location of .26 $\bar{c}$ .

Lift coefficient plotted vs angle of attack for zero rotation rate is presented in the Appendix for several configurations cited in Table II.



#### REFERENCE:

1. Mechtly, E.A.: The International System of Units - Physical Constants and Conversion Factors. NASA SP-7012, 1973.
2. Bihle, William, Jr.; Hultberg, Randy S.; and Mulcay, William: Rotary Balance Data for a Typical Single-Engine Low-Wing General Aviation Design for an Angle-of-Attack Range of  $30^{\circ}$  to  $90^{\circ}$ . NASA CR-2972, 1978.

TABLE I.- DIMENSIONAL CHARACTERISTICS OF THE BASIC MODEL

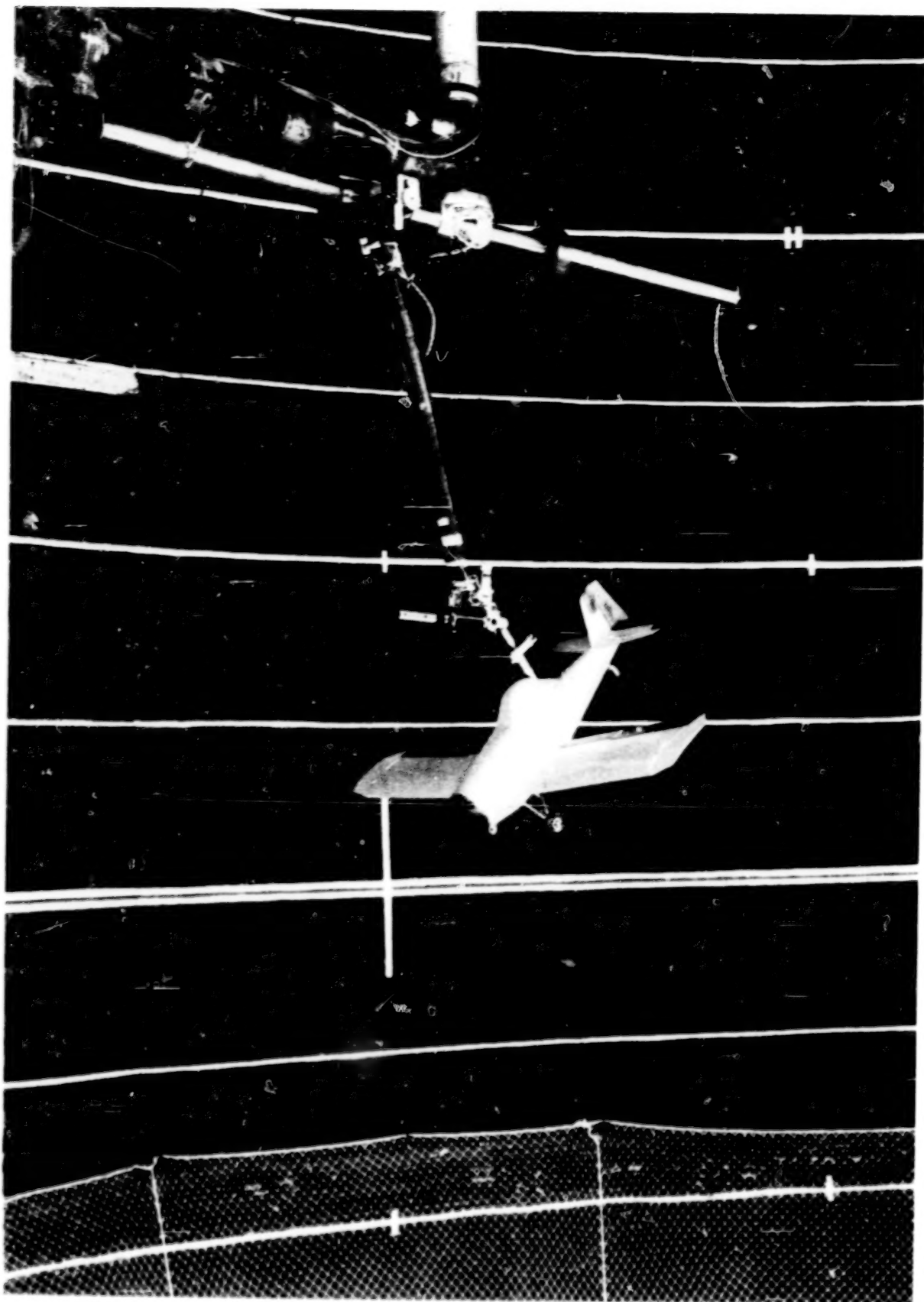
Overall length, m (ft) . . . . .	.89 (2.92)
Wing:	
Span, m (ft) . . . . .	1.35 (4.43)
Area, m <sup>2</sup> (ft <sup>2</sup> ) . . . . .	.304 (3.27)
Root chord, cm (in.) . . . . .	22.9 (9.0)
Tip chord, cm (in.) . . . . .	22.9 (9.0)
Mean aerodynamic chord, cm (in.) . . . . .	22.9 (9.0)
Aspect ratio . . . . .	6.0
Dihedral, deg . . . . .	3.5
Incidence:	
Root, deg . . . . .	2.07
Tip (of constant chord section), deg . . . . .	0.39
Airfoil section . . . . .	NACA 4412
Horizontal tail:	
Span, m (ft) . . . . .	.49 (1.60)
Area, m <sup>2</sup> (ft <sup>2</sup> ) . . . . .	.050 (.54)
Incidence, deg . . . . .	-1.55
Airfoil Section . . . . .	Flat plate
Vertical tail:	
Area, m <sup>2</sup> (ft <sup>2</sup> ) . . . . .	.021 (.222)
Airfoil section . . . . .	Flat plate

TABLE II.- CONFIGURATIONS TESTED AND FIGURE INDEX

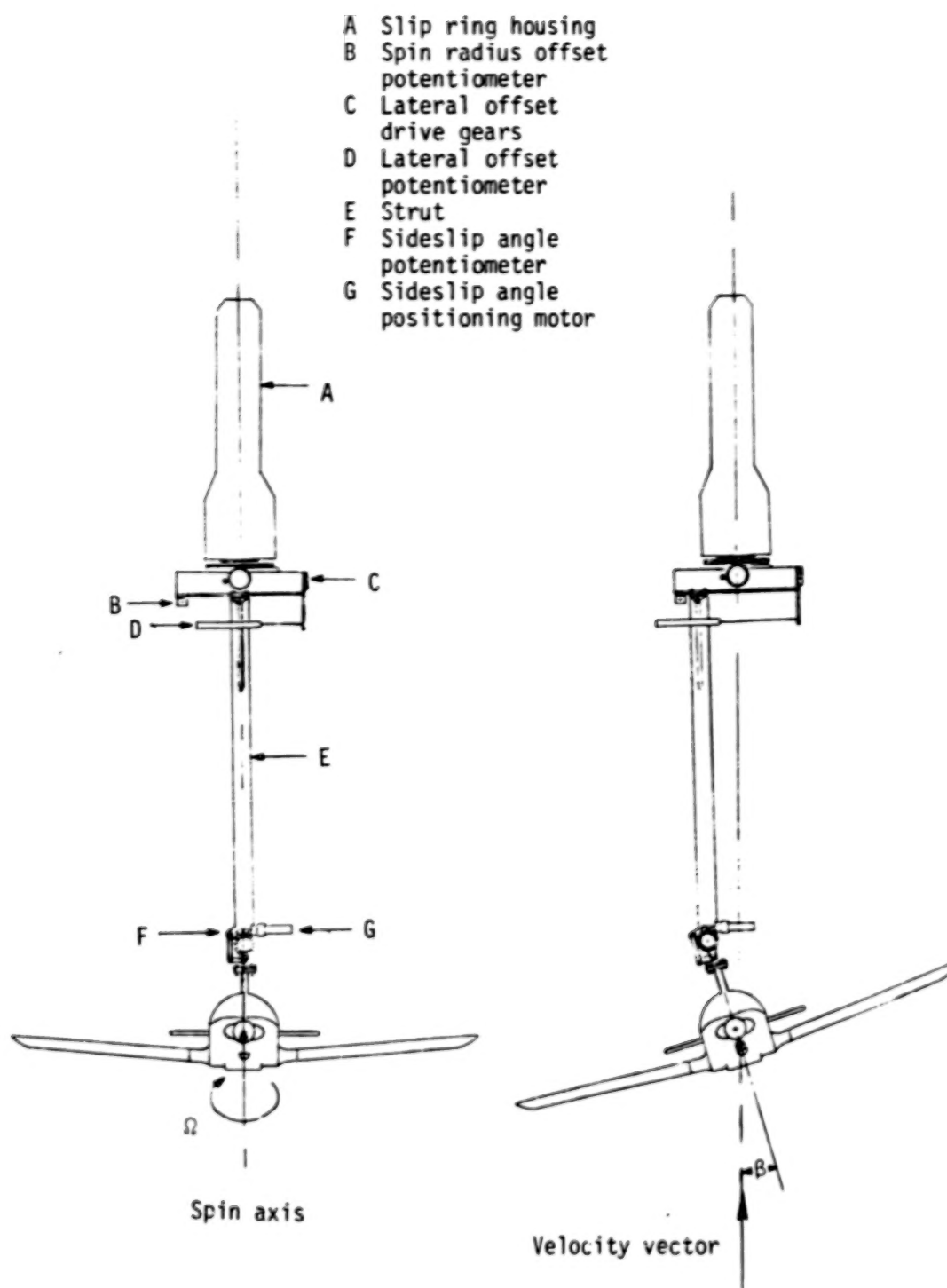
(Unless noted otherwise, all configurations tested through  $\alpha=8$  to  $35^\circ$  at SR=152.4 cm (60 in.) and  $\beta=0^\circ$ .)

FIGURE NO	CONFIGURATION	$\delta_e$ deg	$\delta_a$ deg	$\delta_r$ deg	REMARKS
a,b,c A1-A6	Basic	0	0	0	also $\alpha=30$ to $90^\circ$ at SR=0
A7-A12		17		-24	
A12-A18		-27	†		
A19-A24			+19		
A25-A30	†		-19		
A31-A36	Turbine nose	0	0	0	also $\alpha=30$ to $90^\circ$ at SR=0
A37-A42	Canopy fairing				
C A43-A48	Wing-fuselage fillet				
C A49-A54	with outboard LE wing droop				also $\alpha=30$ to $90^\circ$ at SR=0
C A55-A60	† with outboard LE wing slat				
a A61-A66	Full-span wing slat				
a A67-A72	Segmented wing slat				
b A73-A78	Winglets				
b A79-A84	Wing tip sails				
b A85-A90	Lockheed Vortex Diffuser Vanes	†	†	†	

a  $C_L$  vs.  $\alpha$  presented in figure A91.b  $C_L$  vs.  $\alpha$  presented in figure A92.†  $C_L$  vs.  $\alpha$  presented in figure A93.

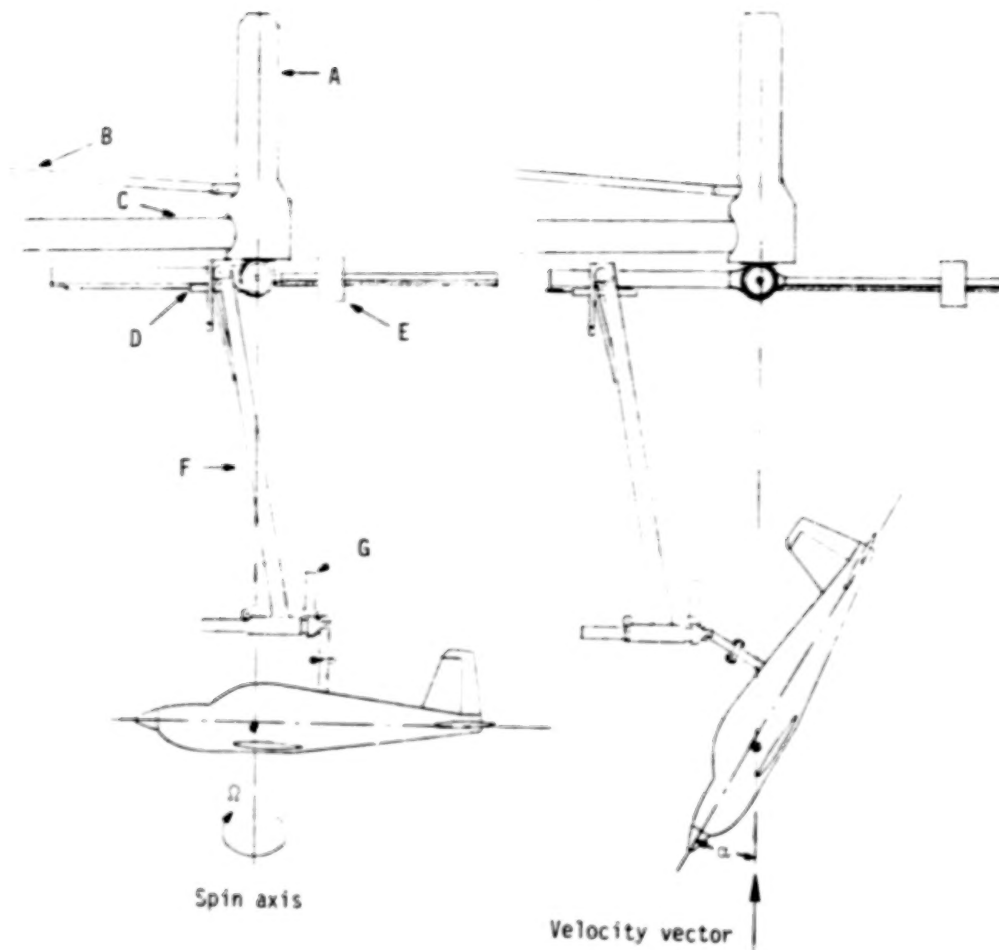


12      Figure 1. - 1/10 - scale model installed on rotary balance apparatus.



(b) Front view of model.

- A Slip ring housing
- B Drive shaft
- C Support boom
- D Spin radius offset potentiometer
- E Counterweight
- F Strut
- G Angle of attack positioning motor



(a) Side view of model.

Figure 2.- Sketch of rotary balance apparatus.

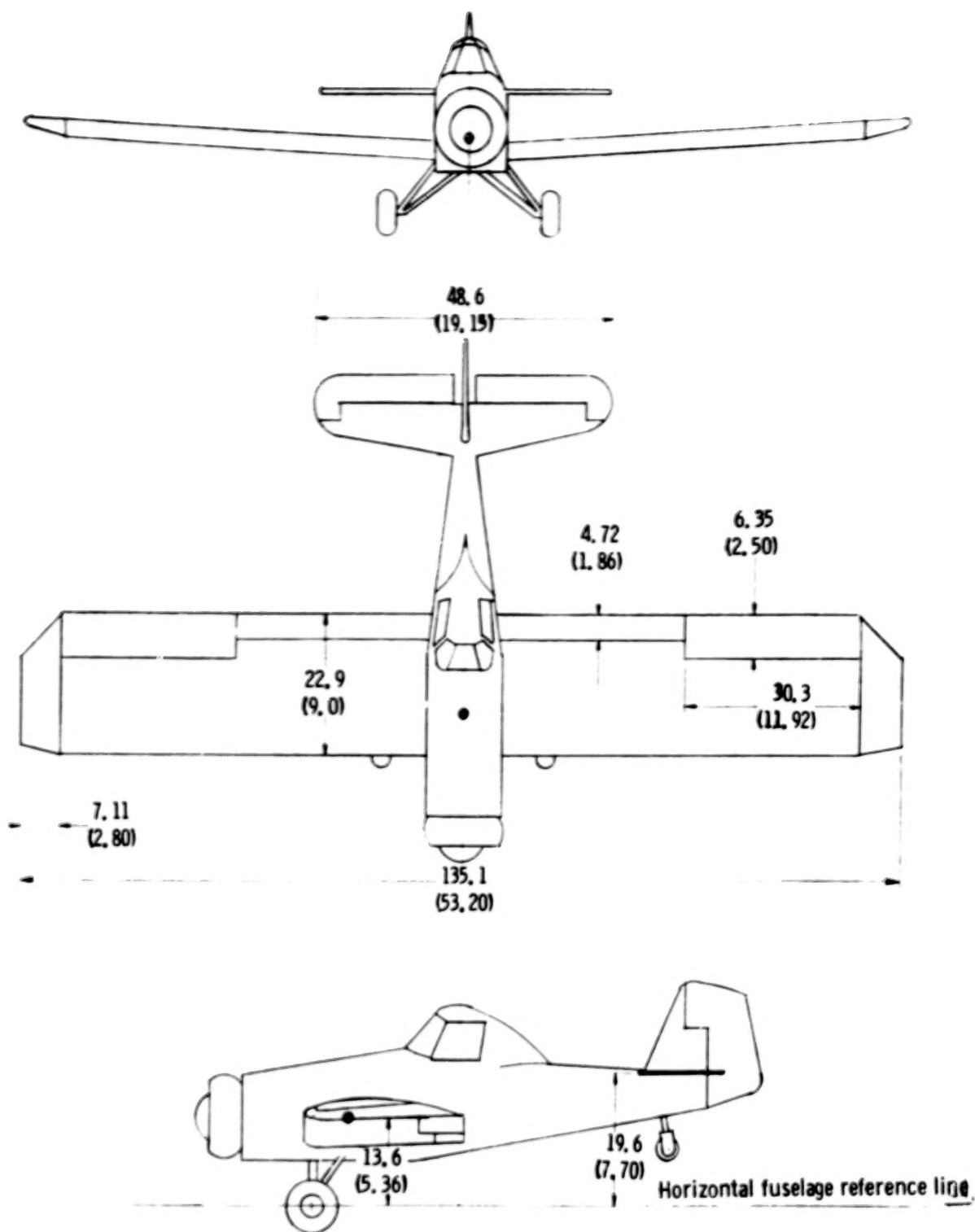


Figure 3. - Three-view of 1/10 - scale basic configuration. Center of gravity positioned at 0.26C. Dimensions are given in centimeters (inches), model scale.

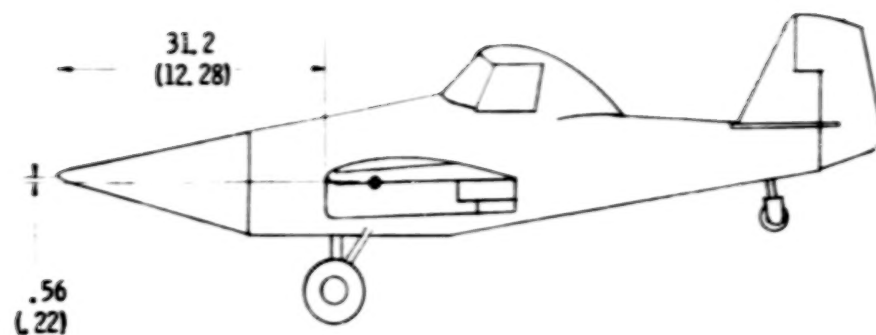


Figure 4. - Turbine nose tested on model. Dimensions are given in centimeters (inches), model scale.



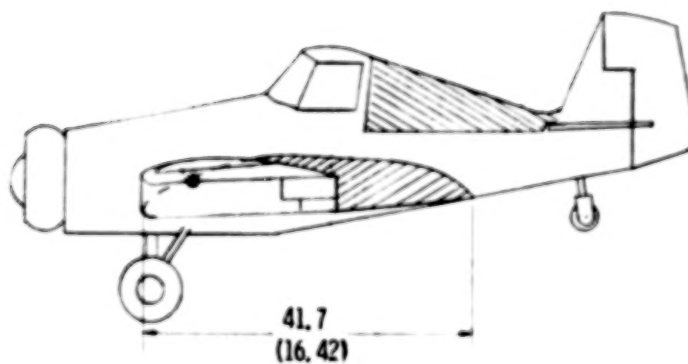
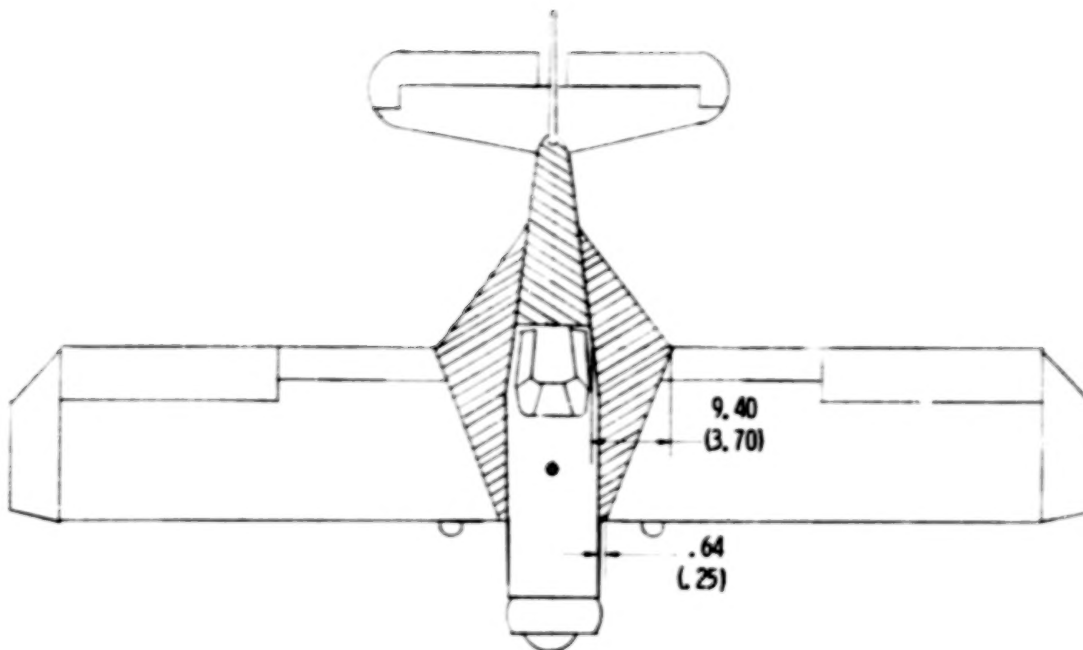
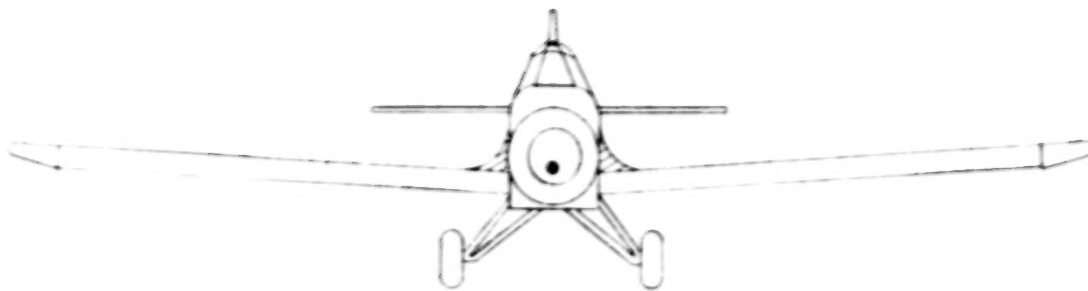


Figure 5. - Canopy fairing and wing-fuselage fillet tested on model. Dimensions are given in centimeters(inches), model scale.

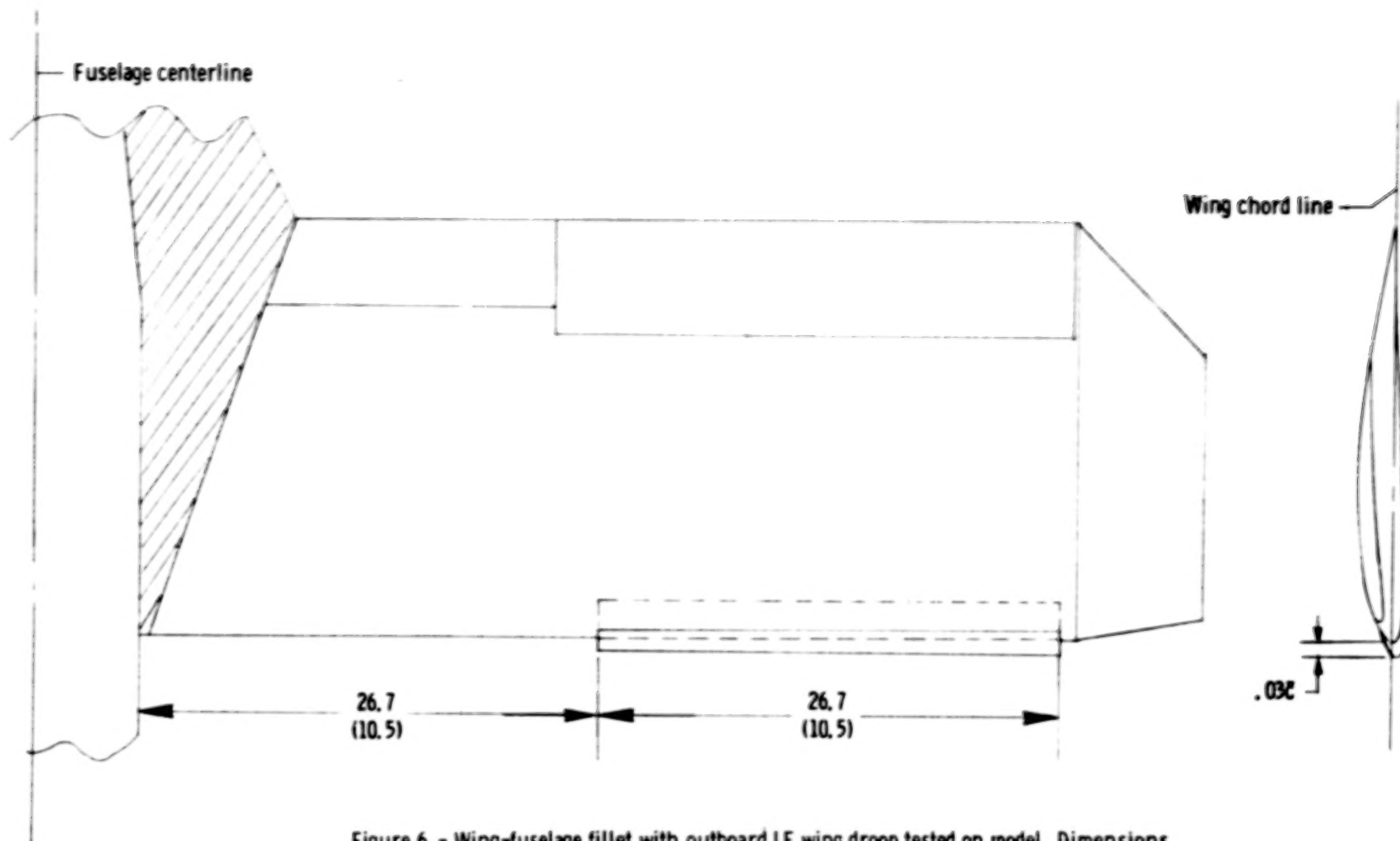


Figure 6. - Wing-fuselage fillet with outboard LE wing droop tested on model. Dimensions are given in centimeters (inches), model scale.

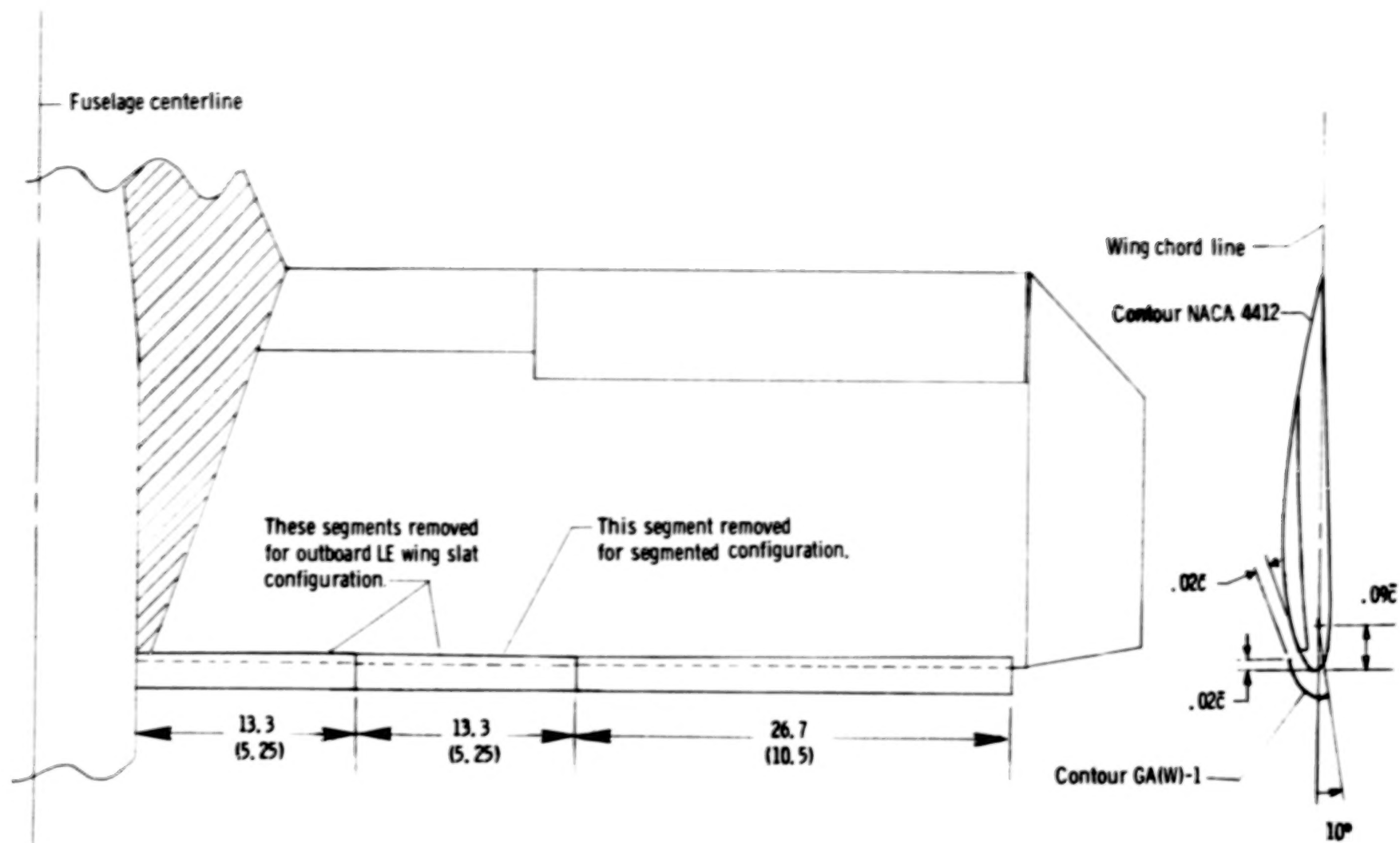


Figure 7. - Wing-fuselage fillet and LE wing slat configurations tested on model. Dimensions are given in centimeters(inches), model scale.

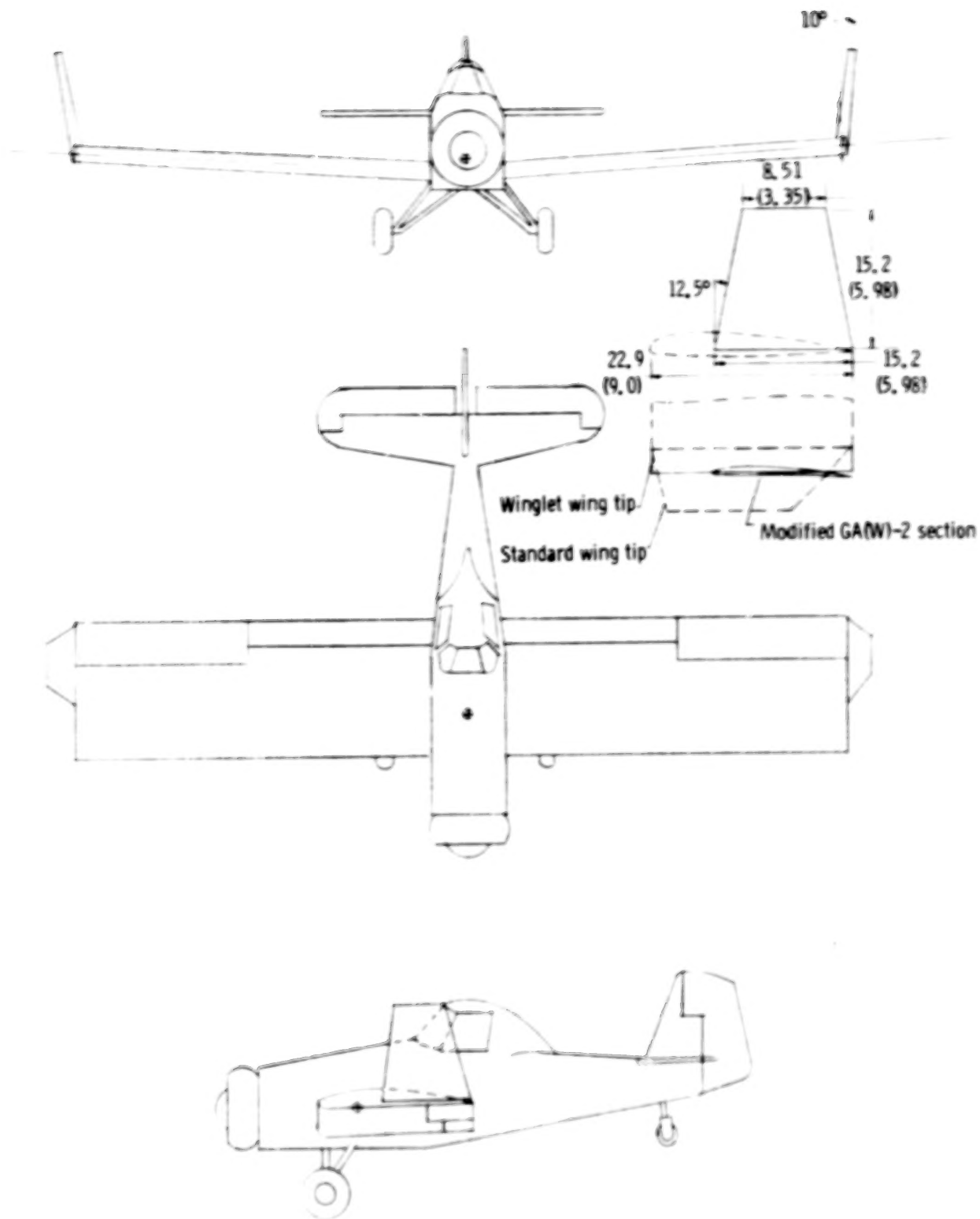
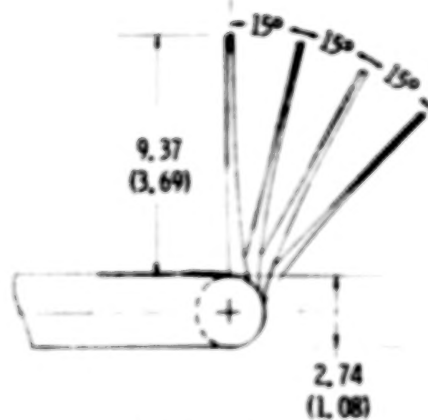
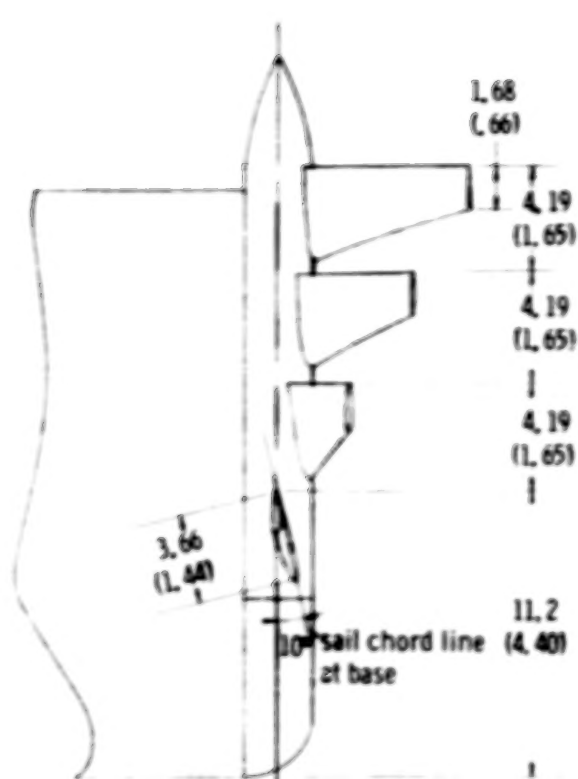
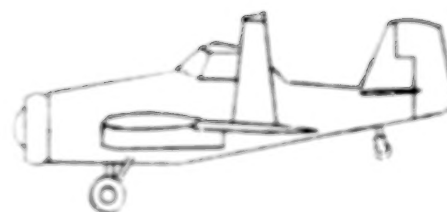
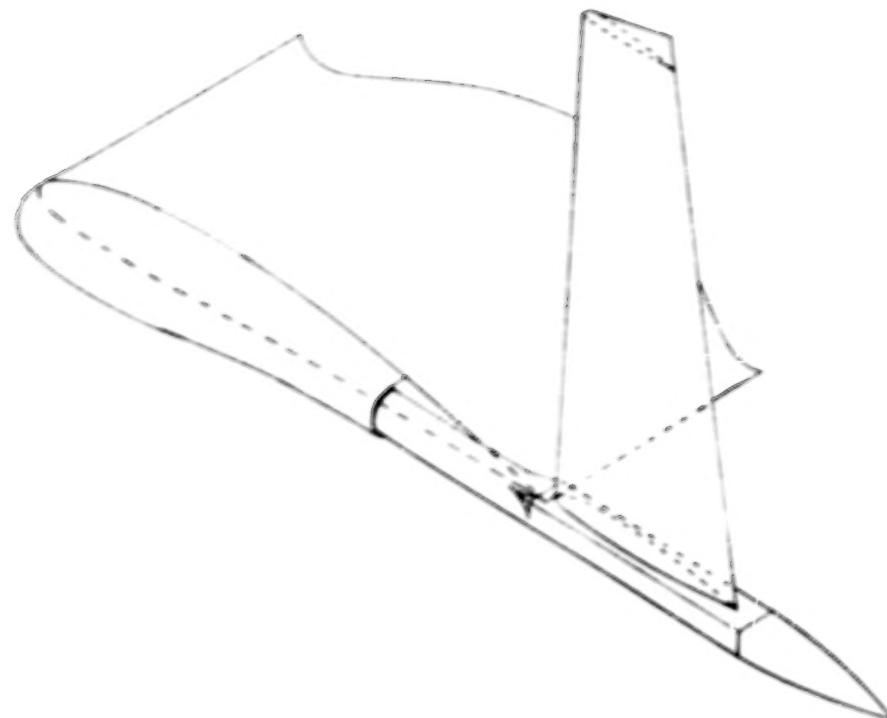


Figure 8. - Winglet installation tested on model. Dimensions are given in centimeters (inches), model scale.



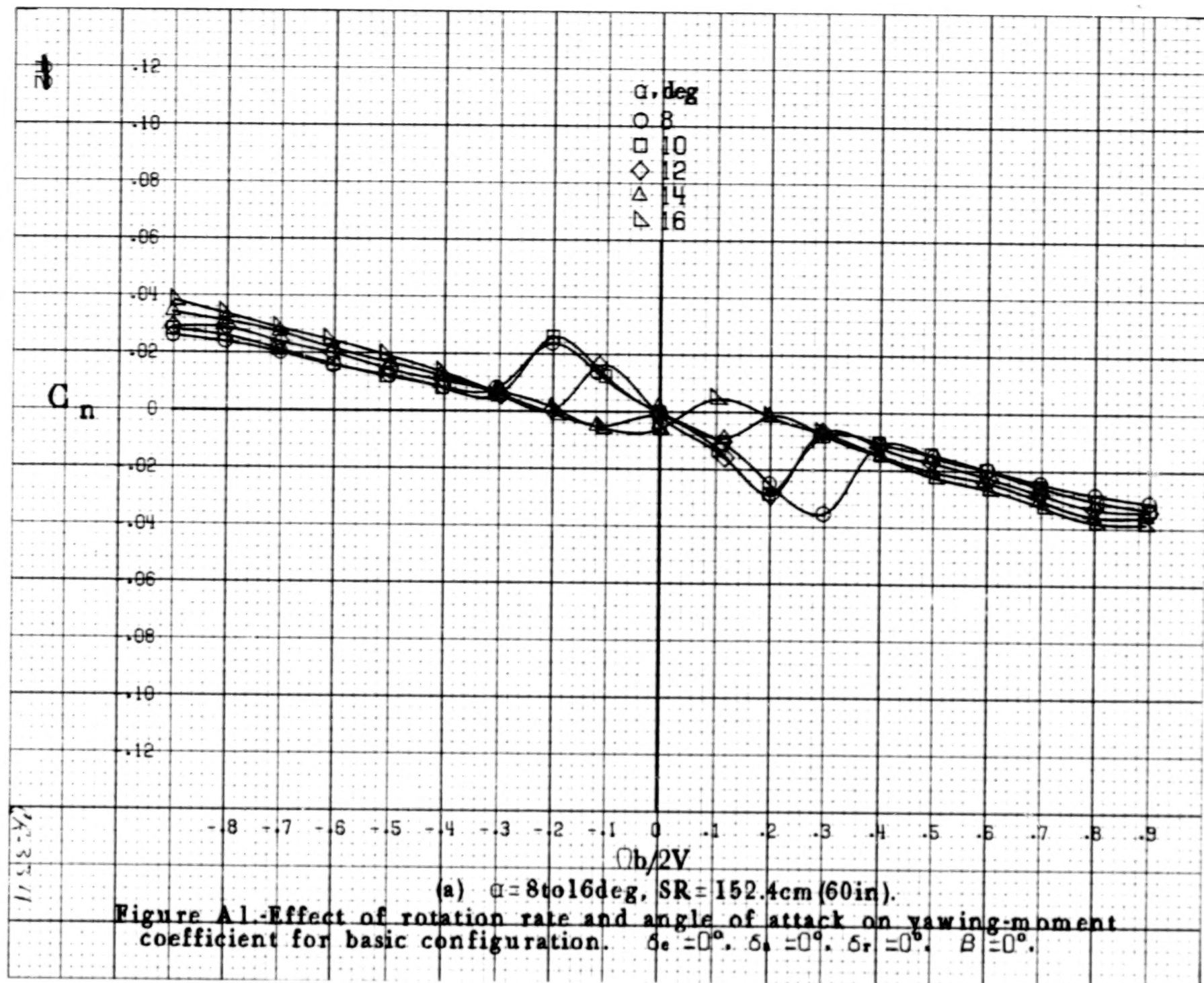
Right wing tip sail

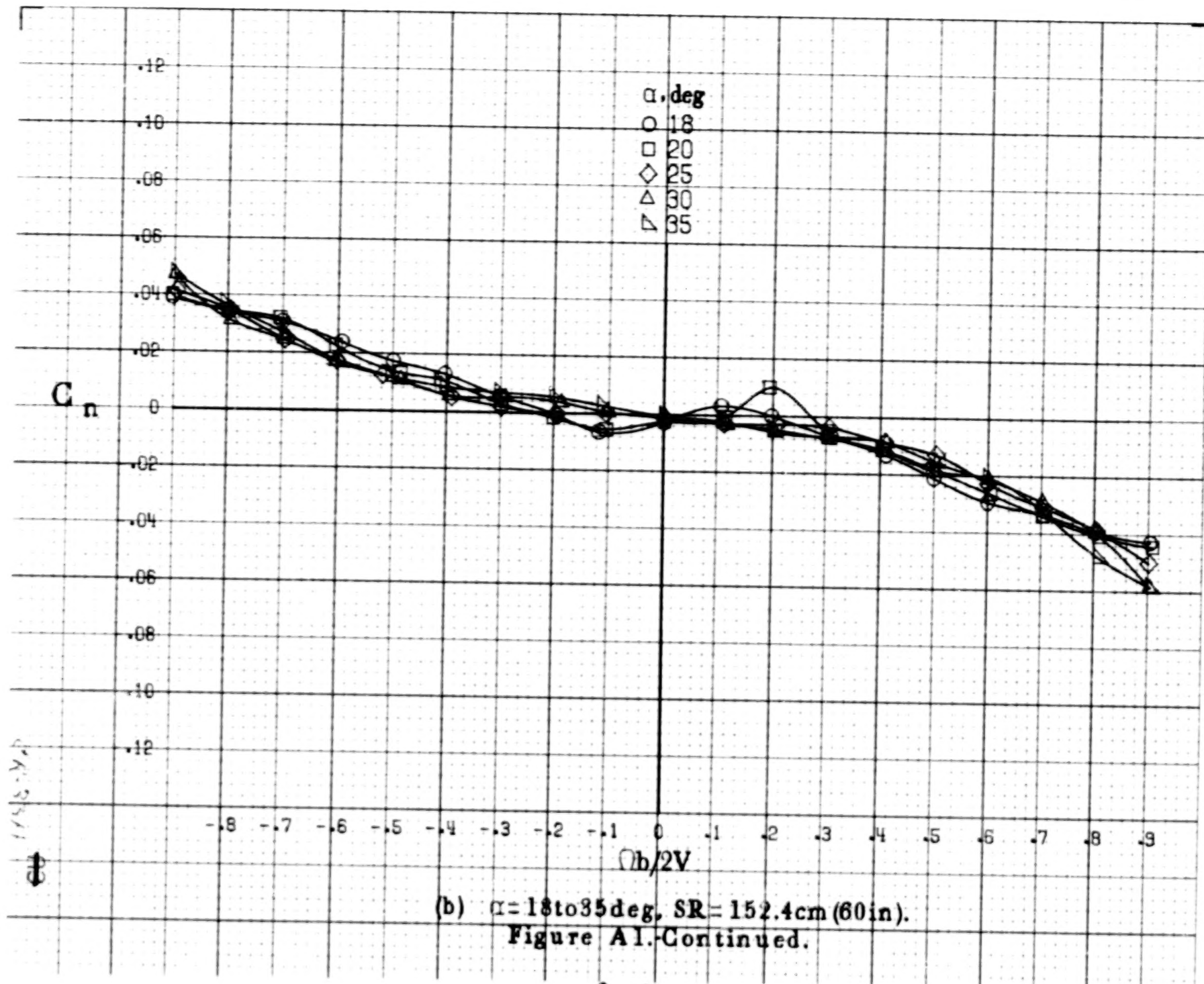


Lockheed vortex diffuser vane

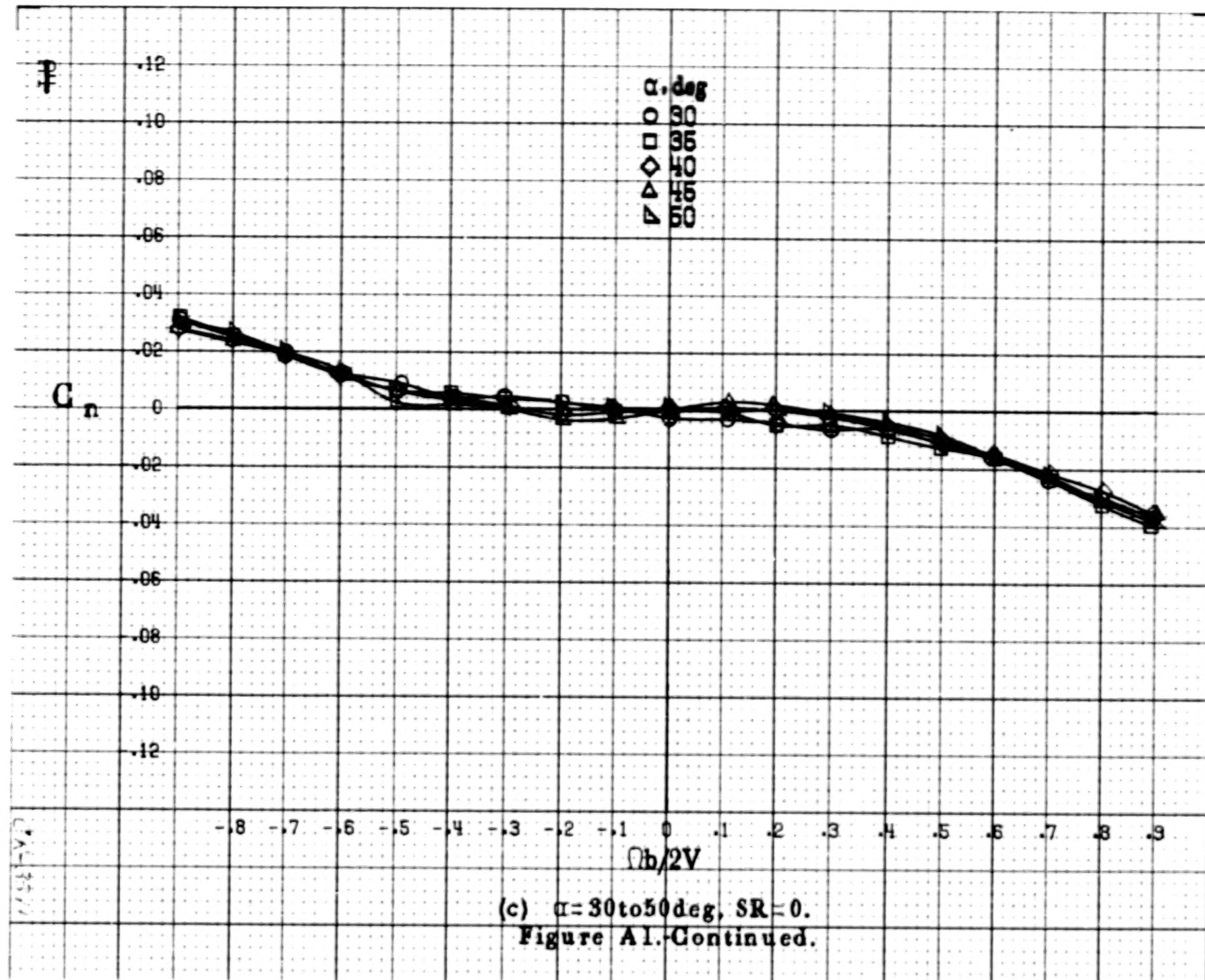
Figure 9. - Wingtip sails and tip vortex diffusers tested on model. Dimensions are given in centimeters (inches), model scale.

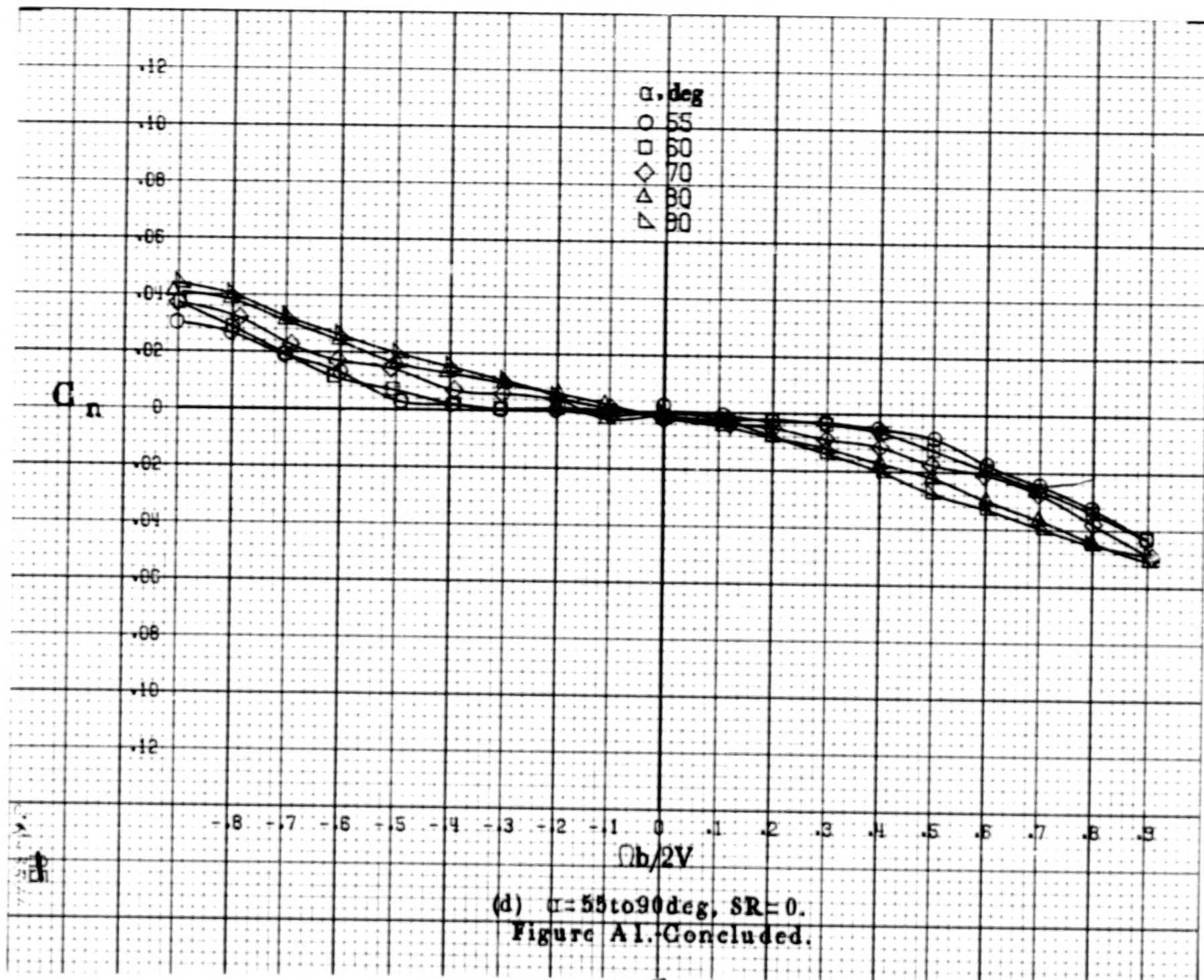
## APPENDIX

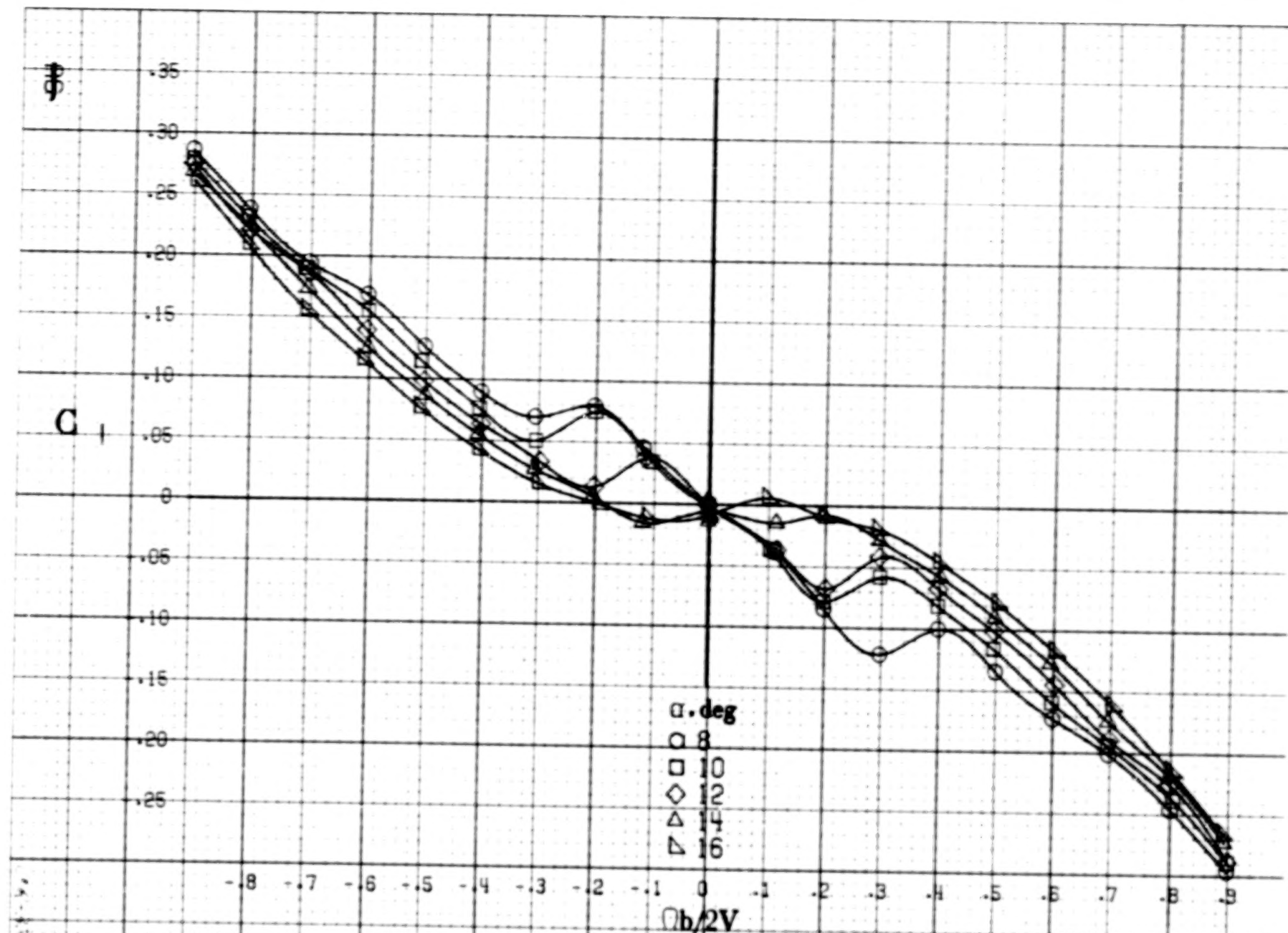




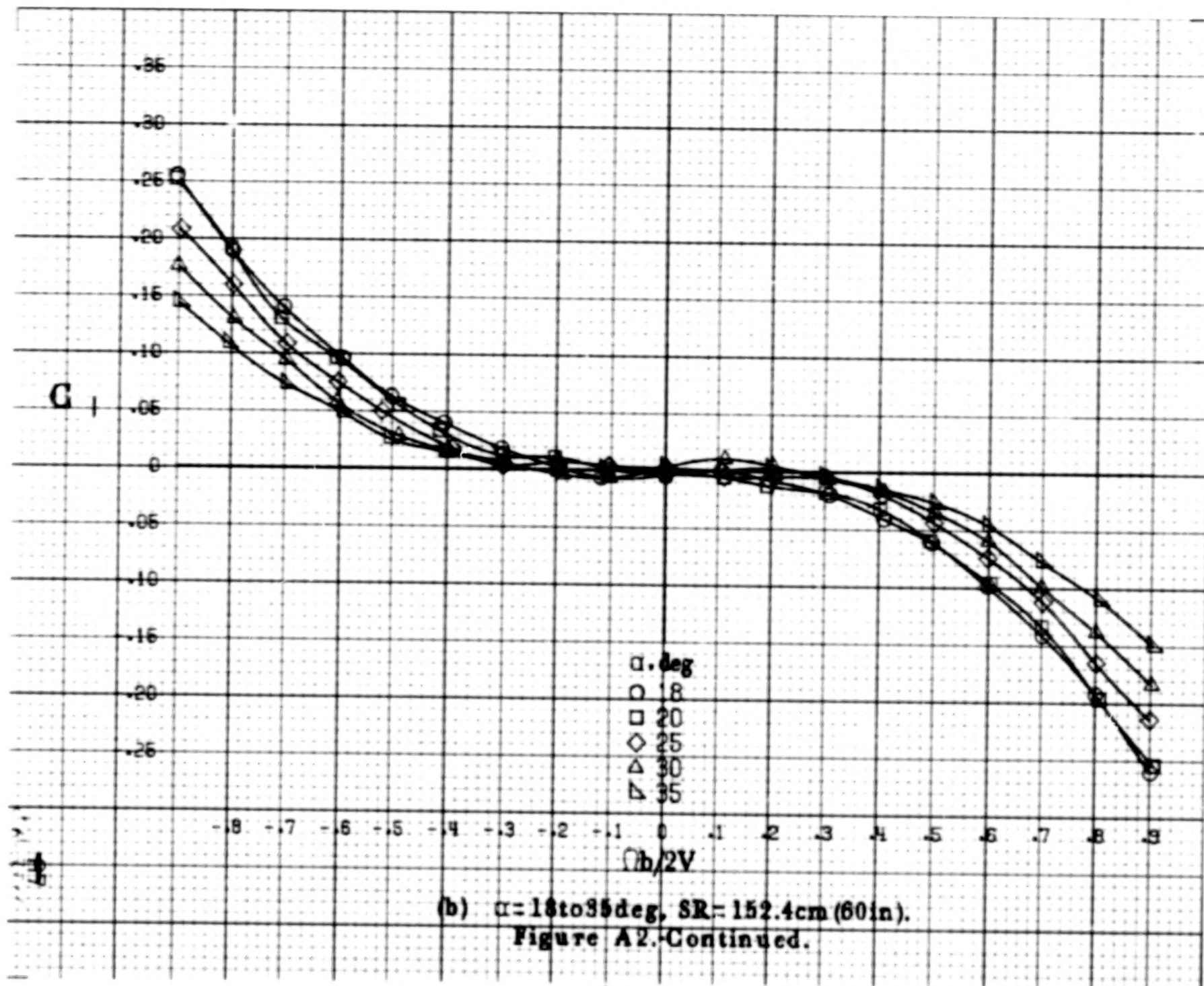








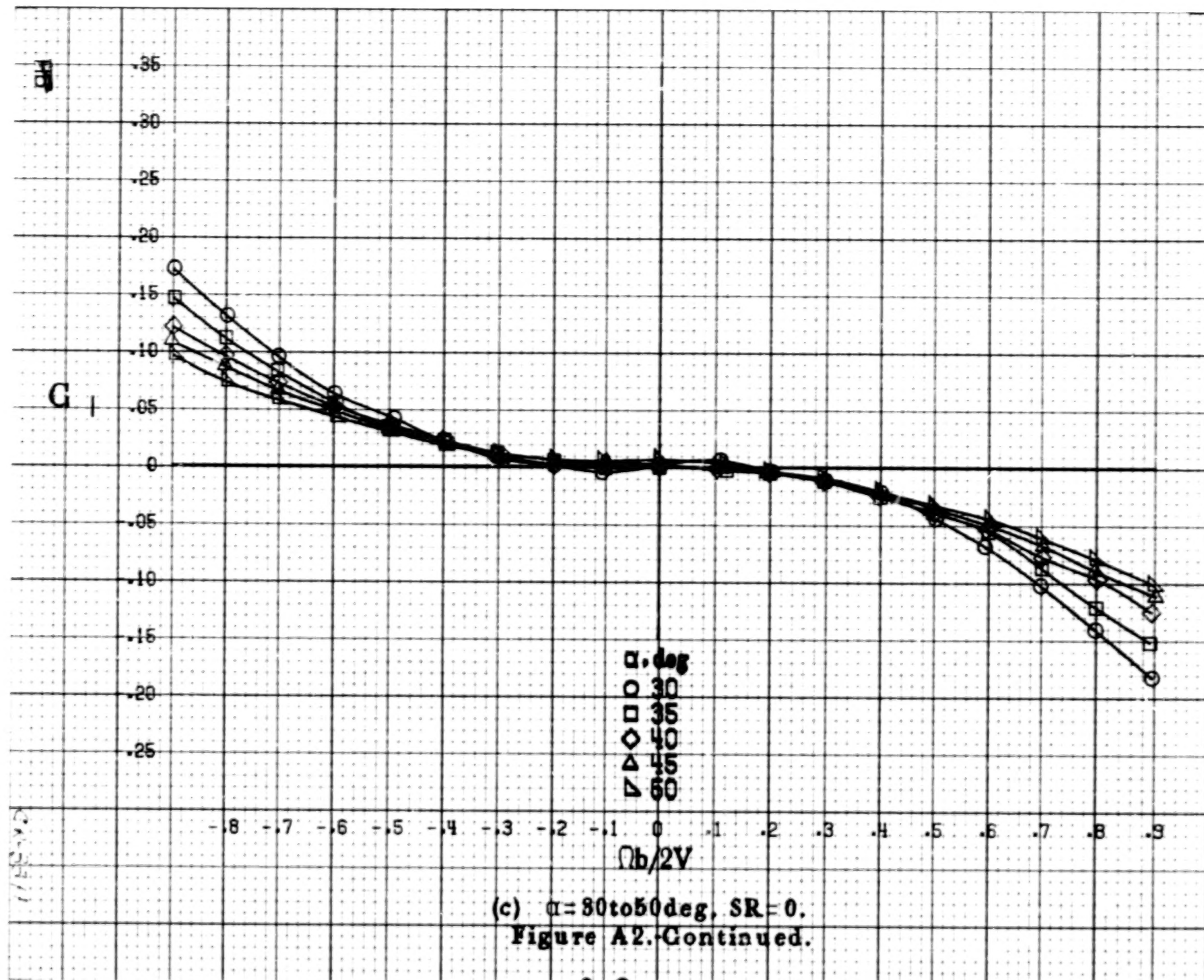
(a)  $\alpha = 8$  to  $16^\circ$ ,  $SR = 152.4 \text{ cm (60 in)}$ .  
 Figure A2.-Effect of rotation rate and angle of attack on rolling-moment coefficient for basic configuration.  $\delta_e = 0^\circ$ ,  $\delta_a = 0^\circ$ ,  $\delta_r = 0^\circ$ ,  $\beta = 0^\circ$ .

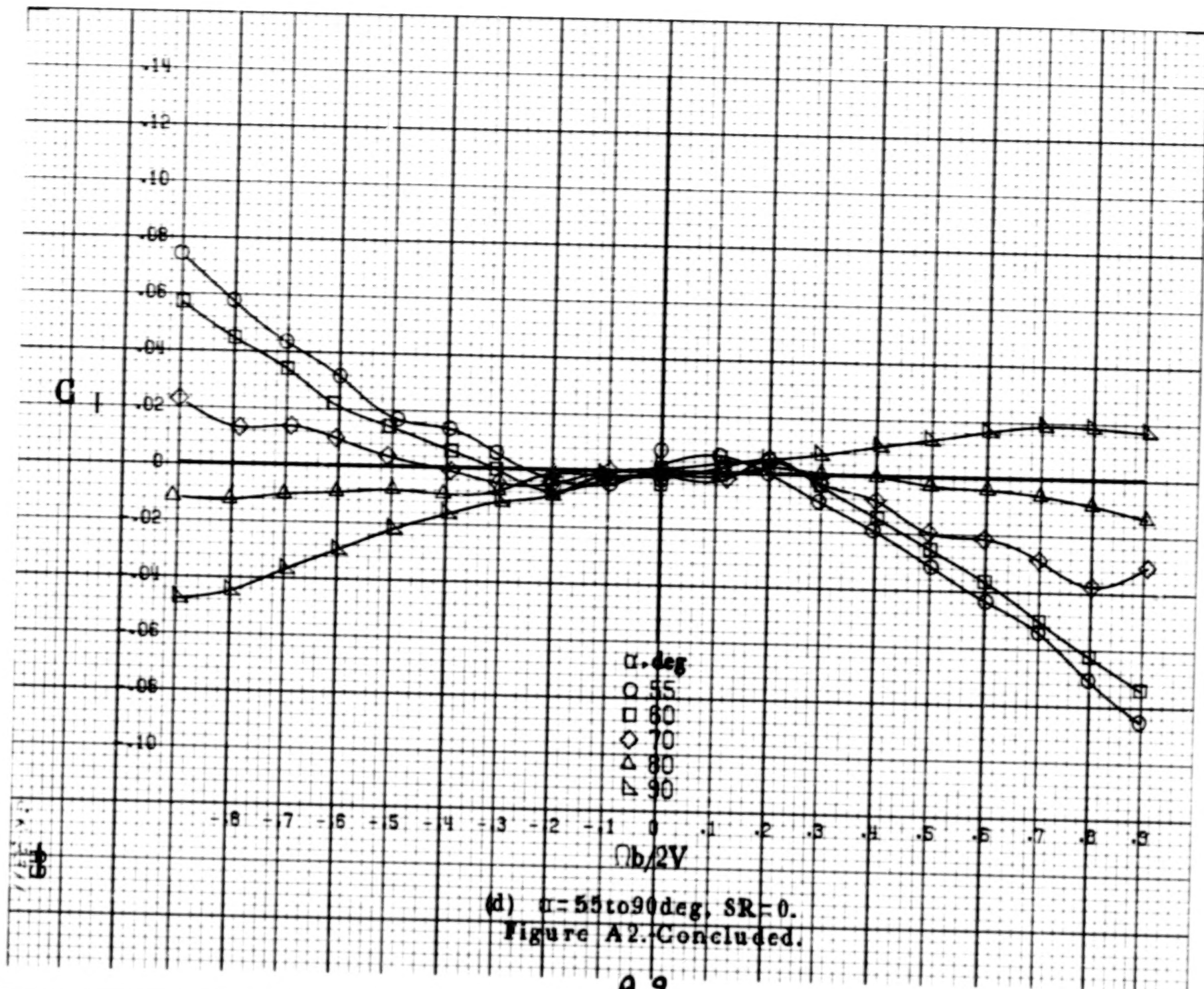


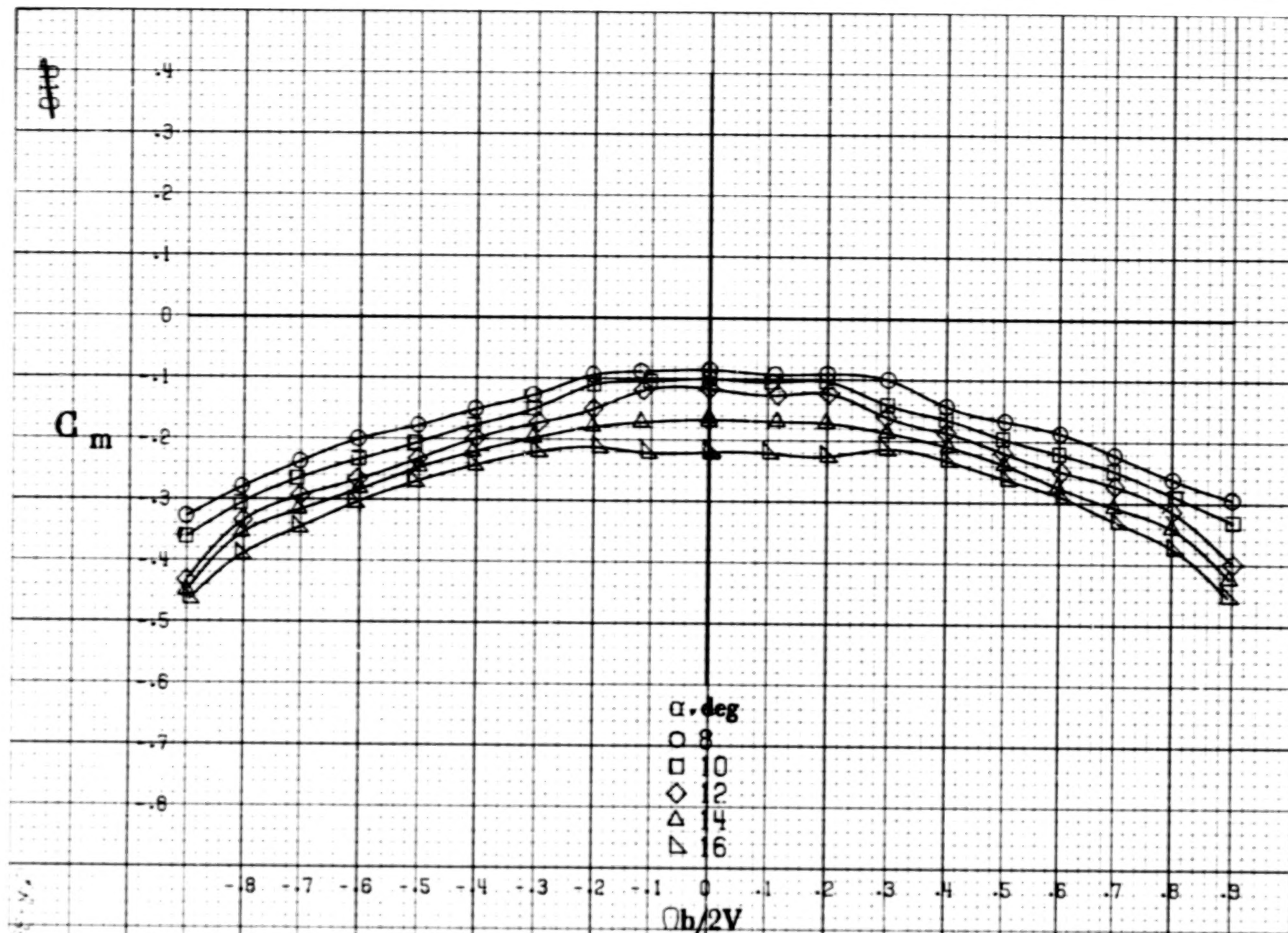
**BLANK PAGE**

**BLANK PAGE**





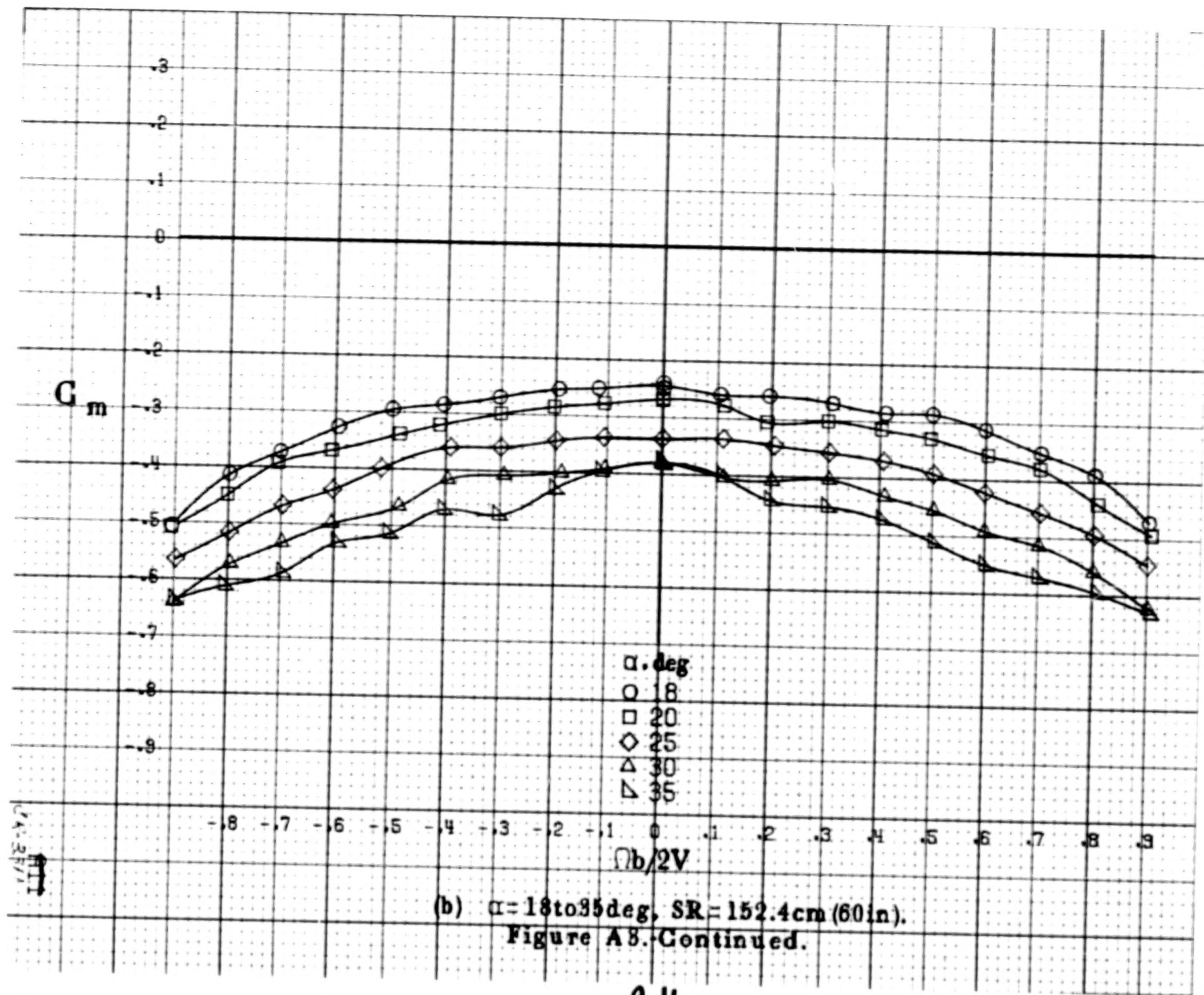


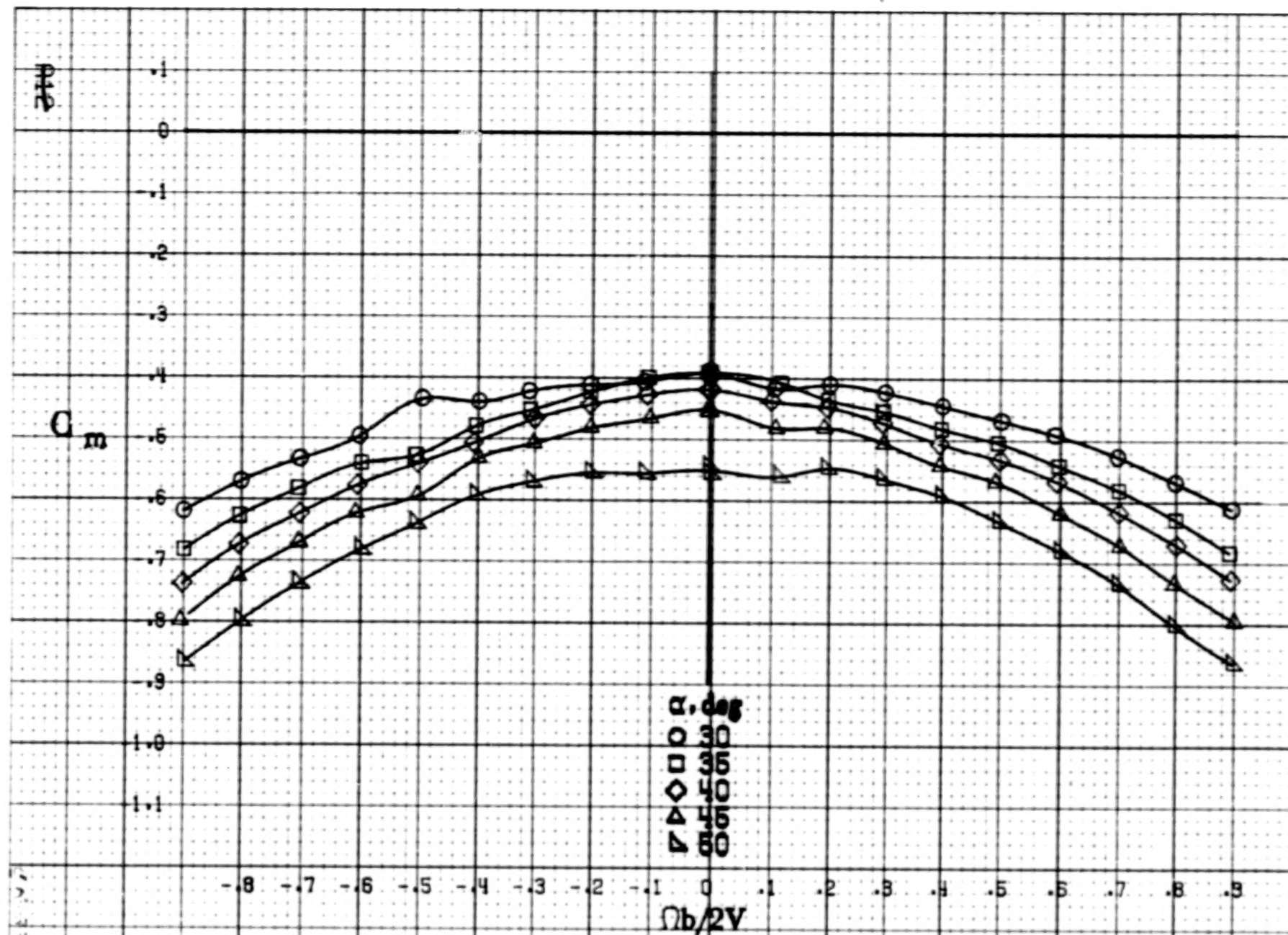


(a)  $\alpha = 8$  to  $16$  deg,  $SR = 152.4$  cm (60 in).

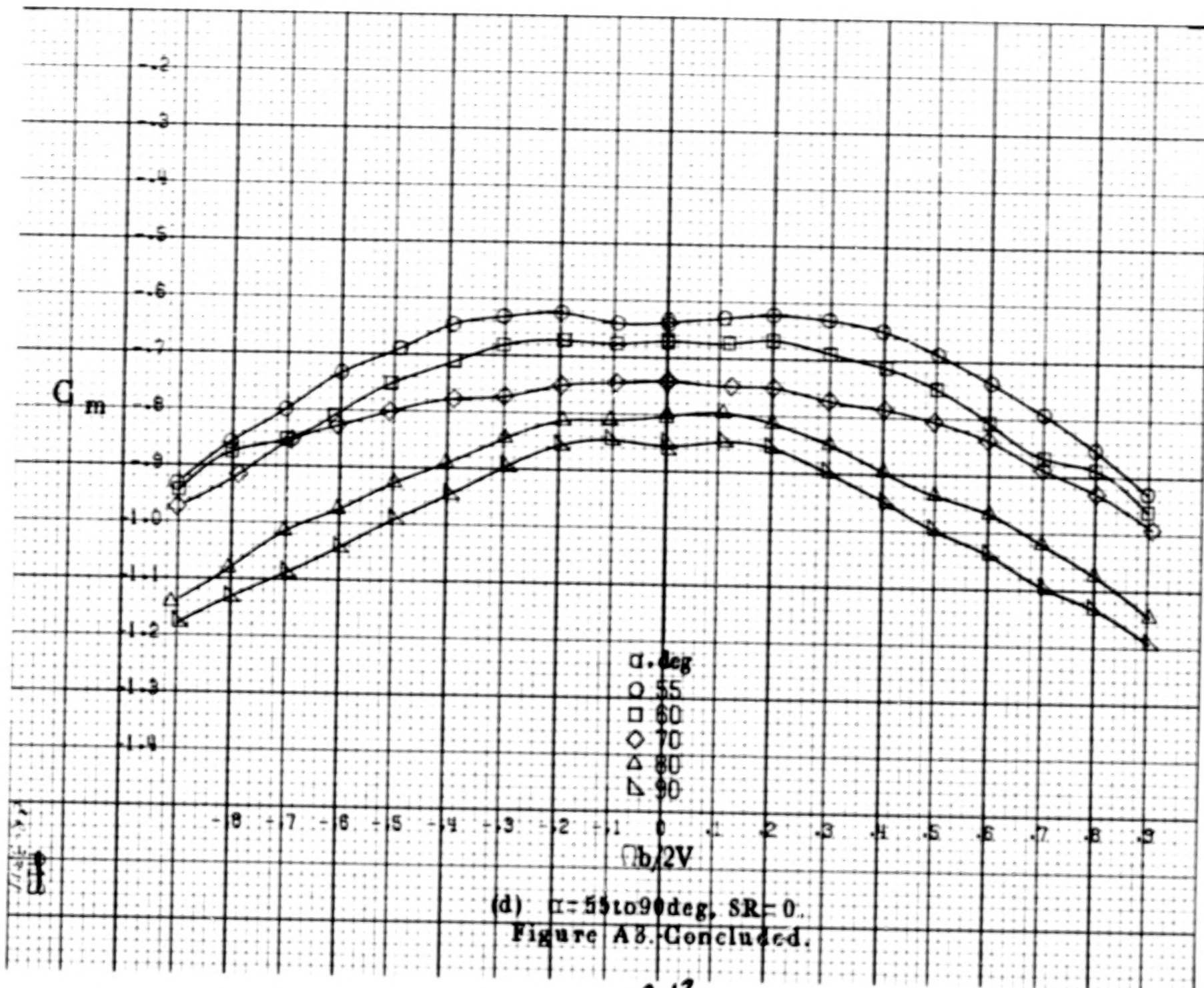
Figure A3.-Effect of rotation rate and angle of attack on pitching-moment coefficient for basic configuration.  $\delta_e = 0^\circ$ ,  $\delta_a = 0^\circ$ ,  $\delta_r = 0^\circ$ ,  $B = 0^\circ$ .

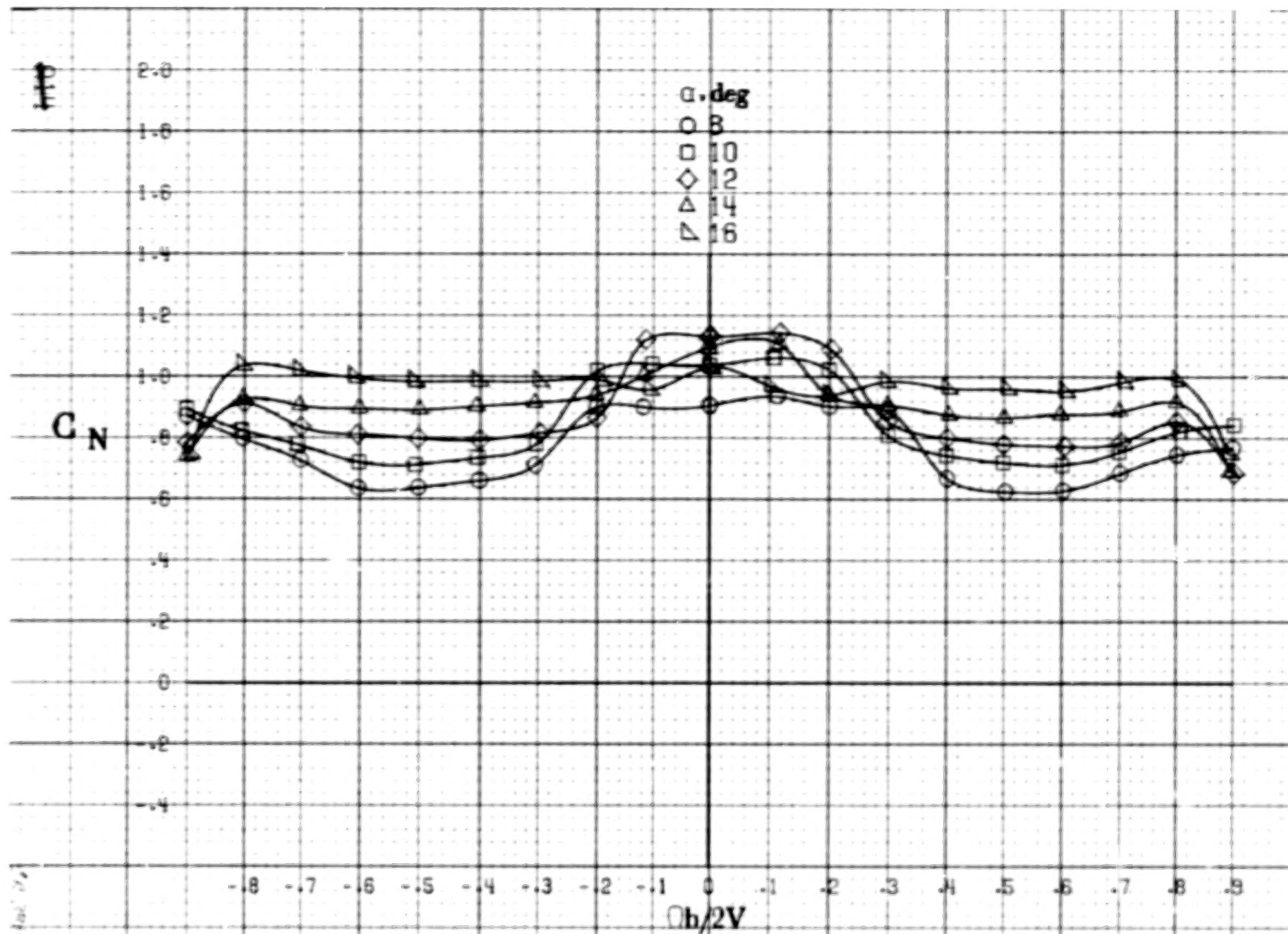






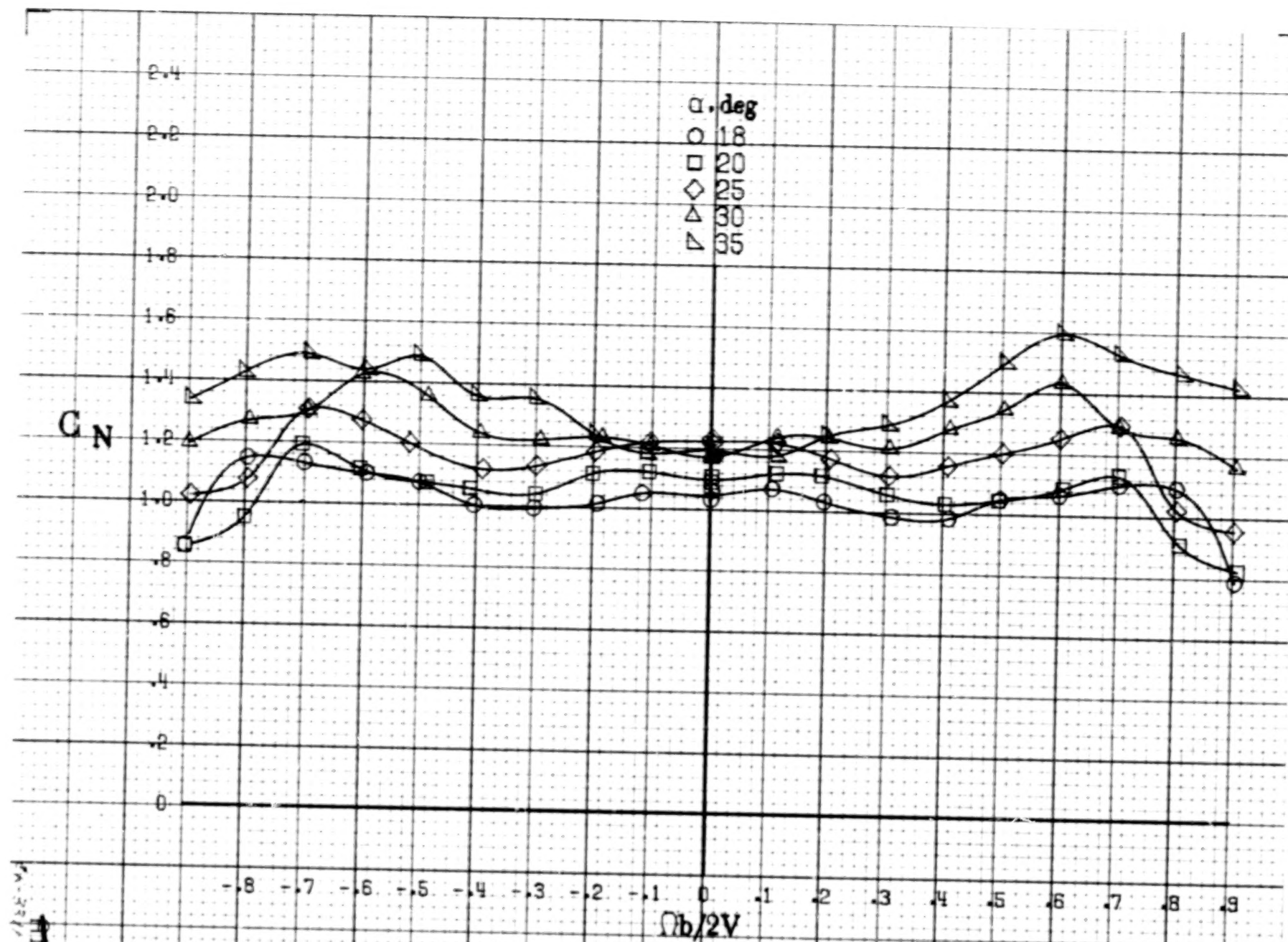
(c)  $\alpha = 30$  to  $50^\circ$  deg,  $SR = 0$ .  
Figure A3. Continued.



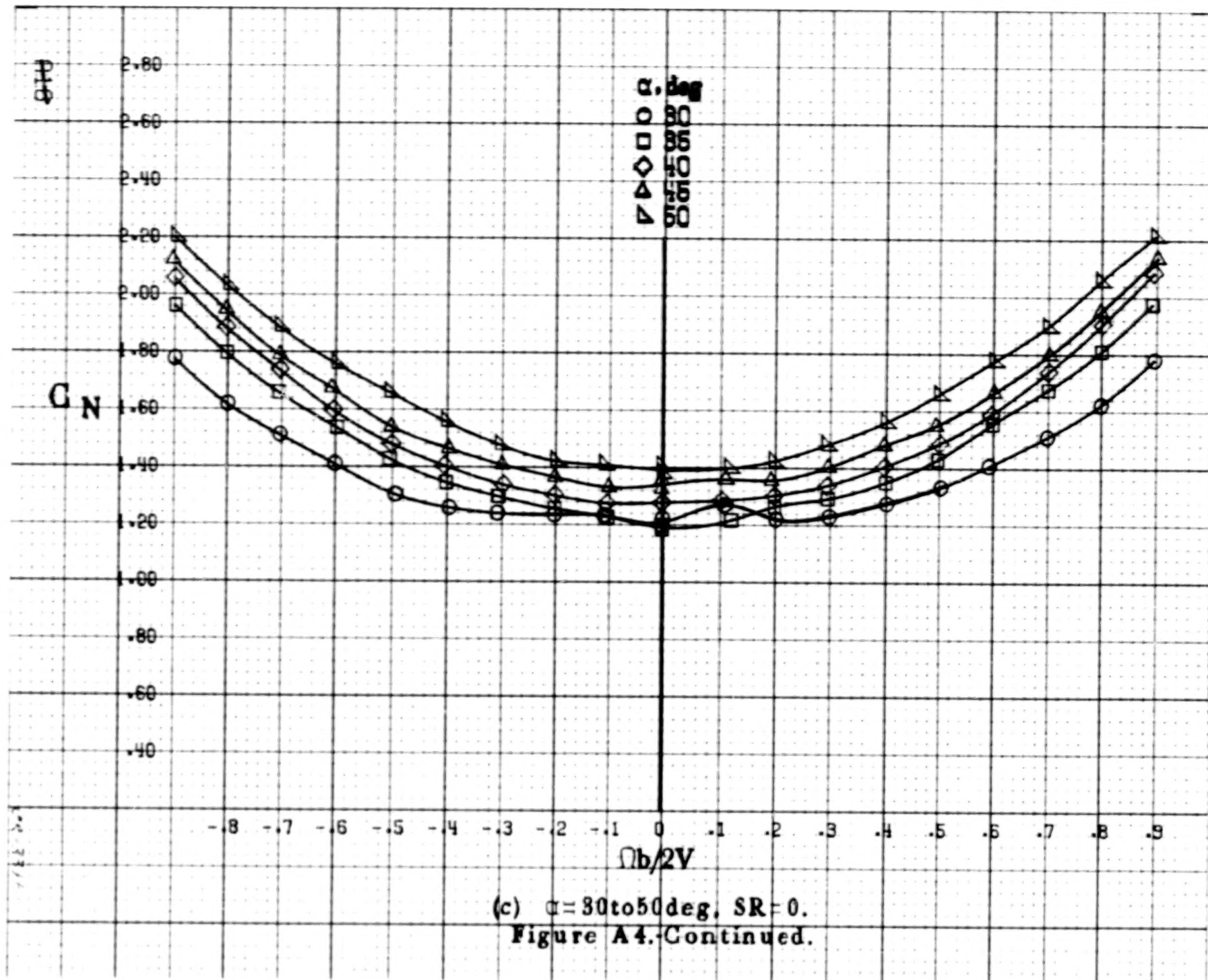


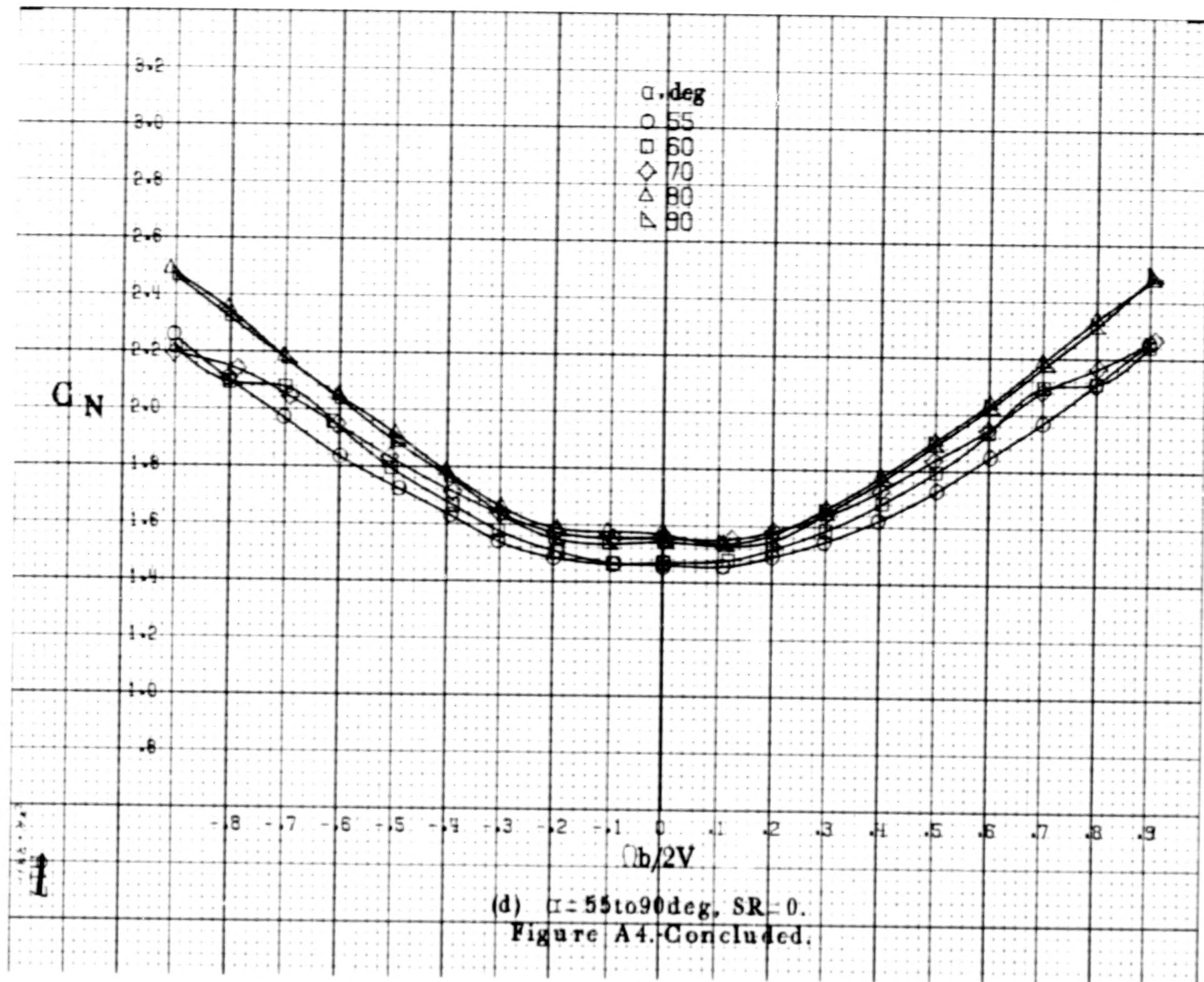
(a)  $\alpha = 8$  to  $16^\circ$ ,  $SR = 152.4 \text{ cm (60 in.)}$ .  
 Figure A4.-Effect of rotation rate and angle of attack on normal-force coefficient for basic configuration.  $\delta_e = 0^\circ$ ,  $\delta_a = 0^\circ$ ,  $\delta_r = 0^\circ$ ,  $\beta = 0^\circ$ .

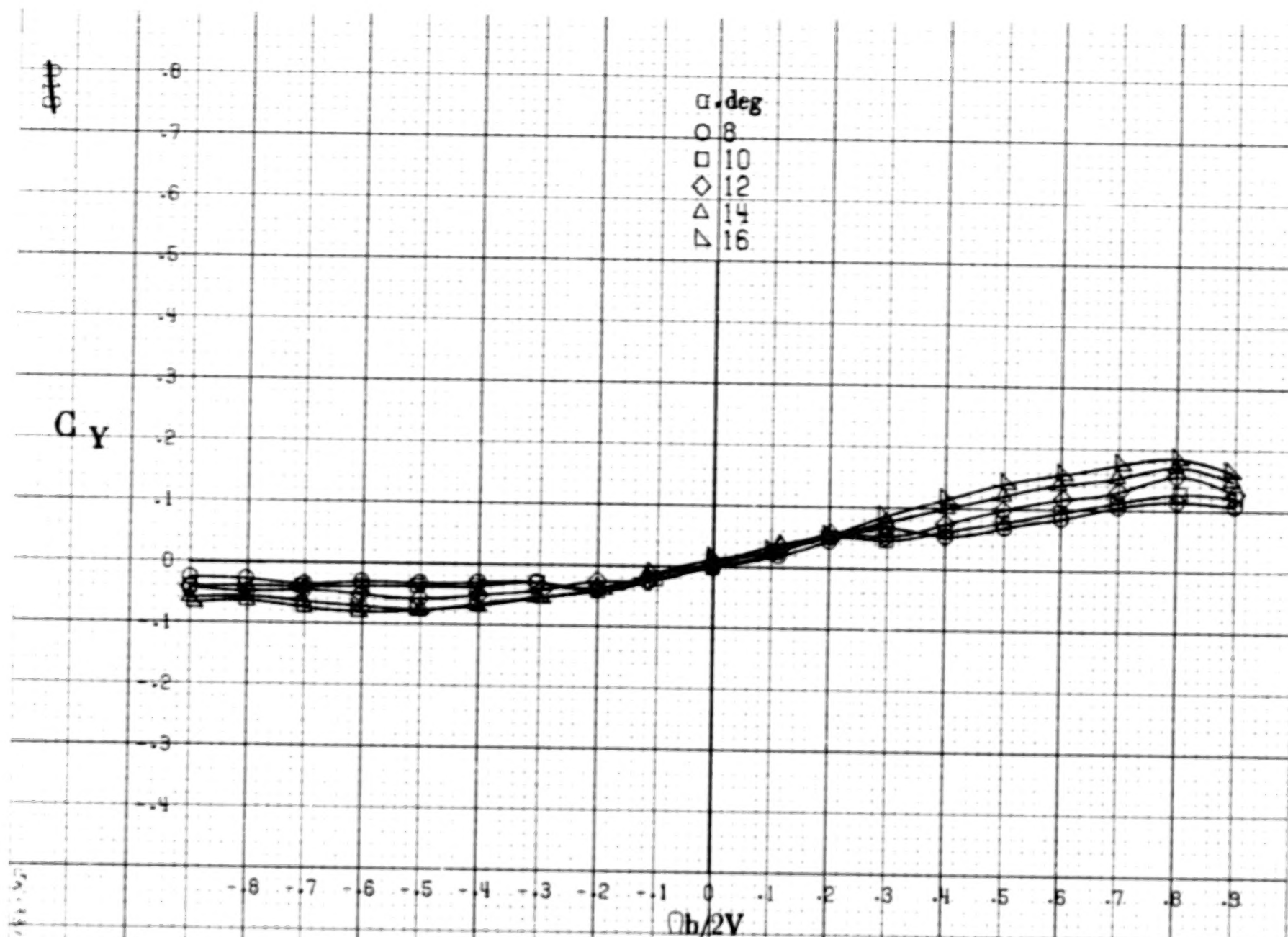




(b)  $\alpha = 18$  to  $35$  deg,  $SR = 152.4$  cm (60 in).  
Figure A4. Continued.

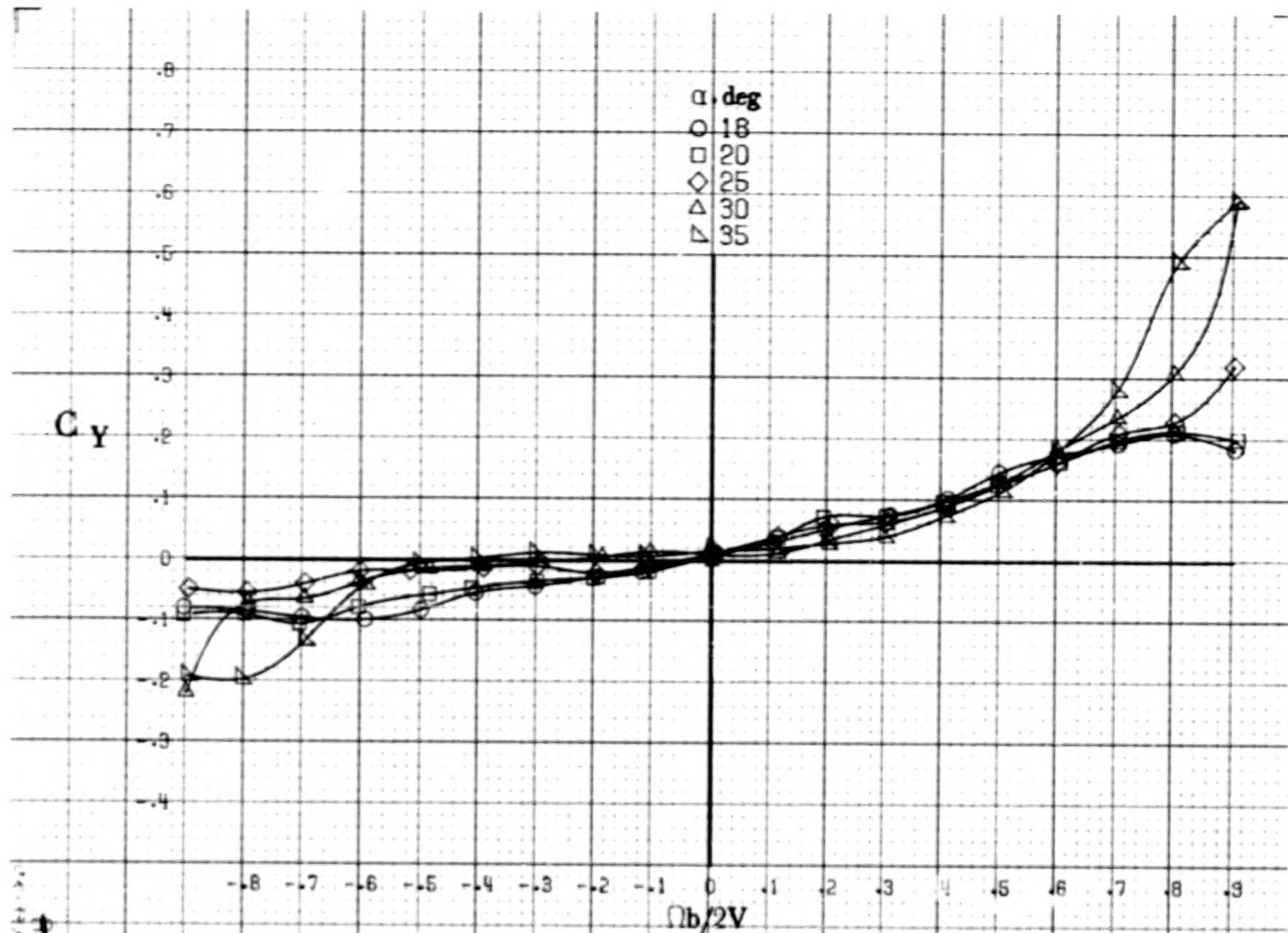






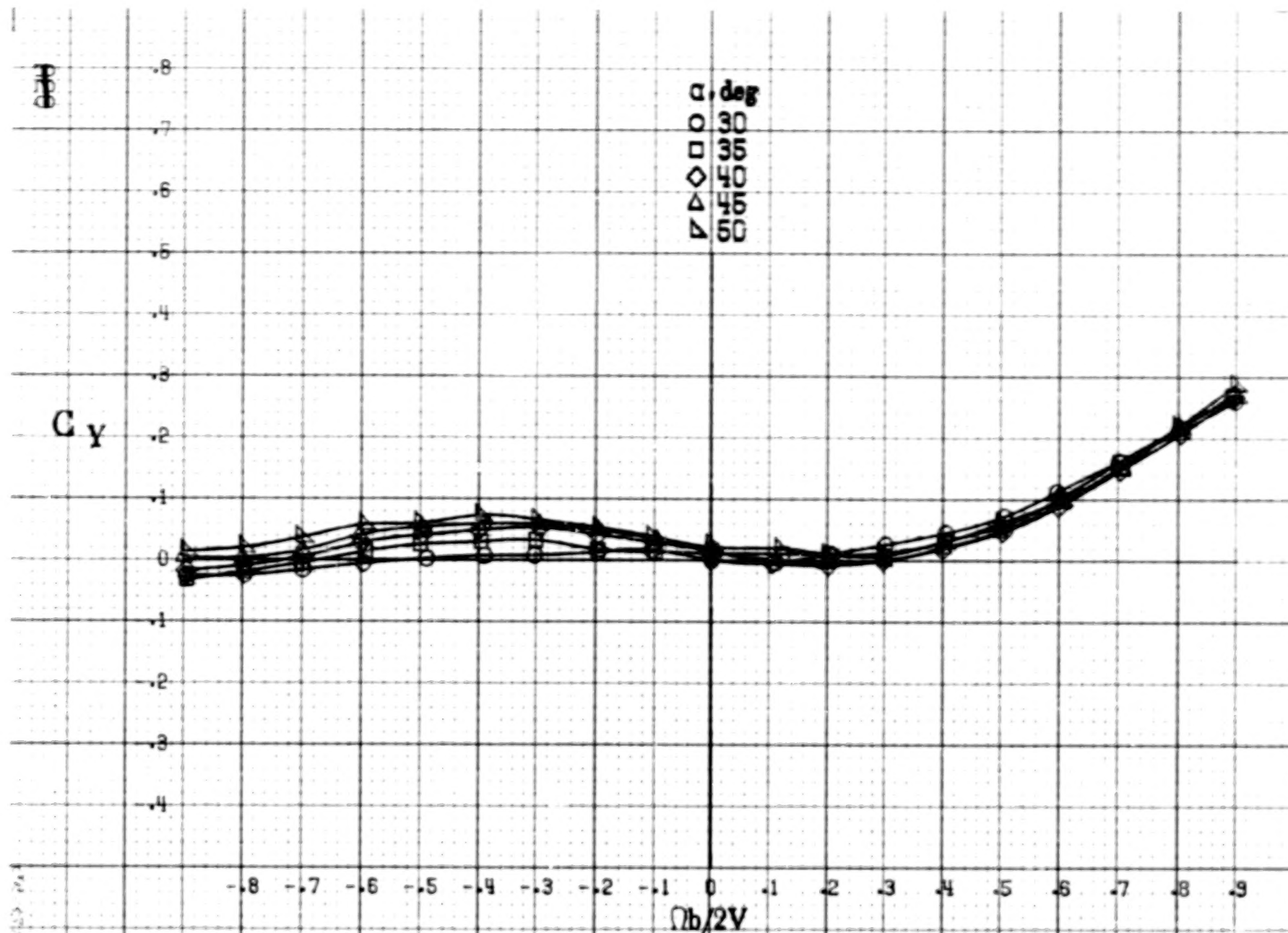
(a)  $\alpha = 8$  to  $16^\circ$ ,  $SR = 152.4\text{cm (60in)}$ .  
 Figure A5.-Effect of rotation rate and angle of attack on side-force coefficient for basic configuration.  $\delta_e = 0^\circ$ ,  $\delta_a = 0^\circ$ ,  $\delta_r = 0^\circ$ ,  $\beta = 0^\circ$ .





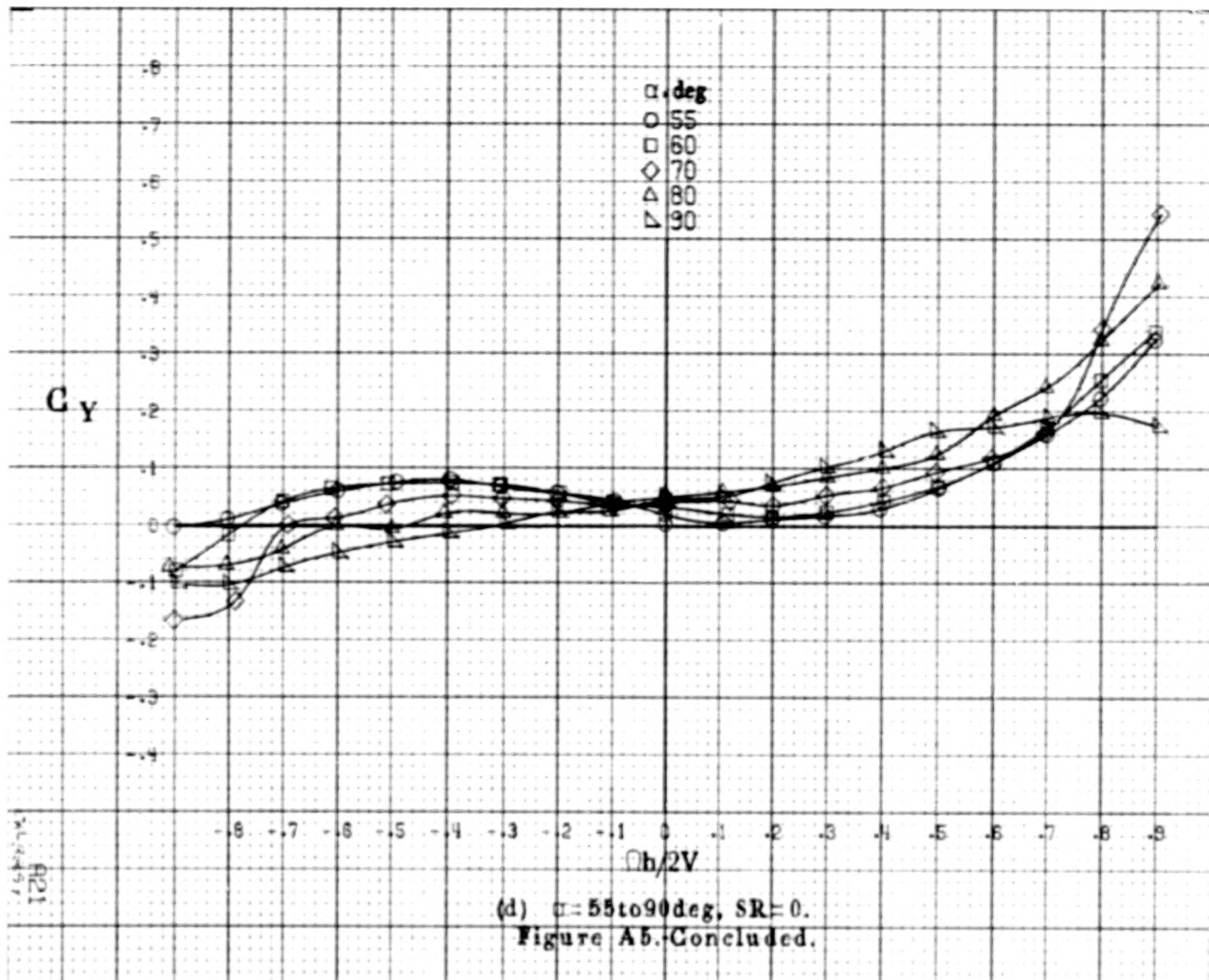
(b)  $\alpha = 18$  to  $35$  deg,  $SR = 152.4$  cm (60 in).

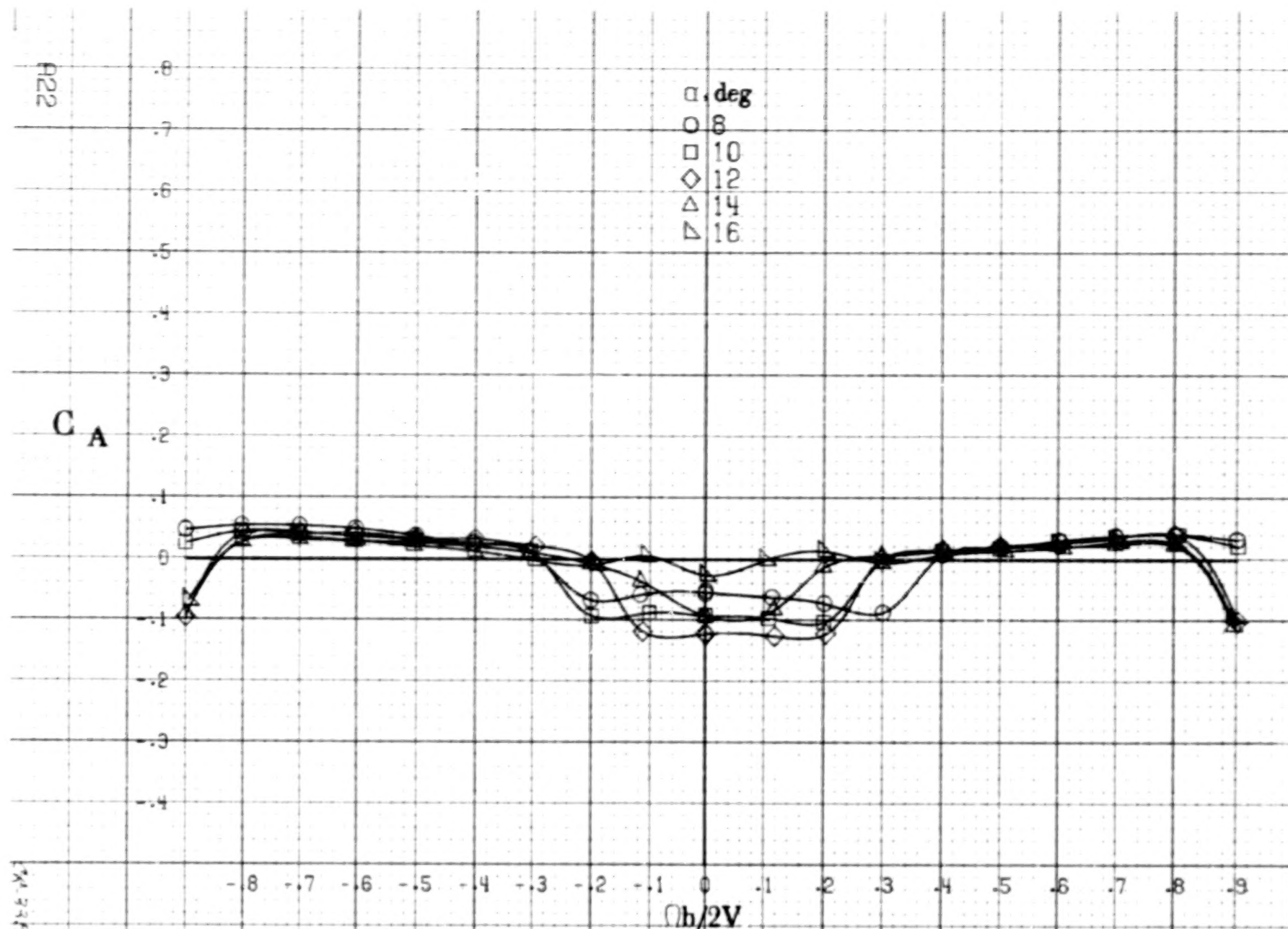
Figure A5-Continued.



(c)  $\alpha = 30$  to  $50$  deg,  $SR = 0$ .

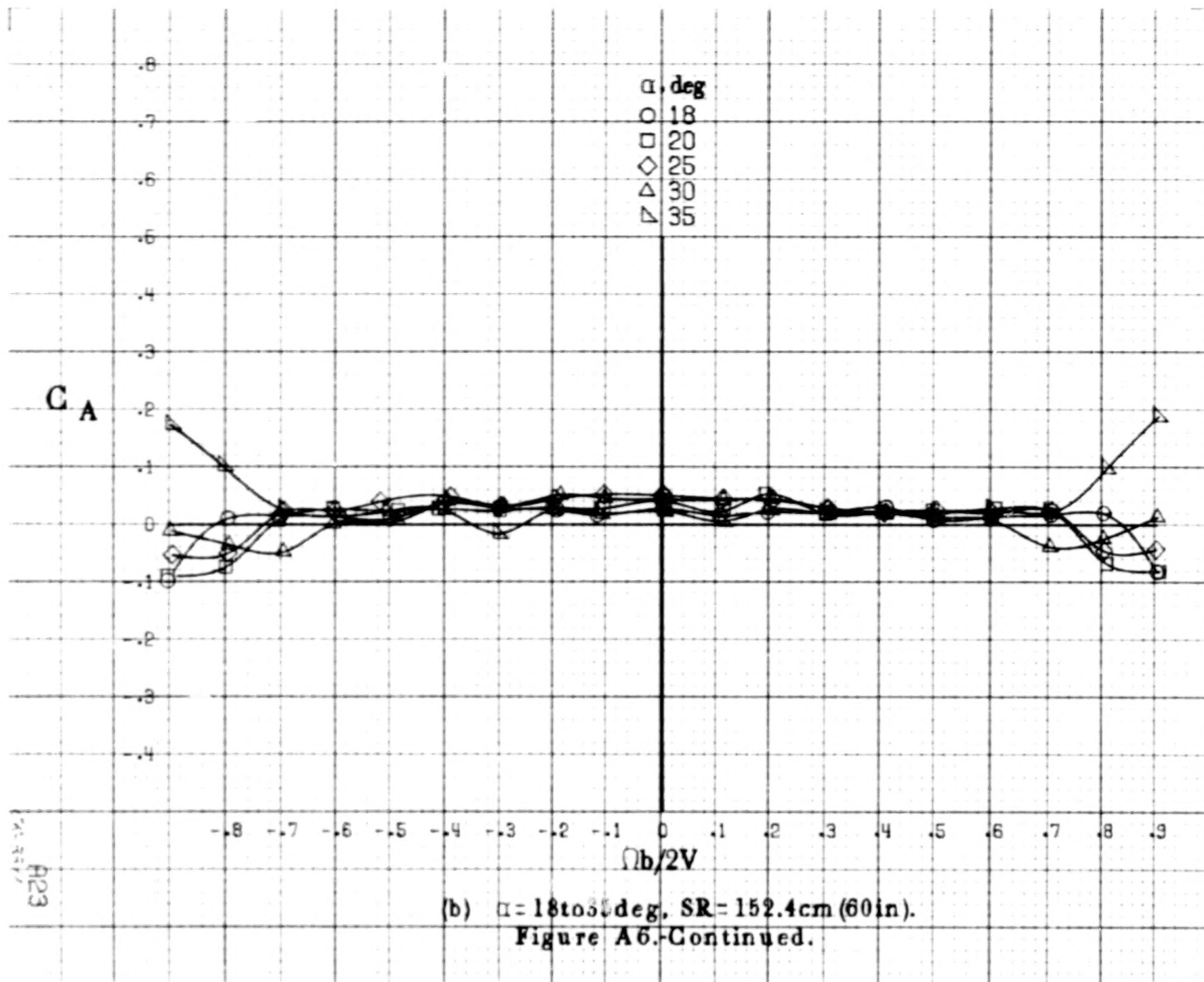
Figure A5. Continued.



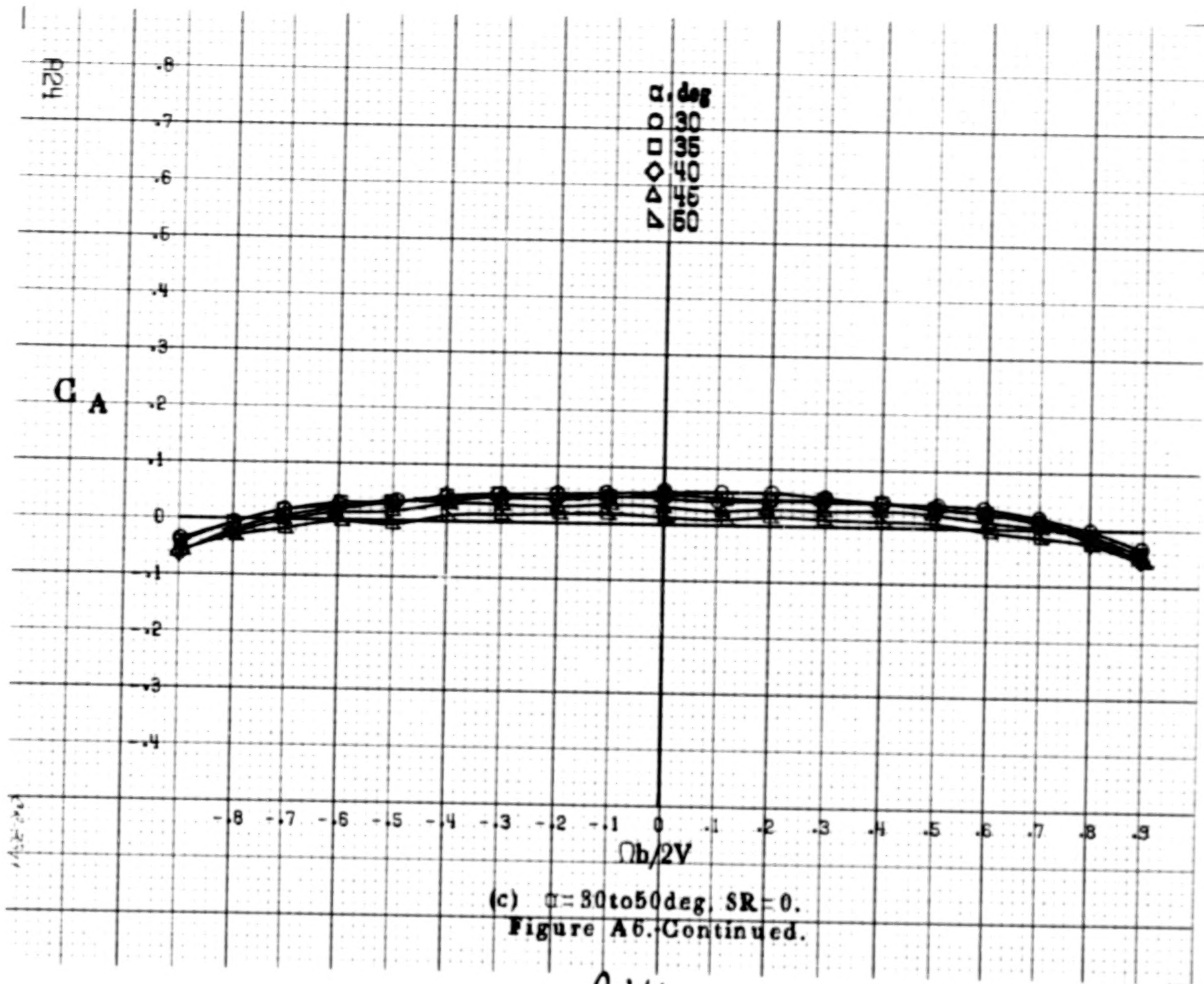


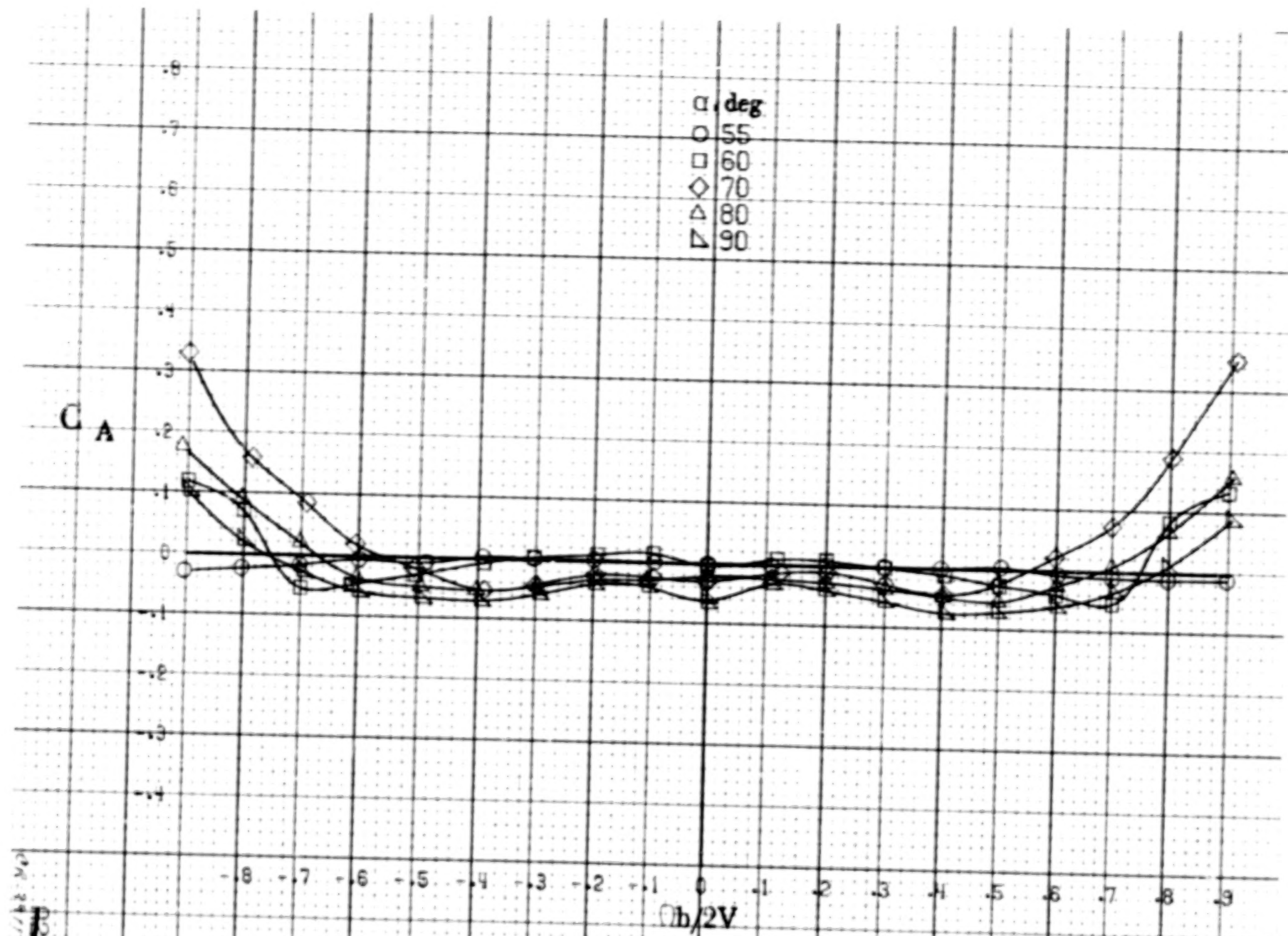
(a)  $\alpha = 8 \text{ to } 16 \text{ deg}$ ,  $SR = 152.4 \text{ cm (60 in)}$ .

Figure A6. Effect of rotation rate and angle of attack on axial-force coefficient for basic configuration.  $\delta_e = 0^\circ$ ,  $\delta_a = 0^\circ$ ,  $\delta_r = 0^\circ$ ,  $\beta = 0^\circ$ .

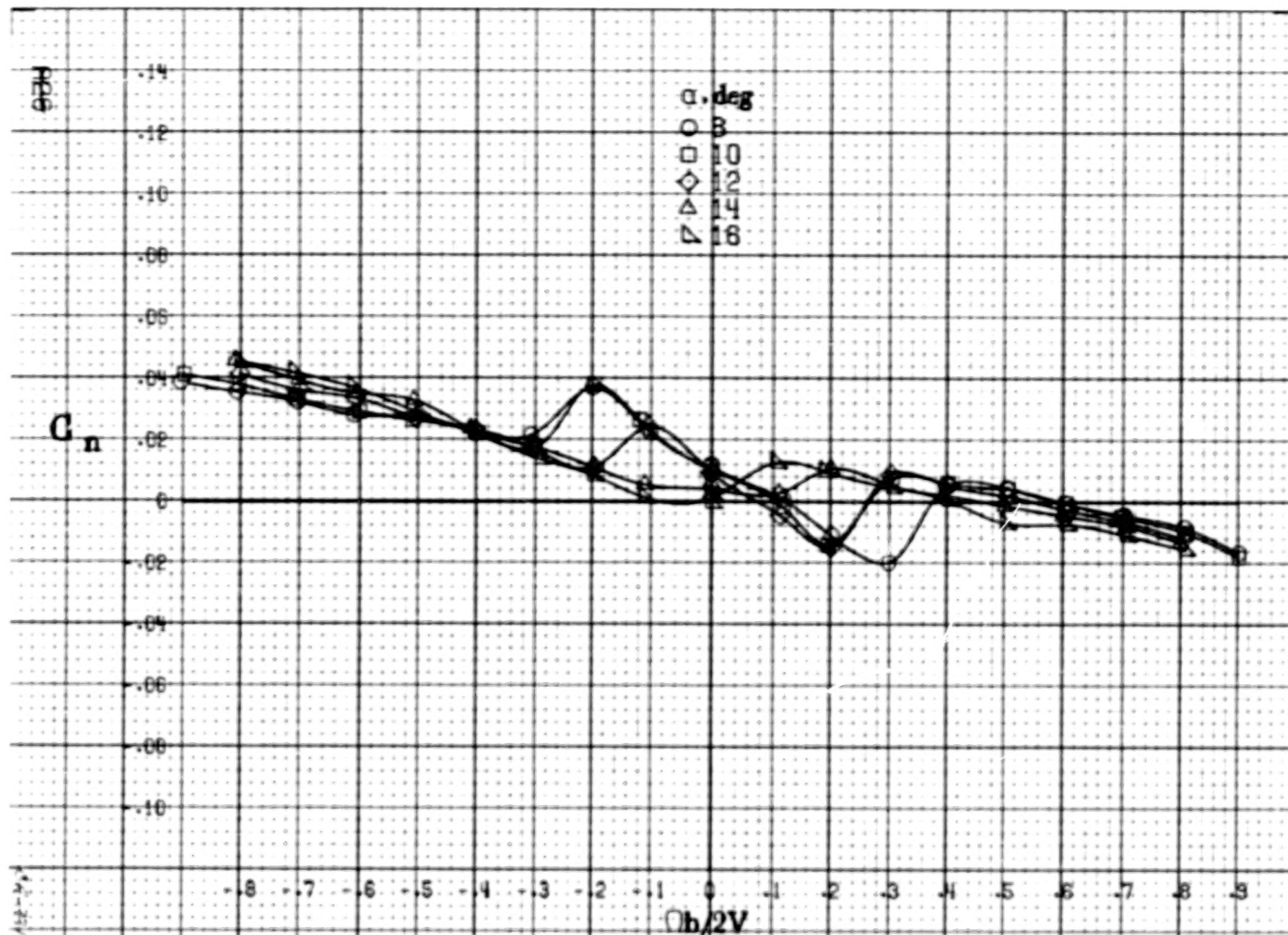








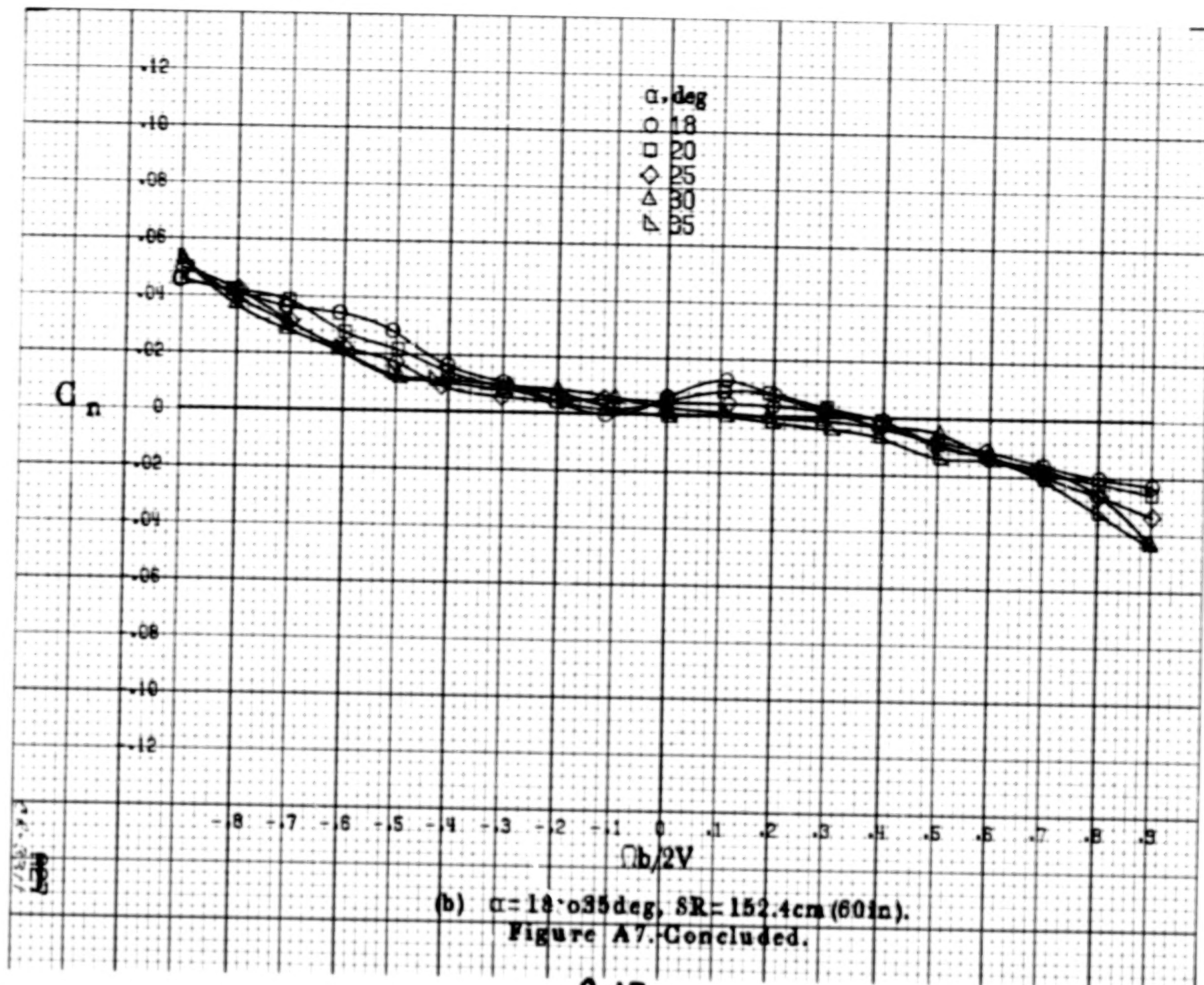
(d)  $\alpha = 55$  to  $90$  deg,  $SR = 0$ .  
Figure A6. Concluded.

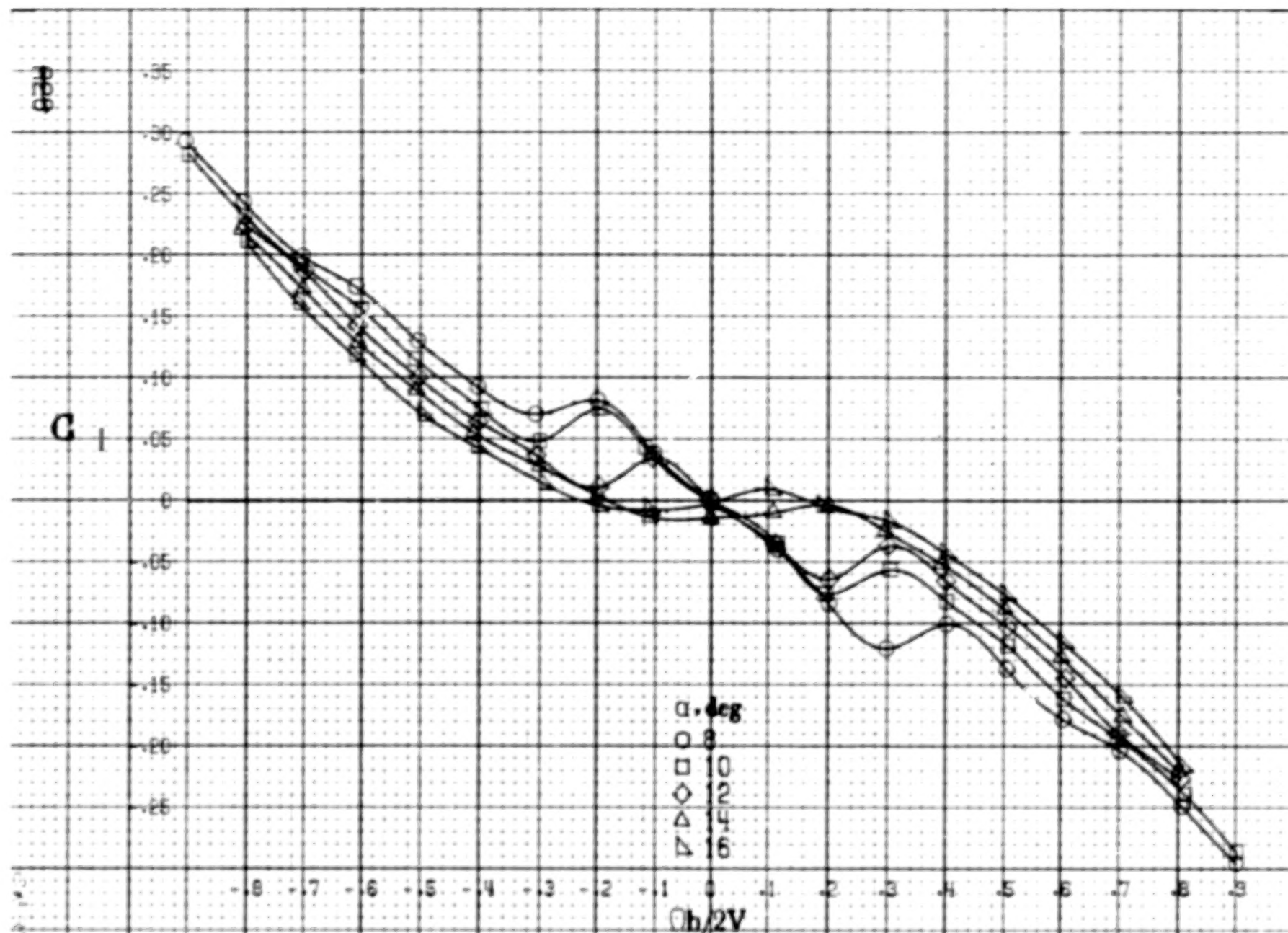


(a)  $\alpha = 8$  to  $16^\circ$ ,  $SR = 152.4 \text{ cm (60 in.)}$ .

Figure A7.-Effect of rotation rate and angle of attack on yawing-moment coefficient for basic configuration.  $\delta_e = 17^\circ$ ,  $\delta_a = 0^\circ$ ,  $\delta_r = -24^\circ$ ,  $\beta = 0^\circ$ .

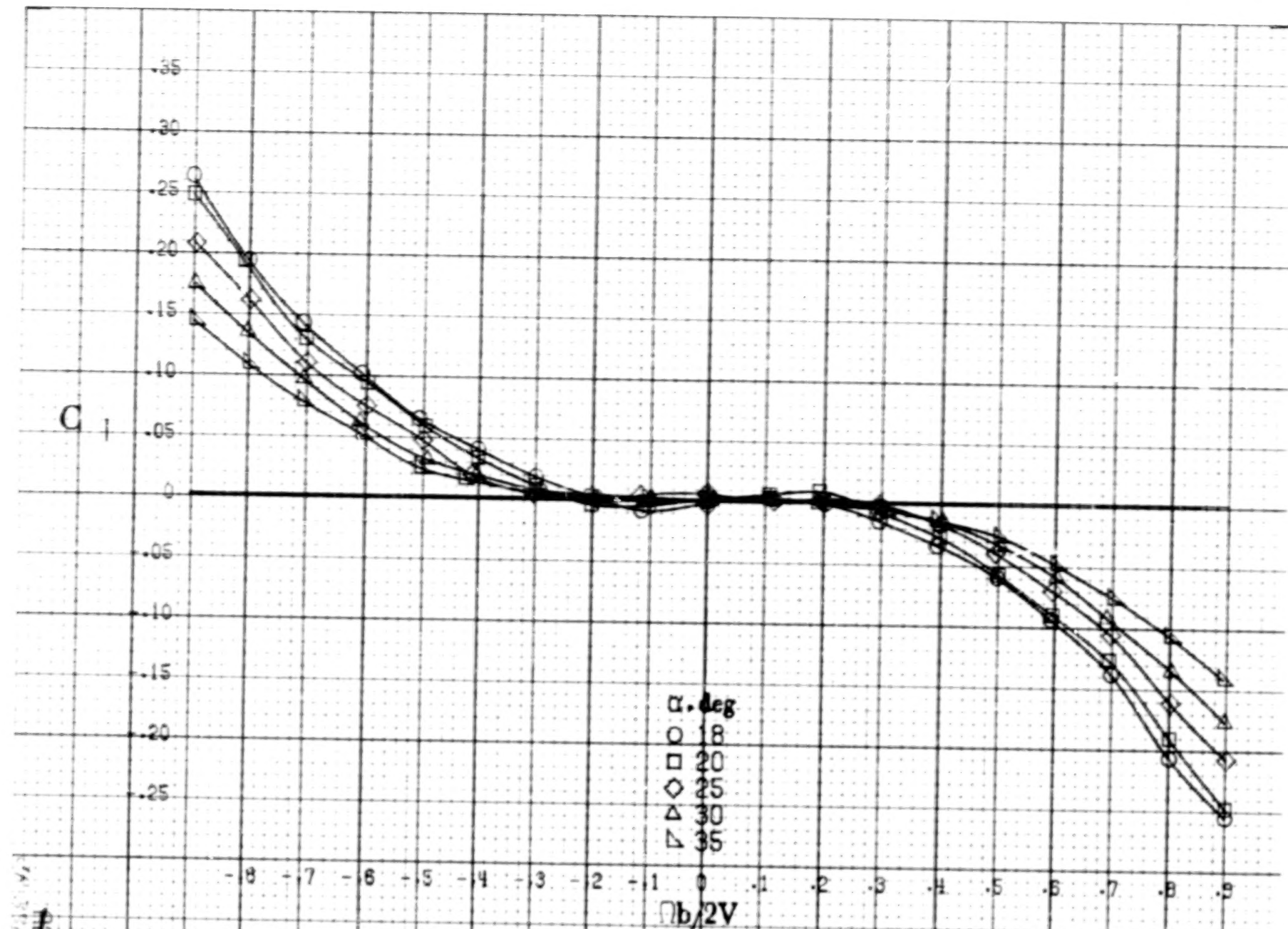




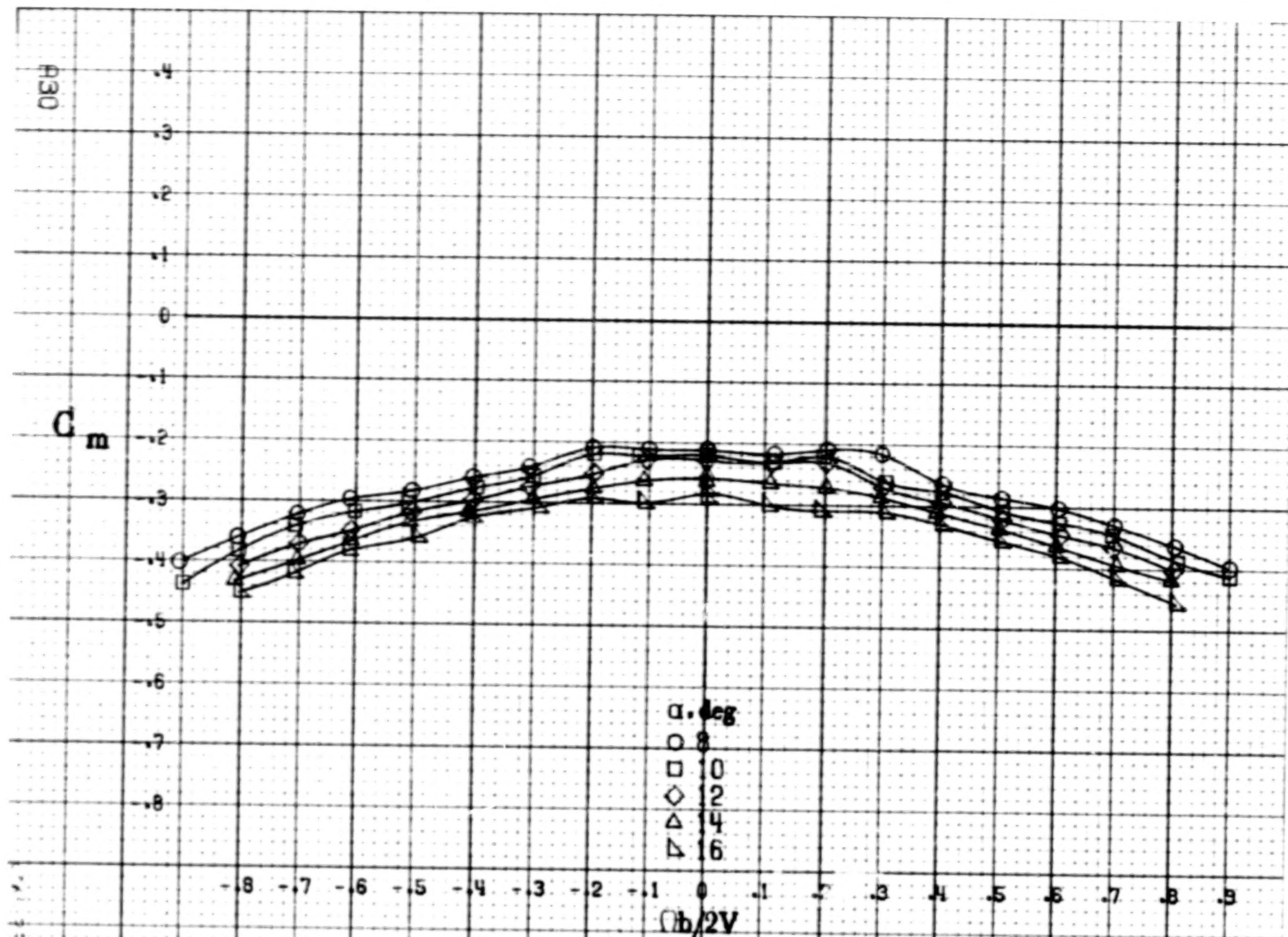


(a)  $\alpha = 8 \text{ to } 16 \text{ deg}$ ,  $SR = 152.4 \text{ cm (60 in)}$ .

Figure A8.-Effect of rotation rate and angle of attack on rolling-moment coefficient for basic configuration.  $\delta_s = 17^\circ$ ,  $\delta_a = 0^\circ$ ,  $\delta_r = -24^\circ$ ,  $\beta = 0^\circ$ .

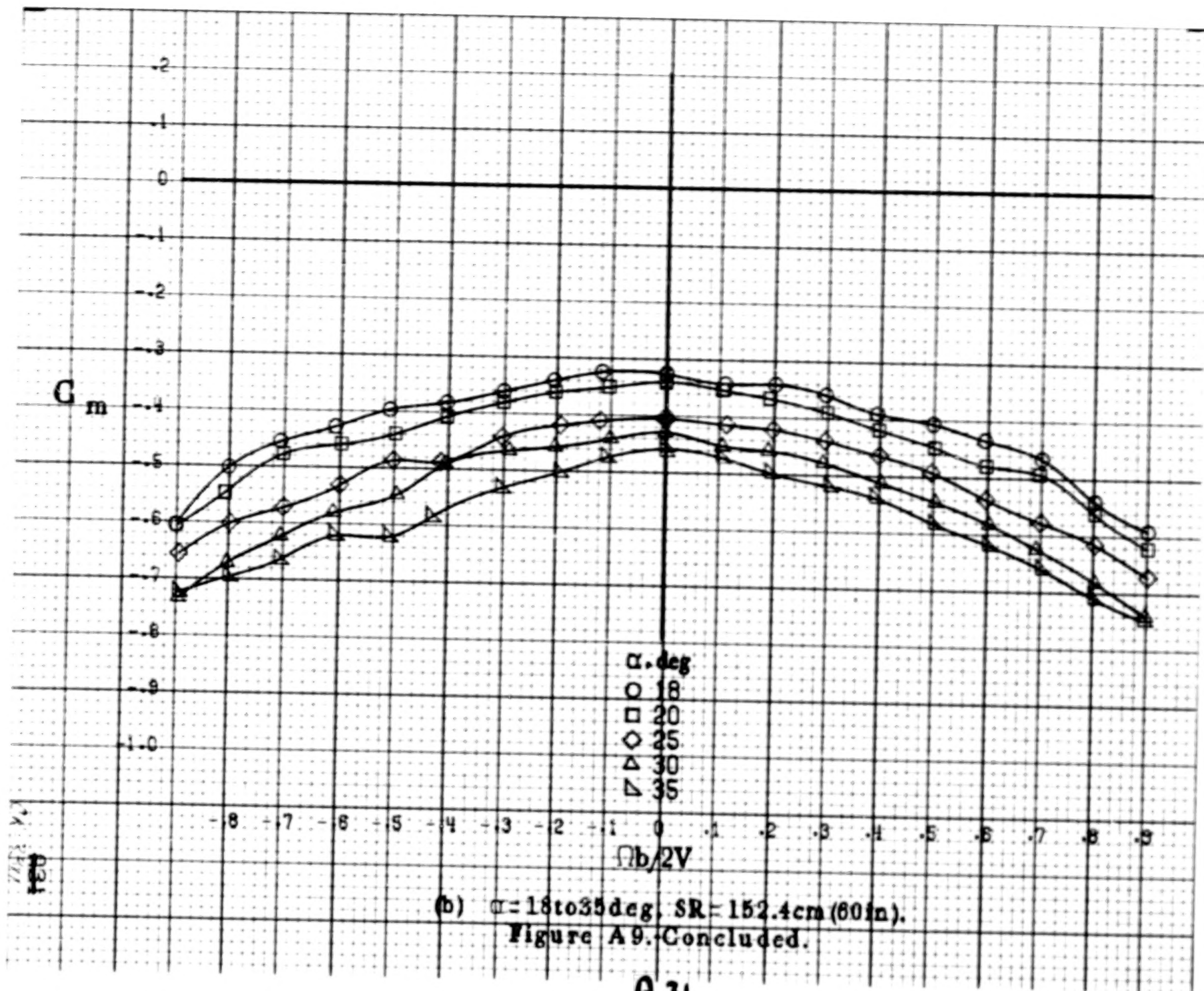


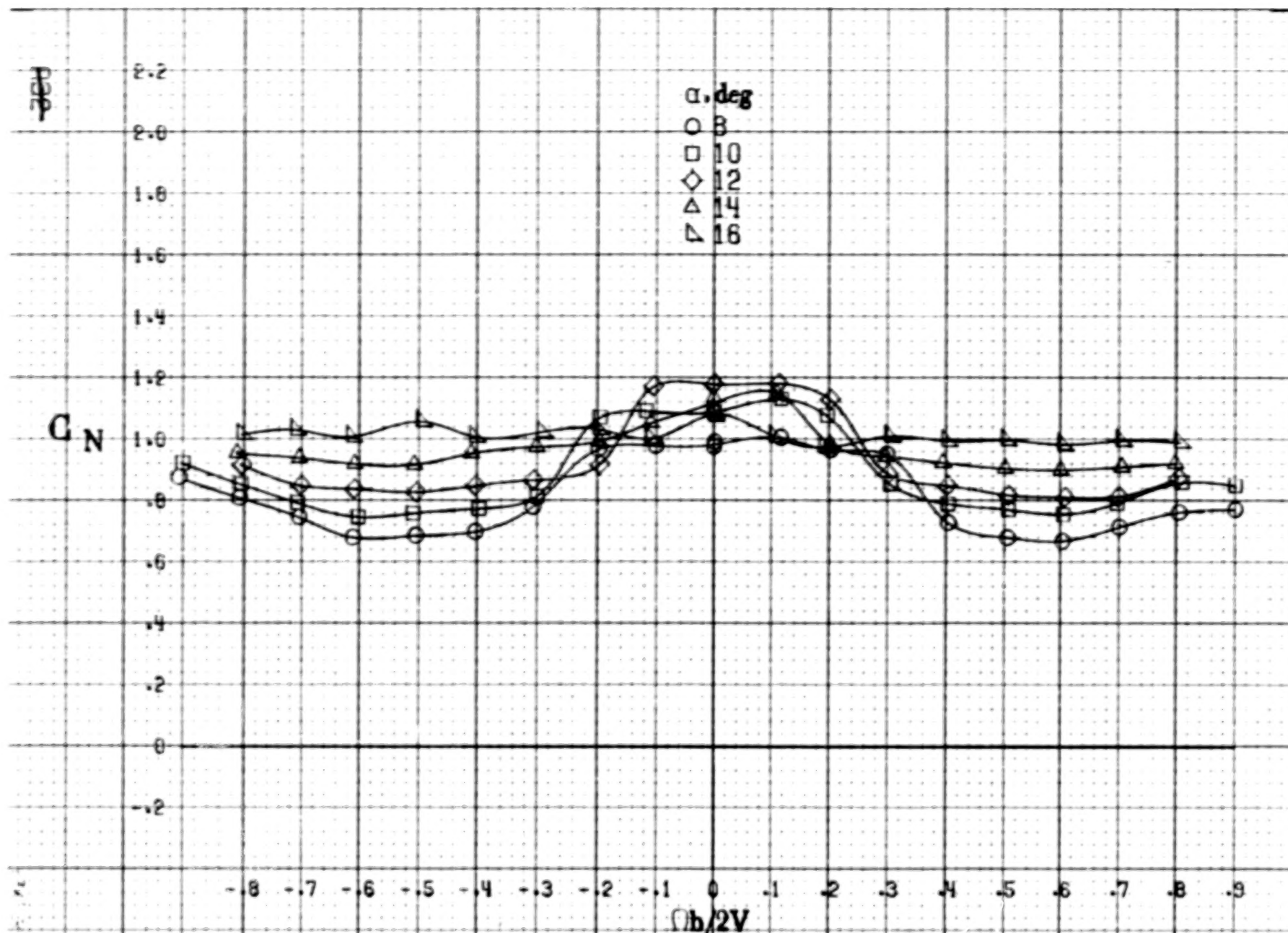
(b)  $\alpha = 18$  to  $35^\circ$ ,  $SR = 152.4 \text{ cm (60 in.)}$ .  
Figure A8. Concluded.



(a)  $\alpha = 8$  to  $16^\circ$ ,  $SR = 152.4\text{cm (60in)}$ .  
 Figure A9. Effect of rotation rate and angle of attack on pitching-moment coefficient for basic configuration.  $\delta_s = 17^\circ$ ,  $\delta_a = 0^\circ$ ,  $\delta_r = -24^\circ$ ,  $\beta = 0^\circ$ .

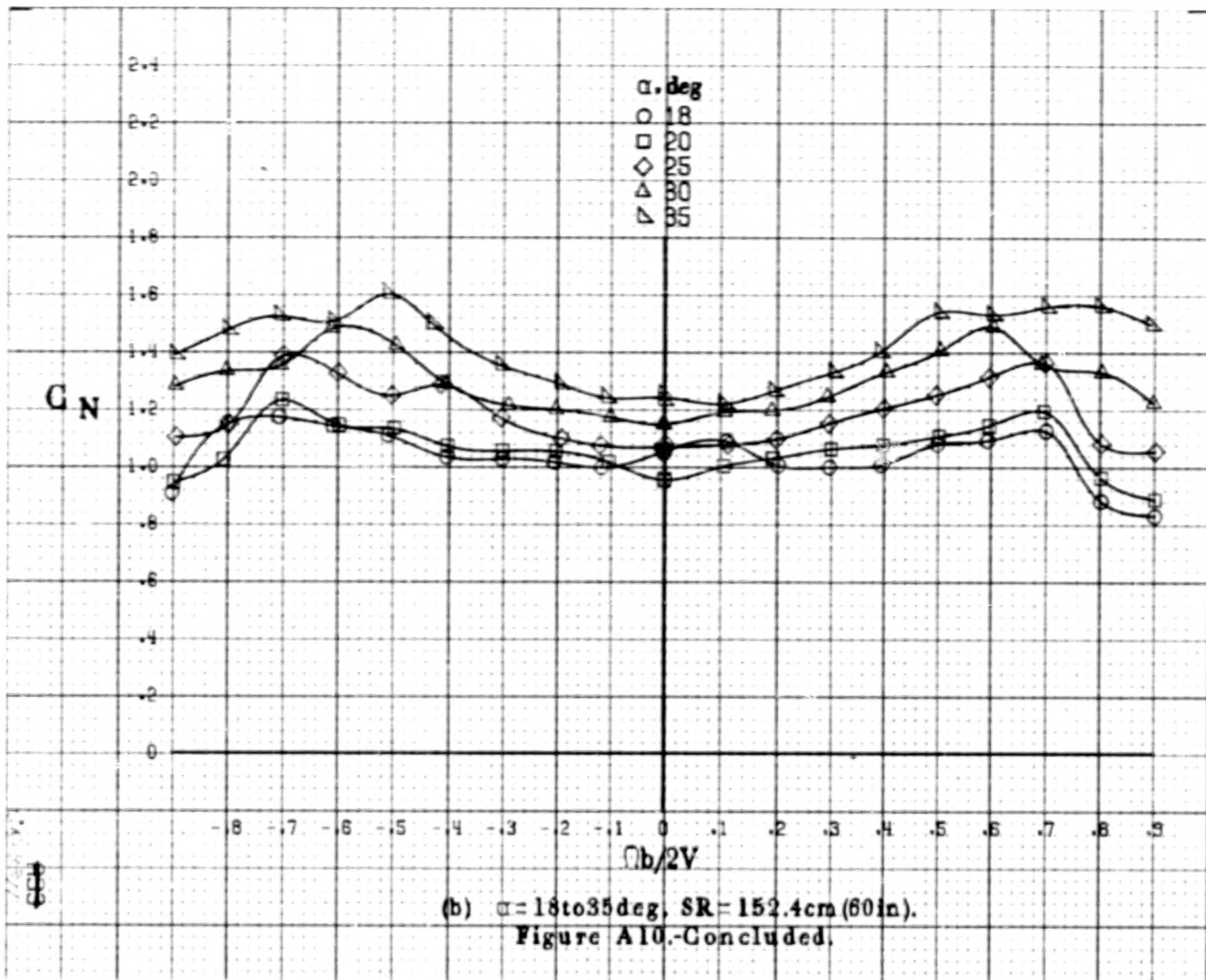


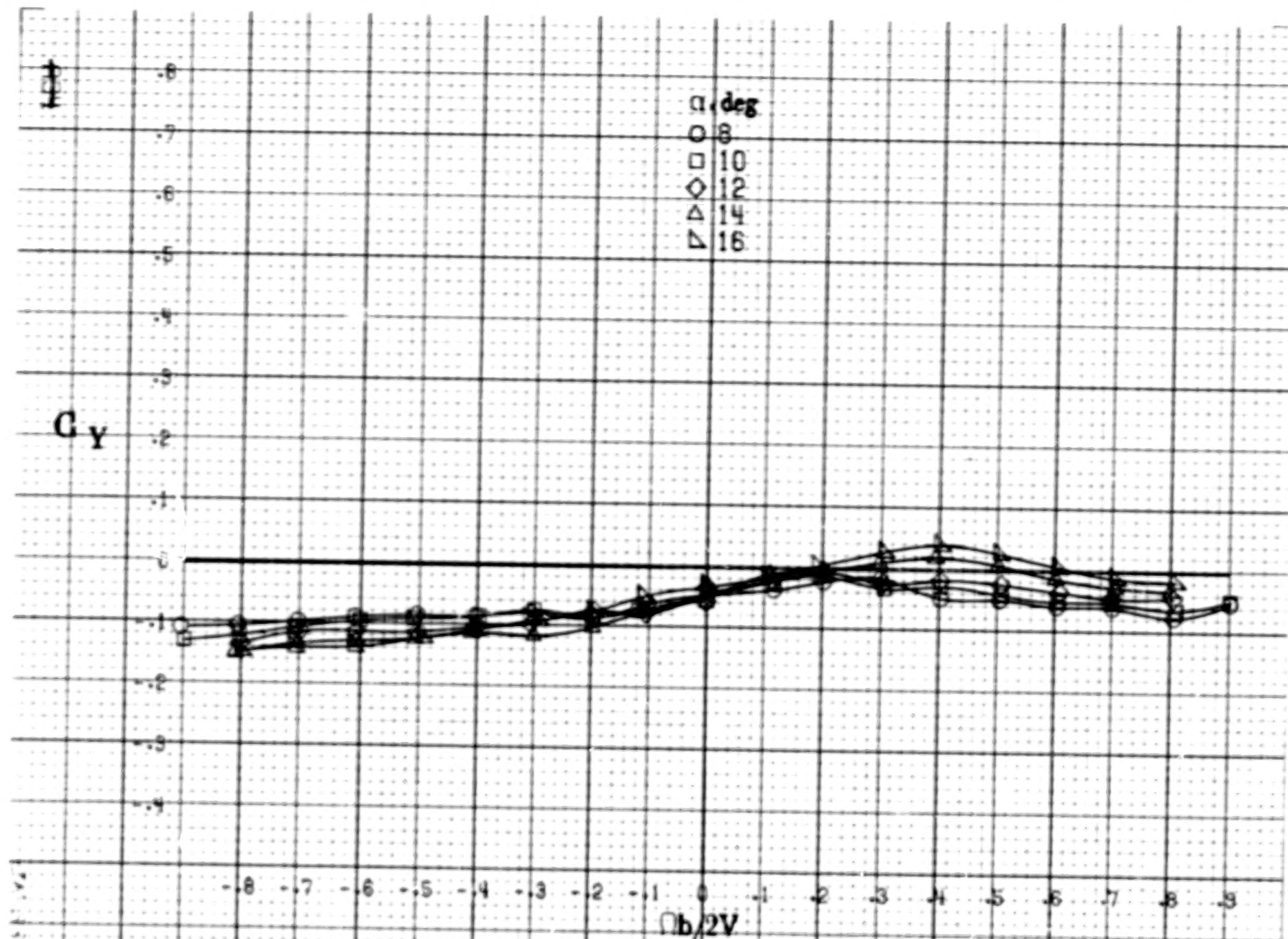




(a)  $\alpha = 8 \text{ to } 16 \text{ deg}$ ,  $SR = 152.4 \text{ cm (60 in)}$ .

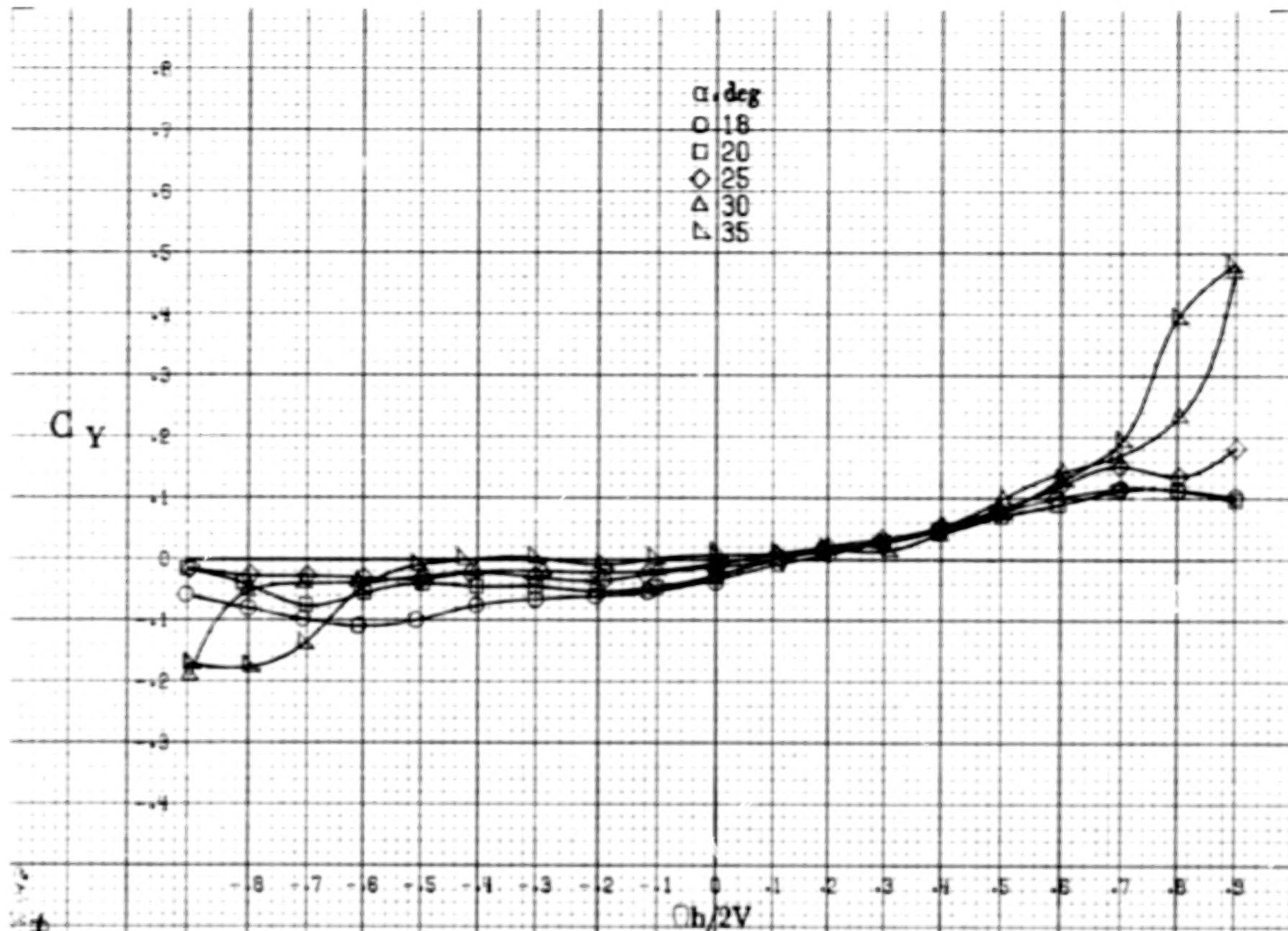
Figure A10. Effect of rotation rate and angle of attack on normal-force coefficient for basic configuration.  $\delta_s = 17^\circ$ ,  $\delta_a = 0^\circ$ ,  $\delta_r = -24^\circ$ ,  $\beta = 0^\circ$ .



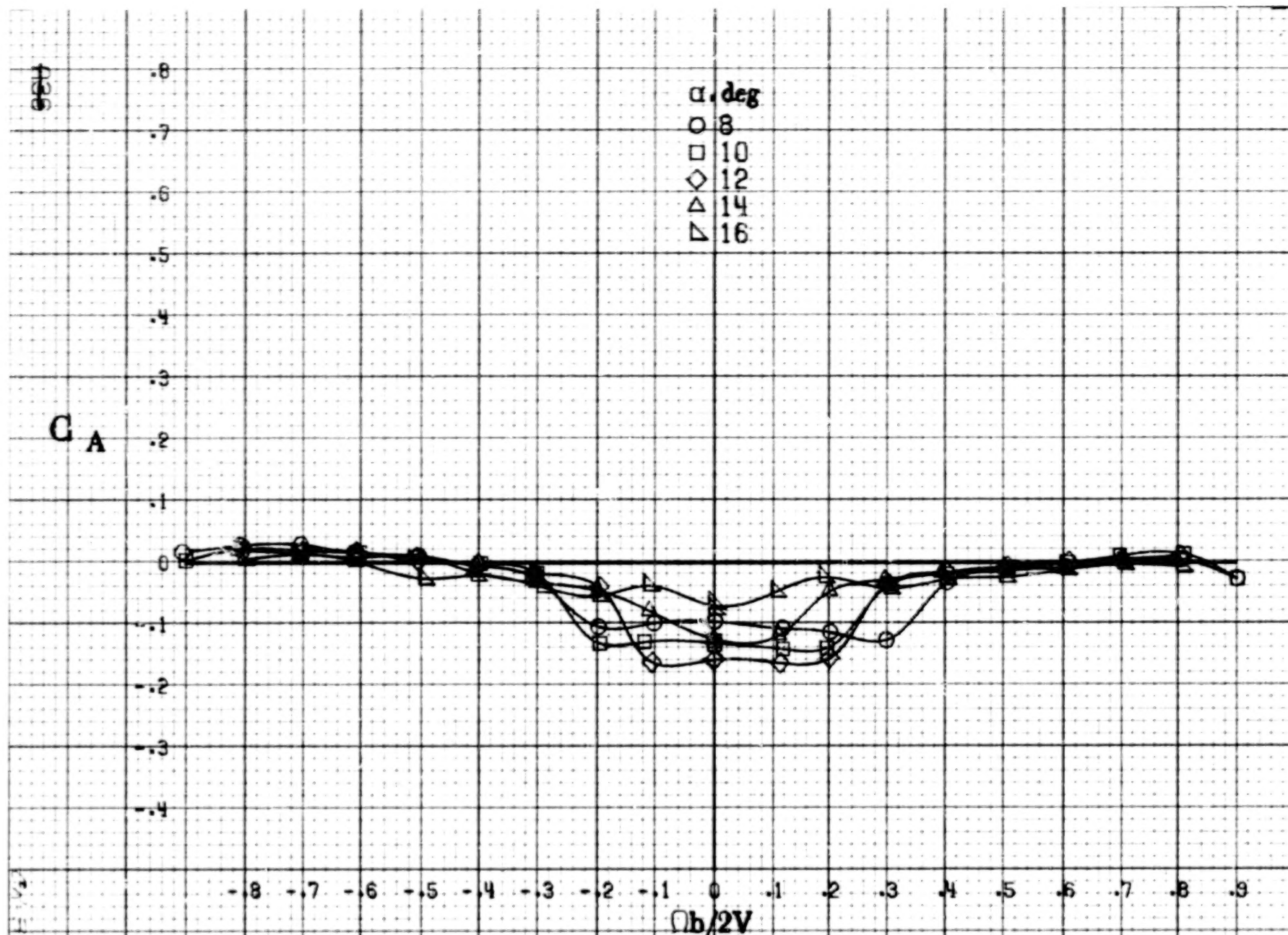


(a)  $\alpha = 8$  to  $16^\circ$ ,  $SR = 152.4 \text{ cm (60 in.)}$ .  
 Figure A11. Effect of rotation rate and angle of attack on side-force coefficient for basic configuration.  $\delta_s = 17^\circ$ ,  $\delta_a = 0^\circ$ ,  $\delta_r = -24^\circ$ ,  $\theta = 0^\circ$ .



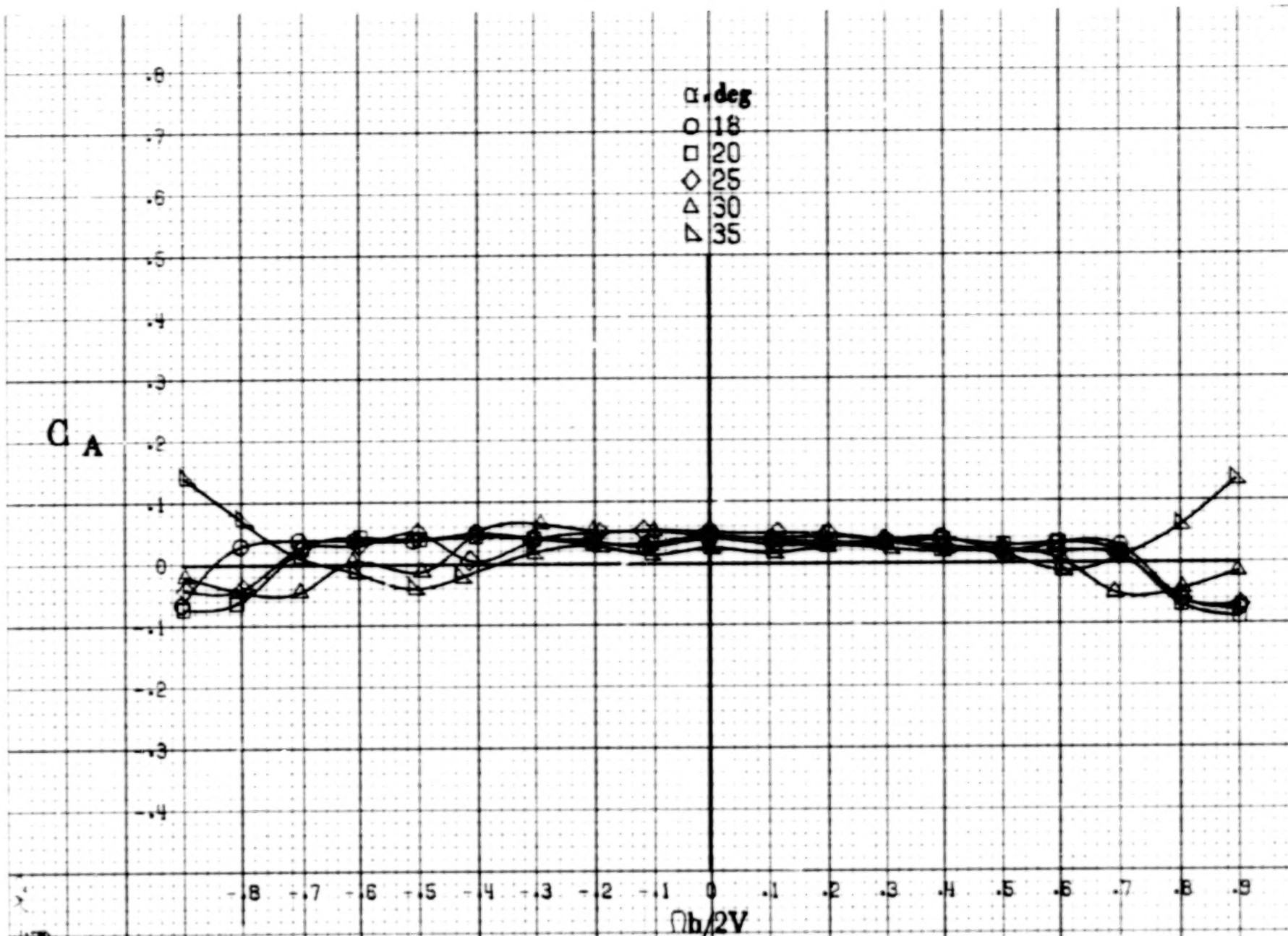


(b)  $\alpha = 18$  to  $35^\circ$ ,  $SR = 152.4$  cm (60 in).  
Figure A11.-Concluded.



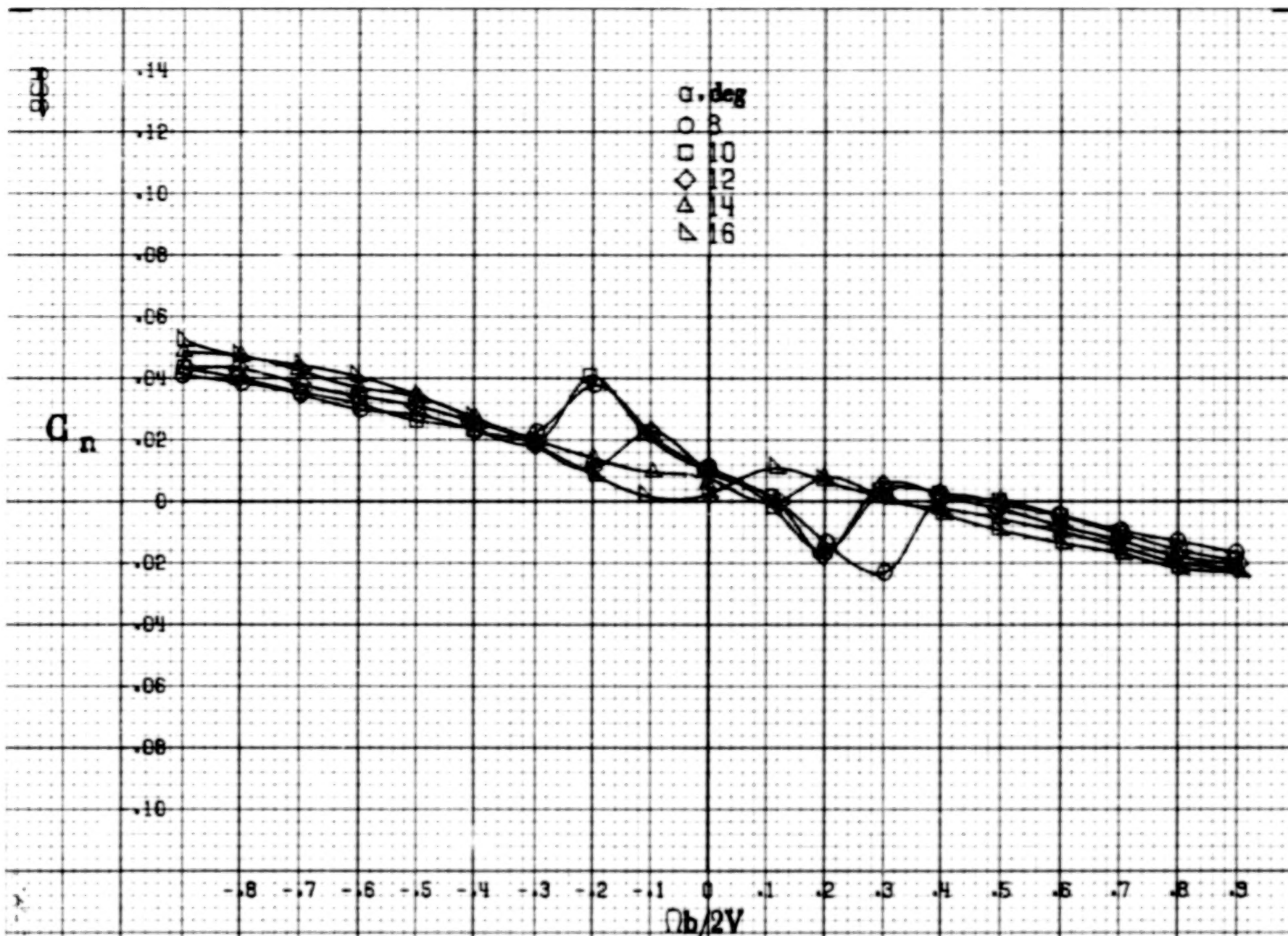
(a)  $\alpha = 8$  to  $16^\circ$ ,  $SR = 152.4\text{cm (60in)}$ .

Figure A12. Effect of rotation rate and angle of attack on axial force coefficient for basic configuration.  $\delta_s = 17^\circ$ ,  $\delta_a = 0^\circ$ ,  $\delta_r = -24^\circ$ ,  $\beta = 0^\circ$ .



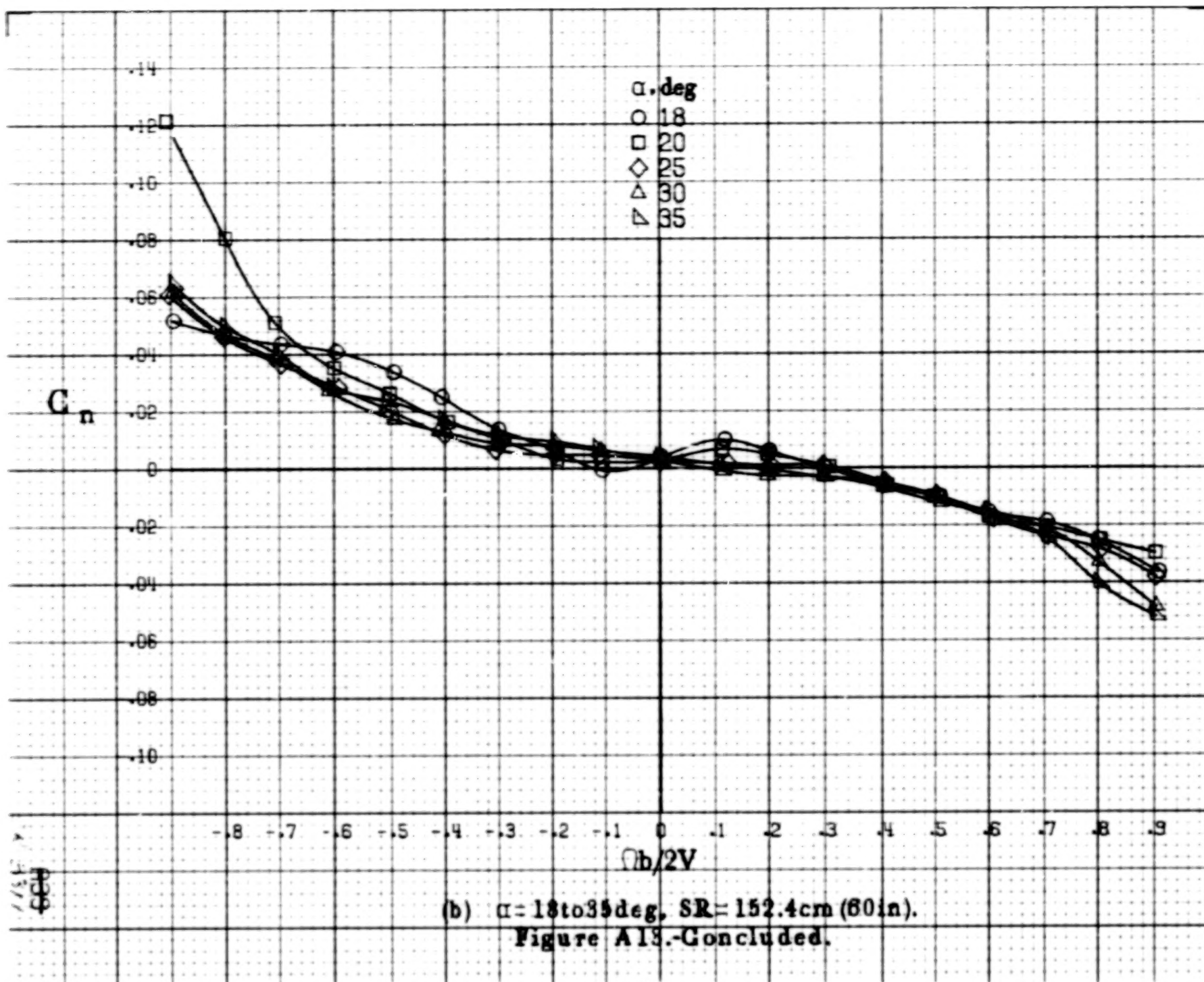
(b)  $\alpha = 18$  to  $35$  deg,  $SR = 152.4$  cm (60 in).

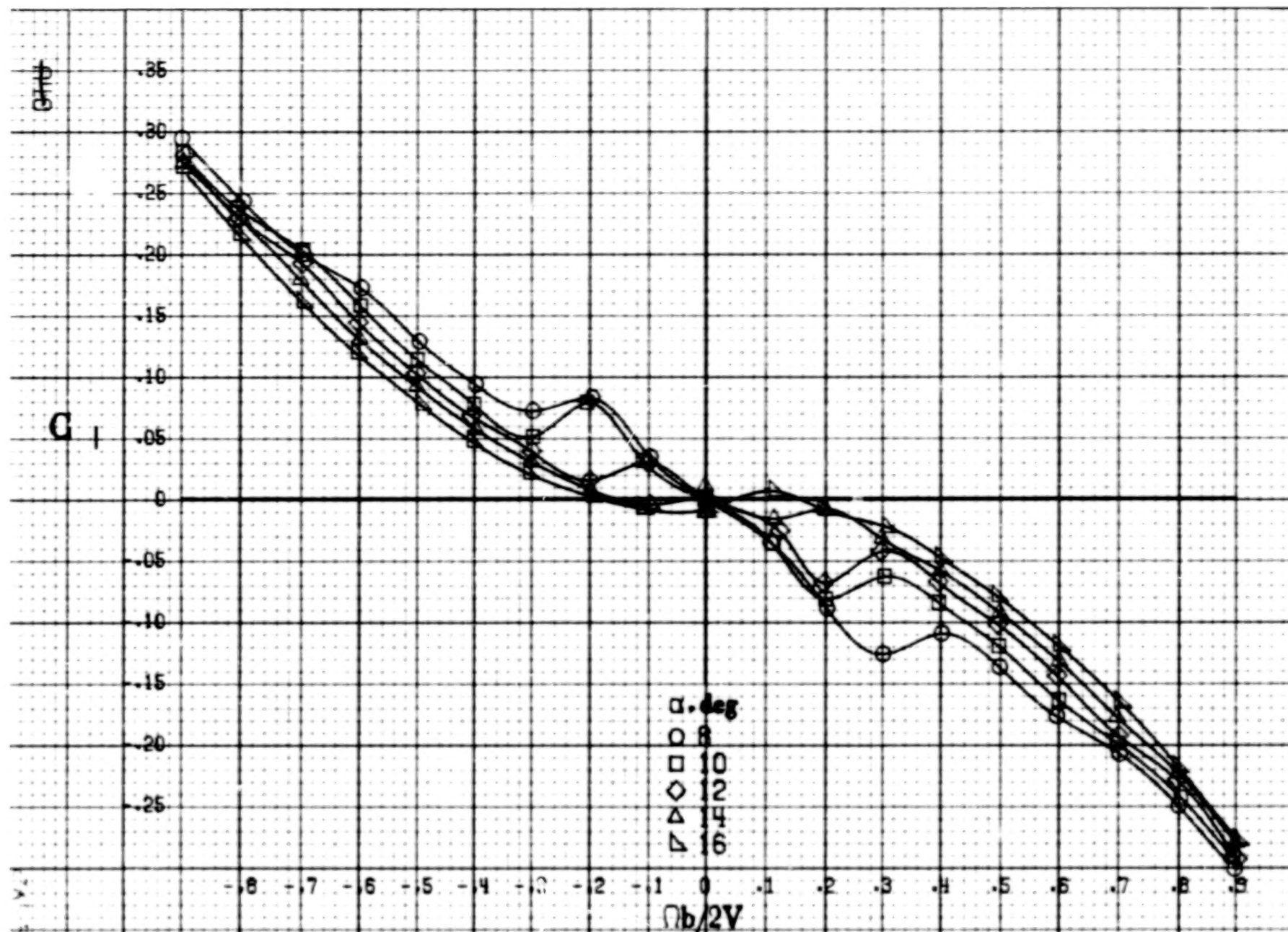
Figure A12.-Concluded.



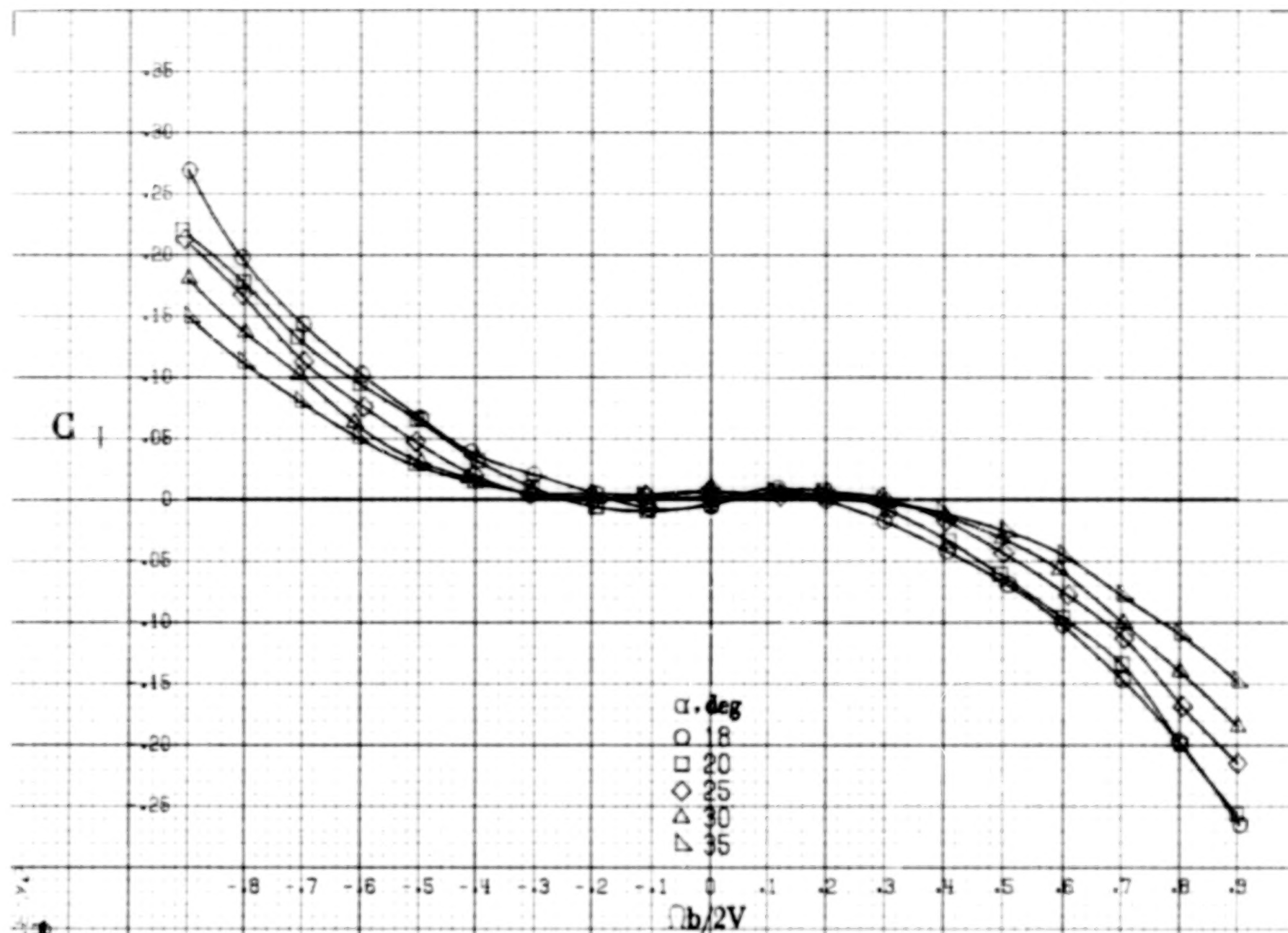
(a)  $\alpha = 8$  to  $16$  deg,  $SR = 152.4$  cm (60 in).  
 Figure A13. Effect of rotation rate and angle of attack on yawing-moment coefficient for basic configuration.  $\delta_e = -27^\circ$ ,  $\delta_a = 0^\circ$ ,  $\delta_r = -24^\circ$ ,  $\beta = 0^\circ$ .





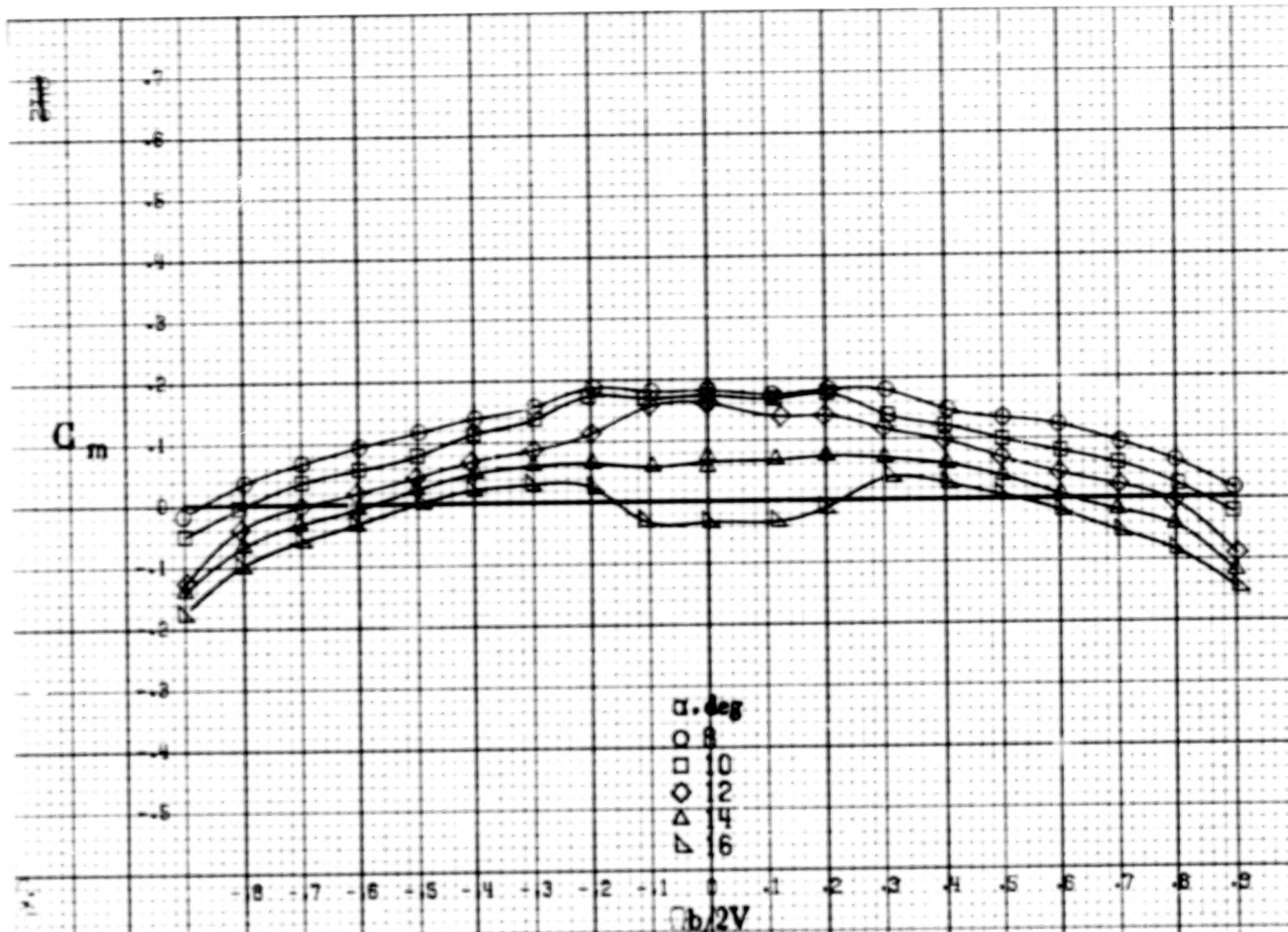


(a)  $\alpha = 8$  to  $16^\circ$ ,  $SR = 152.4 \text{ cm (60 in)}$ .  
 Figure A14. Effect of rotation rate and angle of attack on rolling-moment coefficient for basic configuration.  $\delta_c = -27^\circ$ ,  $\delta_a = 0^\circ$ ,  $\delta_r = -24^\circ$ ,  $\beta = 0^\circ$ .



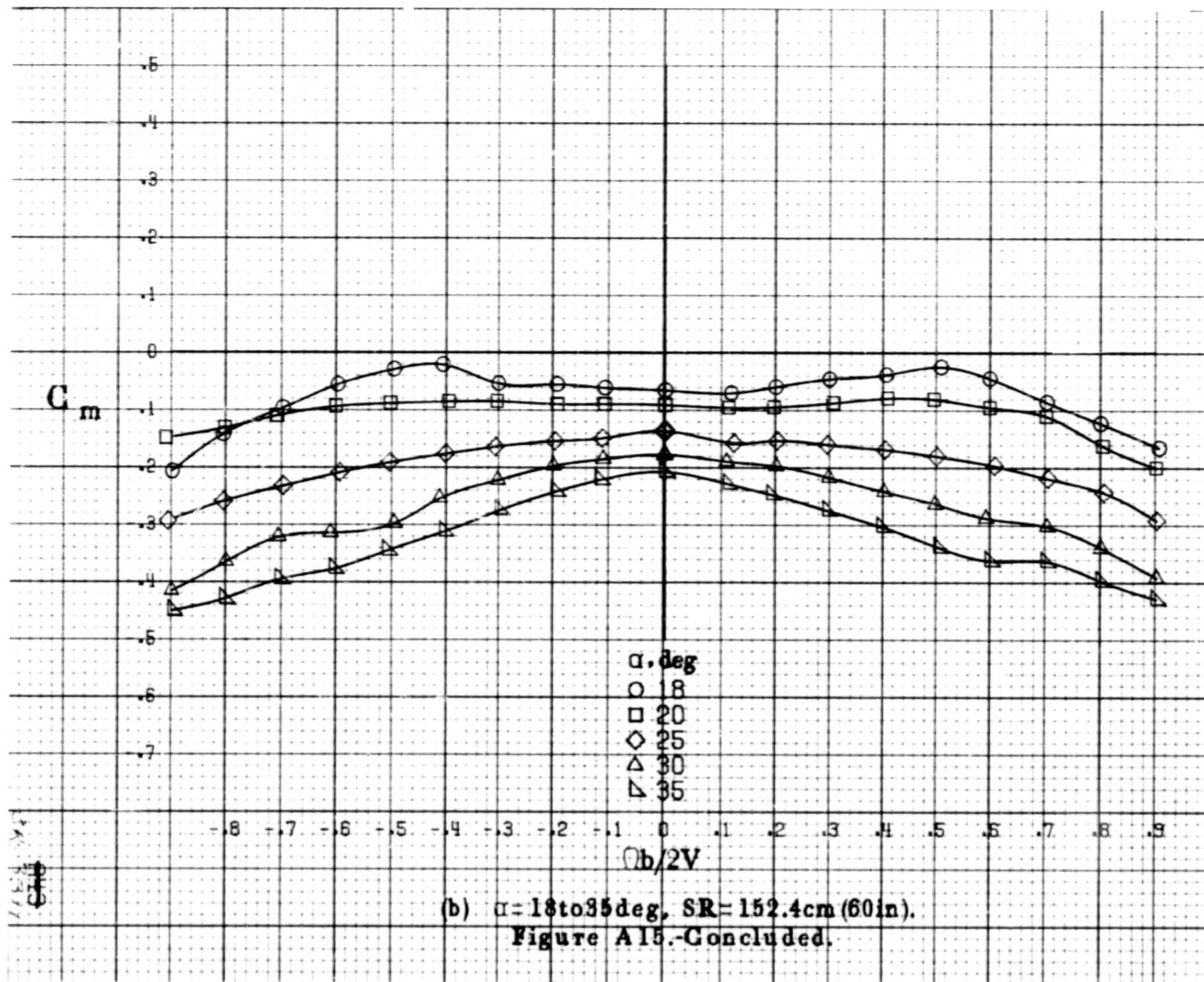
(b)  $\alpha = 18$  to  $35^\circ$ ,  $SR = 152.4\text{cm}$  (60 in).

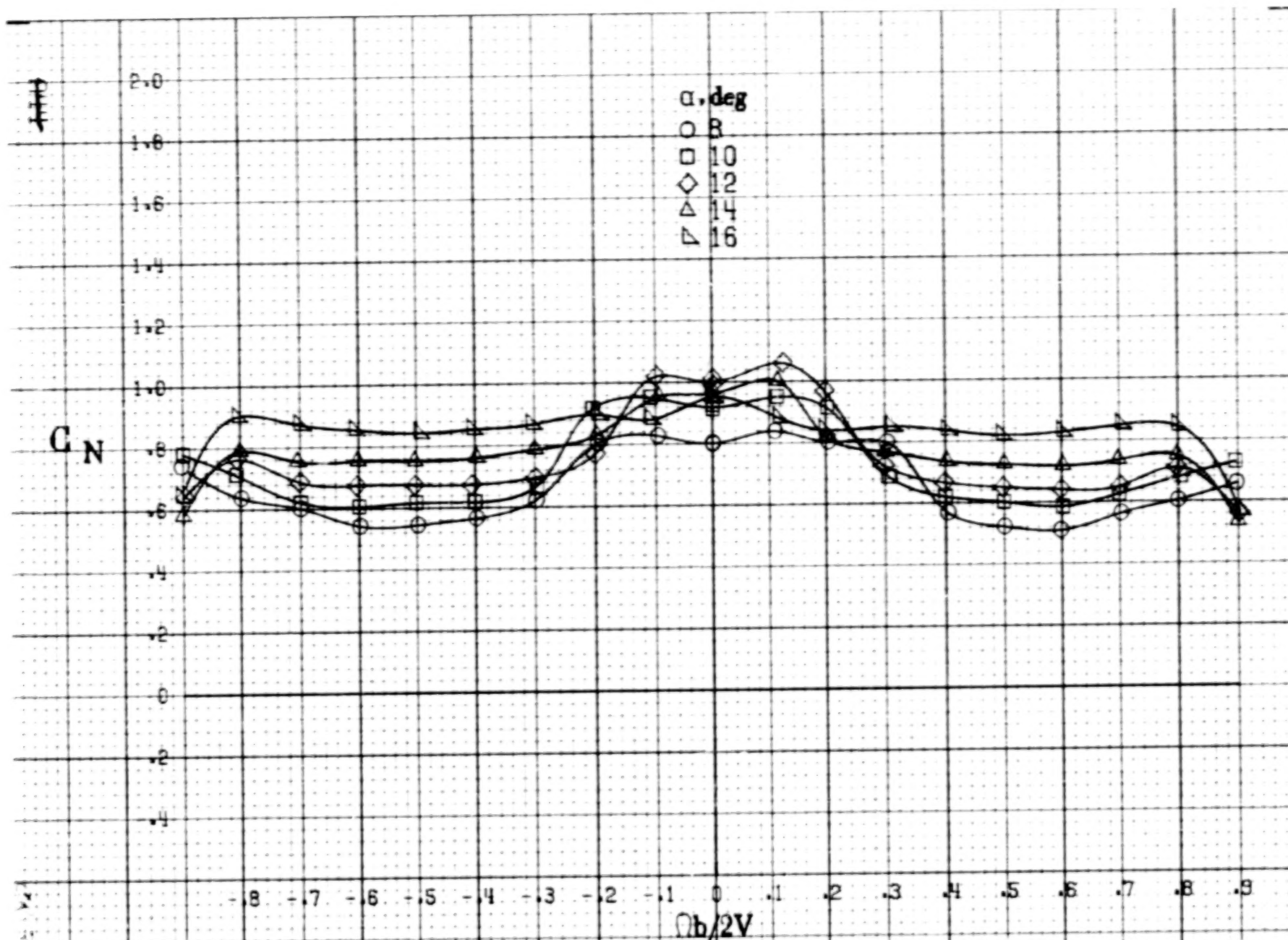
Figure A14.-Concluded.



(a)  $\alpha = 8$  to  $16$  deg,  $SR = 152.4$  cm (60 in).  
 Figure A15. Effect of rotation rate and angle of attack on pitching moment coefficient for basic configuration.  $\delta_s = -27^\circ$ ,  $\delta_a = 0^\circ$ ,  $\delta_r = -24^\circ$ ,  $\beta = 0^\circ$ .

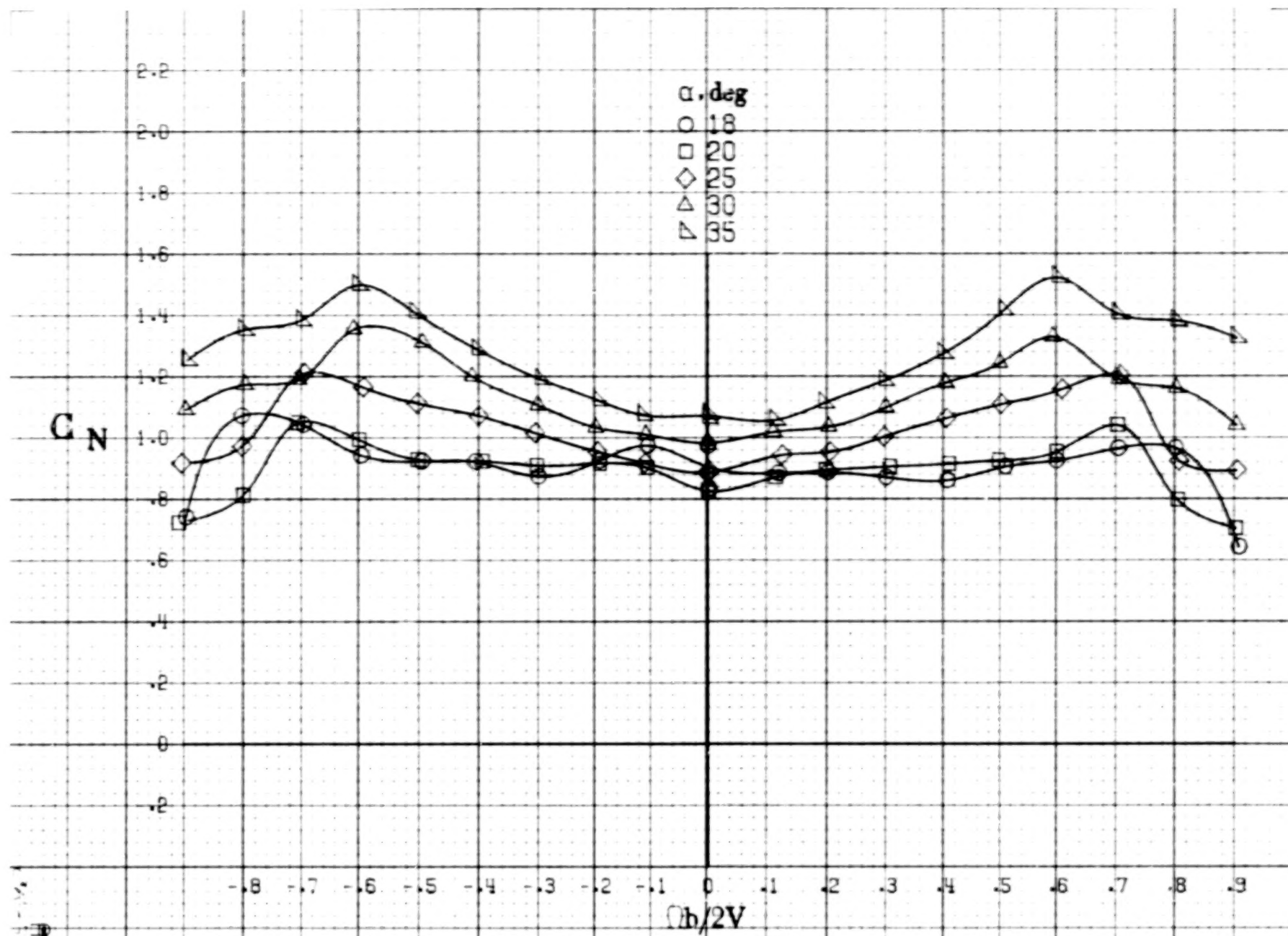




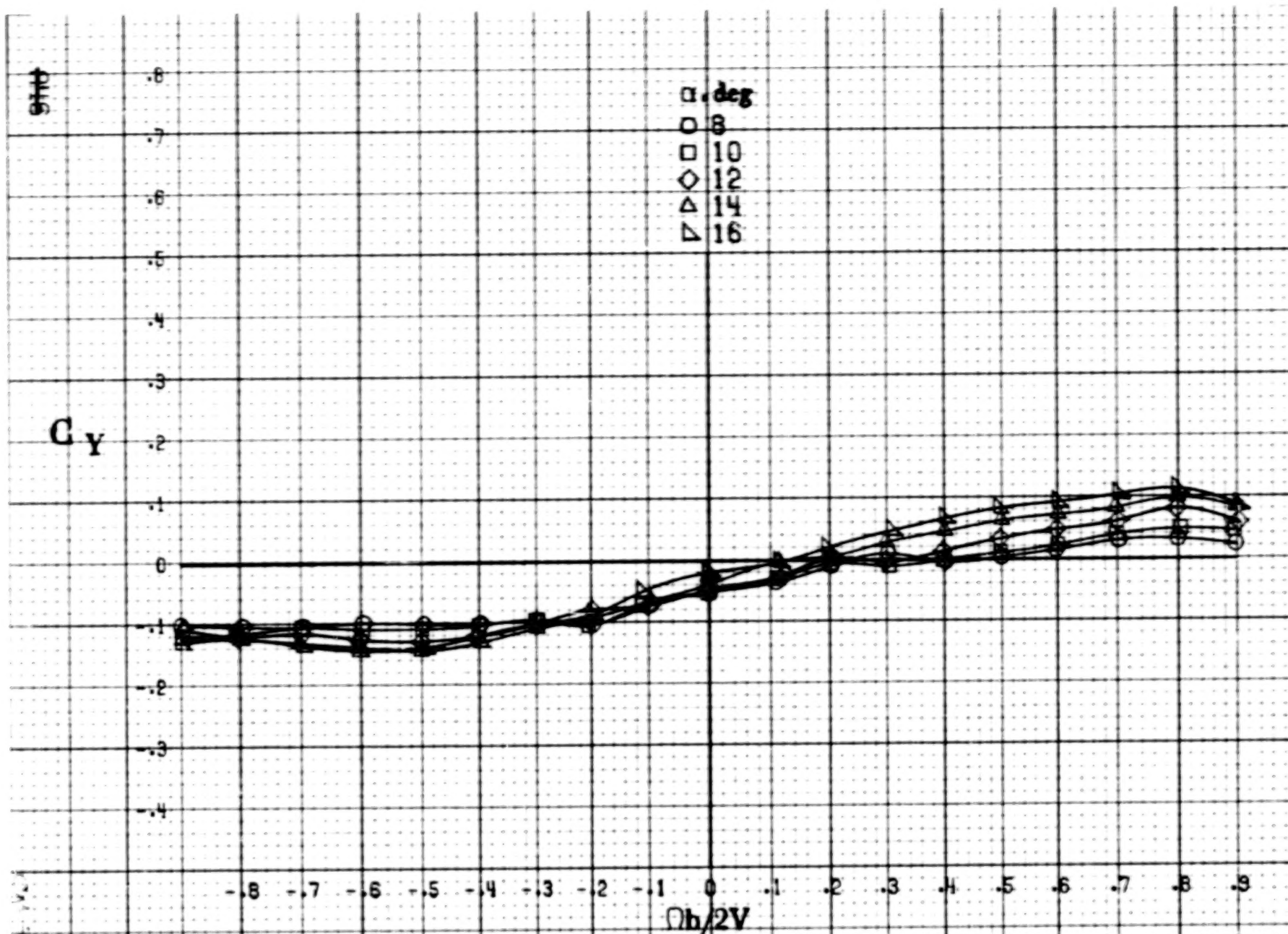


(a)  $\alpha = 8$  to  $16$  deg,  $SR = 152.4$  cm (60 in).

Figure A16. Effect of rotation rate and angle of attack on normal-force coefficient for basic configuration.  $\delta_e = -27^\circ$ ,  $\delta_a = 0^\circ$ ,  $\delta_r = -24^\circ$ ,  $\beta = 0^\circ$ .



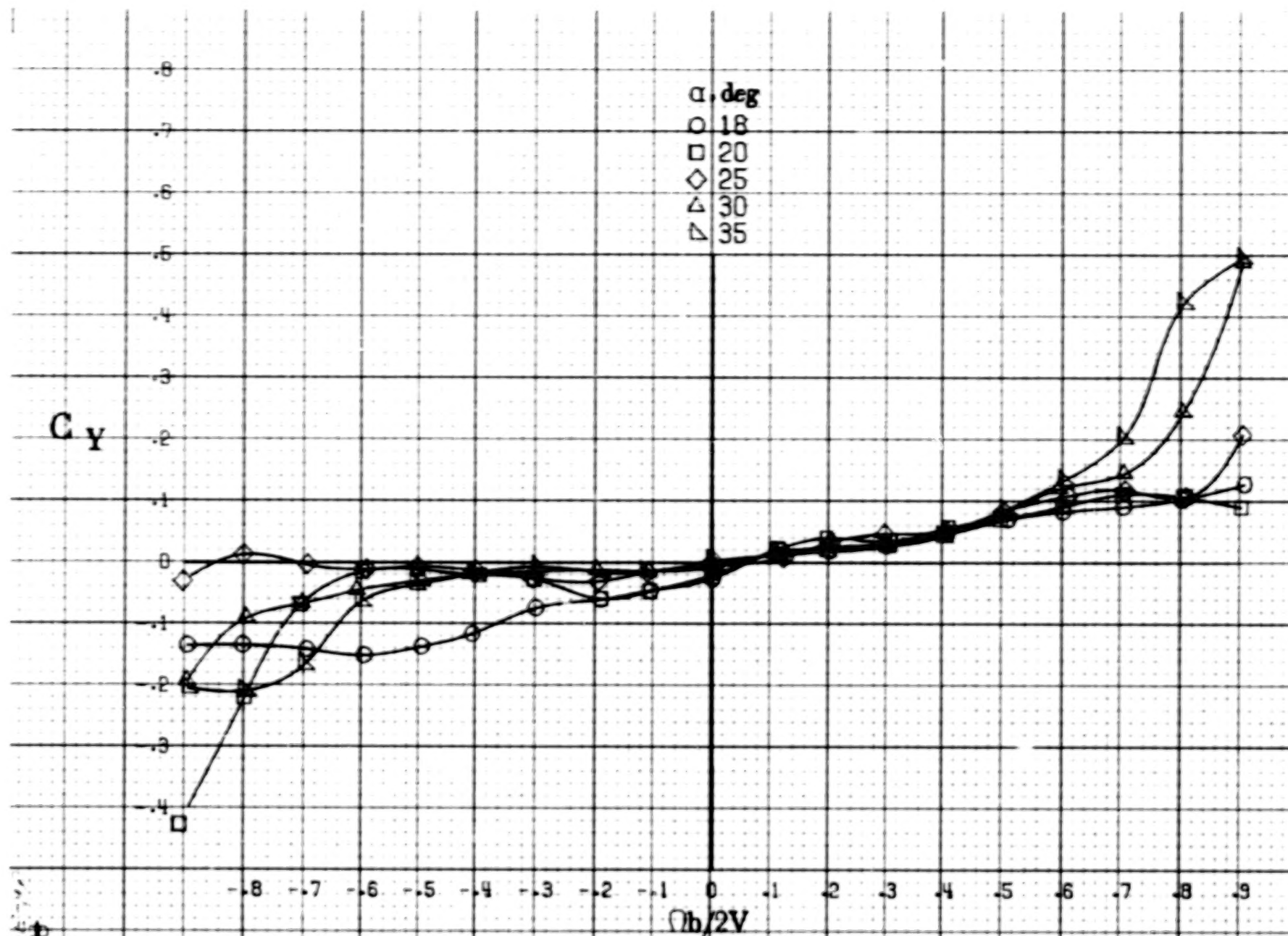
(b)  $\alpha = 18$  to  $35^\circ$ ,  $SR = 152.4\text{cm}$  (60 in).  
Figure A16.-Concluded.



(a)  $\alpha = 8$  to  $16^\circ$ ,  $SR = 152.4\text{cm (60in.)}$ .

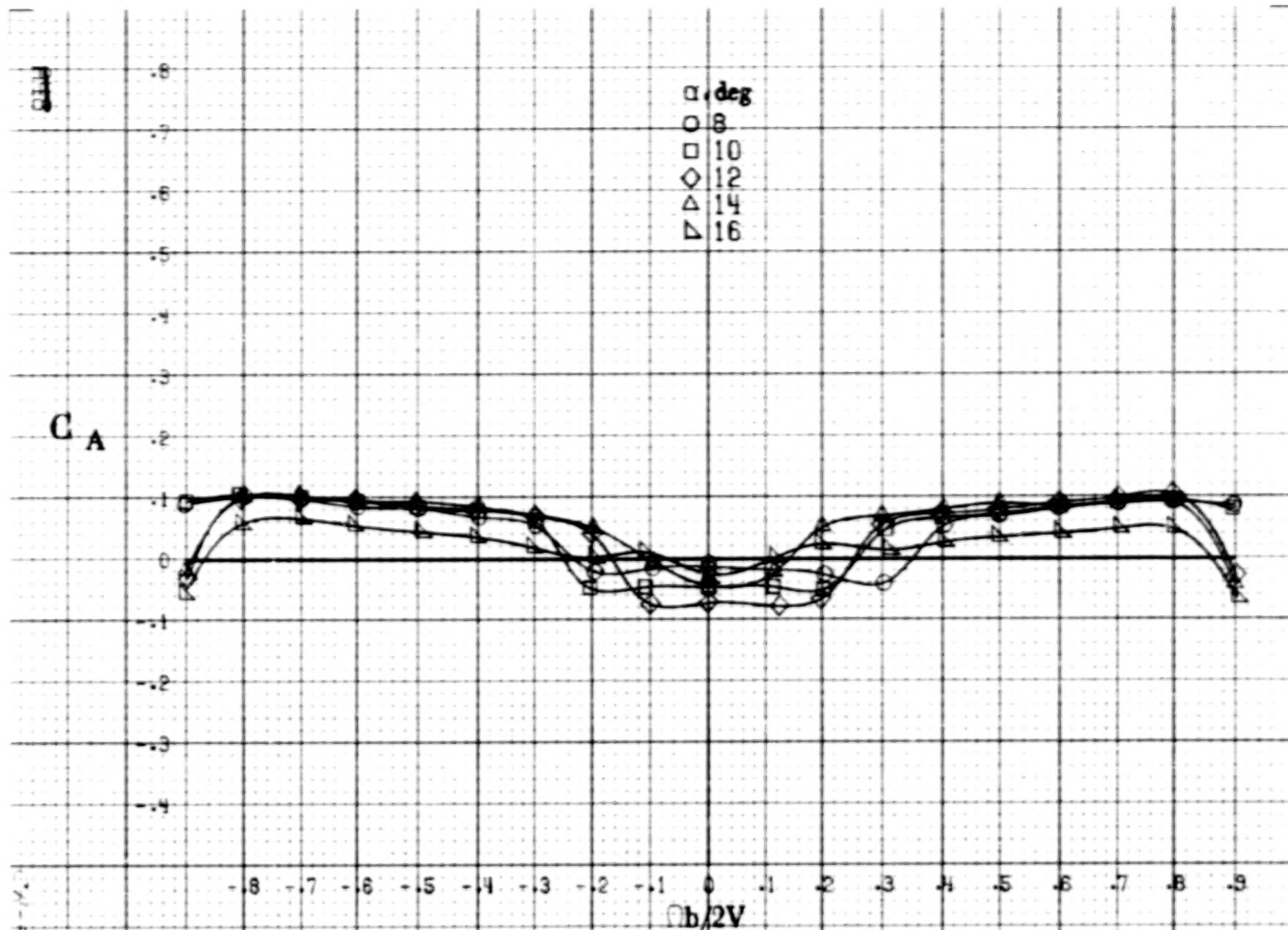
Figure A17. Effect of rotation rate and angle of attack on side-force coefficient for basic configuration.  $\delta_s = -27^\circ$ ,  $\delta_a = 0^\circ$ ,  $\delta_r = -24^\circ$ ,  $\beta = 0^\circ$ .



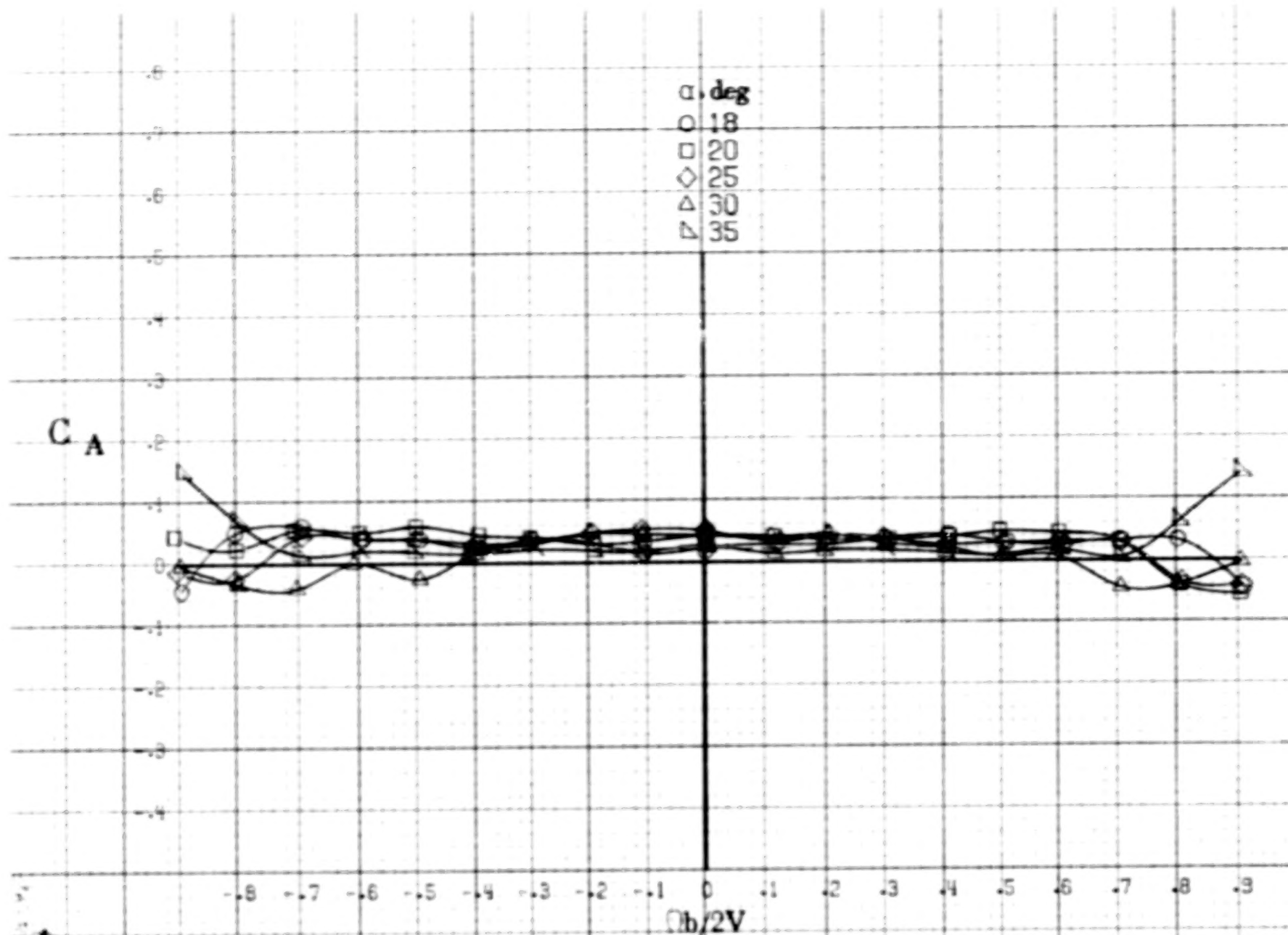


(b)  $\alpha = 18$  to  $35$  deg, SR = 152.4 cm (60 in).

Figure A17.-Concluded.

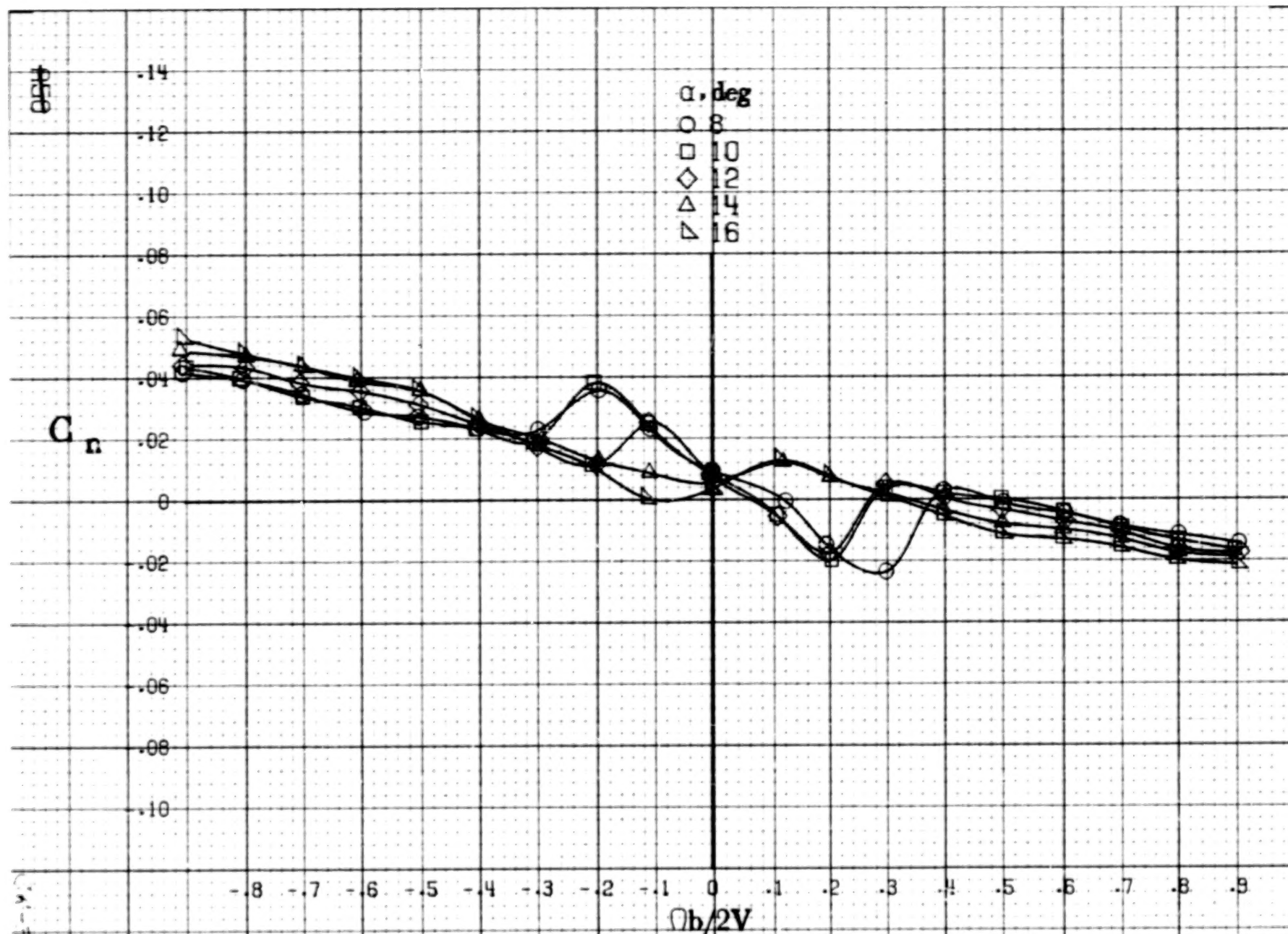


(a)  $\alpha = 8$  to  $16^\circ$ ,  $SR = 152.4 \text{ cm (60 in.)}$ .  
 Figure A18. Effect of rotation rate and angle of attack on axial-force coefficient for basic configuration.  $\delta_s = -27^\circ$ ,  $\delta_n = 0^\circ$ ,  $\delta_r = -24^\circ$ ,  $\beta = 0^\circ$ .



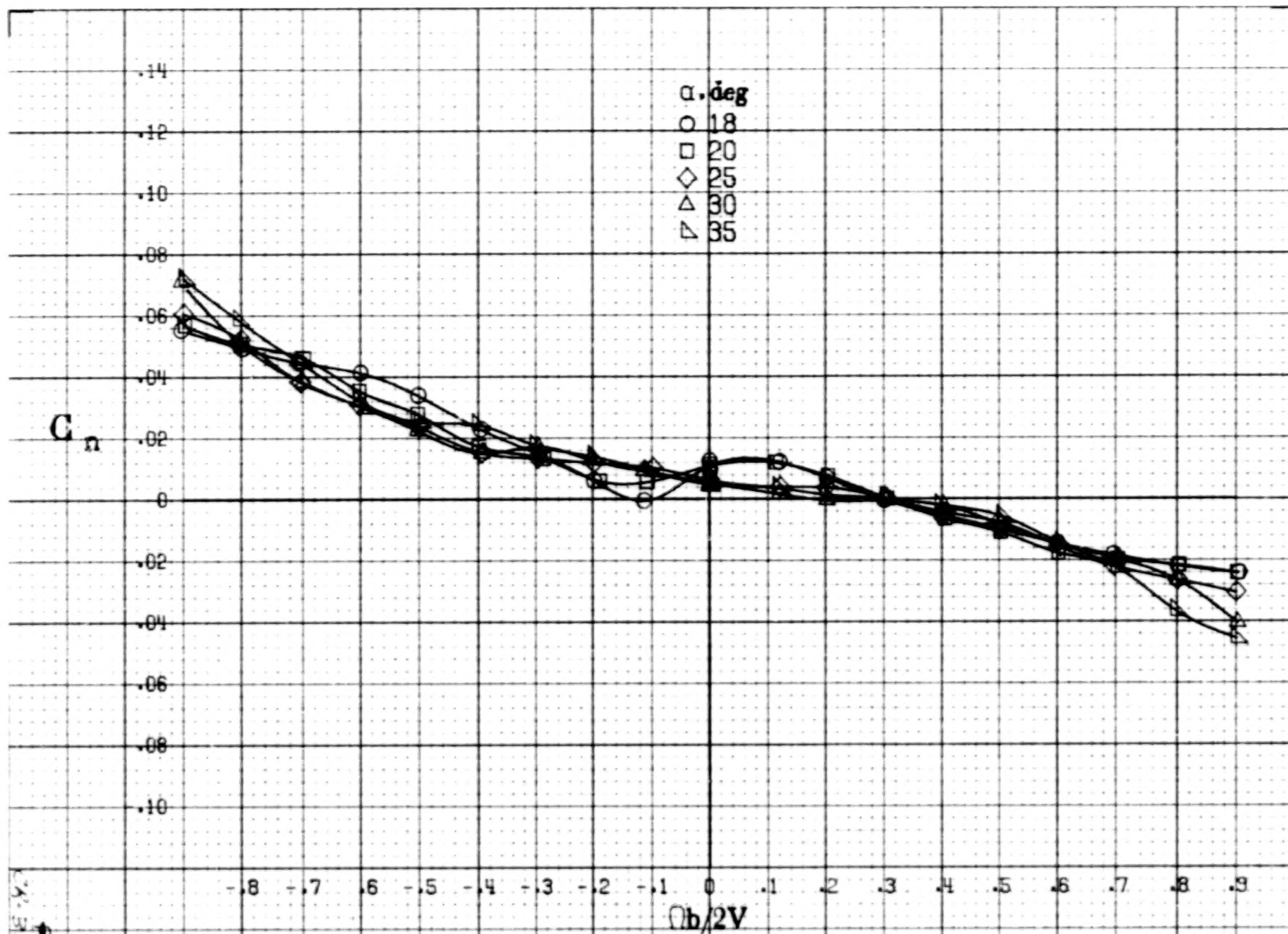
(b)  $\alpha = 18$  to  $35^\circ$ ,  $SR = 152.4\text{cm}$  (60 in).  
Figure A18.-Concluded.





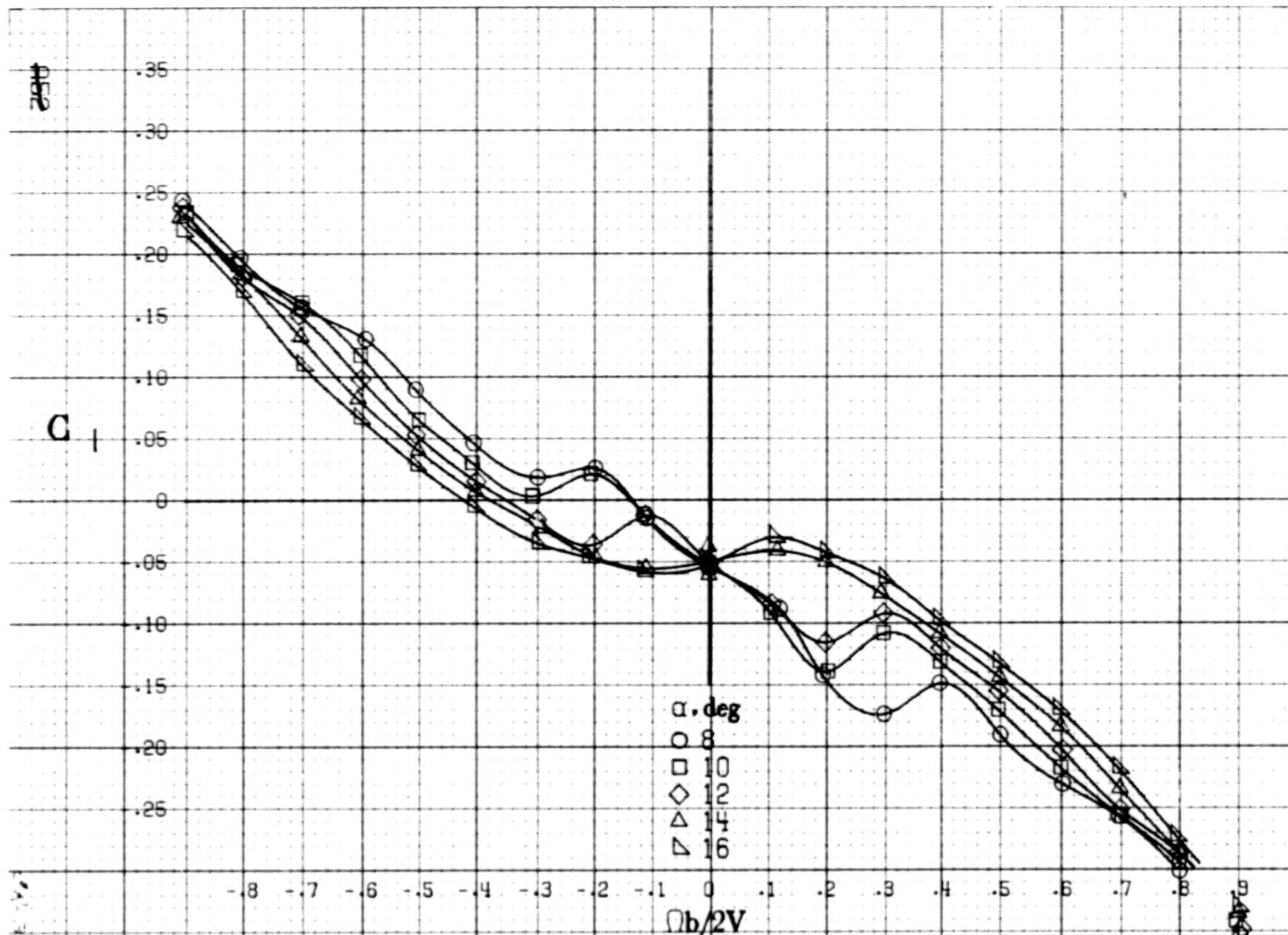
(a)  $\alpha = 8$  to  $16$  deg,  $SR = 152.4$  cm (60 in).

Figure A19. Effect of rotation rate and angle of attack on yawing-moment coefficient for basic configuration.  $\delta_e = -27^\circ$ ,  $\delta_a = 19.0^\circ$ ,  $\delta_r = -24^\circ$ ,  $B = 0^\circ$ .



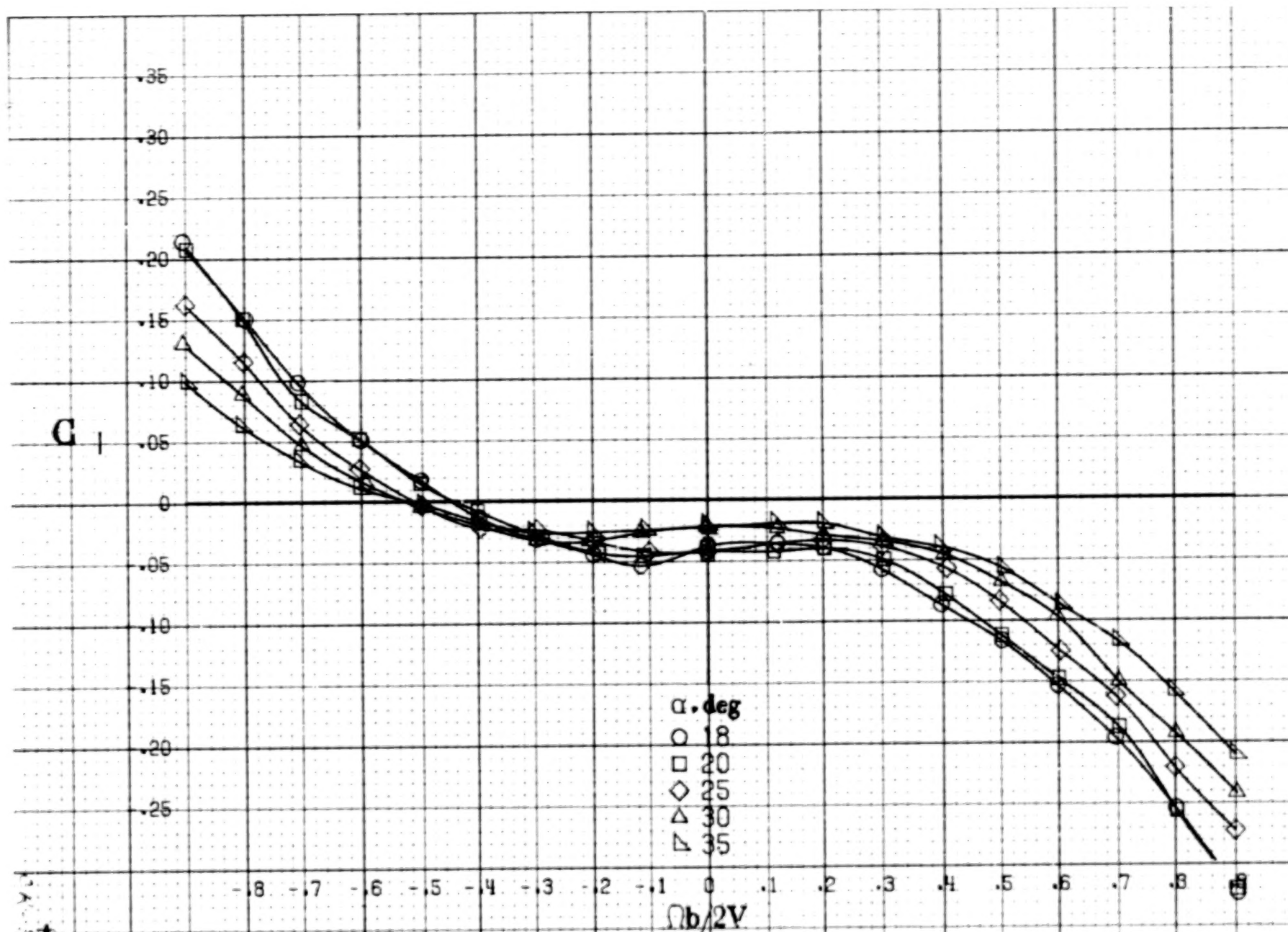
(b)  $\alpha = 18$  to  $35^\circ$ ,  $SR = 152.4\text{cm}$  (60 in).

Figure A19.-Concluded.



(a)  $\alpha = 8$  to  $16$  deg,  $SR = 152.4$  cm (60 in).

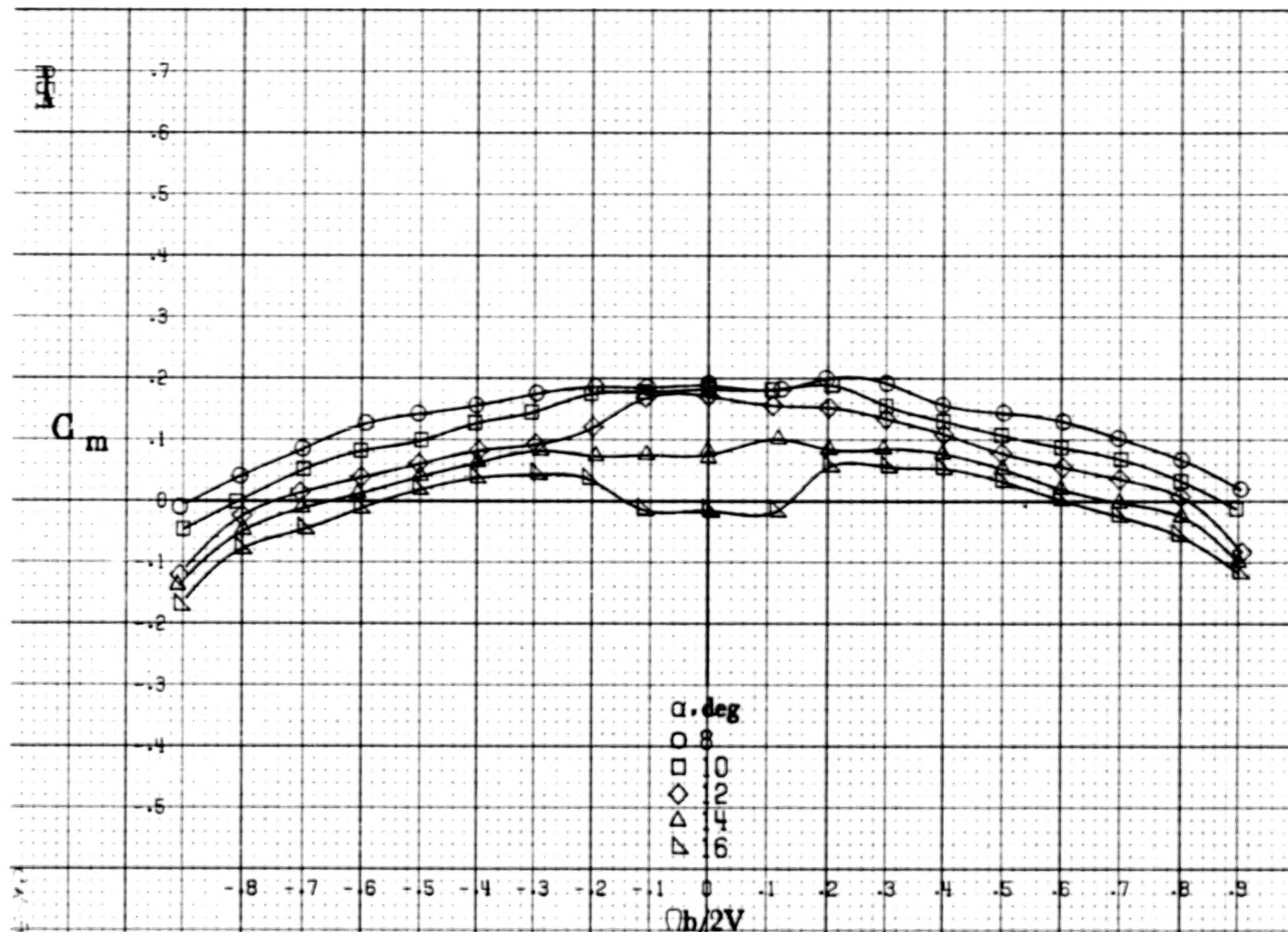
Figure A20. Effect of rotation rate and angle of attack on rolling-moment coefficient for basic configuration.  $\delta_c = -27^\circ$ ,  $\delta_a = 19.0^\circ$ ,  $\delta_r = -24^\circ$ ,  $B = 0^\circ$ .



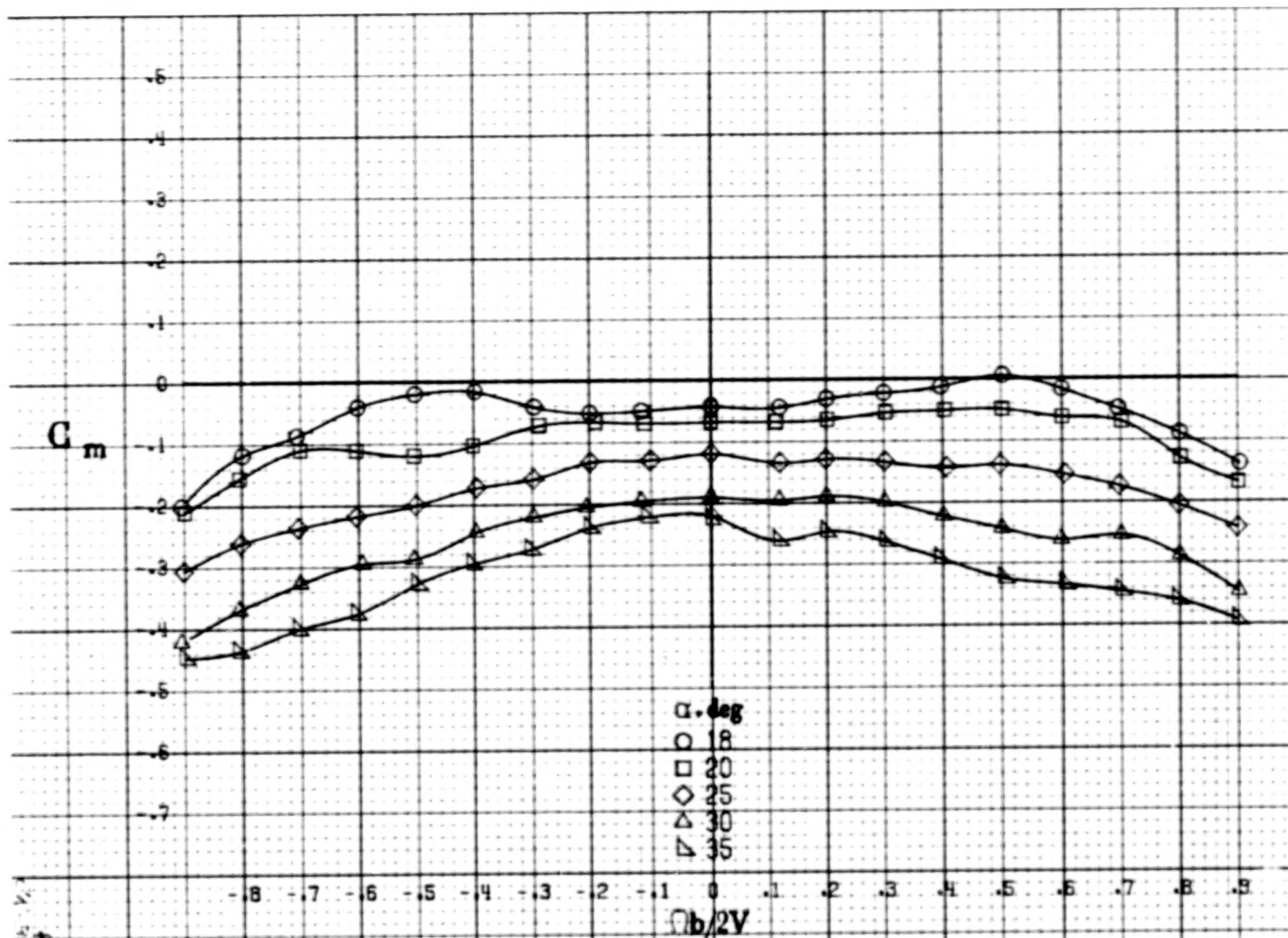
(b)  $\alpha = 18$  to  $35$  deg, SR = 152.4 cm (60 in).

Figure A20.-Concluded.



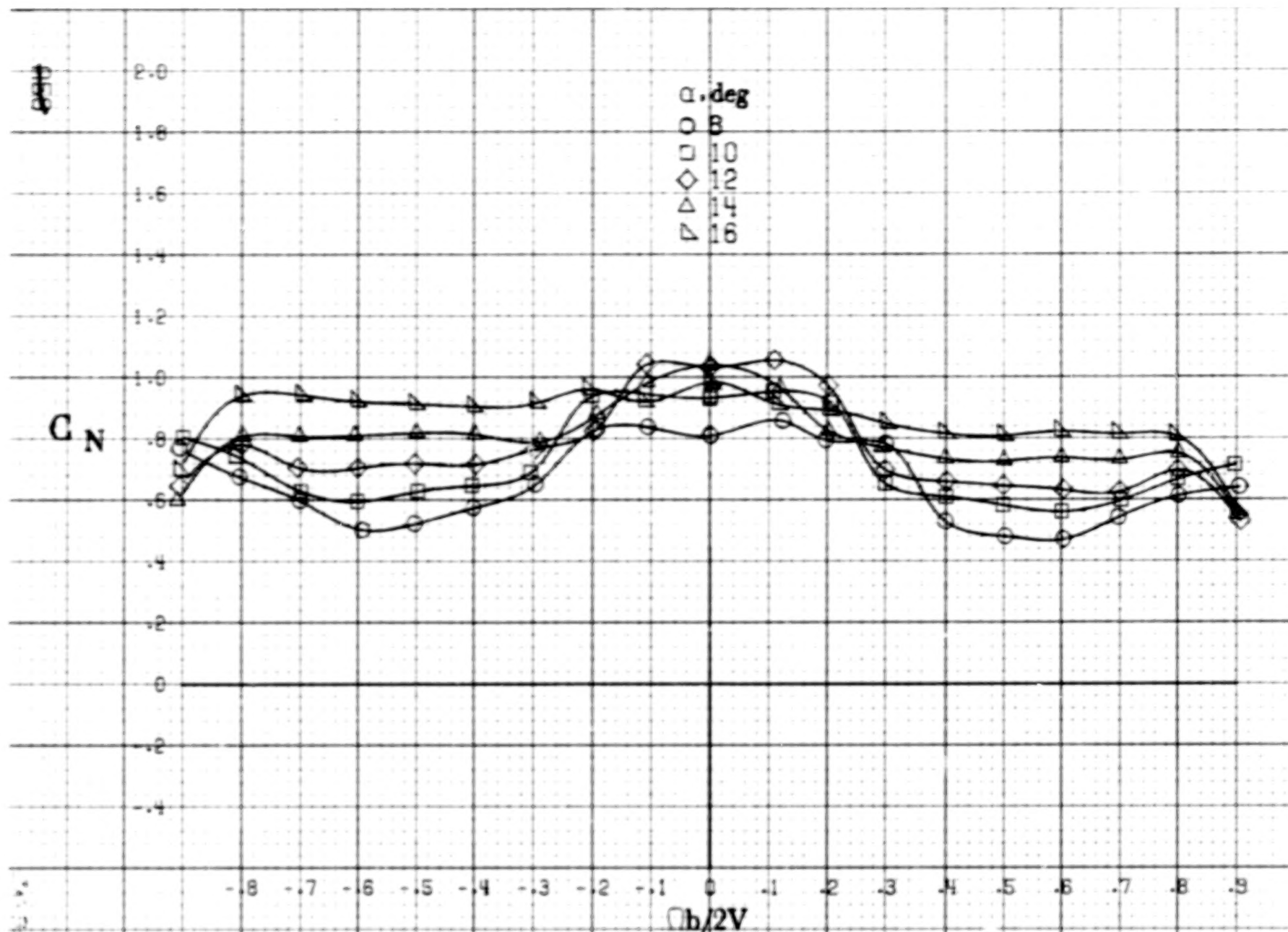


(a)  $\alpha = 8$  to  $16^\circ$ ,  $SR = 152.4 \text{ cm (60 in)}$ .  
 Figure A21. Effect of rotation rate and angle of attack on pitching-moment coefficient for basic configuration.  $\delta_e = -27^\circ$ ,  $\delta_a = 19.0^\circ$ ,  $\delta_r = -24^\circ$ ,  $\beta = 0^\circ$ .

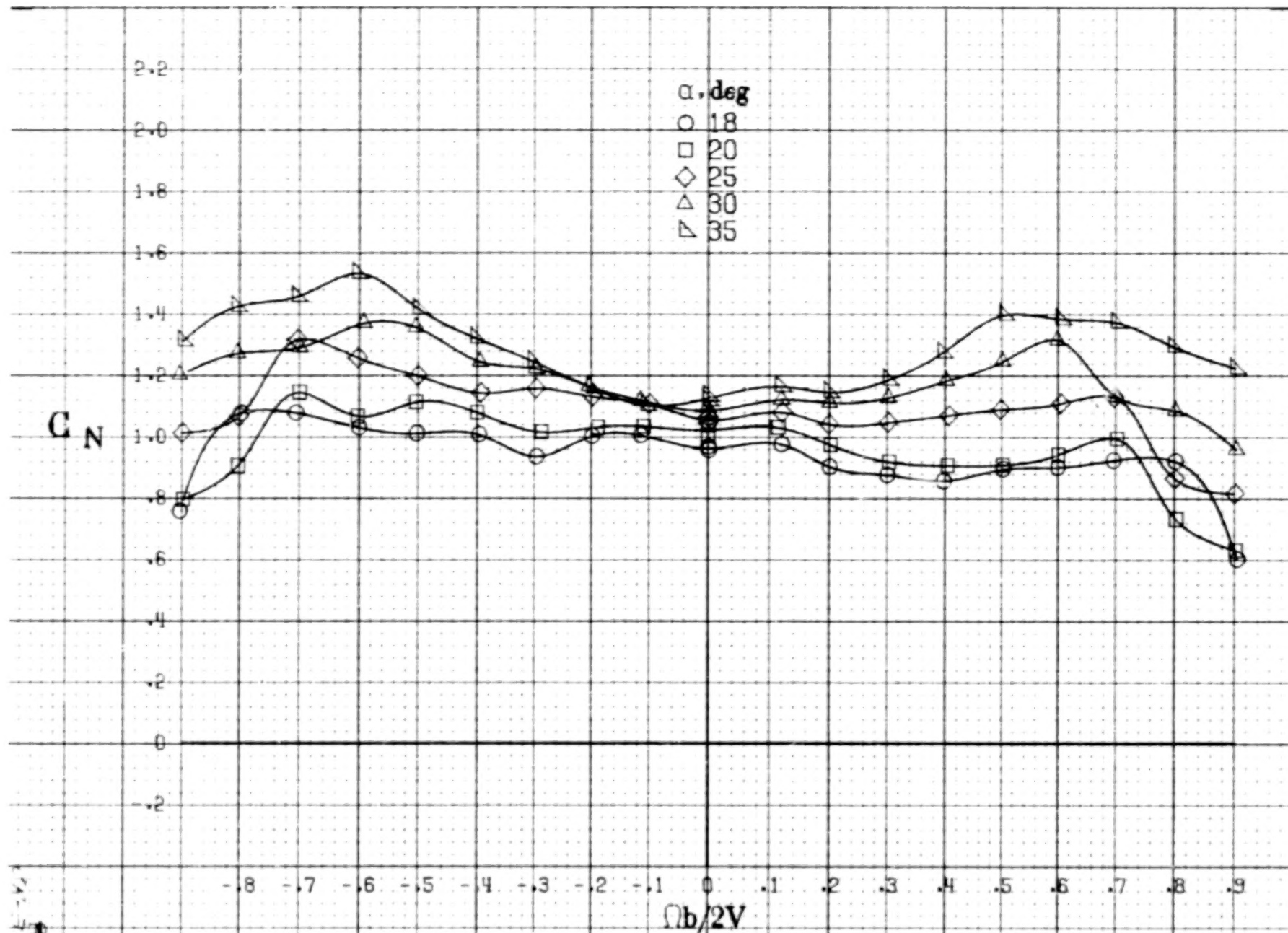


(b)  $\alpha = 18$  to  $35$  deg,  $SR = 152.4$  cm (60 in).  
Figure A21.-Concluded.



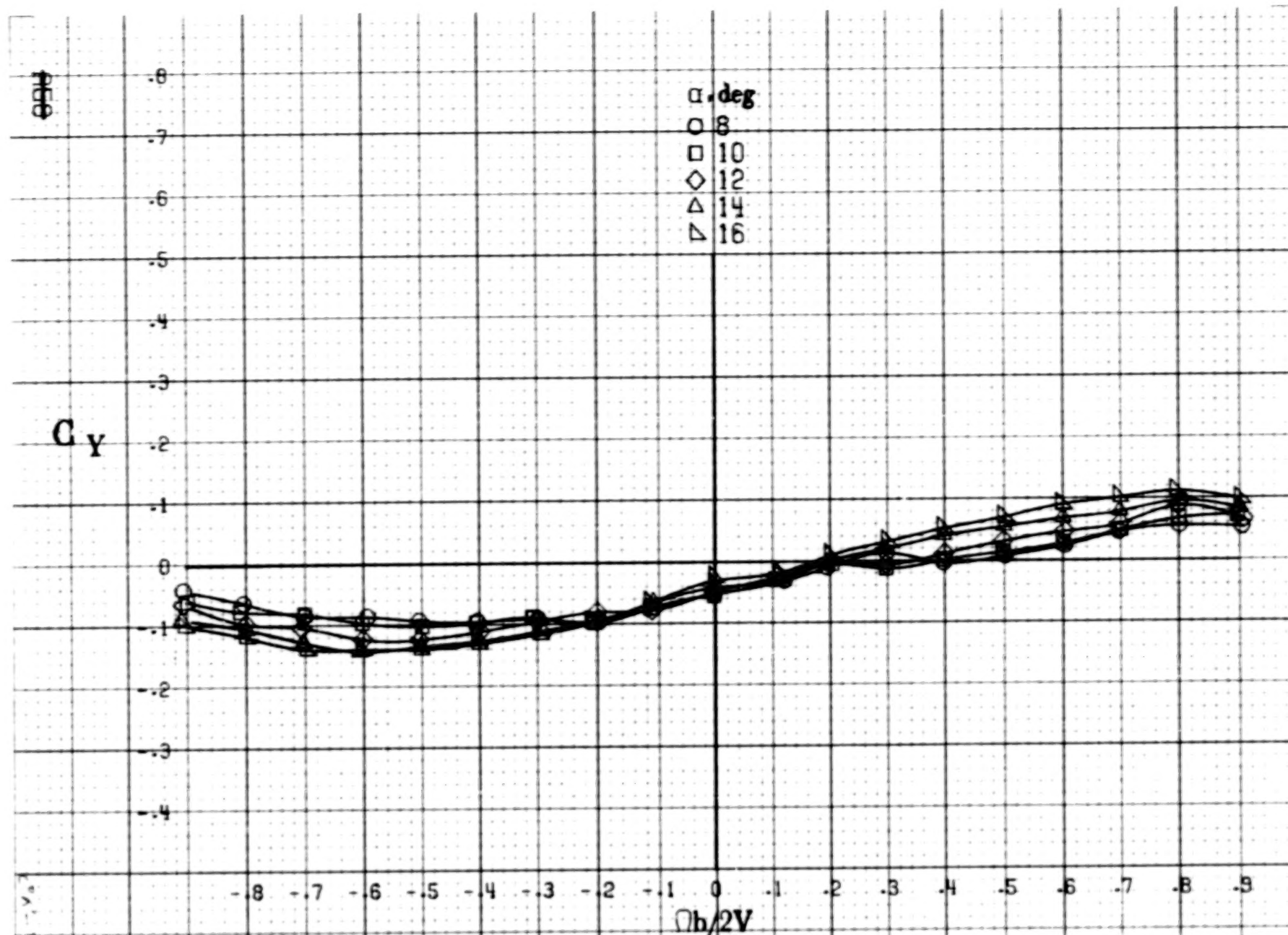


(a)  $\alpha = 8$  to  $16^\circ$ ,  $SR = 152.4 \text{ cm (60 in)}$ .  
 Figure A22. Effect of rotation rate and angle of attack on normal-force coefficient for basic configuration.  $\delta_e = -27^\circ$ ,  $\delta_s = 19.0^\circ$ ,  $\delta_r = -24^\circ$ ,  $\beta = 0^\circ$ .

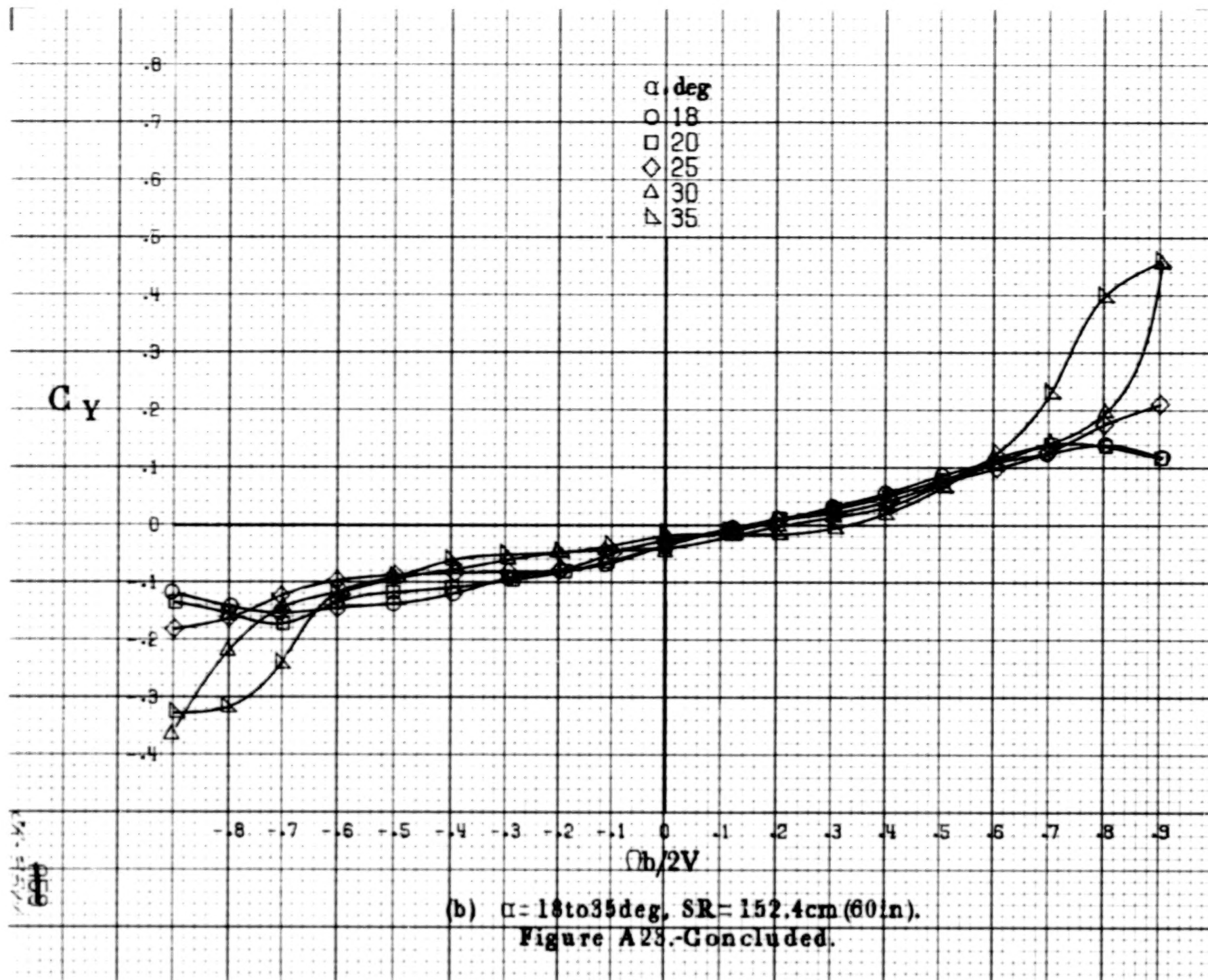


(b)  $\alpha = 18$  to  $35^\circ$ ,  $SR = 152.4\text{cm}$  (60in).

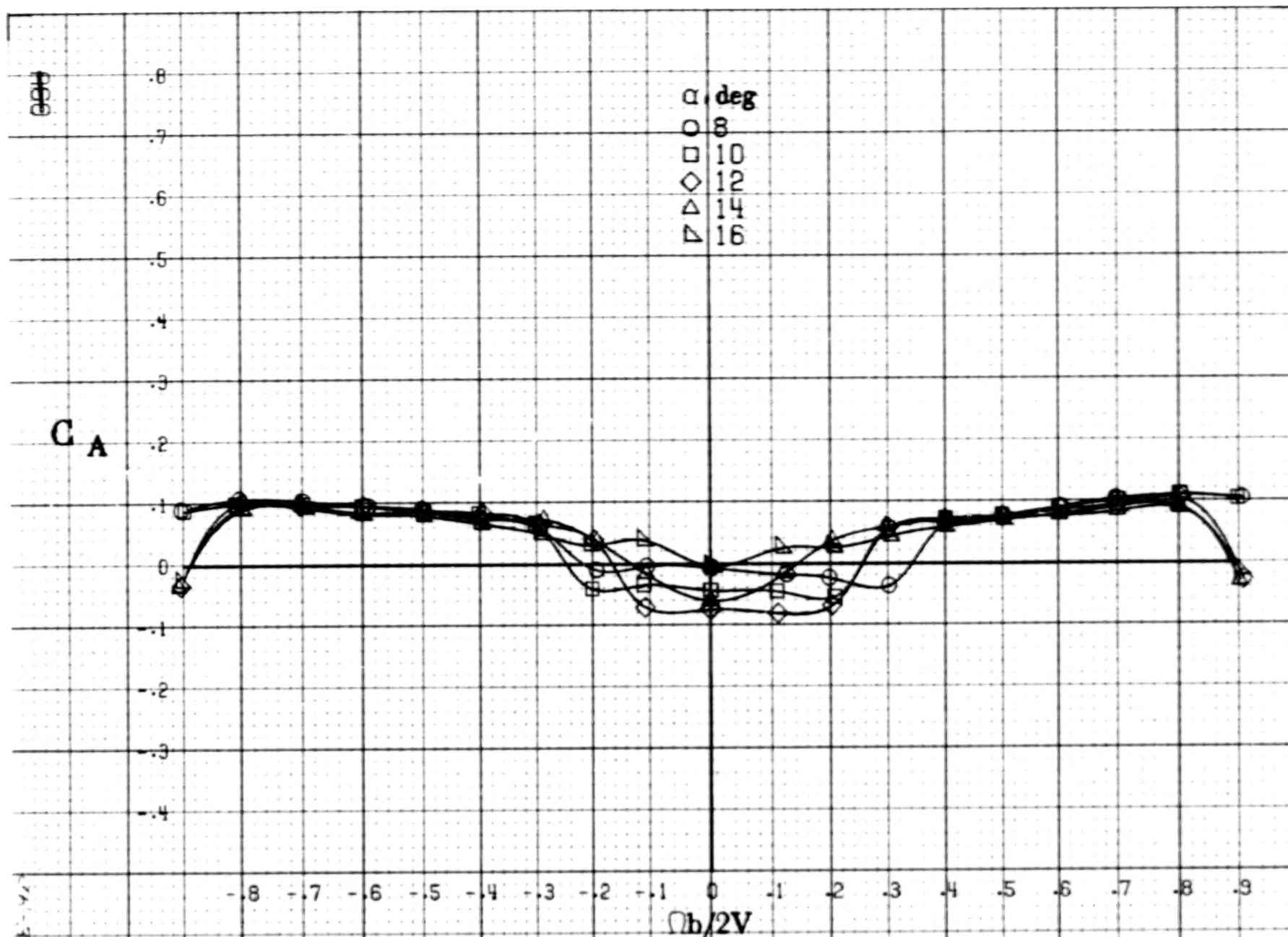
Figure A22.-Concluded.



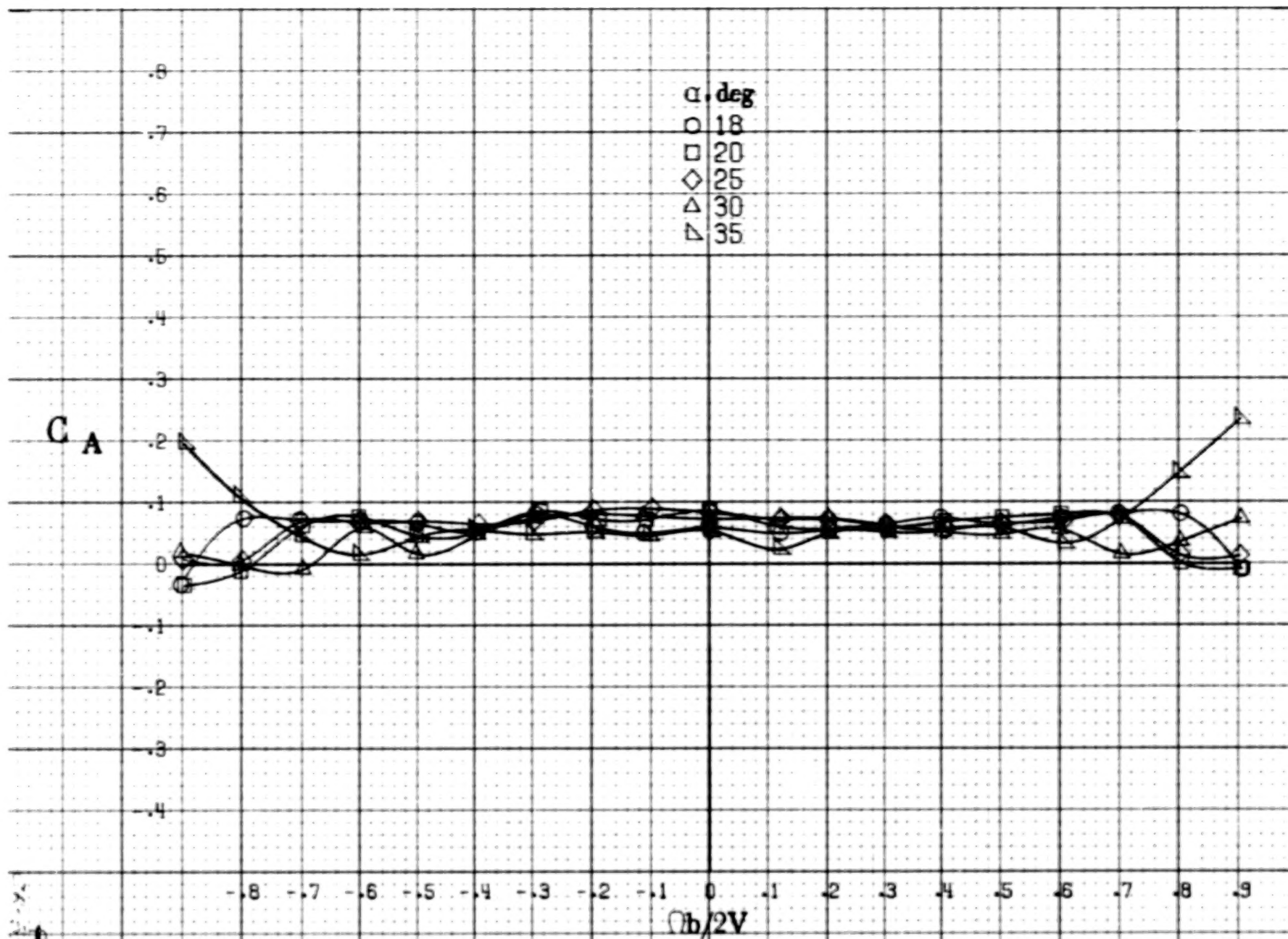
(a)  $\alpha = 8$  to  $16^\circ$ ,  $SR = 152.4 \text{ cm (60 in.)}$ .  
 Figure A28. Effect of rotation rate and angle of attack on side-force coefficient for basic configuration.  $\delta_e = -27^\circ$ ,  $\delta_a = 19.0^\circ$ ,  $\delta_r = -24^\circ$ ,  $\beta = 0^\circ$ .





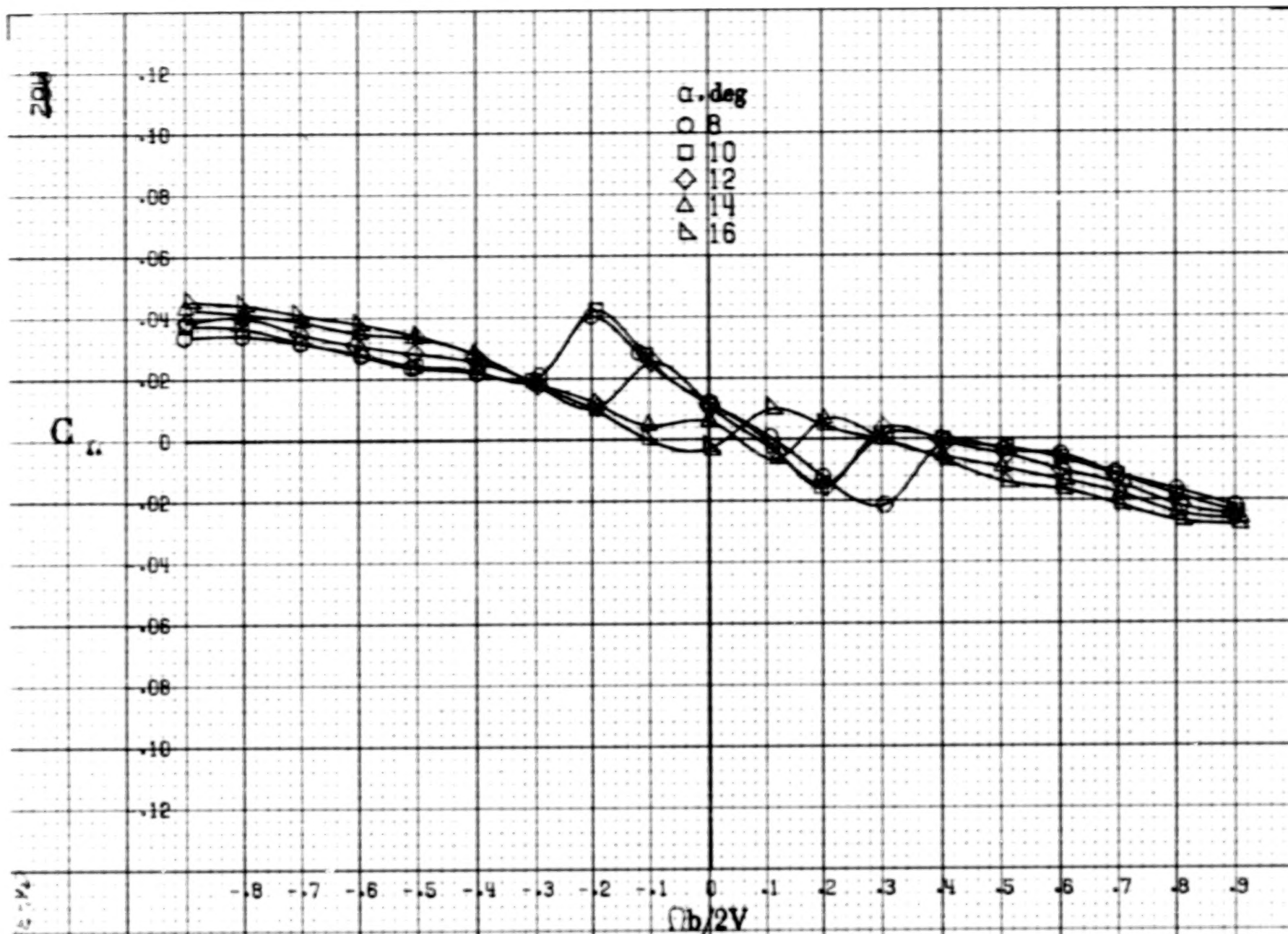


(a)  $\alpha = 8$  to  $16$  deg,  $SR = 152.4$  cm (60 in).  
 Figure A24. Effect of rotation rate and angle of attack on axial-force coefficient for basic configuration.  $\delta_e = -27^\circ$ ,  $\delta_a = 19.0^\circ$ ,  $\delta_r = -24^\circ$ ,  $\beta = 0^\circ$ .

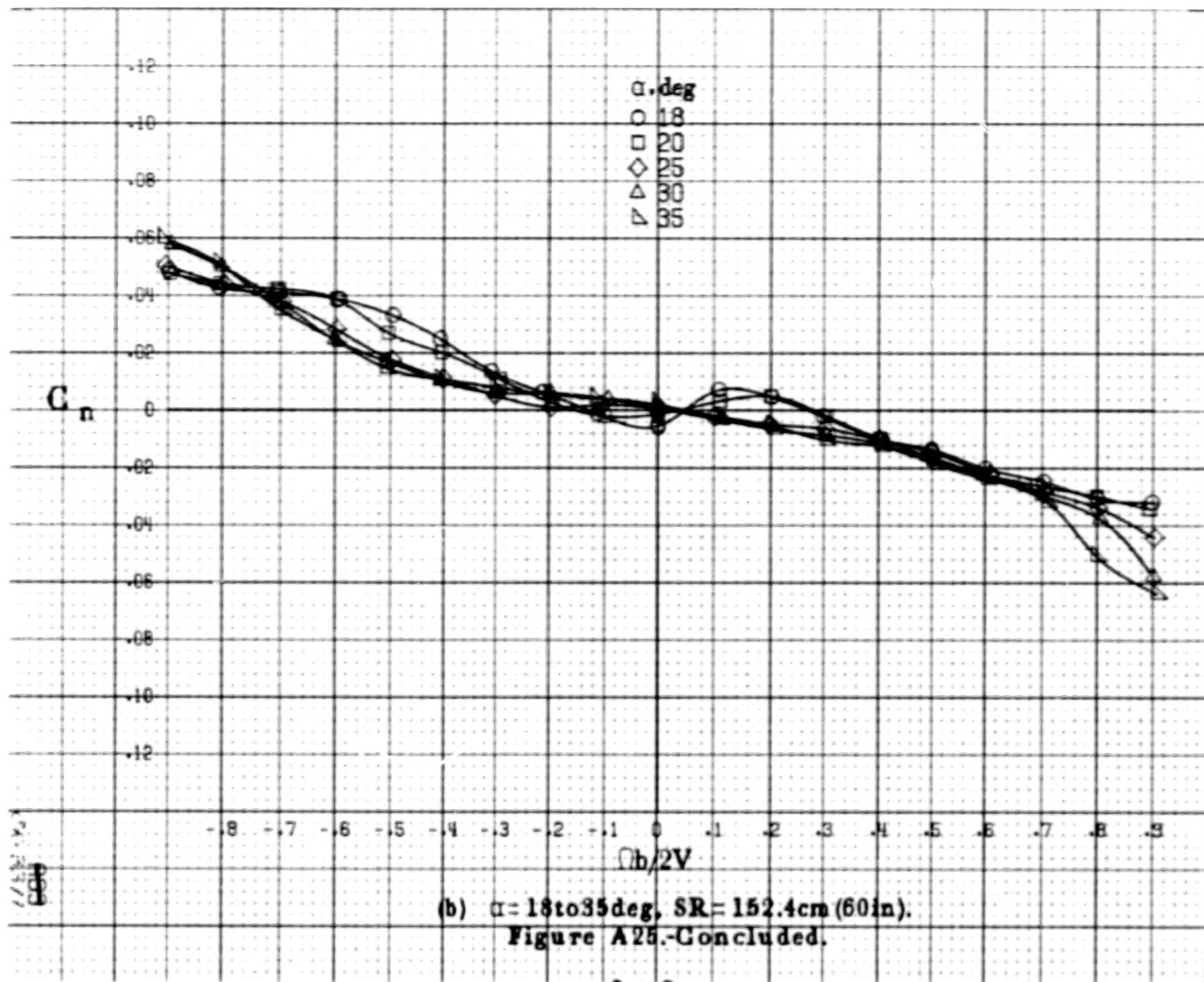


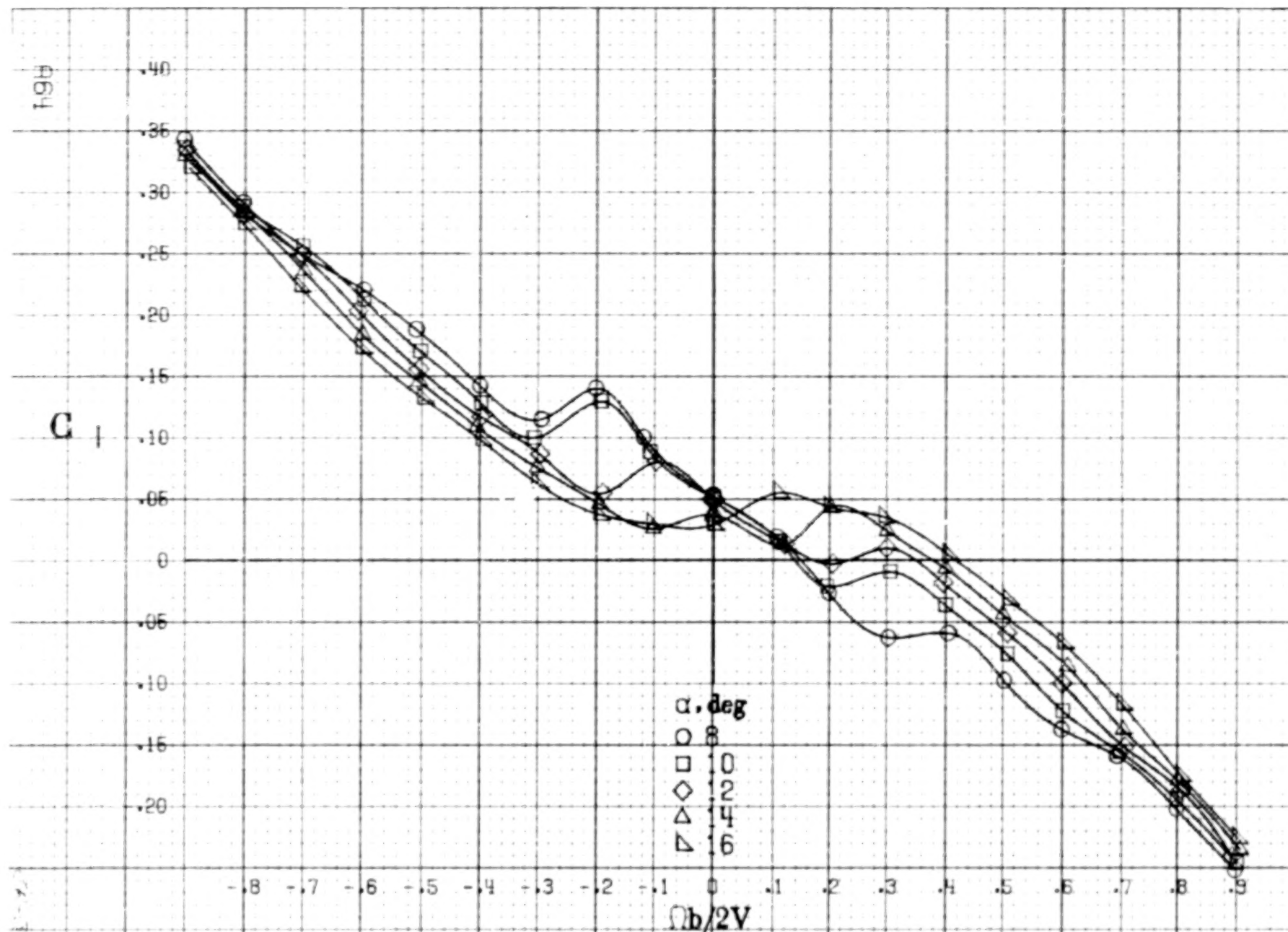
(b)  $\alpha = 18$  to  $35$  deg,  $SR = 152.4$  cm (60 in).  
Figure A24.-Concluded.



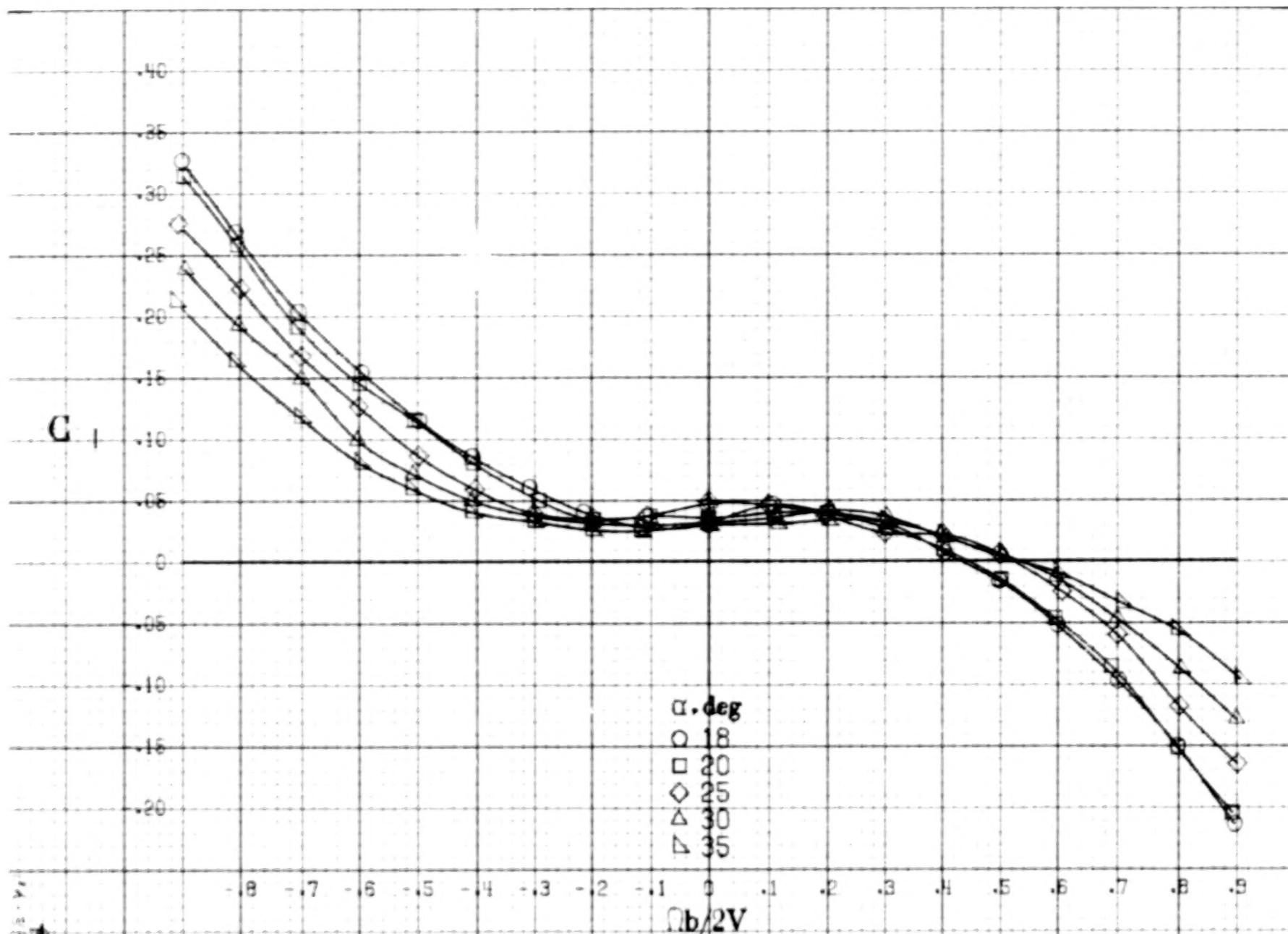


(a)  $\alpha = 8$  to  $16$  deg,  $SR = 152.4$  cm (60 in).  
 Figure A25. Effect of rotation rate and angle of attack on yawing moment coefficient for basic configuration.  $\delta_e = -27^\circ$ ,  $\delta_a = -19.0^\circ$ ,  $\delta_r = -24^\circ$ ,  $\beta = 0^\circ$ .





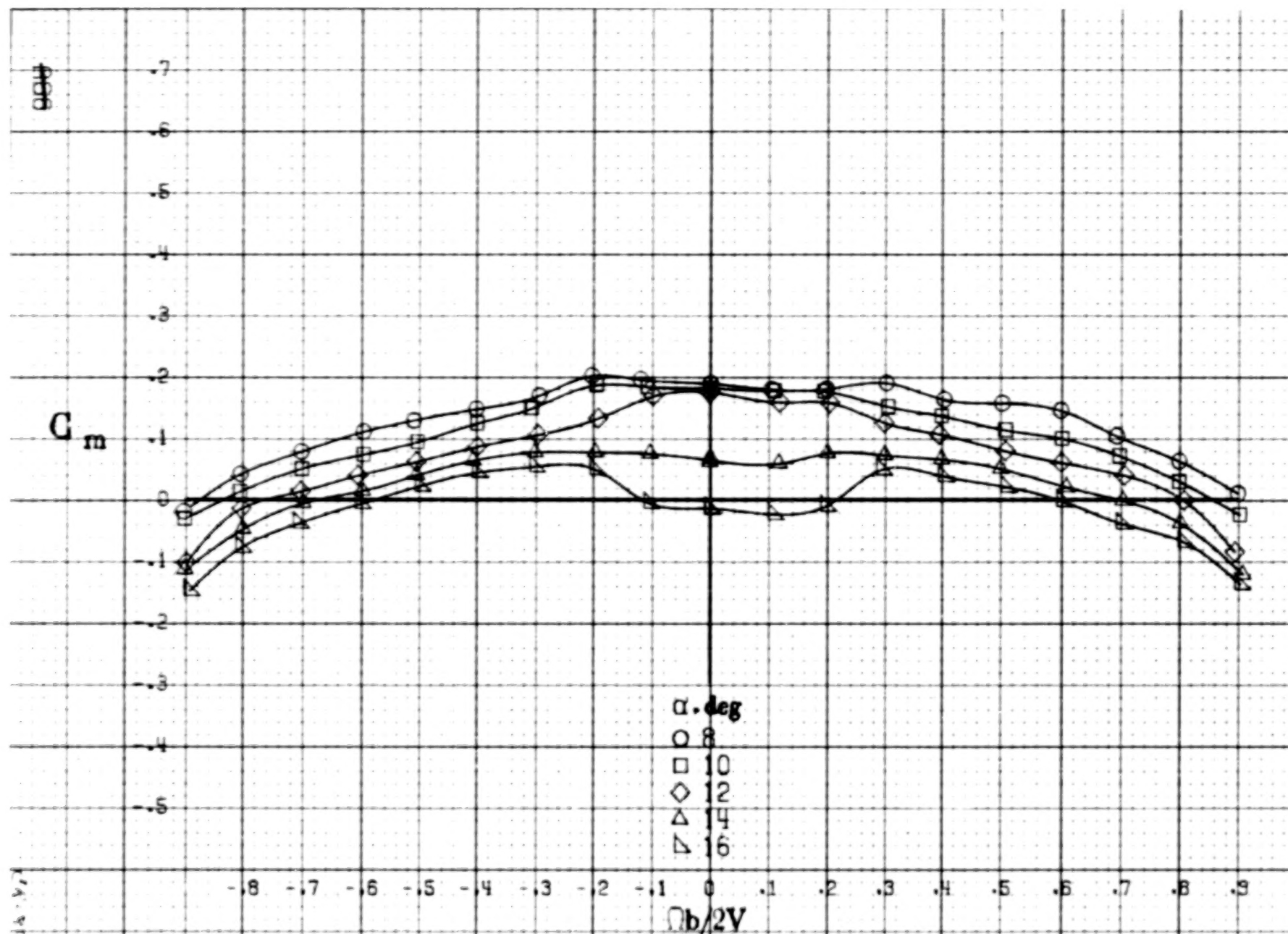
(a)  $\alpha = 8$  to  $16^\circ$ ,  $SR = 152.4 \text{ cm (60 in.)}$ .  
 Figure A26. Effect of rotation rate and angle of attack on rolling-moment coefficient for basic configuration.  $\delta_e = -27^\circ$ ,  $\delta_n = -19.0^\circ$ ,  $\delta_r = -24^\circ$ ,  $\beta = 0^\circ$ .



(b)  $\alpha = 18$  to  $35^\circ$ ,  $SR = 152.4 \text{ cm (60 in.)}$ .

Figure A26.-Concluded.

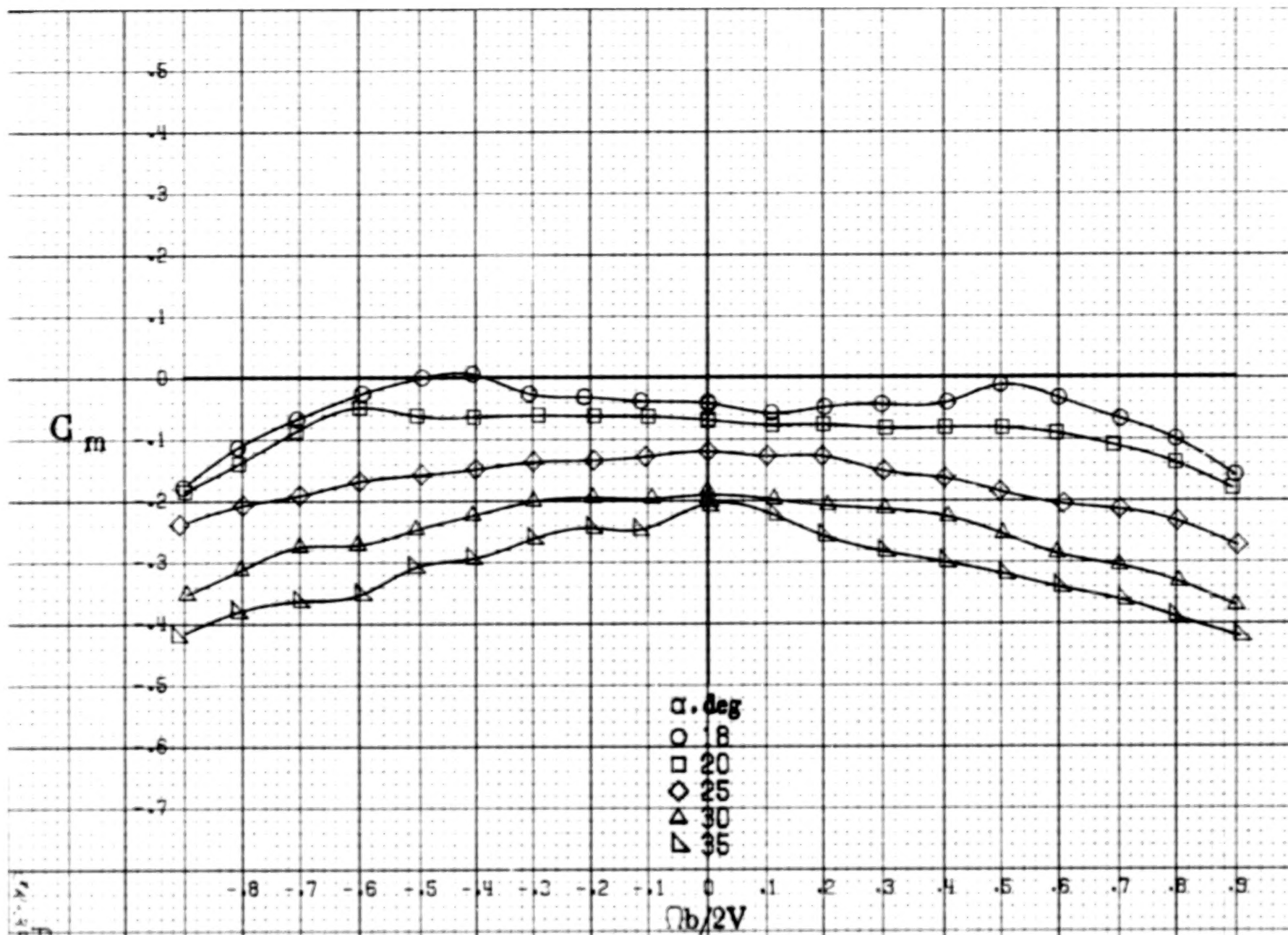




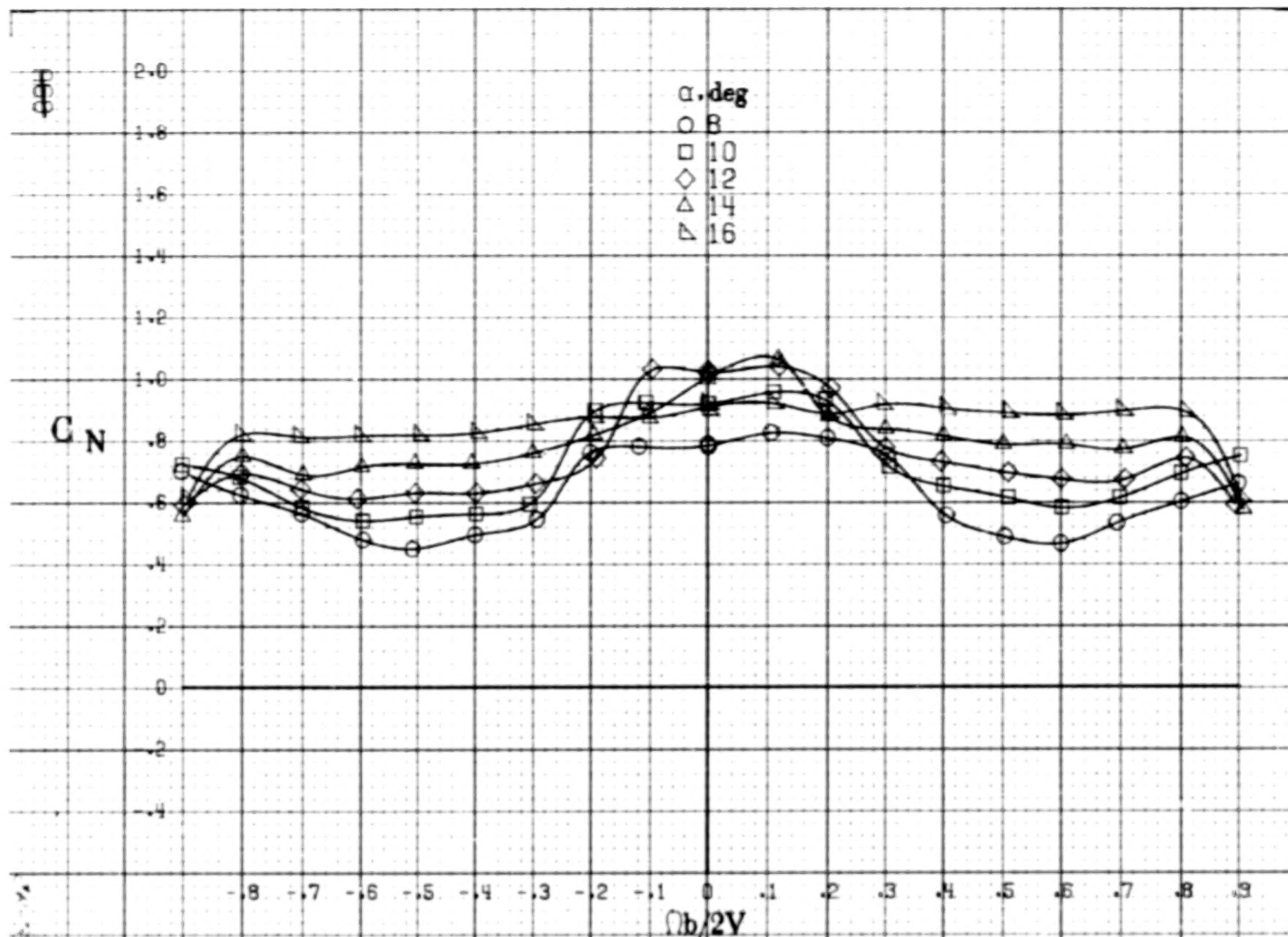
(a)  $\alpha = 8$  to  $16^\circ$ ,  $SR = 152.4 \text{ cm (60 in.)}$ .

Figure A27. Effect of rotation rate and angle of attack on pitching-moment coefficient for basic configuration.  $\delta_e = -27^\circ$ ,  $\delta_a = -19.0^\circ$ ,  $\delta_r = -24^\circ$ ,  $\beta = 0^\circ$ .

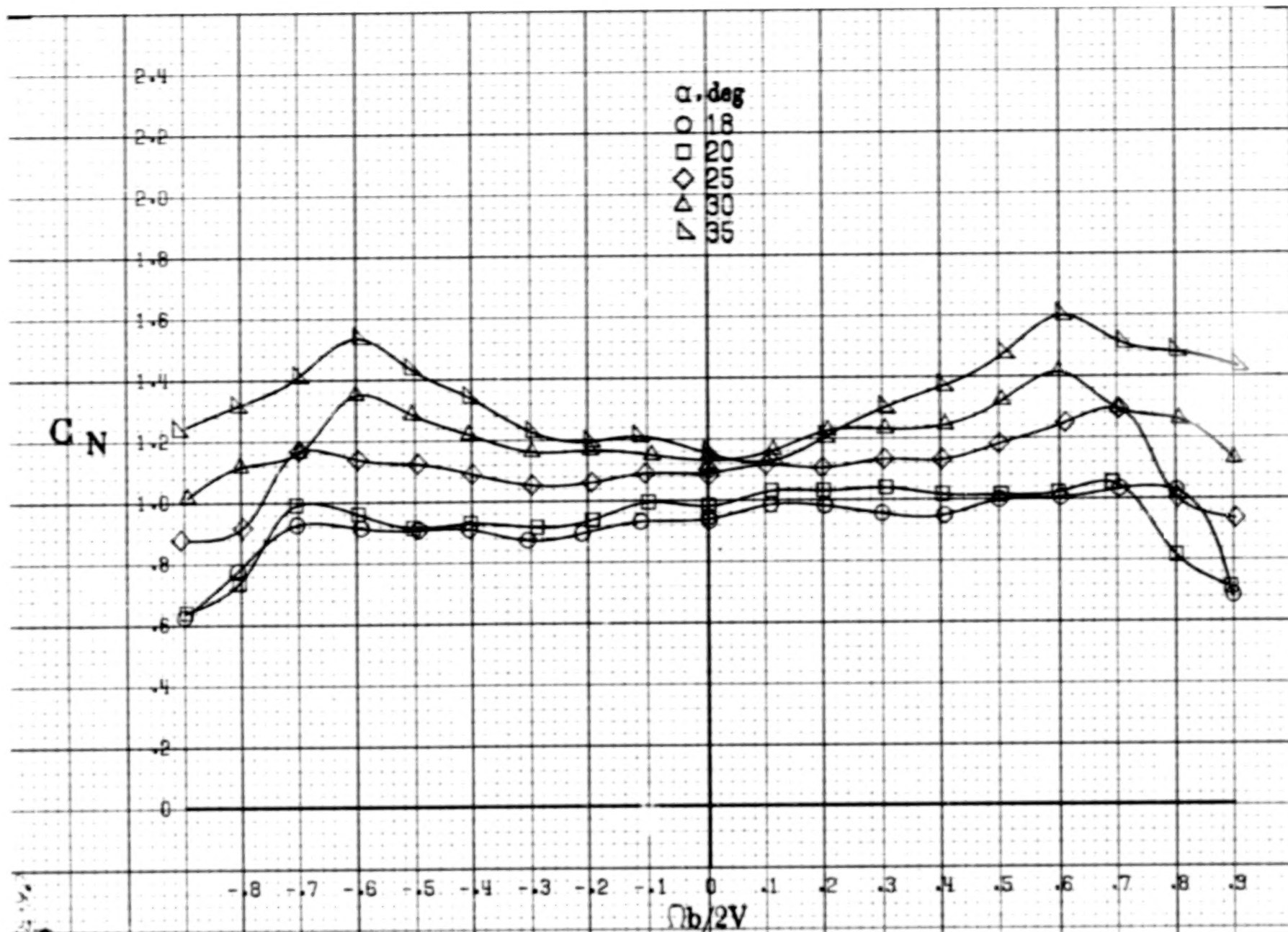




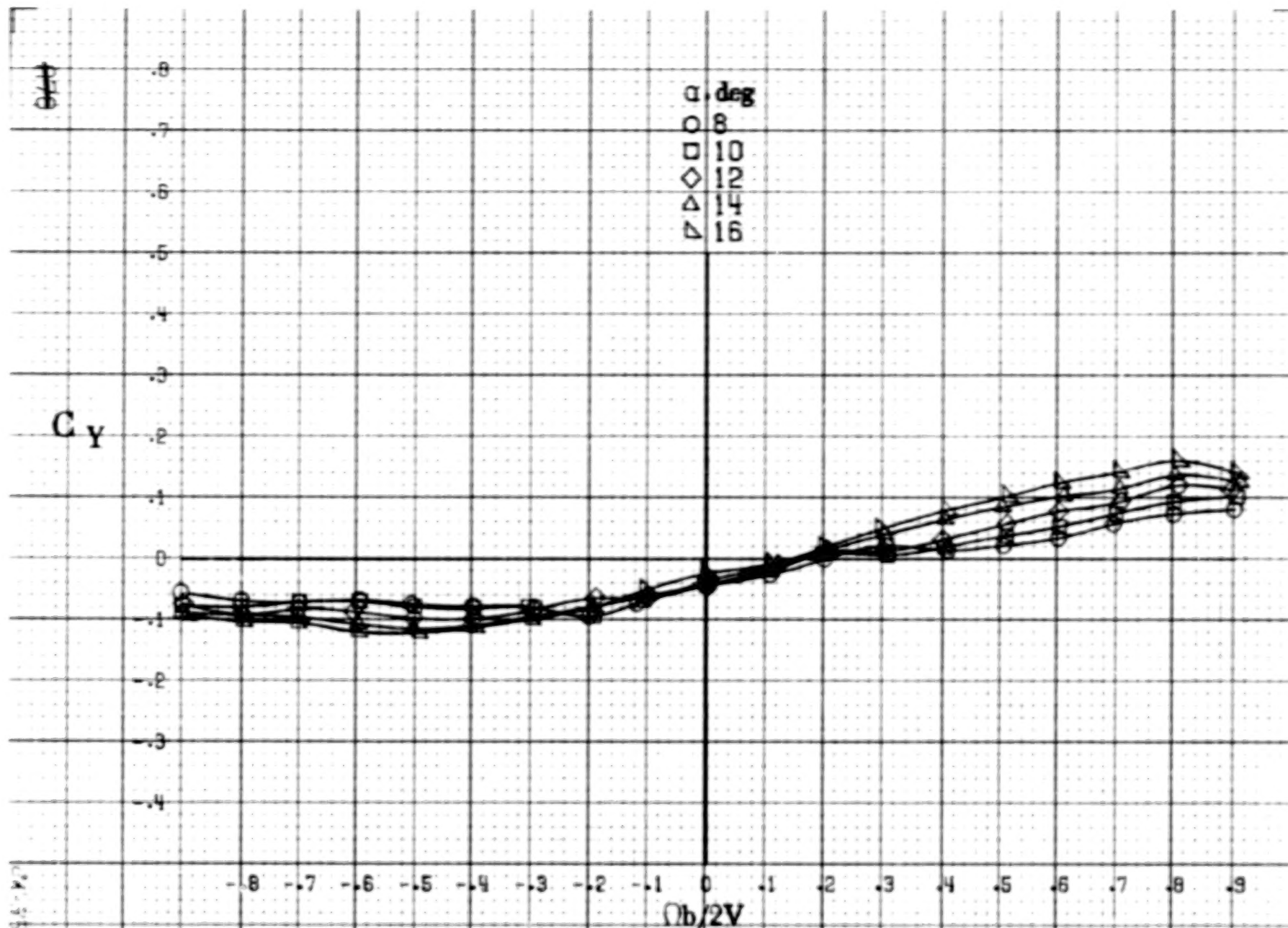
(b)  $\alpha = 18$  to  $35$  deg,  $SR = 152.4$  cm (60 in).  
Figure A27.-Concluded.



(a)  $\alpha = 8$  to  $16$  deg,  $SR = 152.4$  cm (60 in).  
 Figure A28.-Effect of rotation rate and angle of attack on normal-force coefficient for basic configuration.  $\delta_e = -27^\circ$ ,  $\delta_a = -19.0^\circ$ ,  $\delta_r = -24^\circ$ ,  $\beta = 0^\circ$ .

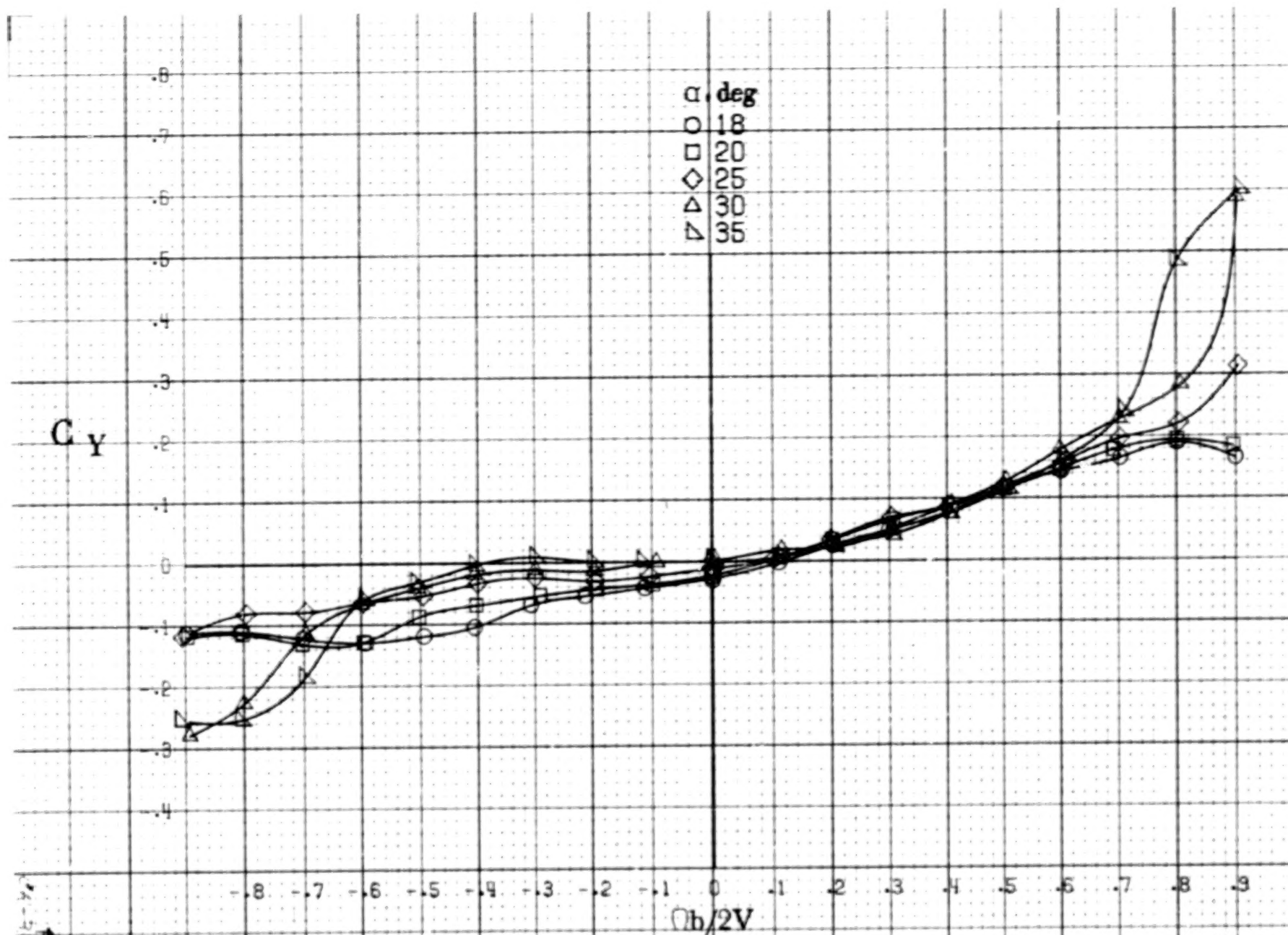


(b)  $\alpha = 18$  to  $35$  deg, SR = 152.4 cm (60 in).  
Figure A28.-Concluded.



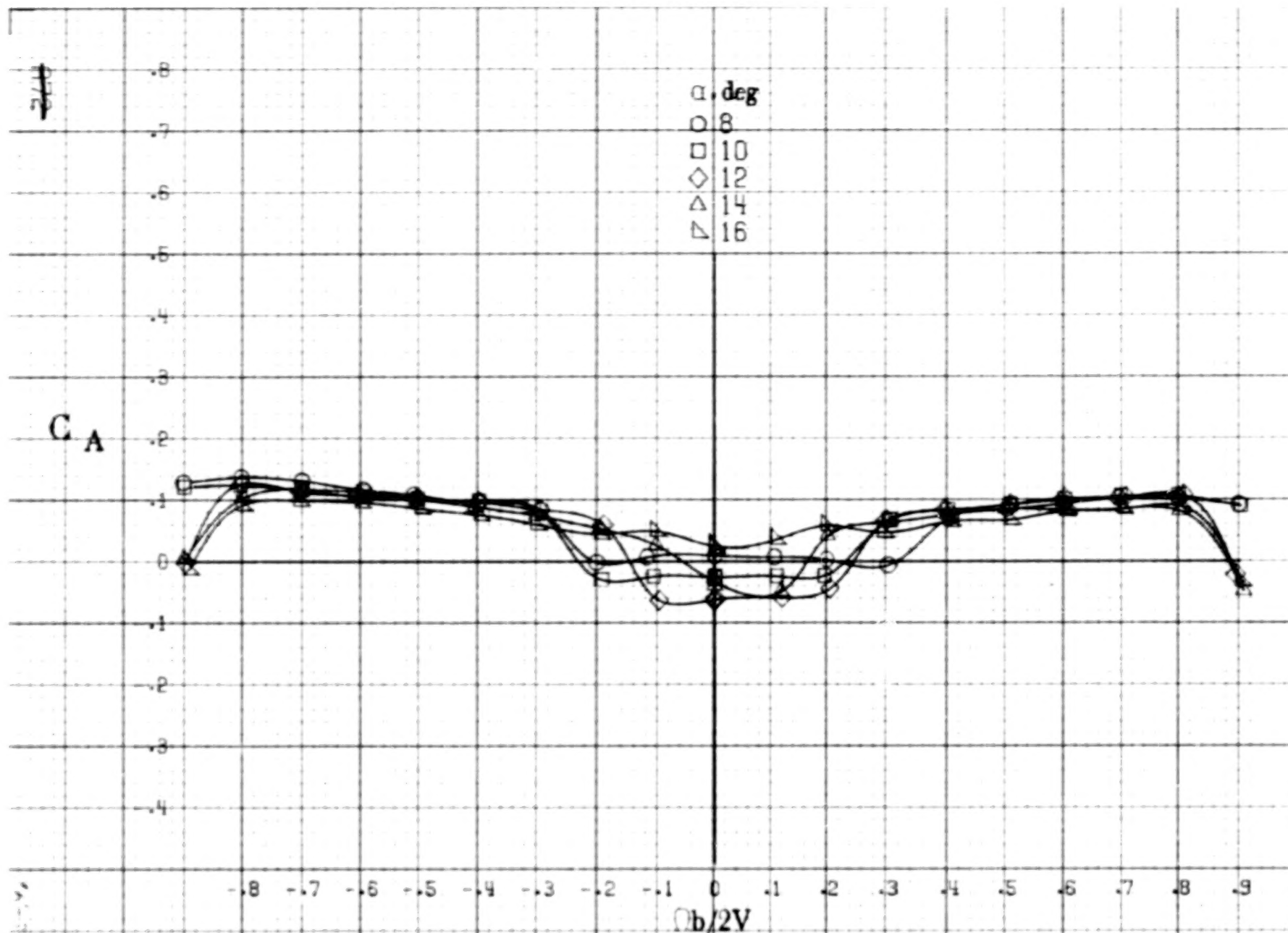
(a)  $\alpha = 8$  to  $16^\circ$ ,  $SR = 152.4 \text{ cm (60 in.)}$ .  
 Figure A29. Effect of rotation rate and angle of attack on side-force coefficient for basic configuration.  $\delta_e = -27^\circ$ ,  $\delta_a = -19.0^\circ$ ,  $\delta_r = -24^\circ$ ,  $\beta = 0^\circ$ .





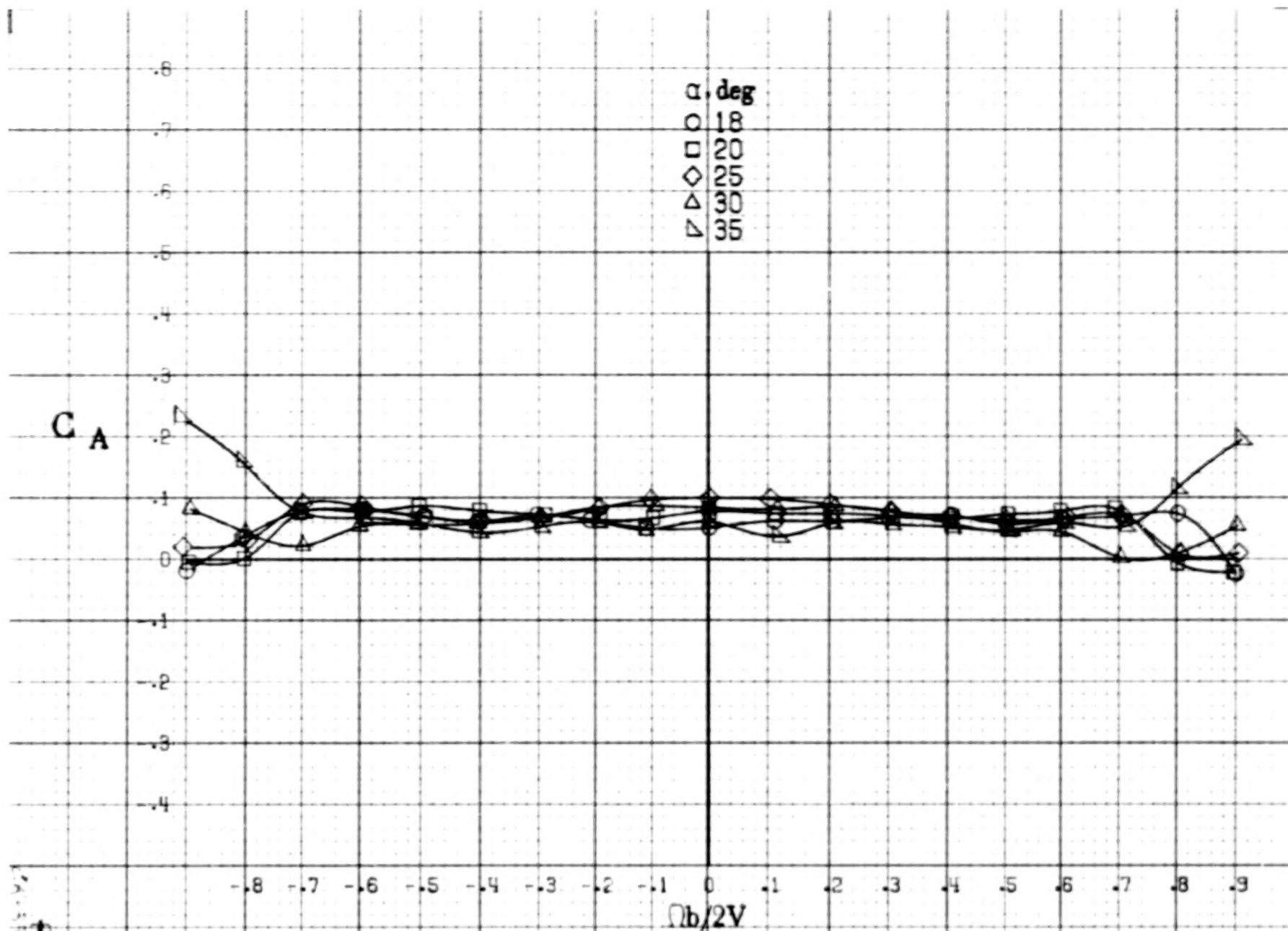
(b)  $\alpha = 18$  to  $35^\circ$ ,  $SR = 152.4\text{cm}$  (60 in).  
Figure A29.-Concluded.



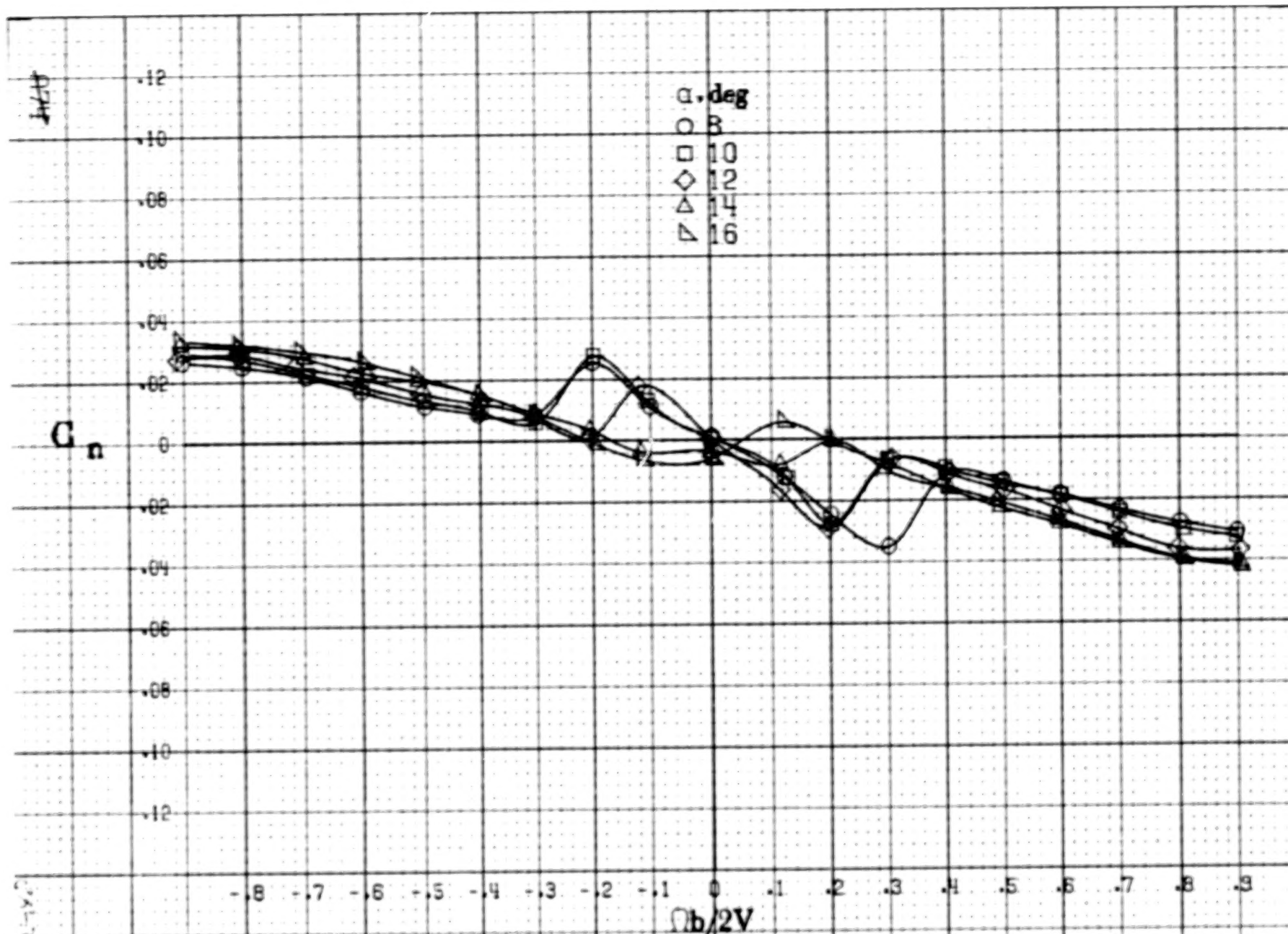


(a)  $\alpha = 8$  to  $16^\circ$ ,  $SR = 152.4 \text{ cm (60 in.)}$ .

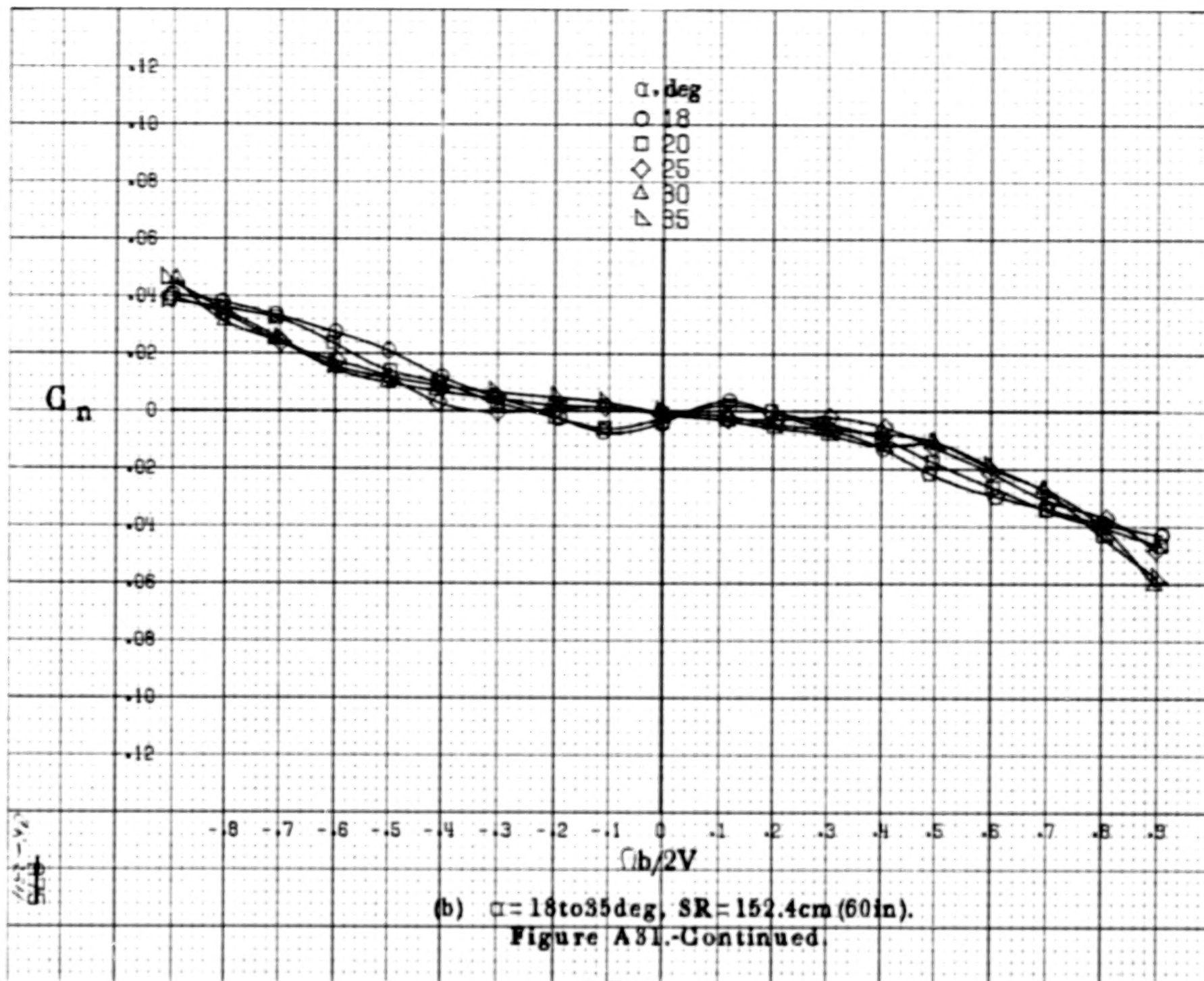
Figure A30.-Effect of rotation rate and angle of attack on axial-force coefficient for basic configuration.  $\delta_e = -27^\circ$ ,  $\delta_a = -19.0^\circ$ ,  $\delta_r = -24^\circ$ ,  $\beta = 0^\circ$ .



(b)  $\alpha = 18$  to  $35^\circ$ ,  $SR = 152.4\text{cm (60 in.)}$ .  
Figure A30.-Concluded.



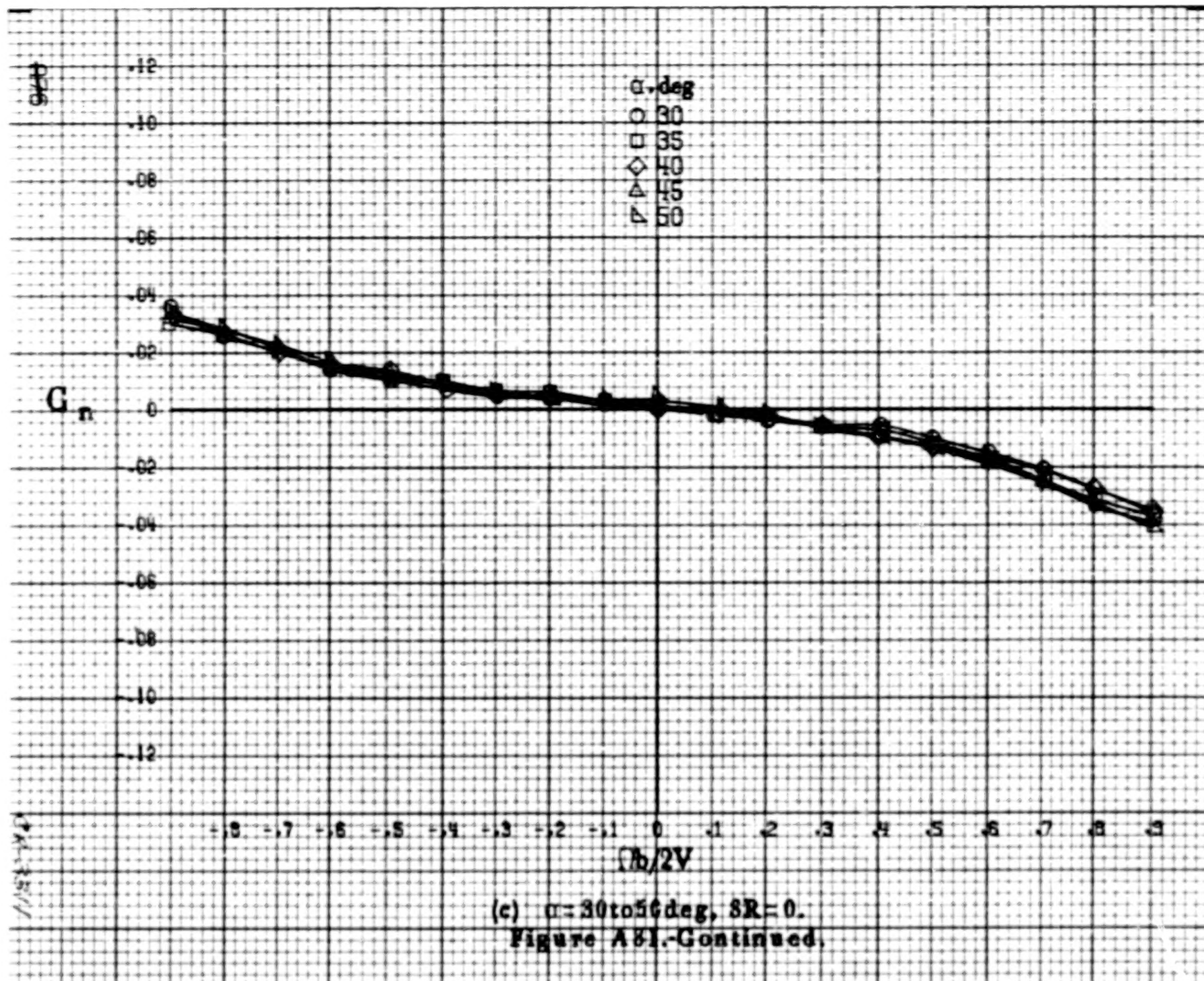
(a)  $\alpha = 8$  to  $16^\circ$ ,  $SR = 152.4 \text{ cm (60 in.)}$ .  
 Figure A31. Effect of rotation rate and angle of attack on yawing-moment coefficient for turbine nose configuration.  $\delta_s = 0^\circ$ ,  $\delta_a = 0^\circ$ ,  $\delta_r = 0^\circ$ ,  $\beta = 0^\circ$ .



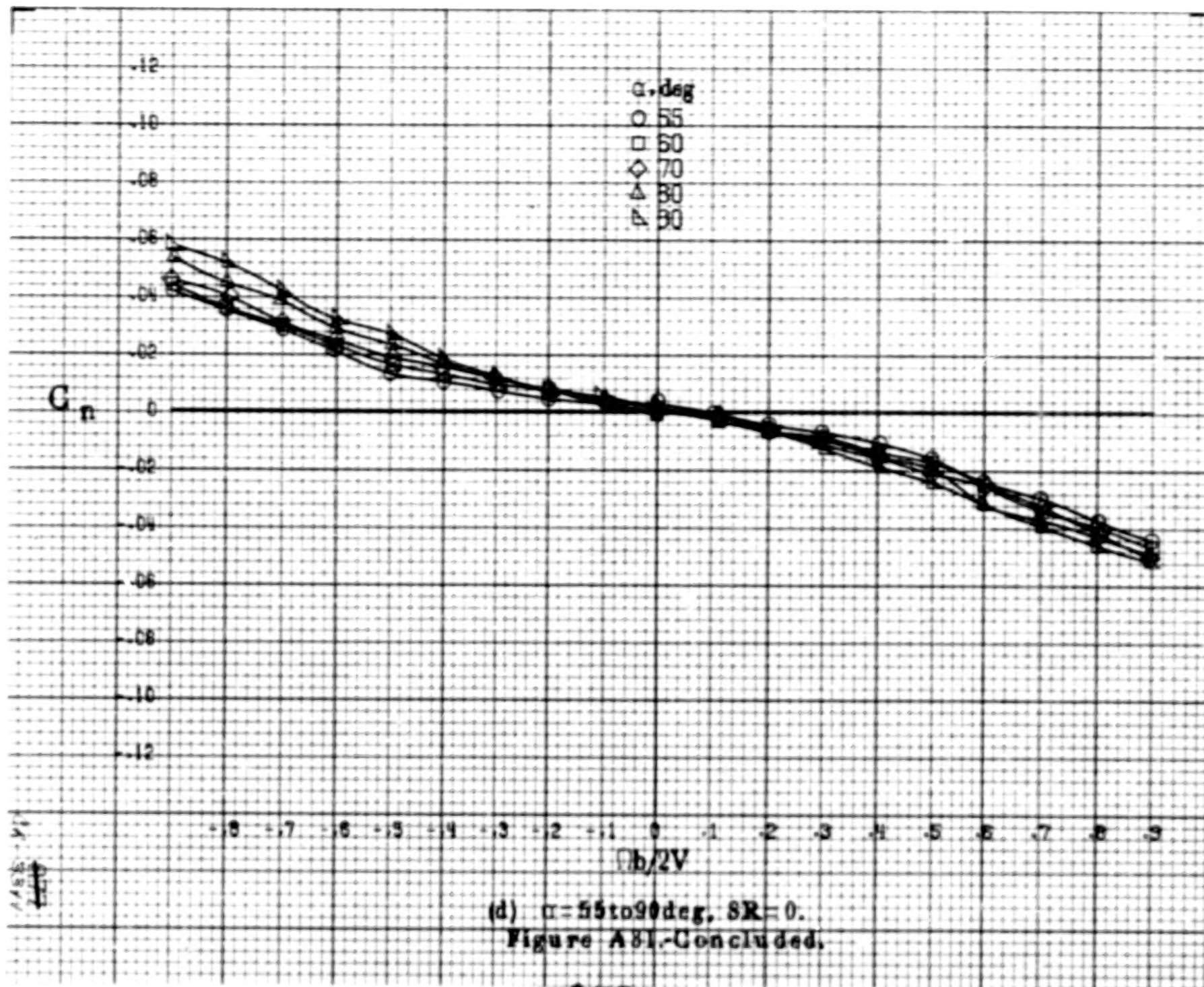
(b)  $\alpha = 18$  to  $35^\circ$ ,  $SR = 152.4\text{cm}$  (60 in).

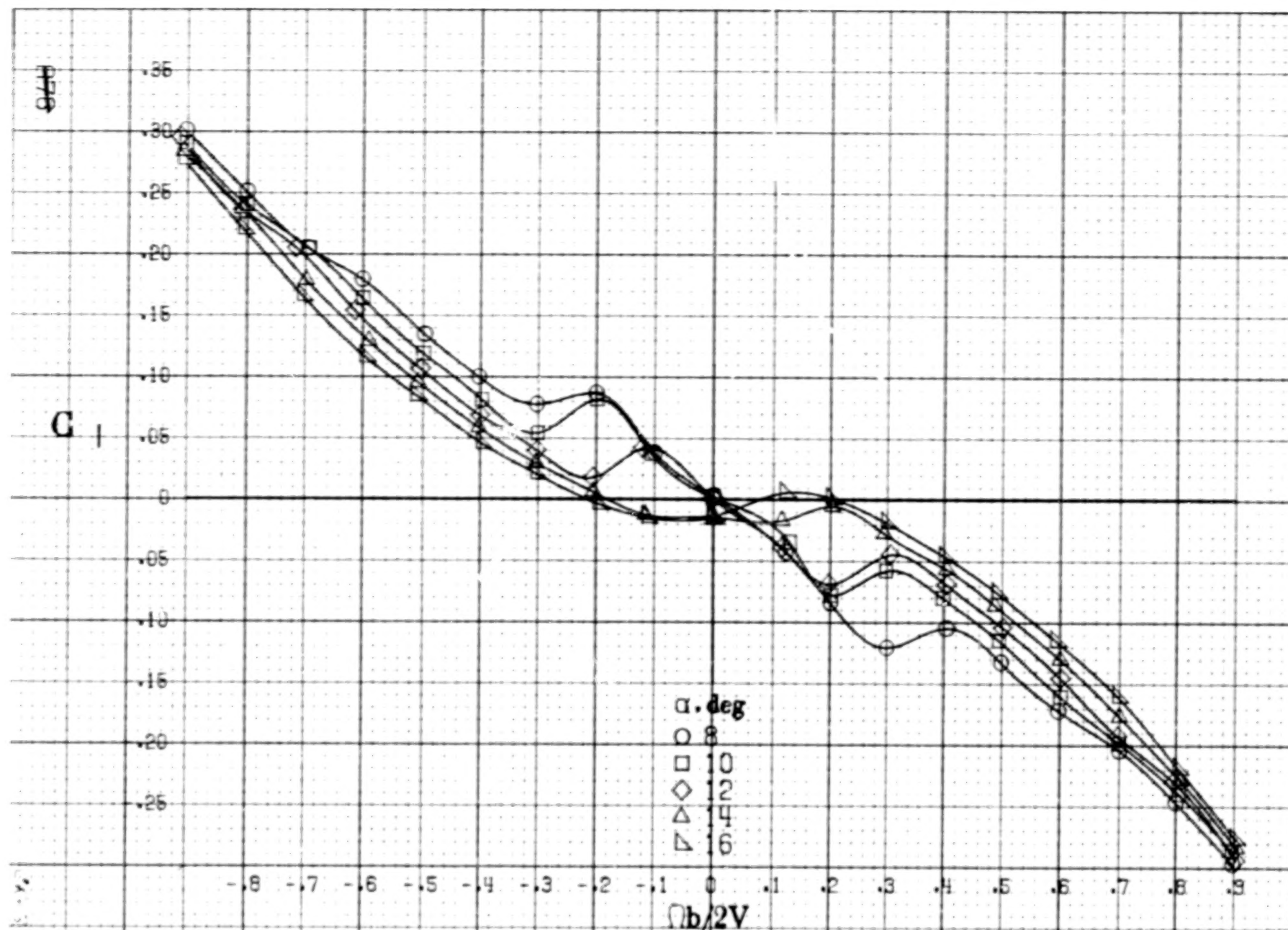
Figure A81.-Continued.





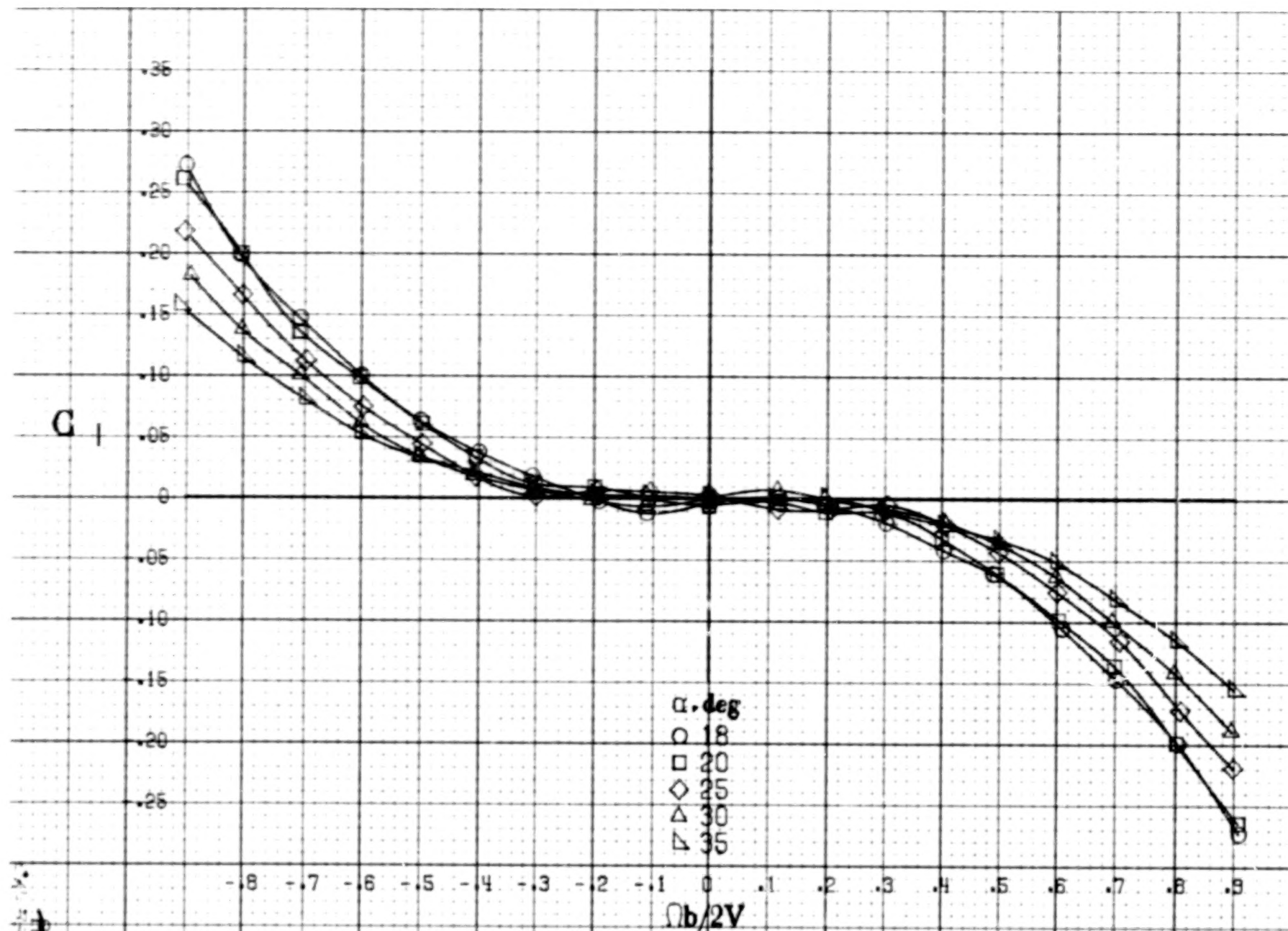






(a)  $\alpha = 8$  to  $16^\circ$ ,  $SR = 152.4 \text{ cm (60 in.)}$ .

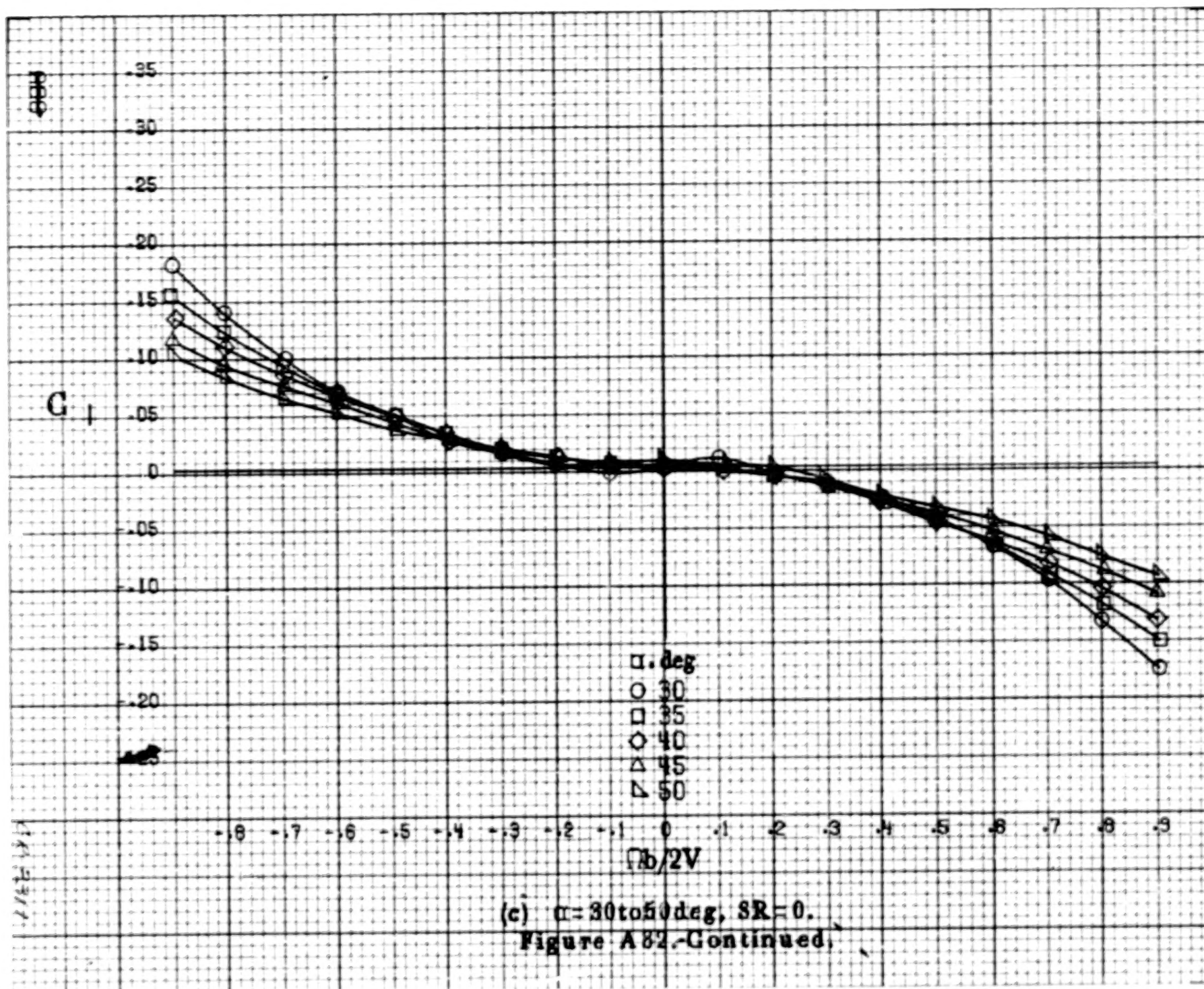
Figure A32.-Effect of rotation rate and angle of attack on rolling-moment coefficient for turbine nose configuration.  $\delta_s = 0^\circ$ ,  $\delta_a = 0^\circ$ ,  $\delta_r = 0^\circ$ ,  $\beta = 0^\circ$ .

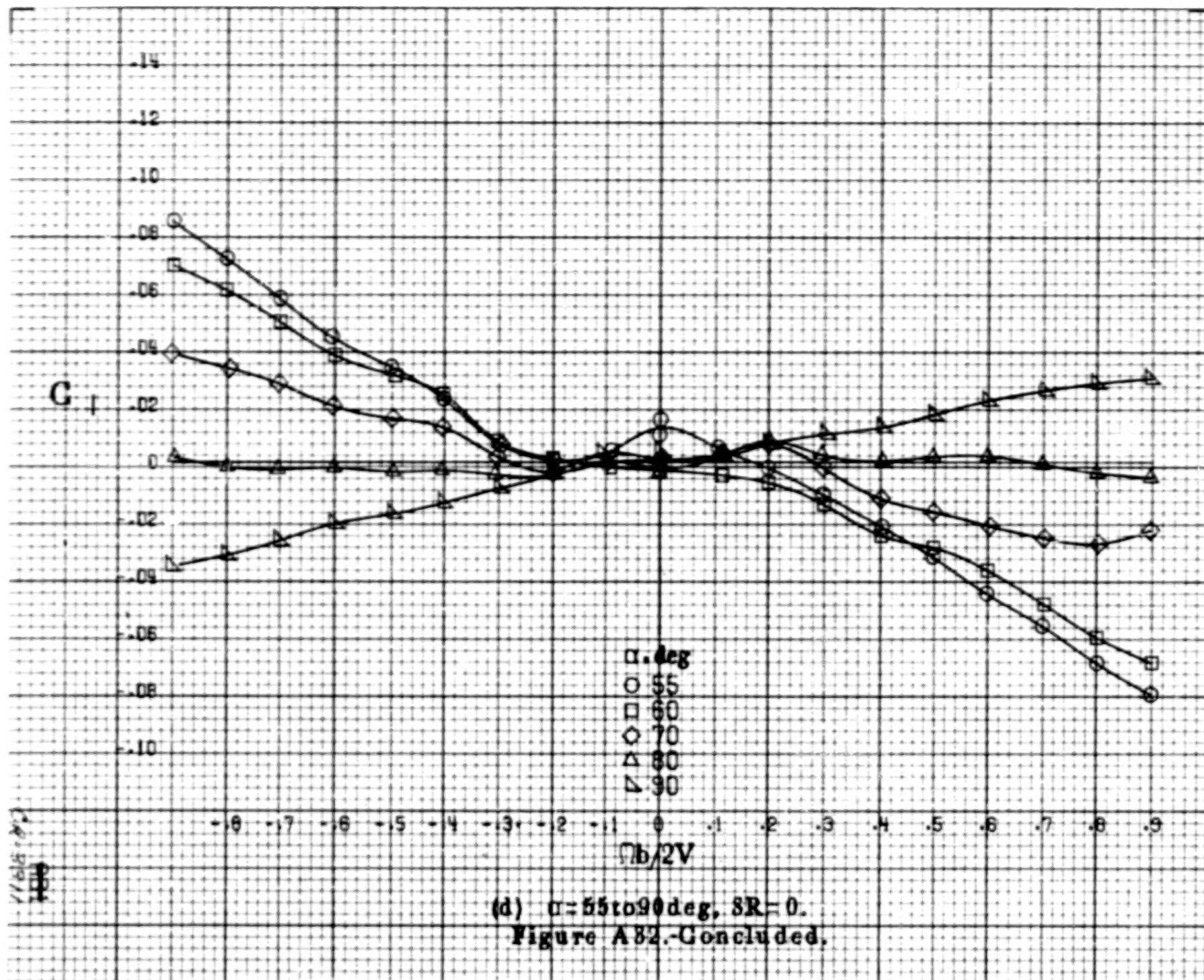


(b)  $\alpha = 18$  to  $35^\circ$ ,  $SR = 152.4\text{ cm (60 in.)}$ .

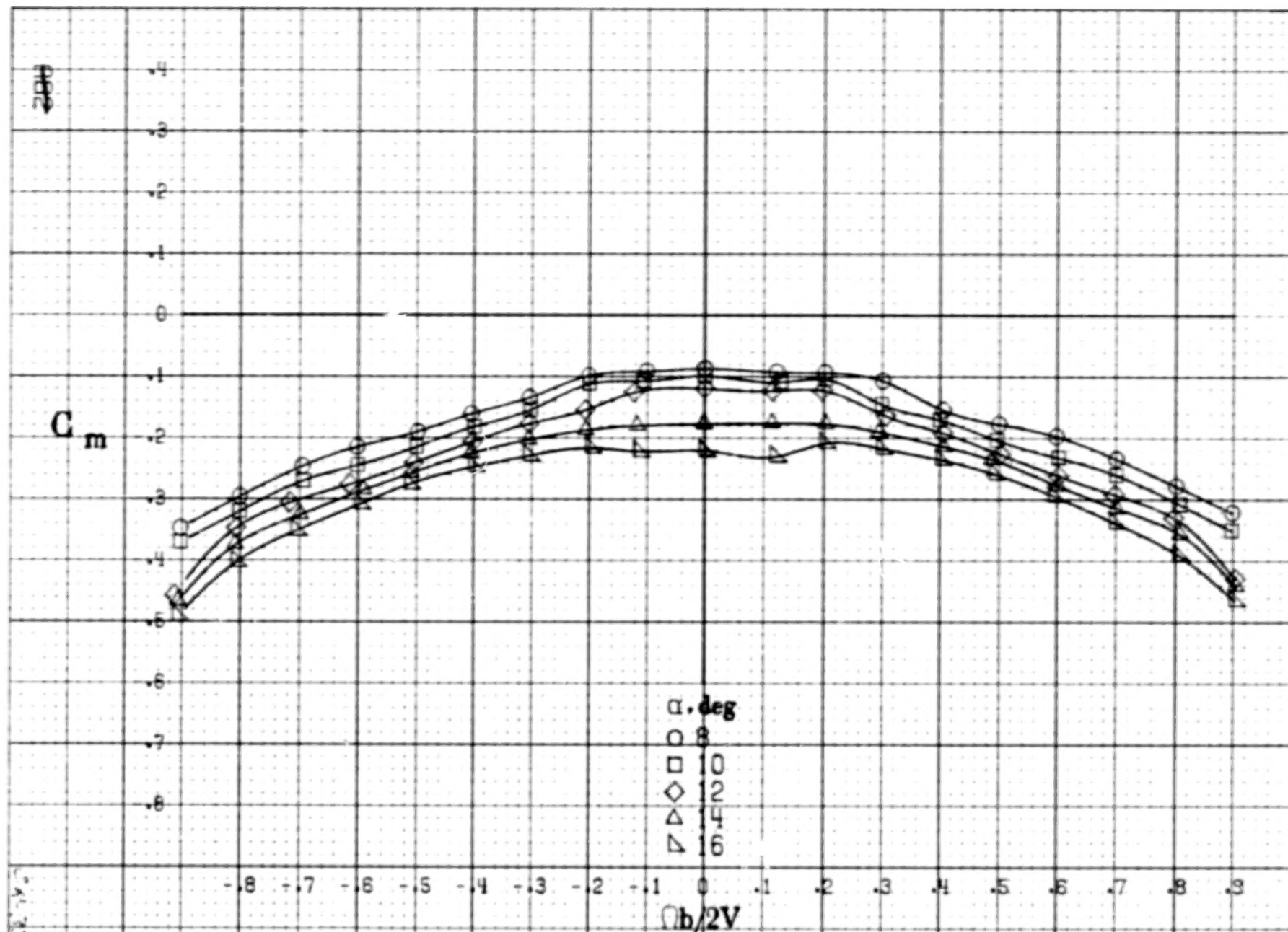
Figure A82.-Continued.





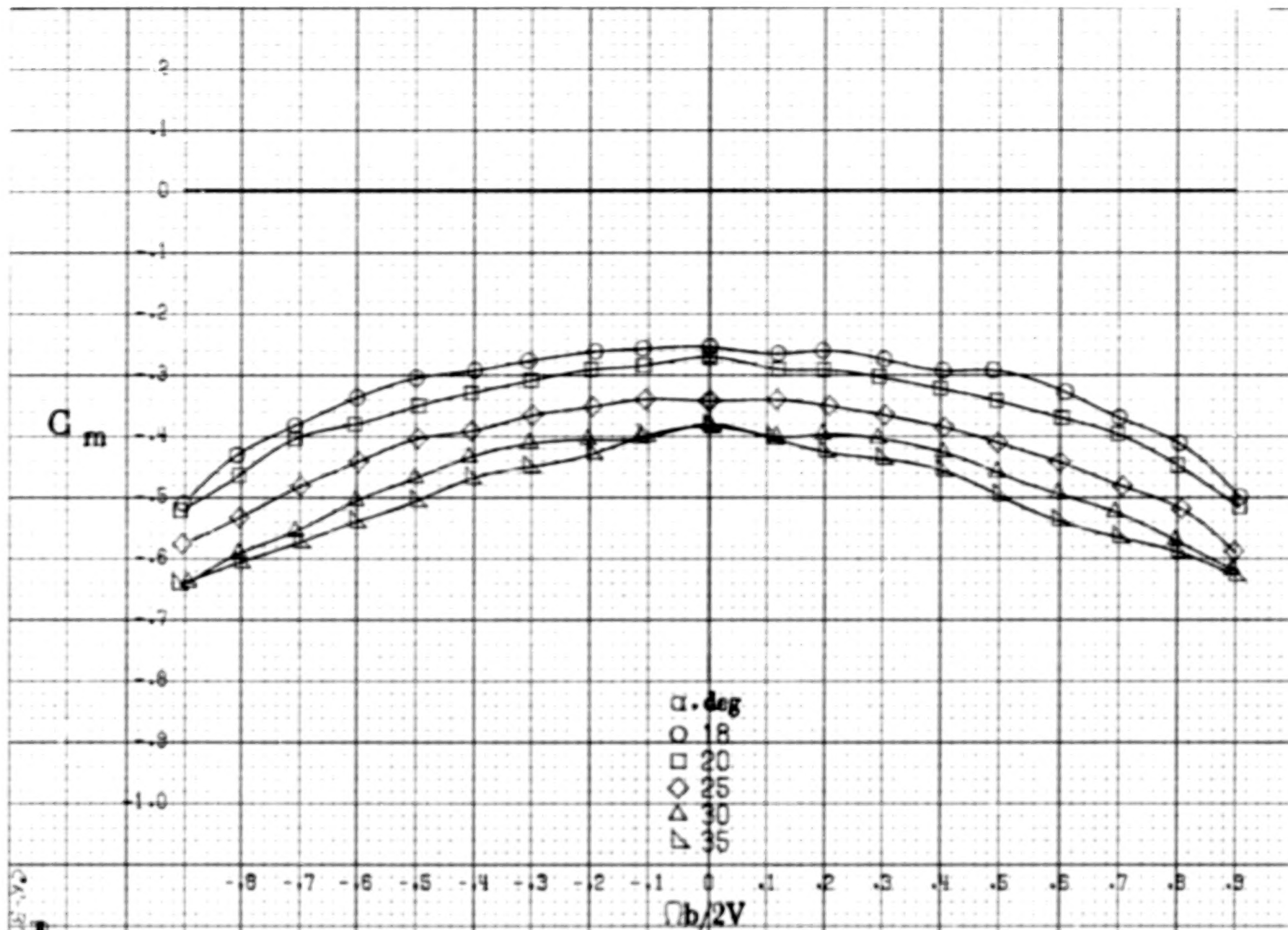




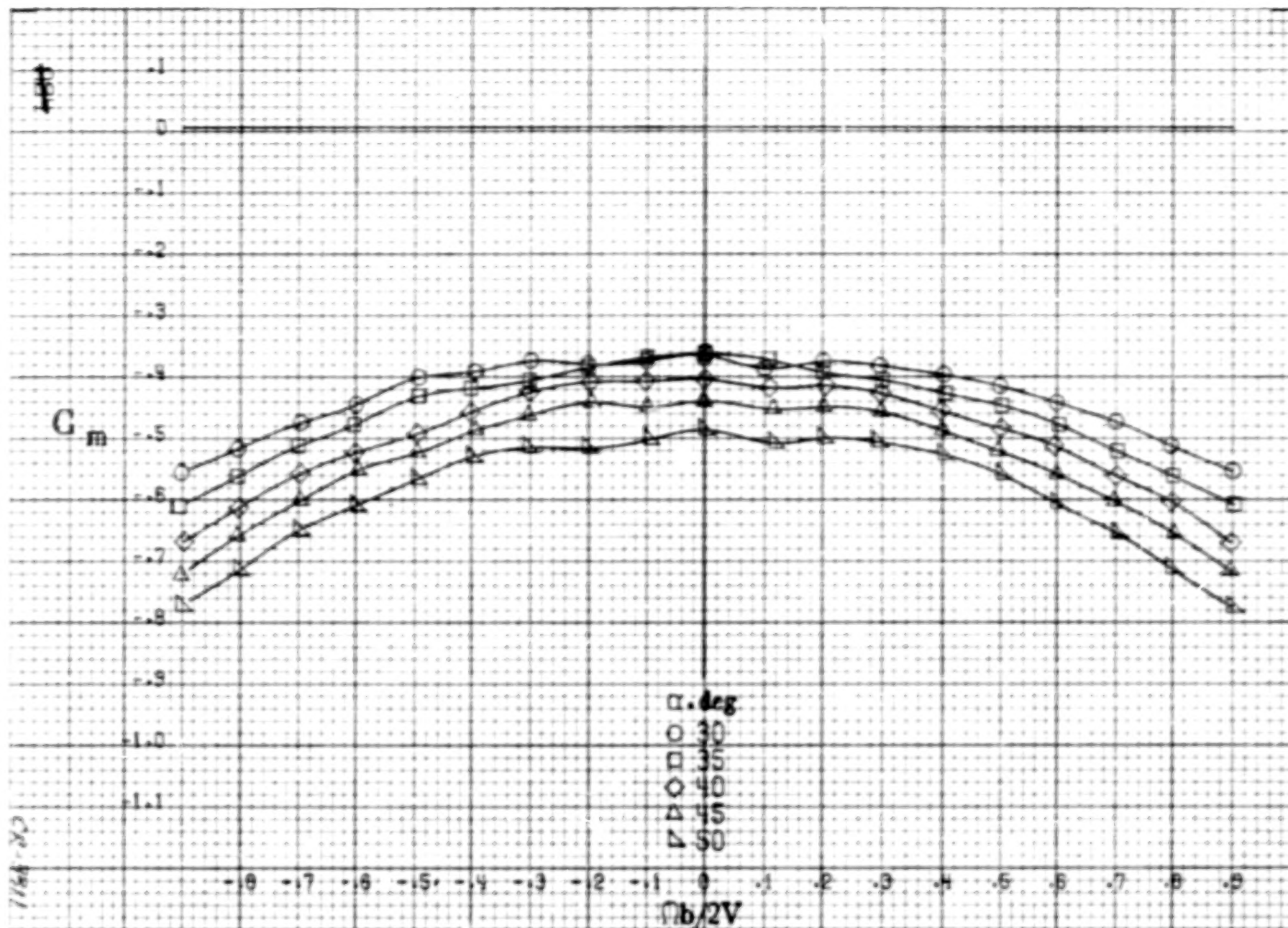


(a)  $\alpha = 8$  to  $16$  deg,  $SR = 152.4$  cm (60 in).

Figure A33. Effect of rotation rate and angle of attack on pitching-moment coefficient for turbine nose configuration,  $\delta_s = 0^\circ$ ,  $\delta_a = 0^\circ$ ,  $\delta_r = 0^\circ$ ,  $\beta = 0^\circ$ .

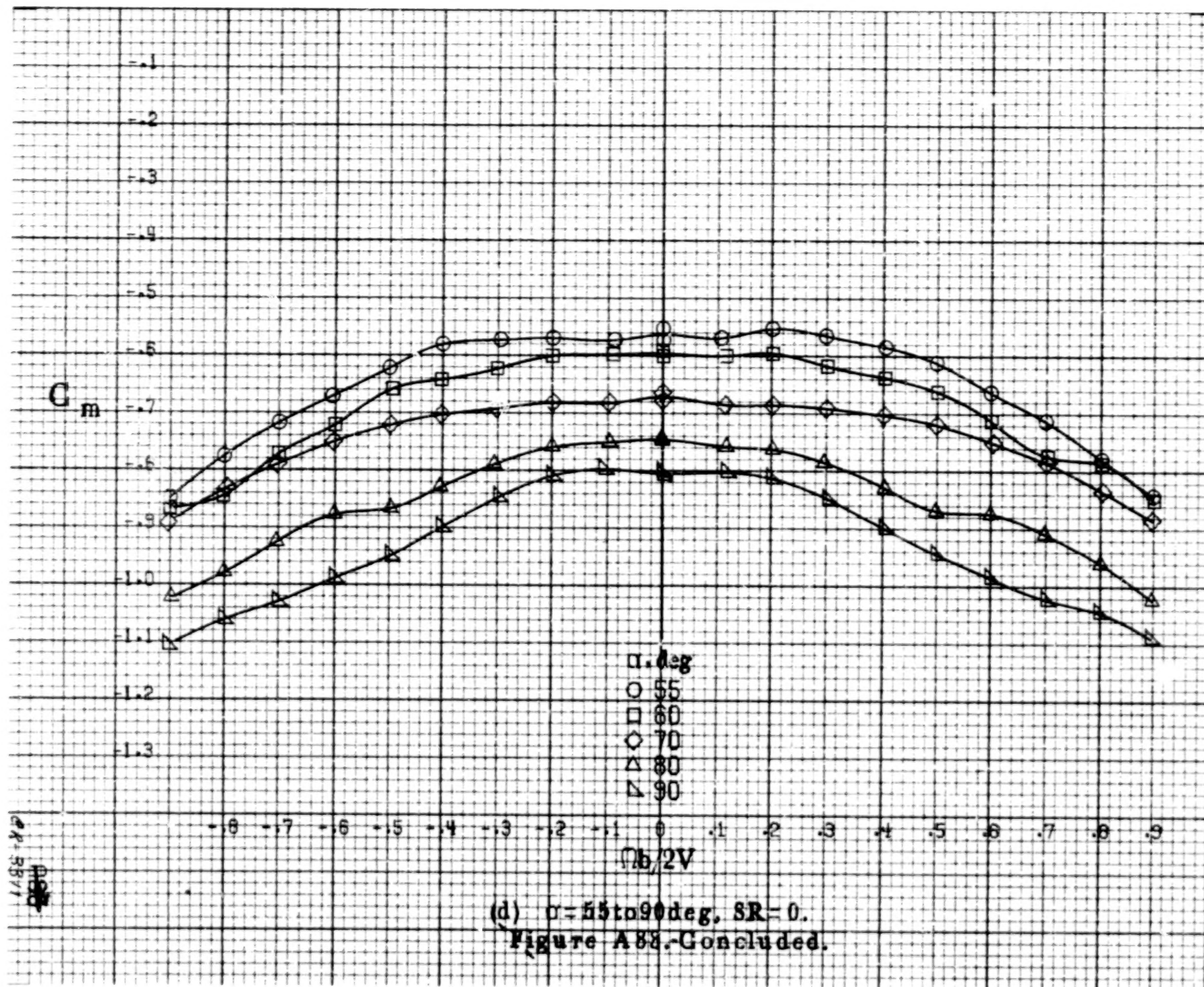


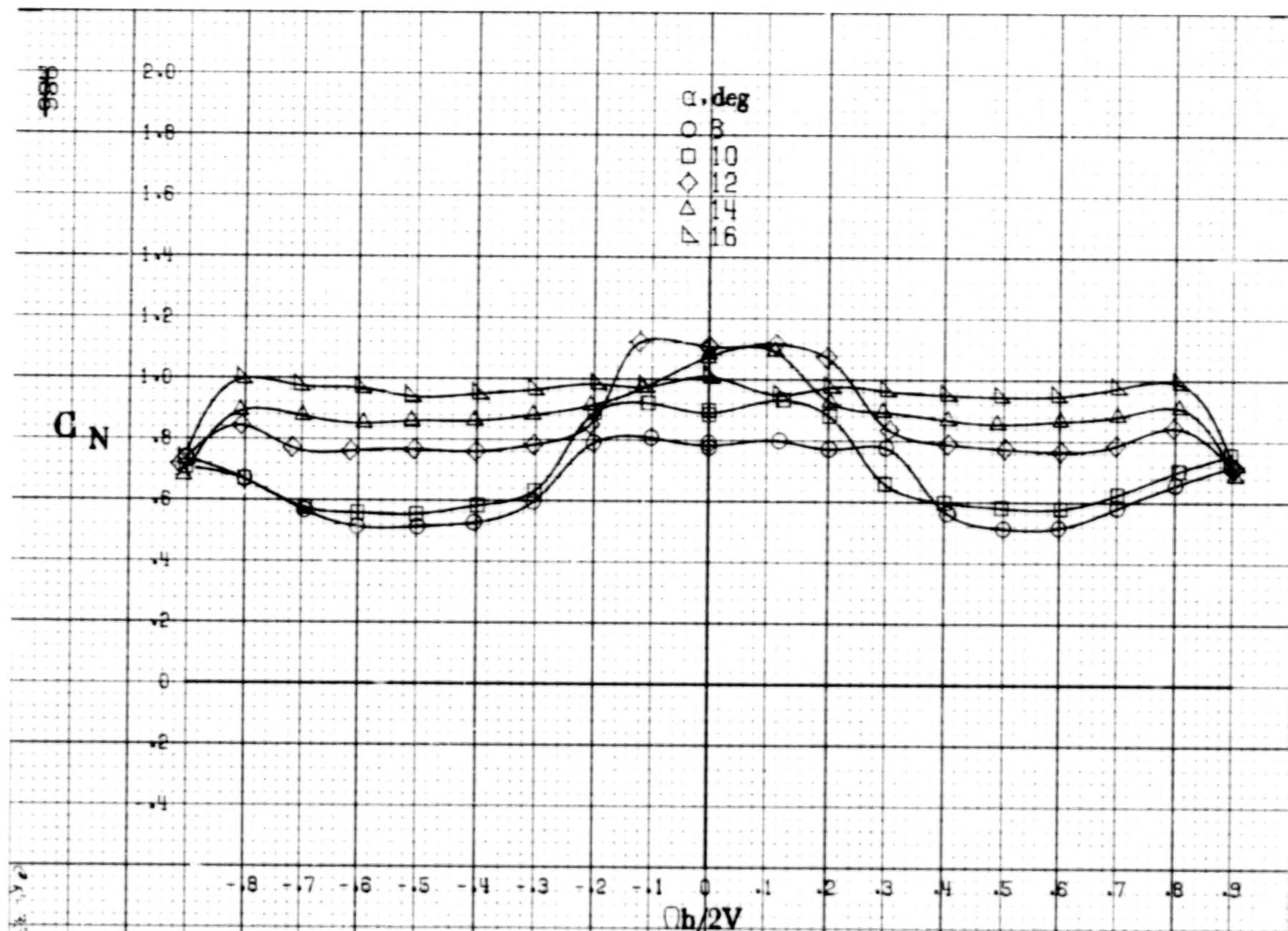
(b)  $\alpha = 18$  to  $35^\circ$ ,  $SR = 152.4\text{cm}$  (60 in).  
Figure A83.-Continued.



(c)  $\alpha = 30$  to  $50$  deg,  $SR = 0$ .  
Figure A83.-Continued.

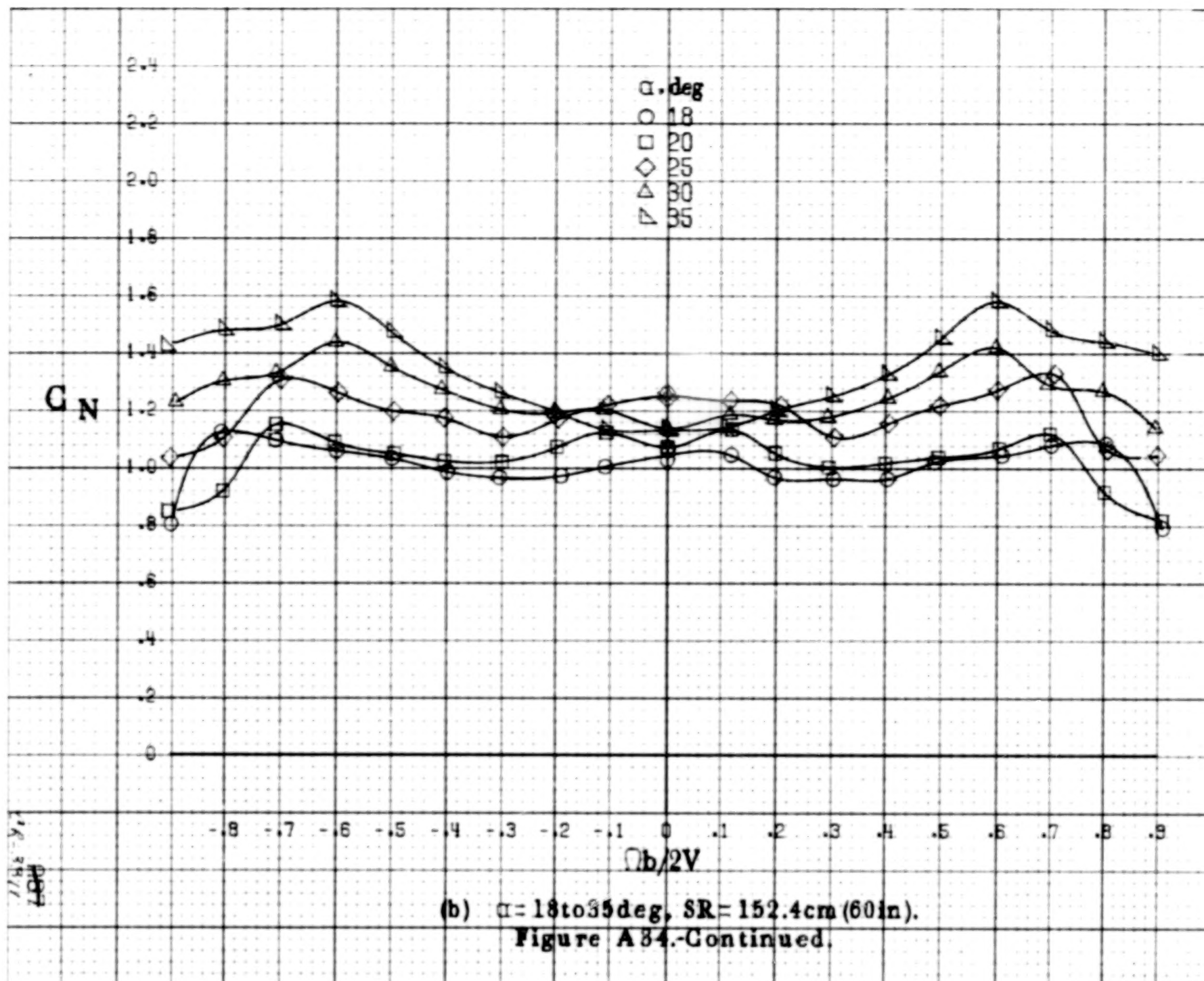


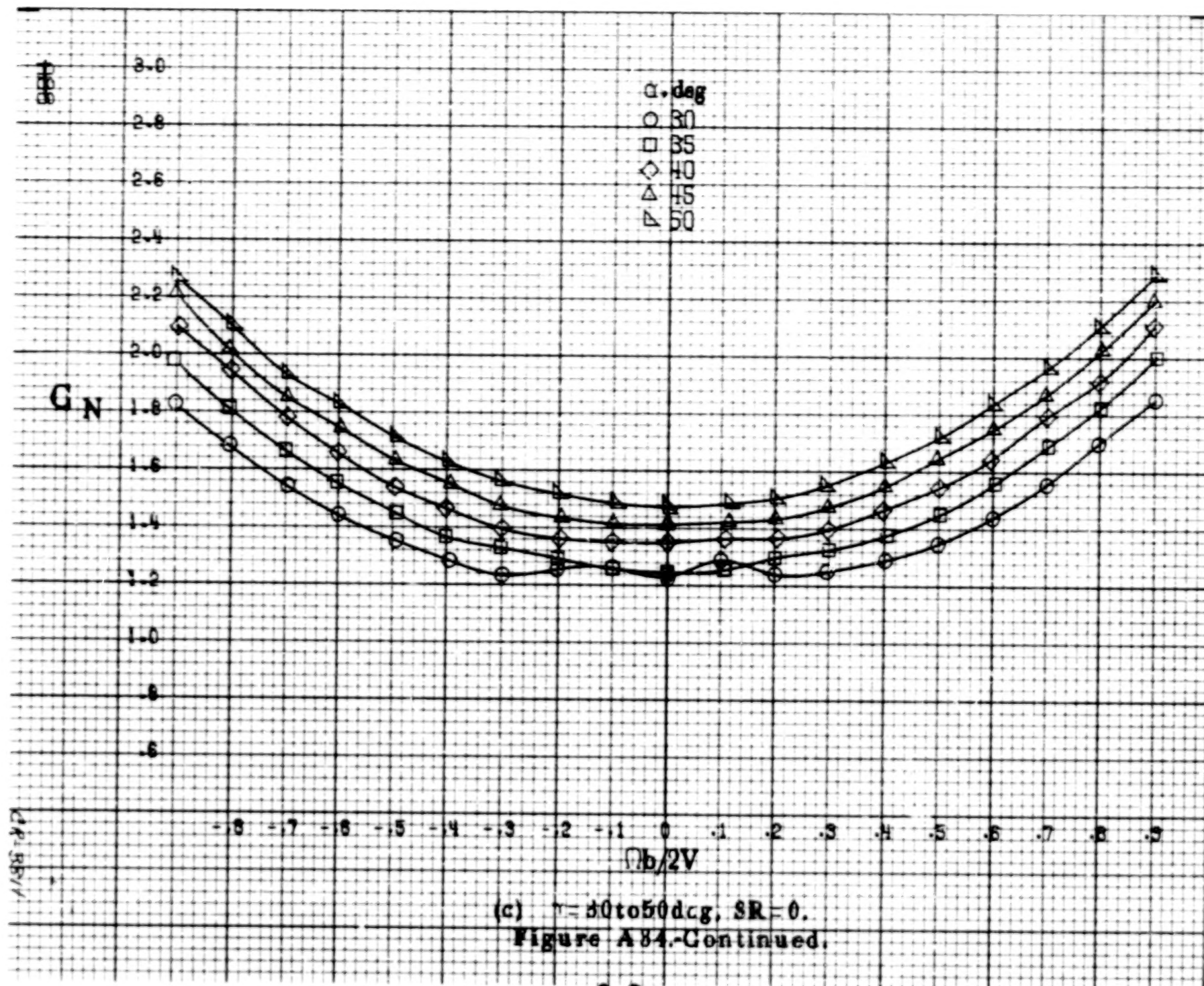


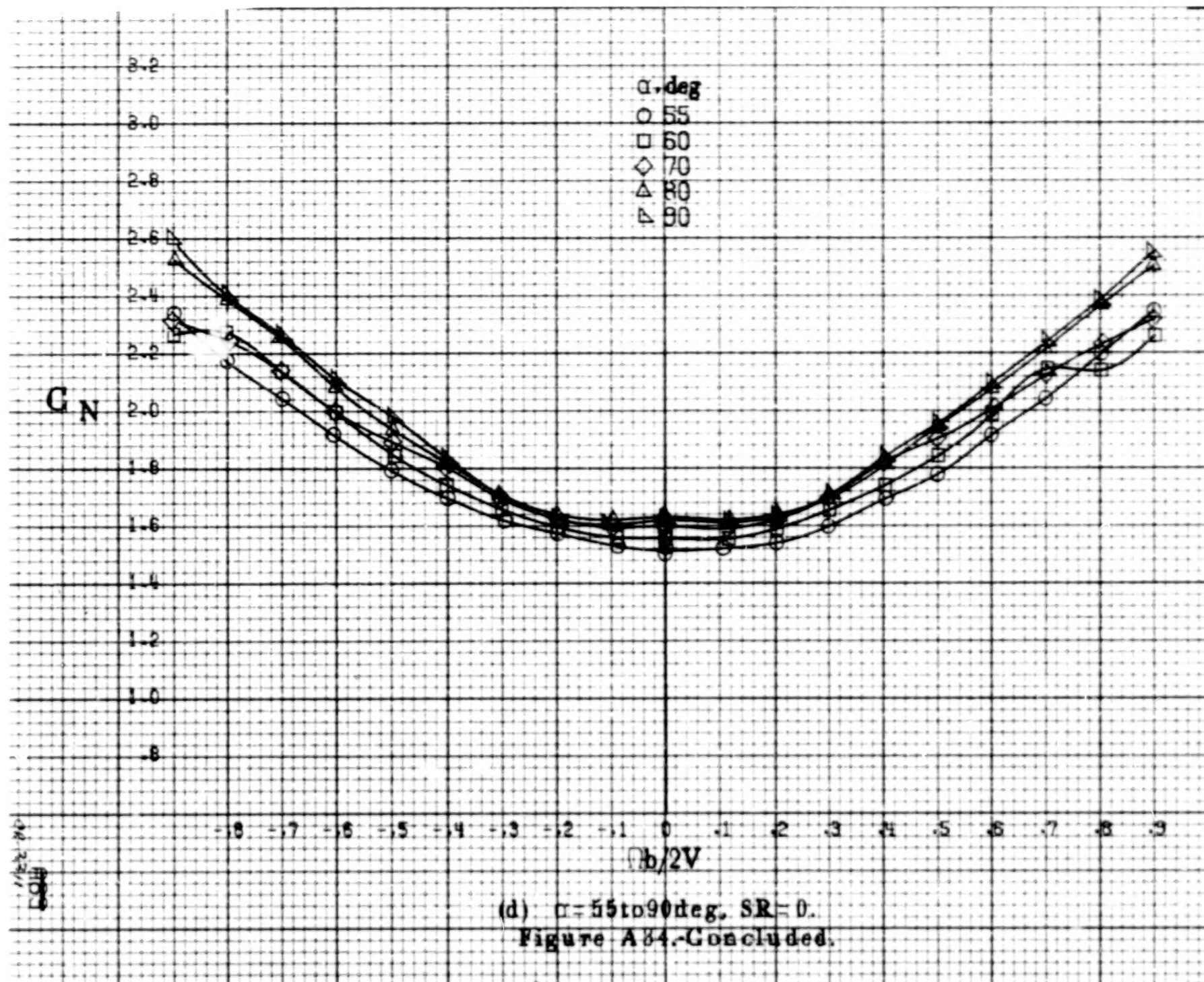


(a)  $\alpha = 8$  to  $16^\circ$ ,  $SR = 152.4 \text{ cm (60 in.)}$ .  
 Figure A34: Effect of rotation rate and angle of attack on normal-force coefficient for turbine nose configuration.  $\delta_s = 0^\circ$ ,  $\delta_a = 0^\circ$ ,  $\delta_r = 0^\circ$ ,  $\beta = 0^\circ$ .

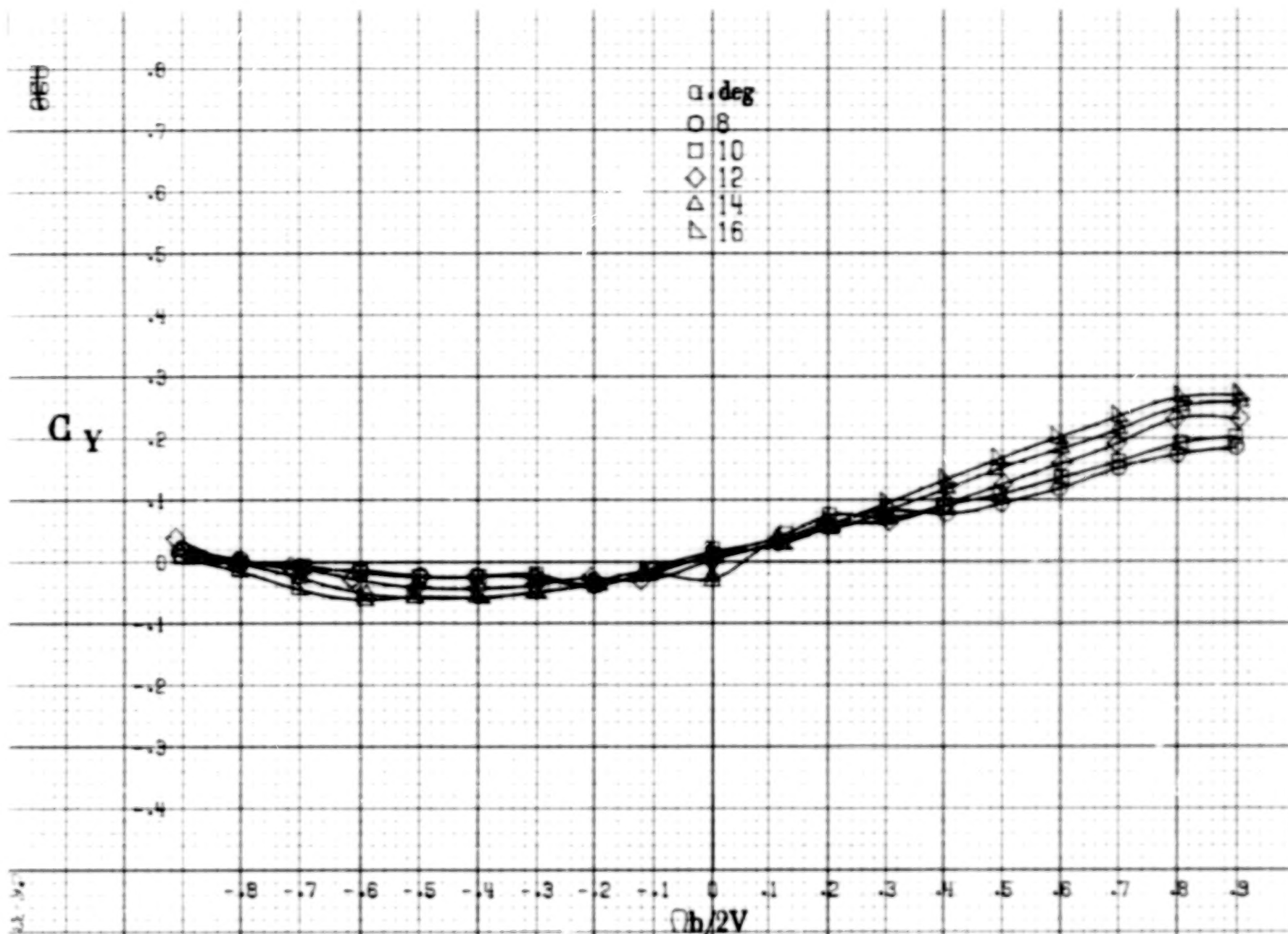




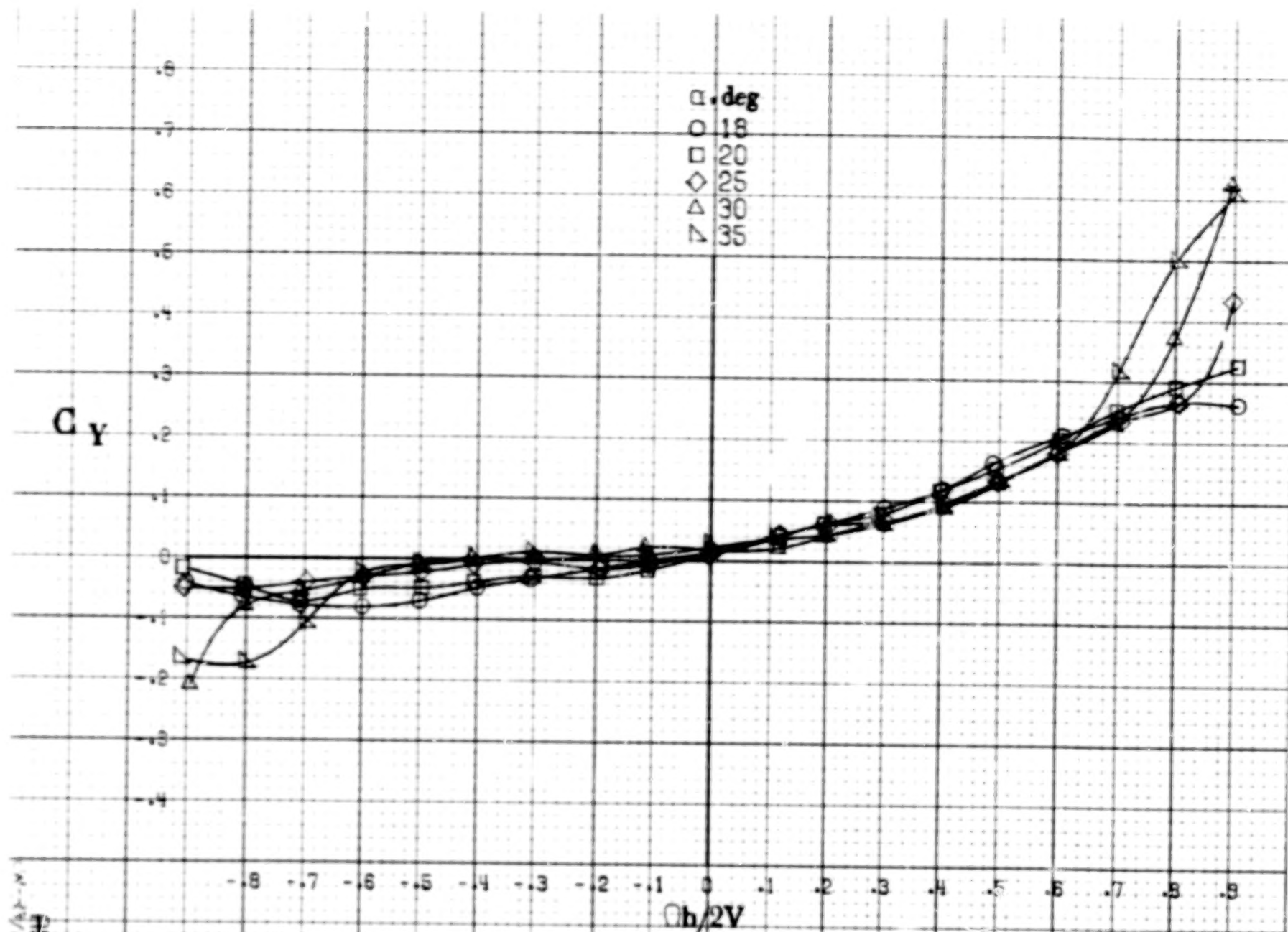








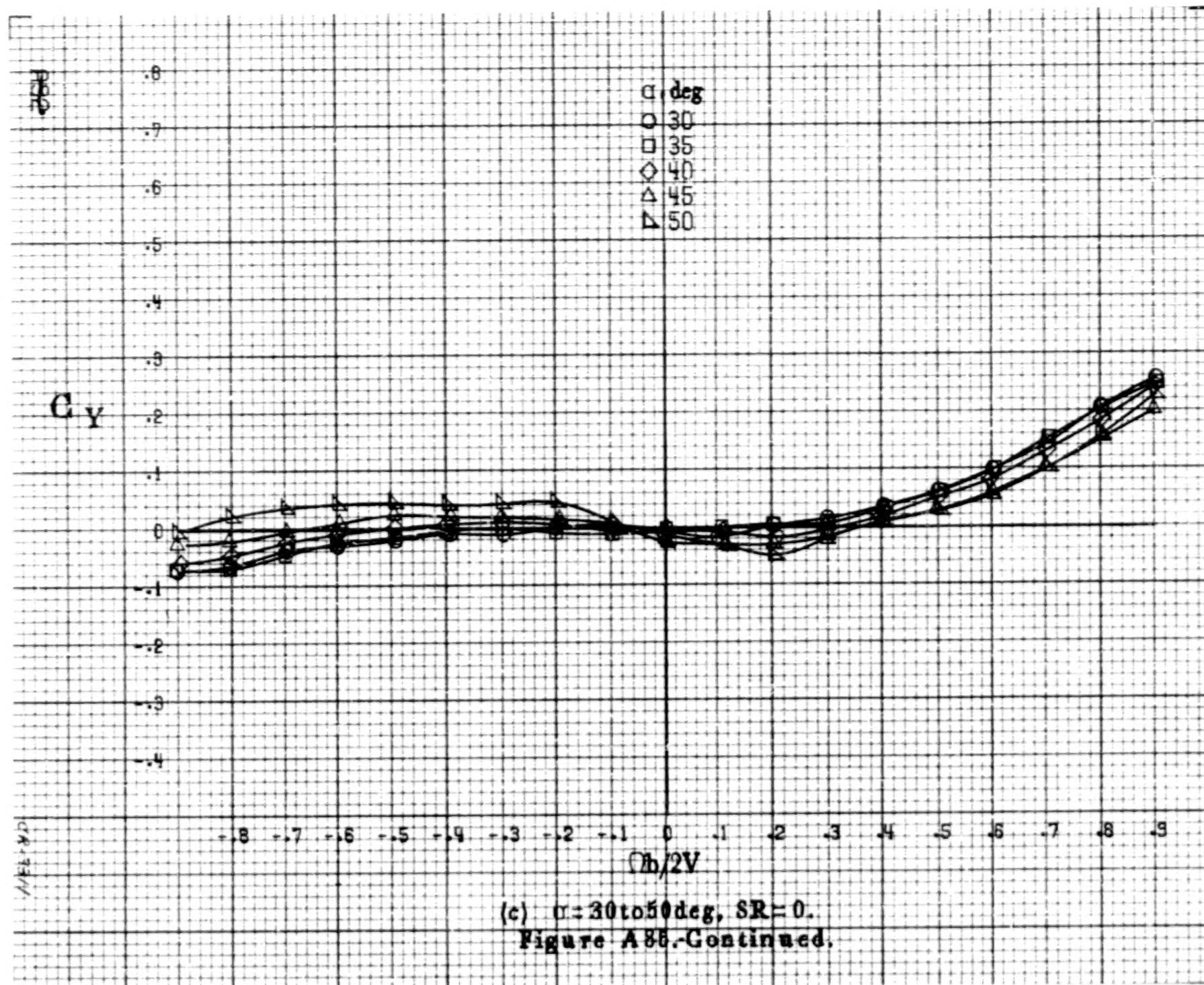
(a)  $\alpha = 8$  to  $16^\circ$ ,  $SR = 152.4 \text{ cm (60 in.)}$ .  
 Figure A35.-Effect of rotation rate and angle of attack on side-force coefficient for turbine nose configuration.  $\delta_s = 0^\circ$ ,  $\delta_a = 0^\circ$ ,  $\delta_r = 0^\circ$ ,  $\theta = 0^\circ$ .

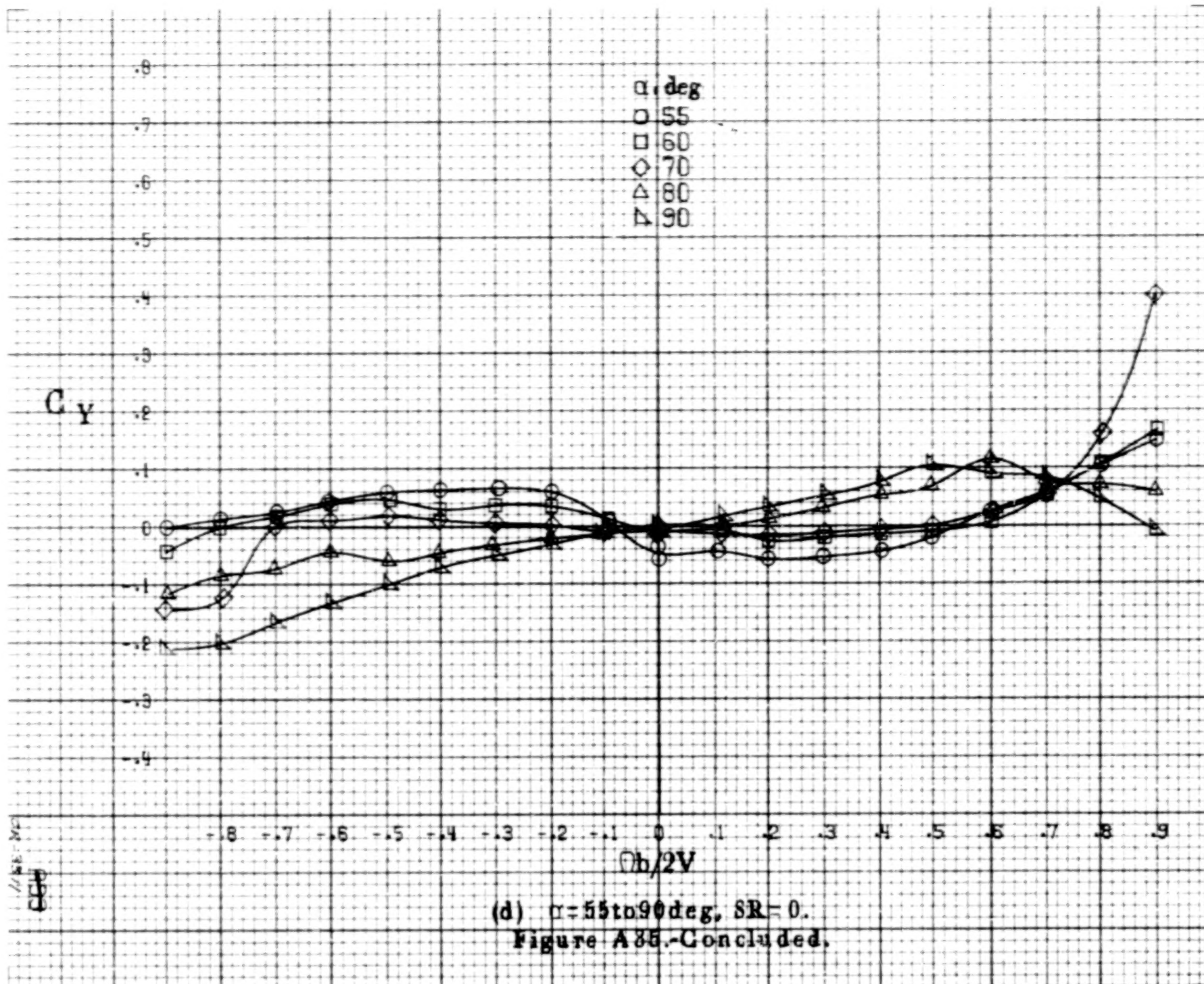


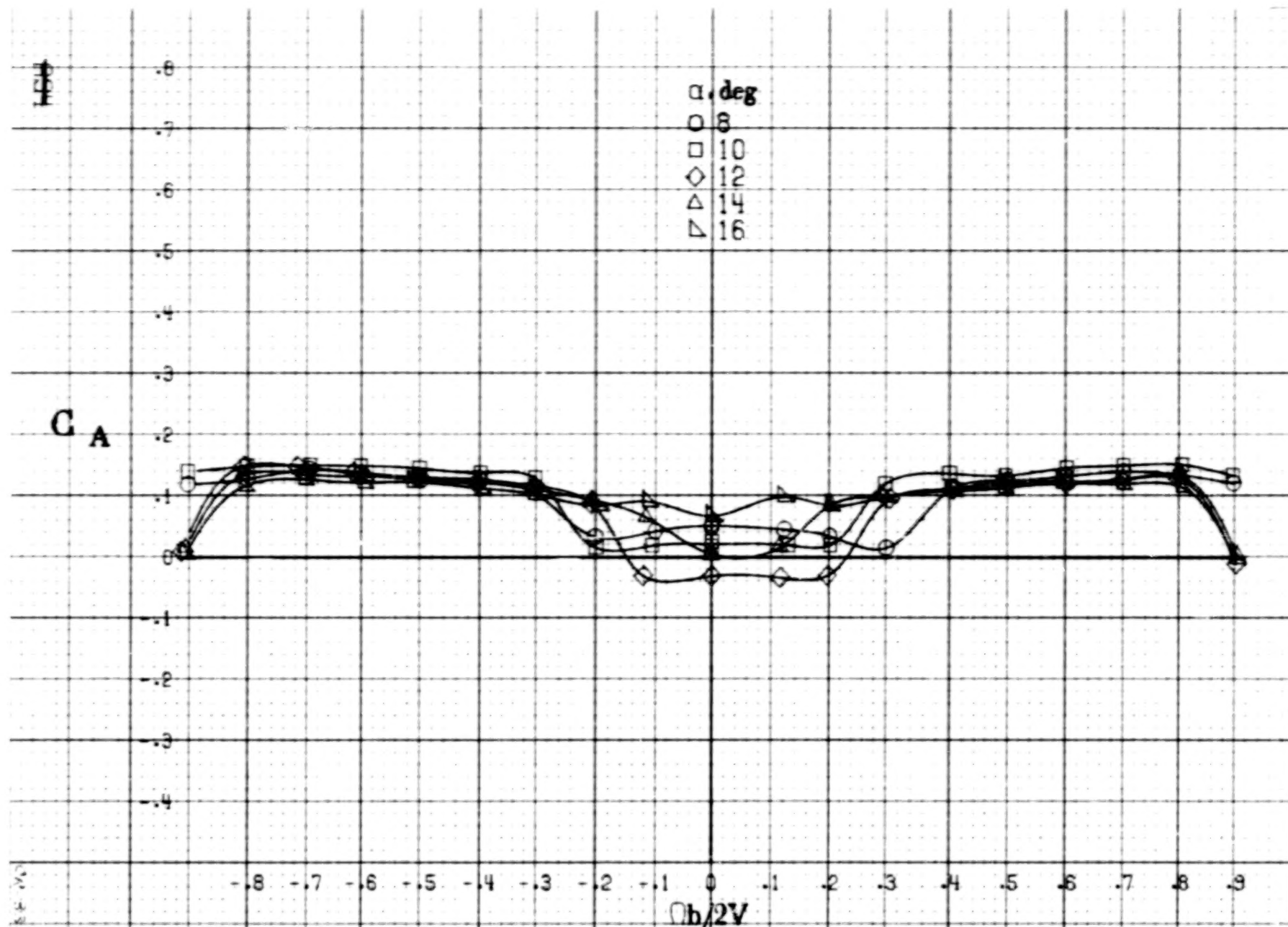
(b)  $\alpha = 18$  to  $35^\circ$ ,  $SR = 152.4 \text{ cm (60 in.)}$ .

Figure A85.-Continued.





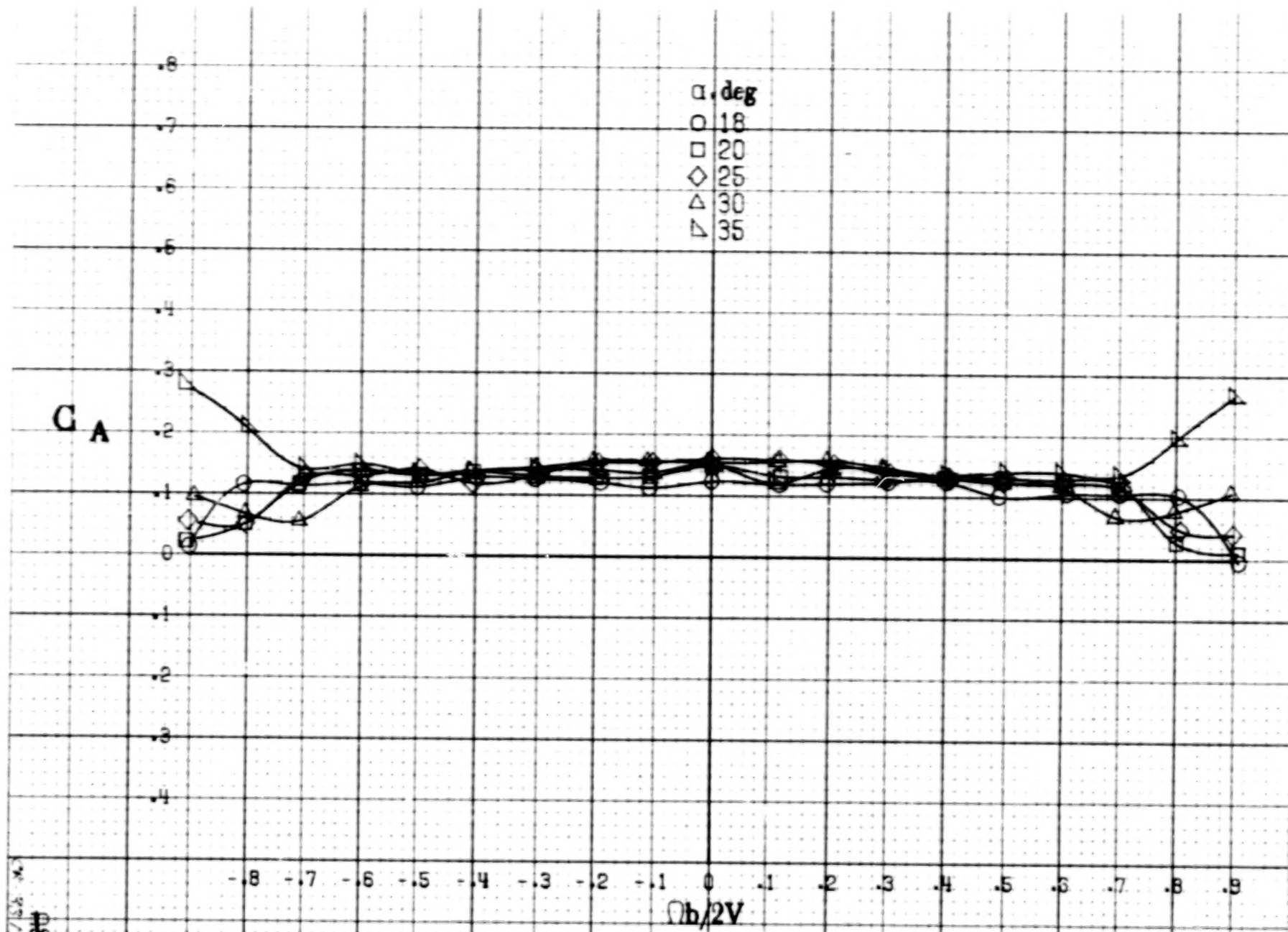




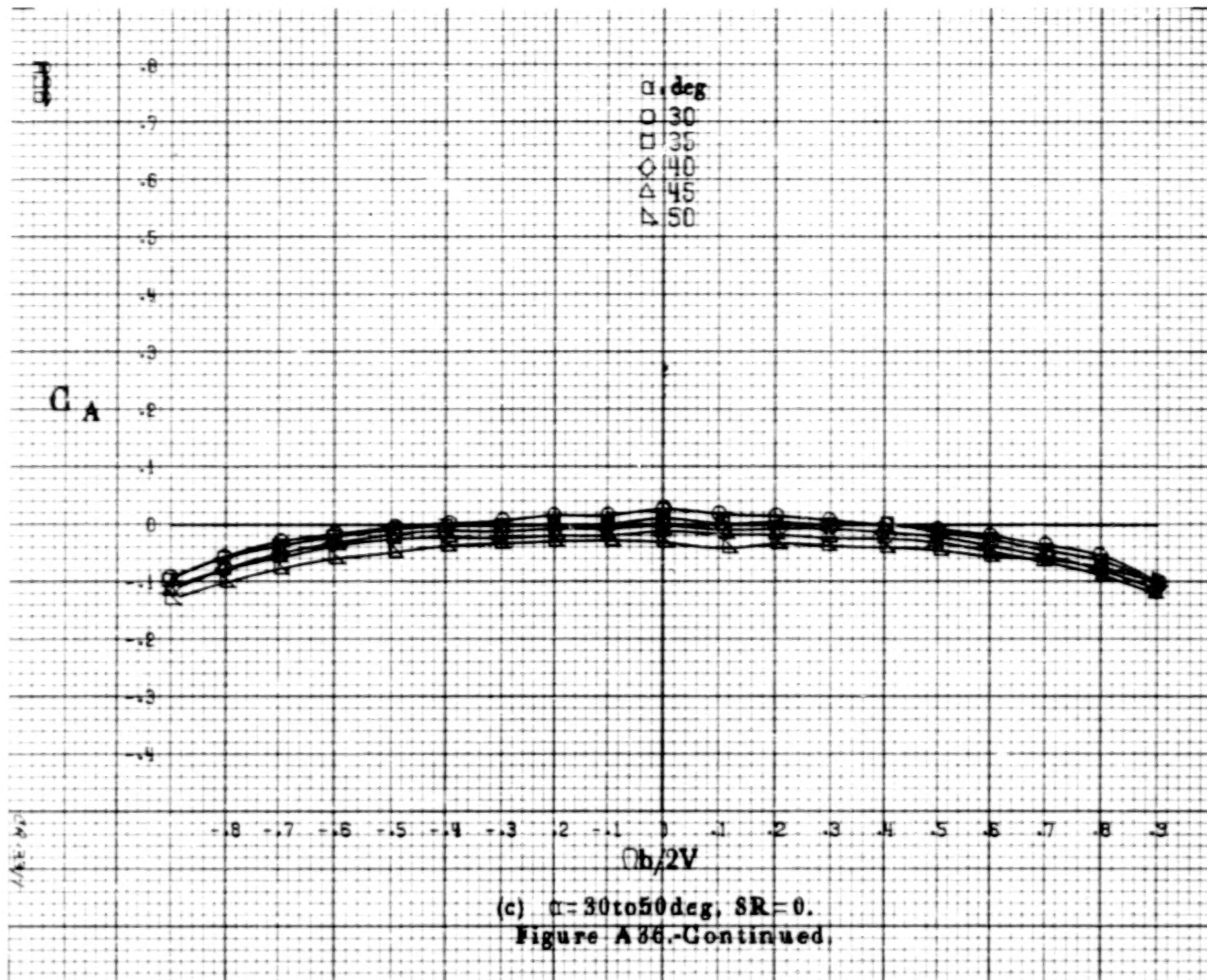
(a)  $\alpha = 8$  to  $16^\circ$ ,  $SR = 152.4\text{cm (60in)}$ .

Figure A36. Effect of rotation rate and angle of attack on axial-force coefficient for turbine nose configuration.  $\delta_s = 0^\circ$ ,  $\delta_a = 0^\circ$ ,  $\delta_r = 0^\circ$ ,  $\beta = 0^\circ$ .

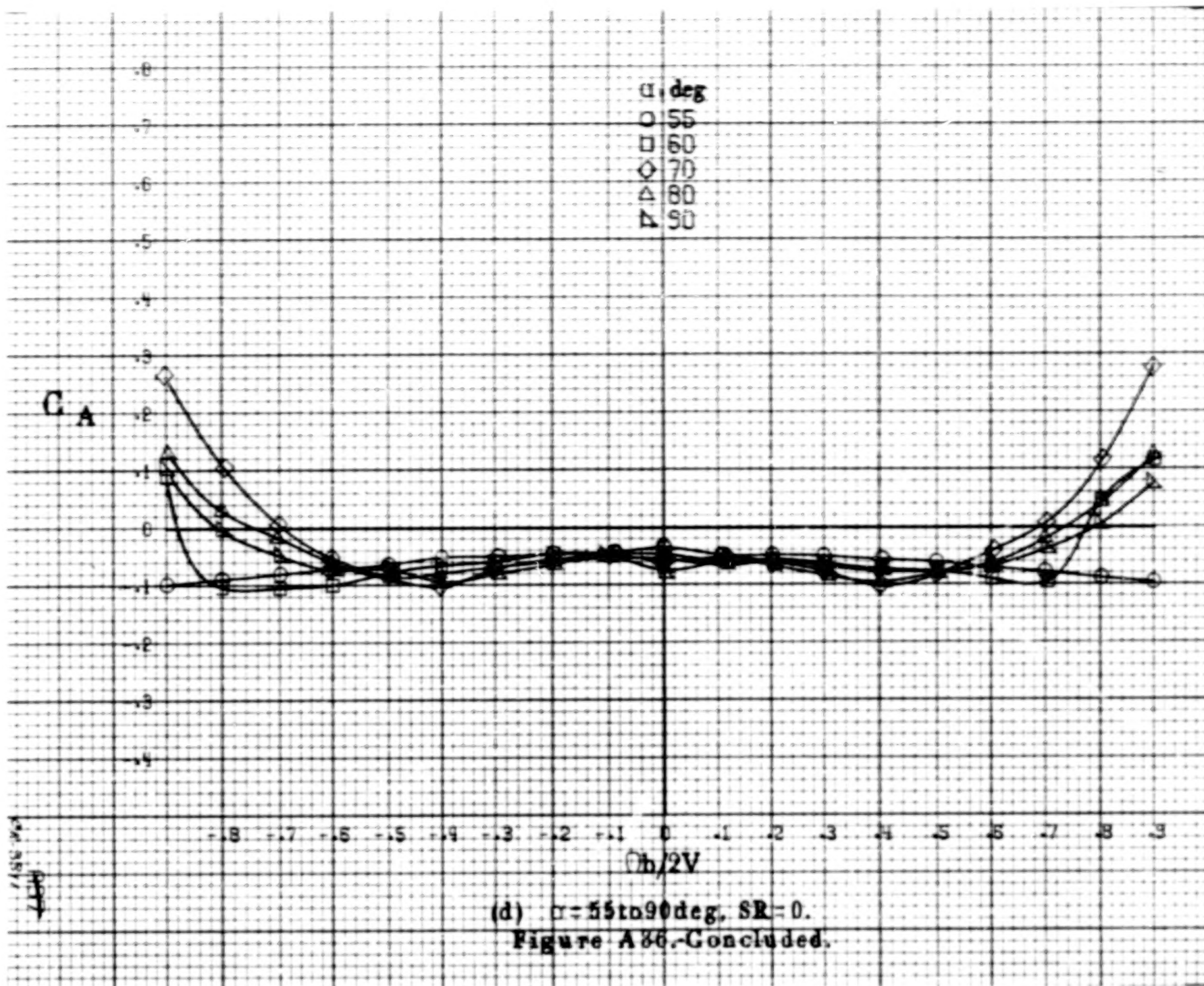


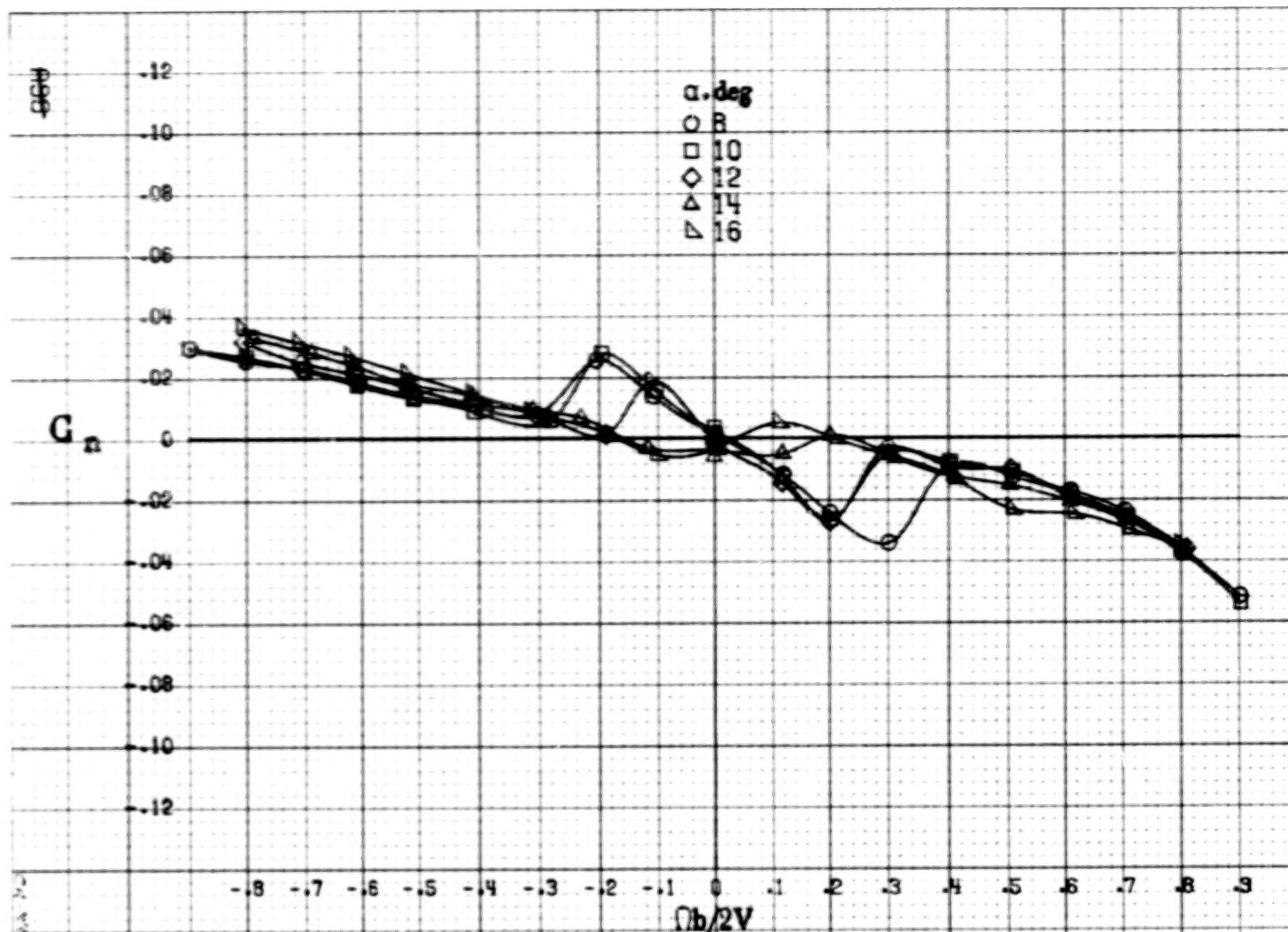


(b)  $\alpha = 18$  to  $35$  deg,  $SR = 152.4$  cm (60 in).  
Figure A86.-Continued.

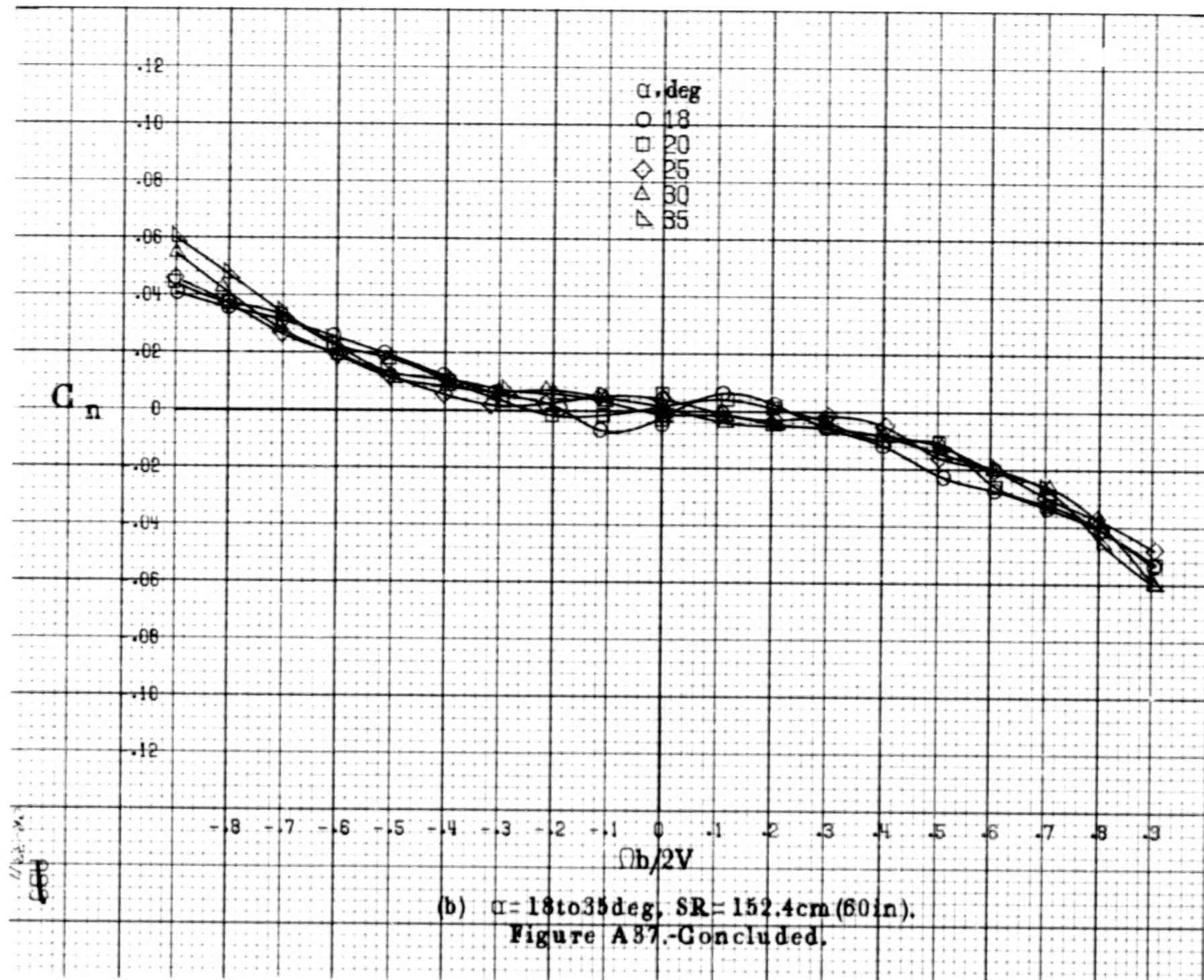


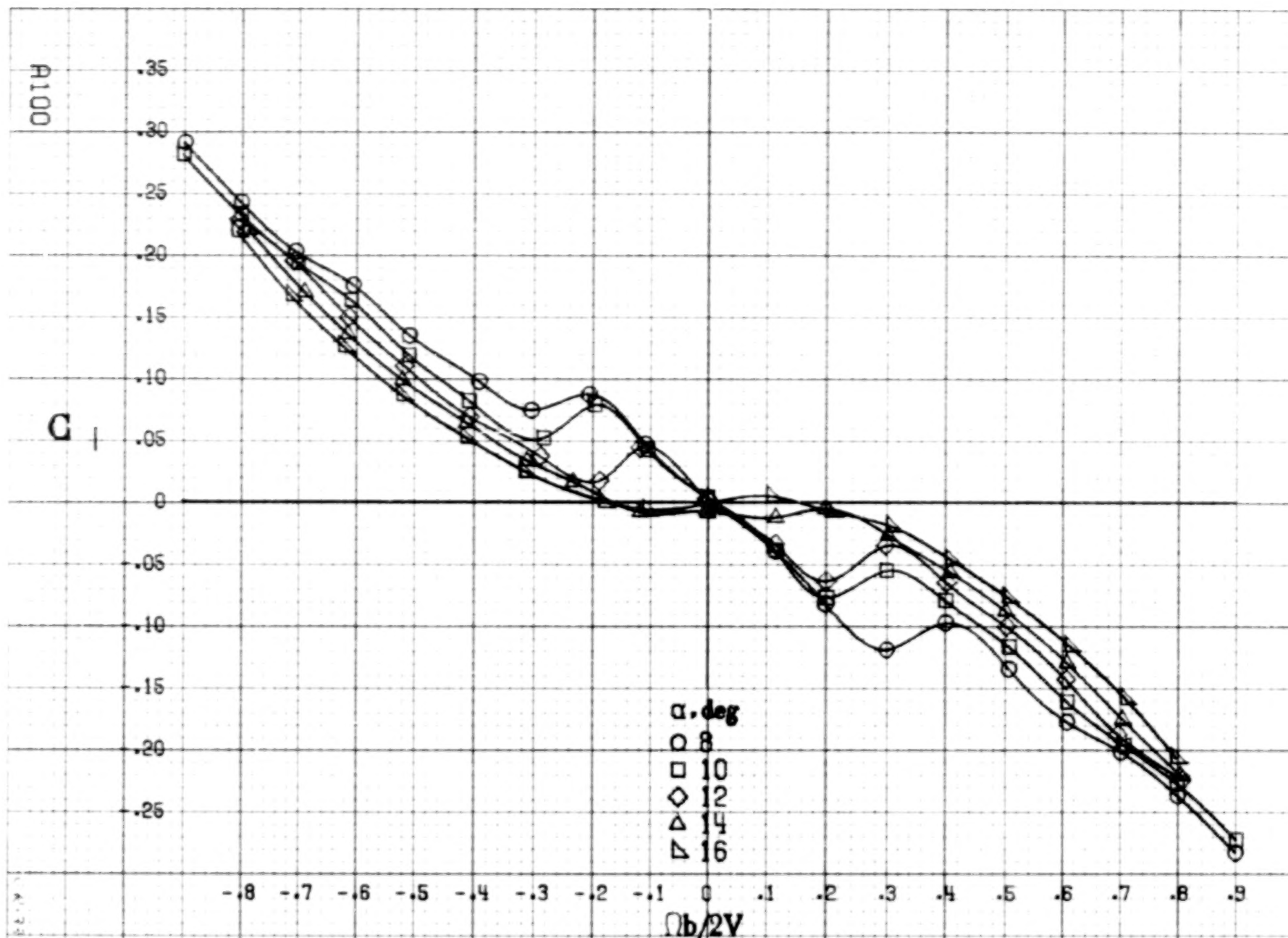






(a)  $\alpha = 8$  to  $16^\circ$ ,  $SR = 152.4\text{cm (60in)}$ .  
 Figure A97. Effect of rotation rate and angle of attack on yawing-moment coefficient for canopy fairing configuration.  $\delta_a = 0^\circ$ ,  $\delta_s = 0^\circ$ ,  $\delta_r = 0^\circ$ ,  $\beta = 0^\circ$ .

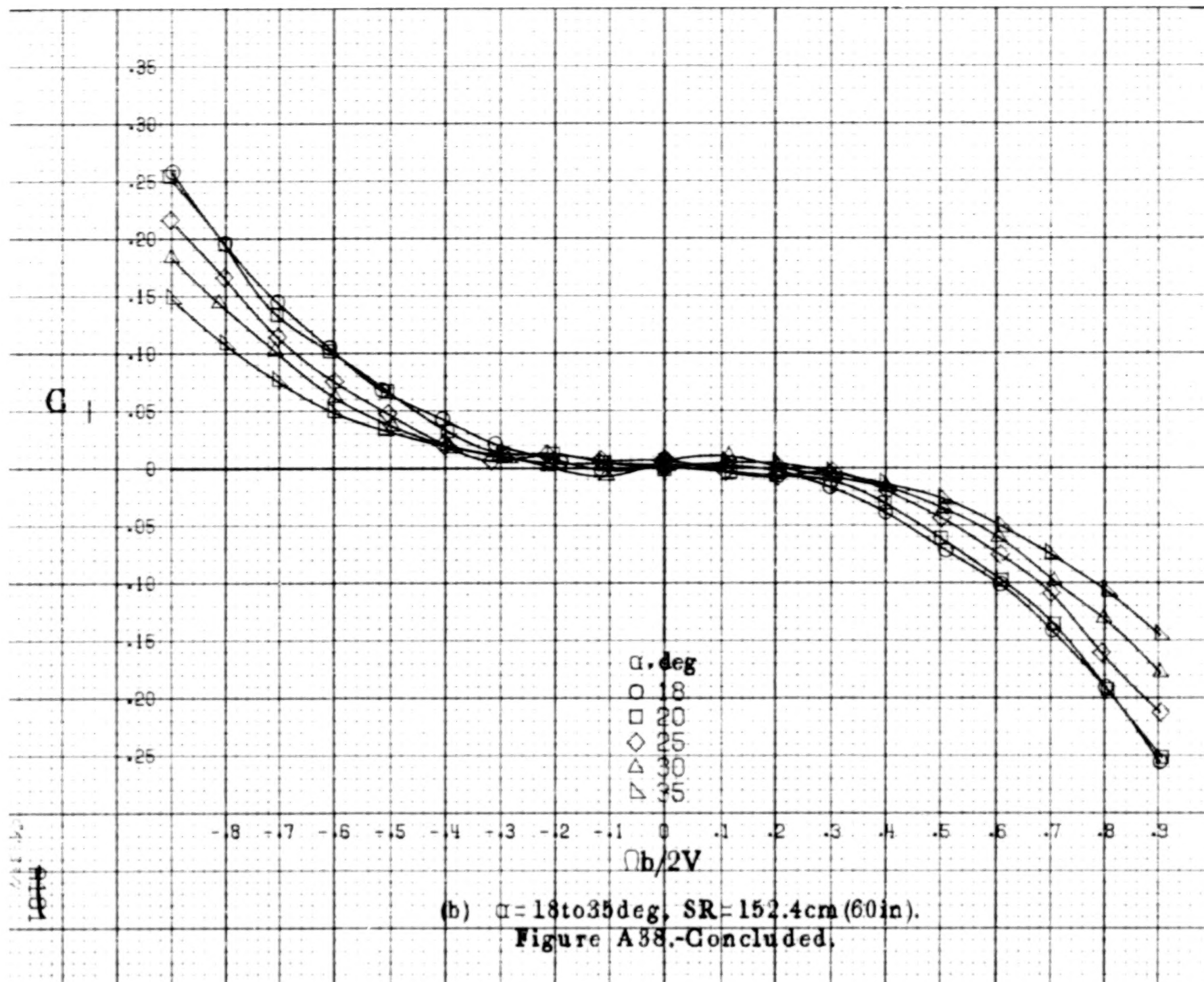




(a)  $\alpha = 8$  to  $16^\circ$ ,  $SR = 152.4 \text{ cm (60 in)}$ .

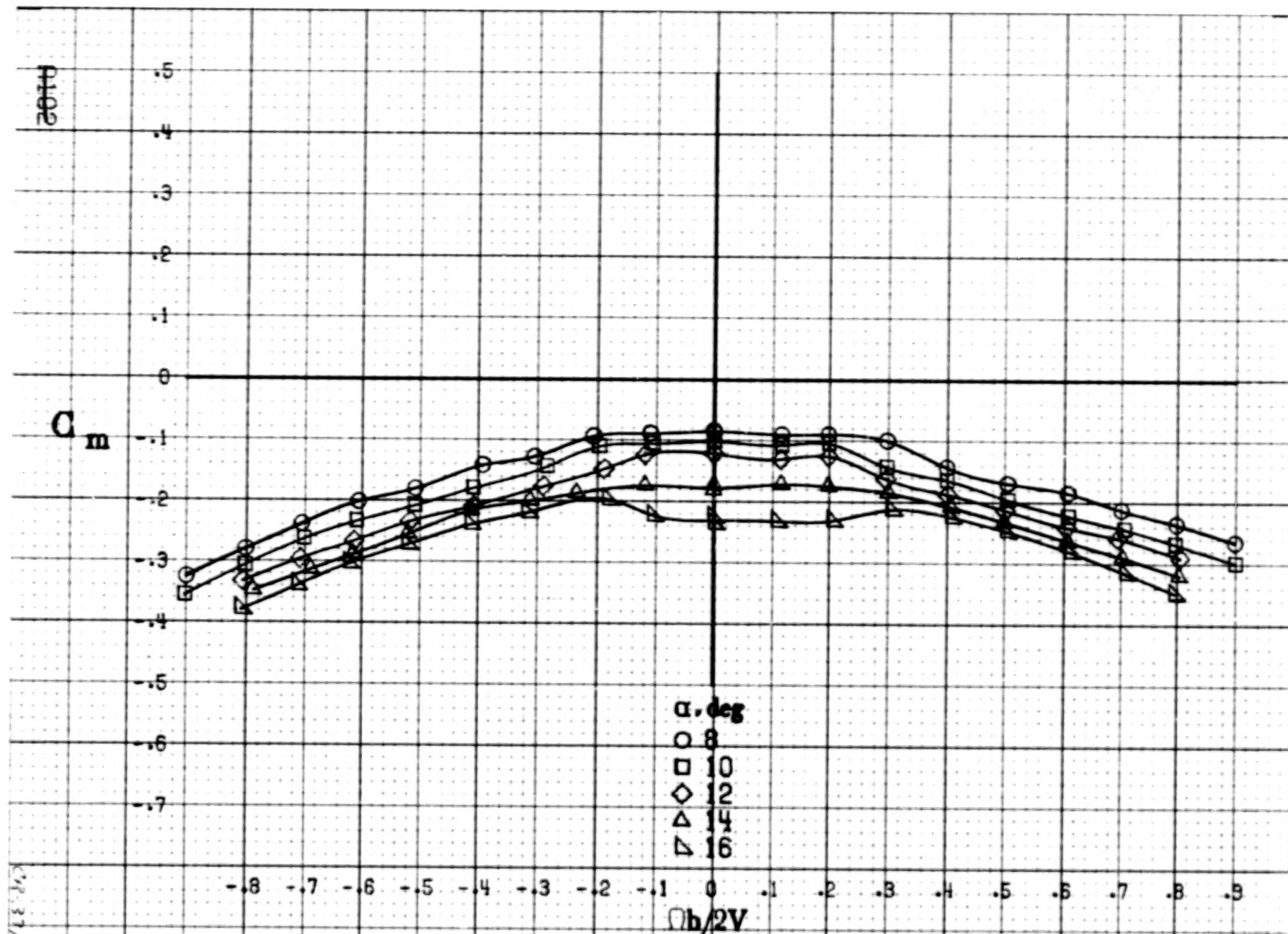
Figure A38.-Effect of rotation rate and angle of attack on rolling-moment coefficient for canopy fairing configuration.  $\delta_e = 0^\circ$ ,  $\delta_a = 0^\circ$ ,  $\delta_r = 0^\circ$ ,  $\beta = 0^\circ$ .





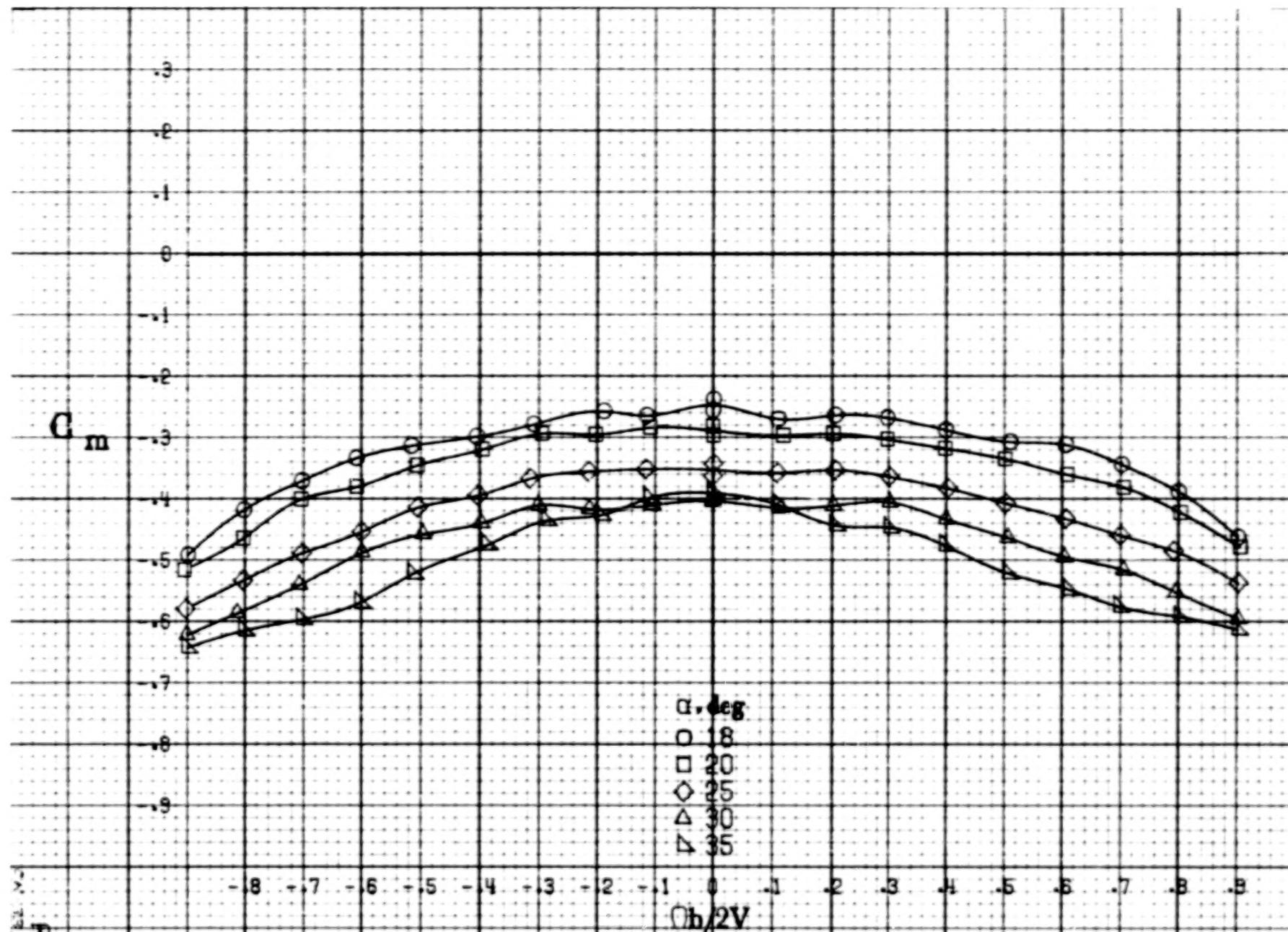
(b)  $\alpha = 18$  to  $35^\circ$ ,  $SR = 152.4 \text{ cm (60 in.)}$ .

Figure A88.-Concluded.

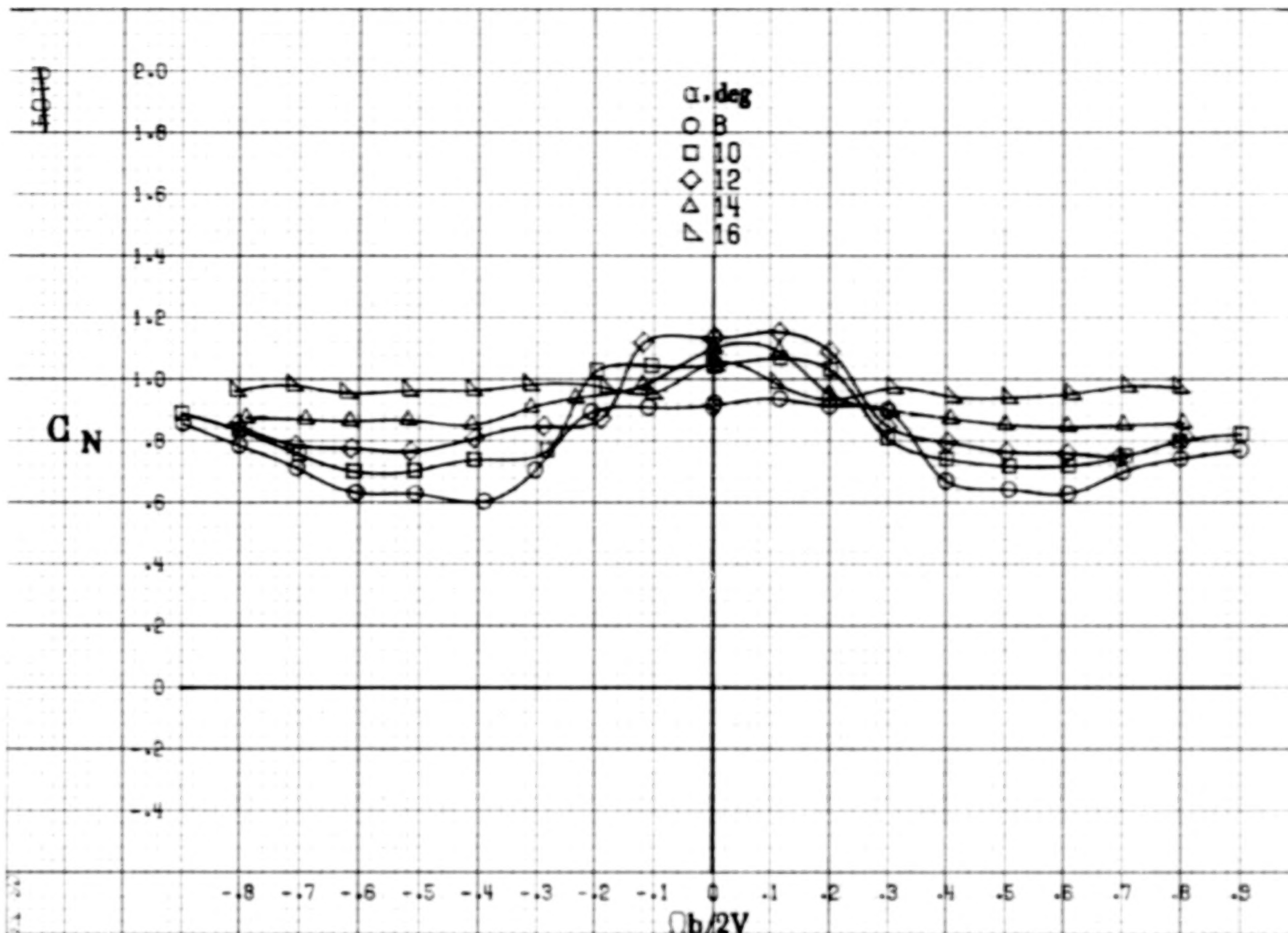


(a)  $\alpha = 8$  to  $16^\circ$ ,  $SR = 152.4\text{cm (60in)}$ .

Figure A39. Effect of rotation rate and angle of attack on pitching-moment coefficient for canopy fairing configuration.  $\delta_e = 0^\circ$ ,  $\delta_a = 0^\circ$ ,  $\delta_r = 0^\circ$ ,  $\beta = 0^\circ$ .

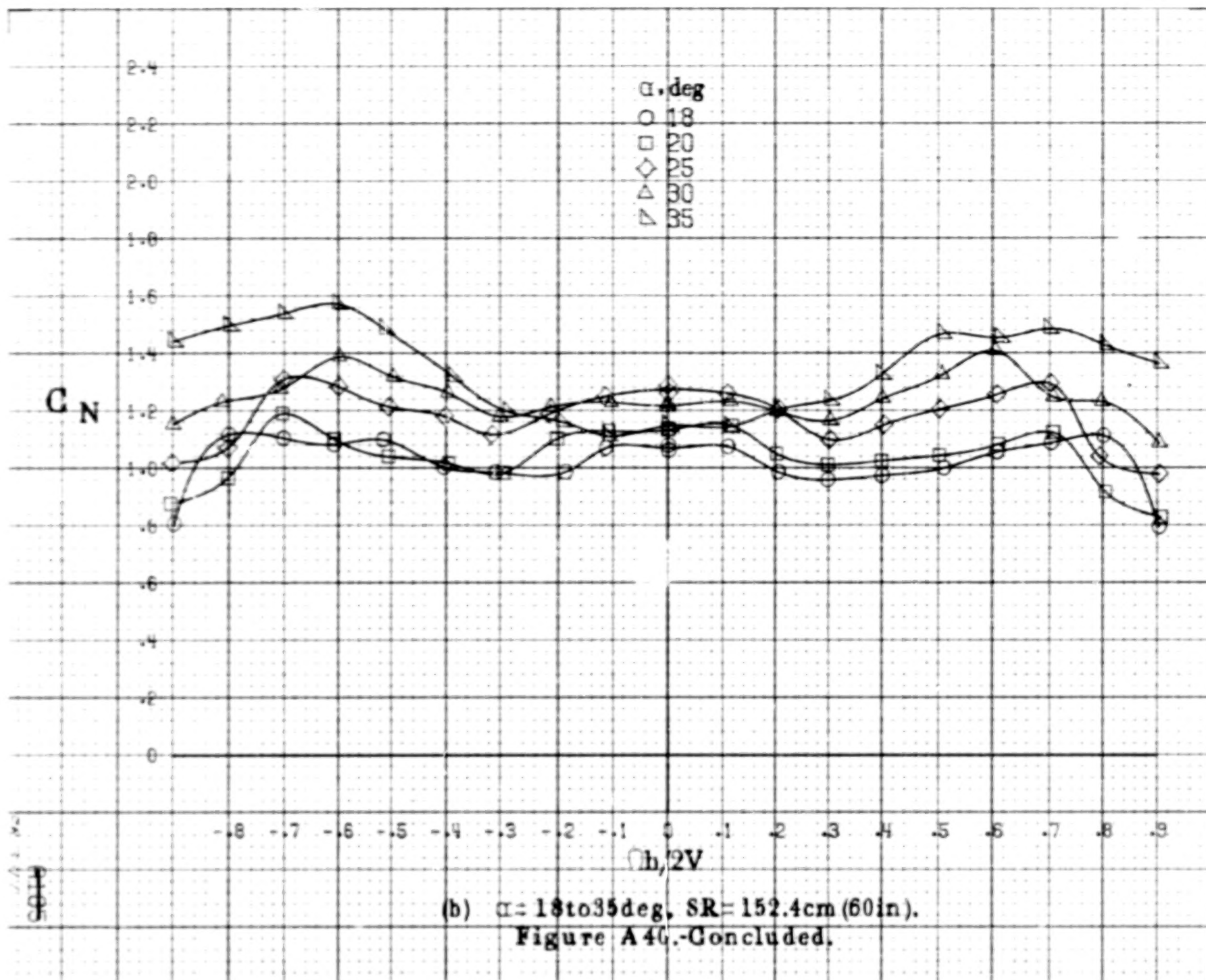


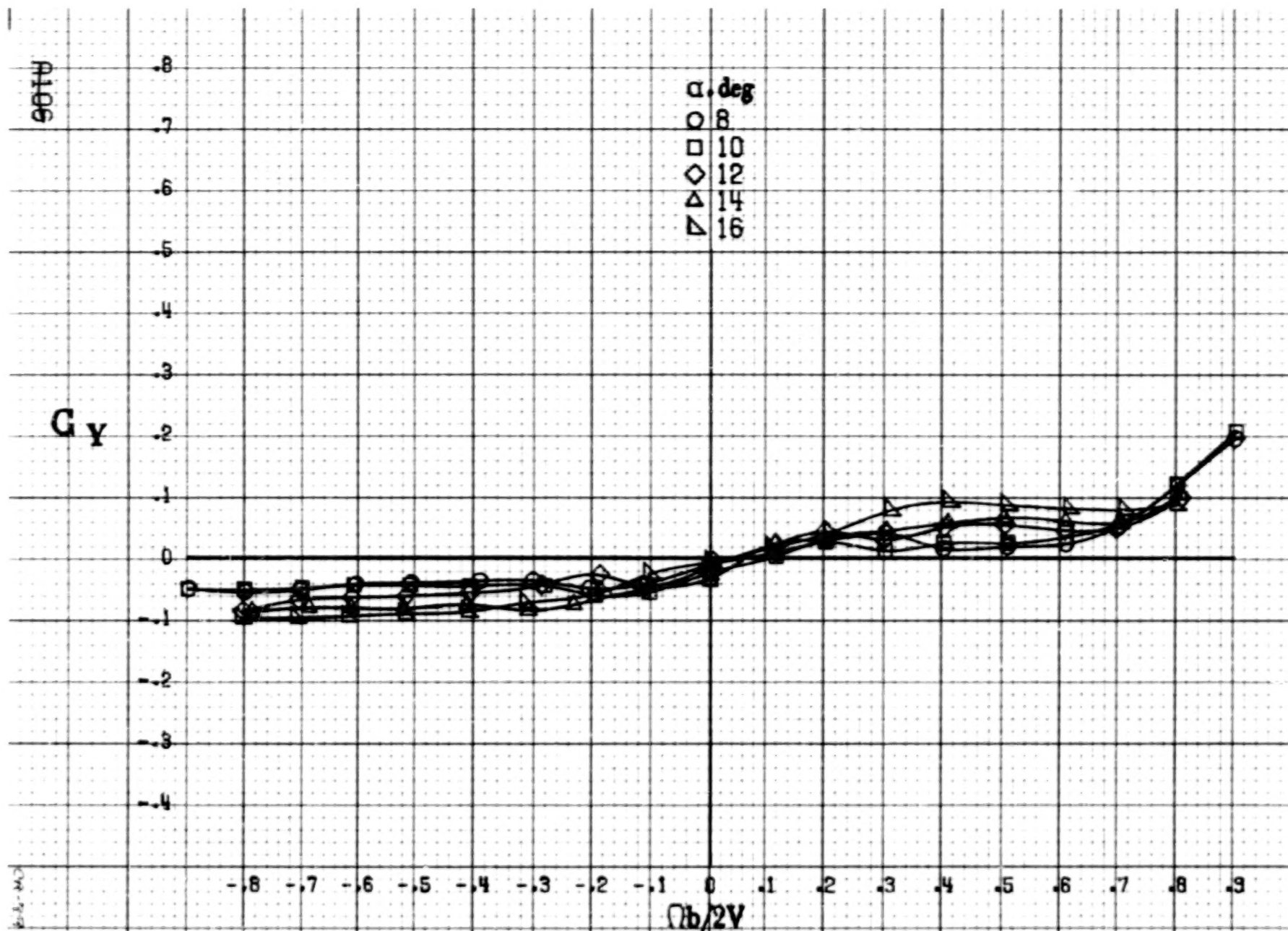
(b)  $\alpha = 18$  to  $35^\circ$ ,  $SR = 152.4\text{cm}$  (60 in).  
Figure A89.-Concluded.



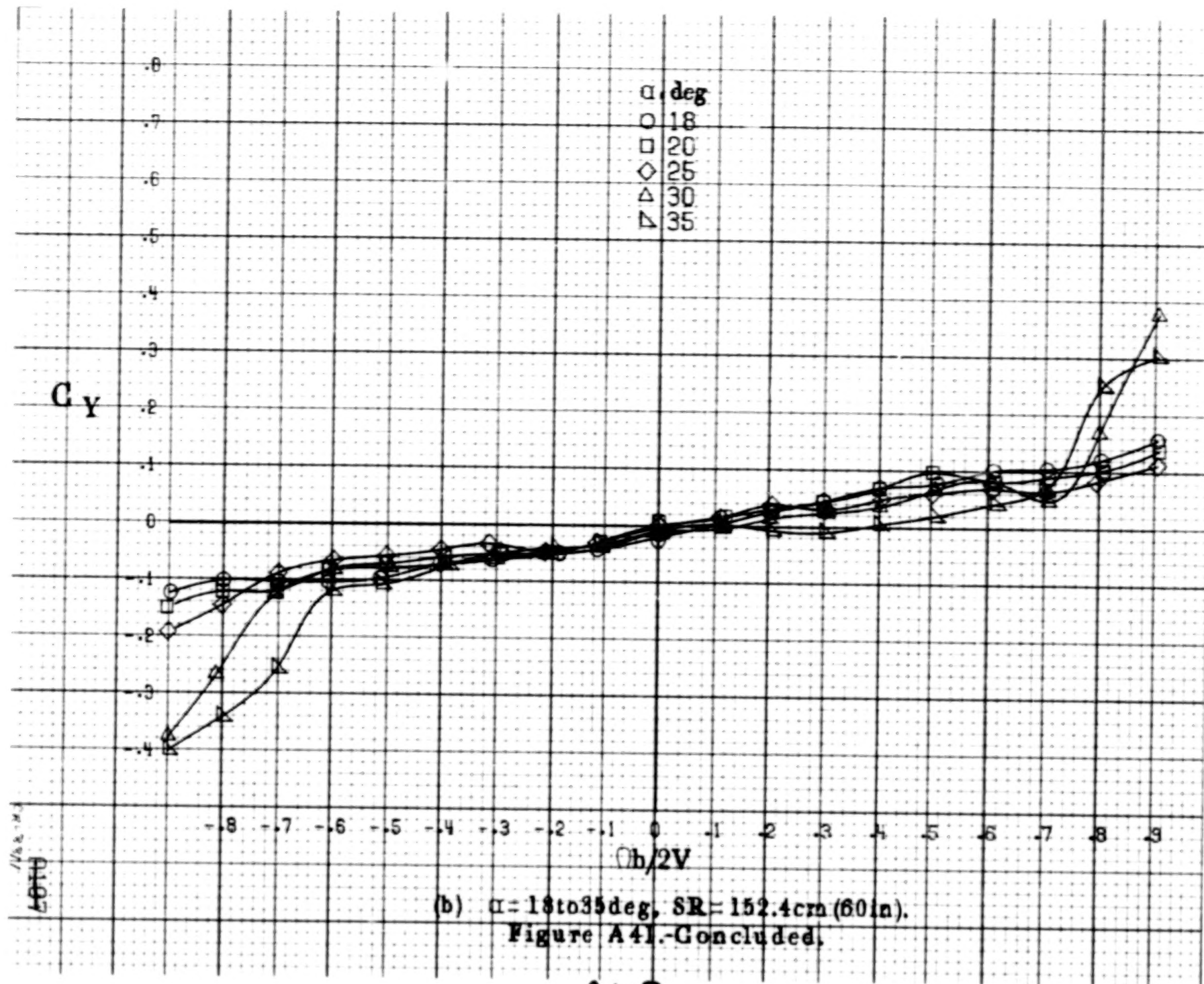
(a)  $\alpha = 8$  to  $16$  deg,  $SR = 152.4$  cm (60 in).  
 Figure A40. Effect of rotation rate and angle of attack on normal-force coefficient for canopy fairing configuration.  $\delta_s = 0^\circ$ ,  $\delta_a = 0^\circ$ ,  $\delta_r = 0^\circ$ ,  $\beta = 0^\circ$ .

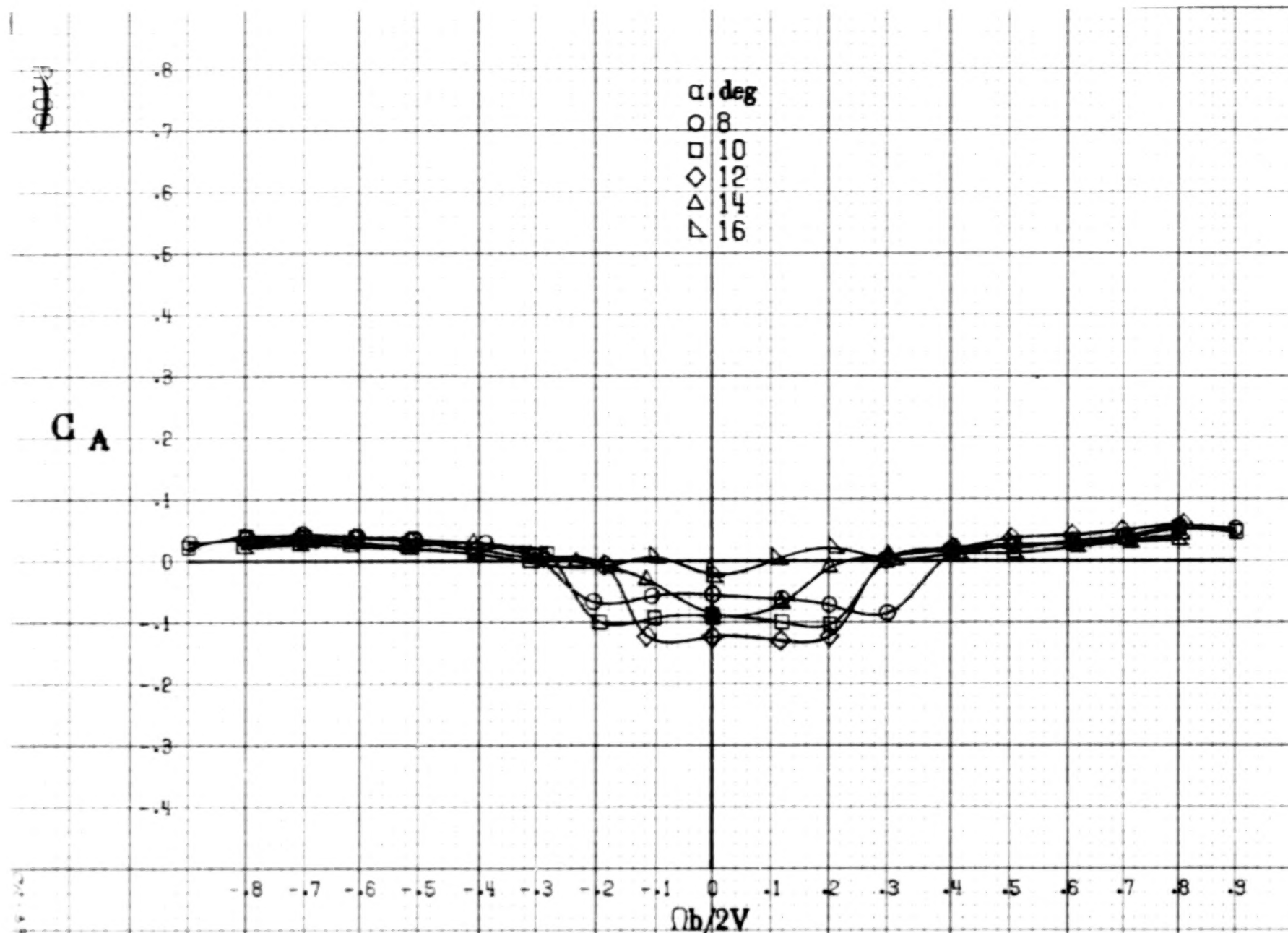






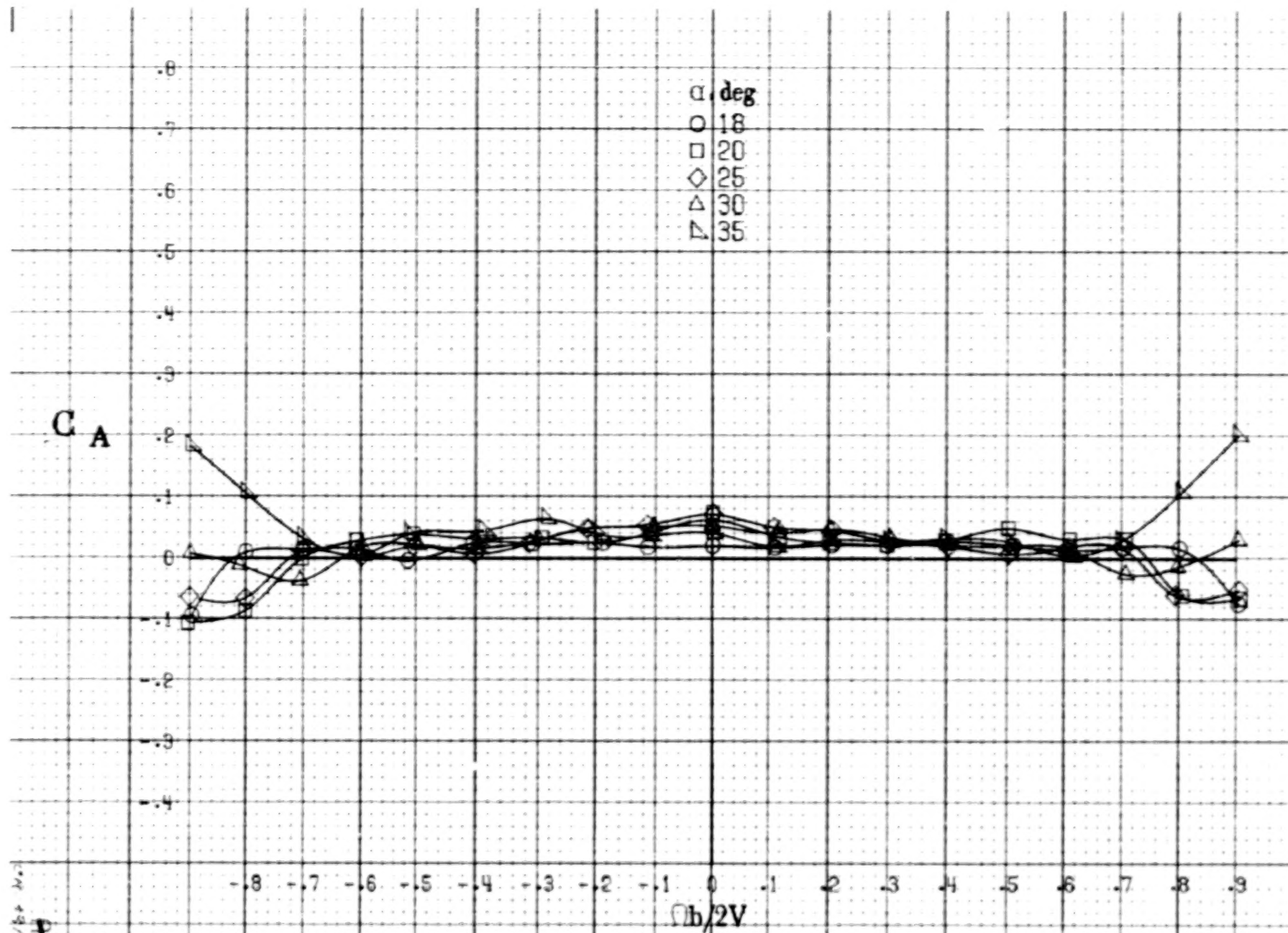
(a)  $\alpha = 8$  to  $16^\circ$ ,  $SR = 152.4\text{cm (60in)}$ .  
 Figure A41. Effect of rotation rate and angle of attack on side-force coefficient for canopy fairing configuration.  $\delta_e = 0^\circ$ ,  $\delta_a = 0^\circ$ ,  $\delta_r = 0^\circ$ .  $\beta = 0^\circ$ .



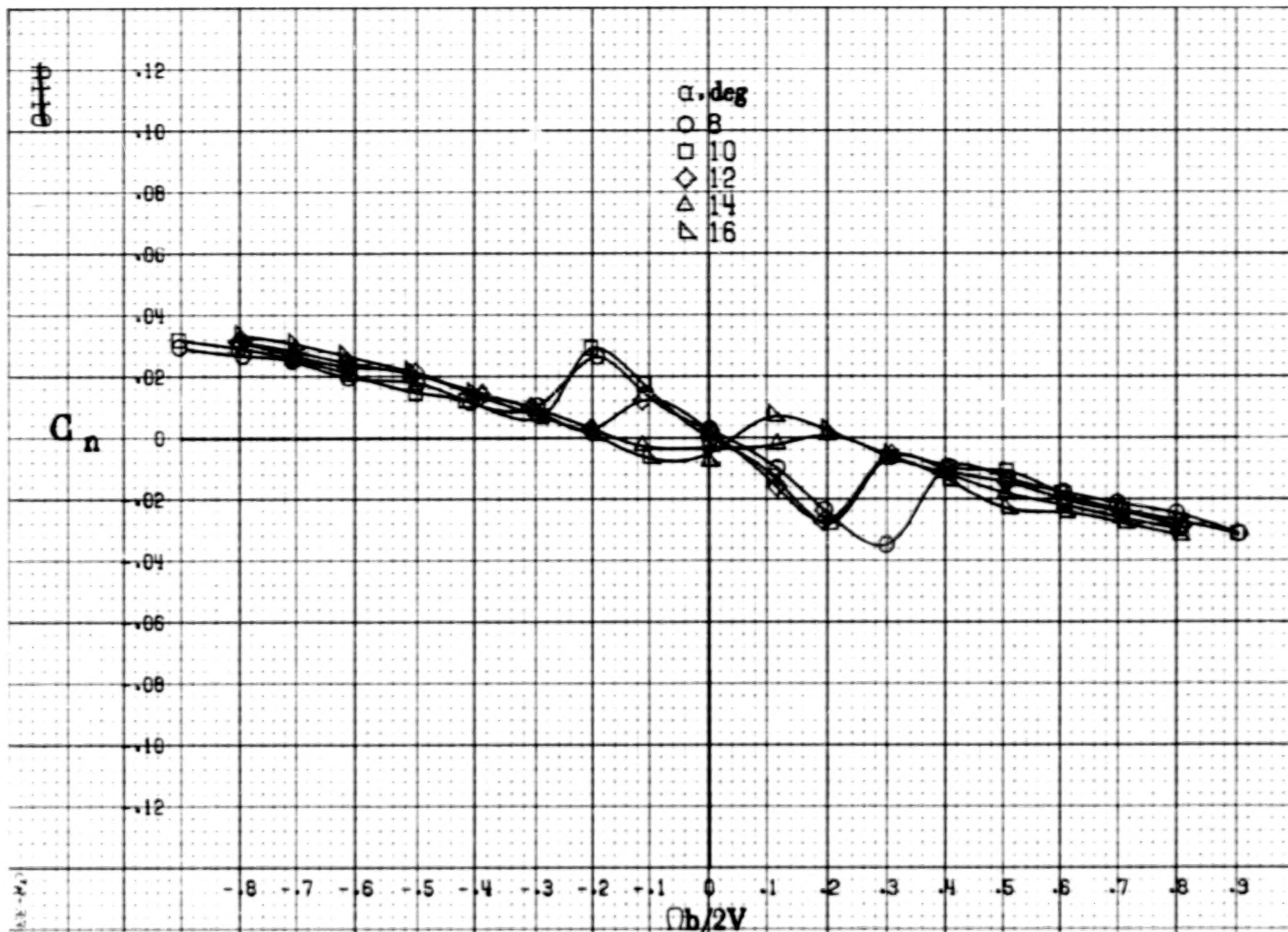


(a)  $\alpha = 8$  to  $16^\circ$ ,  $SR = 152.4 \text{ cm (60 in)}$ .  
 Figure A42.-Effect of rotation rate and angle of attack on axial-force coefficient for canopy fairing configuration.  $\delta_s = 0^\circ$ ,  $\delta_a = 0^\circ$ ,  $\delta_r = 0^\circ$ ,  $\beta = 0^\circ$ .

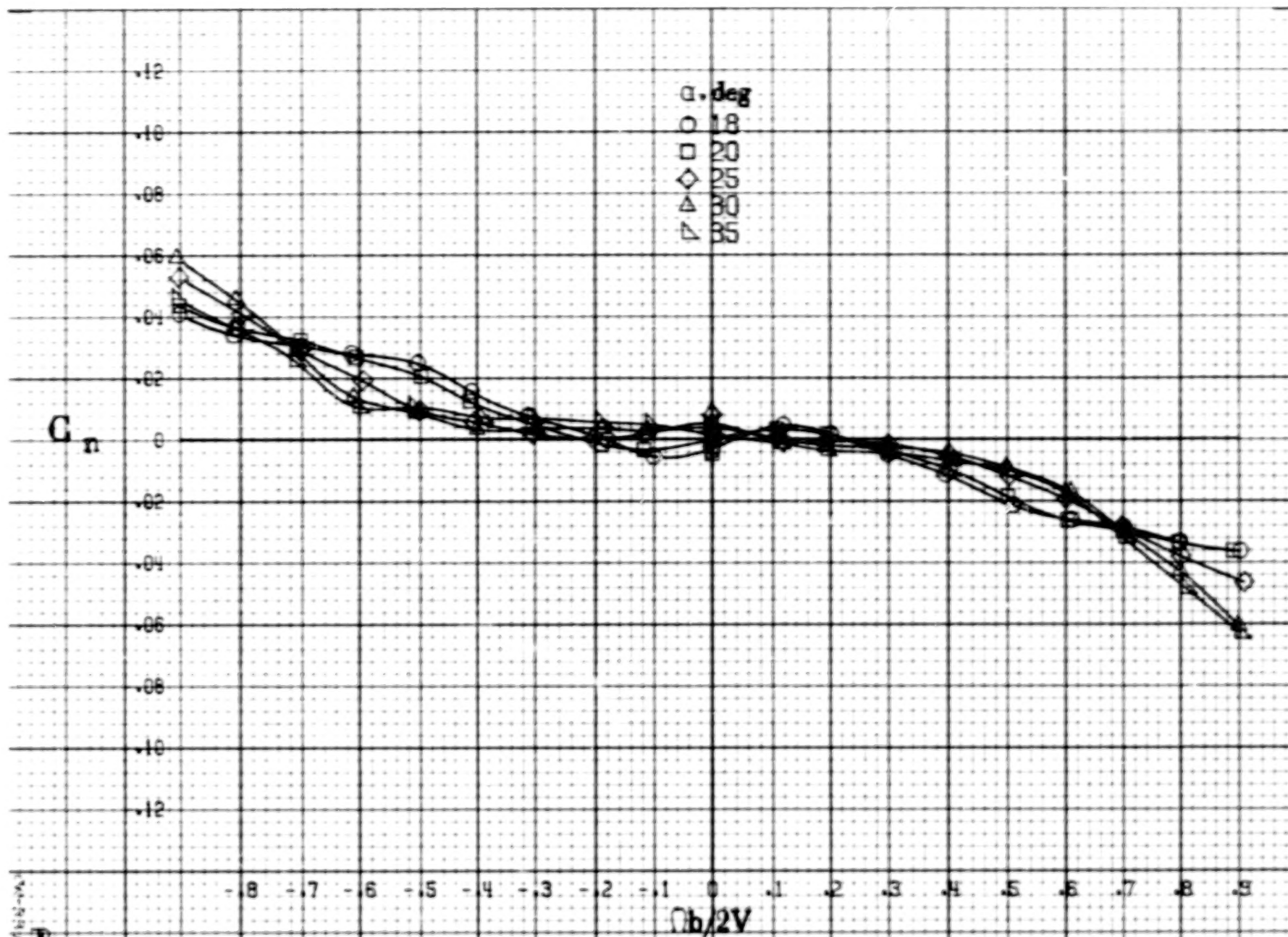




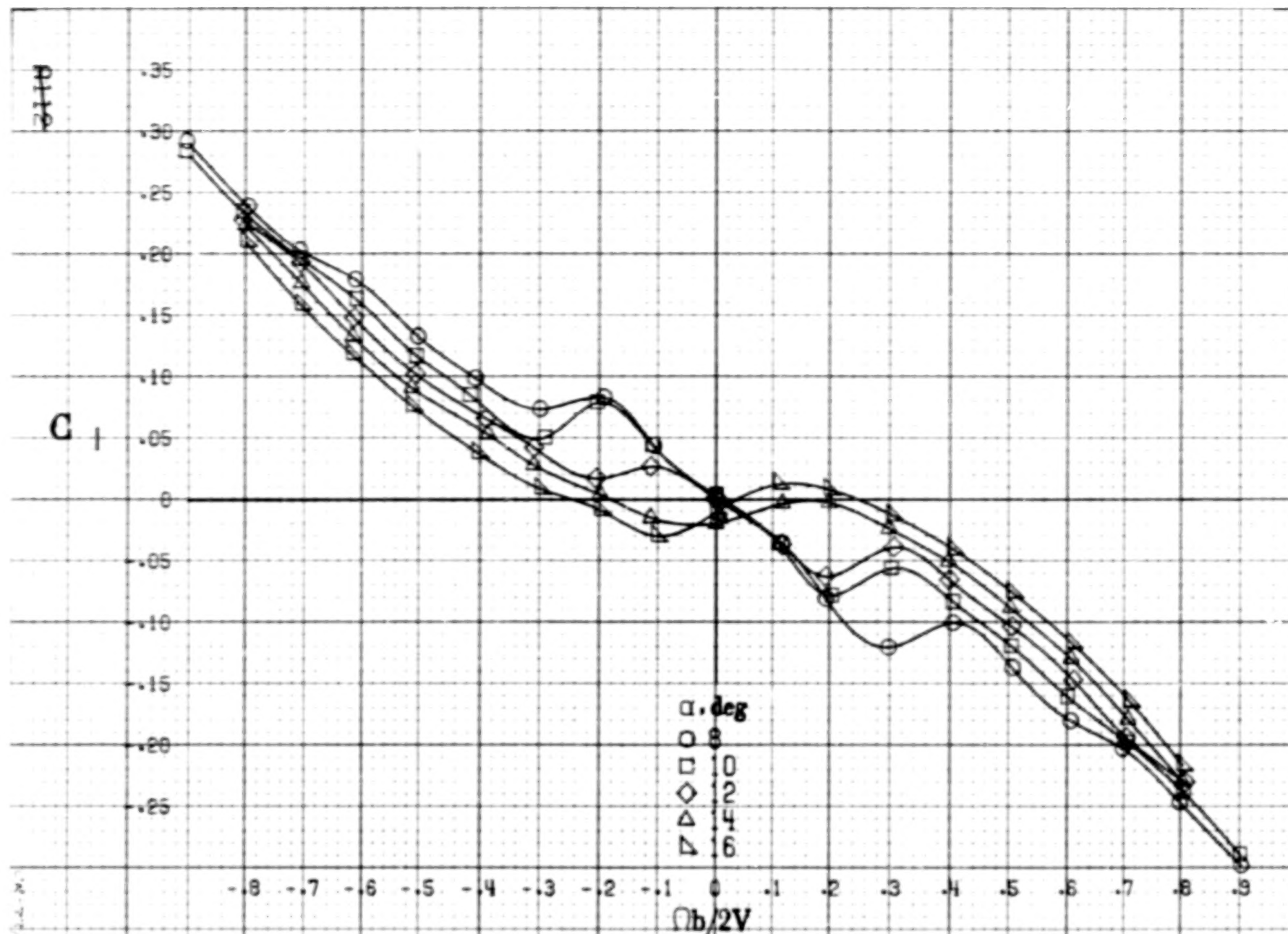
(b)  $\alpha = 18$  to  $35^\circ$ ,  $SR = 152.4\text{ cm (60 in.)}$ .  
Figure A42.-Concluded.



(a)  $\alpha = 8$  to  $16^\circ$ ,  $SR = 152.4 \text{ cm (60 in.)}$ .  
 Figure A43.-Effect of rotation rate and angle of attack on yawing-moment coefficient for wing-fuselage fillet configuration.  $\delta_e = 0^\circ$ ,  $\delta_a = 0^\circ$ ,  $\delta_r = 0^\circ$ .  
 $\beta = 0^\circ$ .

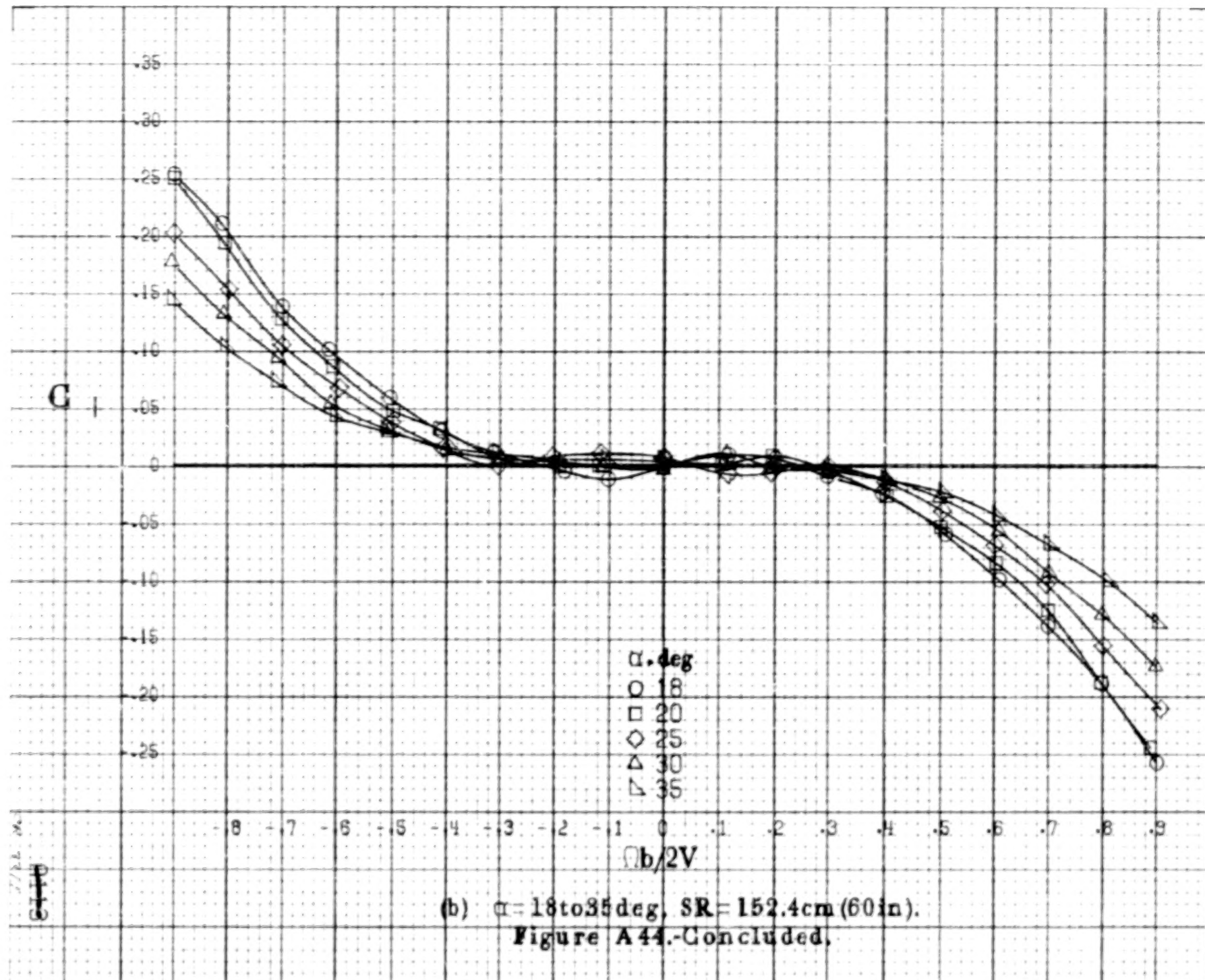


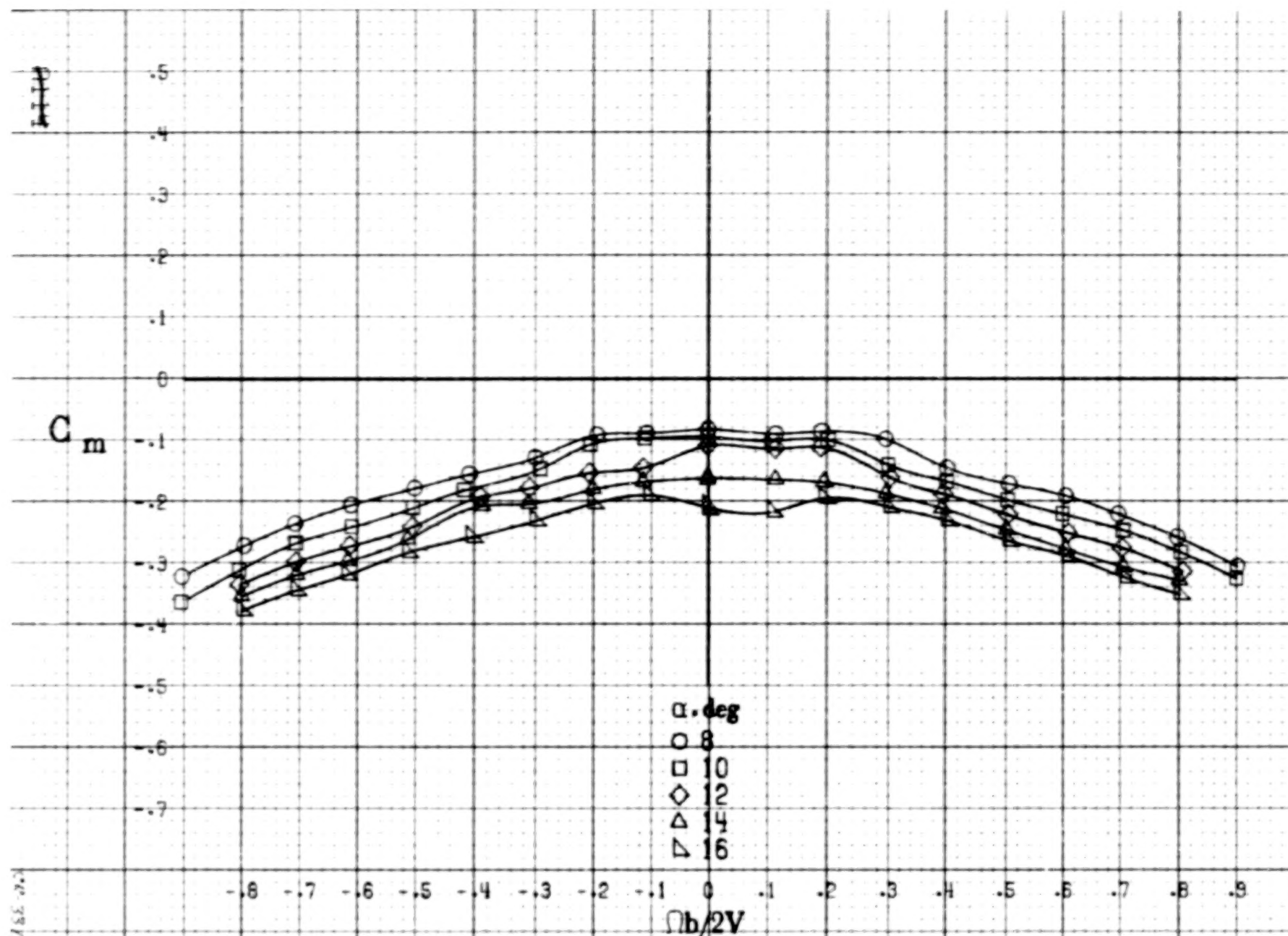
(b)  $\alpha = 18$  to  $35^\circ$ ,  $SR = 152.4\text{cm}$  (60 in).  
Figure A43.-Concluded.



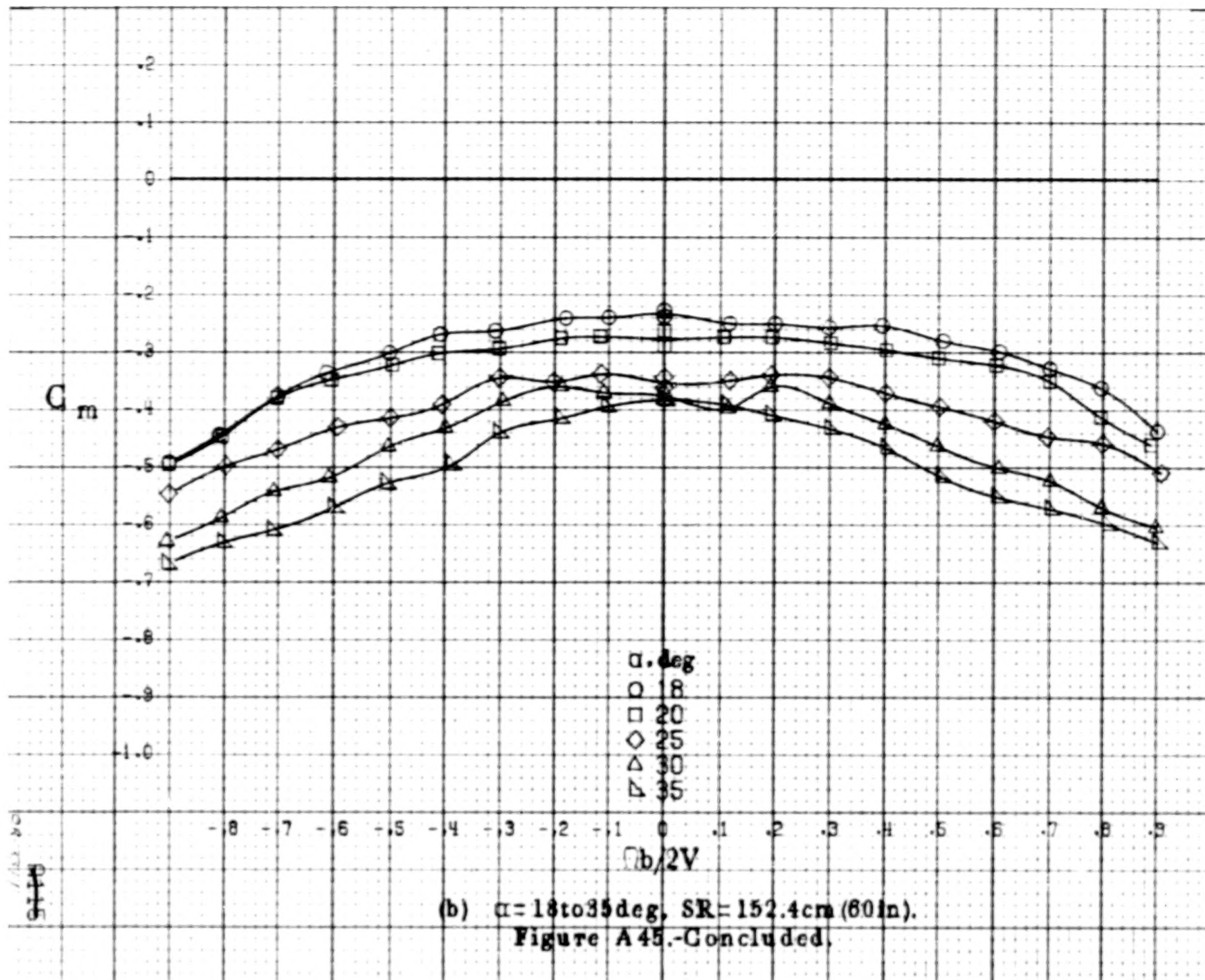
(a)  $\alpha = 8$  to  $16^\circ$ ,  $SR = 152.4 \text{ cm (60 in.)}$ .  
 Figure A44.-Effect of rotation rate and angle of attack on rolling-moment coefficient for wing-fuselage fillet configuration.  $\delta_e = 0^\circ$ ,  $\delta_a = 0^\circ$ ,  $\delta_r = 0^\circ$ .  
 $B = 0^\circ$ .

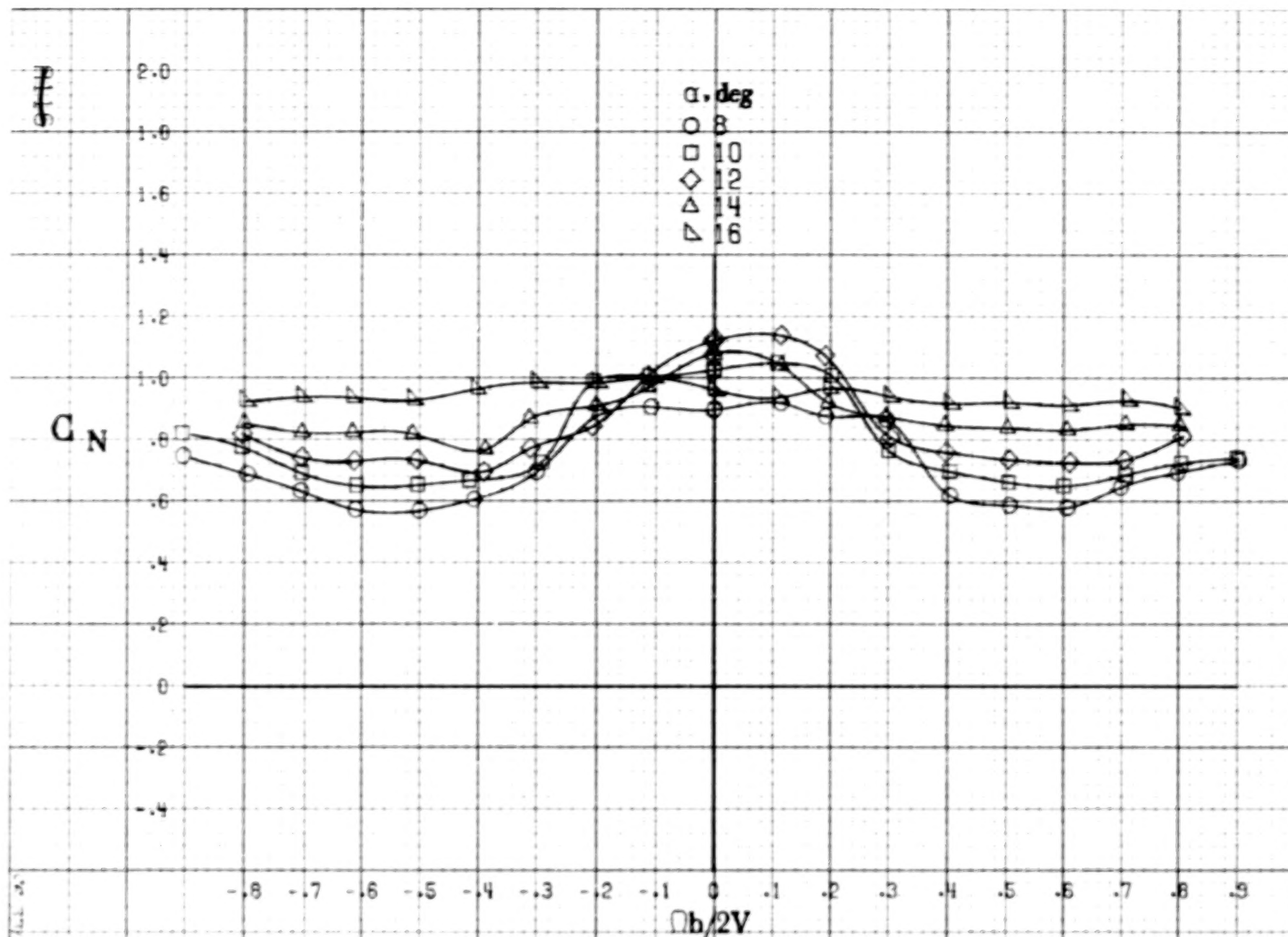






(a)  $\alpha = 8$  to  $16$  deg,  $SR = 152.4$  cm (60 in).  
 Figure A45.-Effect of rotation rate and angle of attack on pitching-moment coefficient for wing-fuselage fillet configuration.  $\delta_e = 0^\circ$ ,  $\delta_a = 0^\circ$ ,  $\delta_r = 0^\circ$ ,  $\beta = 0^\circ$ .

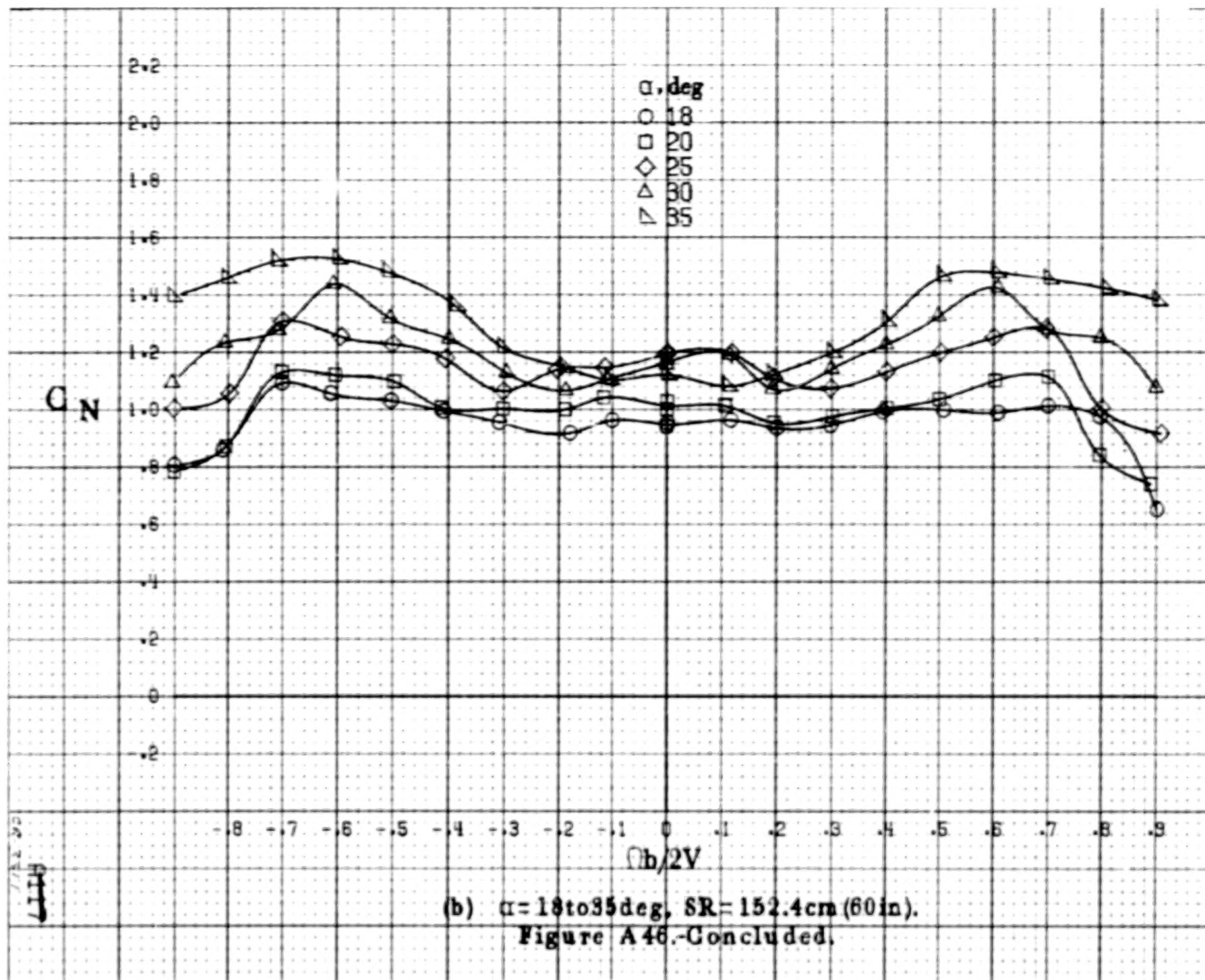


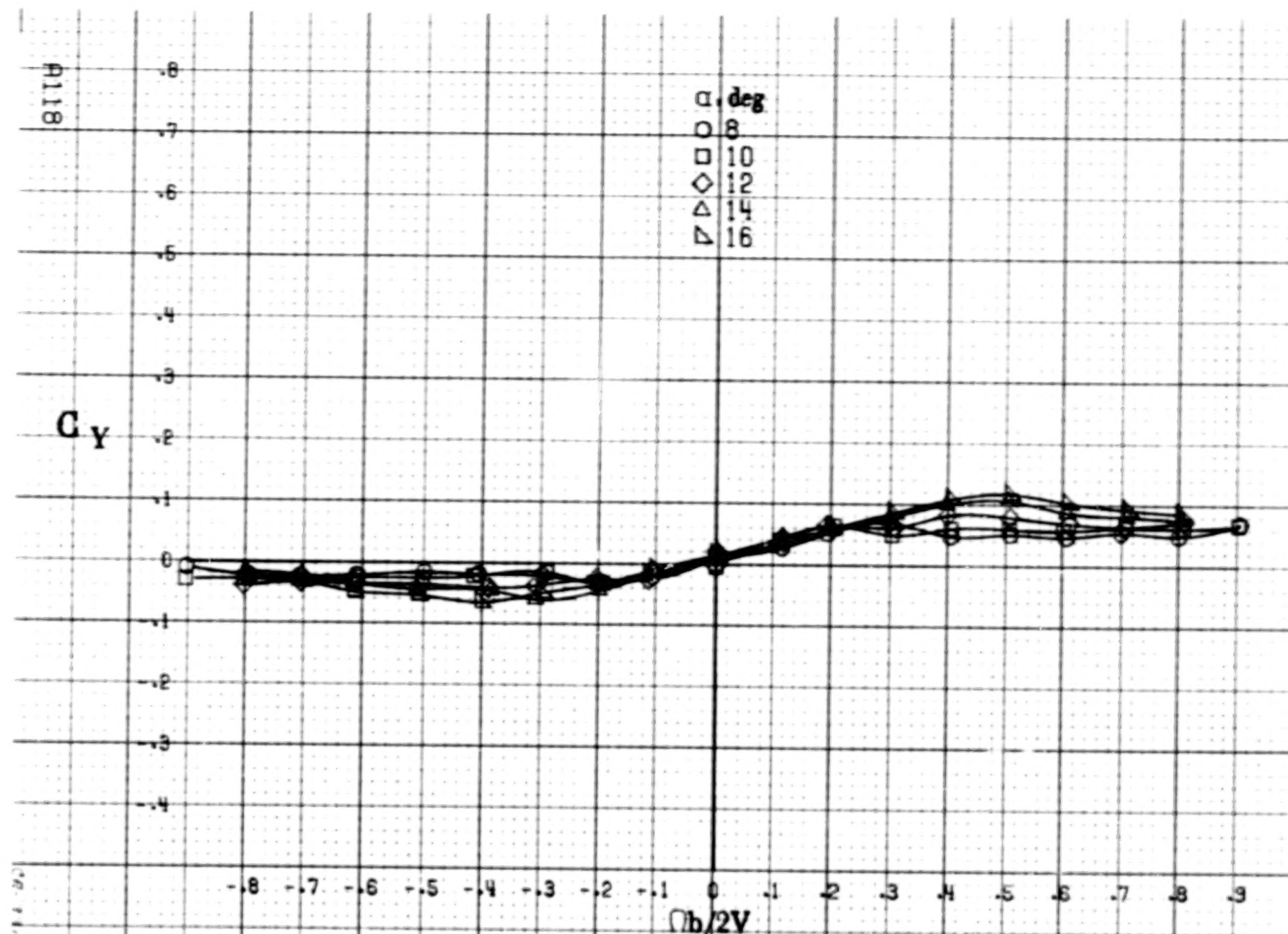


(a)  $\alpha = 8$  to  $16^\circ$ ,  $SR = 152.4\text{ cm (60 in.)}$ .

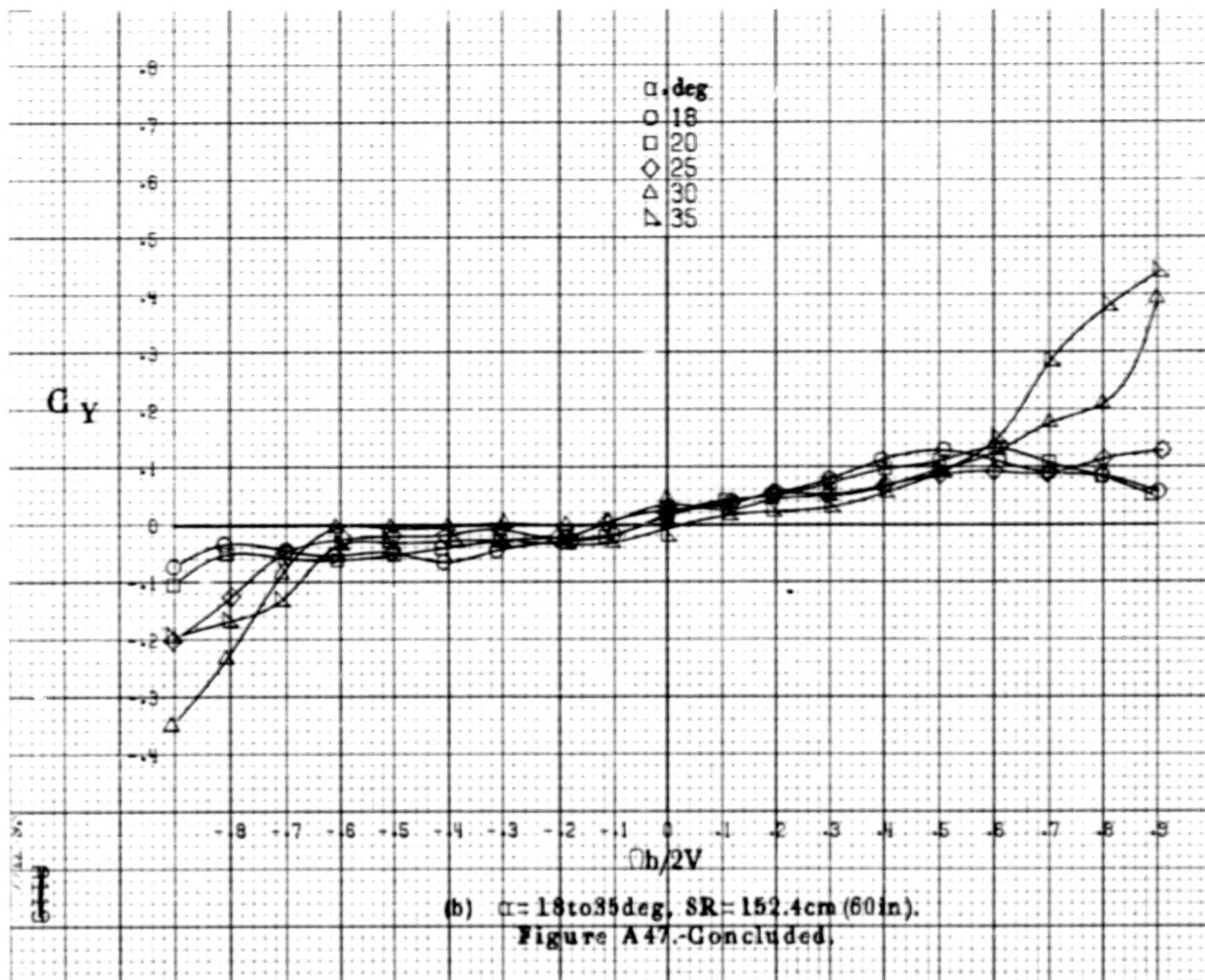
Figure A46. Effect of rotation rate and angle of attack on normal-force coefficient for wing-fuselage fillet configuration.  $\delta_e = 0^\circ$ ,  $\delta_a = 0^\circ$ ,  $\delta_r = 0^\circ$ .  $\beta = 0^\circ$ .

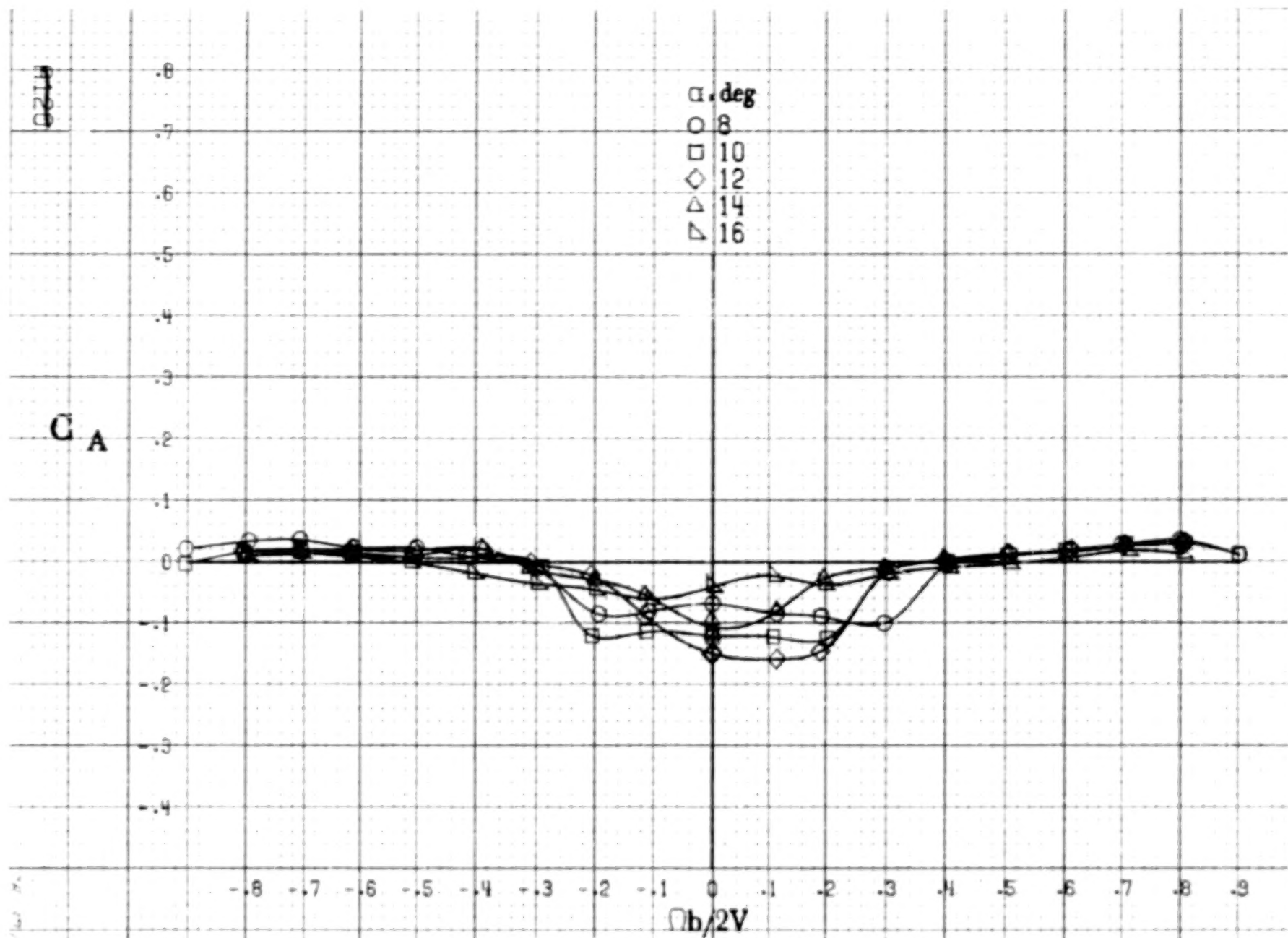






(a)  $\alpha = 8$  to  $16^\circ$ ,  $SR = 152.4 \text{ cm (60 in.)}$ .  
 Figure A47.-Effect of rotation rate and angle of attack on side-force coefficient for wing-fuselage fillet configuration.  $\delta_s = 0^\circ$ ,  $\delta_a = 0^\circ$ ,  $\delta_r = 0^\circ$ .  
 $\beta = 0^\circ$ .

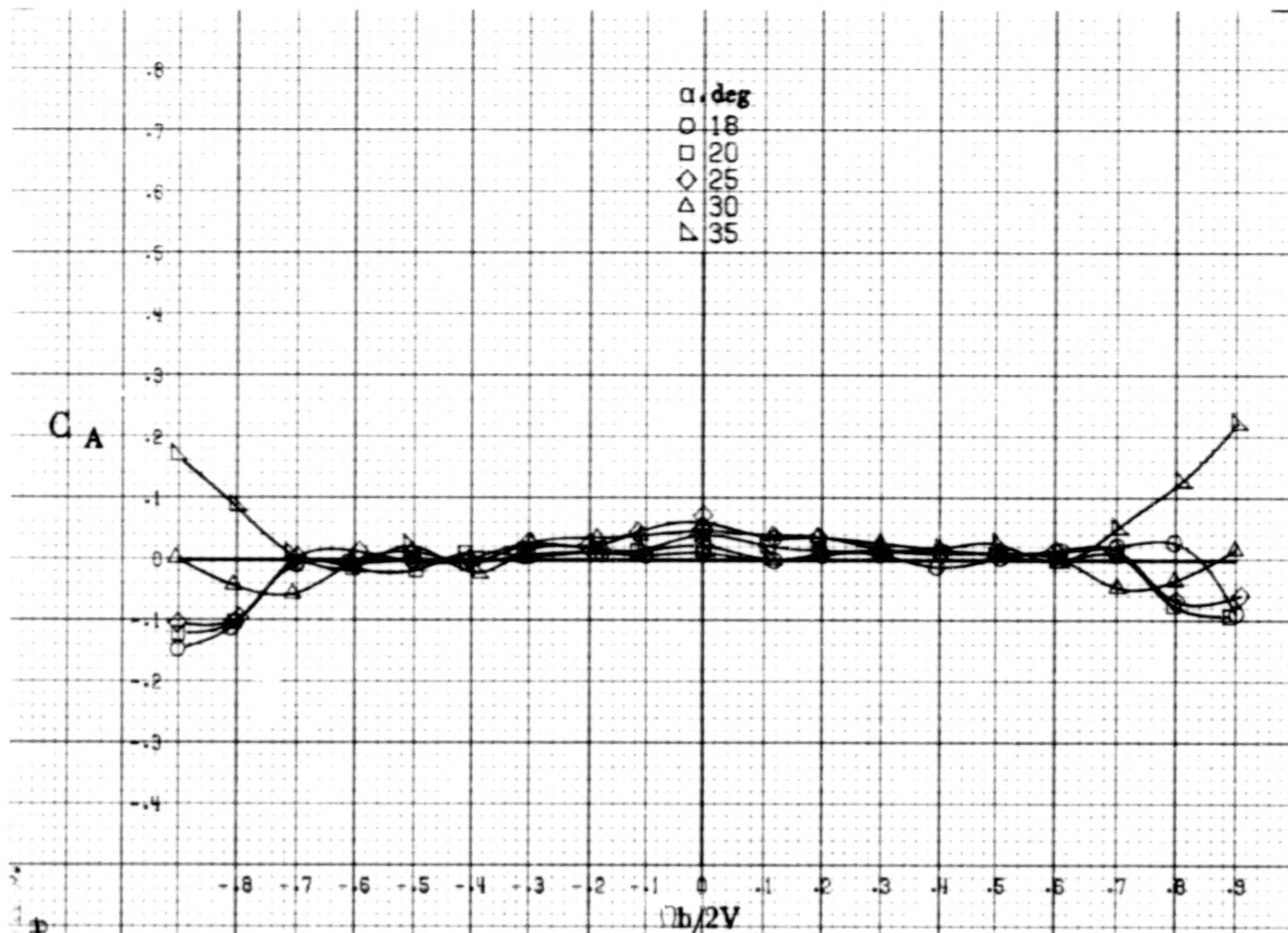




(a)  $\alpha = 8$  to  $16^\circ$ ,  $SR = 152.4 \text{ cm (60 in.)}$ .

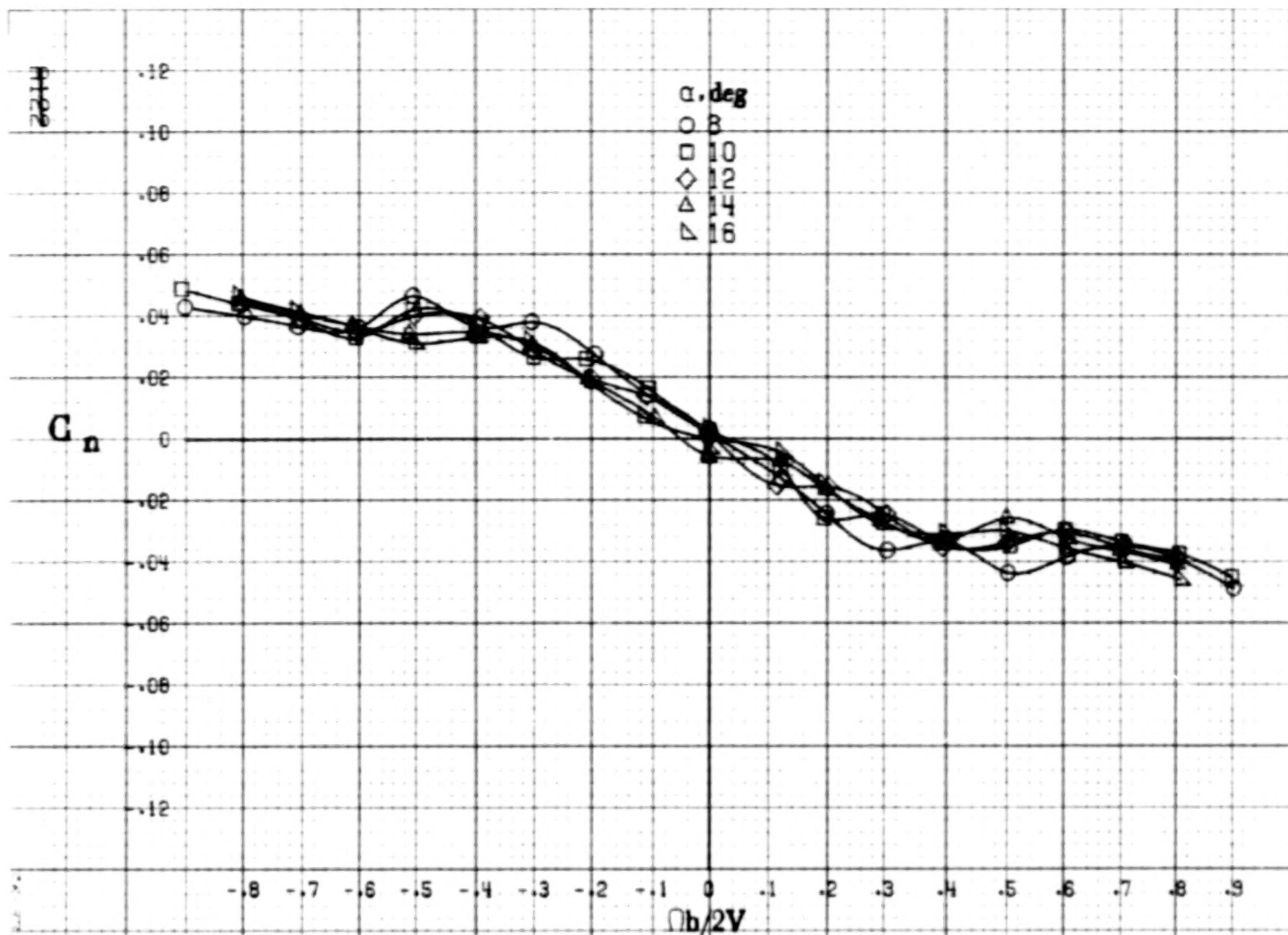
Figure A48.-Effect of rotation rate and angle of attack on axial-force coefficient for wing-fuselage fillet configuration.  $\delta_e = 0^\circ$ ,  $\delta_a = 0^\circ$ ,  $\delta_r = 0^\circ$ .  $\beta = 0^\circ$ .



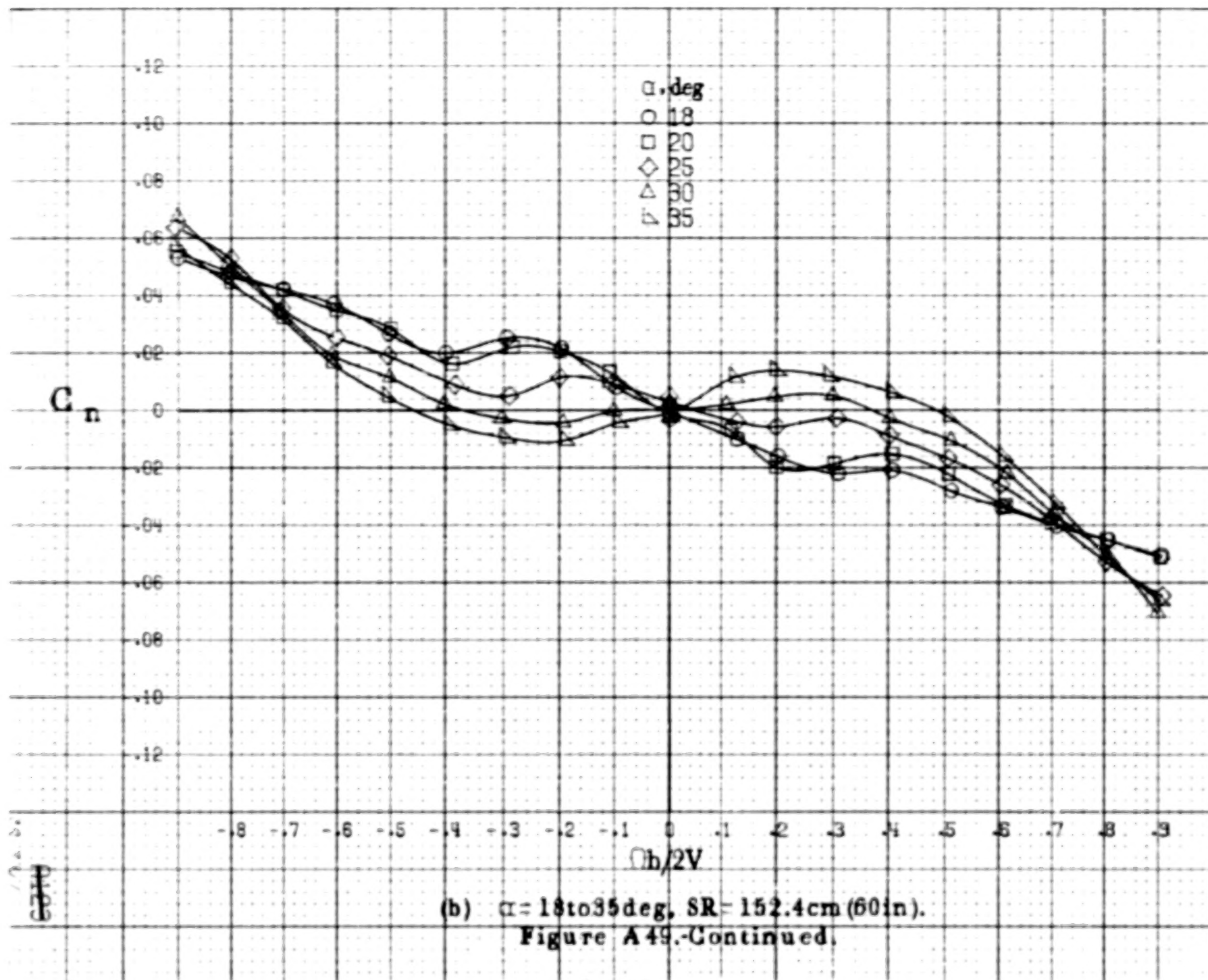


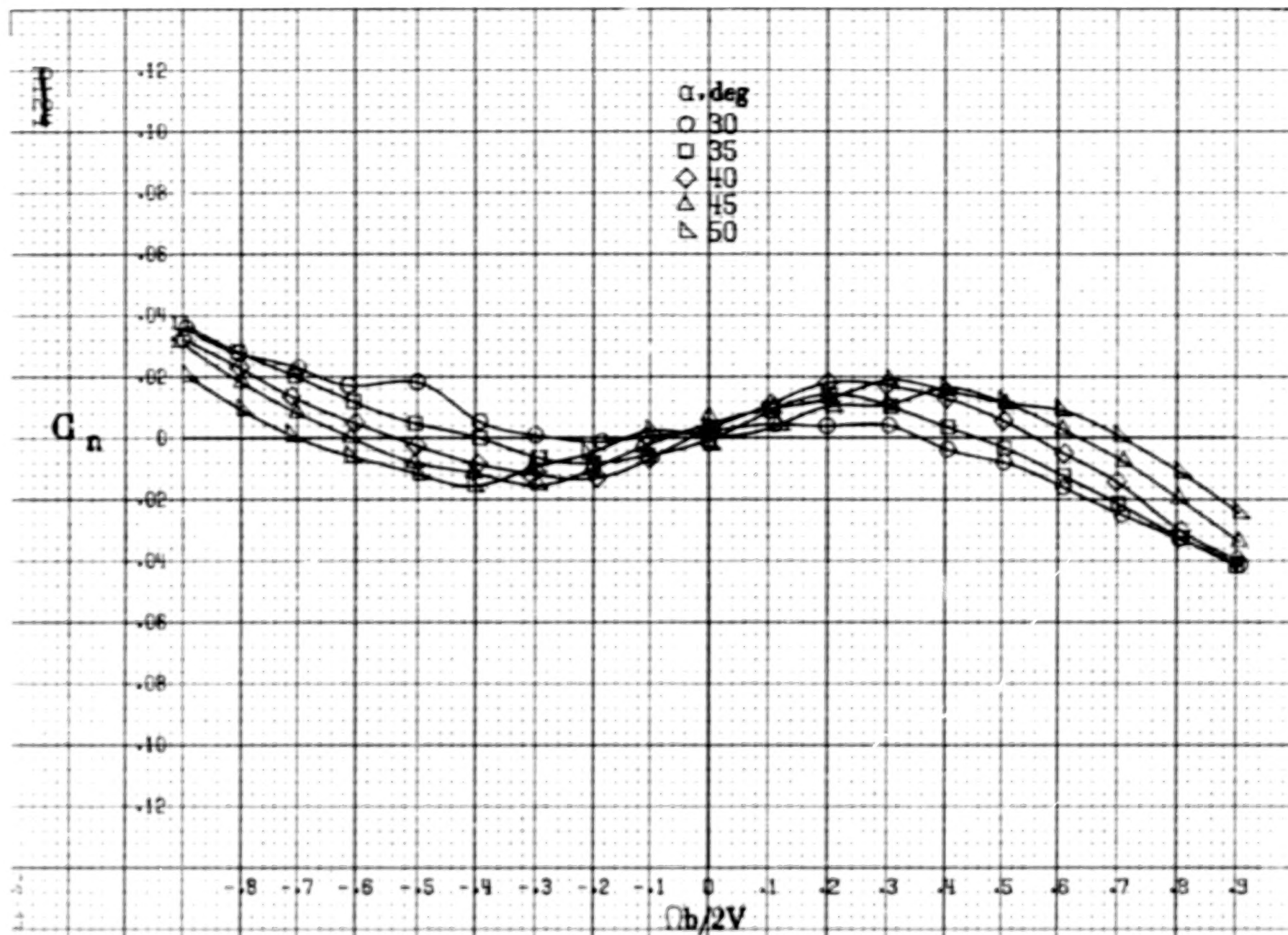
(b)  $\alpha = 18$  to  $35$  deg,  $SR = 152.4$  cm (60 in).

Figure A48.-Concluded.



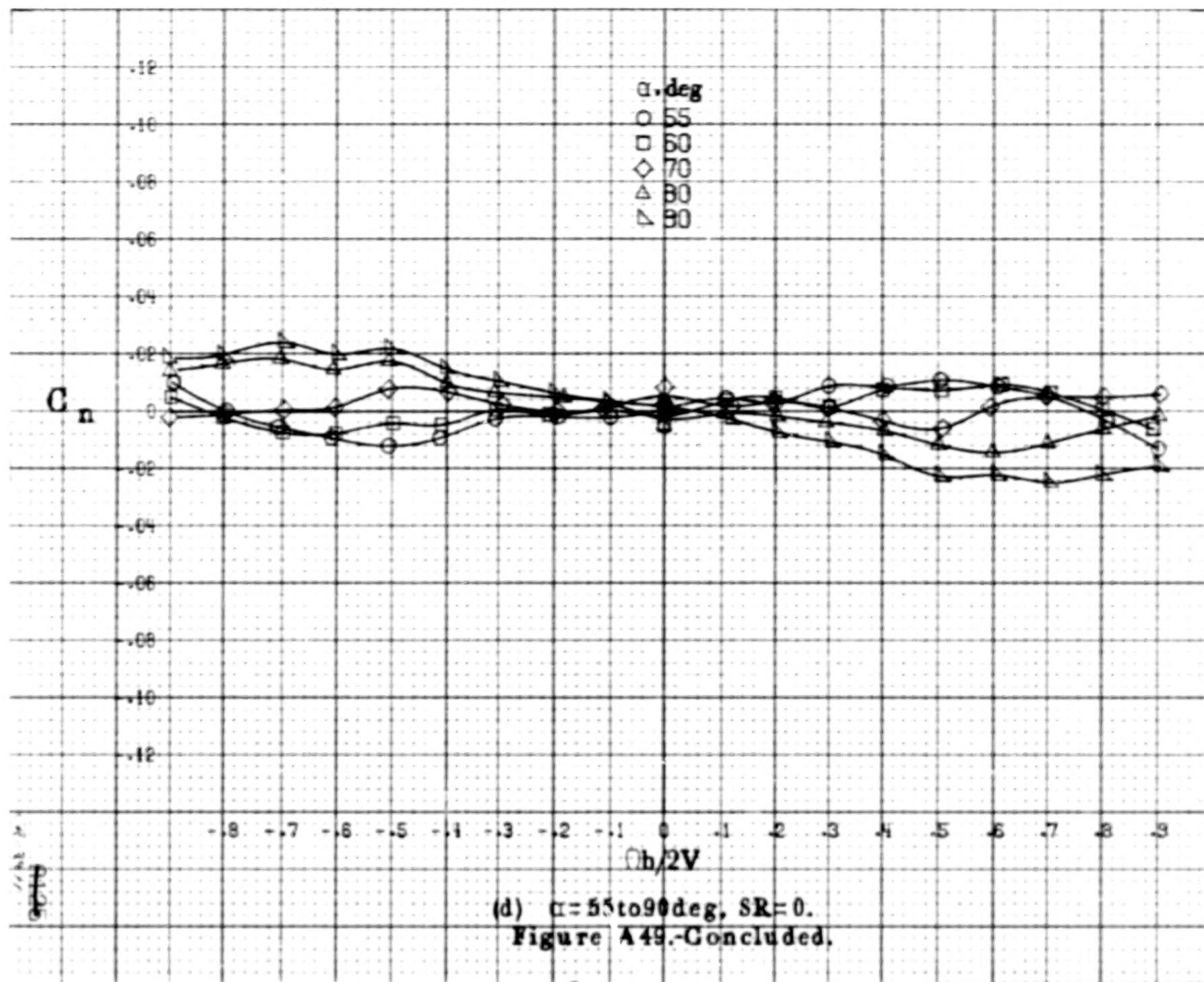
(a)  $\alpha = 8$  to  $16$  deg,  $SR = 152.4$  cm (60 in).  
 Figure A49.-Effect of rotation rate and angle of attack on yawing-moment coefficient for configuration having wing-fuselage fillet with outboard LE wing droop.  $\delta_s = 0^\circ$ ,  $\delta_a = 0^\circ$ ,  $\delta_r = 0^\circ$ .  $\beta = 0^\circ$ .

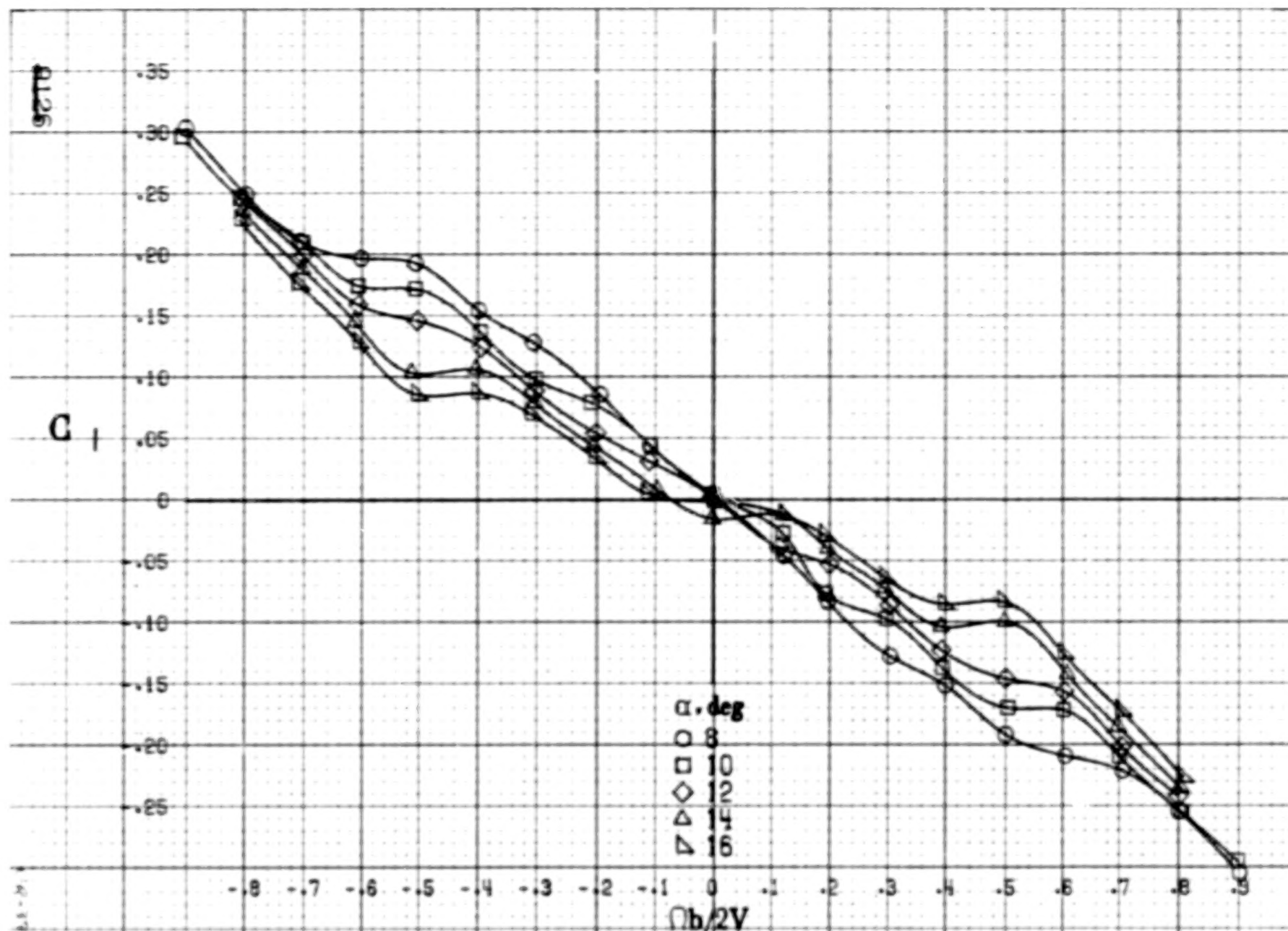




(c)  $\alpha = 30$  to  $50^\circ$ ,  $SR = 0$ .  
Figure A49.-Continued.

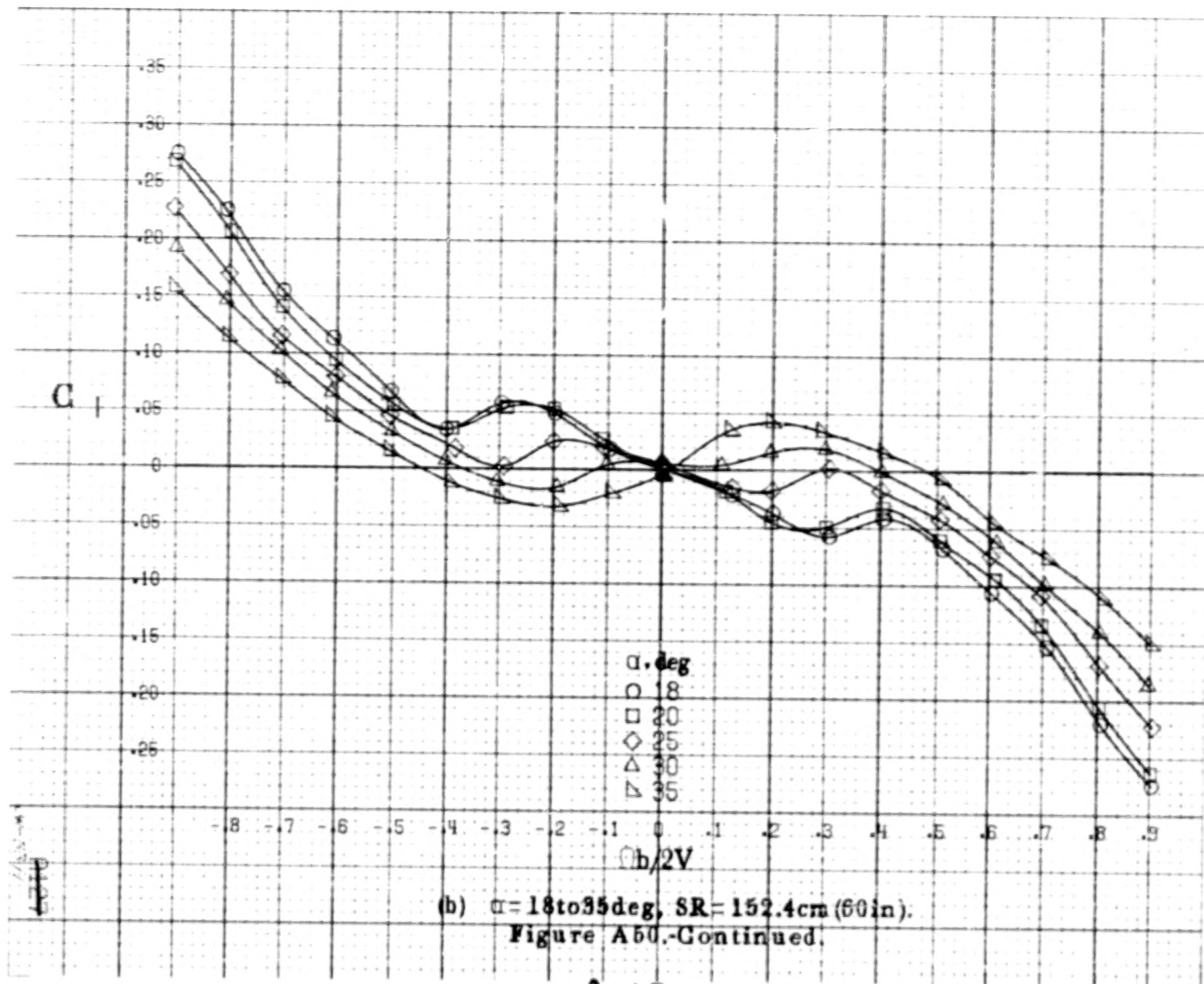


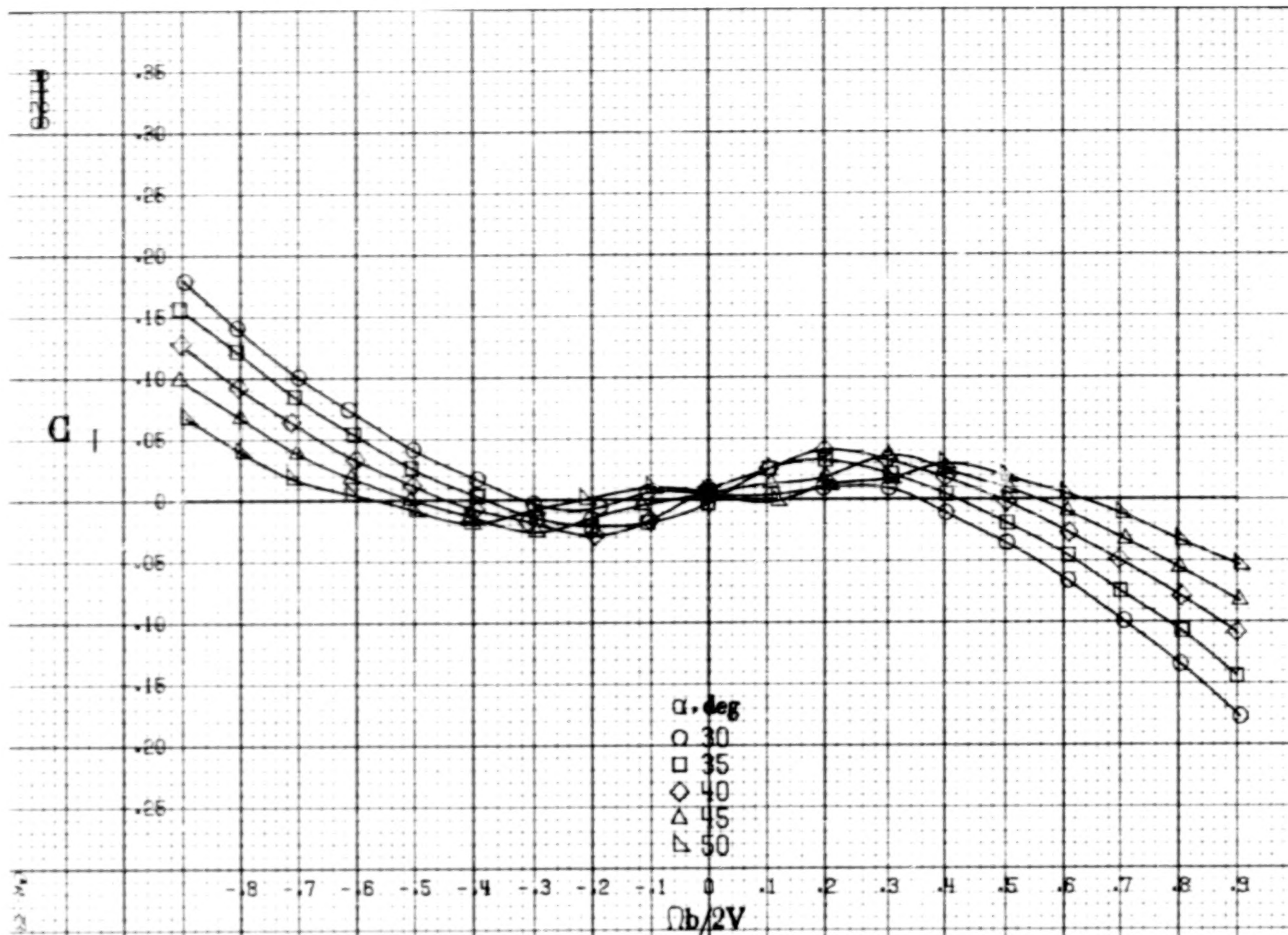




(a)  $\alpha = 8$  to  $16$  deg,  $SR = 152.4$  cm (60 in).

Figure A50. Effect of rotation rate and angle of attack on rolling-moment coefficient for configuration having wing-fuselage fillet with outboard LE wing droop.  $\delta_s = 0^\circ$ ,  $\delta_e = 0^\circ$ ,  $\delta_f = 0^\circ$ ,  $\beta = 0^\circ$ .

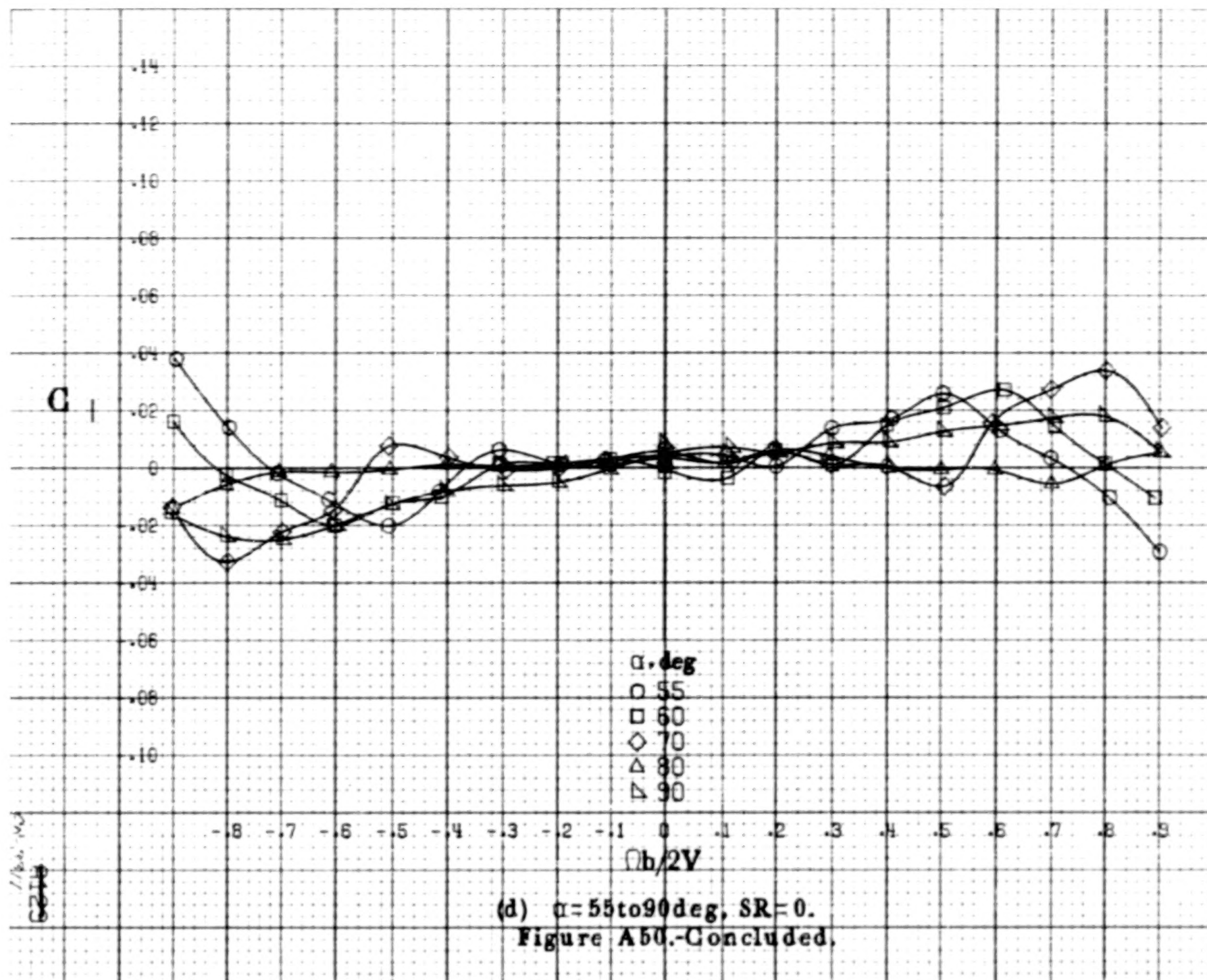


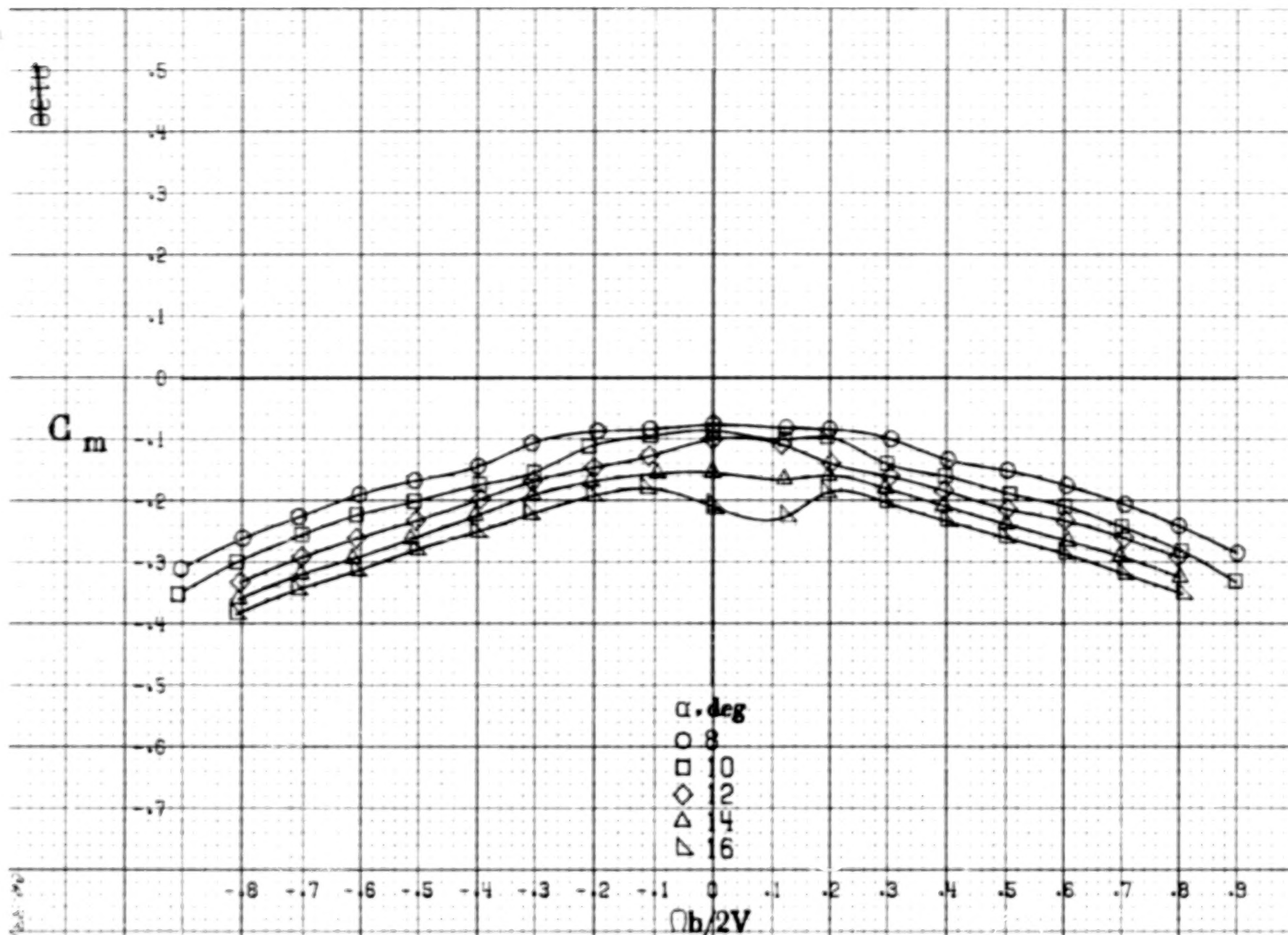


(c)  $\alpha = 30$  to  $50$  deg,  $SR = 0$ .

Figure A50.-Continued.

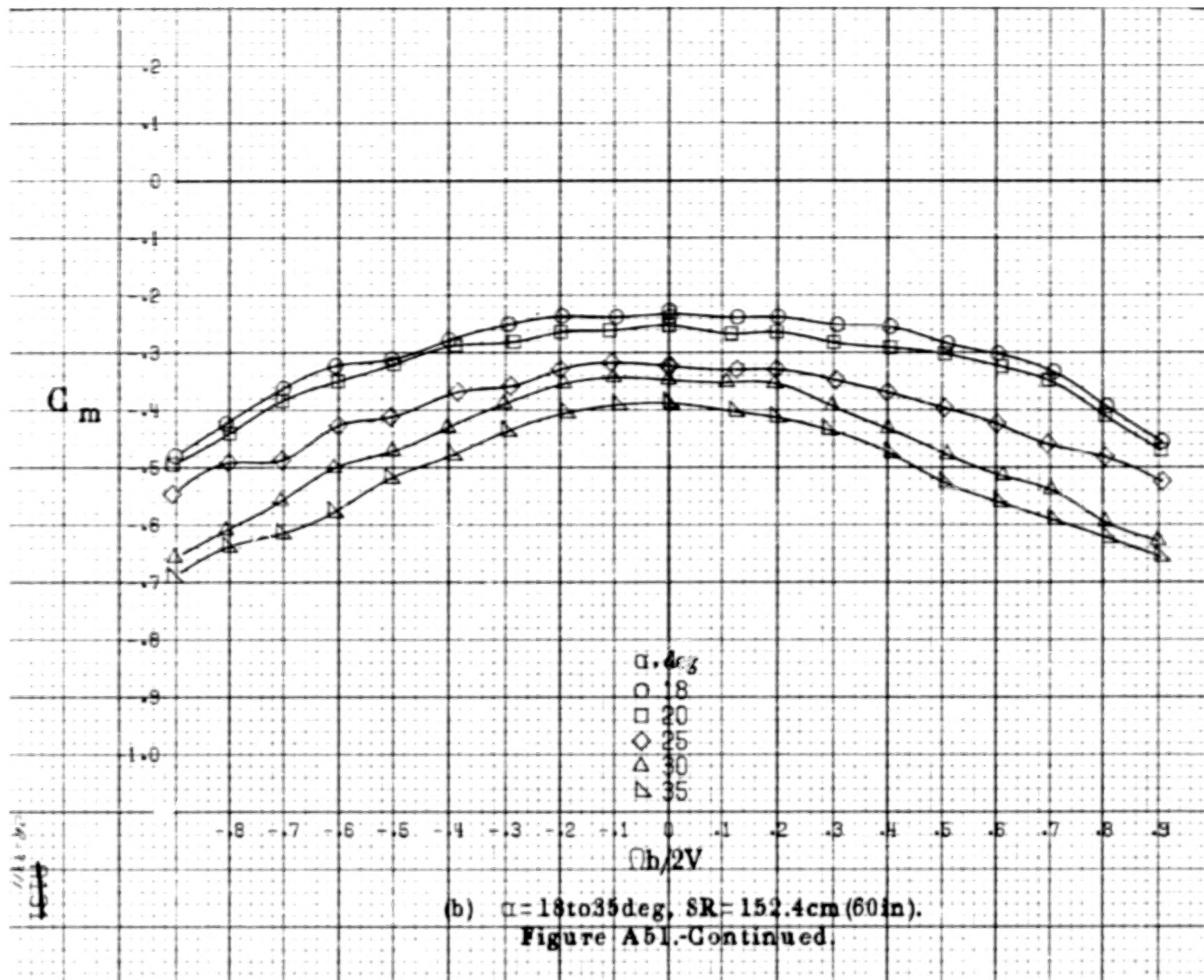


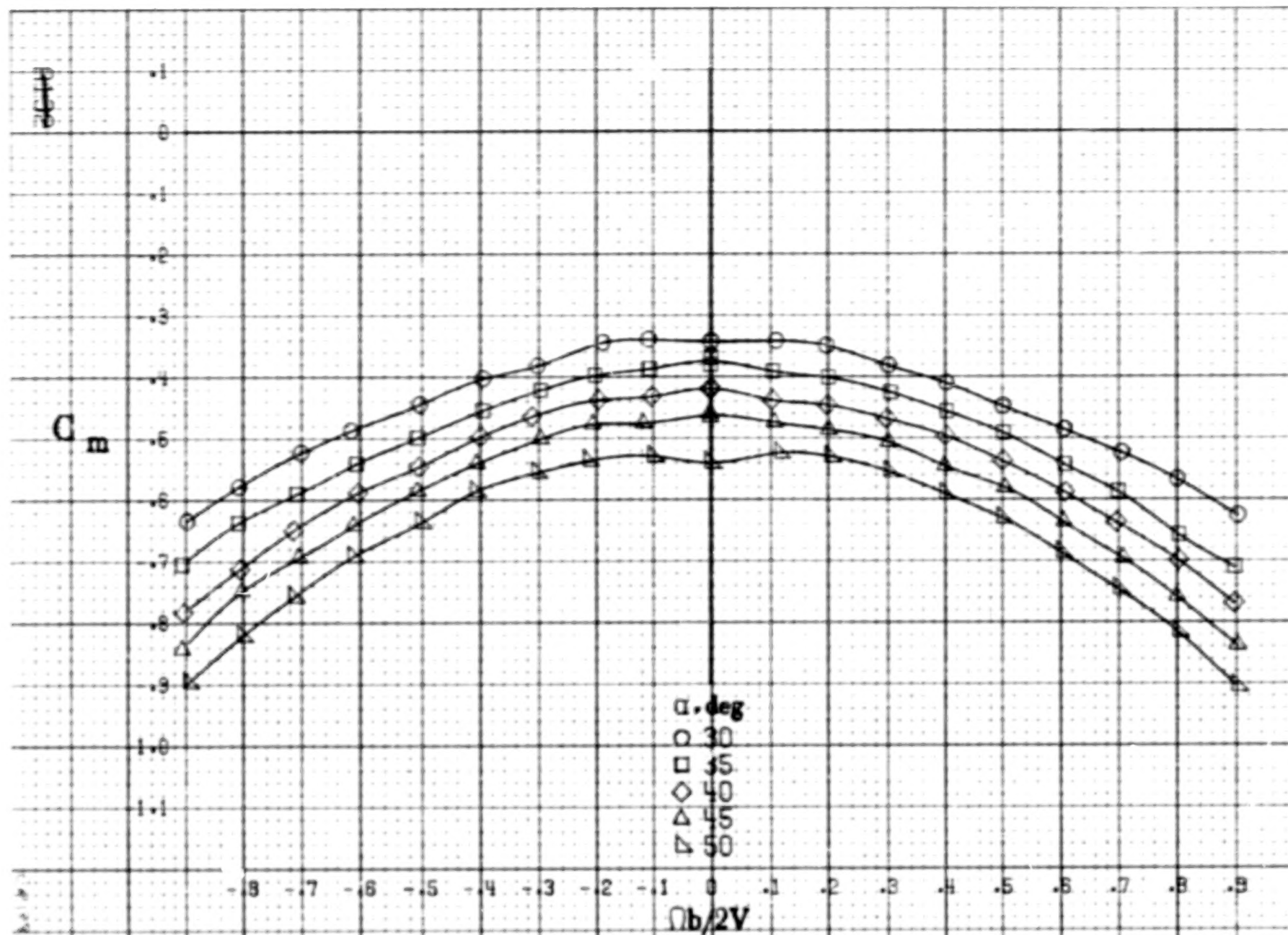




(a)  $\alpha = 8$  to  $16^\circ$ ,  $SR = 152.4\text{cm (60in)}$ .

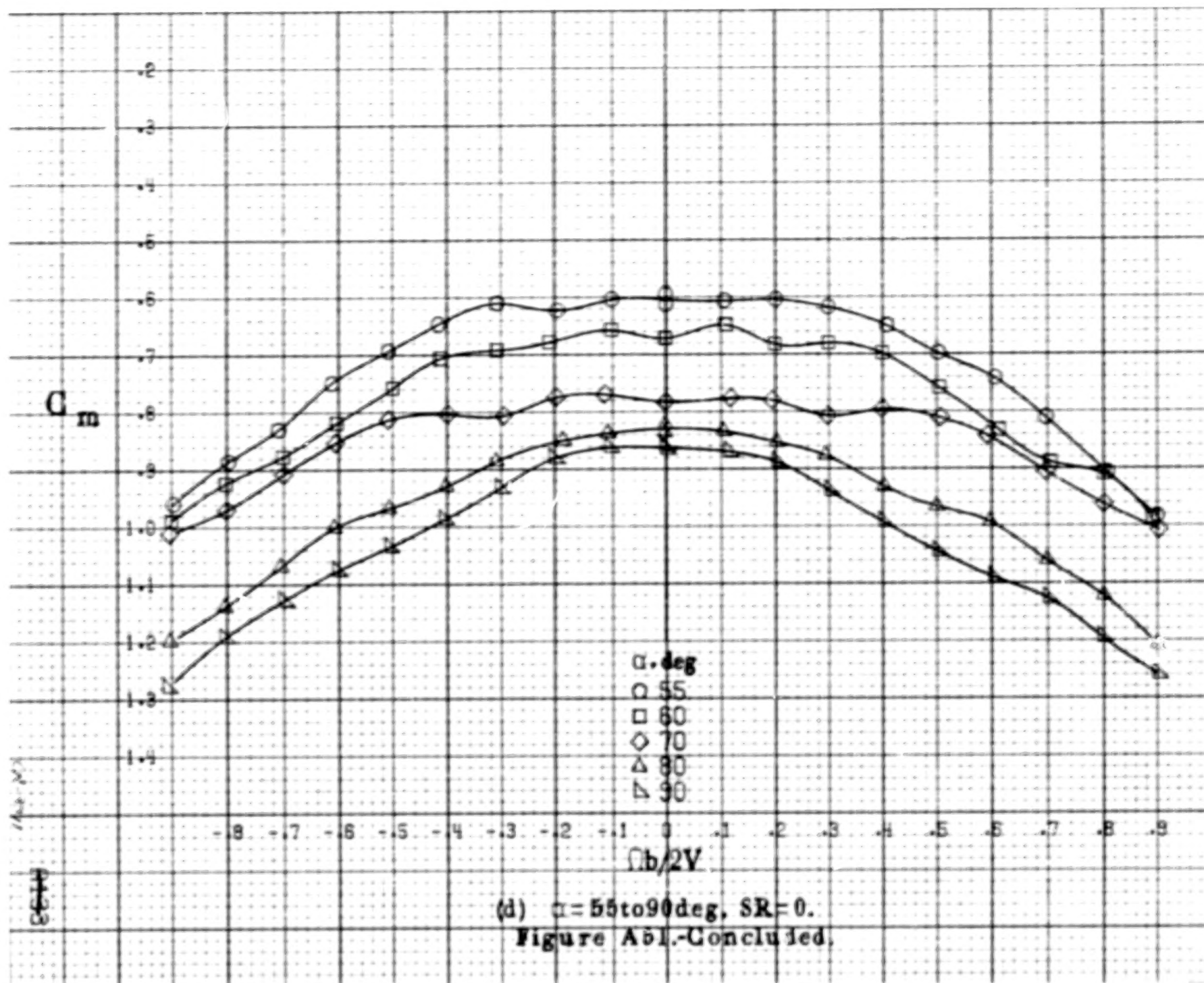
Figure A51. Effect of rotation rate and angle of attack on pitching-moment coefficient for configuration having wing-fuselage fillet with outboard LE wing droop.  $\delta_e = 0^\circ$ ,  $\delta_a = 0^\circ$ ,  $\delta_r = 0^\circ$ .  $B = 0$ .

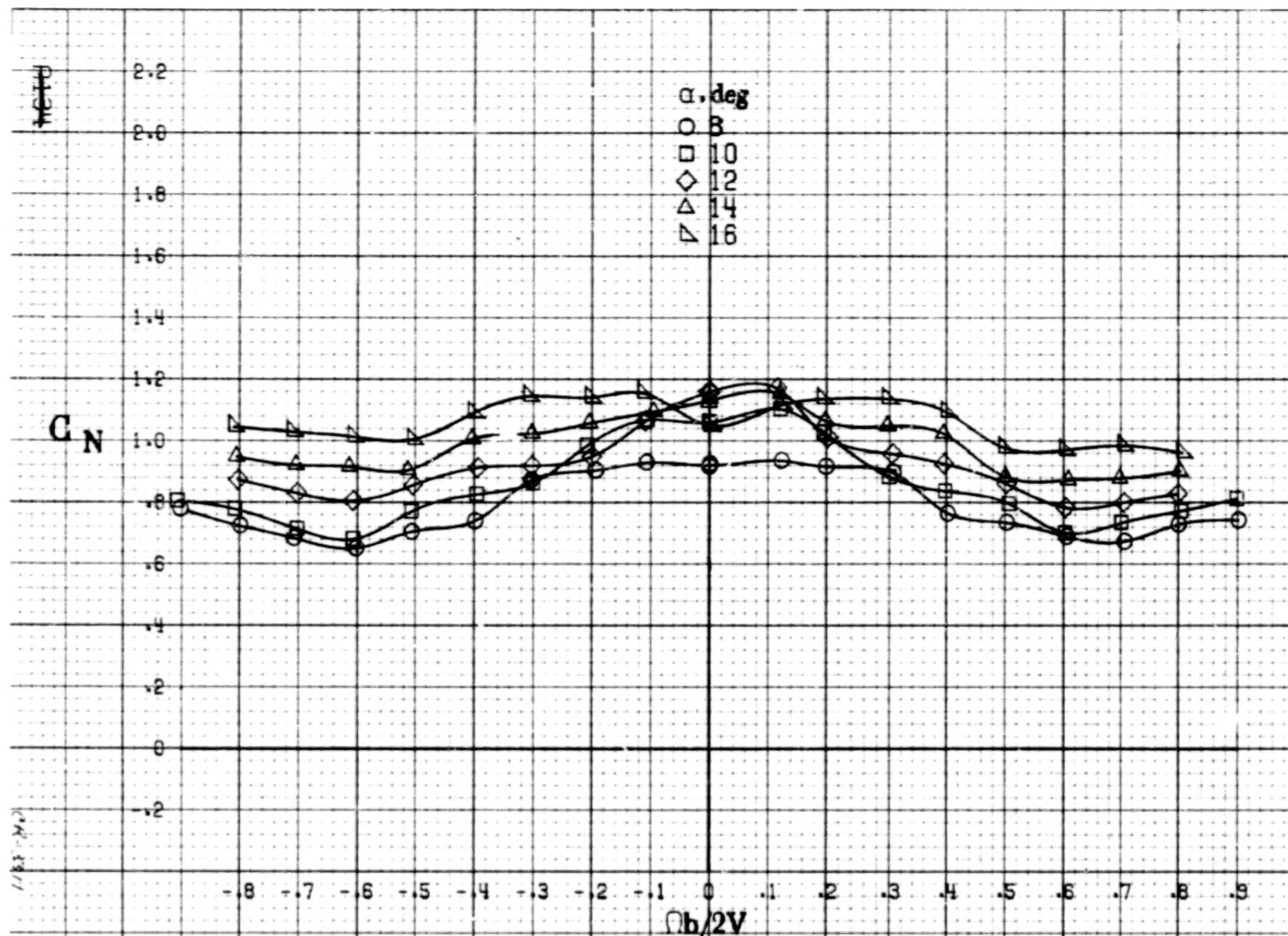




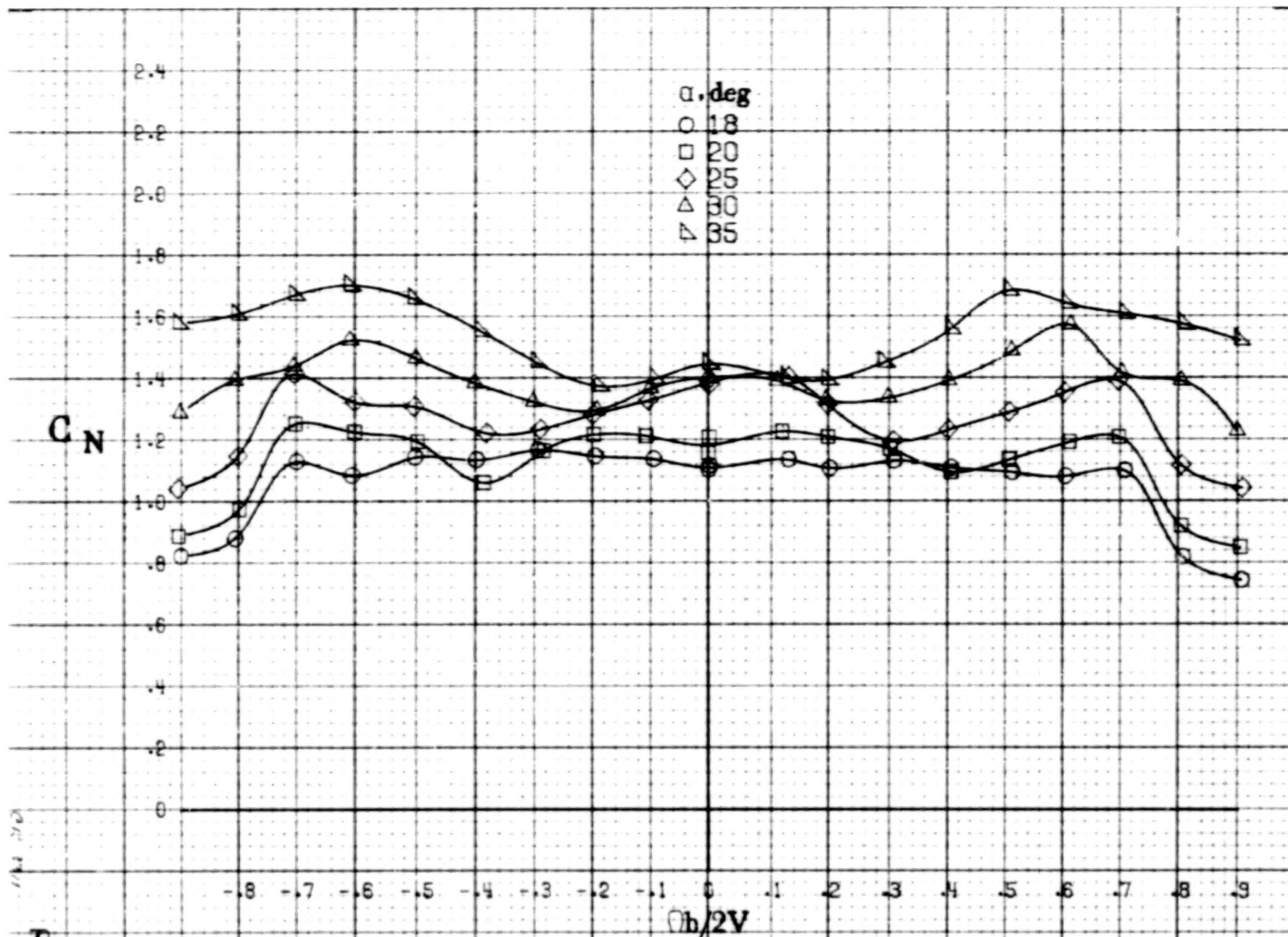
(c)  $\alpha = 30$  to  $50$  deg,  $SR = 0$ .  
Figure A51.-Continued.



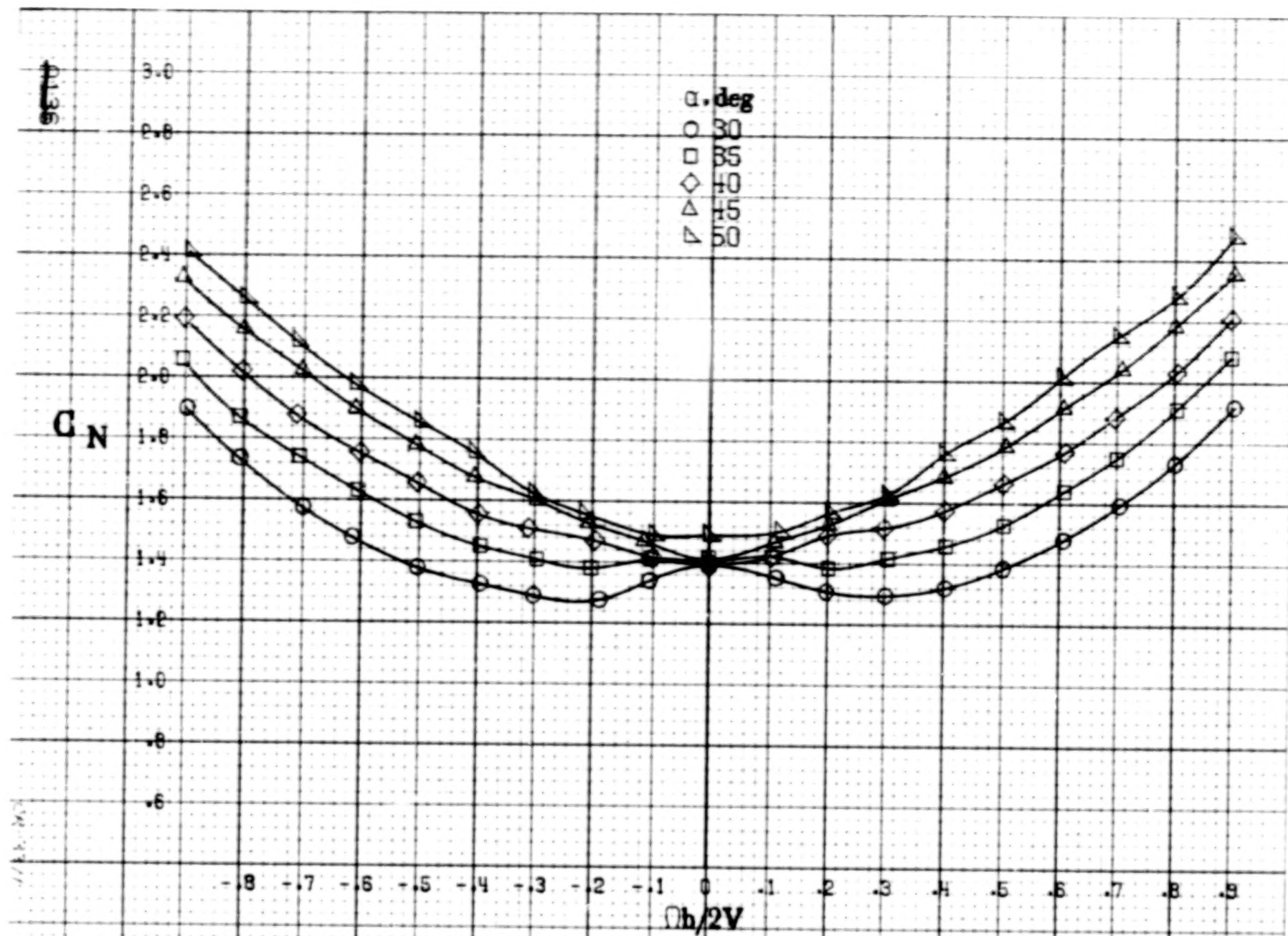




(a)  $\alpha = 8$  to  $16^\circ$ ,  $SR = 152.4 \text{ cm (60 in.)}$ .  
 Figure A52. Effect of rotation rate and angle of attack on normal-force coefficient for configuration having wing-fuselage fillet with outboard I.E wing droop.  $\delta_e = 0^\circ$ ,  $\delta_a = 0^\circ$ ,  $\delta_r = 0^\circ$ ,  $\beta = 0^\circ$ .



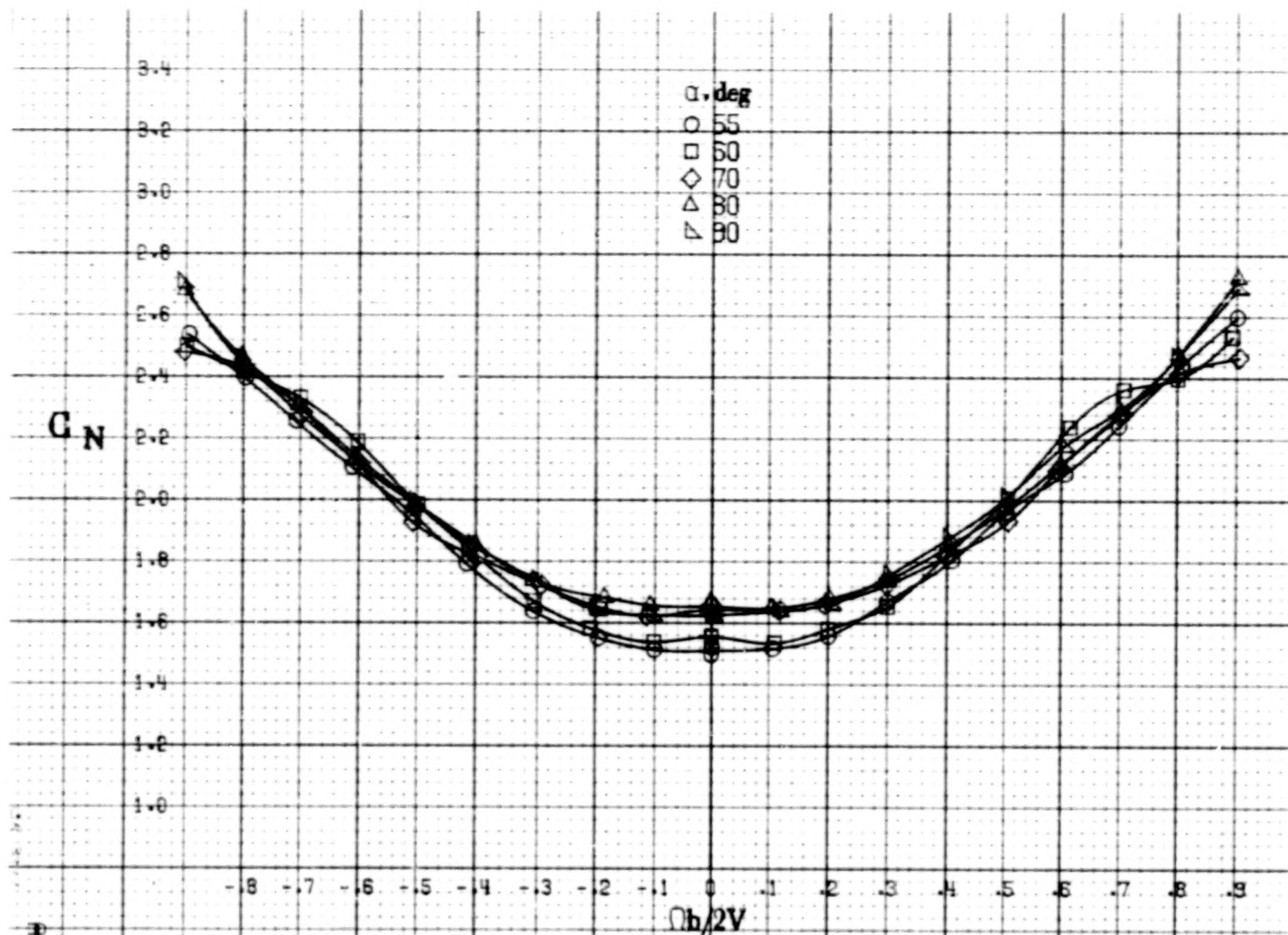
(b)  $\alpha = 18$  to  $35$  deg,  $SR = 152.4$  cm (60 in).  
Figure A52.-Continued.



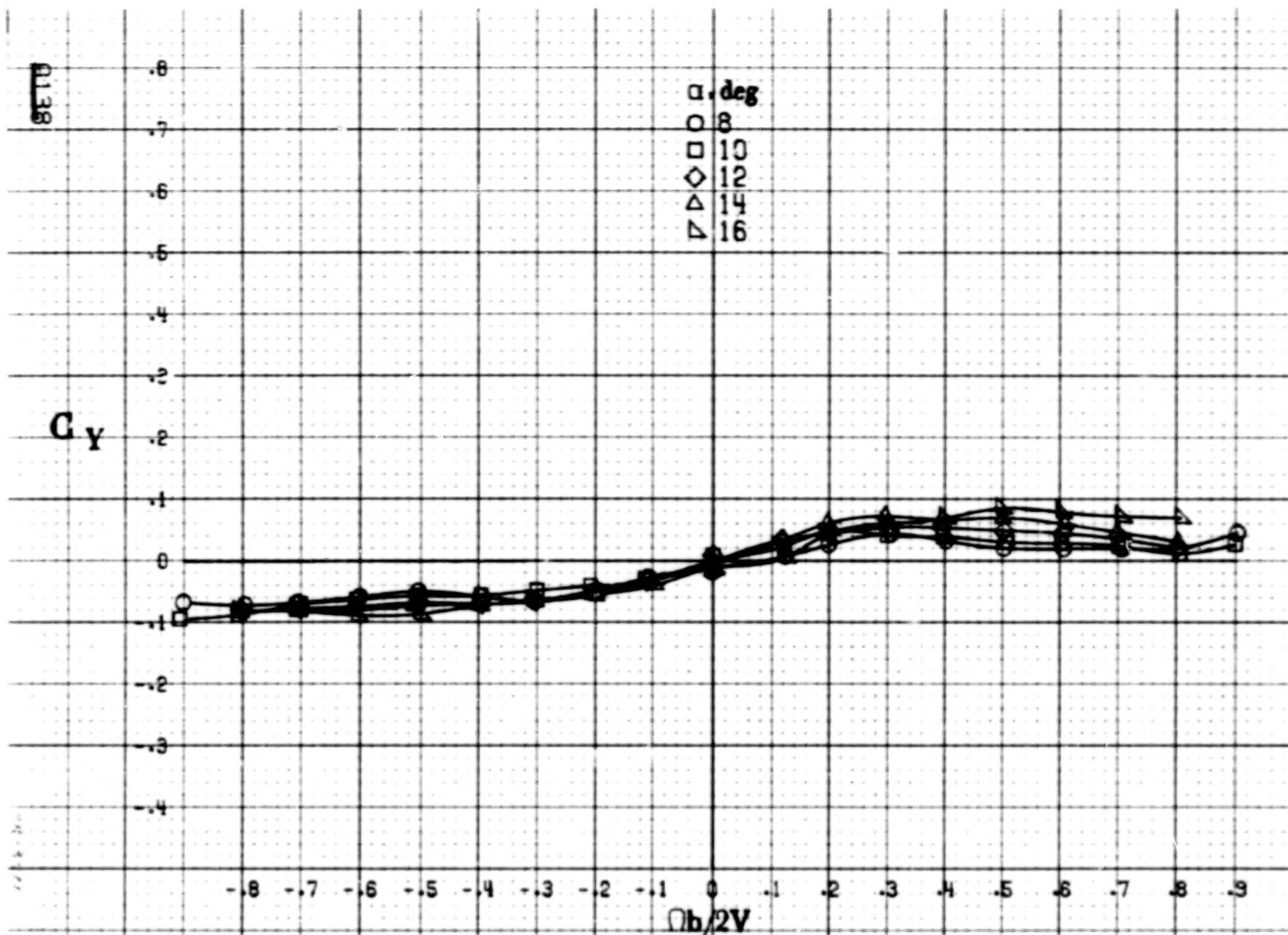
(c)  $\alpha = 30$  to  $50^\circ$ ,  $3R = 0$ .

Figure A52.-Continued.

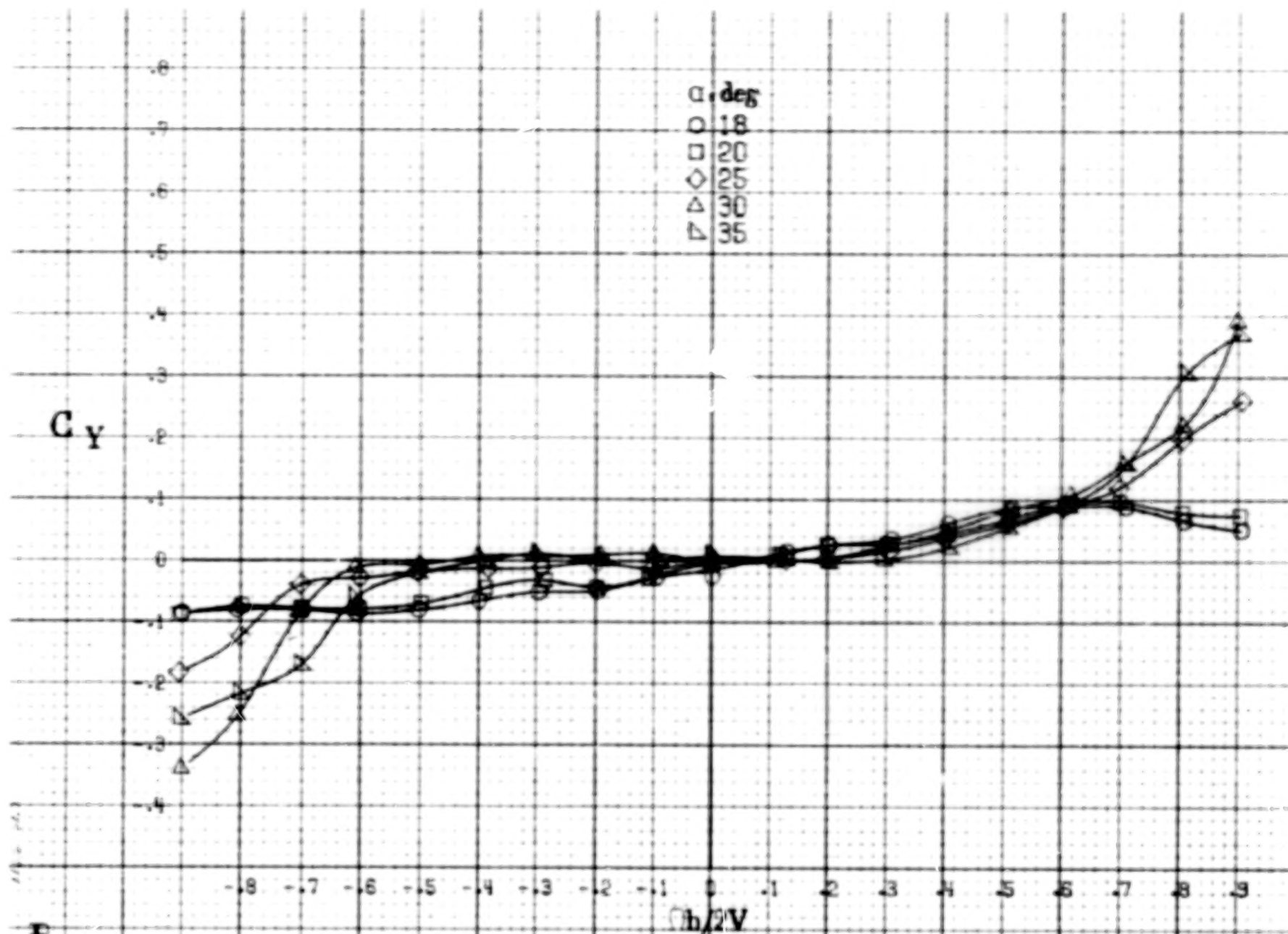




(d)  $\alpha = 55$  to  $90^\circ$ ,  $SR = 0$ .  
Figure A52.-Concluded.

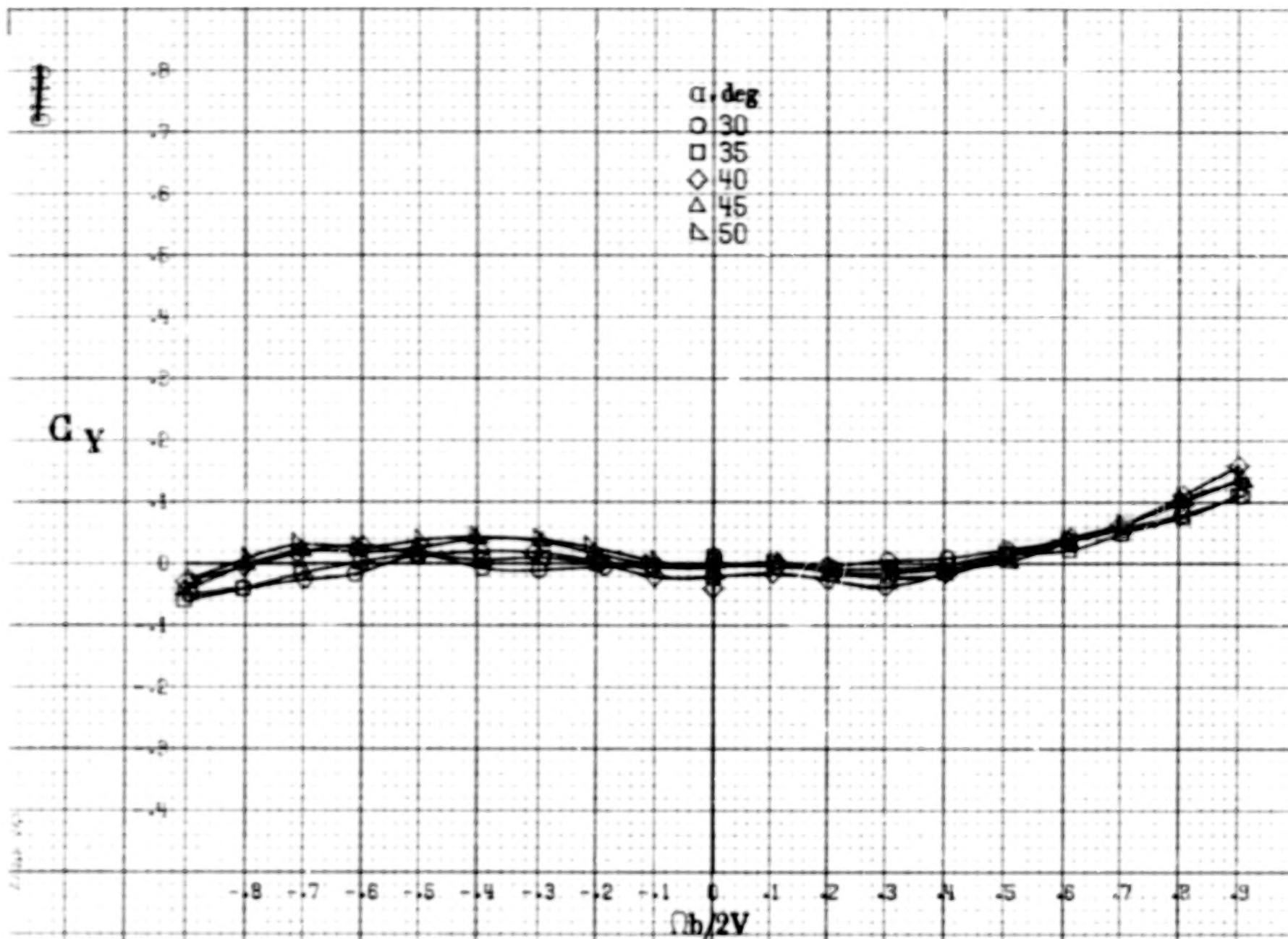


(a)  $\alpha = 8$  to  $16^\circ$ ,  $SR = 152.4\text{cm (60in)}$ .  
 Figure A53.-Effect of rotation rate and angle of attack on side-force coefficient for configuration having wing-fuselage fillet with outboard LE wing droop.  $\delta_s = 0^\circ$ ,  $\delta_e = 0^\circ$ ,  $\delta_f = 0^\circ$ ,  $\beta = 0^\circ$ .



(b)  $\alpha = 18$  to  $35$  deg. SR = 152.4 cm (60 in).

Figure A53.-Continued.

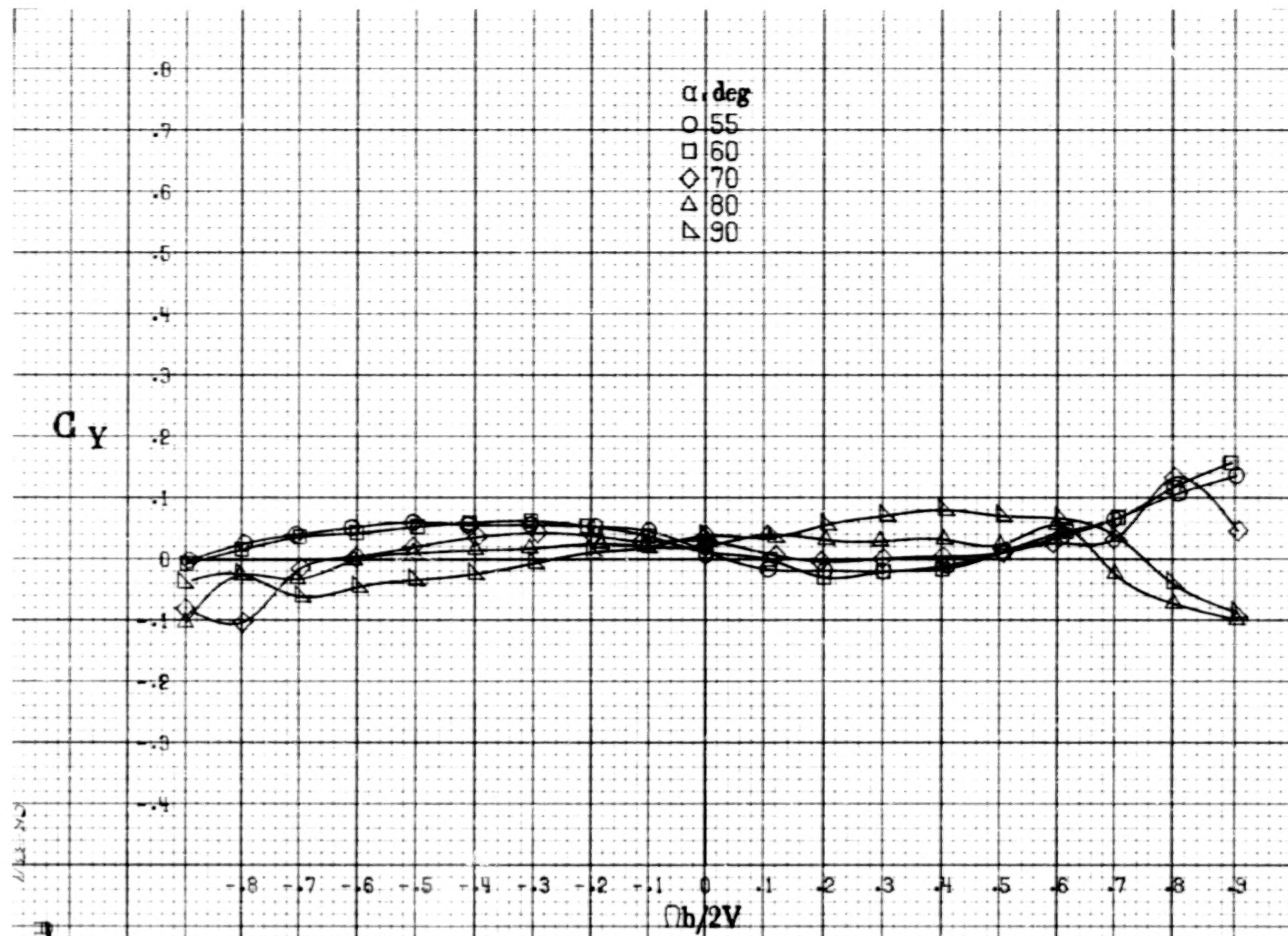


(c)  $\alpha = 30$  to  $50$  deg,  $SR = 0$ .

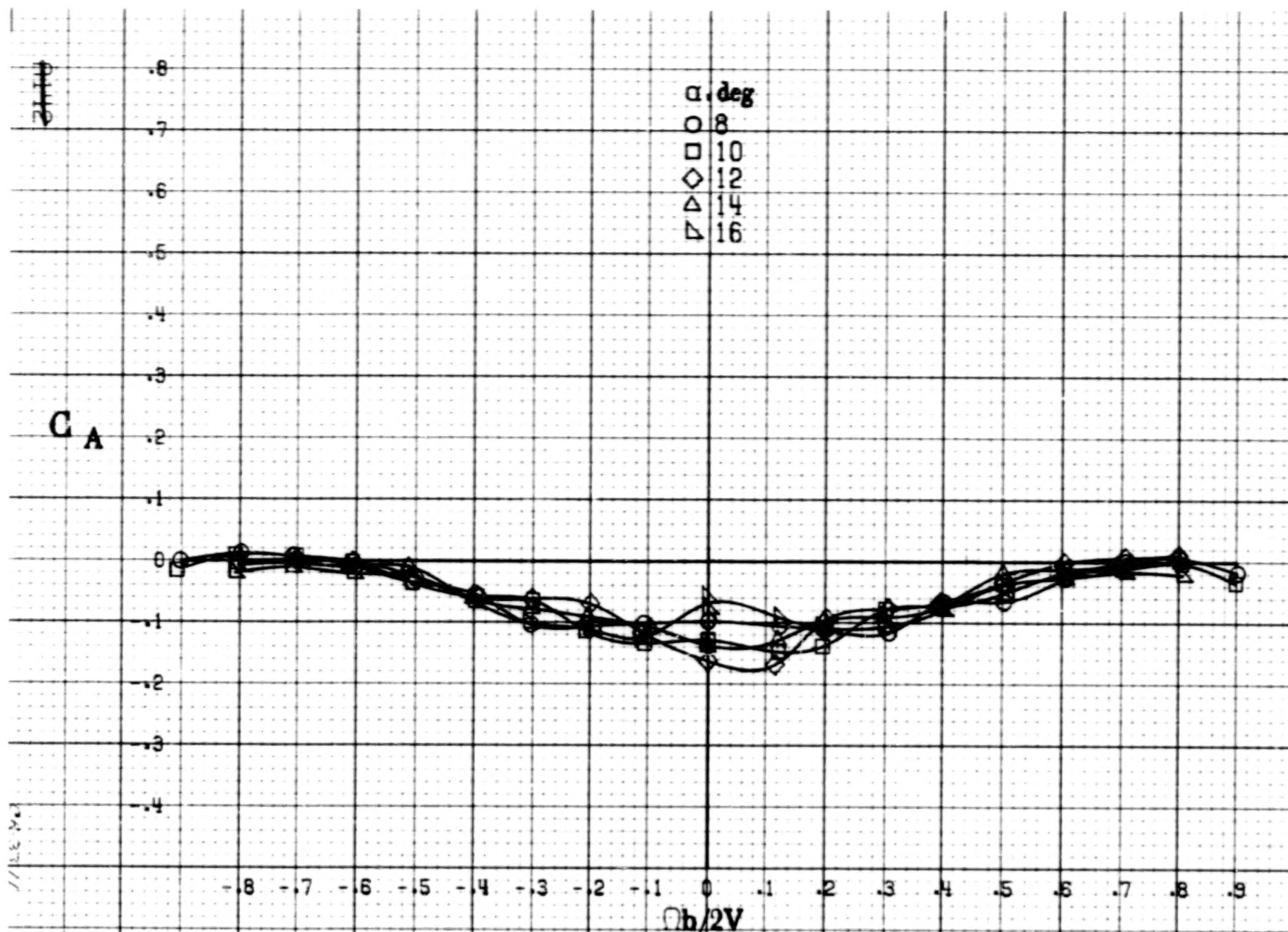
Figure A53.-Continued.

A140



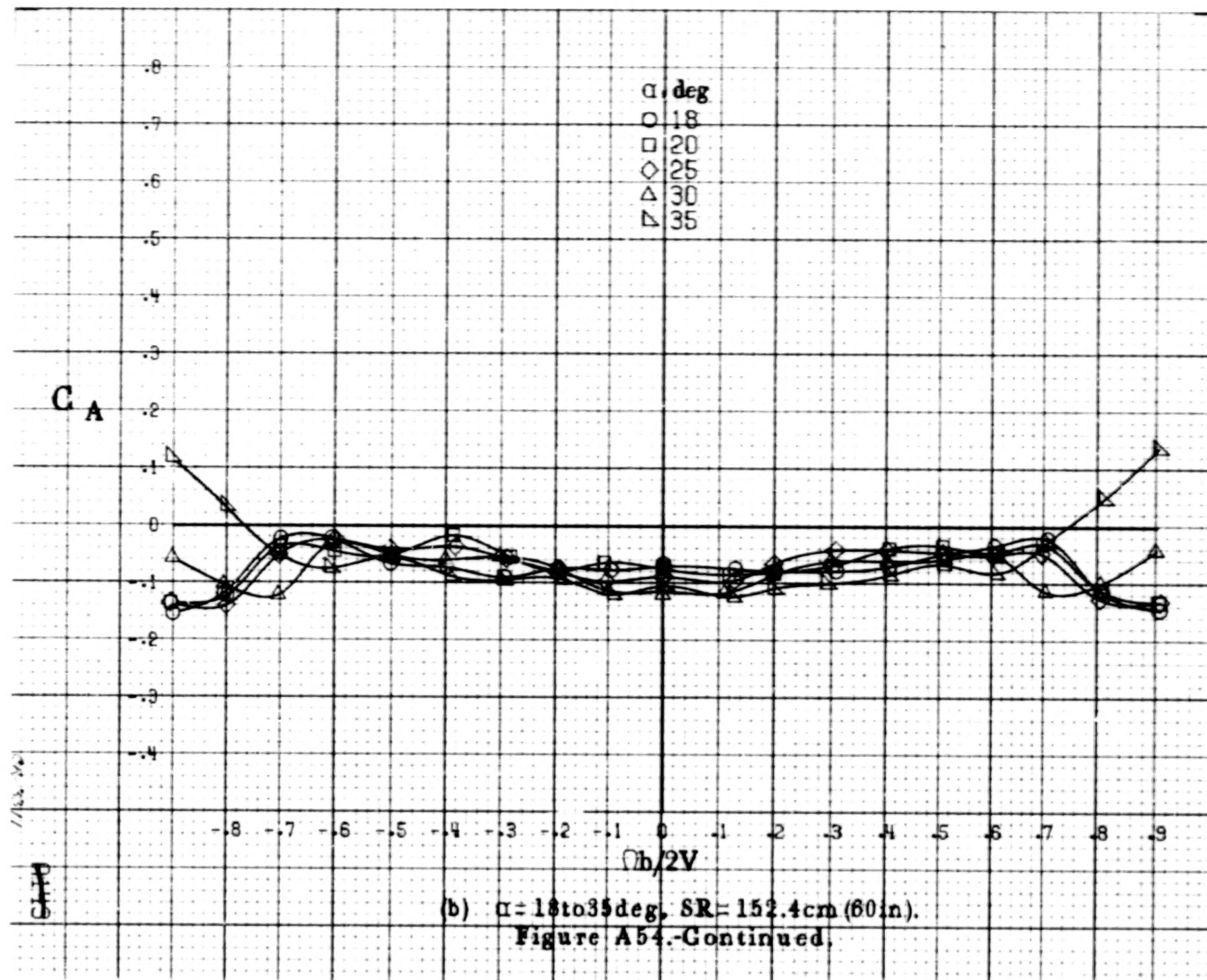


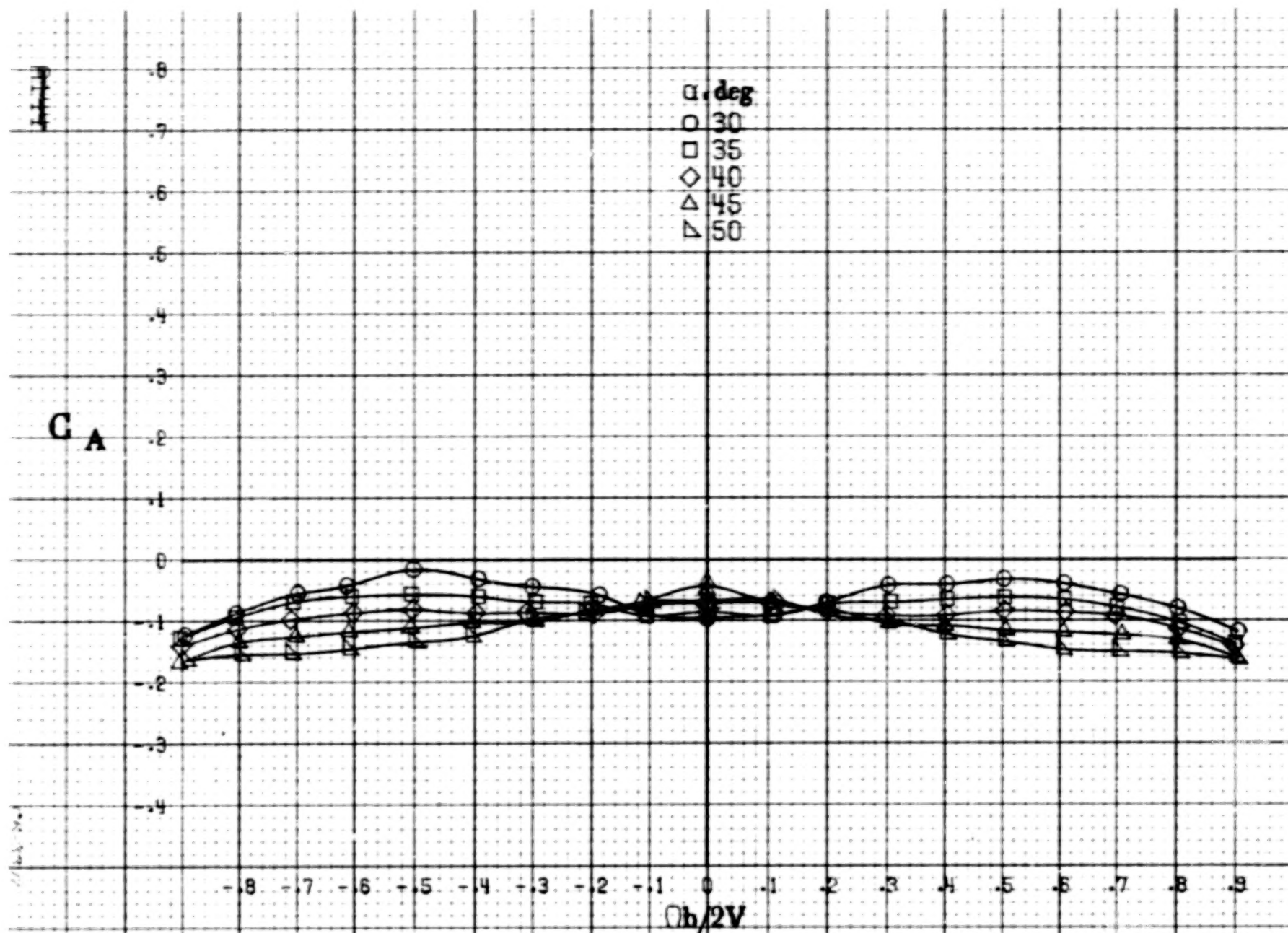
(d)  $\alpha = 55$  to  $90^\circ$ ,  $SR = 0$ .  
Figure A58.-Concluded.



(a)  $\alpha = 8$  to  $16^\circ$ ,  $SR = 152.4 \text{ cm (60 in.)}$ .

Figure A54. Effect of rotation rate and angle of attack on axial-force coefficient for configuration having wing-fuselage fillet with outboard LE wing droop.  $\delta_e = 0^\circ$ ,  $\delta_s = 0^\circ$ ,  $\delta_r = 0^\circ$ .  $\beta = 0^\circ$ .

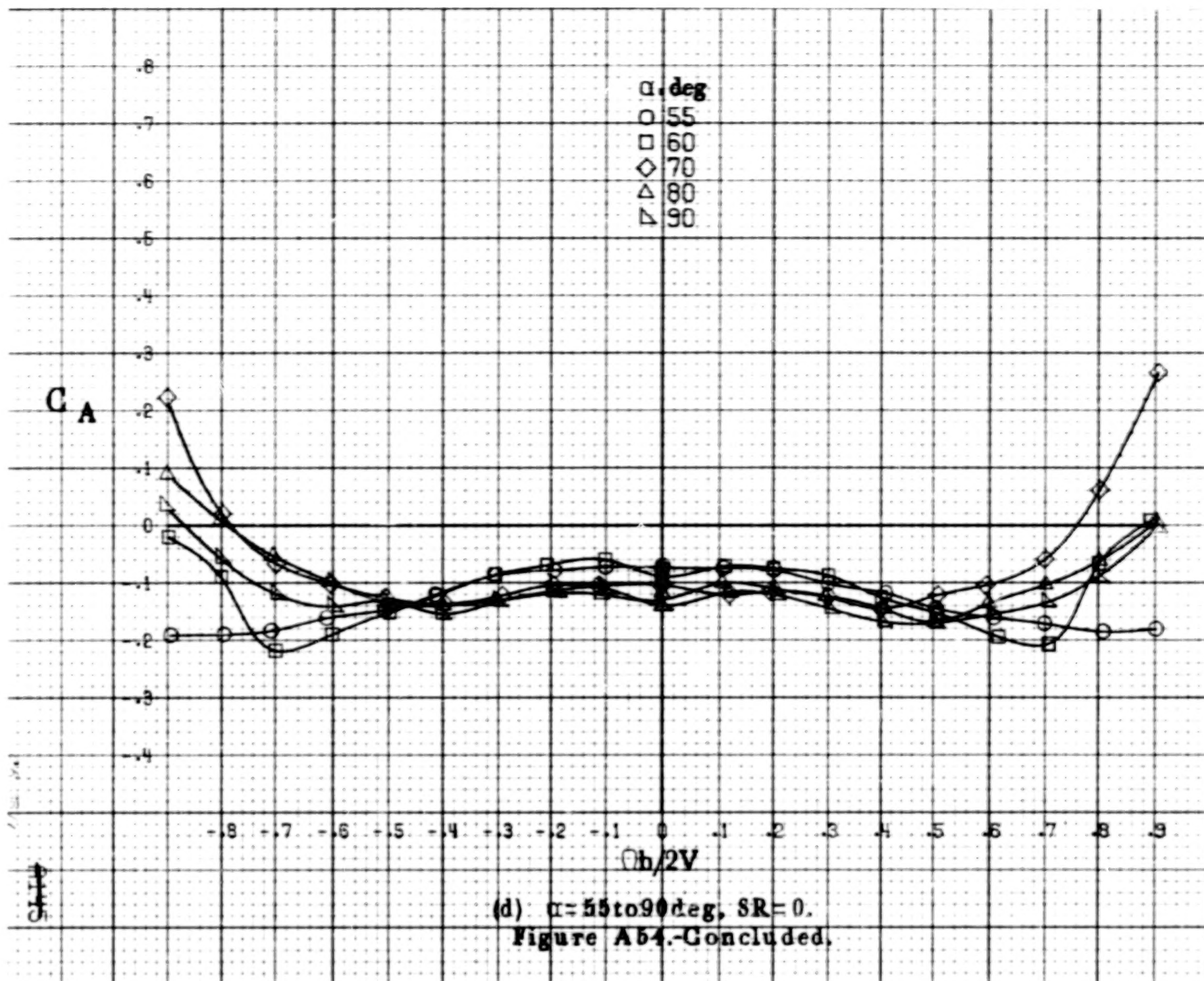


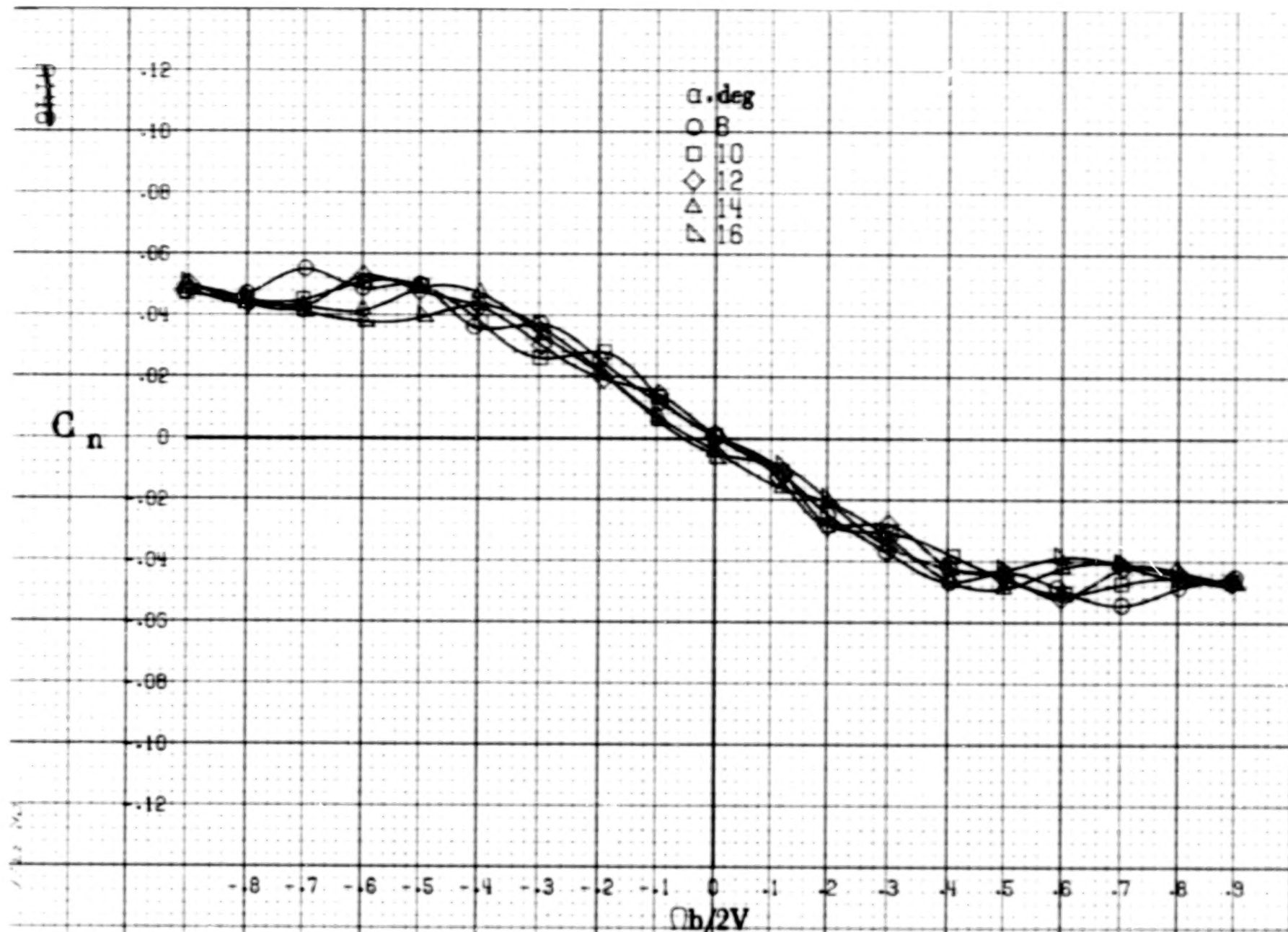


(c)  $\alpha = 30$  to  $50$  deg,  $SR = 0$ .  
Figure A64.-Continued.

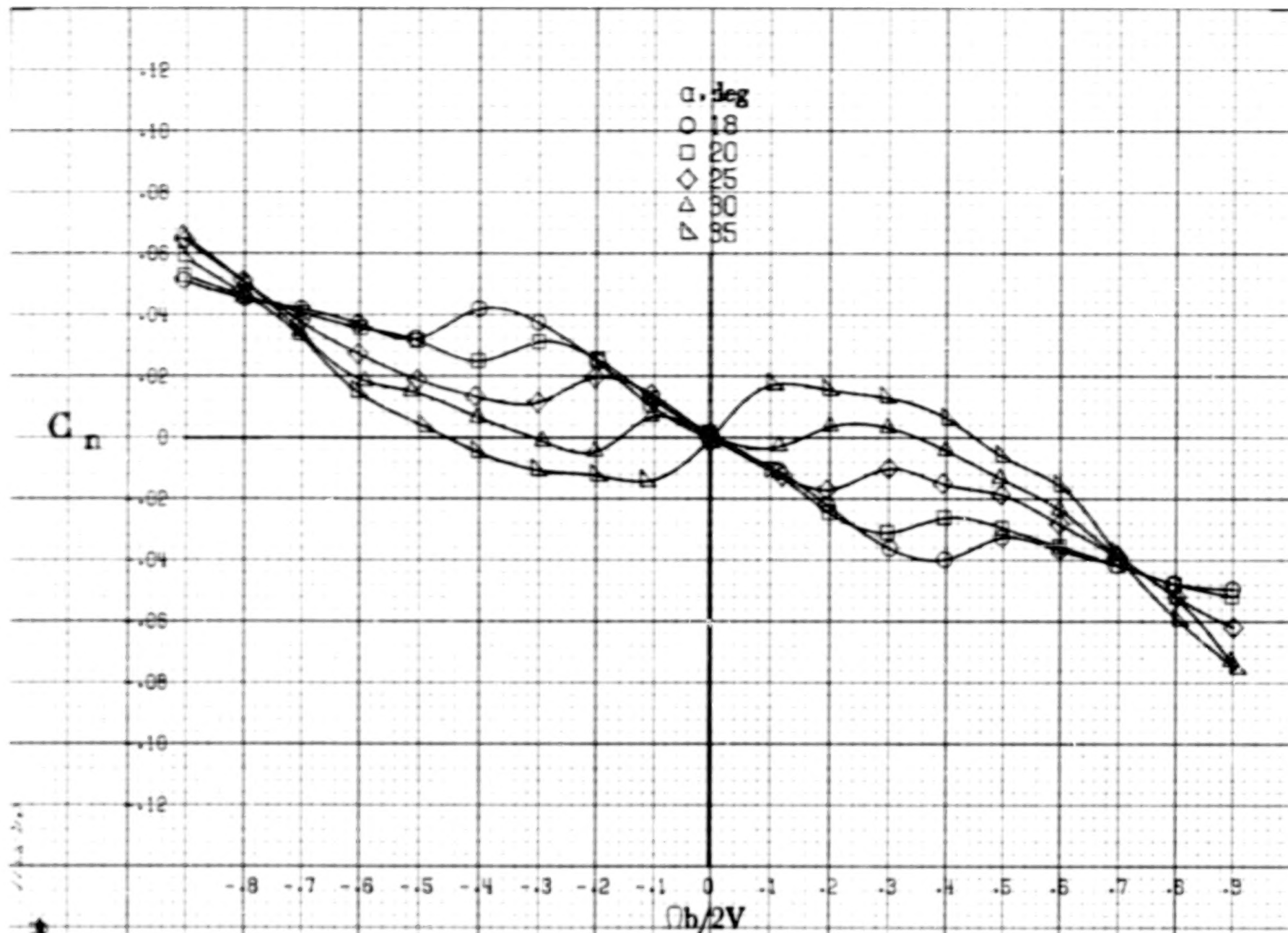
A144



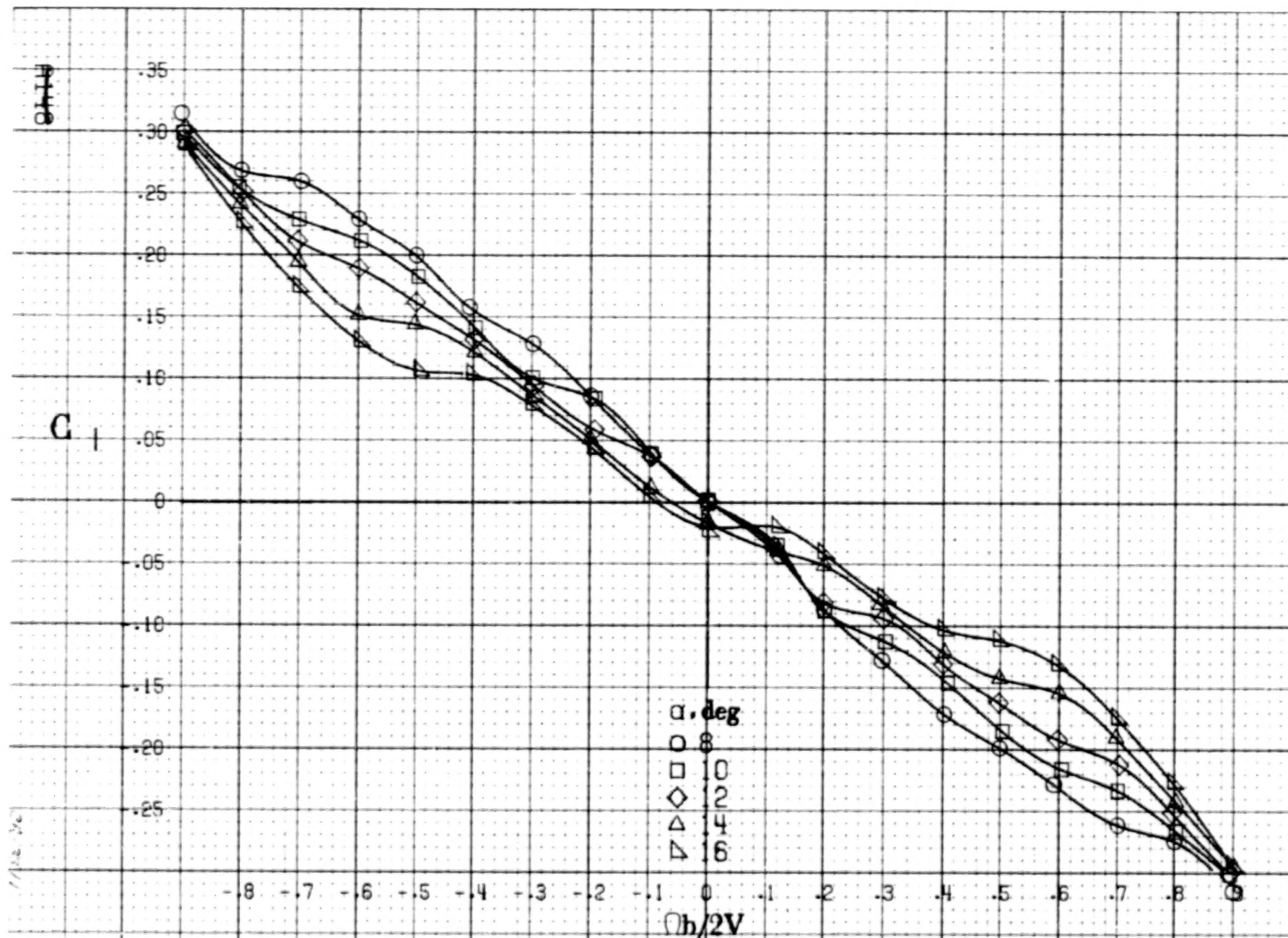




(a)  $\alpha = 8$  to  $16^\circ$ ,  $SR = 152.4 \text{ cm (60 in)}$ .  
 Figure A55.-Effect of rotation rate and angle of attack on yawing-moment coefficient for wing-fuselage fillet with outboard LE wing slat.  $\delta_e = 0^\circ$ ,  $\delta_a = 0^\circ$ ,  $\delta_r = 0^\circ$ ,  $\beta = 0^\circ$ .

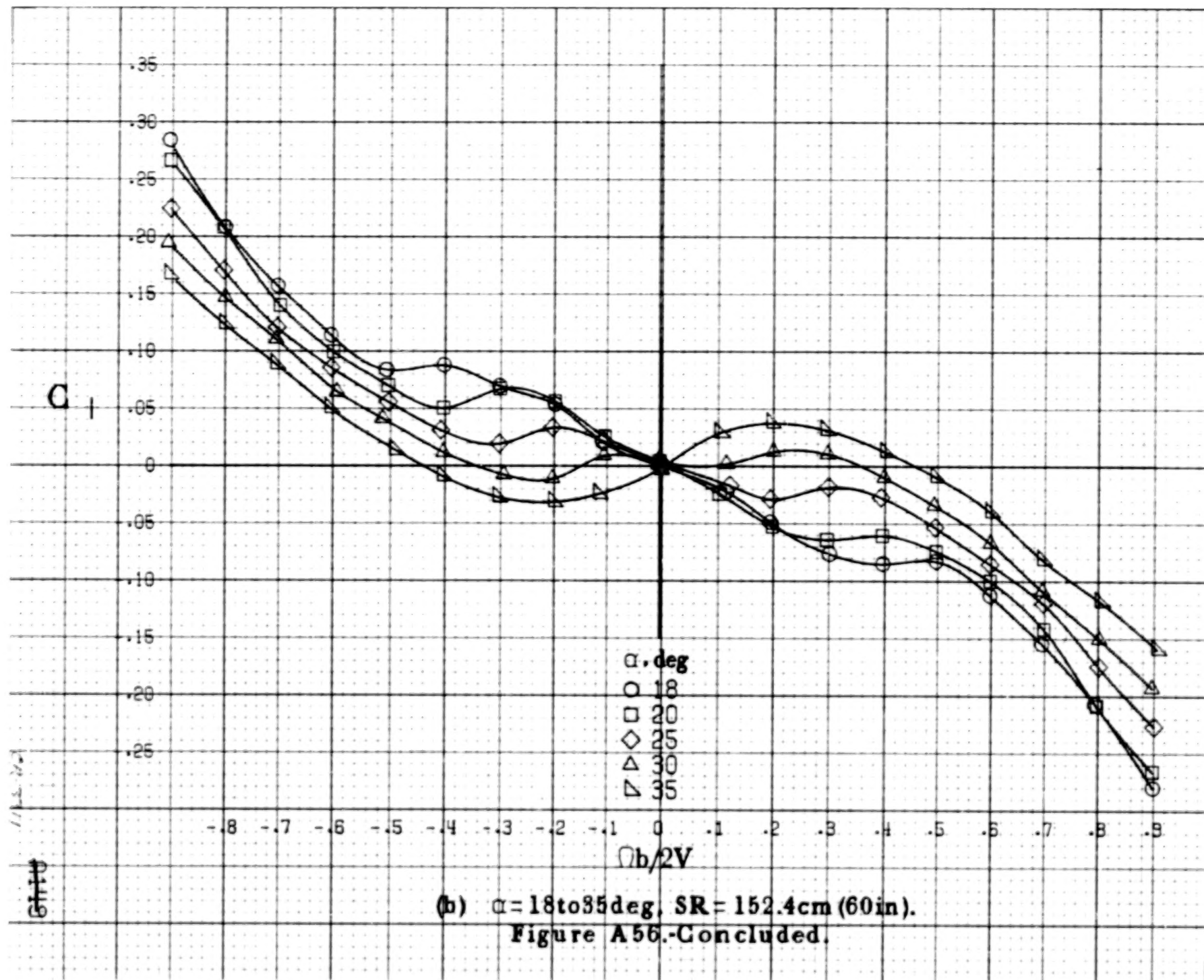


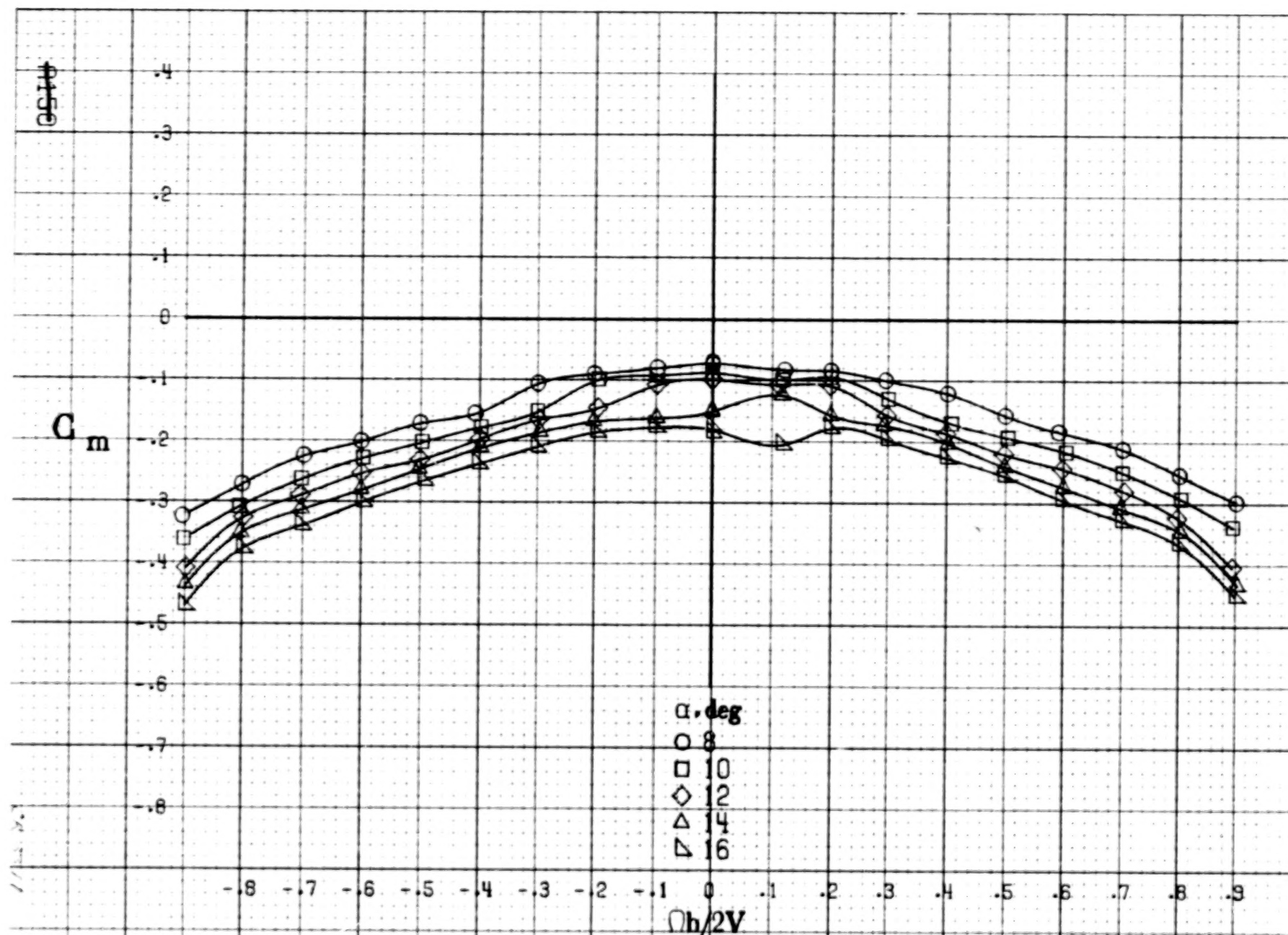
(b)  $\alpha = 18$  to  $35^\circ$ , SR = 152.4 cm (60 in).  
Figure A55.-Concluded.



(a)  $\alpha = 8$  to  $16^\circ$ ,  $SR = 152.4 \text{ cm (60 in.)}$ .  
 Figure A56. Effect of rotation rate and angle of attack on rolling-moment coefficient for wing-fuselage fillet with outboard LE wing slat.  $\delta_a = 0^\circ$ ,  $\delta_r = 0^\circ$ .  $\beta = 0^\circ$ .



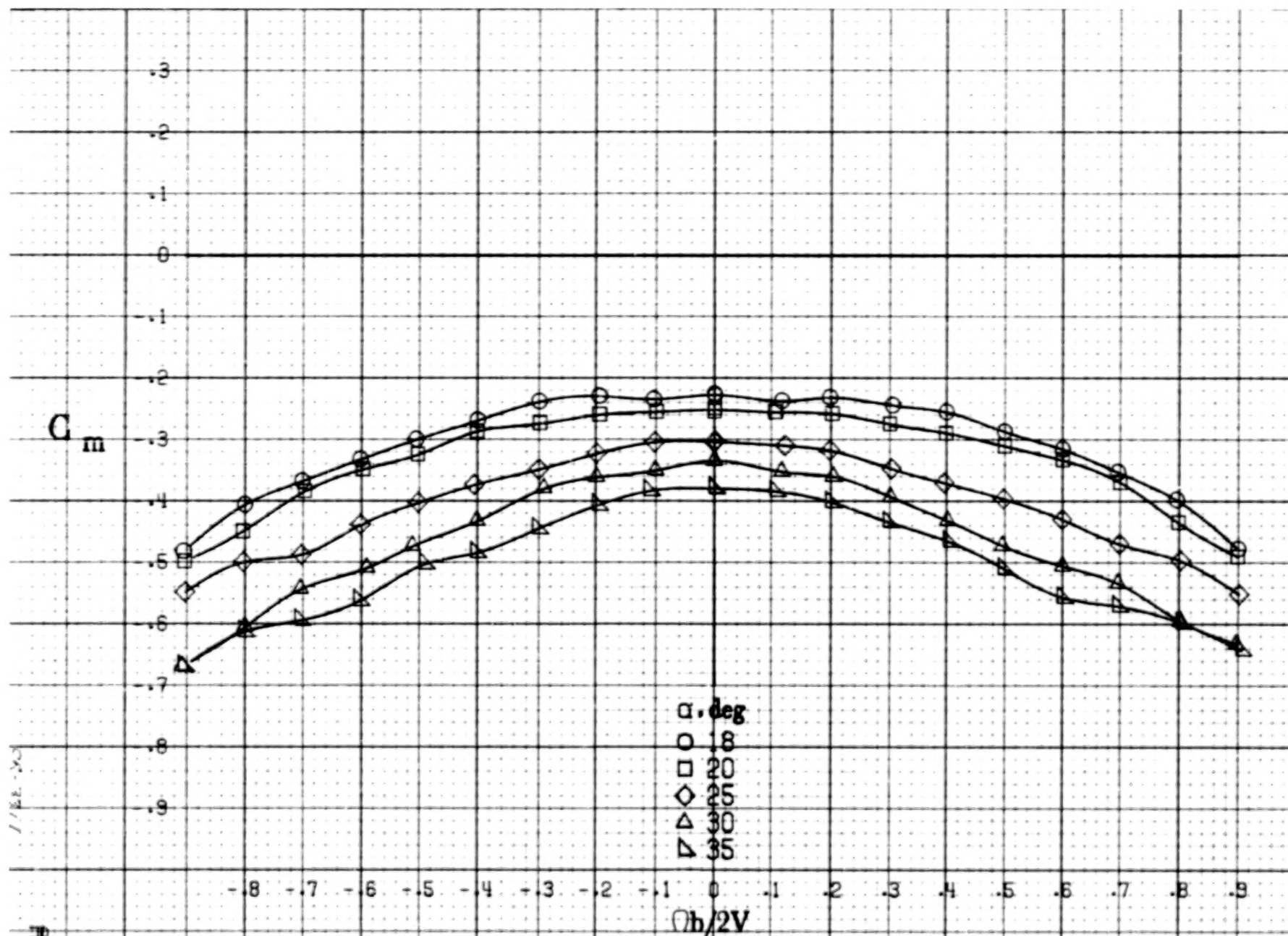




(a)  $\alpha = 8$  to  $16^\circ$ ,  $SR = 152.4\text{cm (60in)}$ .

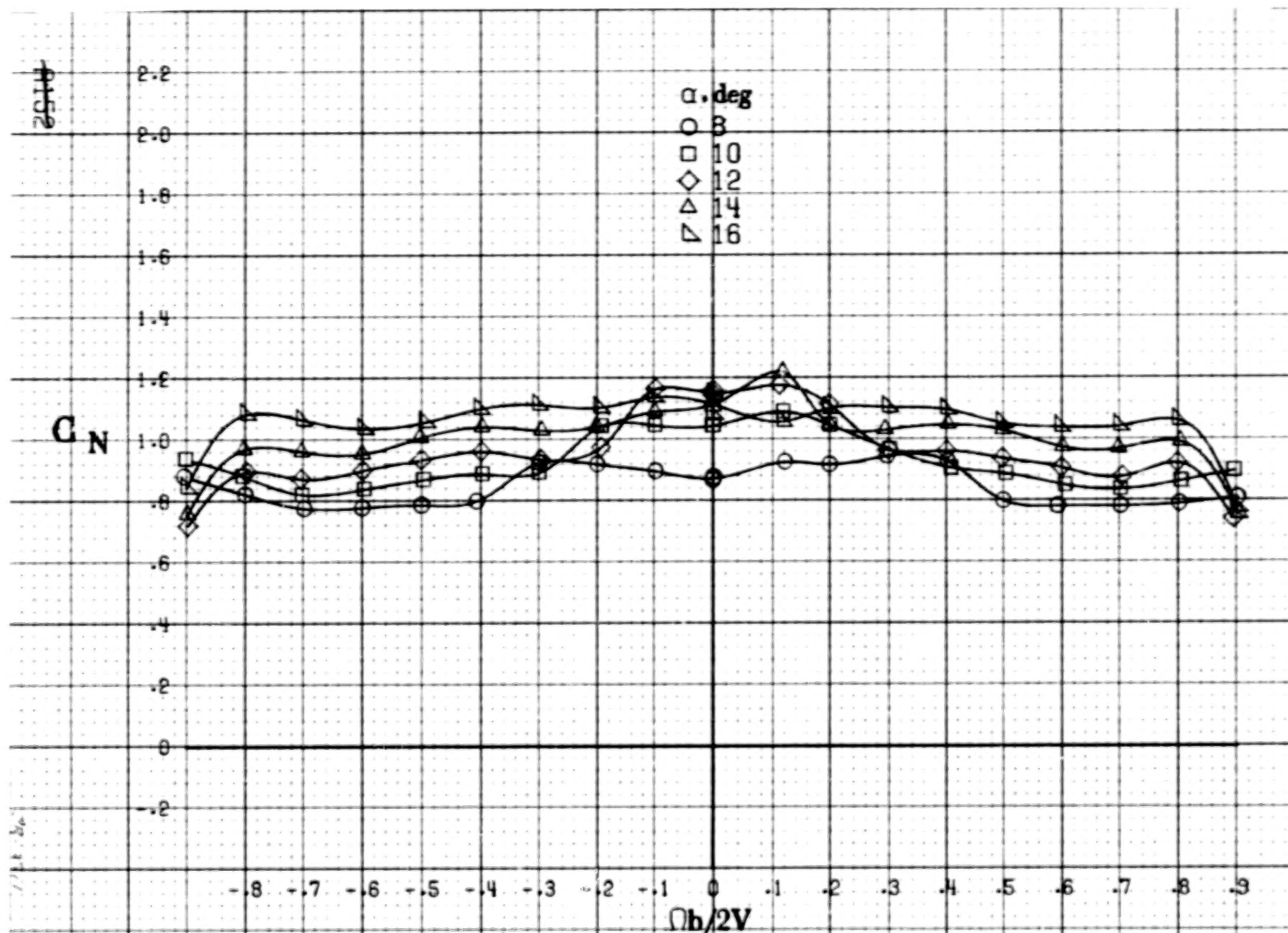
Figure A57. Effect of rotation rate and angle of attack on pitching-moment coefficient for wing-fuselage fillet with outboard LE wing slat.  $\delta_e = 0^\circ$ ,  $\delta_a = 0^\circ$ ,  $\delta_r = 0^\circ$ ,  $\beta = 0^\circ$ .

A150



(b)  $\alpha = 18$  to  $35^\circ$ ,  $SR = 152.4\text{cm}$  (60 in).

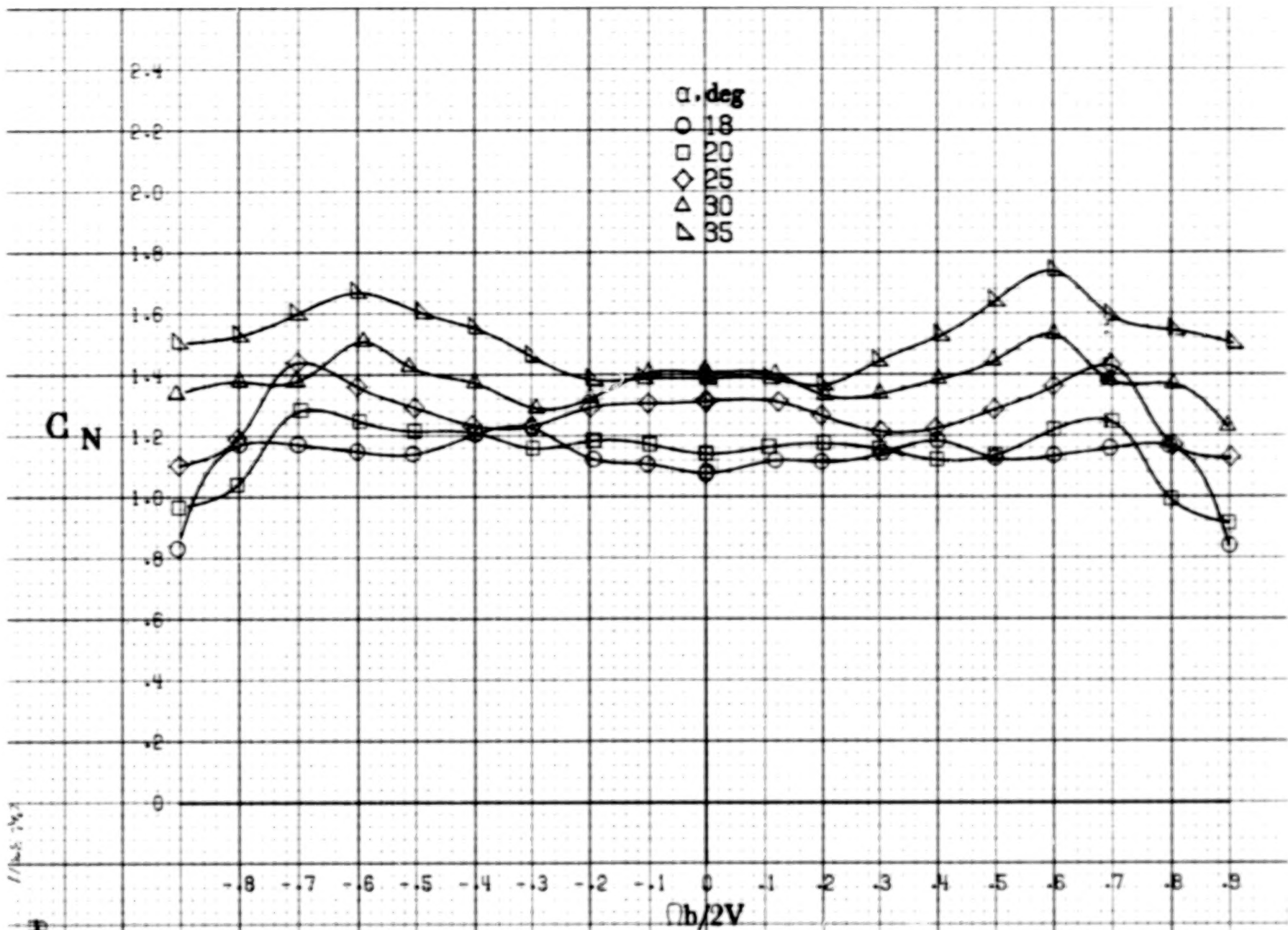
Figure A57.-Concluded.



(a)  $\alpha = 8$  to  $16$  deg,  $SR = 152.4$  cm (60 in).

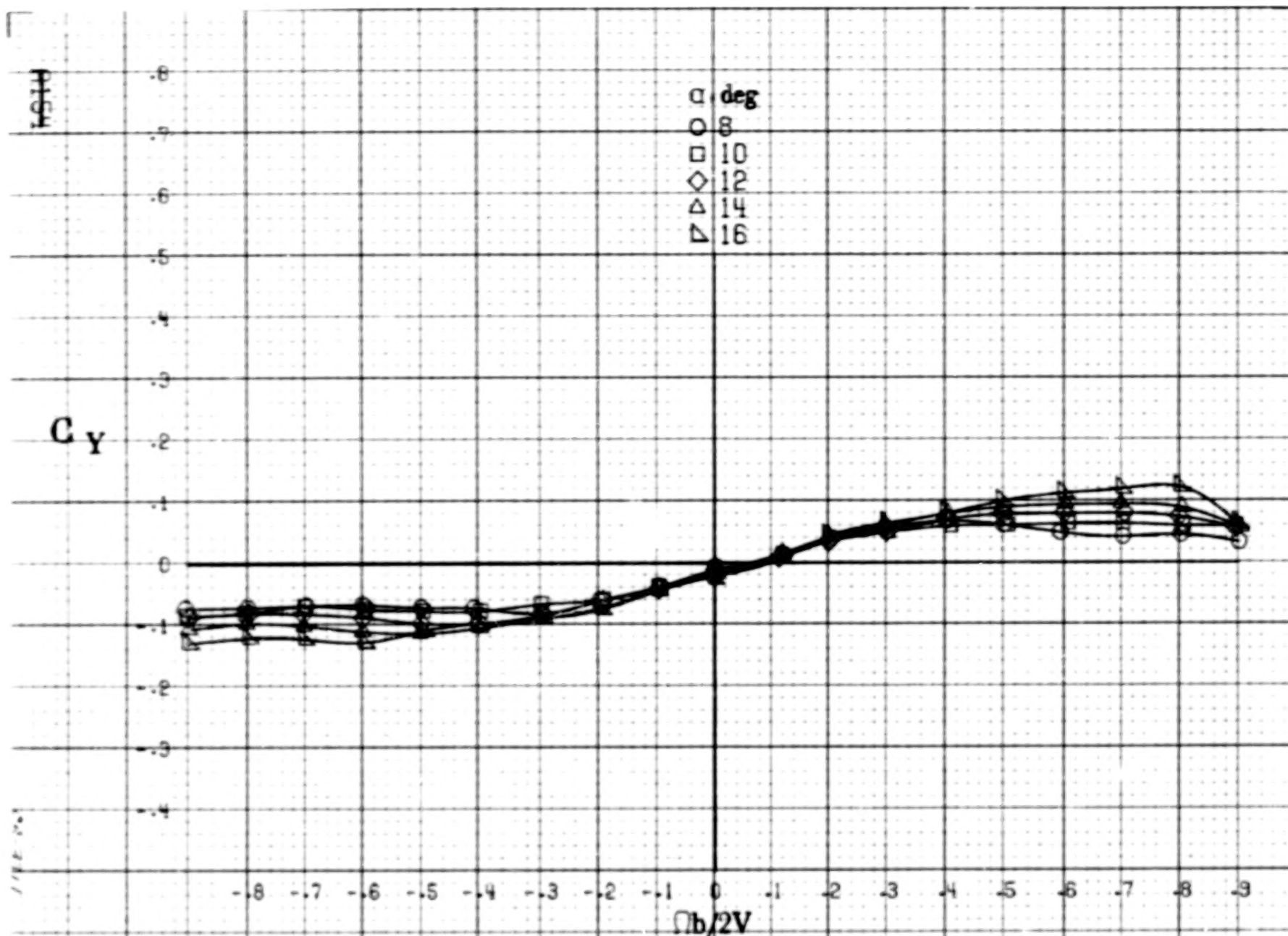
Figure A58.-Effect of rotation rate and angle of attack on normal-force coefficient for wing-fuselage fillet with outboard LE wing slat.  $\delta_e = 0^\circ$ ,  $\delta_a = 0^\circ$ ,  $\delta_r = 0^\circ$ ,  $\beta = 0^\circ$ .





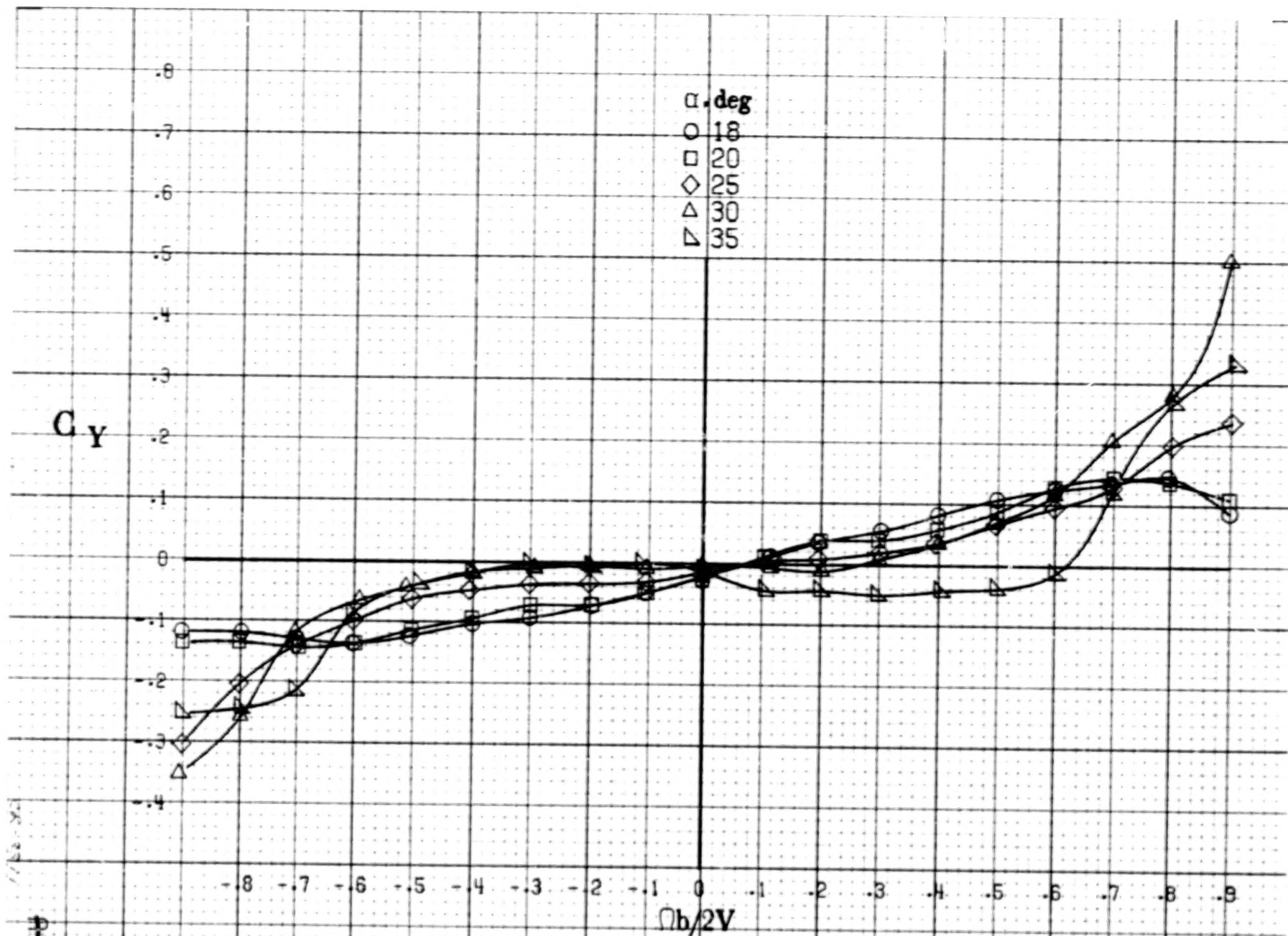
(b)  $\alpha = 18$  to  $35$  deg,  $SR = 152.4$  cm (60 in).

Figure A58.-Concluded.



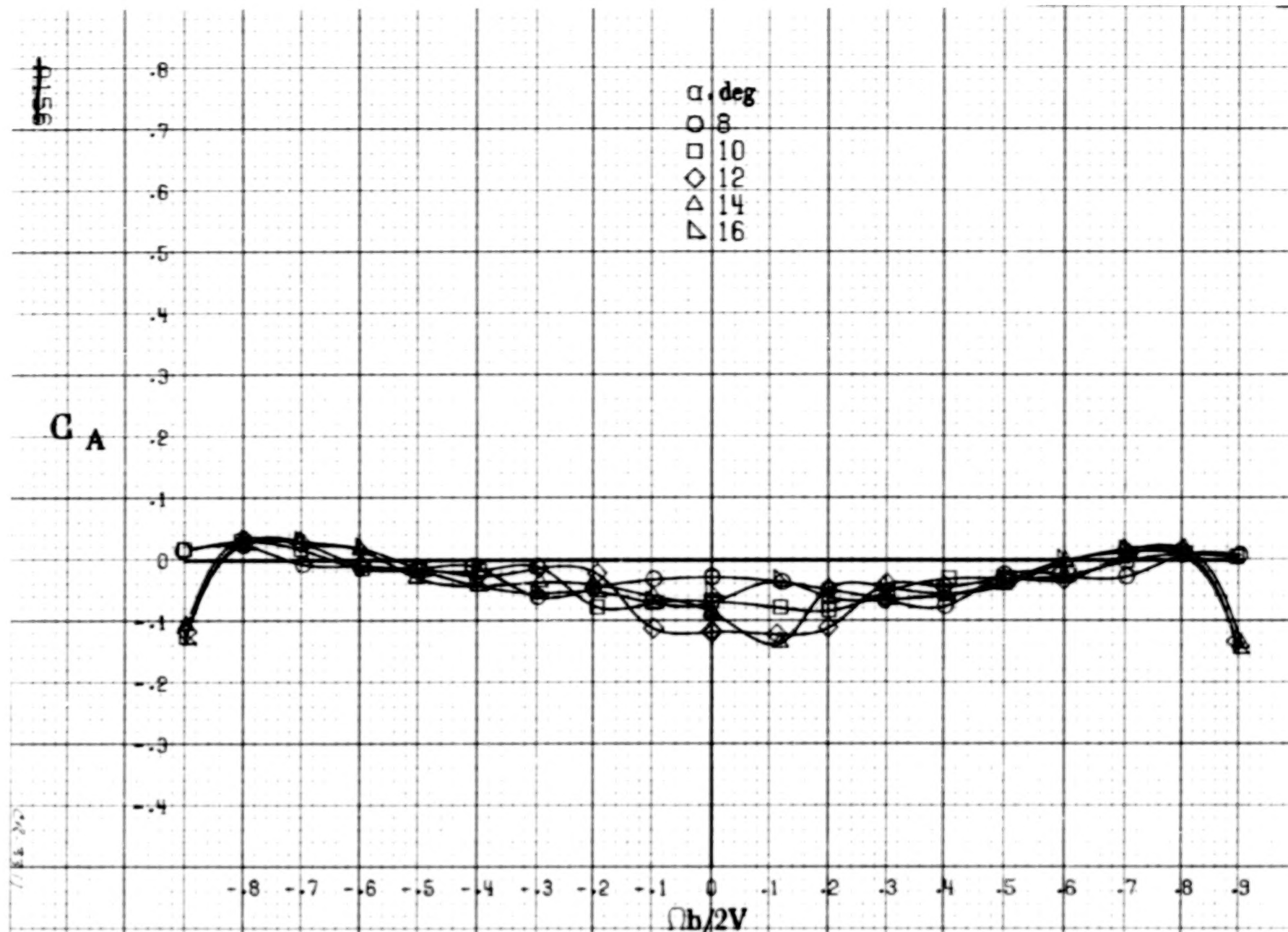
(a)  $\alpha = 8$  to  $16^\circ$ ,  $SR = 152.4\text{cm (60in)}$ .

Figure A59. Effect of rotation rate and angle of attack on side-force coefficient for wing-fuselage fillet with outboard LE wing slat.  $\delta_e = 0^\circ$ ,  $\delta_a = 0^\circ$ ,  $\delta_r = 0^\circ$ ,  $\beta = 0^\circ$ .



(b)  $\alpha = 18$  to  $35^\circ$ ,  $SR = 152.4\text{cm (60in.)}$ .

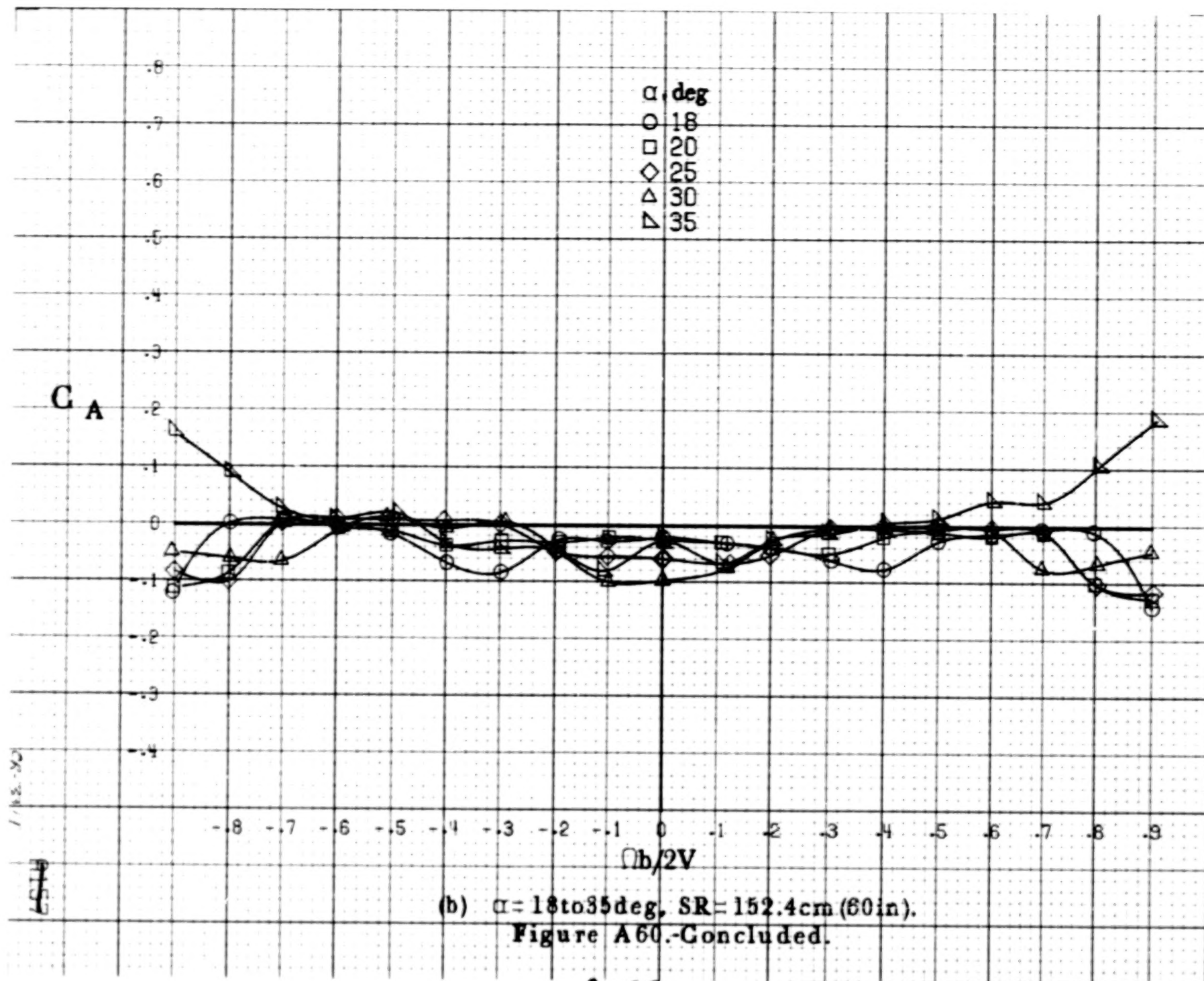
Figure A59.-Concluded.

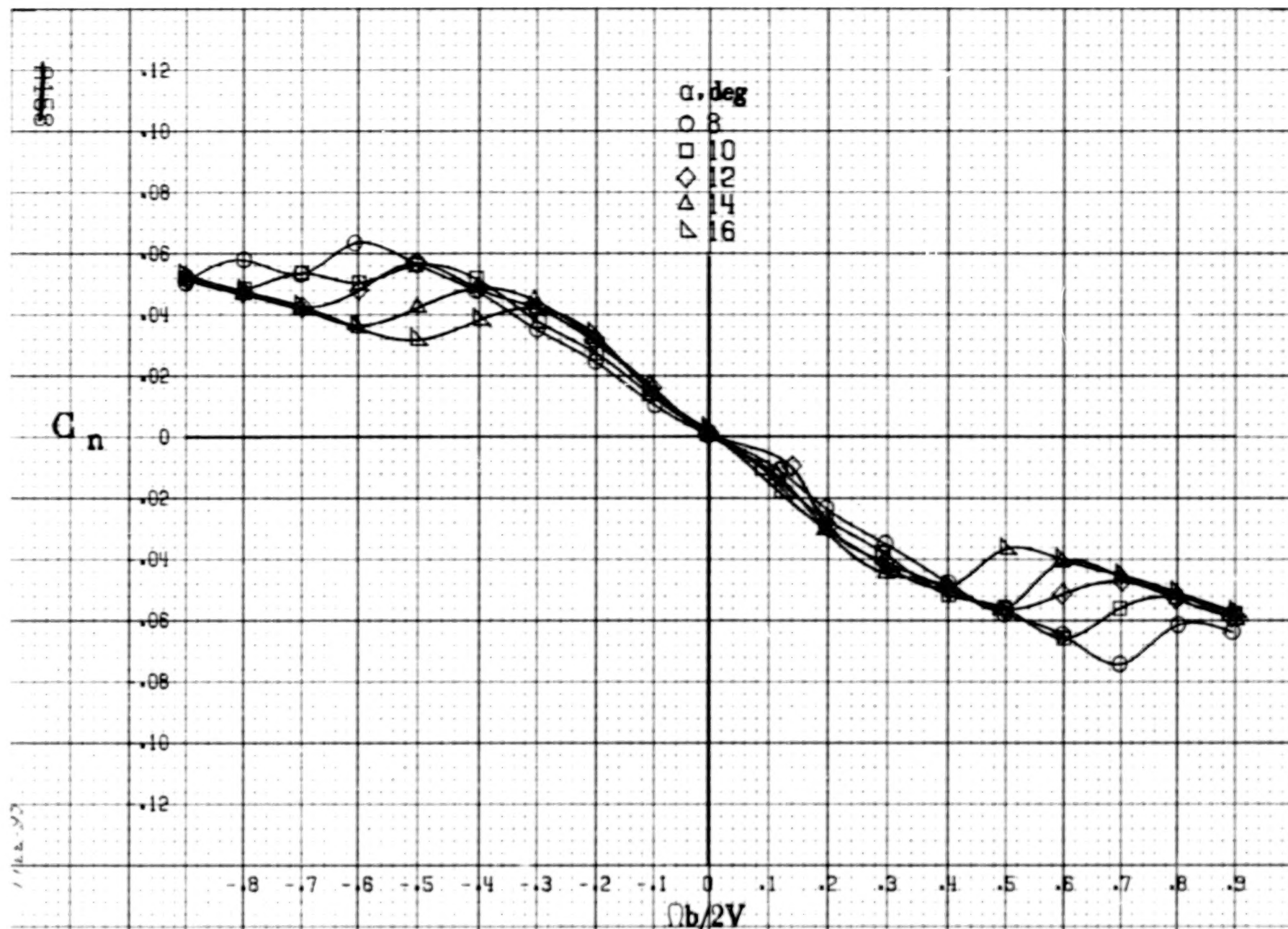


(a)  $\alpha = 8$  to  $16$  deg,  $SR = 152.4$  cm (60 in).

Figure A60.-Effect of rotation rate and angle of attack on axial-force coefficient for wing-fuselage fillet with outboard LE wing slat.  $\delta_e = 0^\circ$ ,  $\delta_a = 0^\circ$ ,  $\delta_r = 0^\circ$ ,  $\beta = 0^\circ$ .

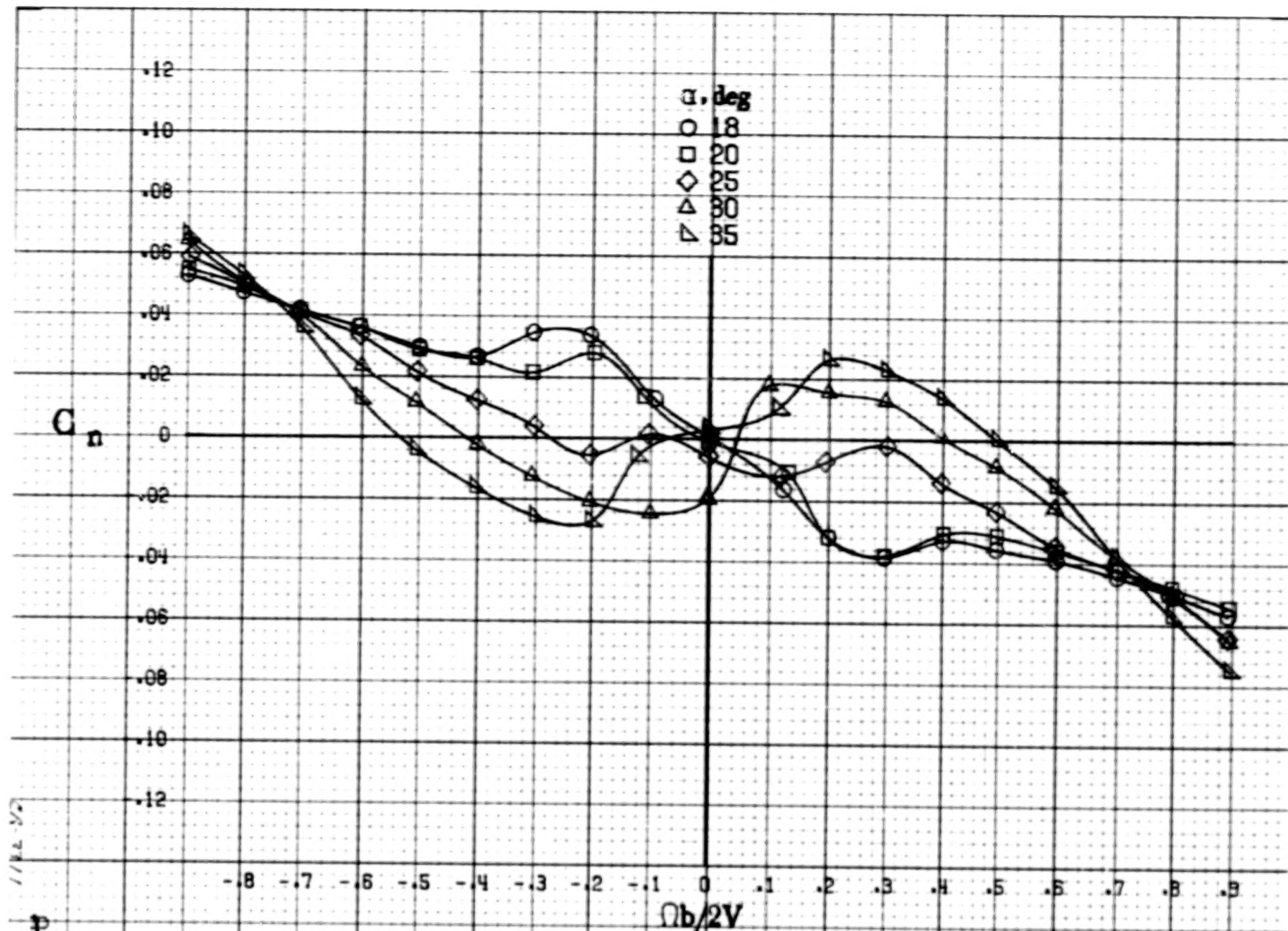




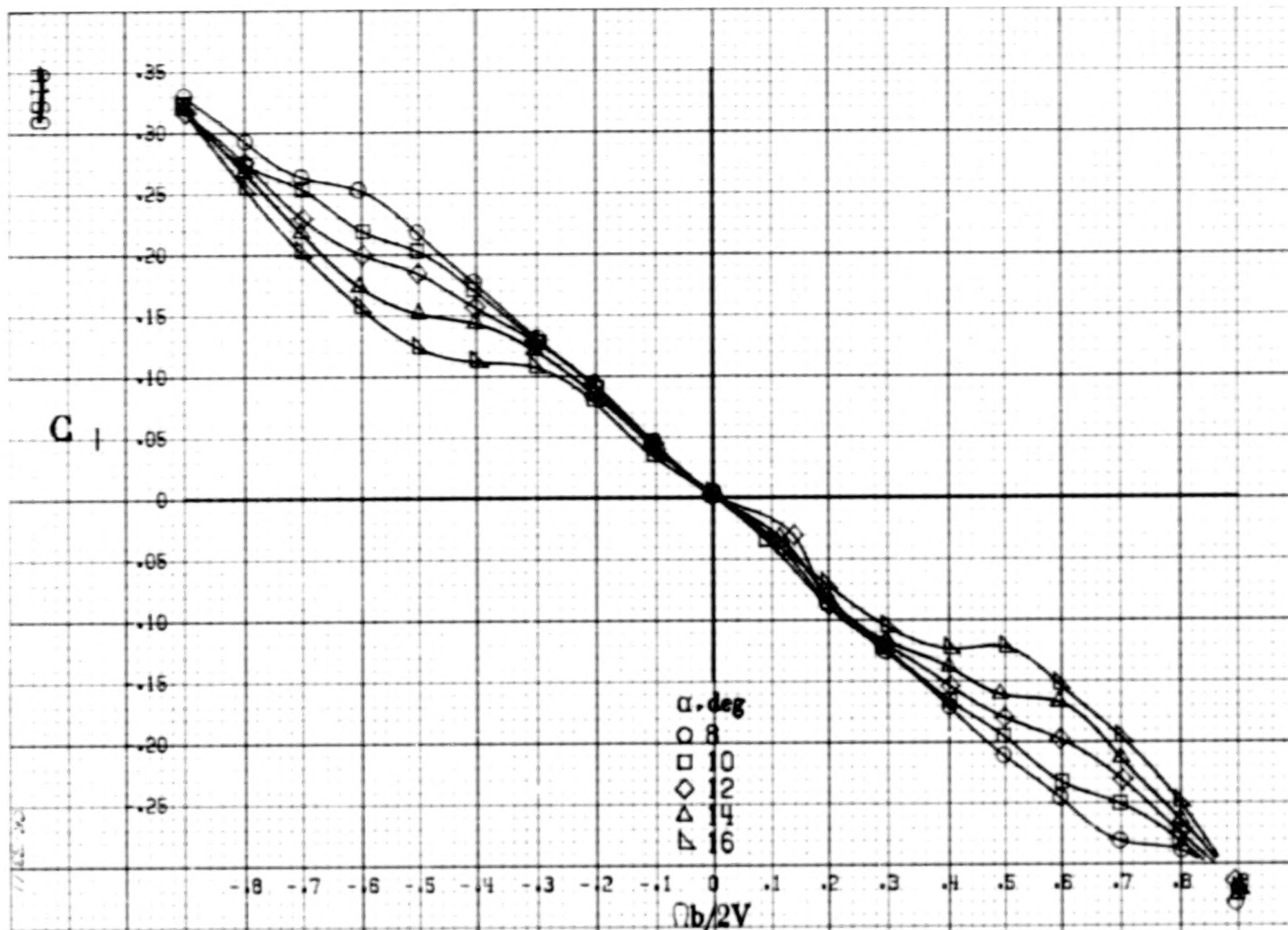


(a)  $\alpha = 8$  to  $16^\circ$ ,  $SR = 152.4\text{cm (60in)}$ .

Figure A61. Effect of rotation rate and angle of attack on yawing-moment coefficient for full-span wing slat configuration.  $\delta_e = 0^\circ$ ,  $\delta_a = 0^\circ$ ,  $\delta_r = 0^\circ$ .  $\beta = 0^\circ$ .



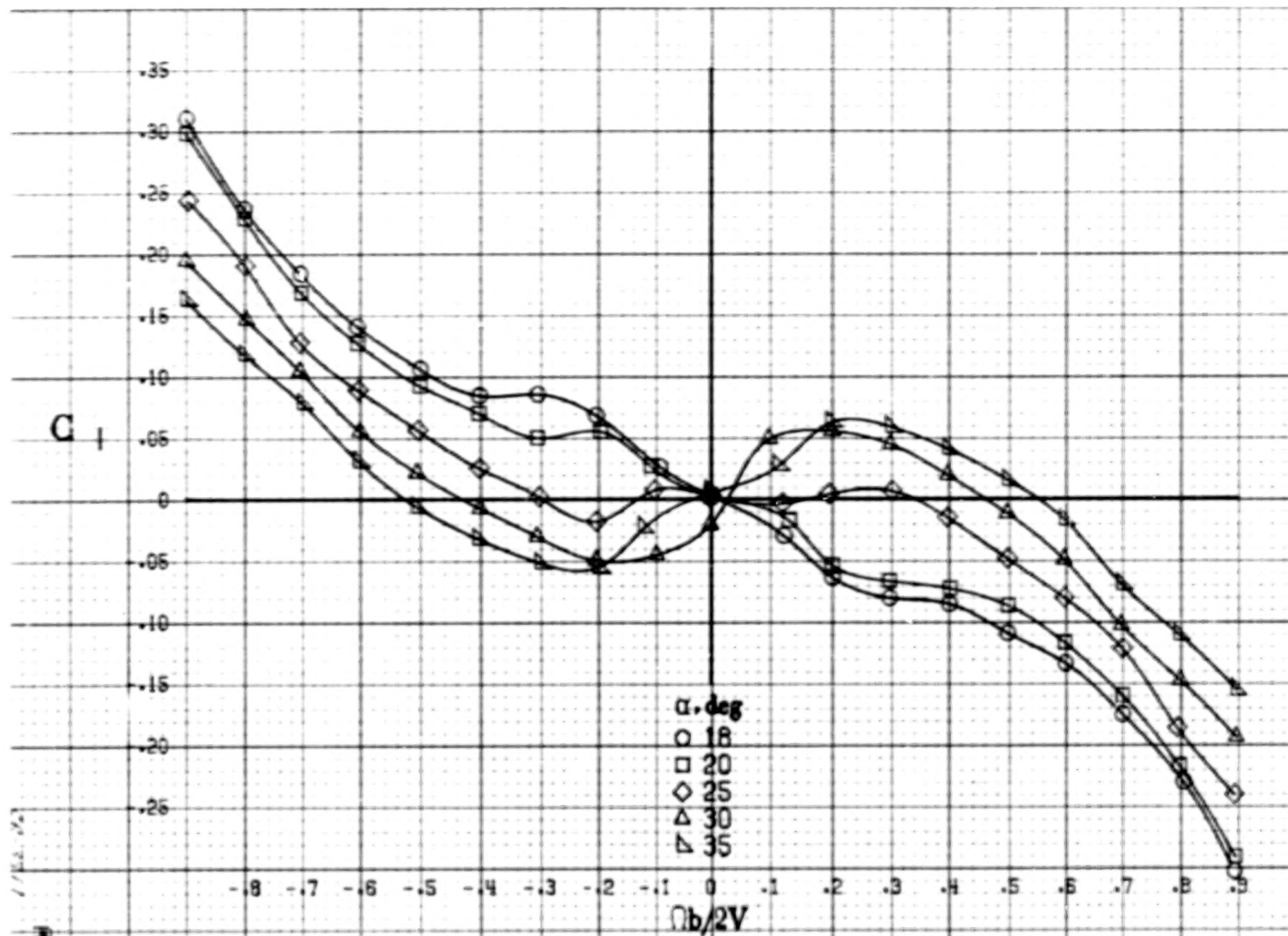
(b)  $\alpha = 18$  to  $35$  deg,  $SR = 152.4$  cm (60 in).  
Figure A61.-Concluded.



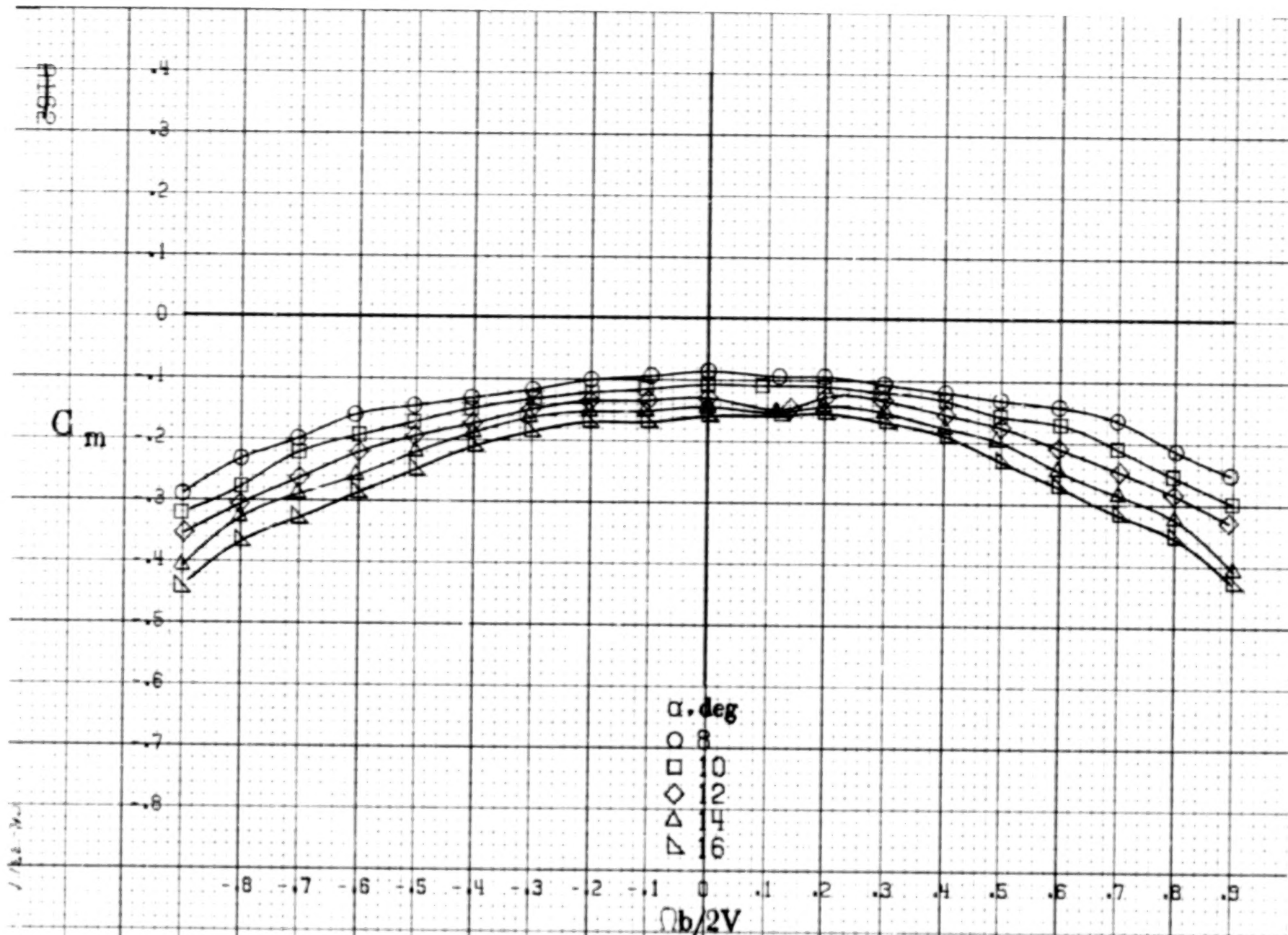
(a)  $\alpha = 8$  to  $16$  deg,  $SR = 152.4$  cm (60 in).

Figure A62. Effect of rotation rate and angle of attack on rolling-moment coefficient for full-span wing slat configuration.  $\delta_e = 0^\circ$ ,  $\delta_a = 0^\circ$ ,  $\delta_r = 0^\circ$ .  $\beta = 0^\circ$ .



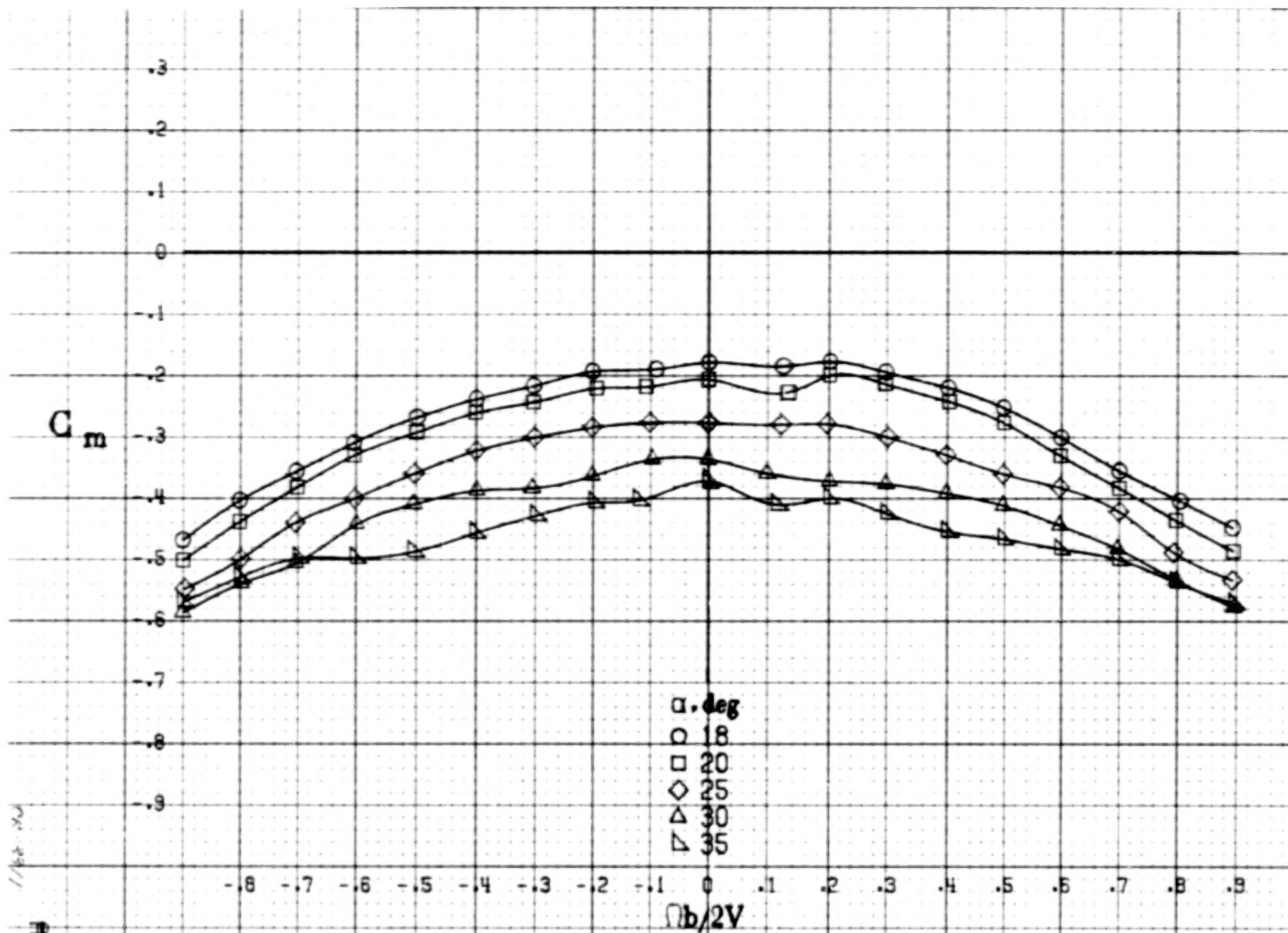


(b)  $\alpha = 18$  to  $35^\circ$ ,  $SR = 152.4\text{cm (60in.)}$ .  
Figure A62.-Concluded.

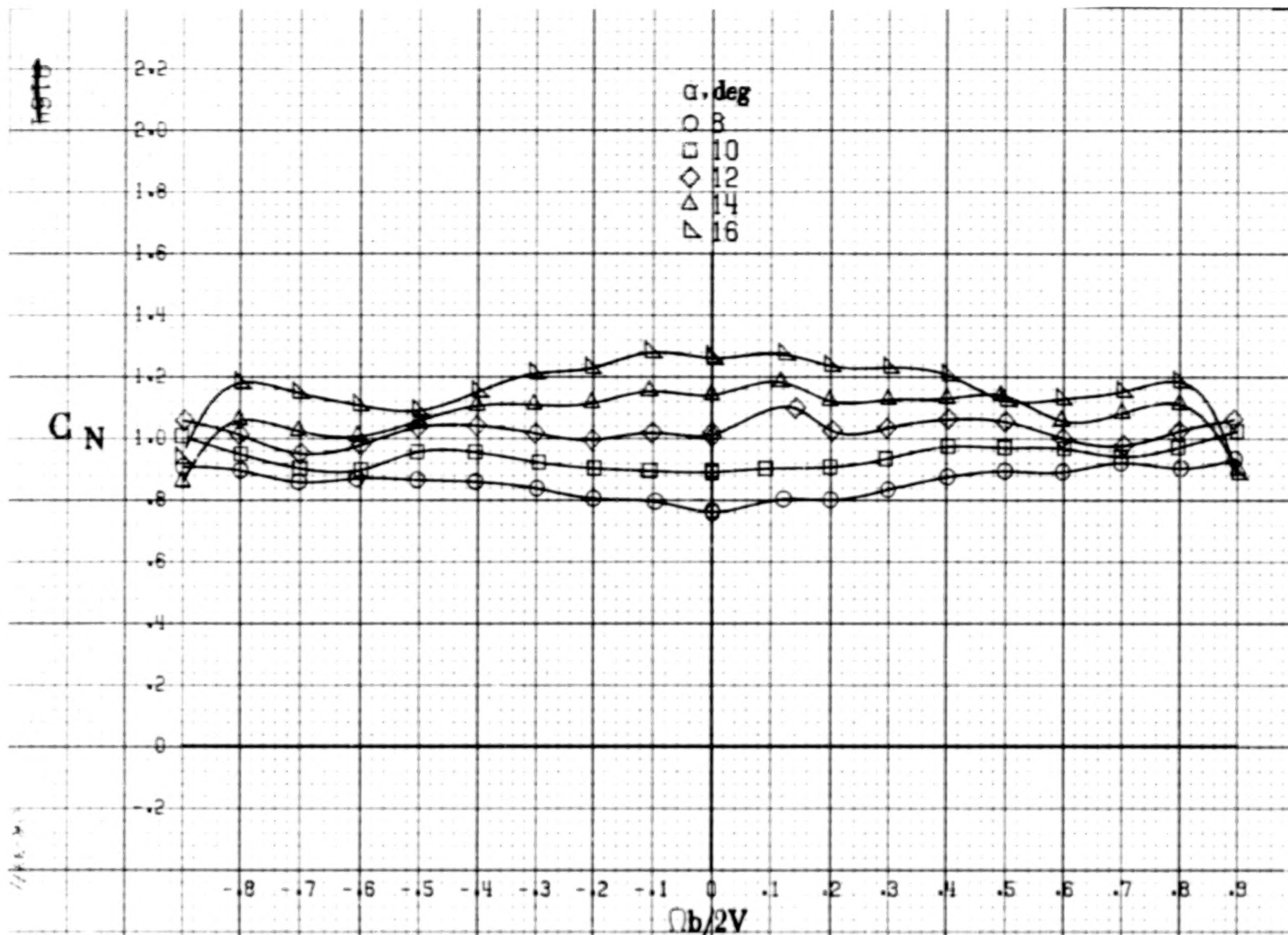


(a)  $\alpha = 8$  to  $16$  deg,  $SR = 152.4$  cm (60 in).

Figure A68. Effect of rotation rate and angle of attack on pitching-moment coefficient for full-span wing slat configuration.  $\delta_e = 0^\circ$ ,  $\delta_a = 0^\circ$ ,  $\delta_r = 0^\circ$ ,  $\beta = 0^\circ$ .



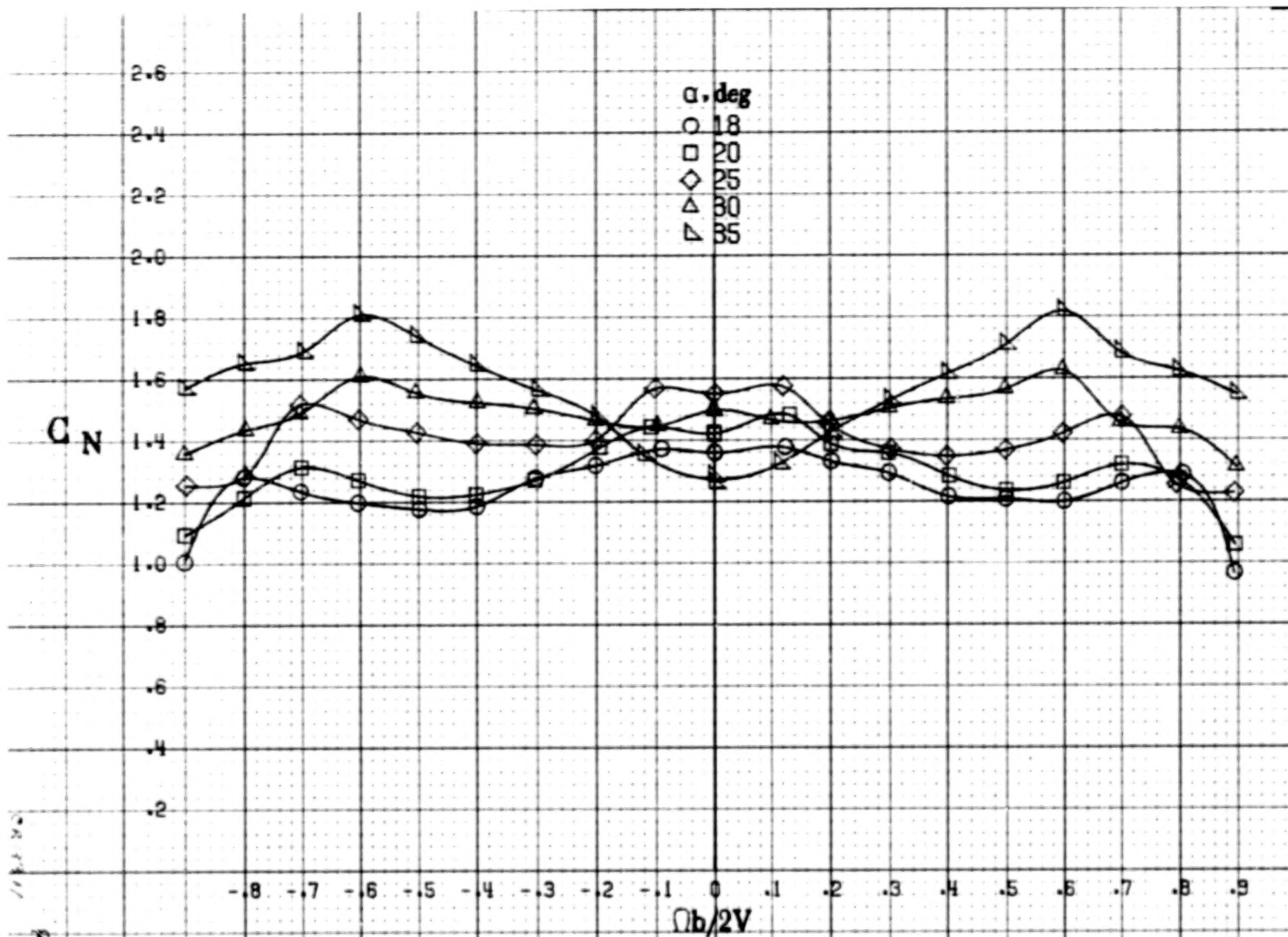
(b)  $\alpha = 18$  to  $35$  deg,  $SR = 152.4$  cm (60 in).  
Figure A63.-Concluded.



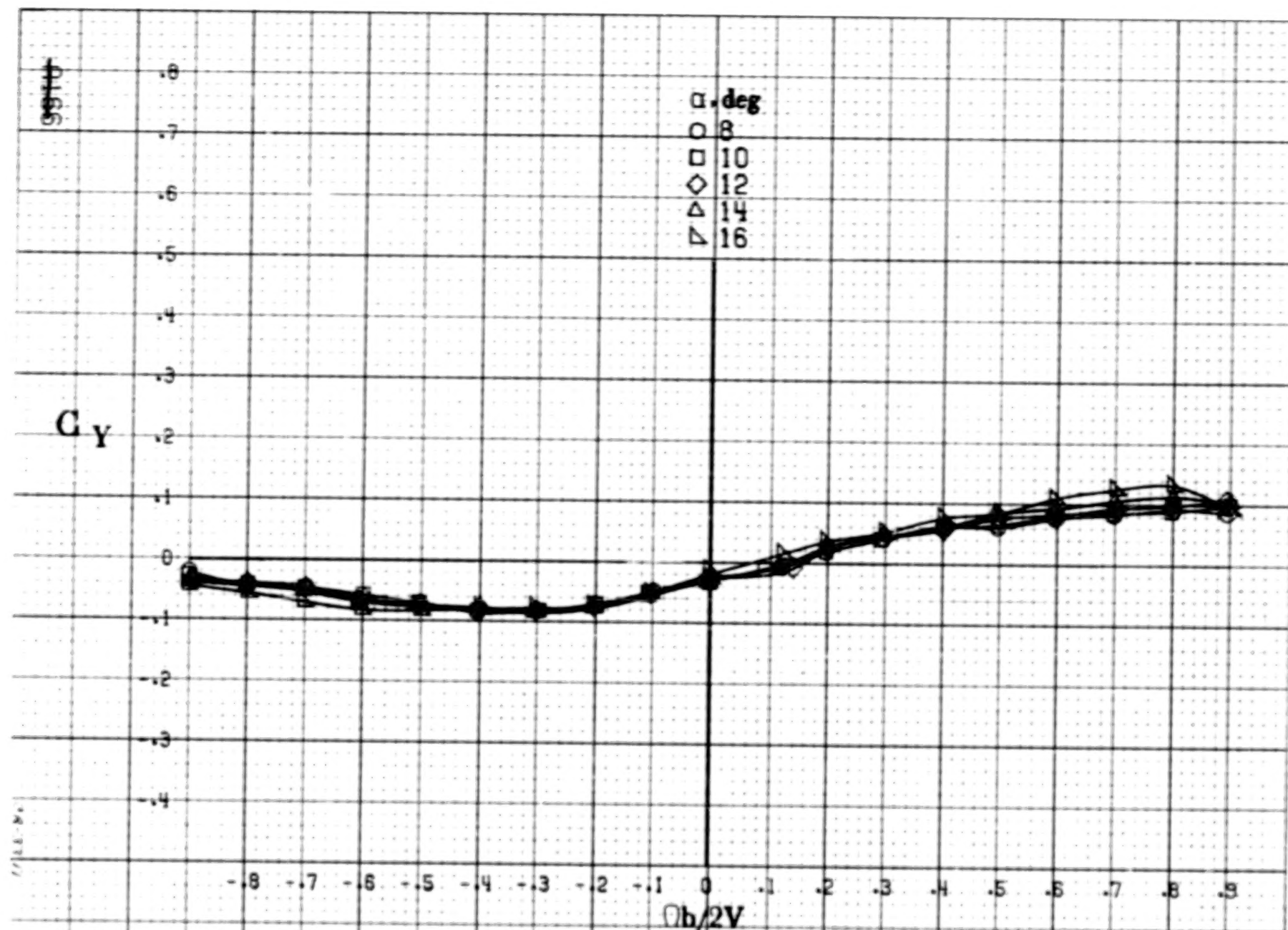
(a)  $\alpha = 8$  to  $16$  deg,  $SR = 152.4$  cm (60 in).

Figure A64. Effect of rotation rate and angle of attack on normal-force coefficient for full-span wing slat configuration.  $\delta_e = 0^\circ$ ,  $\delta_a = 0^\circ$ ,  $\delta_r = 0^\circ$ .  $\beta = 0^\circ$ .



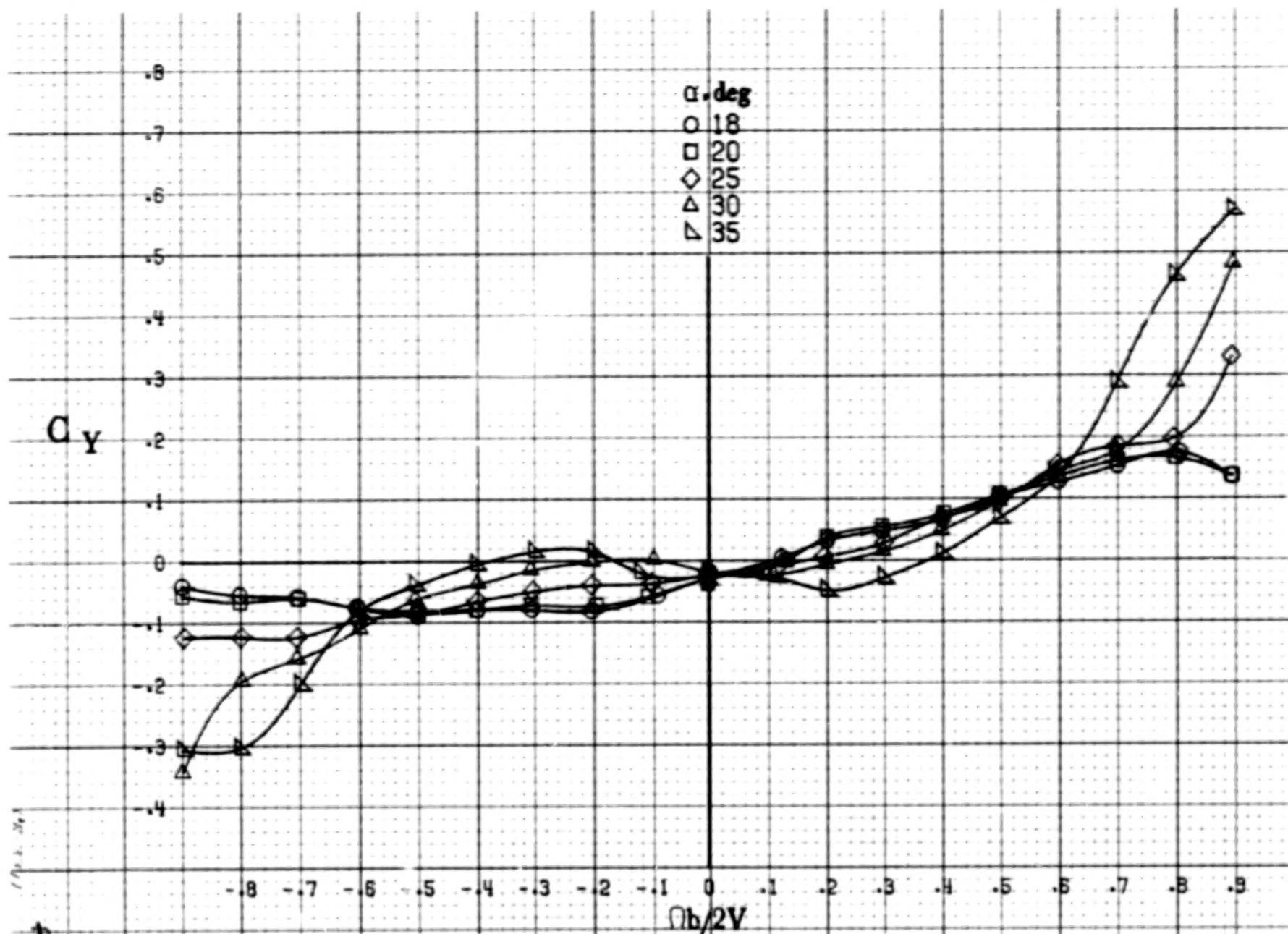


(b)  $\alpha = 18$  to  $35$  deg,  $SR = 152.4$  cm (60 in).  
Figure A64.-Concluded.

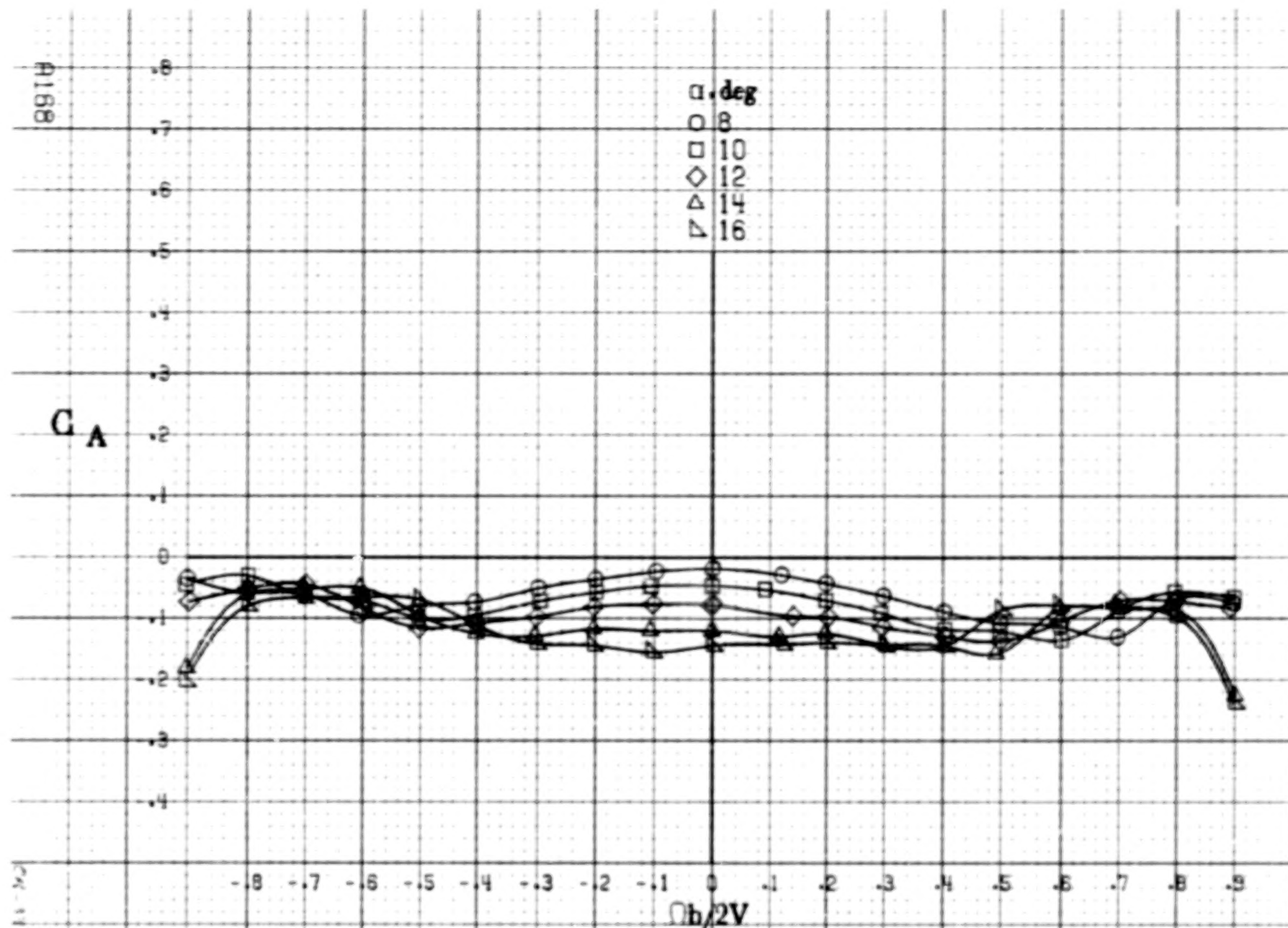


(a)  $\alpha = 8$  to  $16^\circ$ ,  $SR = 152.4\text{cm (60in)}$ .

Figure A65. Effect of rotation rate and angle of attack on side-force coefficient for full-span wing slat configuration.  $\delta_e = 0^\circ$ ,  $\delta_a = 0^\circ$ ,  $\delta_r = 0^\circ$ .  $\beta = 0^\circ$ .



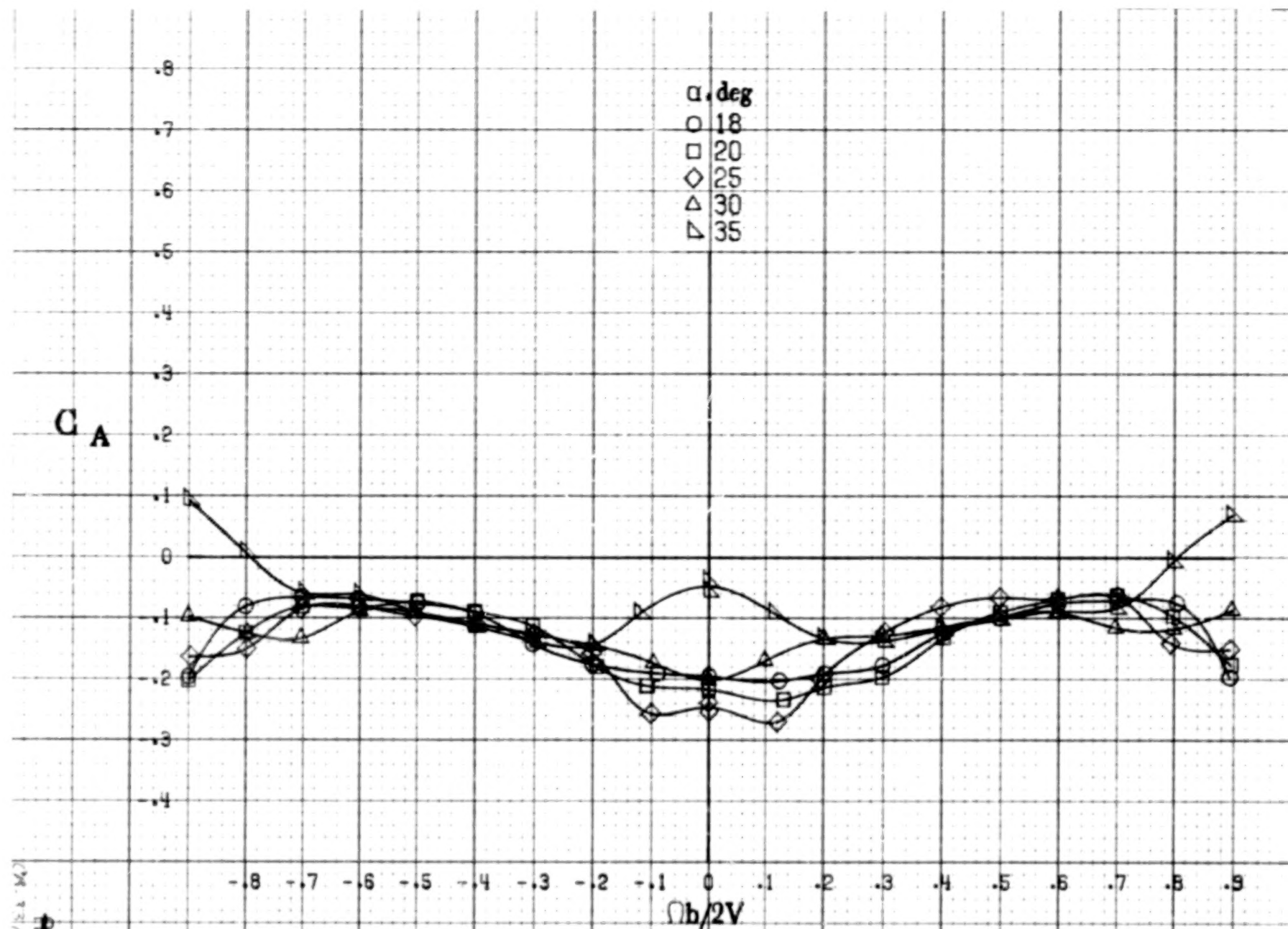
(b)  $\alpha = 18$  to  $35^\circ$ ,  $SR = 152.4\text{ cm (60 in.)}$ .  
Figure A65.-Concluded.



(a)  $\alpha = 8$  to  $16$  deg,  $SR = 152.4$  cm (60 in).

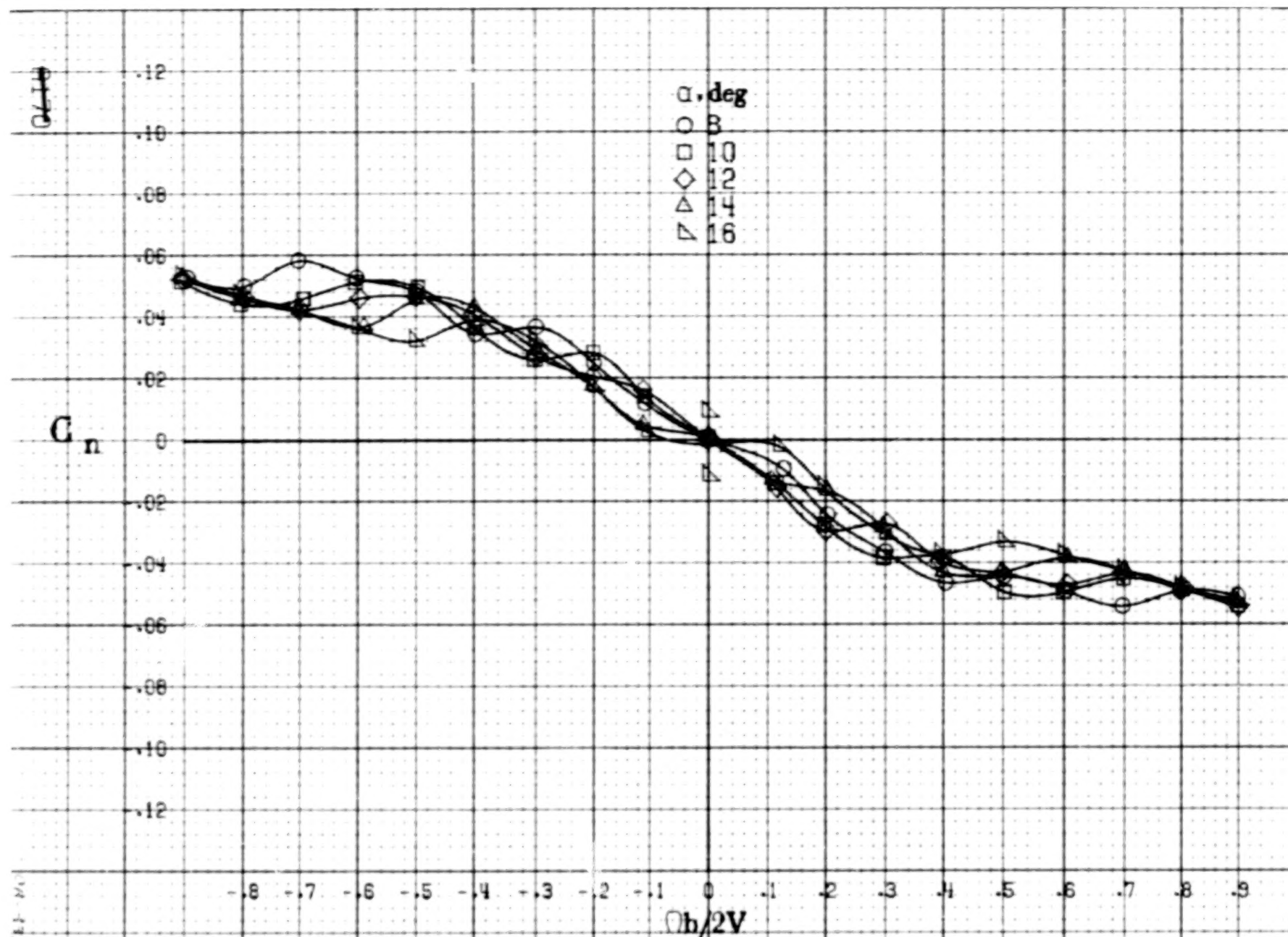
Figure A66. Effect of rotation rate and angle of attack on axial-force coefficient for full-span wing slat configuration.  $\delta_s = 0^\circ$ ,  $\delta_a = 0^\circ$ ,  $\delta_r = 0^\circ$ .  $\beta = 0^\circ$ .



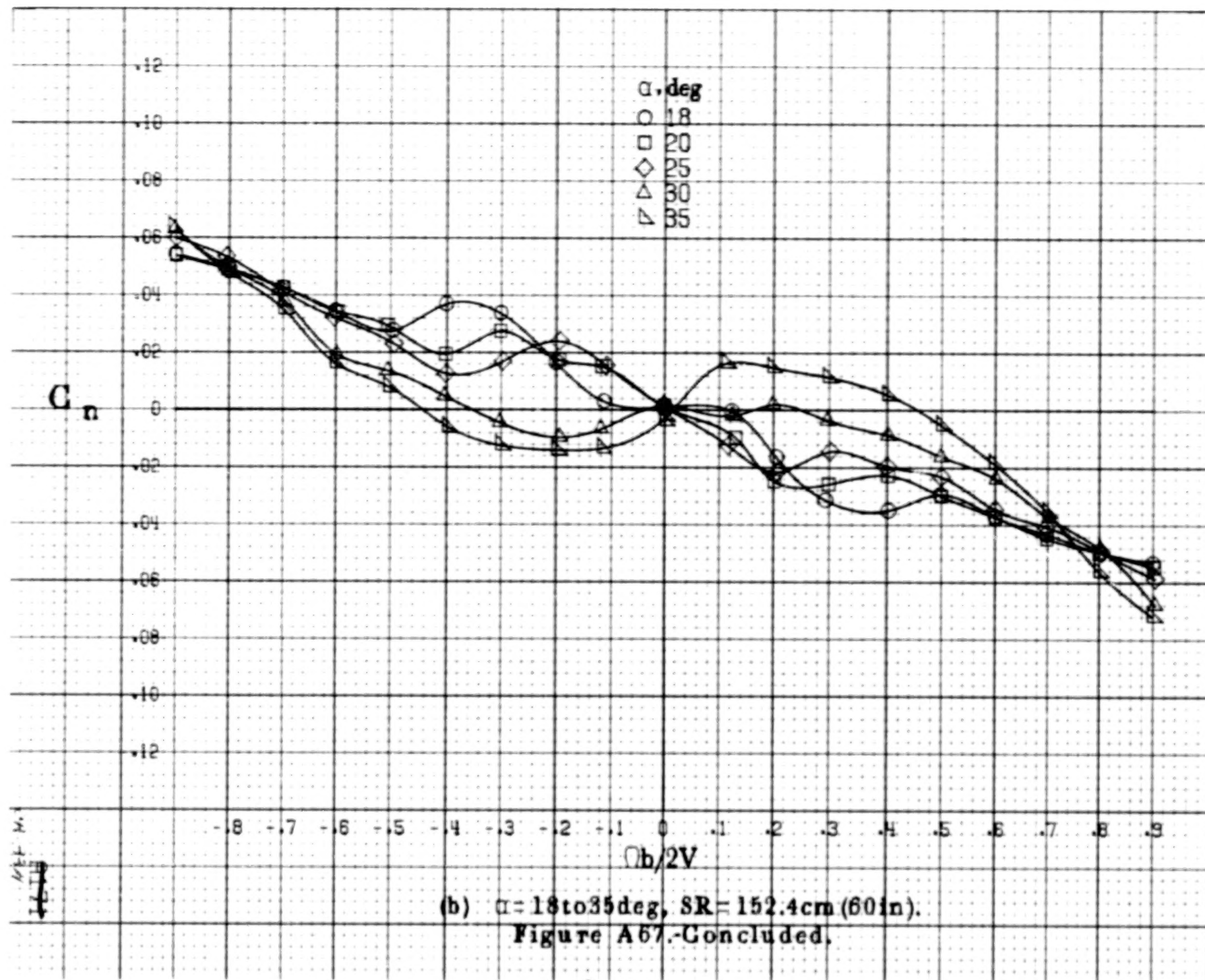


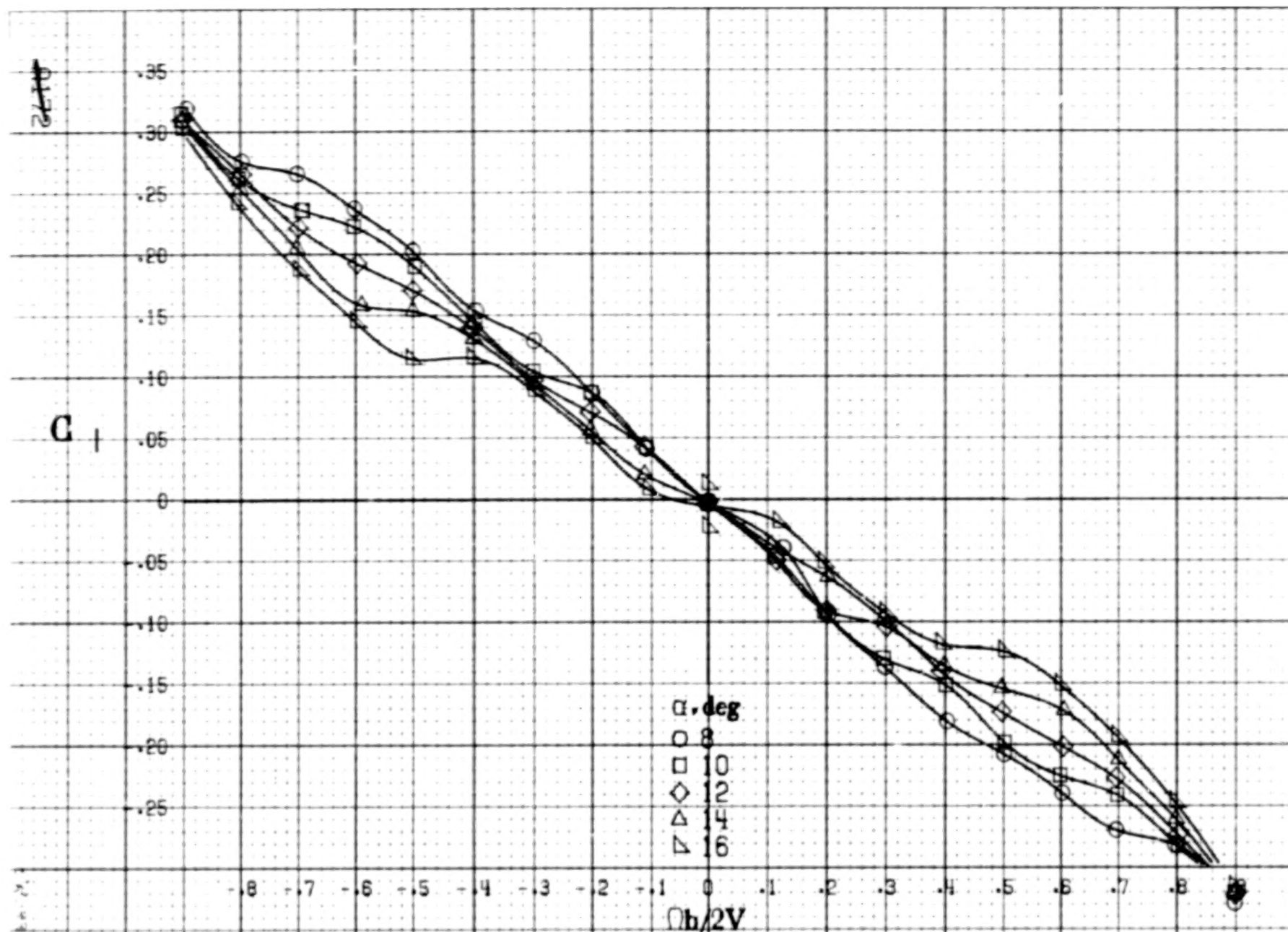
(b)  $\alpha = 18$  to  $25$  deg,  $SR = 152.4$  cm (60 in).  
Figure A66.-Concluded.

A169



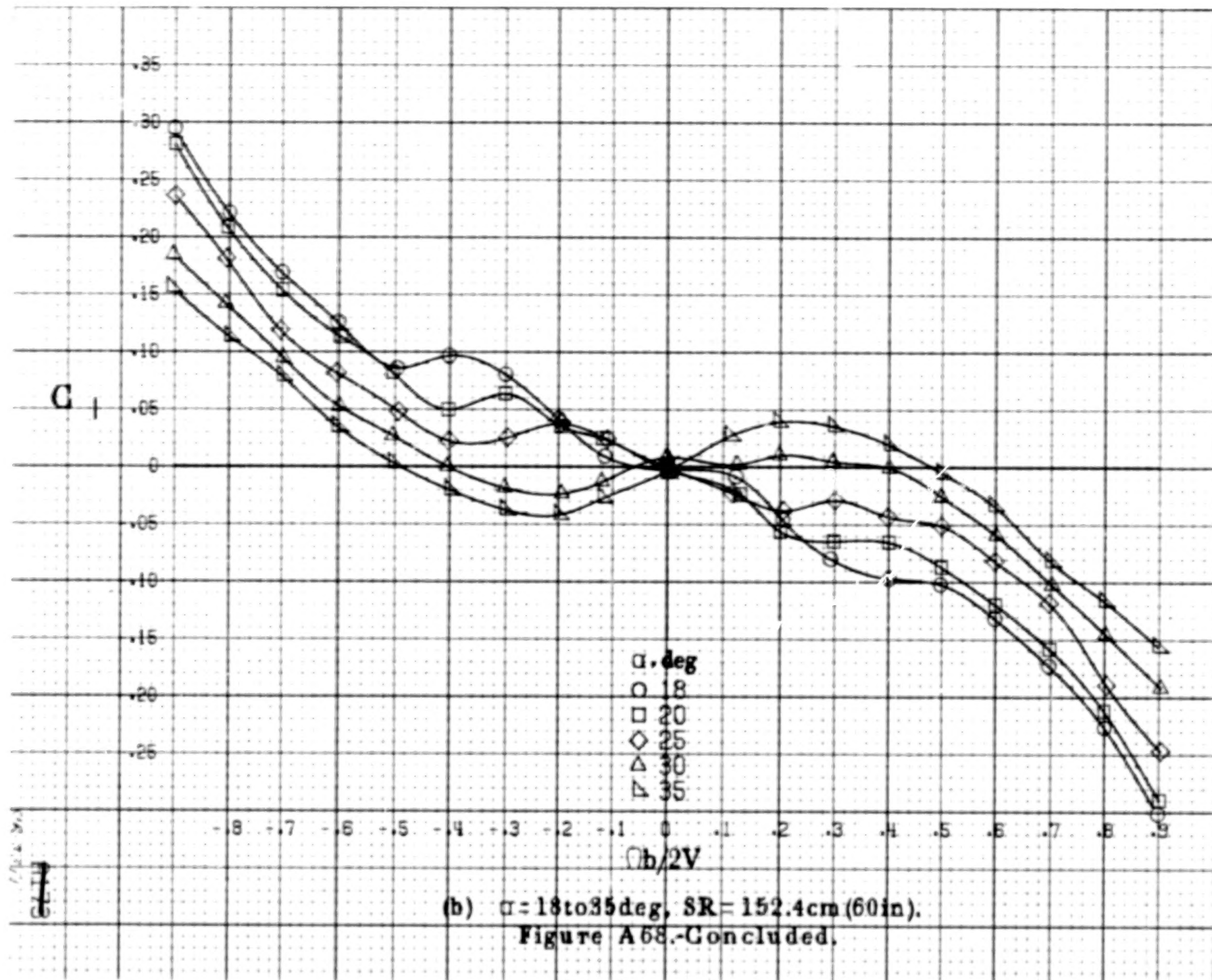
(a)  $\alpha = 8$  to  $16^\circ$ ,  $SR = 152.4 \text{ cm (60 in.)}$ .  
 Figure A67. Effect of rotation rate and angle of attack on yawing-moment coefficient for segmented wing slat configuration.  $\delta_e = 0^\circ$ ,  $\delta_a = 0^\circ$ ,  $\delta_r = 0^\circ$ .  
 $\beta = 0^\circ$ .

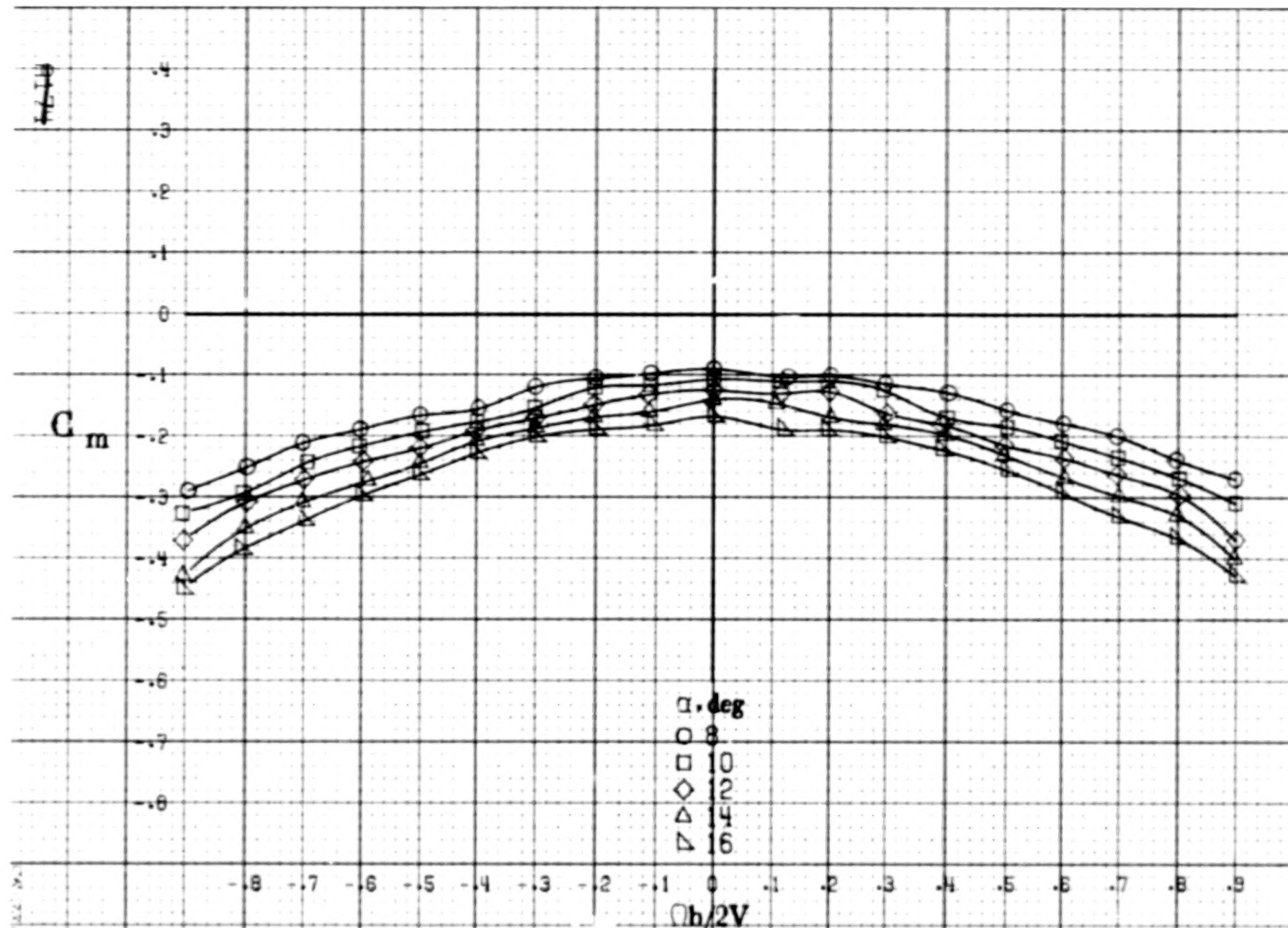




(a)  $\alpha = 8$  to  $16$  deg,  $SR = 152.4$  cm (60 in).  
 Figure A68.-Effect of rotation rate and angle of attack on rolling-moment coefficient for segmented wing slat configuration.  $\delta_s = 0^\circ$ ,  $\delta_a = 0^\circ$ ,  $\delta_r = 0^\circ$ .  
 $\beta = 0^\circ$ .

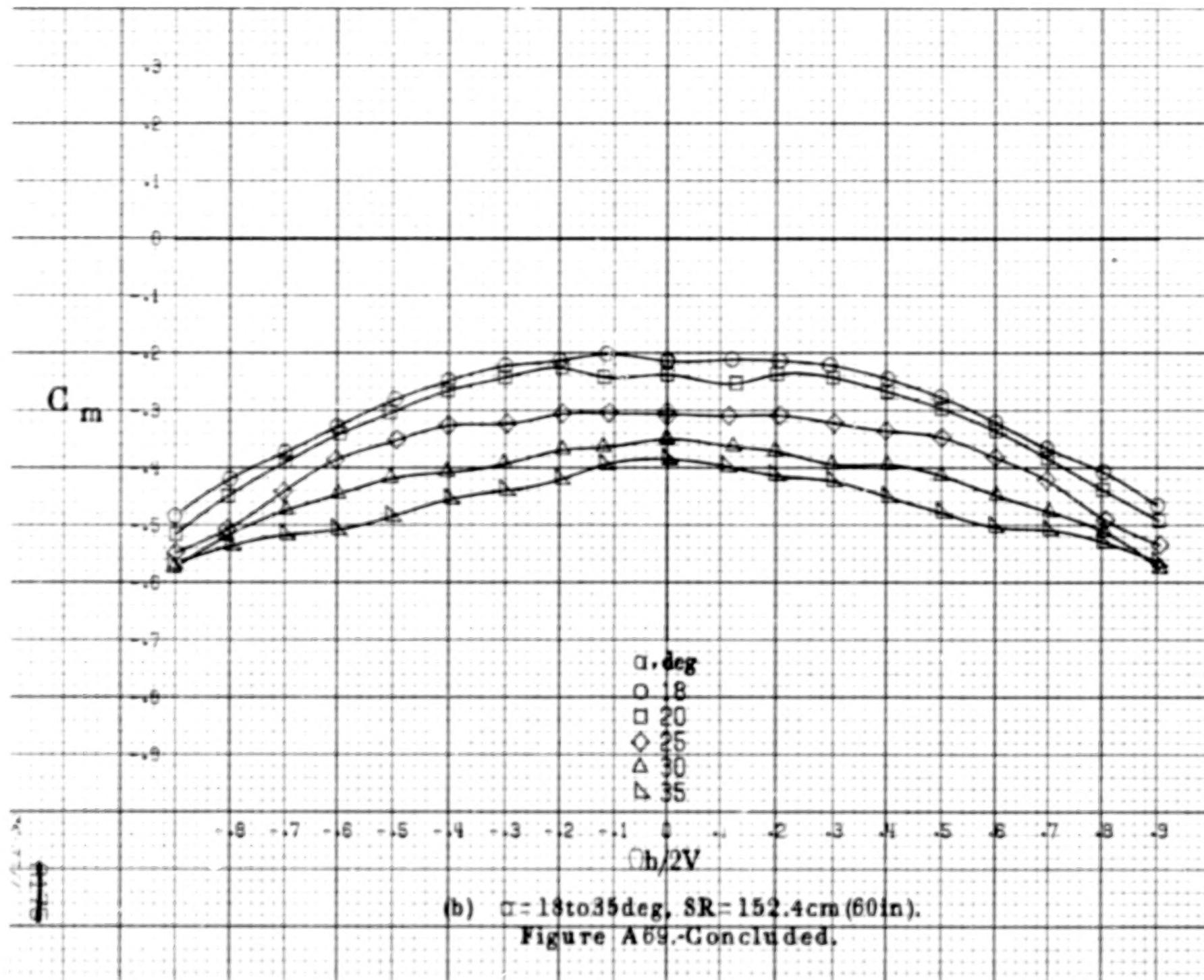


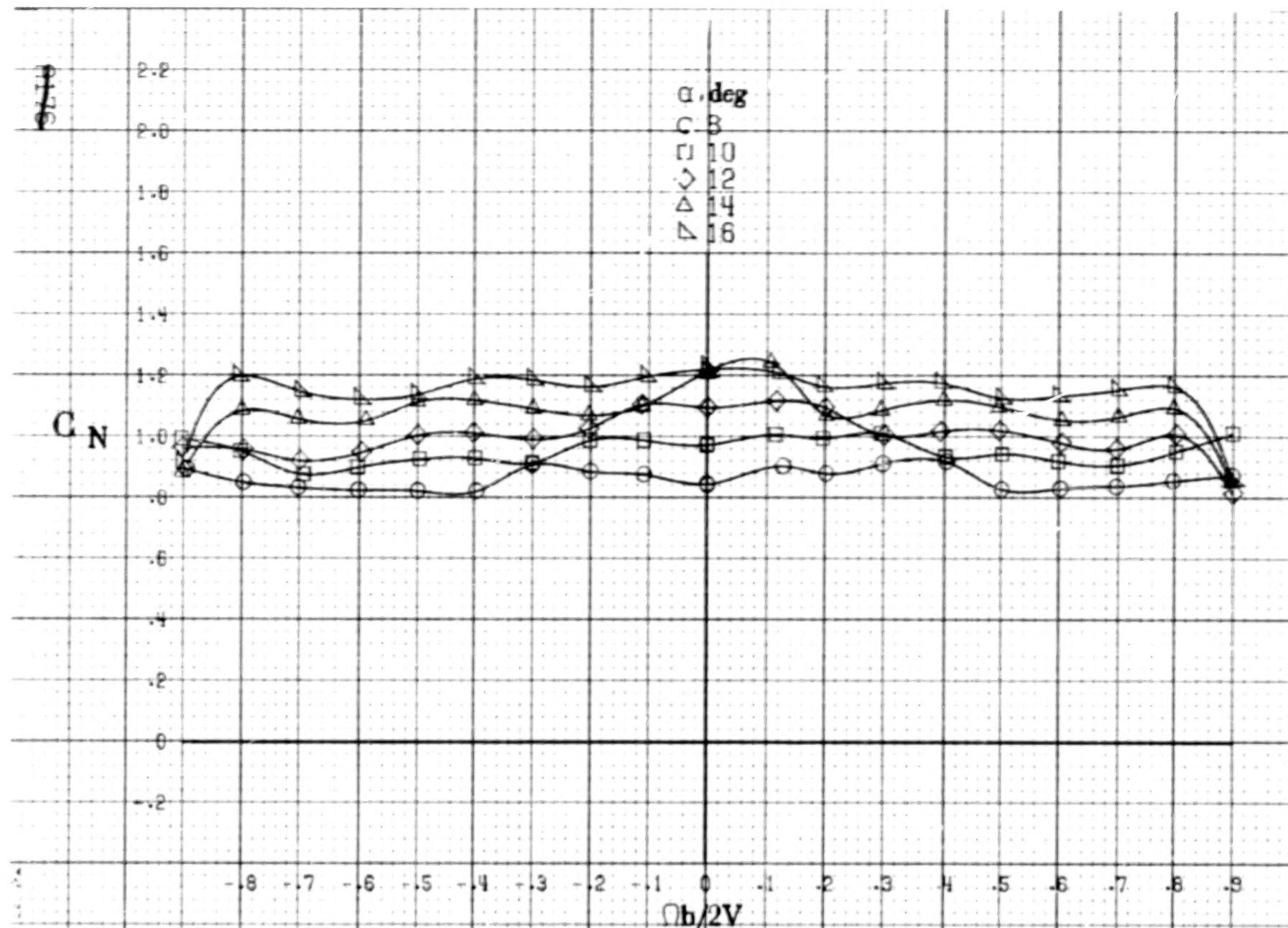




(a)  $\alpha = 8, 16^\circ$ ,  $SR = 152.4\text{cm (60in)}$ .

Figure A69-Effect of rotation rate and angle of attack on pitching-moment coefficient for segmented wing slat configuration.  $\delta_e = 0^\circ$ ,  $\delta_a = 0^\circ$ ,  $\delta_r = 0^\circ$ ,  $\theta = 0^\circ$ .

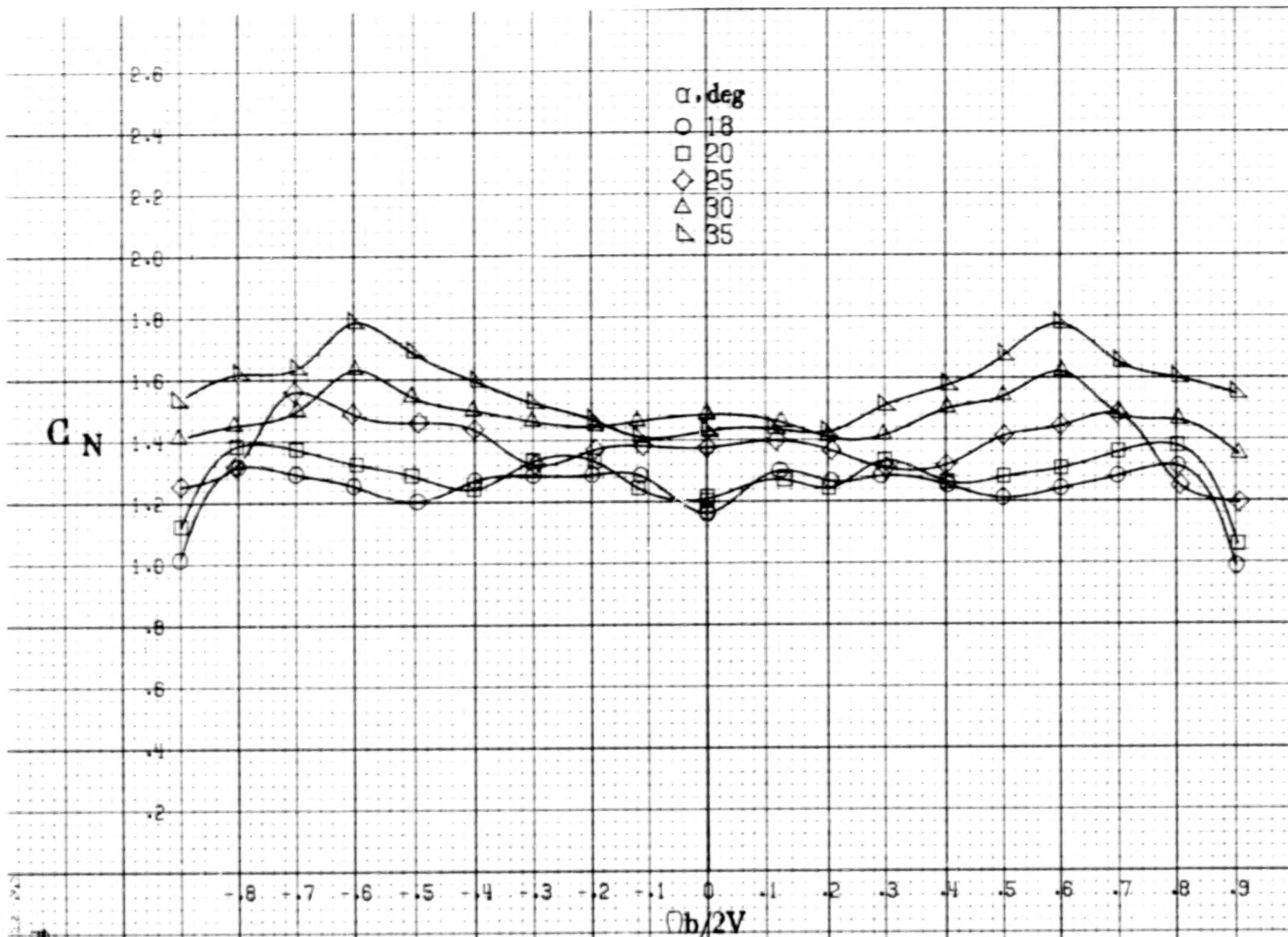




(a)  $\alpha = 8$  to  $16$  deg,  $SR = 152.4$  cm (60 in).

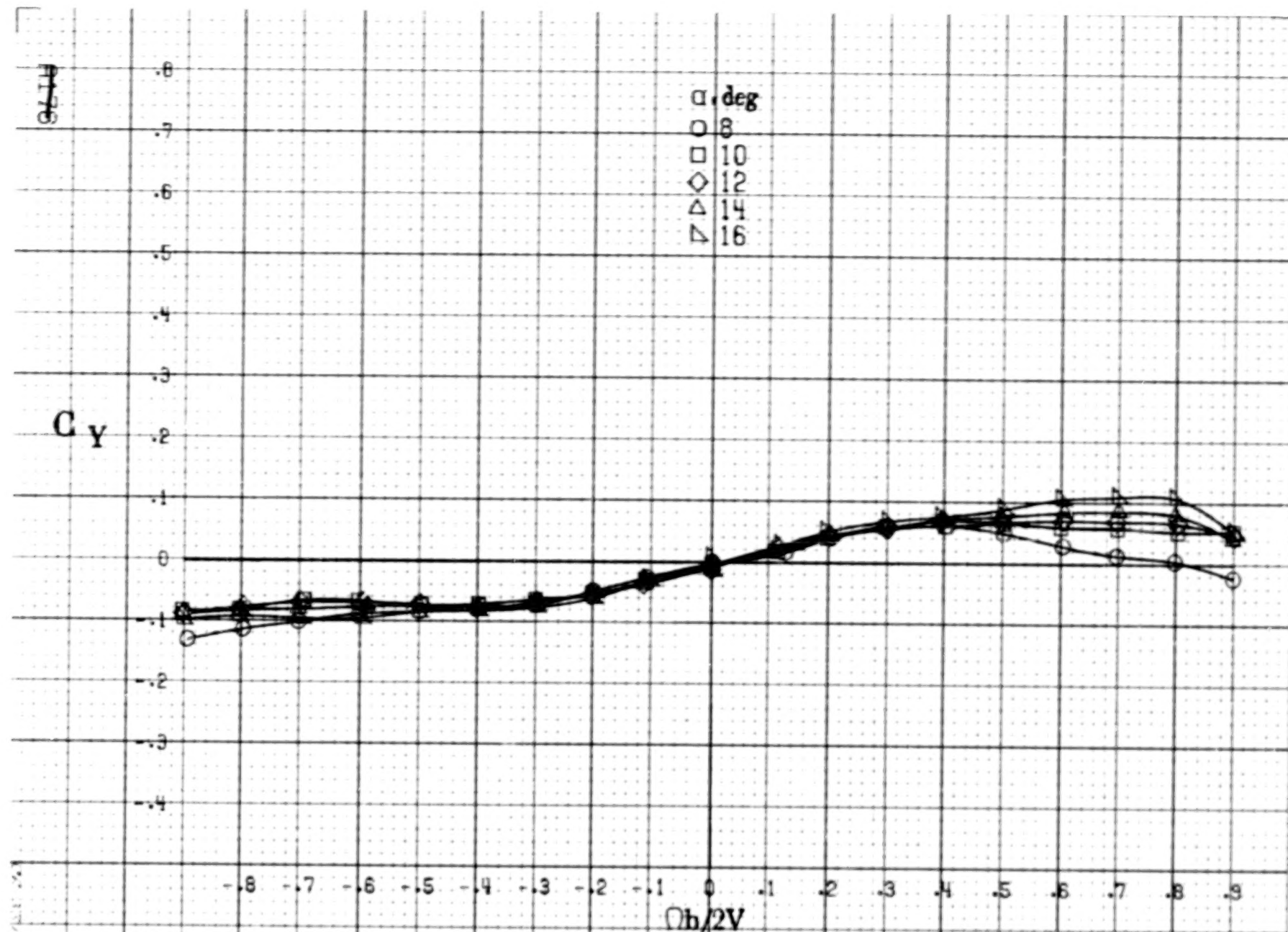
Figure A70.-Effect of rotation rate and angle of attack on normal-force coefficient for segmented wing slat configuration.  $\delta_e = 0^\circ$ ,  $\delta_a = 0^\circ$ ,  $\delta_r = 0^\circ$ ,  $\beta = 0^\circ$ .



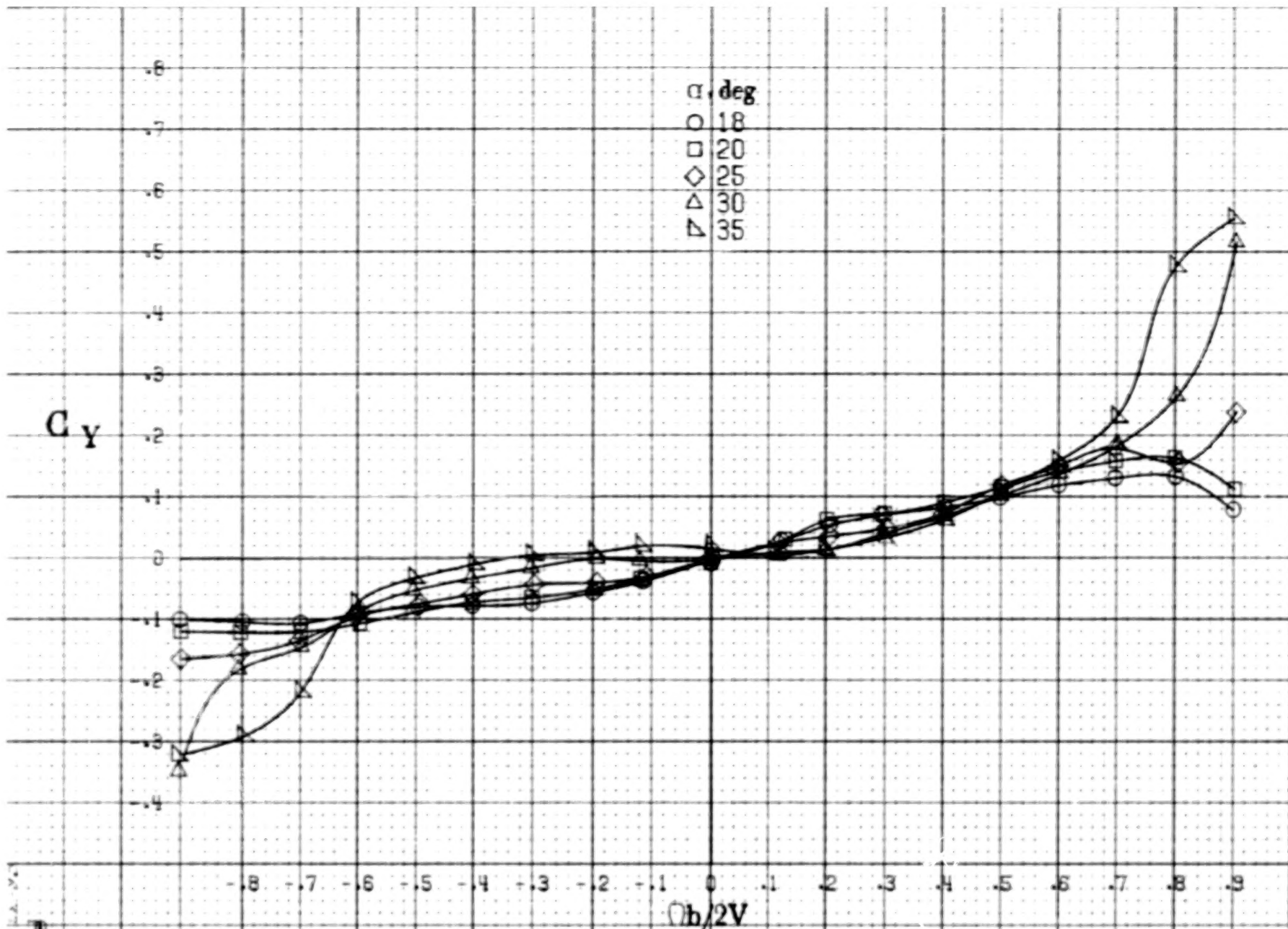


(b)  $\alpha = 18$  to  $35$  deg,  $SR = 152.4$  cm (60 in).

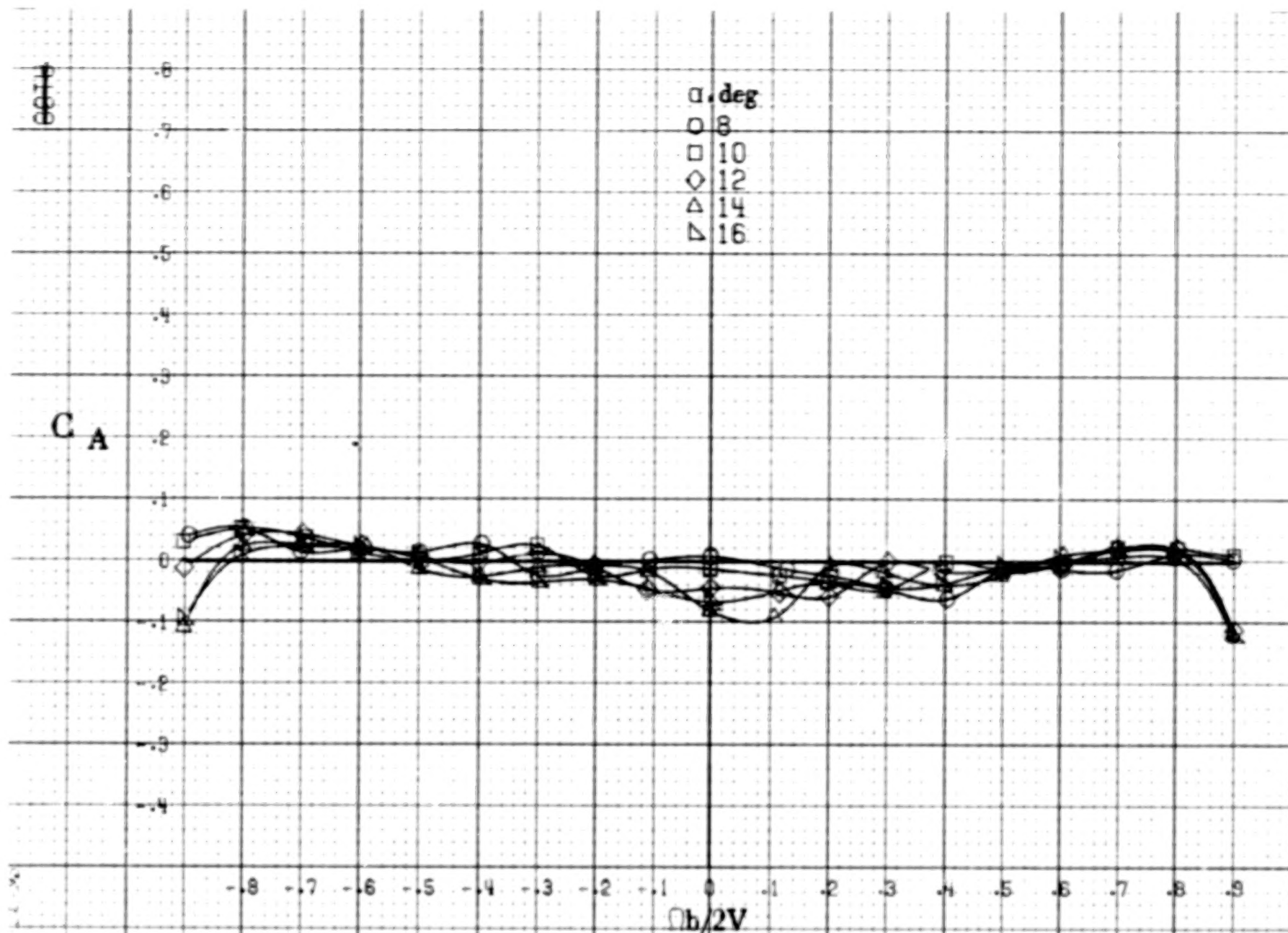
Figure A70.-Concluded.



(a)  $\alpha = 8$  to  $16^\circ$ ,  $SR = 152.4 \text{ cm (60 in.)}$ .  
 Figure A71. Effect of rotation rate and angle of attack on side-force coefficient for segmented wing slat configuration.  $\delta_e = 0^\circ$ ,  $\delta_a = 0^\circ$ ,  $\delta_r = 0^\circ$ .  
 $\beta = 0^\circ$ .

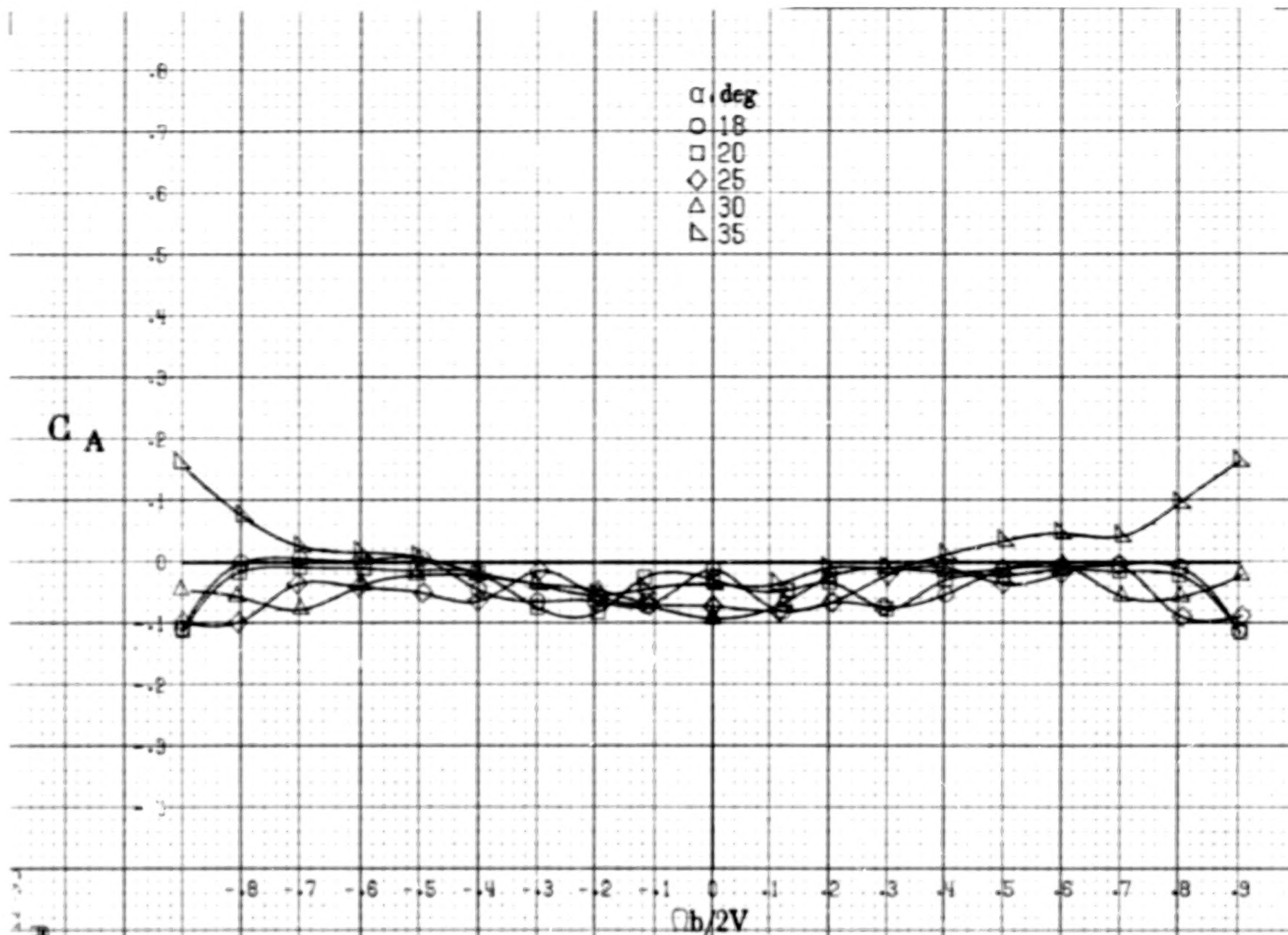


(b)  $\alpha = 18$  to  $35$  deg,  $SR = 152.4$  cm (60 in).  
Figure A71.-Concluded.

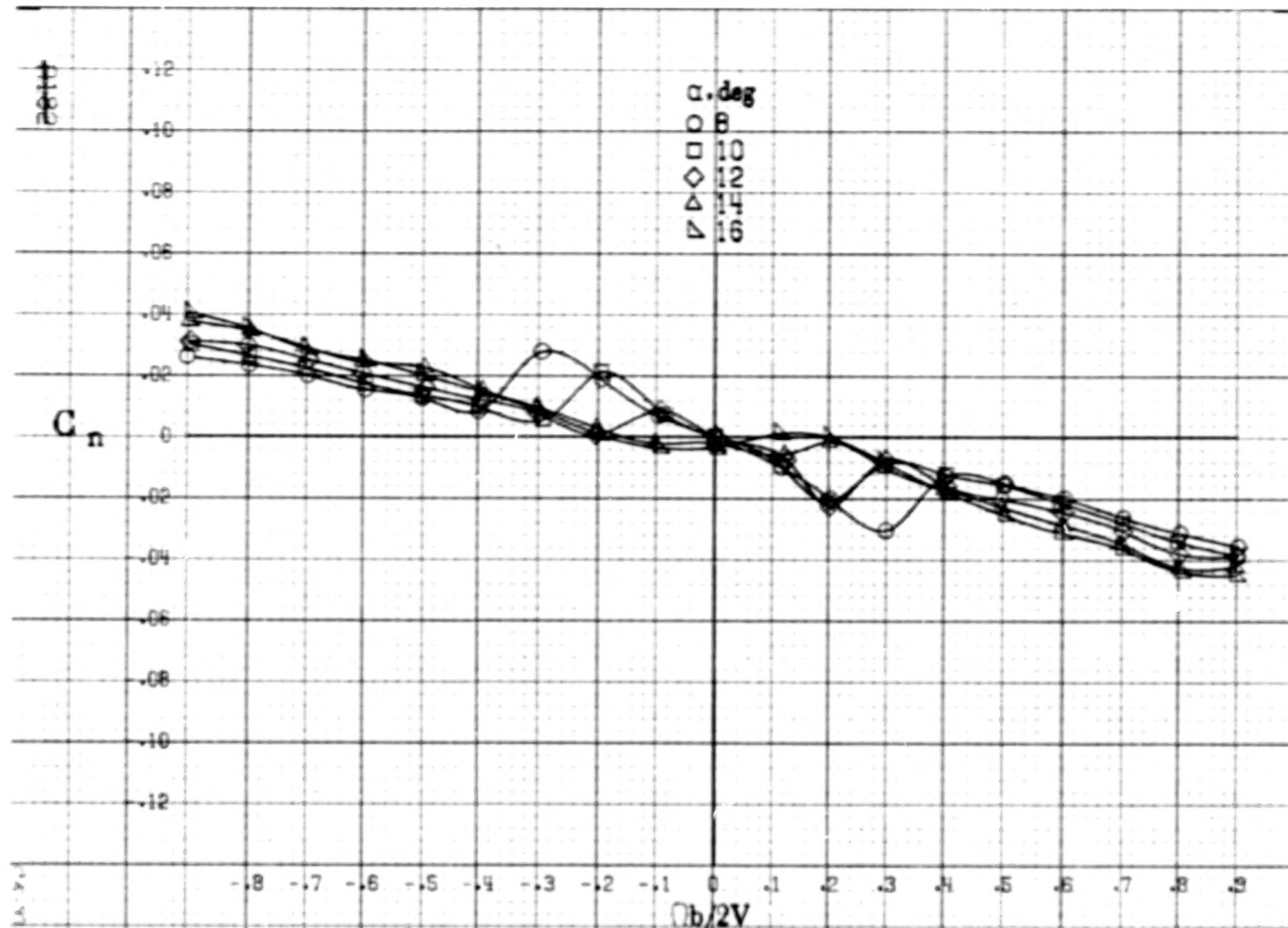


(a)  $\alpha = 8 \text{ to } 16 \text{ deg}$ ,  $SR = 152.4 \text{ cm (60 in)}$ .  
 Figure A72. Effect of rotation rate and angle of attack on axial-force coefficient for segmented wing slat configuration.  $\delta_e = 0^\circ$ ,  $\delta_a = 0^\circ$ ,  $\delta_r = 0^\circ$ ,  $b = 0^\circ$ .



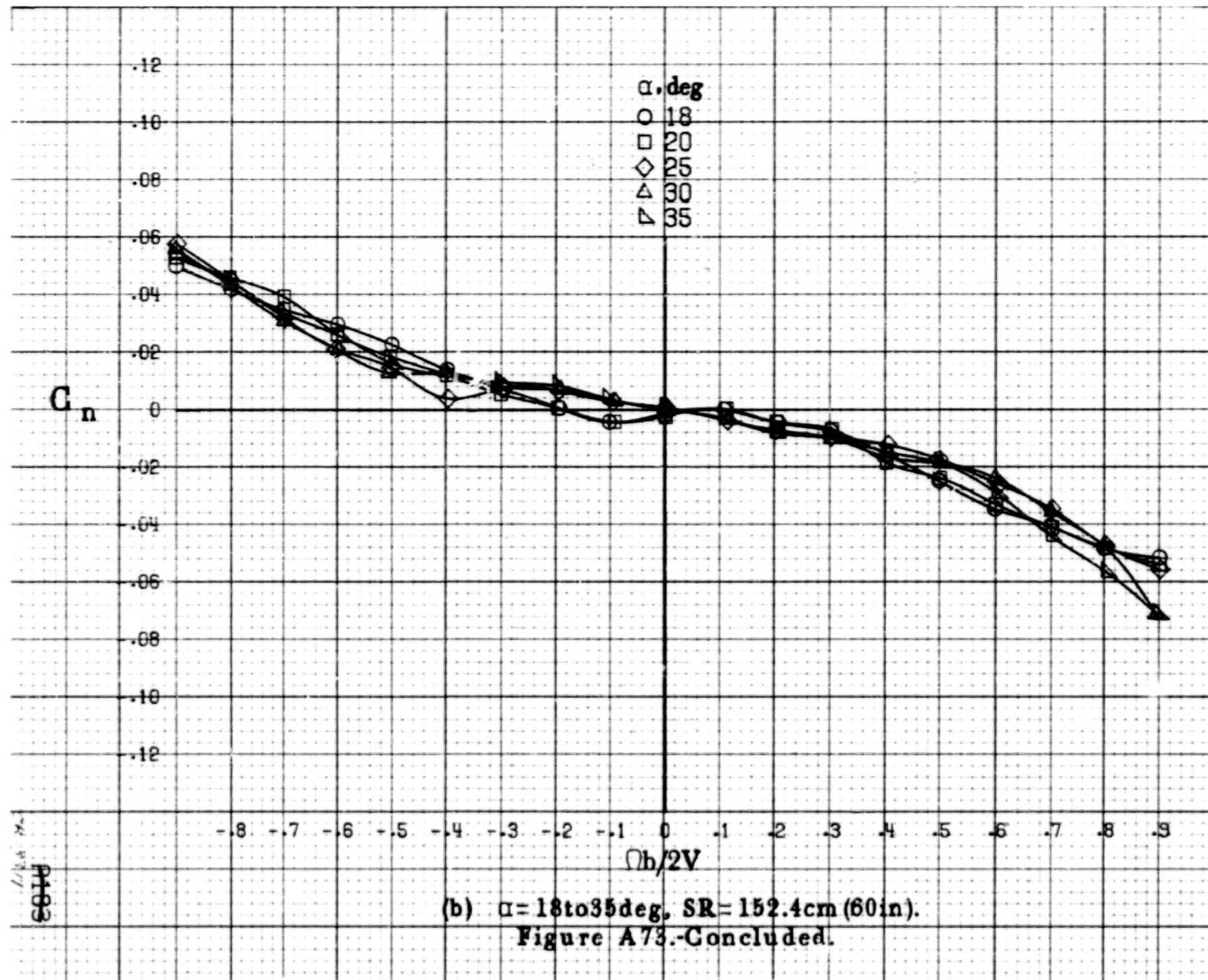


(b)  $\alpha = 18$  to  $35$  deg,  $SR = 152.4$  cm (60 in).  
Figure A72.-Concluded.

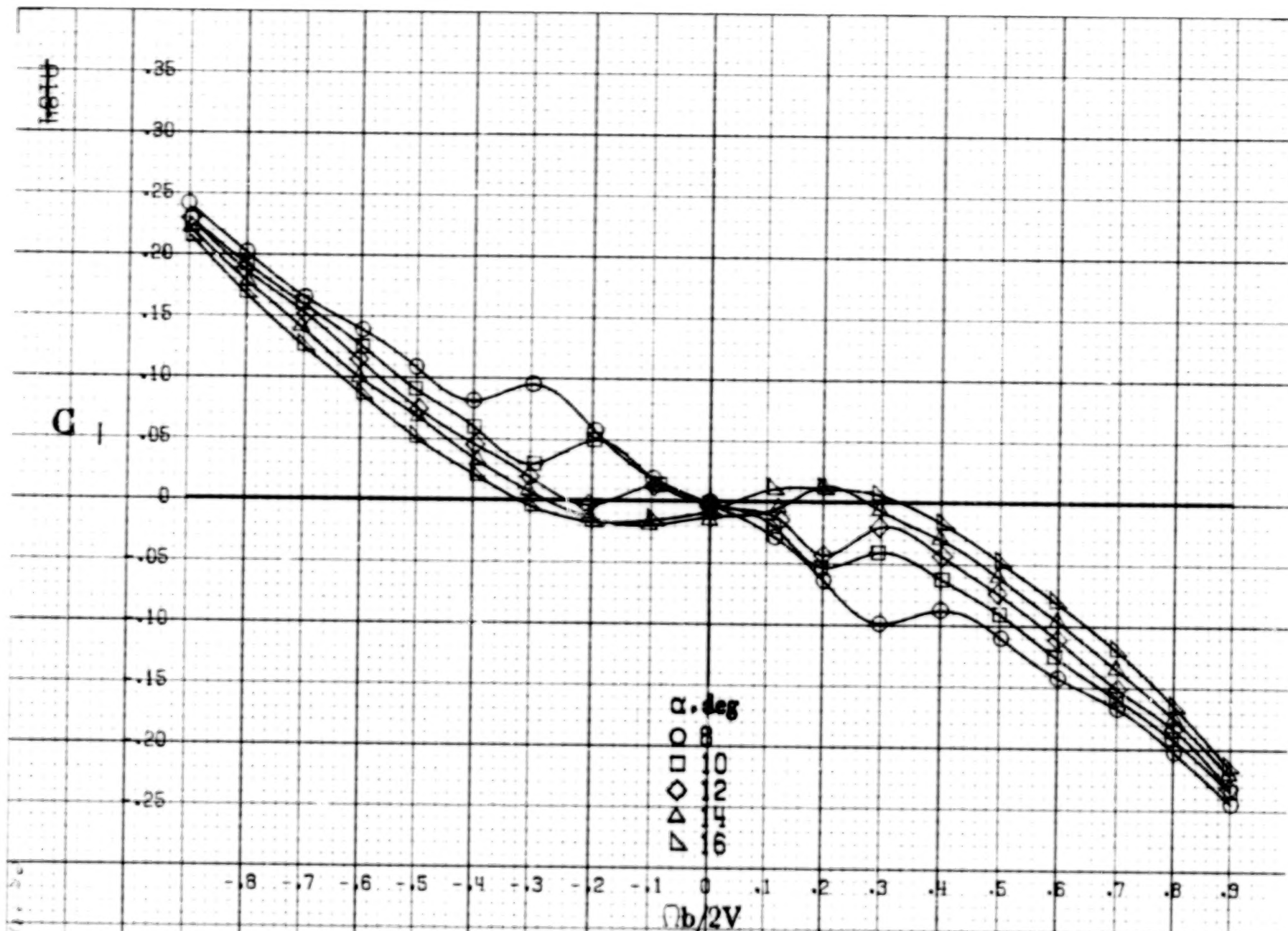


(a)  $\alpha = 8$  to  $16$  deg,  $SR = 152.4$  cm (60 in).

Figure A73. Effect of rotation rate and angle of attack on yawing-moment coefficient for winglet configuration.  $\delta_e = 0^\circ$ ,  $\delta_a = 0^\circ$ ,  $\delta_r = 0^\circ$ ,  $\beta = 0^\circ$ .



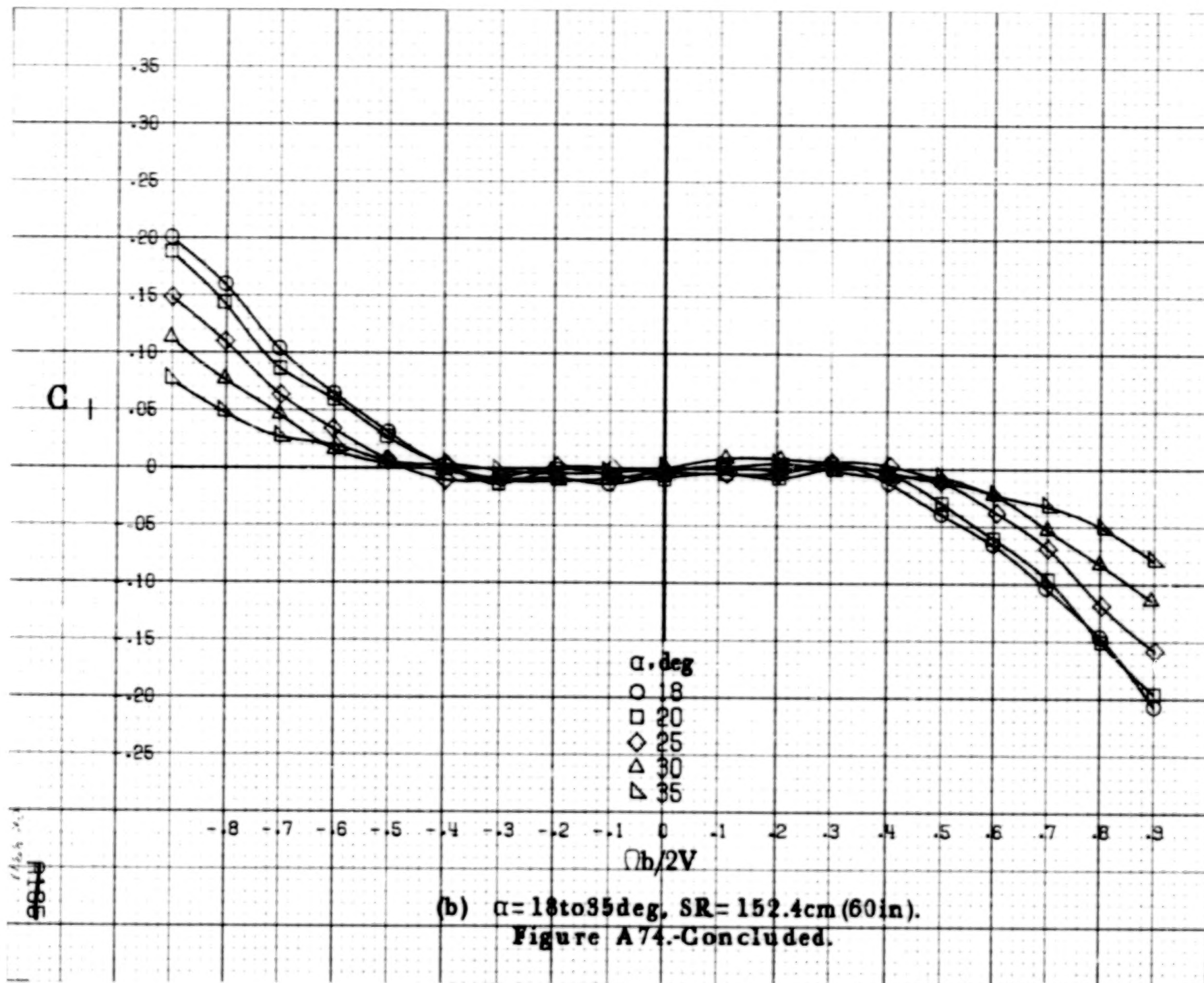
(b)  $\alpha = 18$  to  $35^\circ$ ,  $SR = 152.4\text{cm}$  (60 in).  
Figure A73.-Concluded.

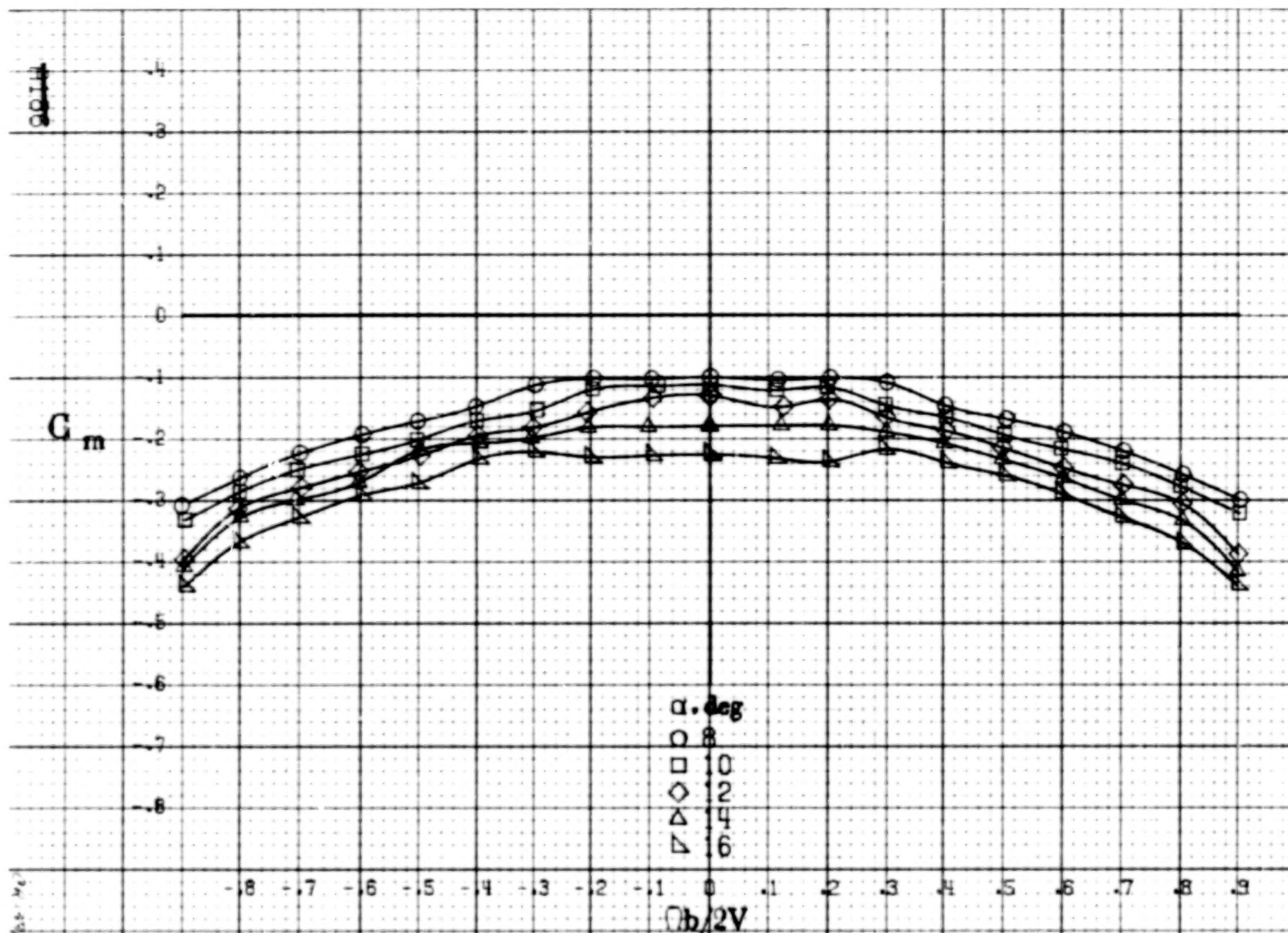


(a)  $\alpha = 8$  to  $16^\circ$ ,  $SR = 152.4 \text{ cm (60 in.)}$ .

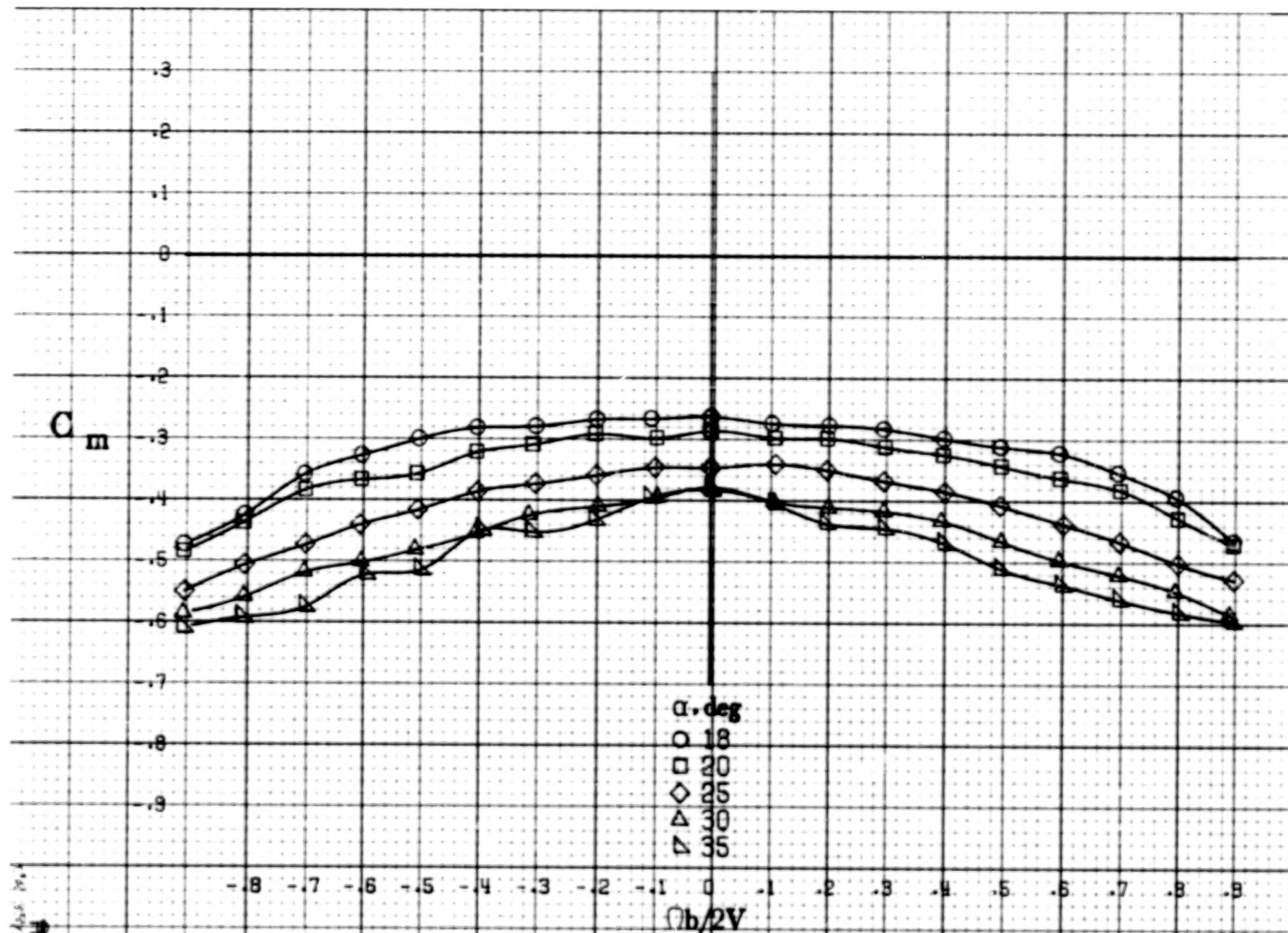
Figure A74.-Effect of rotation rate and angle of attack on rolling-moment coefficient for winglet configuration.  $\delta_s = 0^\circ$ ,  $\delta_a = 0^\circ$ ,  $\delta_r = 0^\circ$ ,  $\beta = 0^\circ$ .







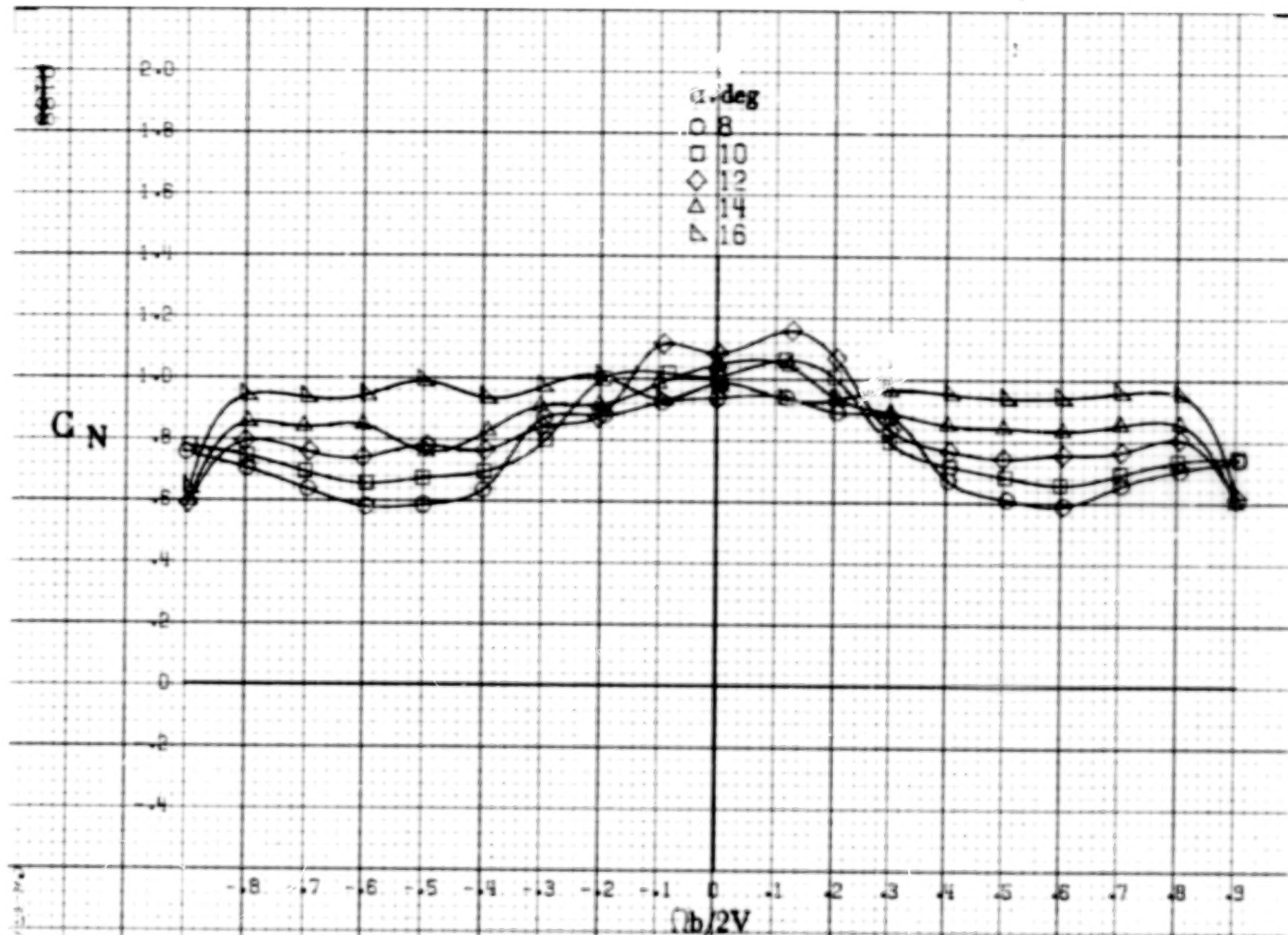
(a)  $\alpha = 8$  to  $16$  deg,  $SR = 152.4$  cm (60 in).  
 Figure A75. Effect of rotation rate and angle of attack on pitching-moment coefficient for winglet configuration.  $\delta_e = 0^\circ$ ,  $\delta_a = 0^\circ$ ,  $\delta_r = 0^\circ$ ,  $\beta = 0^\circ$ .



(b)  $\alpha = 18$  to  $35^\circ$ , SR = 152.4 cm (60 in.).

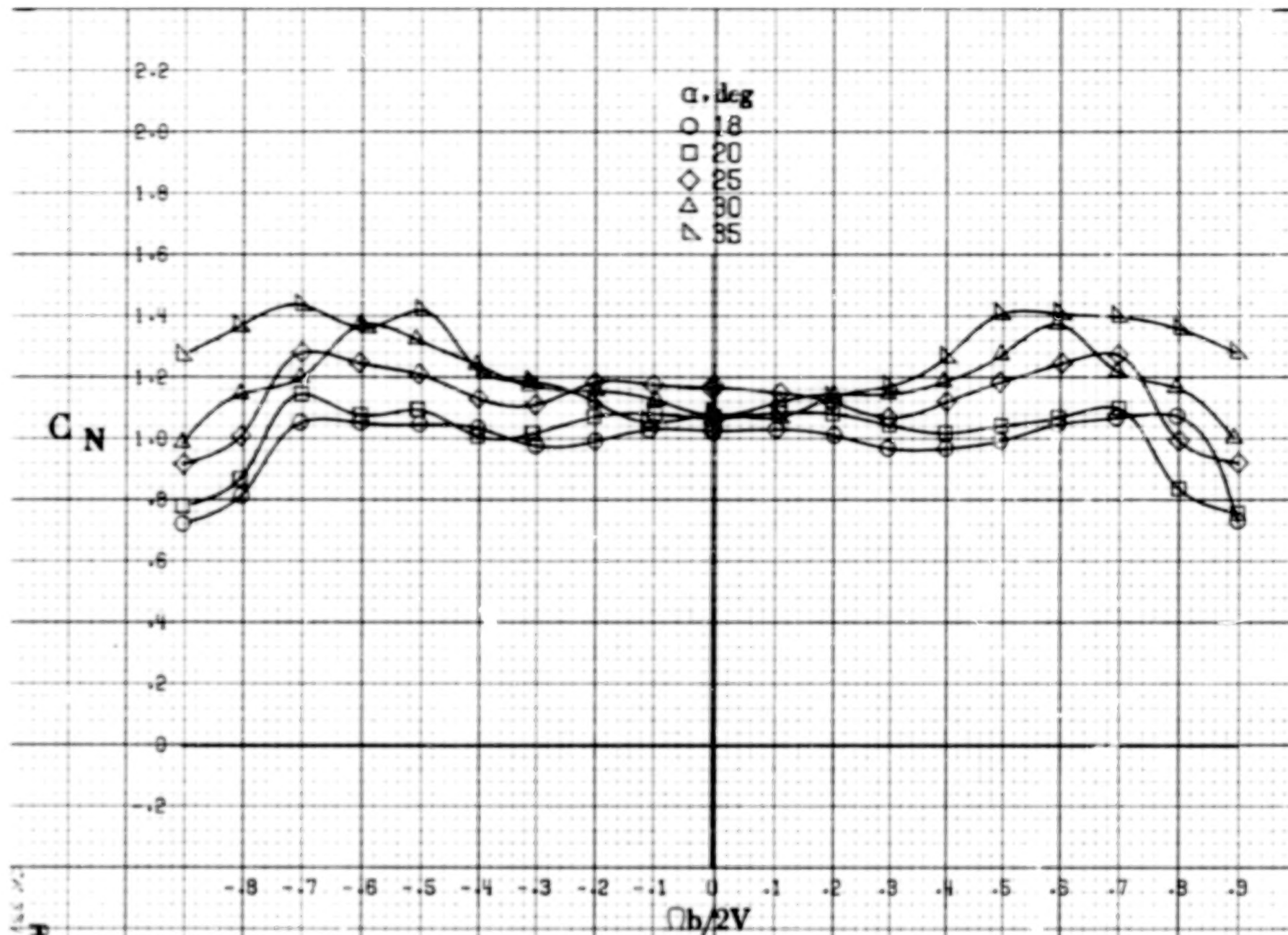
Figure A75.-Concluded.

A187



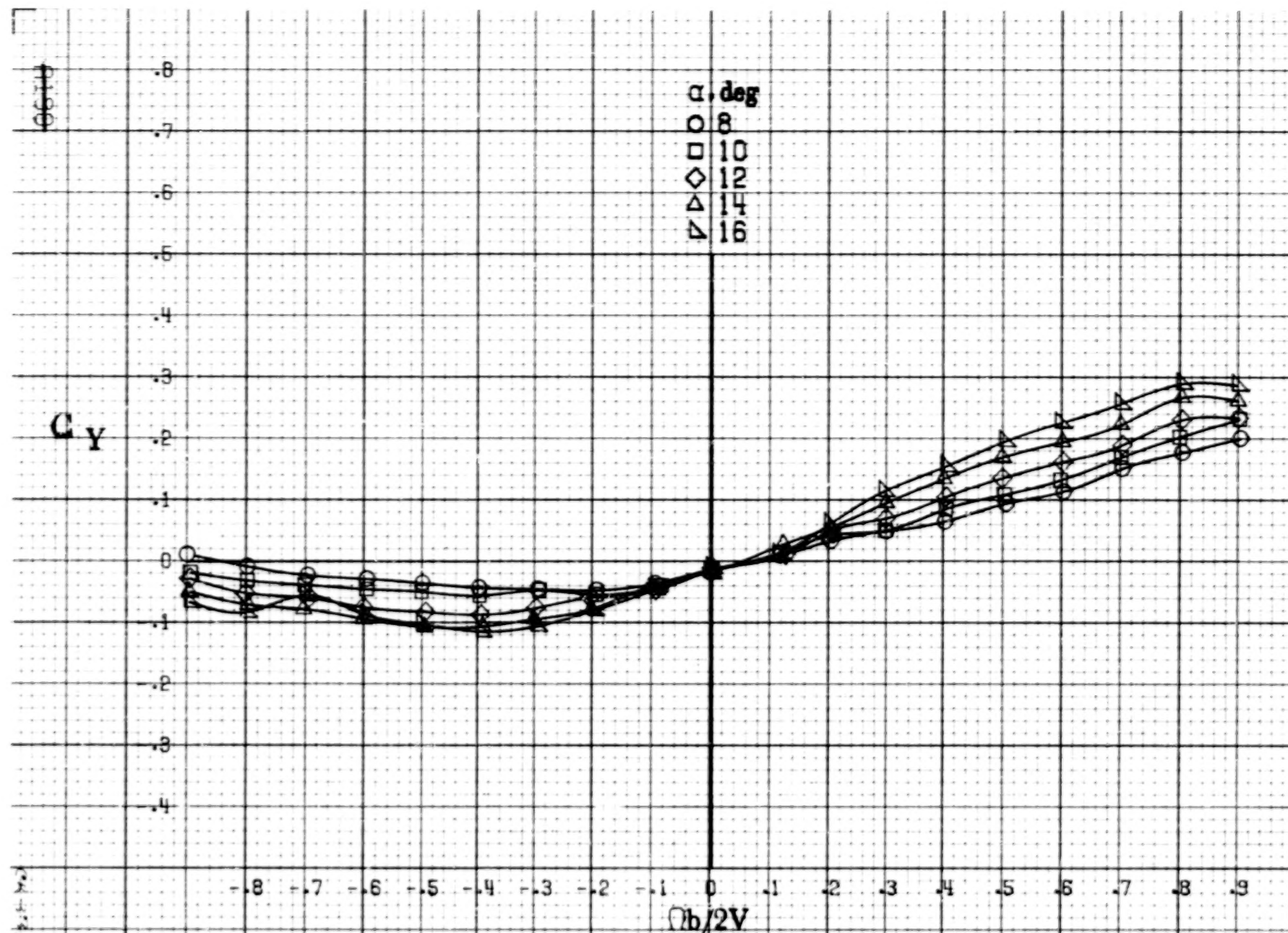
(a)  $\alpha = 8$  to  $16^\circ$ ,  $SK = 152.4 \text{ cm (60 in.)}$ .  
 Figure A76. Effect of rotation rate and angle of attack on normal-force coefficient for winglet configuration.  $\delta_e = 0^\circ$ ,  $\delta_s = 0^\circ$ ,  $\delta_r = 0^\circ$ ,  $\beta = 0^\circ$ .



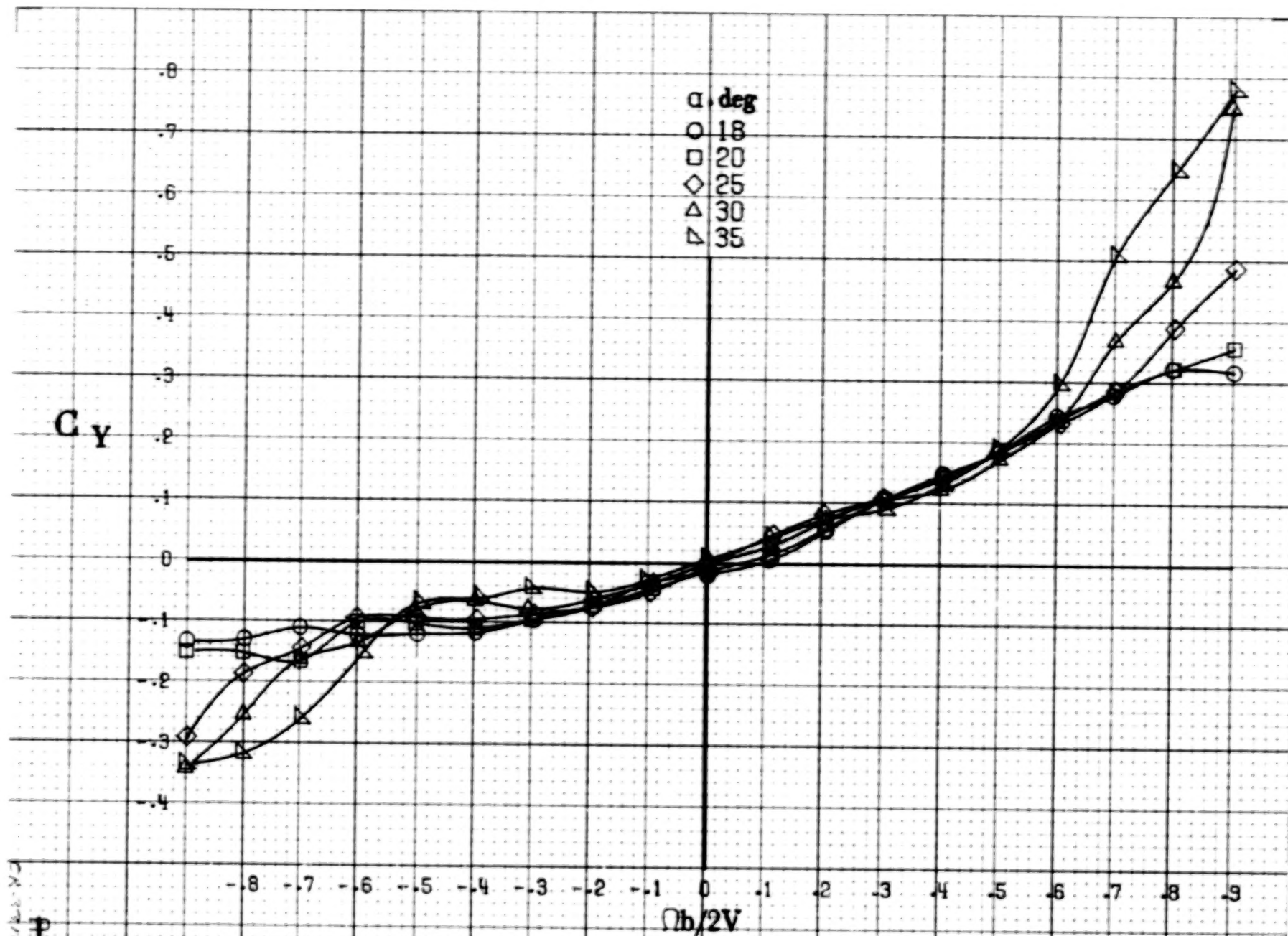


(b)  $\alpha = 18$  to  $35^\circ$ ,  $SR = 152.4\text{cm (60in.)}$ .

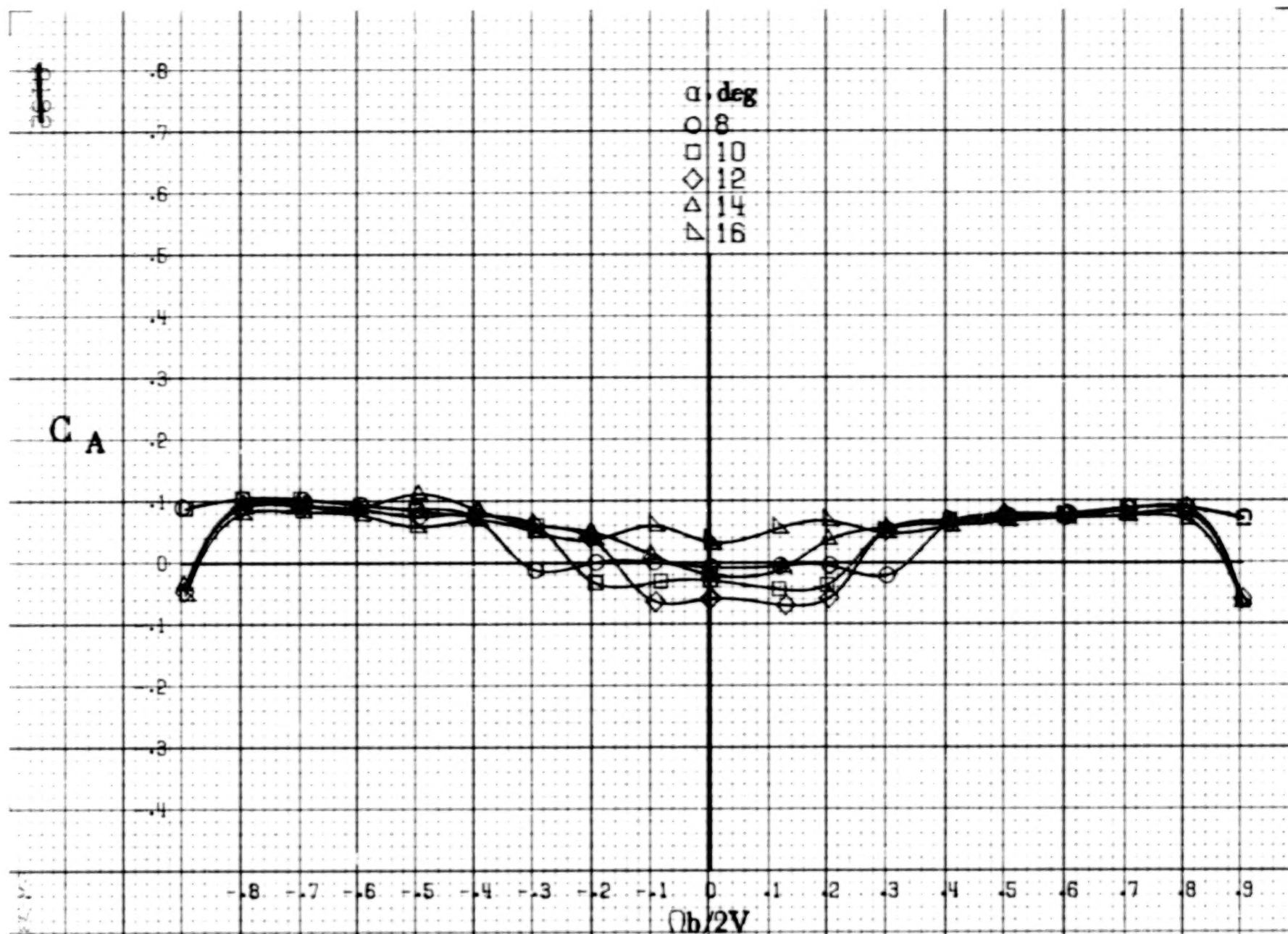
Figure A76-Concluded.



(a)  $\alpha = 8$  to  $16^\circ$ ,  $SR = 152.4\text{cm (60in)}$ .  
 Figure A77.-Effect of rotation rate and angle of attack on side-force coefficient for winglet configuration.  $\delta_e = 0^\circ$ ,  $\delta_a = 0^\circ$ ,  $\delta_r = 0^\circ$ ,  $\beta = 0^\circ$ .



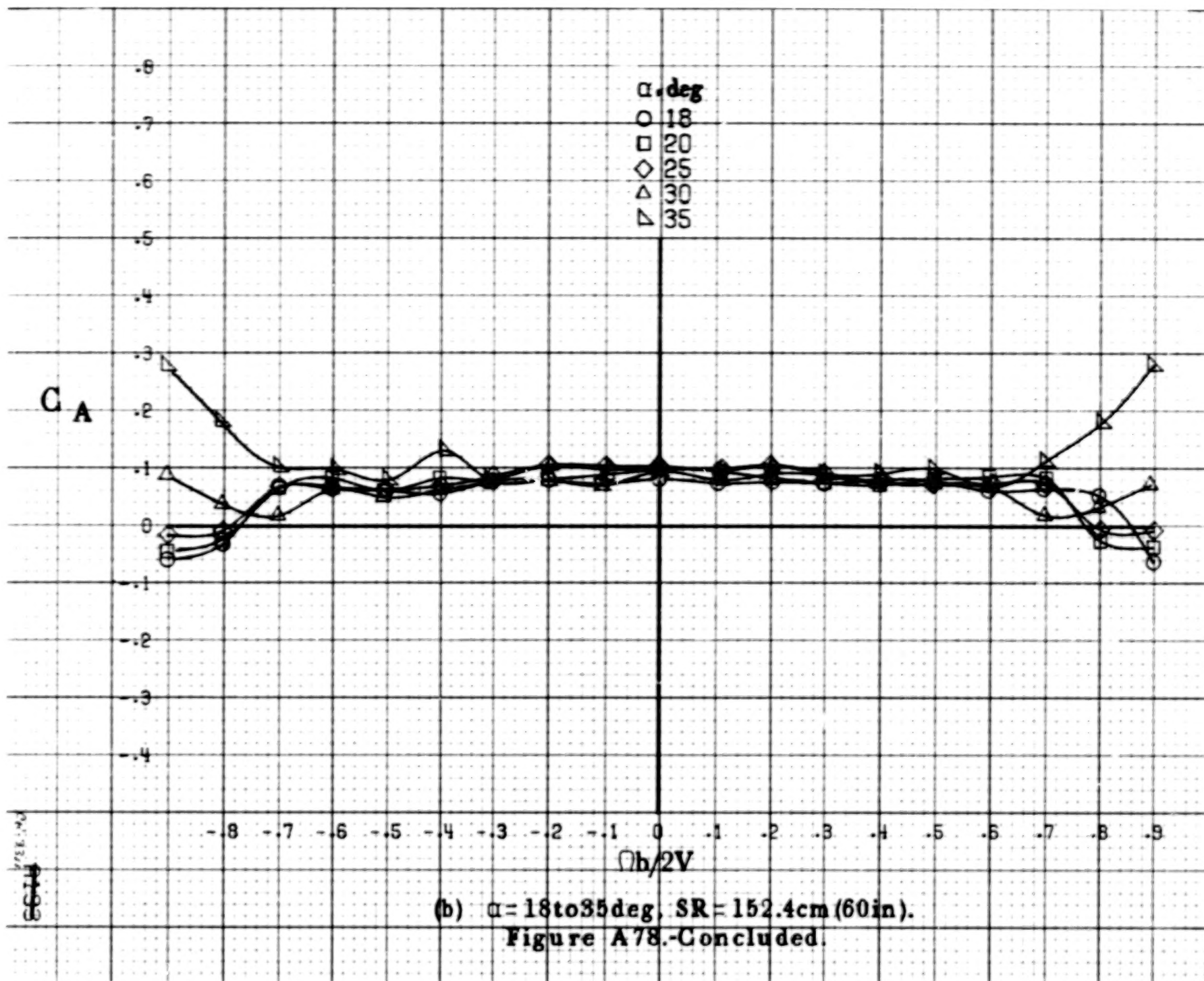
(b)  $\alpha = 18$  to  $35^\circ$ ,  $SR = 152.4\text{cm}$  (60 in).  
Figure A77.-Concluded.

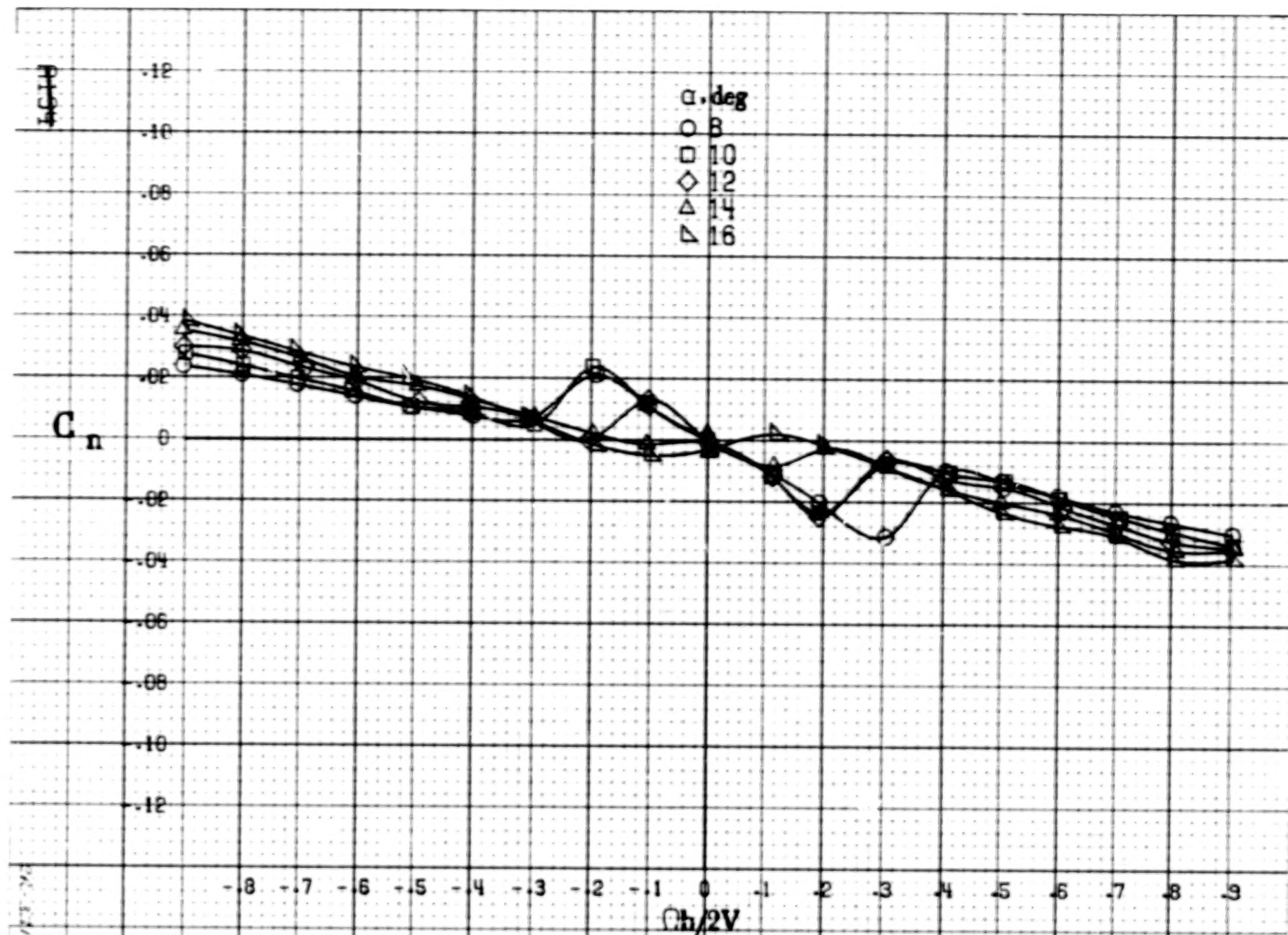


(a)  $\alpha = 8$  to  $16$  deg,  $SR = 152.4$  cm (60 in).

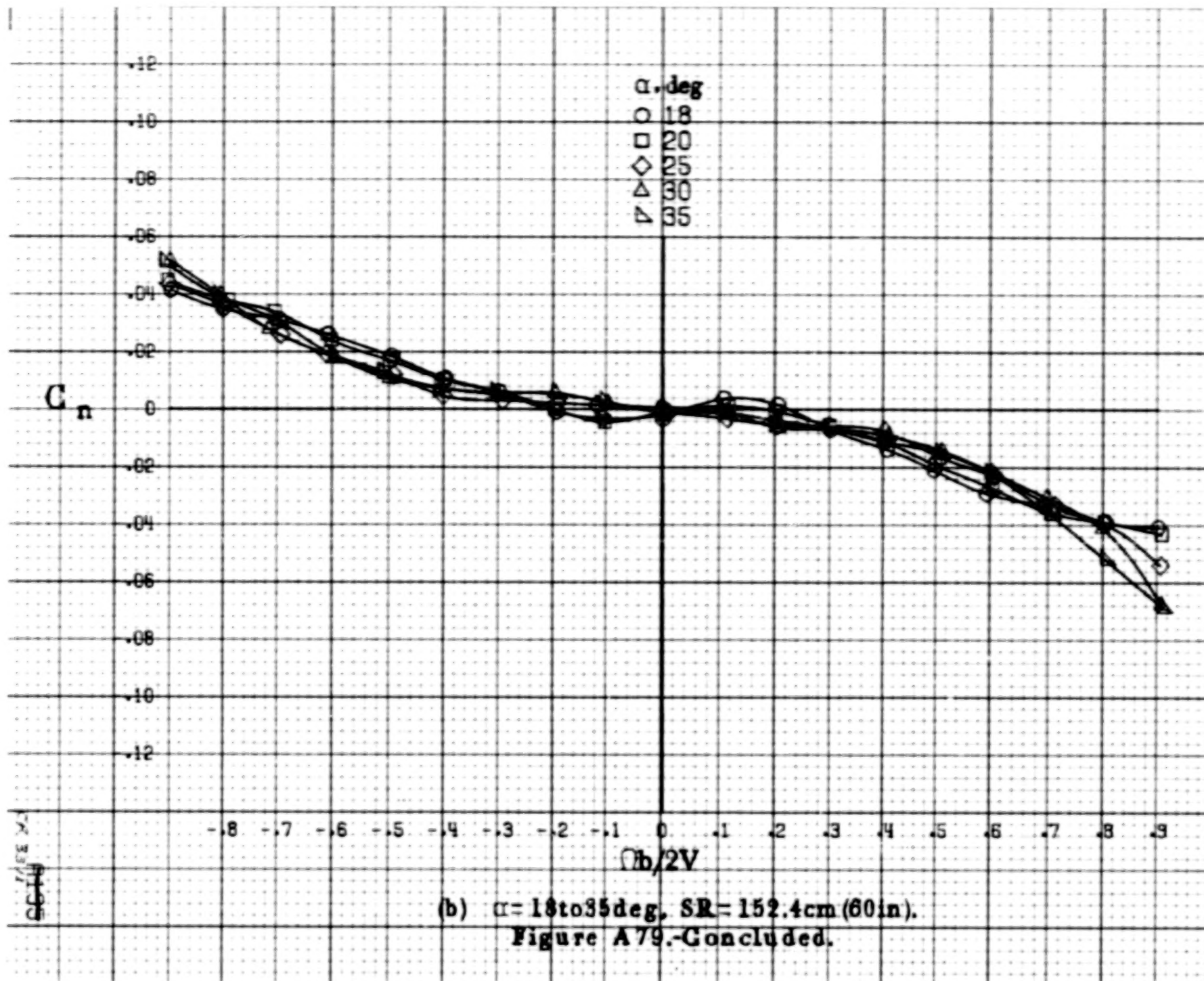
Figure A78.-Effect of rotation rate and angle of attack on axial-force coefficient for winglet configuration.  $\delta_c = 0^\circ$ ,  $\delta_n = 0^\circ$ ,  $\delta_r = 0^\circ$ ,  $\beta = 0^\circ$ .



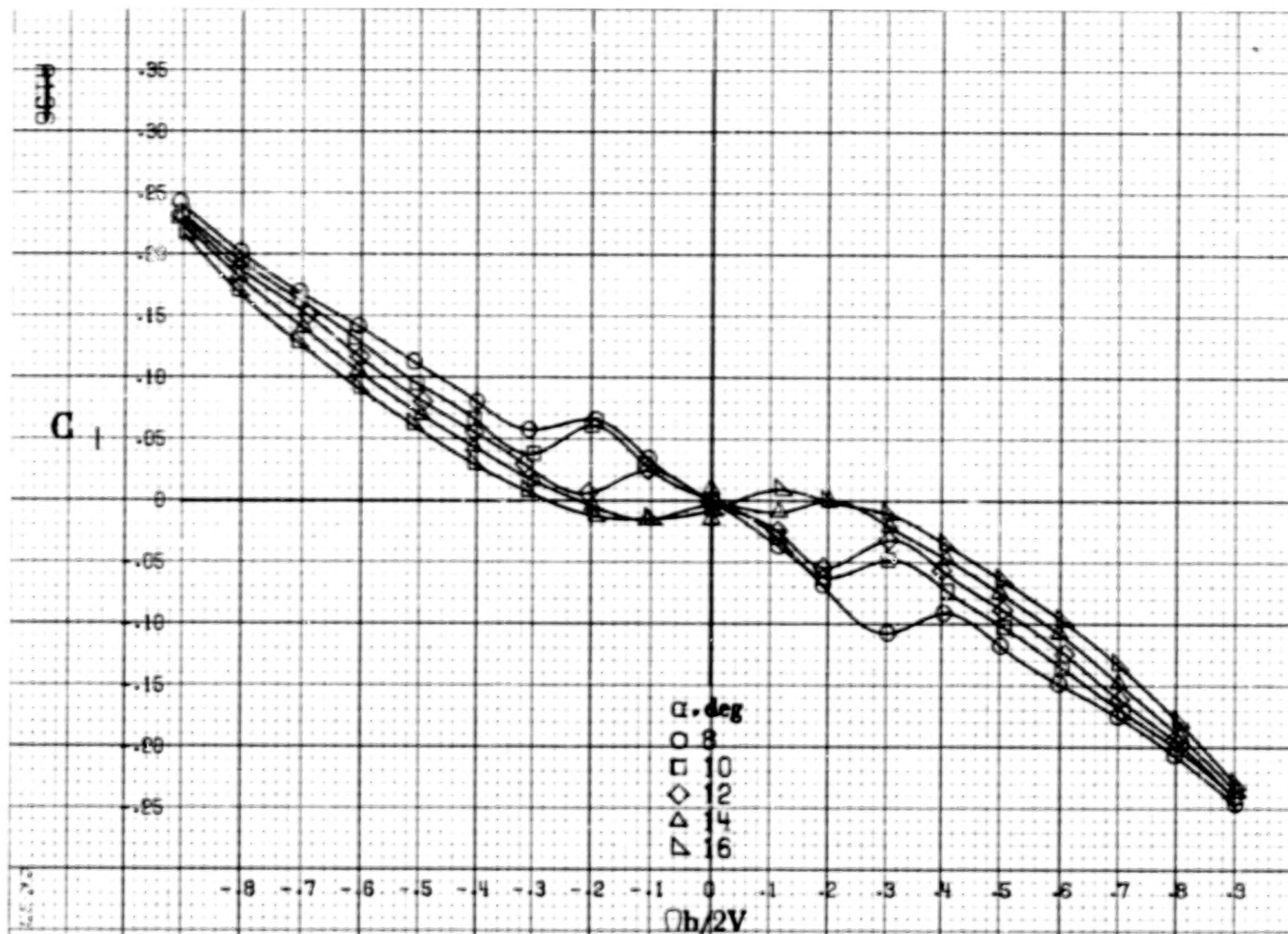




(a)  $\alpha = 8$  to  $16^\circ$ ,  $SR = 152.4\text{cm (60in)}$ .  
 Figure A79. Effect of rotation rate and angle of attack on yawing-moment coefficient for wing tip sails configuration.  $\delta_e = 0^\circ$ ,  $\delta_a = 0^\circ$ ,  $\delta_r = 0^\circ$ ,  $\beta = 0^\circ$ .



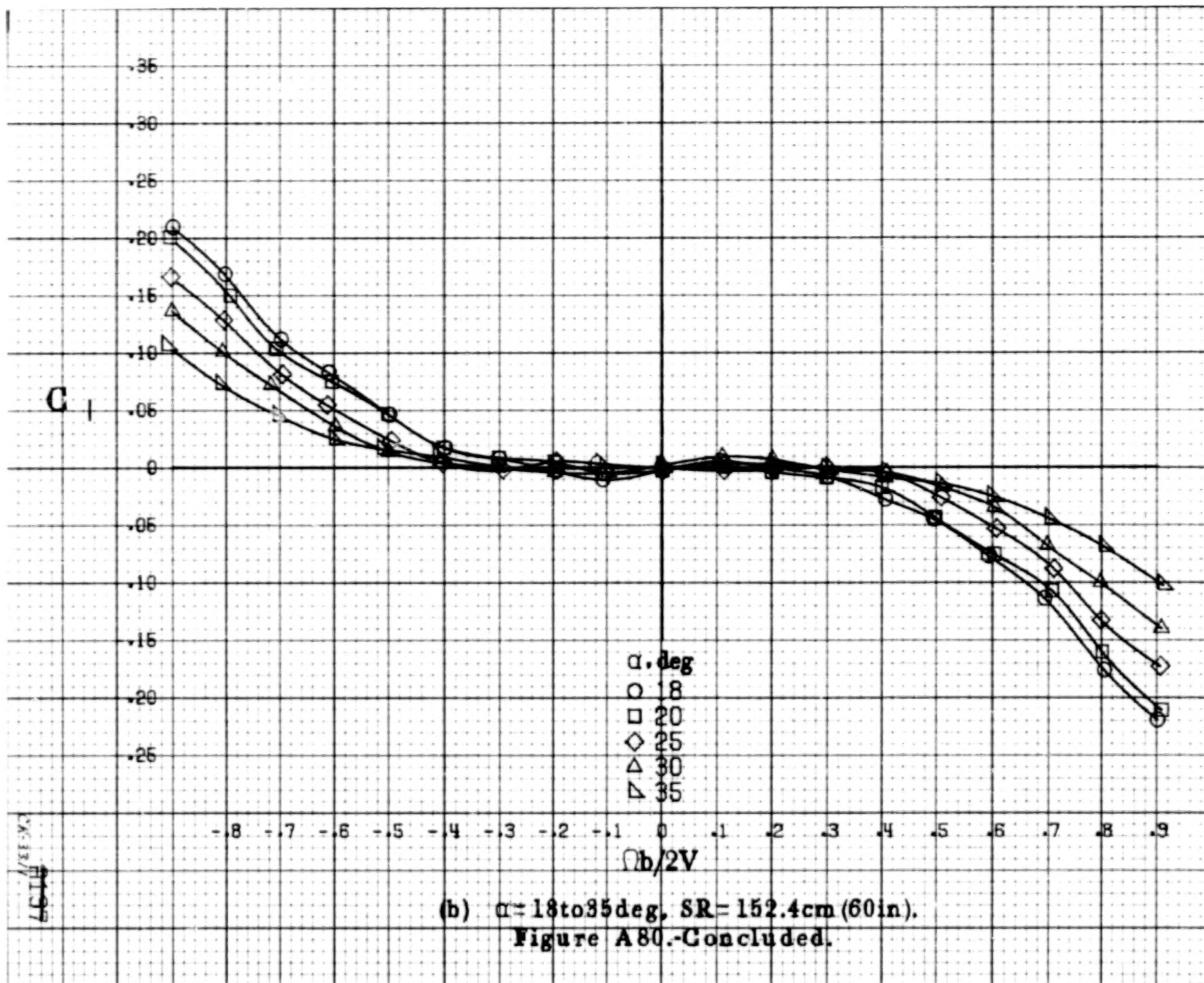
A195

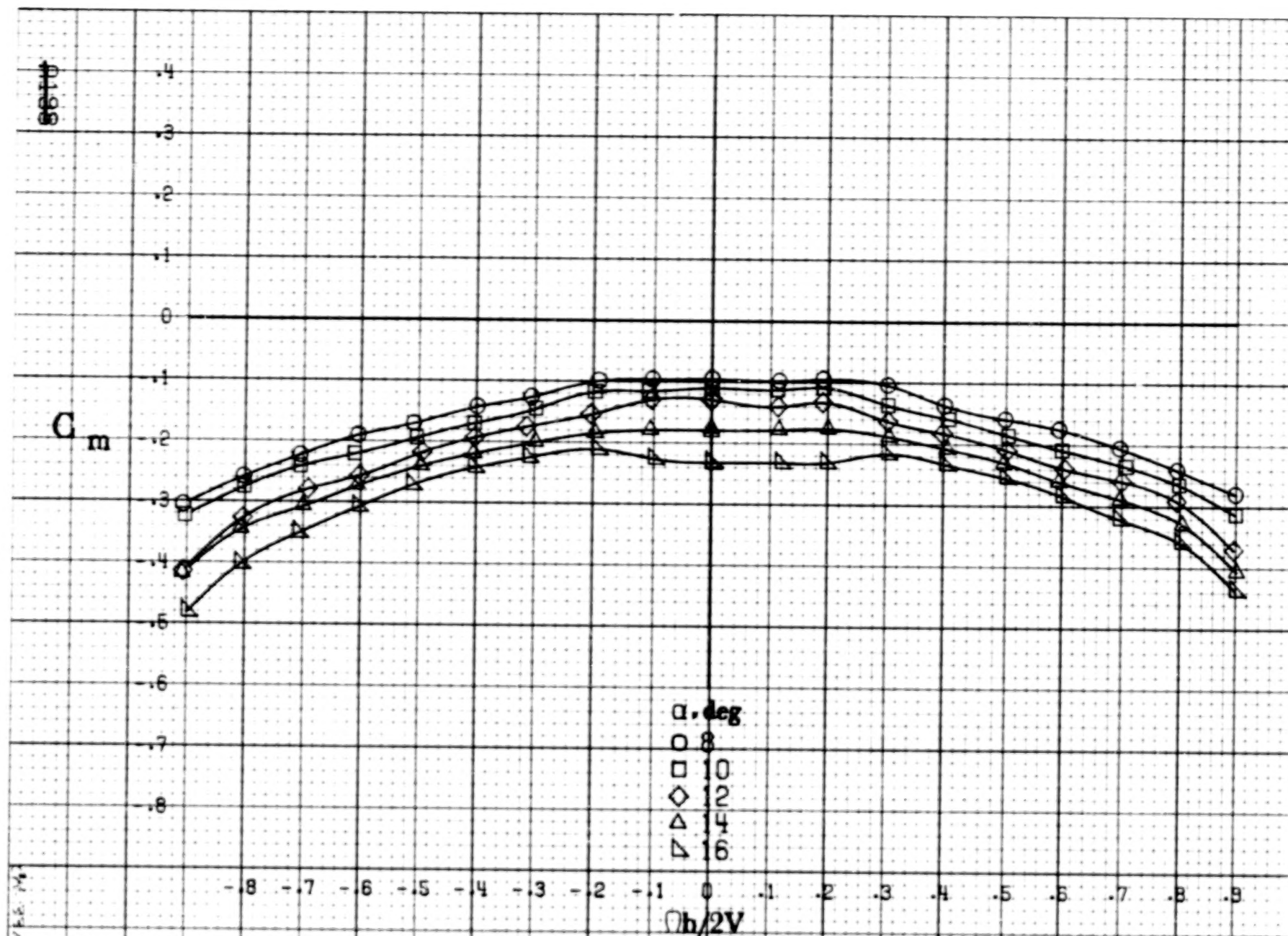


(a)  $\alpha = 8$  to  $16^\circ$ ,  $SR = 152.4 \text{ cm (60 in)}$ .

Figure A80. Effect of rotation rate and angle of attack on rolling-moment coefficient for wing tip sail configuration.  $\delta_s = 0^\circ$ ,  $\delta_a = 0^\circ$ ,  $\delta_r = 0^\circ$ ,  $\beta = 0^\circ$ .

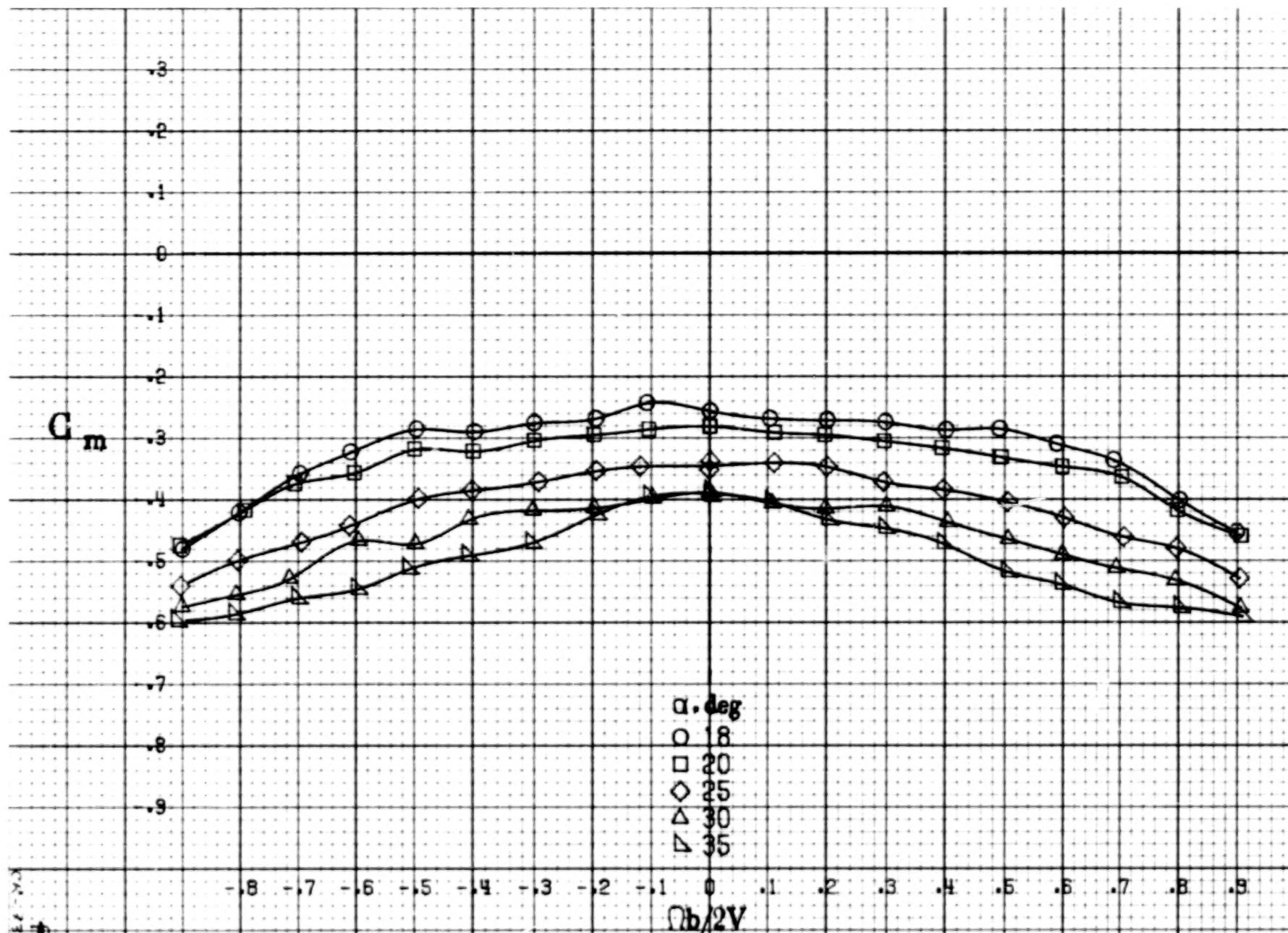






(a)  $\alpha = 8$  to  $16$  deg,  $SR = 152.4$  cm (60 in).

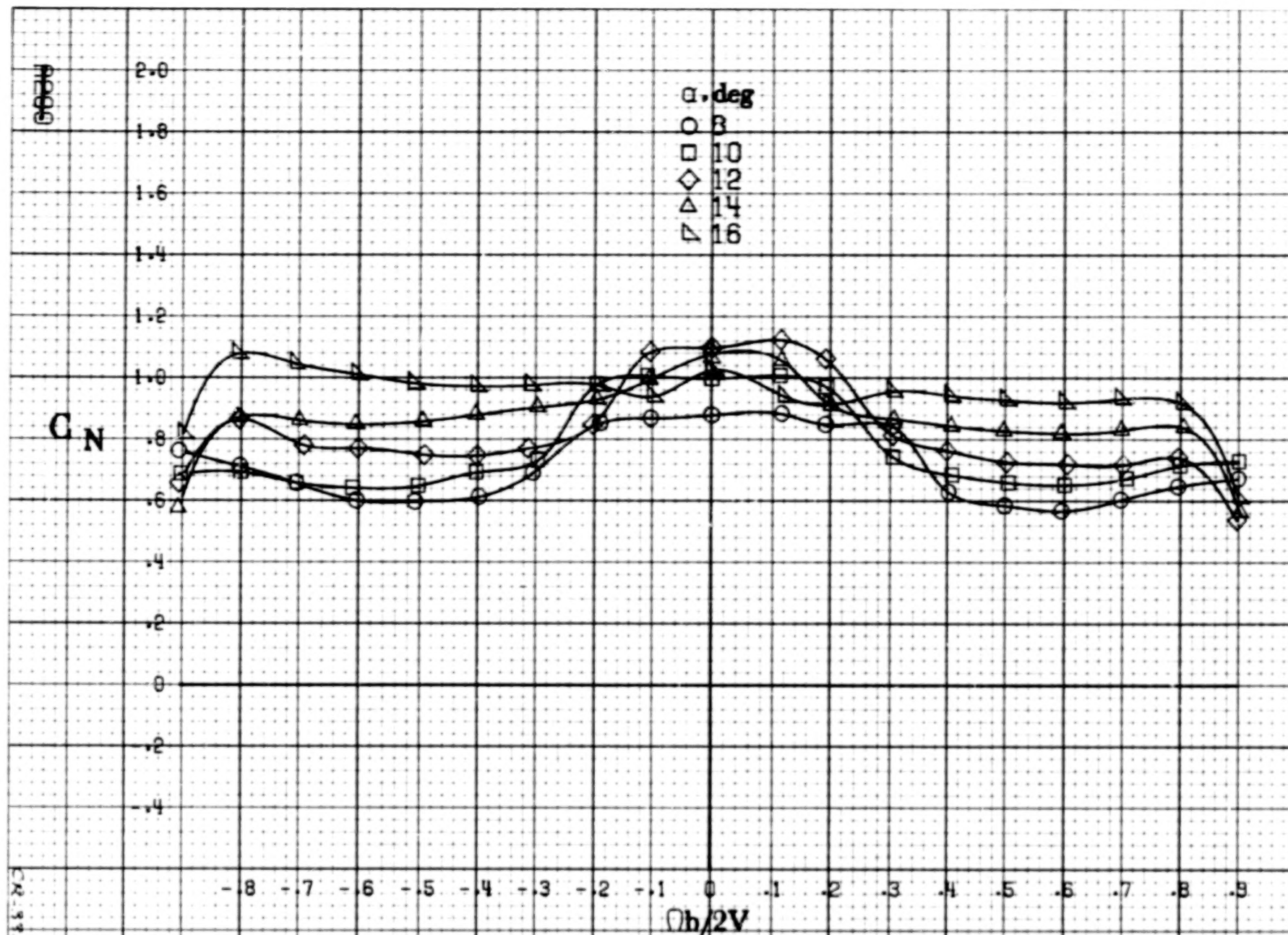
Figure A81. Effect of rotation rate and angle of attack on pitching moment coefficient for wing tip sails configuration.  $\delta_e = 0^\circ$ ,  $\delta_a = 0^\circ$ ,  $\delta_r = 0^\circ$ ,  $\beta = 0^\circ$ .



(b)  $\alpha = 18$  to  $35^\circ$ ,  $SR = 152.4\text{cm}$  (60 in).

Figure A81.-Concluded.

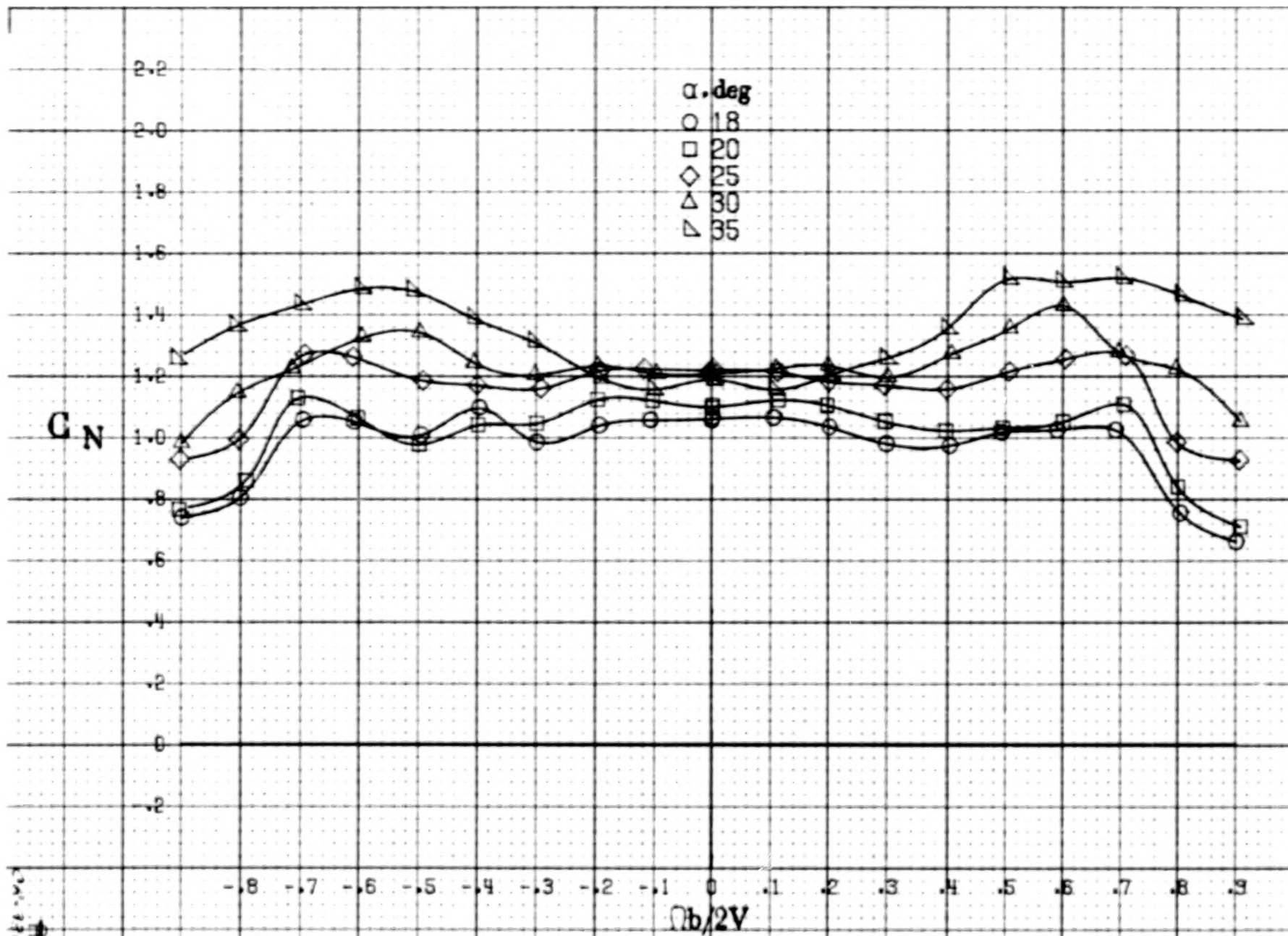




(a)  $\alpha = 8$  to  $16$  deg,  $SR = 152.4$  cm (60 in).

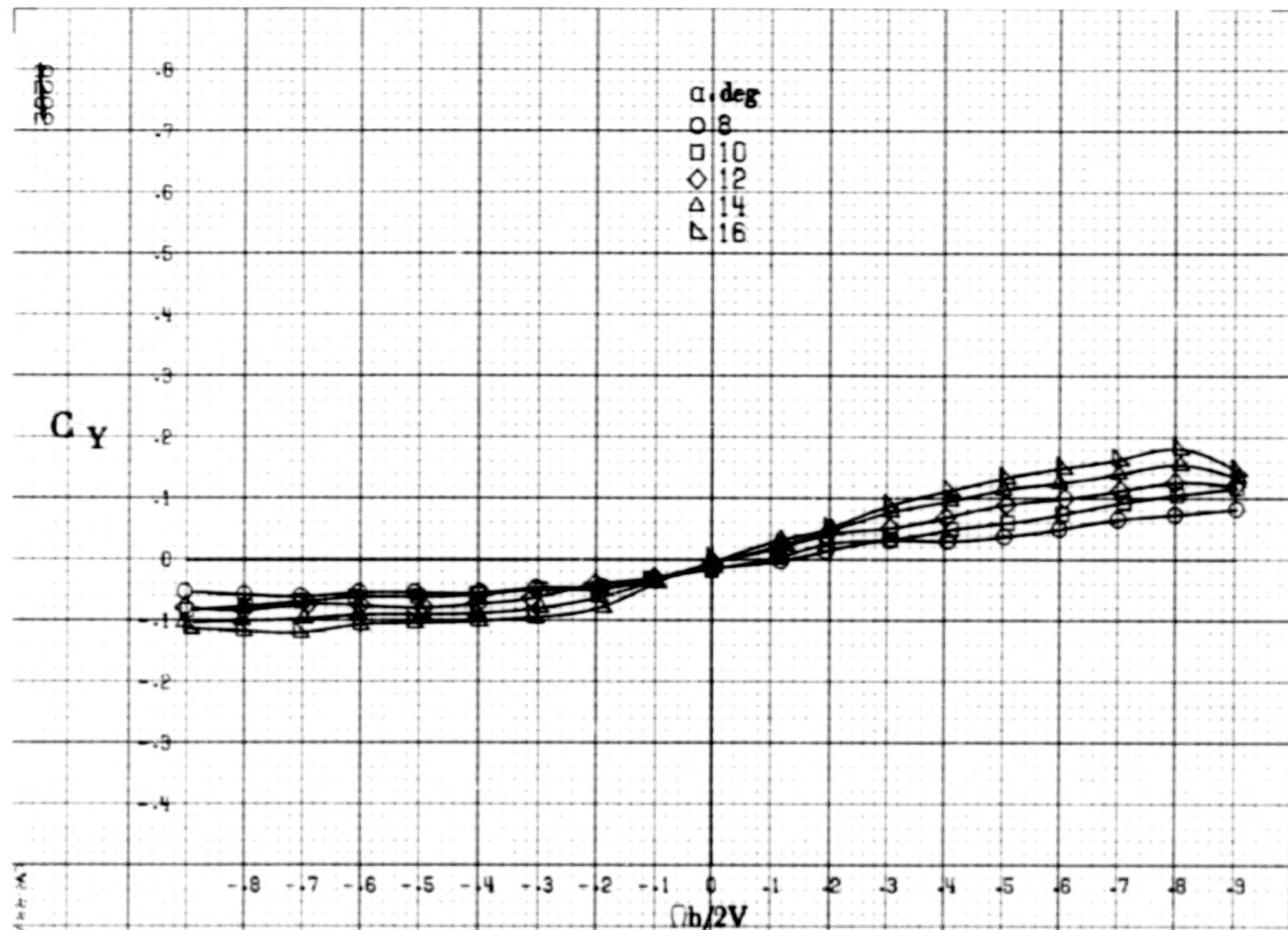
Figure A82. Effect of rotation rate and angle of attack on normal force coefficient for wing tip sails configuration.  $\delta_e = 0^\circ$ ,  $\delta_a = 0^\circ$ ,  $\delta_r = 0^\circ$ ,  $\beta = 0^\circ$ .





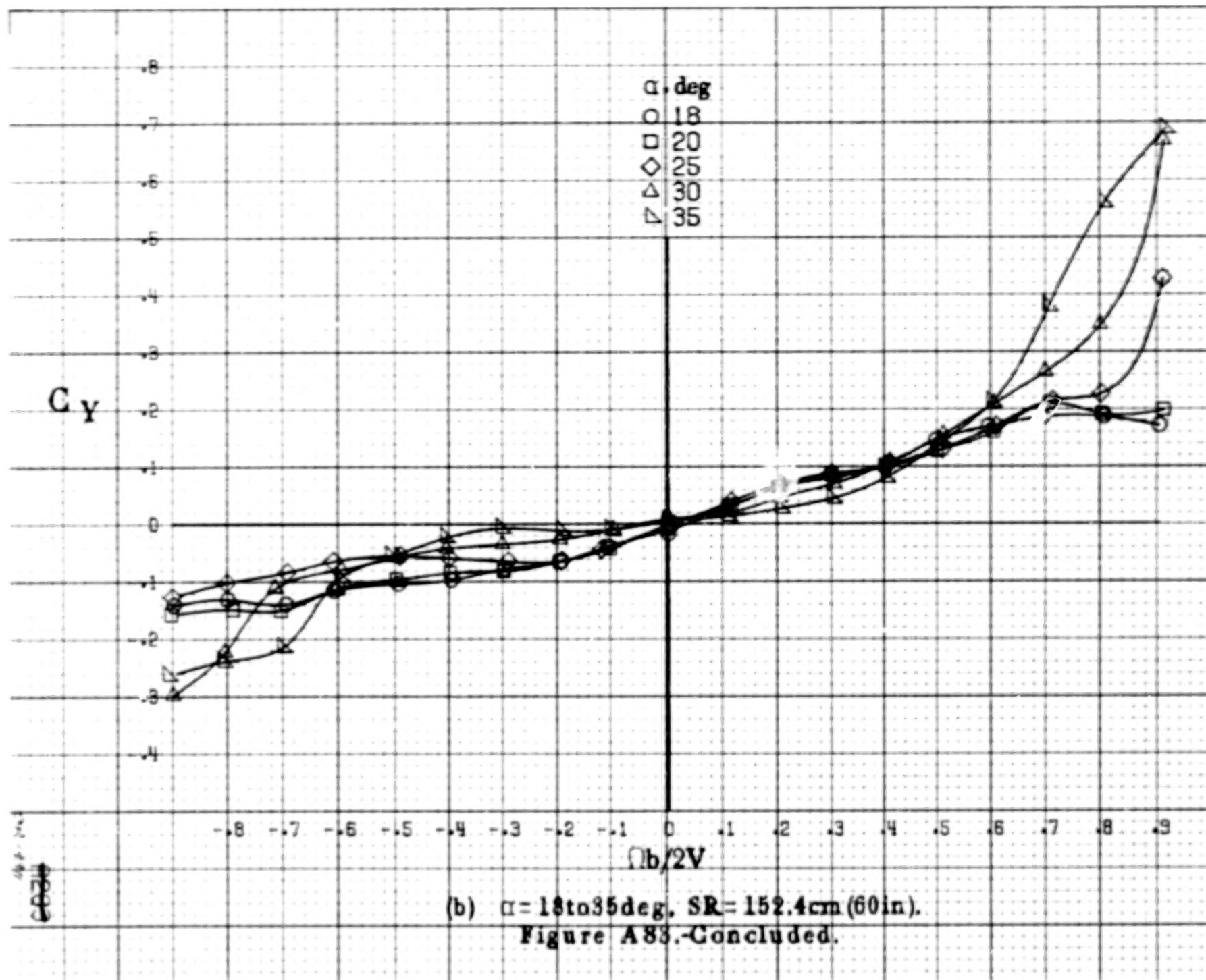
(b)  $\alpha = 18$  to  $35^\circ$ ,  $SR = 152.4\text{cm}$  (60 in).  
Figure A82.-Concluded.

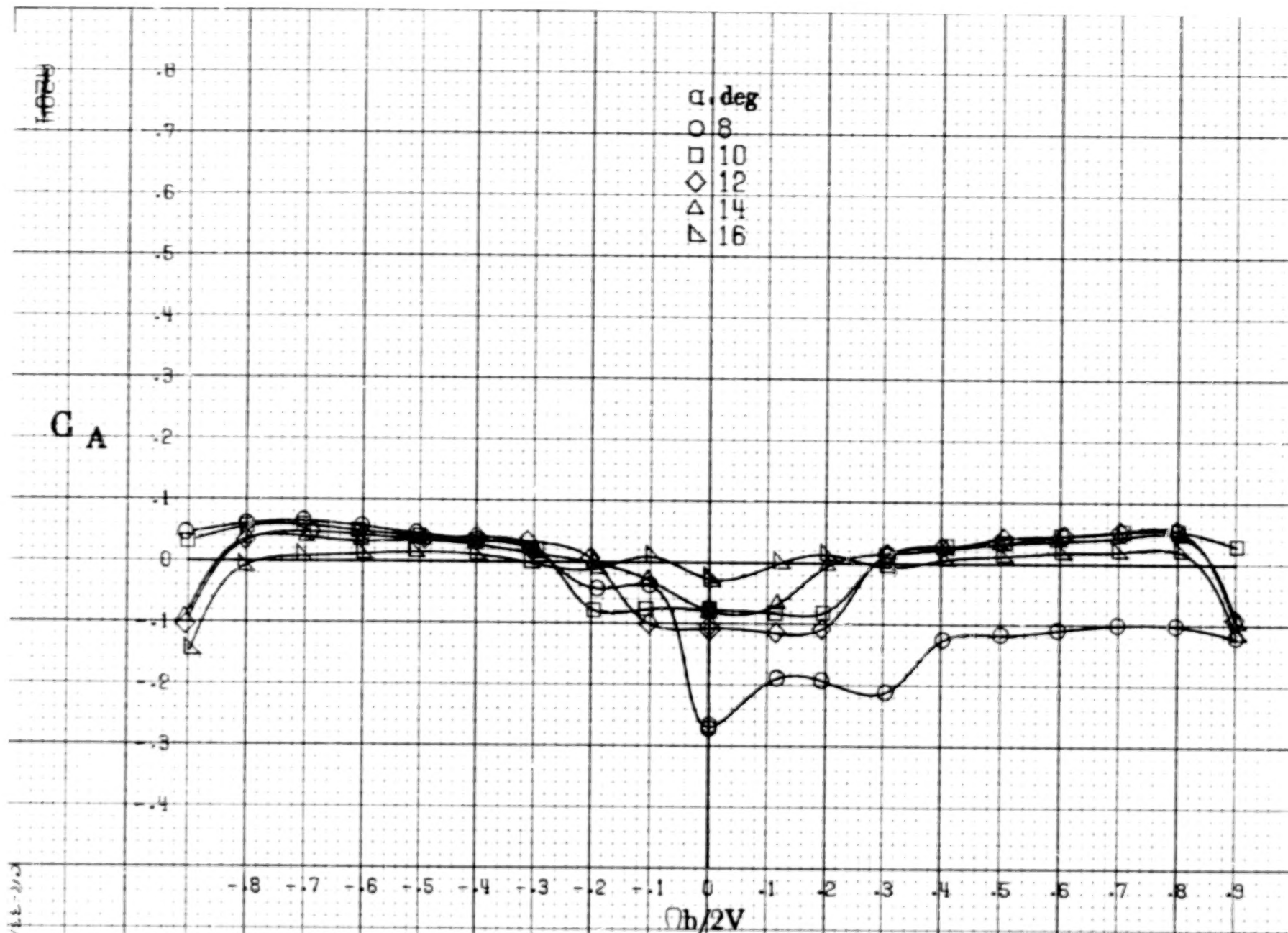
A201



(a)  $\alpha = 8$  to  $16^\circ$ ,  $SR = 152.4 \text{ cm (60 in)}$ .

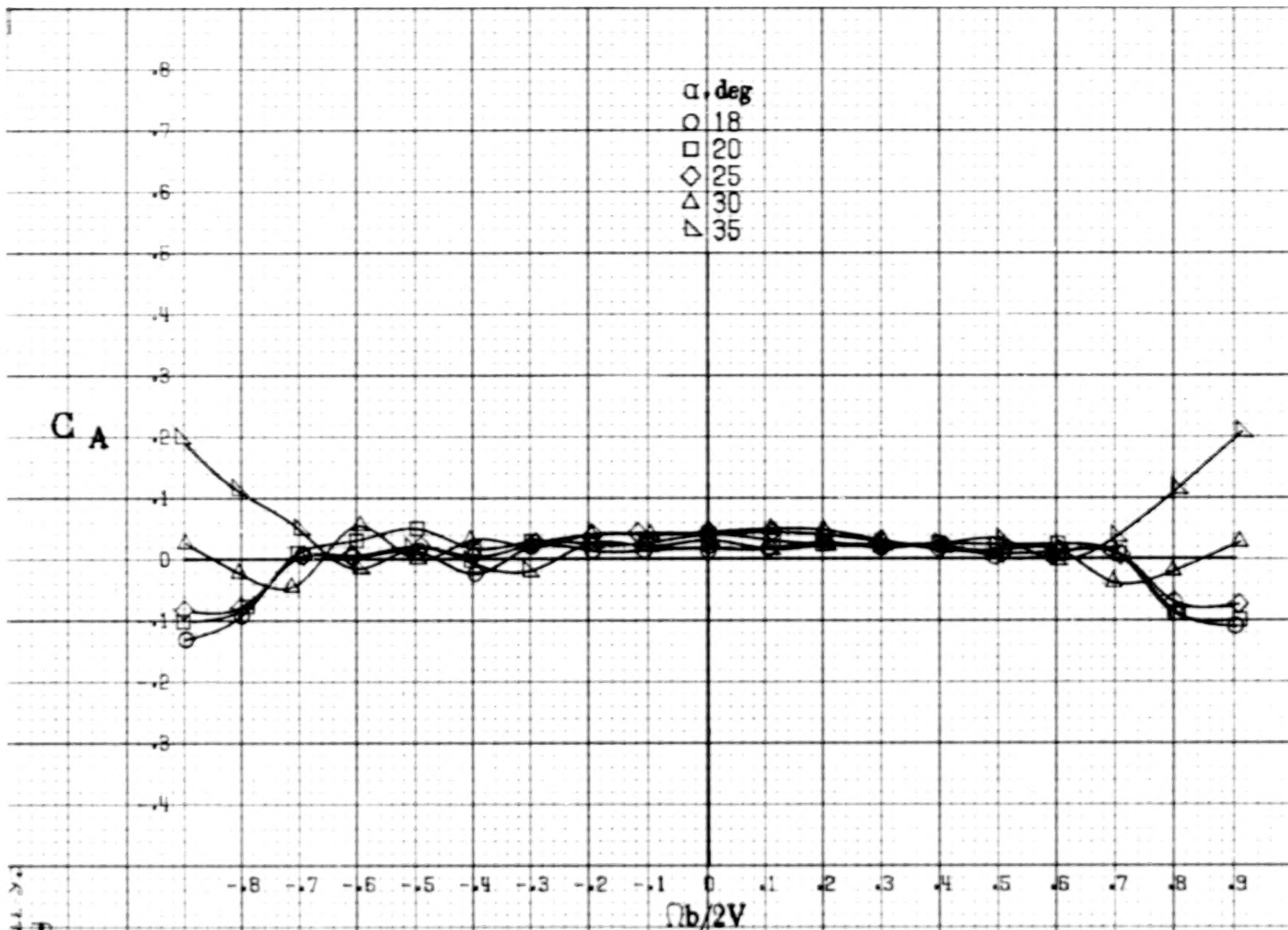
Figure A88. Effect of rotation rate and angle of attack on side force coefficient for wing tip sails configuration.  $\delta_s = 0^\circ$ ,  $\delta_a = 0^\circ$ ,  $\delta_r = 0^\circ$ ,  $\theta = 0^\circ$ .





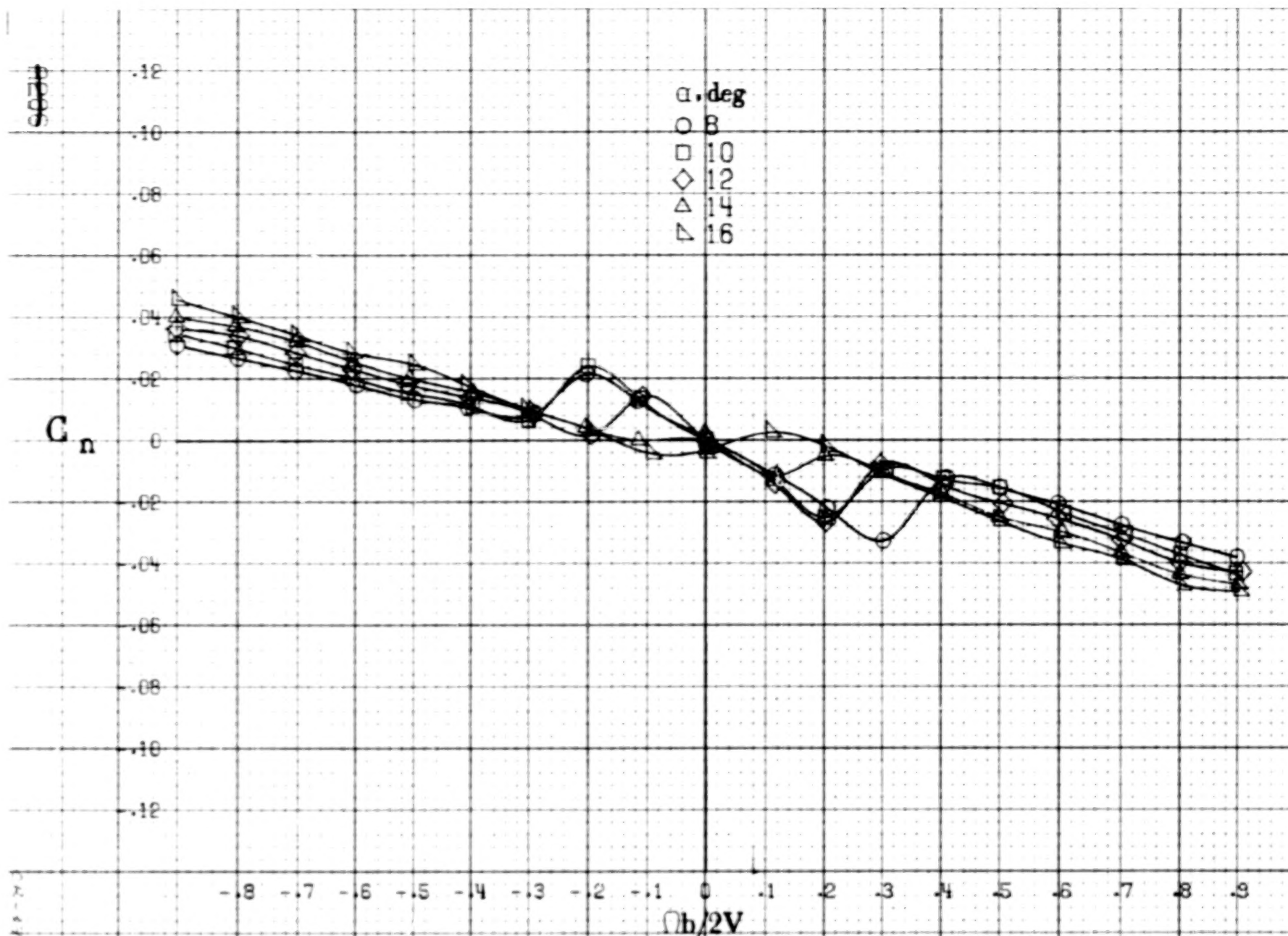
(a)  $\alpha=8$  to  $16^\circ$ ,  $SR=152.4\text{cm}$  (60 in).  
Figure A84.-Effect of rotation rate and angle of attack on axial-force coefficient for wing tip sails configuration.  $\delta_e=0^\circ$ ,  $\delta_s=0^\circ$ ,  $\delta_r=0^\circ$ ,  $\beta=0^\circ$ .





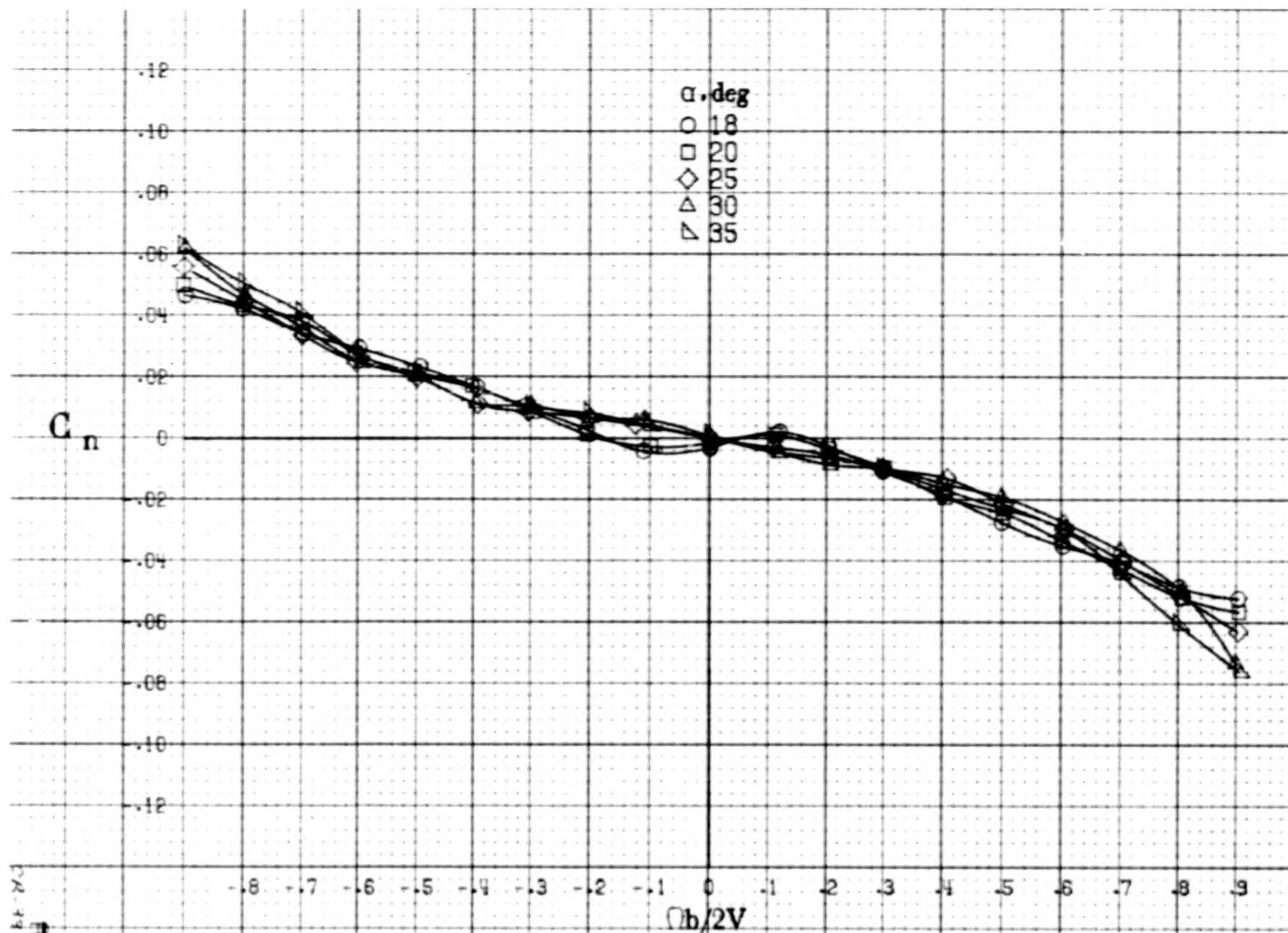
(b)  $\alpha = 18$  to  $35$  deg,  $SR = 152.4$  cm (60 in).

Figure A84.-Concluded.



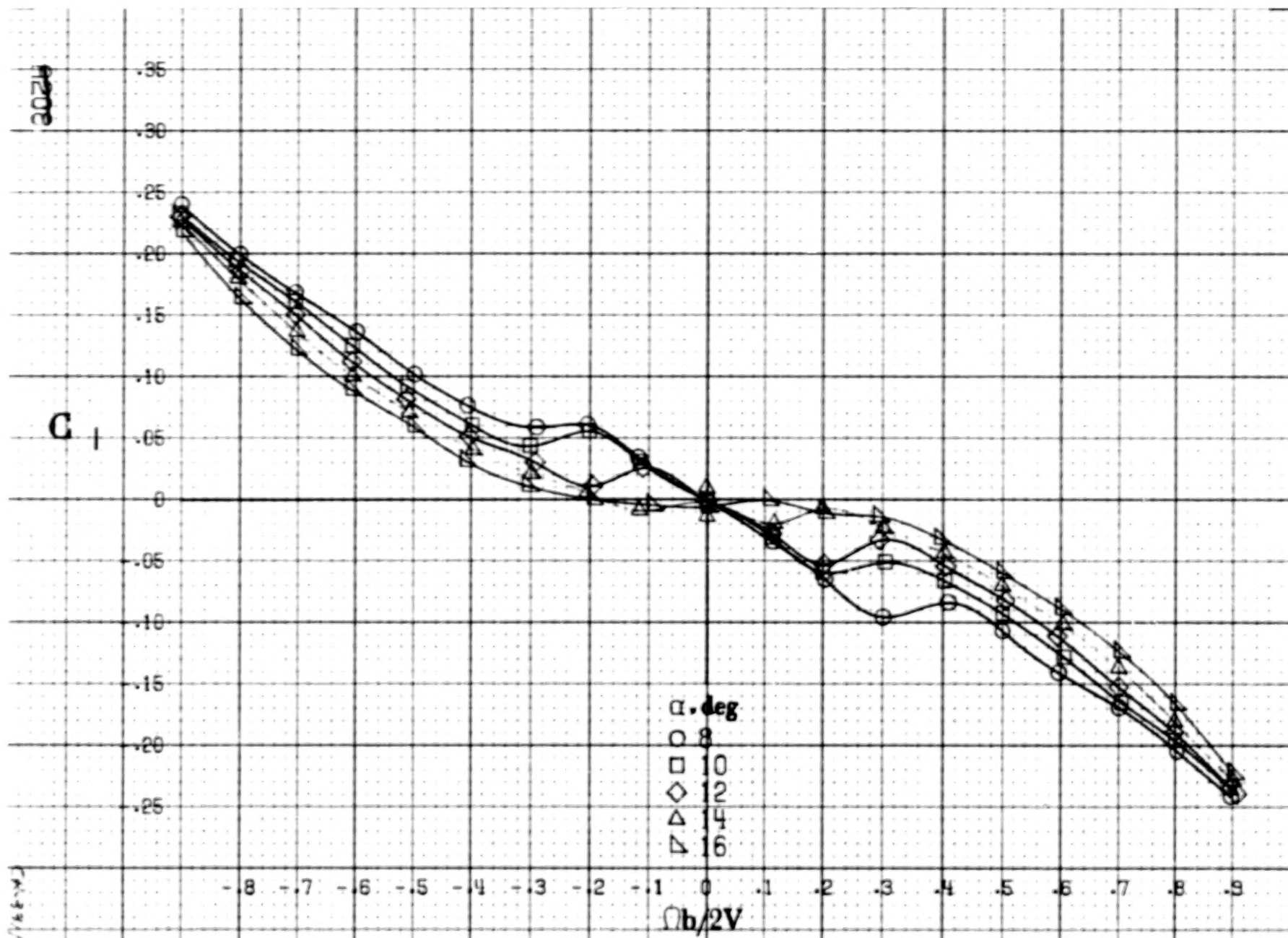
(a)  $\alpha = 8$  to  $16^\circ$ ,  $SR = 152.4 \text{ cm (60 in)}$ .

Figure A85. Effect of rotation rate and angle of attack on yawing-moment coefficient for tip vortex diffusers configuration.  $\delta_e = 0^\circ$ ,  $\delta_a = 0^\circ$ ,  $\delta_r = 0^\circ$ ,  $\beta = 0^\circ$ .



(b)  $\alpha = 18$  to  $35^\circ$ ,  $SR = 152.4 \text{ cm (60 in.)}$ .  
Figure A85.-Concluded.

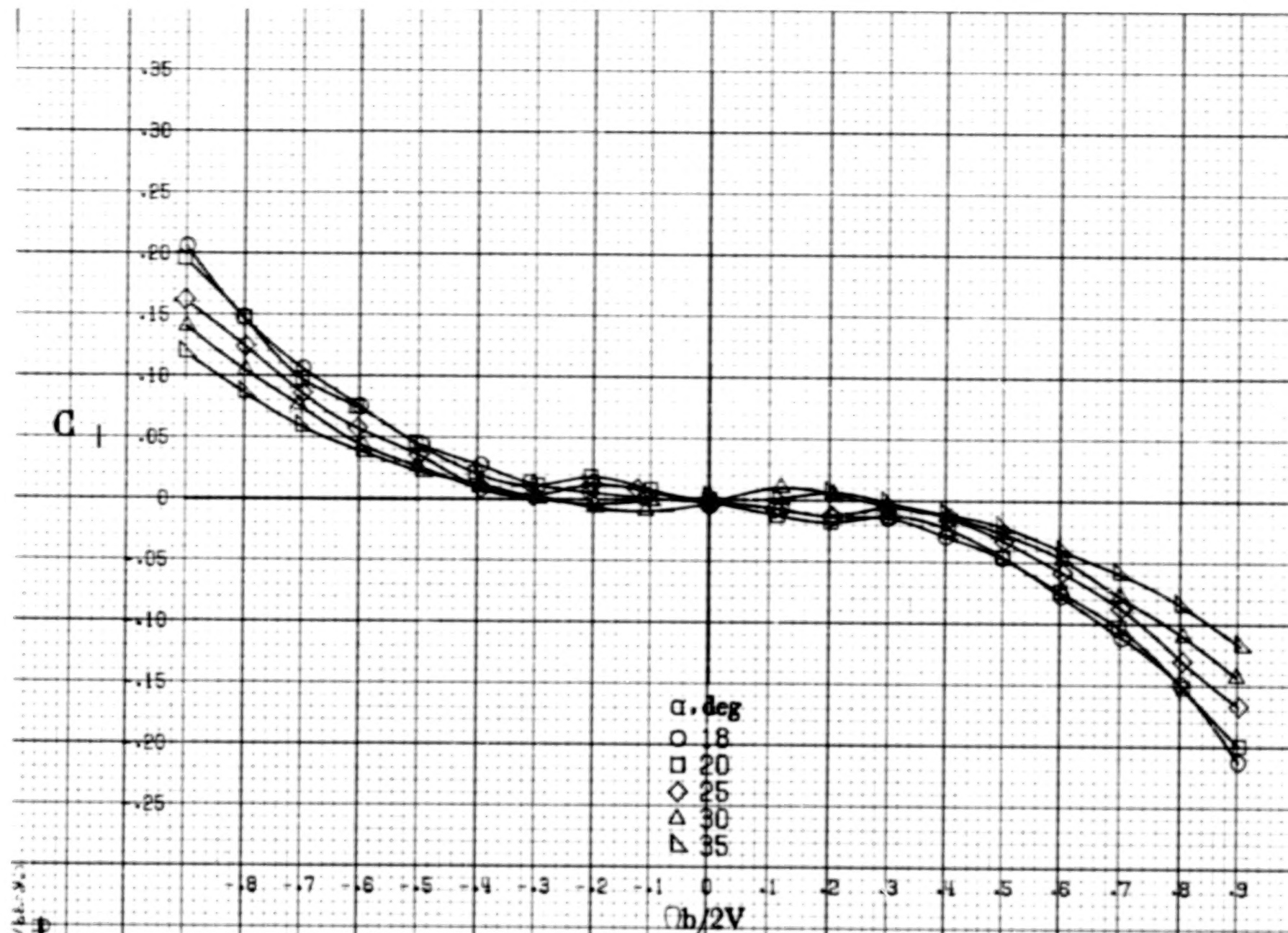
A207



(a)  $\alpha = 8 \text{ to } 16 \text{ deg}$ ,  $SR = 152.4 \text{ cm (60 in)}$ .

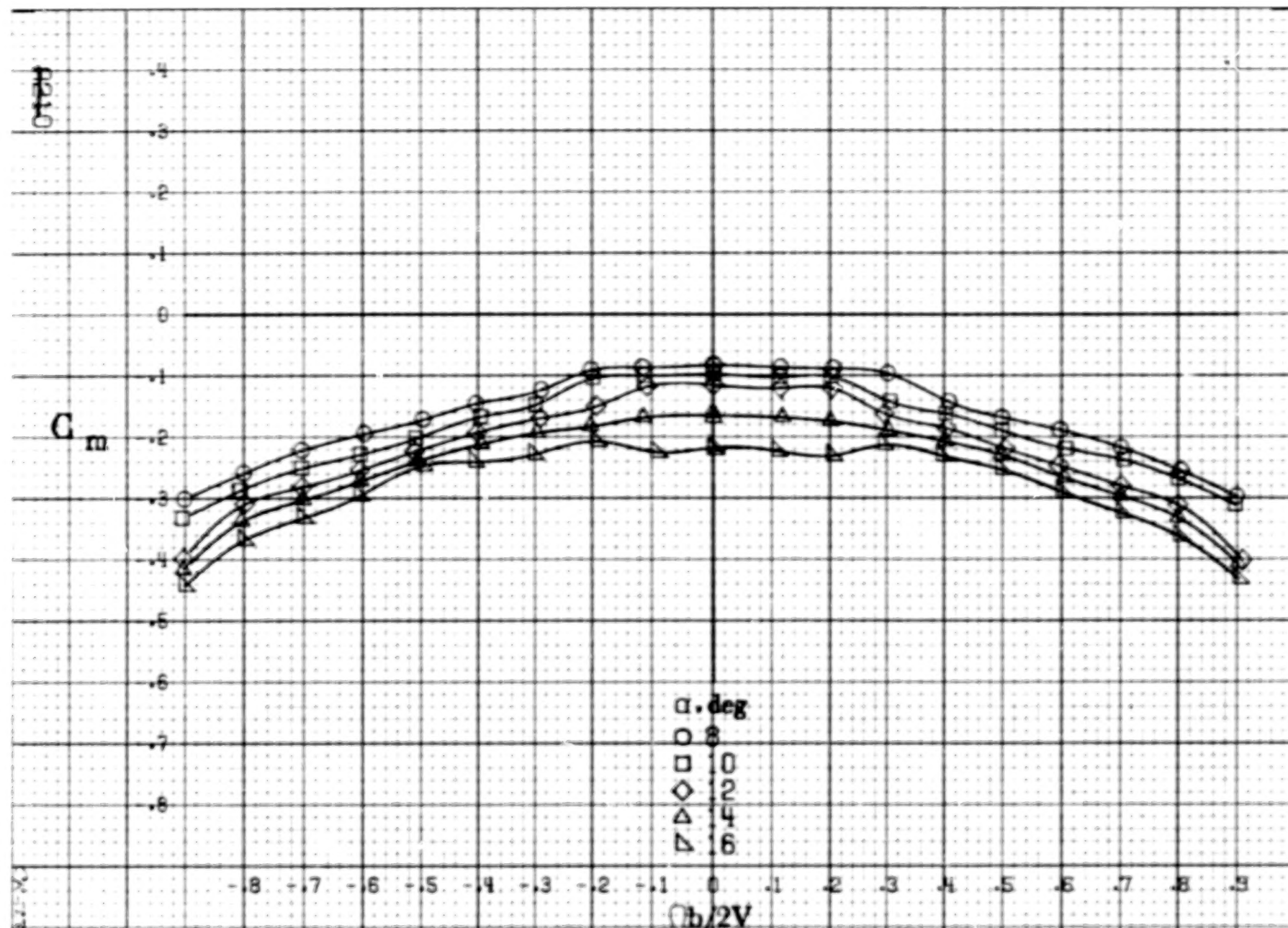
Figure A86. Effect of rotation rate and angle of attack on rolling-moment coefficient for tip vortex diffusers configuration.  $\delta_c = 0^\circ$ ,  $\delta_s = 0^\circ$ ,  $\delta_r = 0^\circ$ .  $\theta = 0^\circ$ .





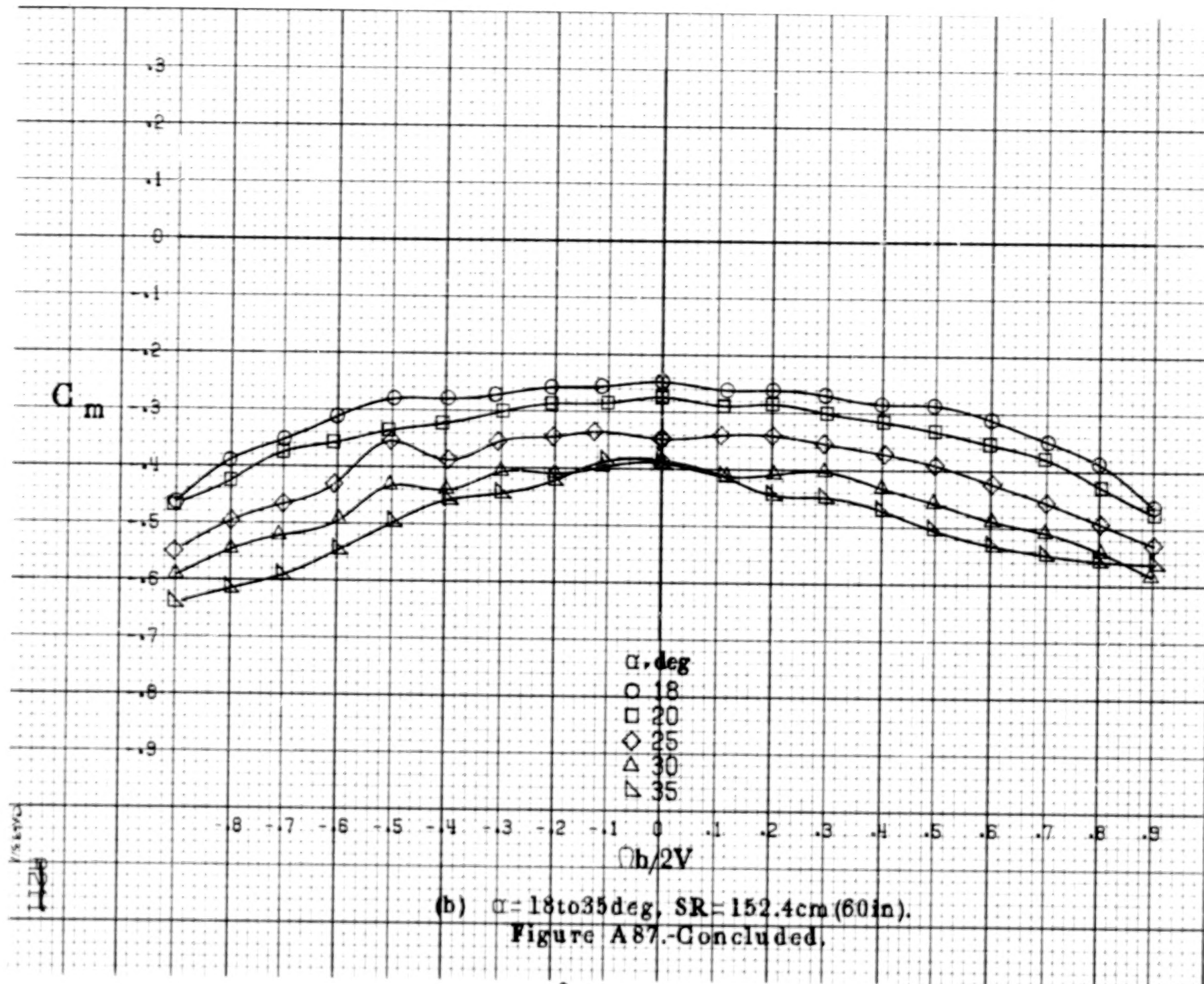
(b)  $\alpha = 18$  to  $35$  deg, SR = 152.4 cm (60 in).

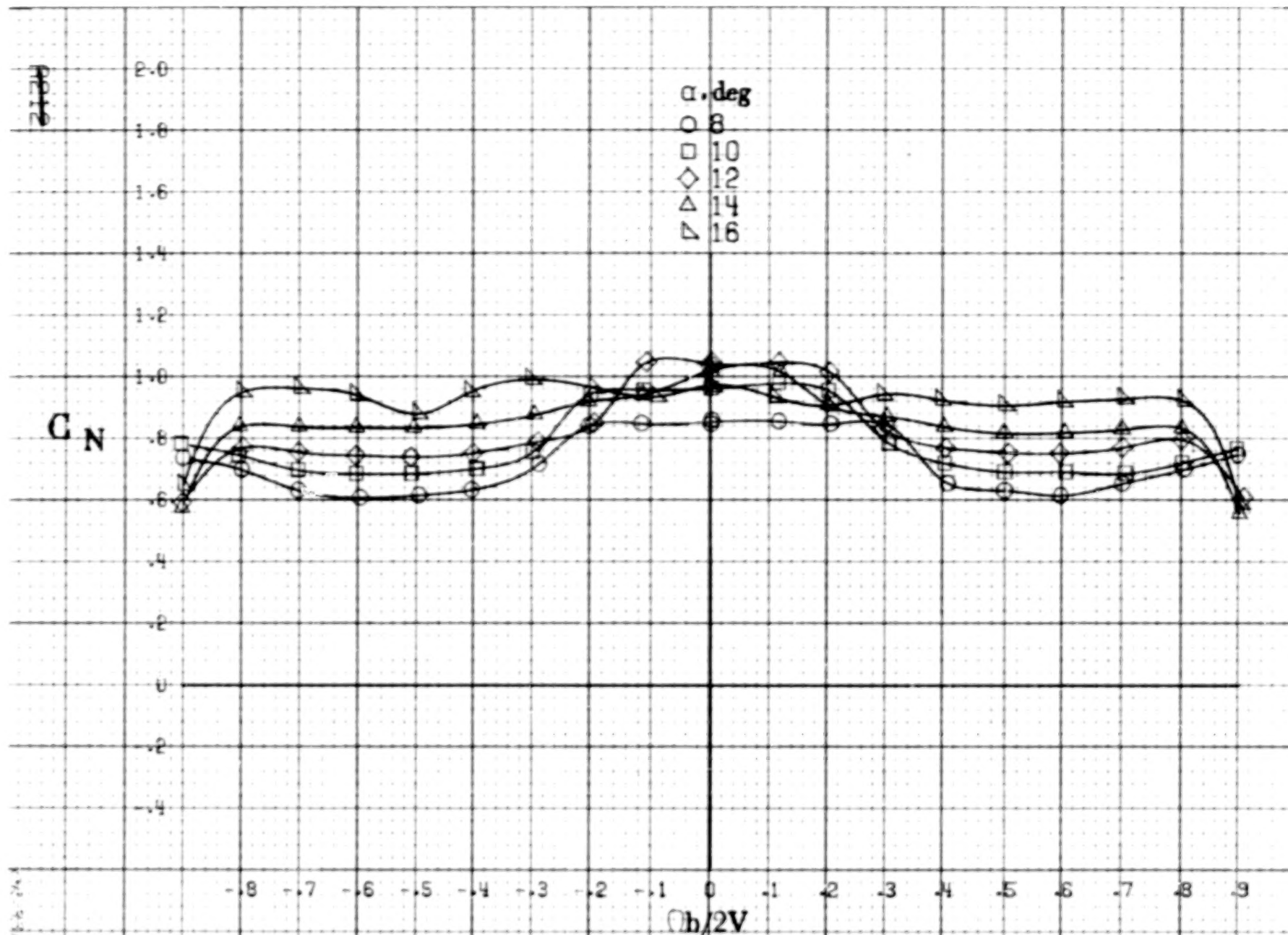
Figure A86.-Concluded.



(a)  $\alpha = 8$  to  $16$  deg,  $SR = 152.4$  cm (60 in).

Figure A87. Effect of rotation rate and angle of attack on pitching moment coefficient for tip vortex diffusers configuration.  $\delta_s = 0^\circ$ ,  $\delta_a = 0^\circ$ ,  $\delta_r = 0^\circ$ ,  $\beta = 0^\circ$ .

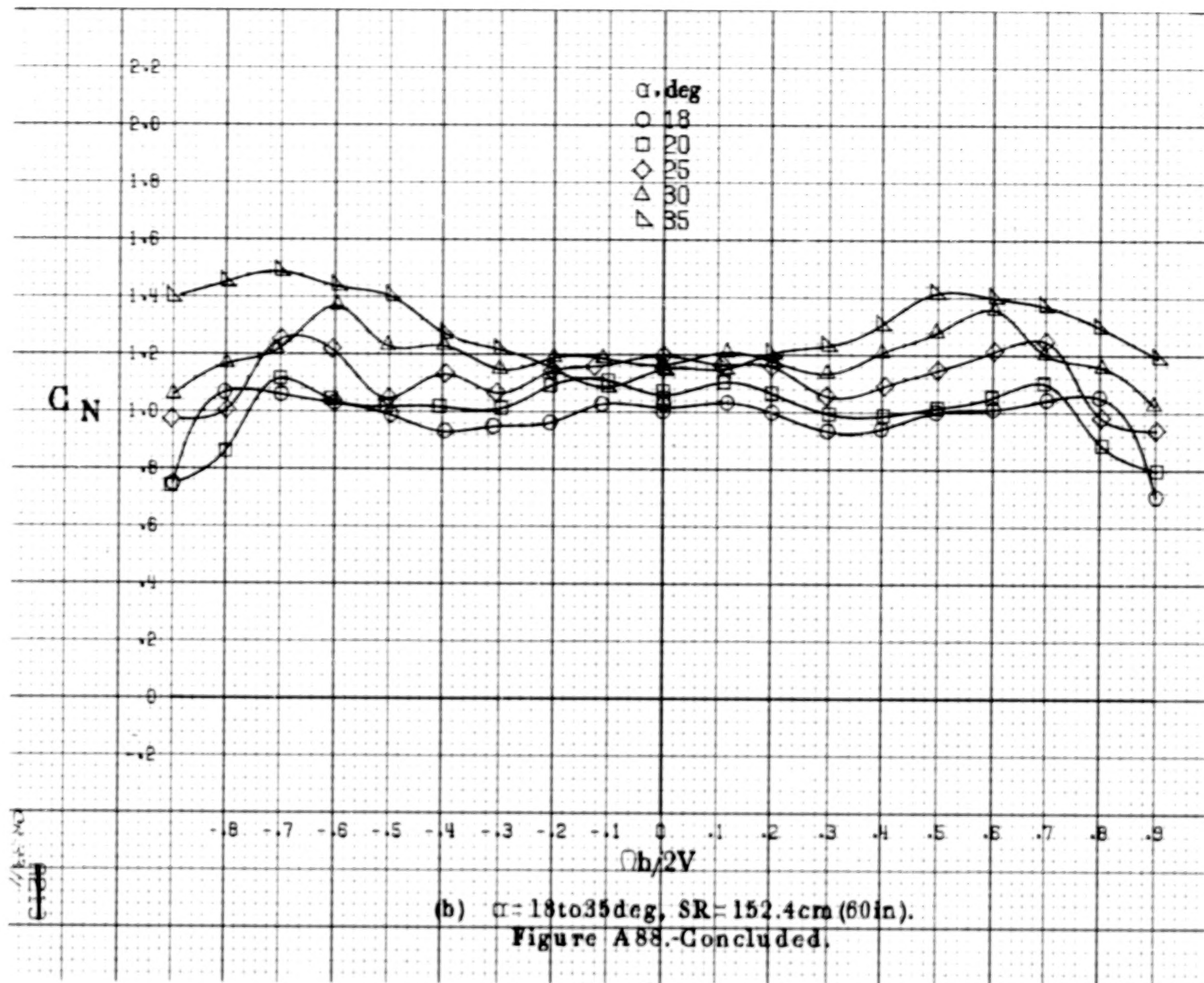


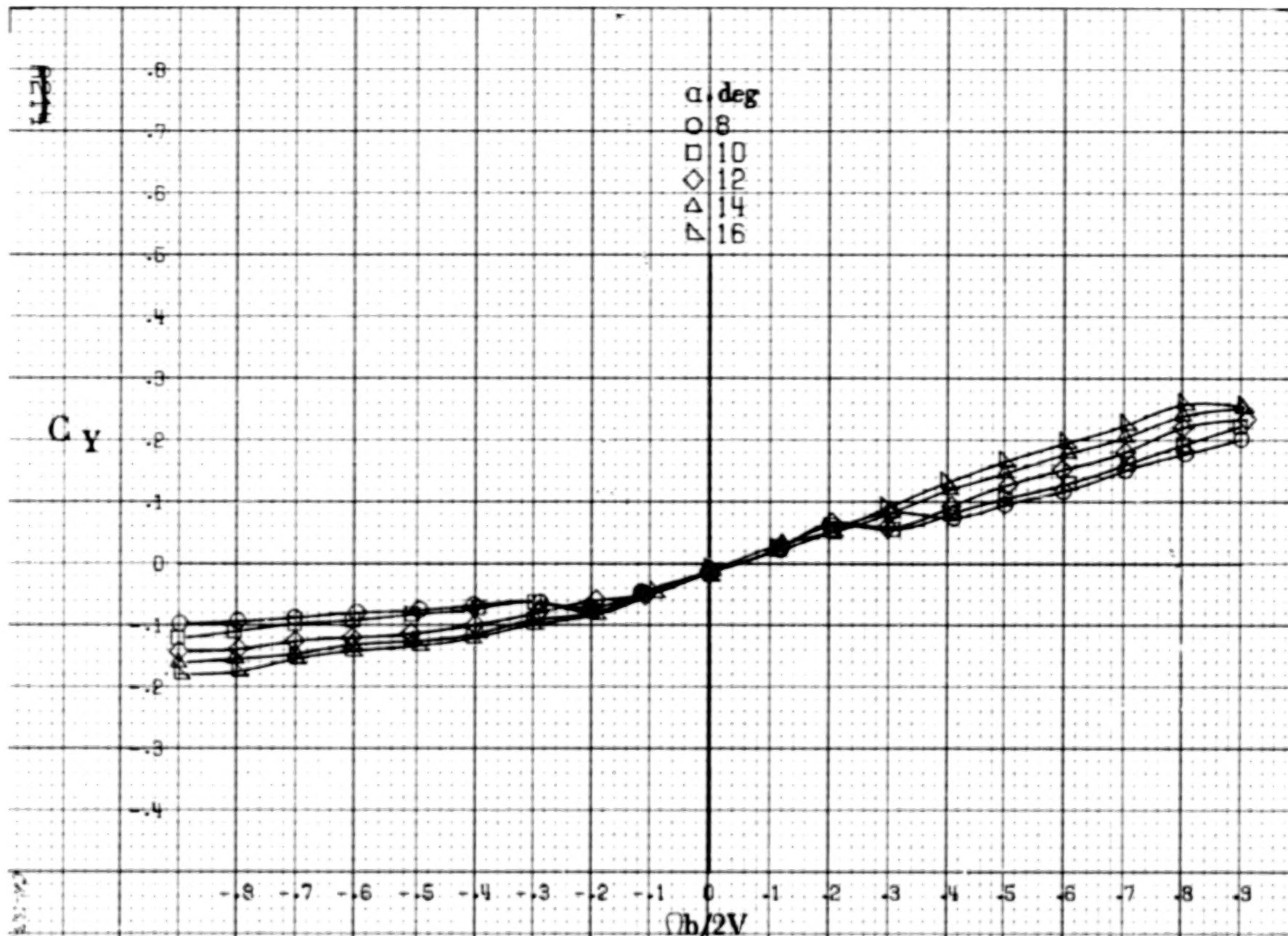


(a)  $\alpha = 8$  to  $16^\circ$ ,  $SR = 152.4 \text{ cm (60 in.)}$ .

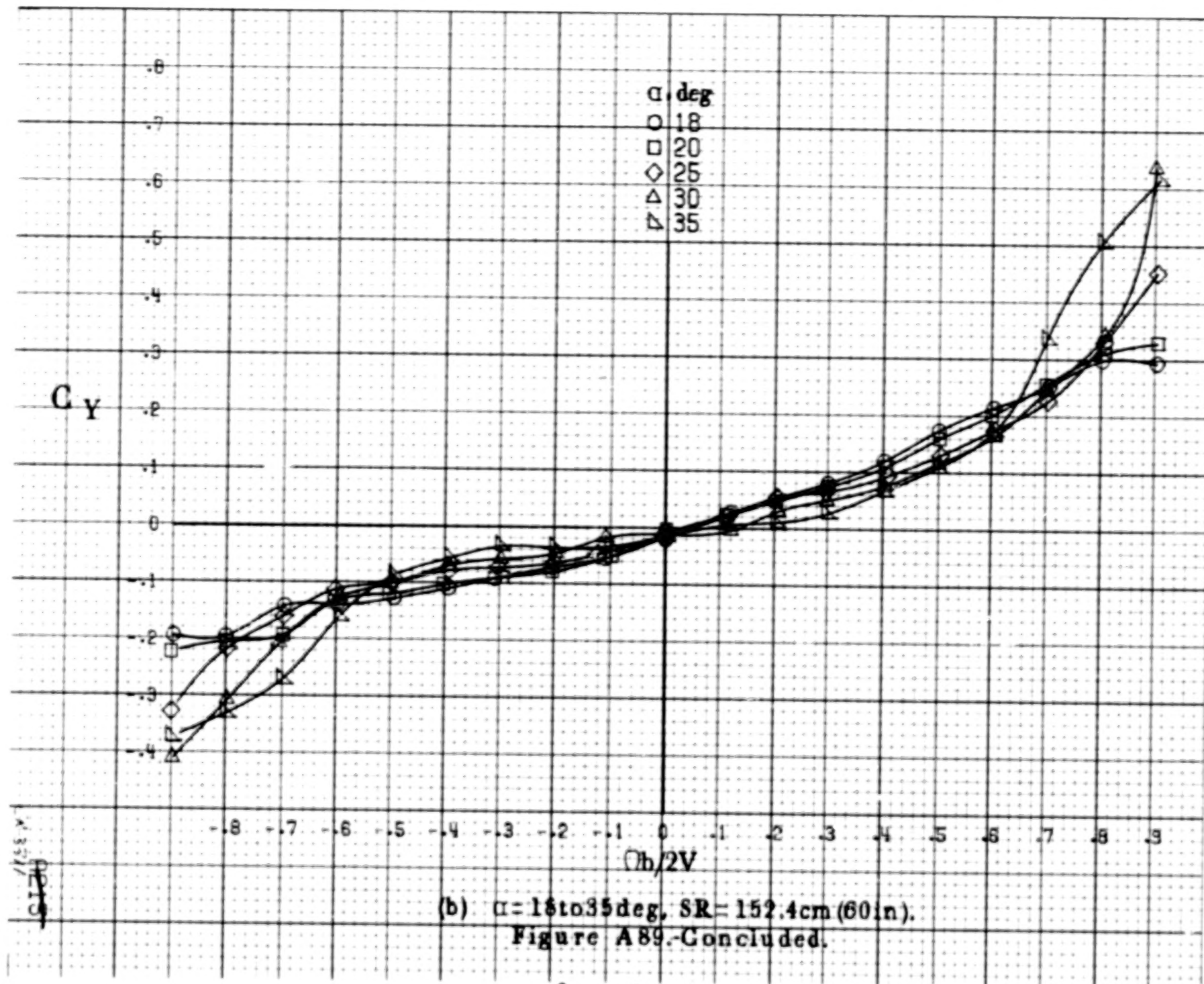
Figure A88.-Effect of rotation rate and angle of attack on normal-force coefficient for tip vortex diffusers configuration.  $\delta_e = 0^\circ$ ,  $\delta_s = 0^\circ$ ,  $\delta_r = 0^\circ$ ,  $\beta = 0^\circ$ .

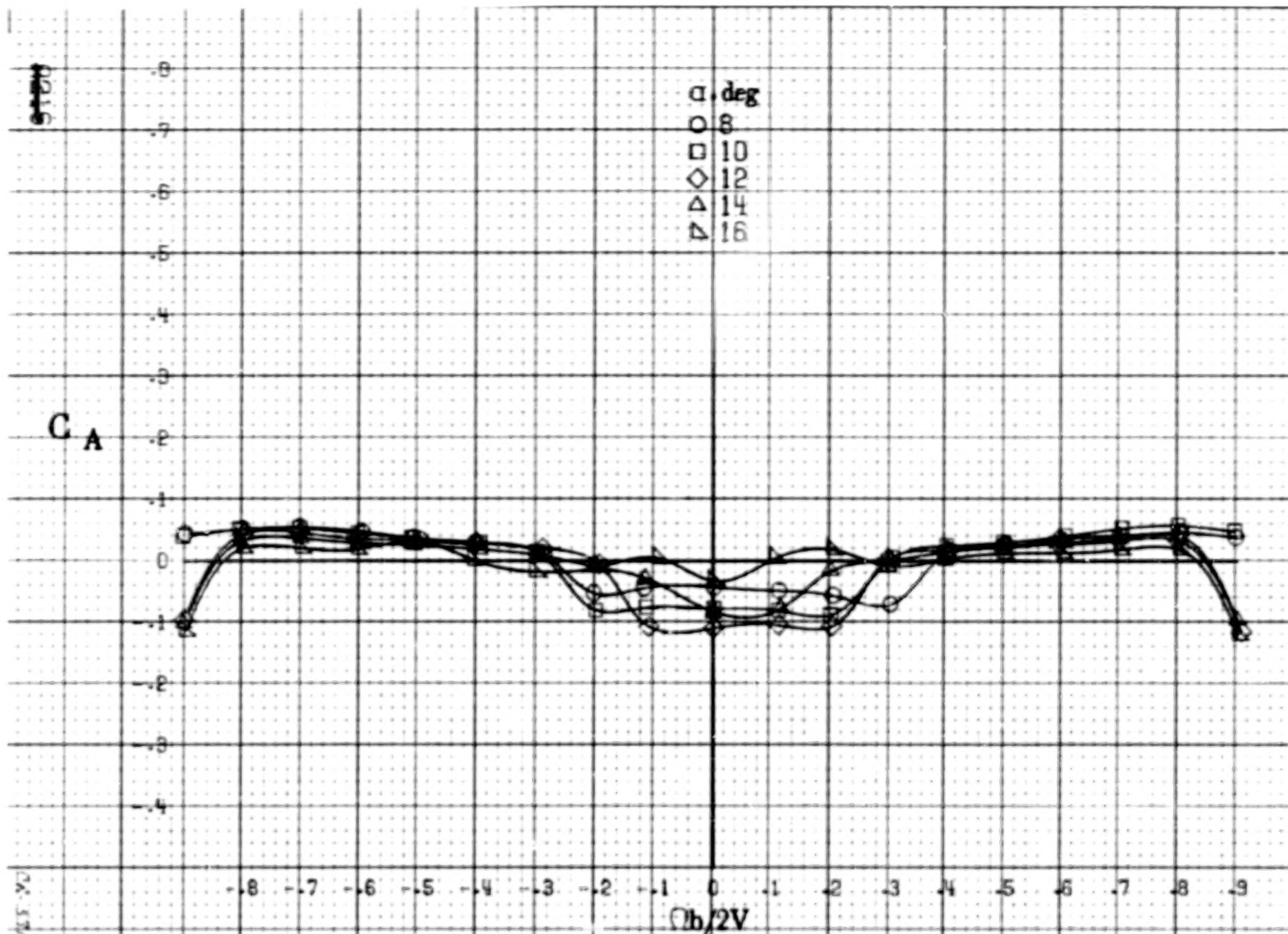






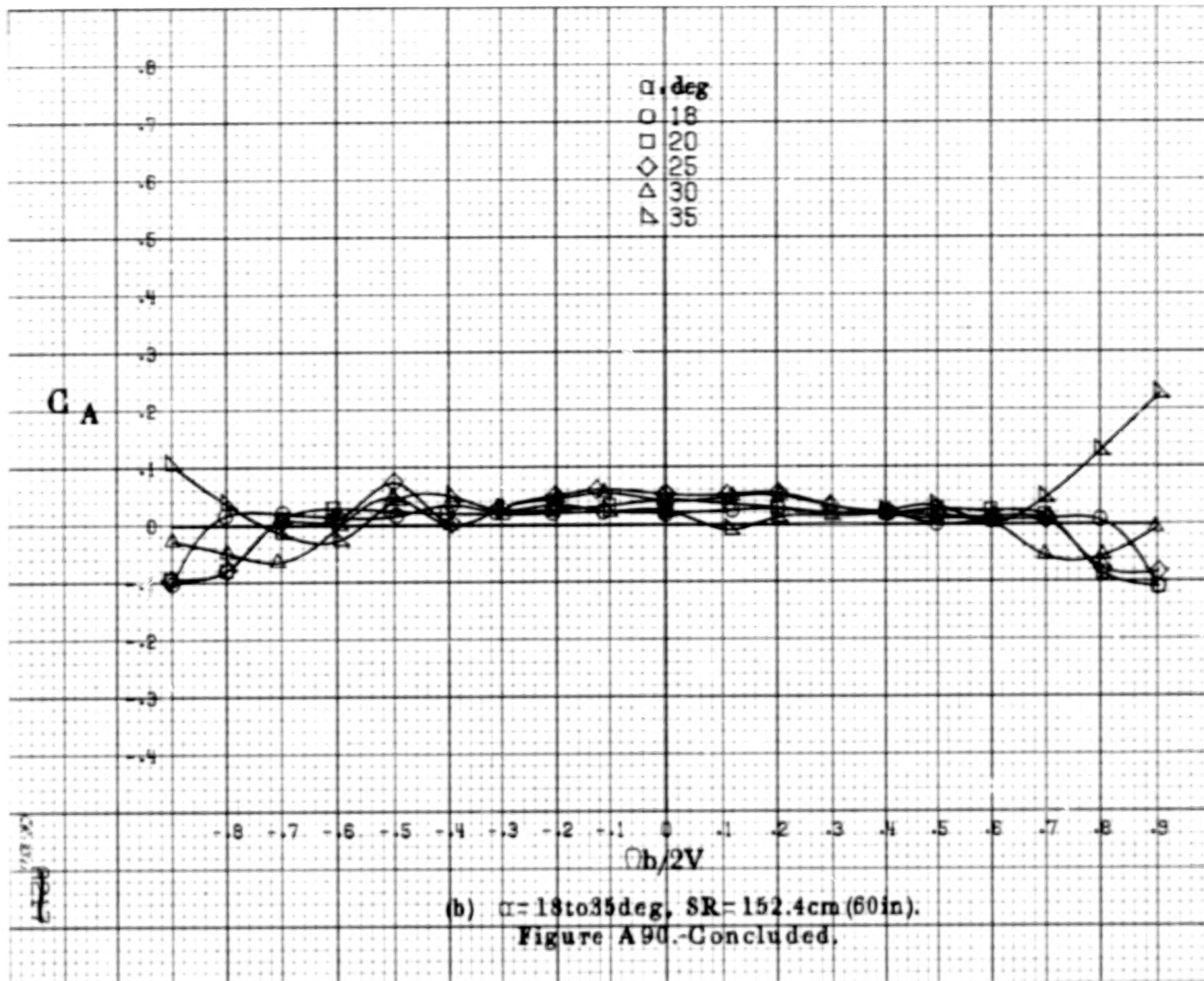
(a)  $\alpha=8$  to  $16^\circ$ ,  $SR=152.4\text{cm}(60\text{in})$ .  
 Figure A89.-Effect of rotation rate and angle of attack on side-force coefficient for tip vortex diffusers configuration.  $\delta_e=0^\circ$ ,  $\delta_a=0^\circ$ ,  $\delta_r=0^\circ$ ,  $\beta=0^\circ$ .





(a)  $\alpha = 8$  to  $16$  deg,  $SR = 152.4$  cm (60 in).  
 Figure A90.-Effect of rotation rate and angle of attack on axial-force coefficient for tip vortex diffusers configuration.  $\delta_e = 0^\circ$ ,  $\delta_s = 0^\circ$ ,  $\delta_r = 0^\circ$ ,  $\beta = 0^\circ$ .





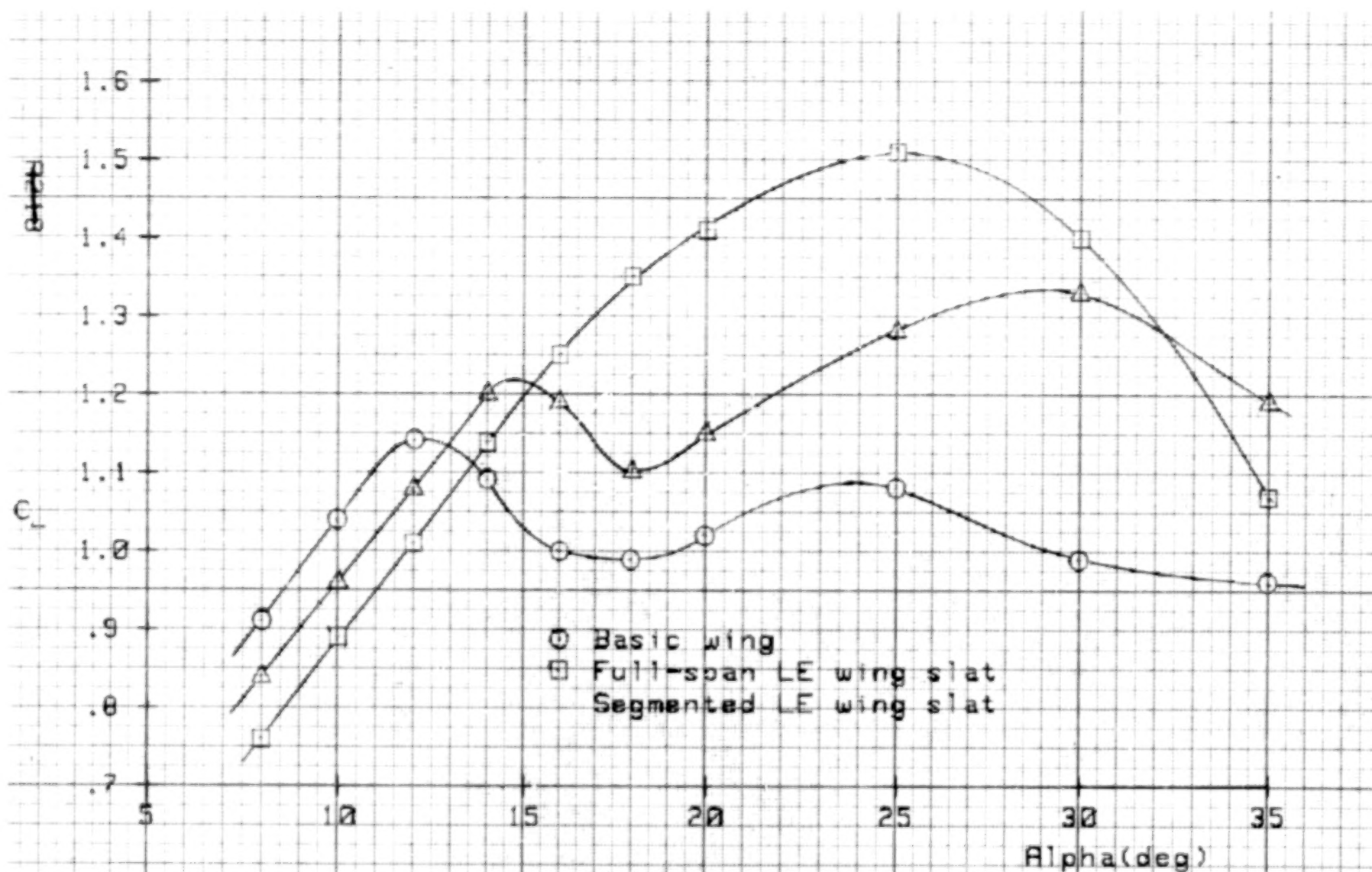


Figure A91.-Lift coefficient as a function of angle of attack for various wing LE devices.

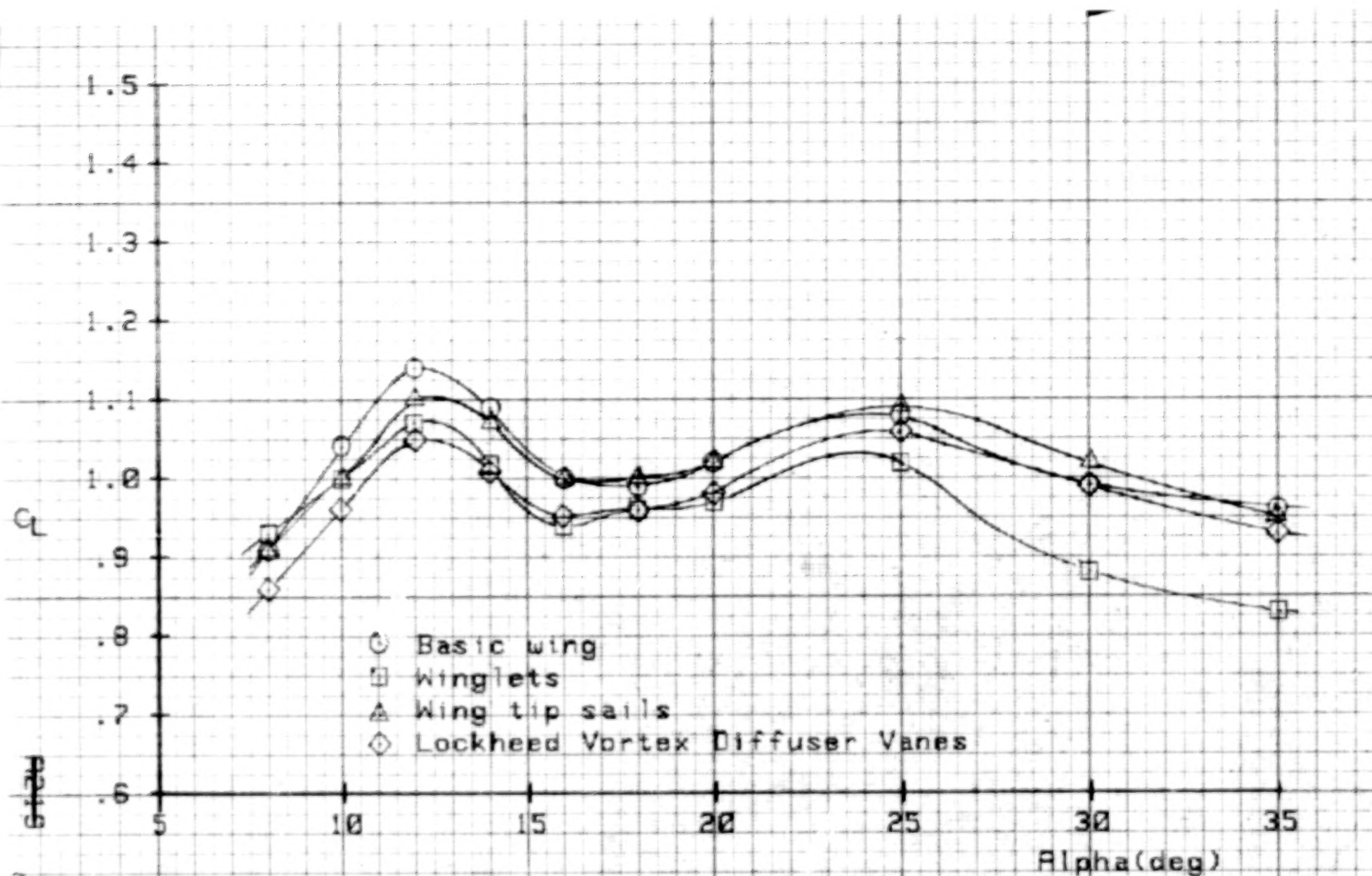


Figure A92.-Lift coefficient as a function of angle of attack for various wing tip devices.

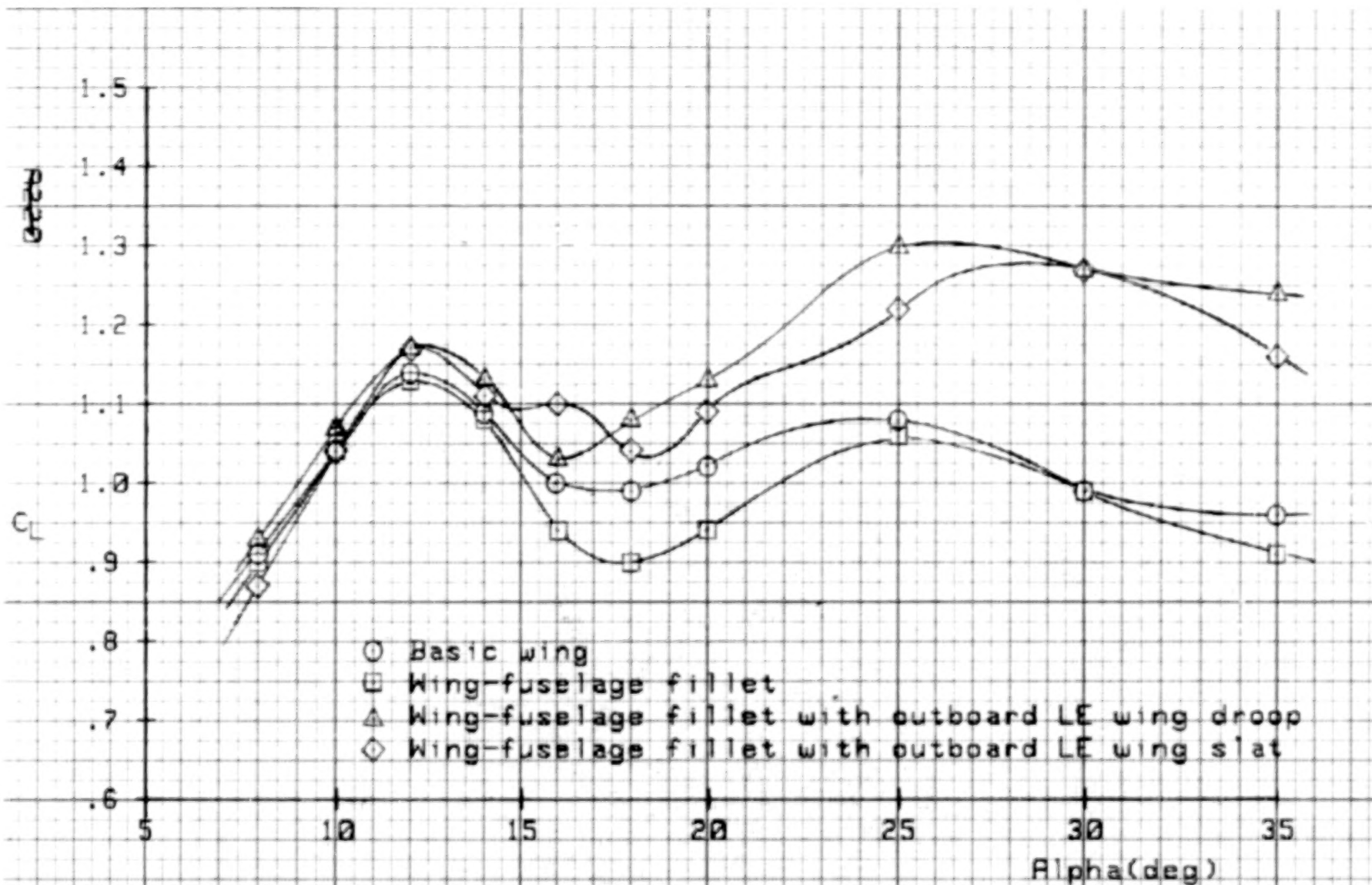


Figure A93.-Lift coefficient as a function of angle of attack for various wing LE devices.



1. Report No. NASA CR-3311		2. Government Accession No.		3. Recipient's Catalog No.	
4. Title and Subtitle Rotary Balance Data for a Single-Engine Agricultural Airplane Configuration for an Angle-of-Attack Range of 8° to 90°				5. Report Date December 1980	
				6. Performing Organization Code	
7. Author(s) William Mulcay Julio Chu				8. Performing Organization Report No.	
				10. Work Unit No.	
9. Performing Organization Name and Address Bihle Applied Research, Inc. 400 Jericho Turnpike Jericho, New York 11753				11. Contract or Grant No. NAS1-14849	
				13. Type of Report and Period Covered Contractor Report	
12. Sponsoring Agency Name and Address National Aeronautics and Space Administration Washington, DC 20546				14. Sponsoring Agency Code 505-10-13-06	
15. Supplementary Notes Langley Technical Monitor: James S. Bowman, Jr. Topical Report					
16. Abstract Aerodynamic characteristics obtained in a helical flow environment utilizing a rotary balance located in the Langley spin tunnel are presented in plotted form for a 1/10-scale single-engine agricultural airplane model. The configurations tested include the basic airplane, various wing leading edge and wing-tip devices, elevator, aileron, and rudder control settings, and other modifications. Data are presented without analysis for an angle-of-attack range of 8° to 90°, and clockwise and counter-clockwise rotations covering an $\frac{\Omega b}{2V}$ range from 0 to .9.					
17. Key Words (Suggested by Author(s)) General Aviation Spinning Rotary Balance High angle-of-attack wind tunnel data				18. Distribution Statement Unclassified - Unlimited  Subject Category 02	
19. Security Classif. (of this report) Unclassified	20. Security Classif. (of this page) Unclassified	21. No. of Pages 242	22. Price All		



**END**

*March 2, 1981*